The aerodynamic loading on an oscillating control

Warsop, Clyde

Award date:
1987

Awarding institution:
University of Bath

THE AERODYNAMIC LOADING ON AN OSCILLATING CONTROL

Submitted for the degree of PhD.
of the university of Bath

by

Clyde Warsop BSc. , May 1987

ProQuest LLC
789 East Eisenhower Parkway
P.O. Box 1346
Ann Arbor, MI 48106-1346

THE AERODYNAMIC LOADING ON AN OSCILLATING CONTROL

SUMMARY

The unsteady, incompressible flow about a fin of aspect ratio 1.5, having a 25% chord trailing edge flap, oscillating harmonically at small amplitude has been investigated.

Unsteady pressures have been measured on a wind tunnel model over a range of reduced frequency from 0 to 2.0 in order to determine the unsteady hinge moments.

The effects of Reynolds number and sealing of the control surface gap were examined.

The formation of vortices, associated with incidence and control surface deflection have been shown to have important effects for low aspect ratio control surfaces, greatly increasing hinge moments.

Comparisons with theoretical predictions obtained from a lifting surface model show reasonable agreement only for the case of zero incidence and mean control deflection.

Topics for further research into the vortex formations and boundary layer interaction with flow through the control surface gap have been identified.

COPYRIGHT

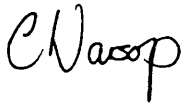

A C K N O W L E D G E M E N T S

I would like to thank Dr. J. F. Henderson for his guidance and the assistance he gave with discussion during all stages of this research.

Thanks are also due to Mr. T. J. Keston for nine months of his skill and patience while constructing the wind tunnel model and to Mr. J. Butt for his co-operation and assistance with preparation of the test facilities.

Finally, I would like to thank the Royal Aircraft Establishment at Farnborough for allowing me access to their theoretical model for the prediction of unsteady airloads on oscillating wings.

NOTATION

SYMBOL	DESCRIPTION
AR	Aspect ratio.
a_0	Local speed of sound.
b	Width of wind tunnel.
b_f	Spanwise dimension of control surface (= 0.4893c).
C	Coefficient to account for effects of flow across orifice of pressure tapping.
C_a	Cross-sectional area of wind tunnel working section.
$C_H = \frac{H}{\frac{1}{2}\rho V^2 c^2 b_f \delta_a}$	Unsteady hinge moment coefficient integrated over entire surface of flap.
$C_h = \frac{h}{\frac{1}{2}\rho V^2 c^2 \delta_a}$	Unsteady sectional hinge moment coefficient on control surface.
$C_{h_s} = \frac{h_s}{\frac{1}{2}\rho V^2 c^2}$	Steady sectional hinge moment coefficient on control surface.
$Cp = \frac{p-p_\infty}{\frac{1}{2}\rho V^2}$	Steady pressure coefficient.
$\Delta Cp = (Cp_l - Cp_u)$	Steady pressure loading.
Cp_l	Steady pressure coefficient on lower surface.
Cp_u	Steady pressure coefficient on upper surface.

SYMBOL	DESCRIPTION
$Cp^u = \frac{\Delta p}{\frac{1}{2}\rho V^2 \delta_a}$	Amplitude normalised unsteady pressure coefficient.
Cp_l^u	Amplitude normalised unsteady pressure coefficient on lower surface.
Cp_u^u	Amplitude normalised unsteady pressure coefficient on upper surface.
$\Delta Cp^u = (Cp_l^u - Cp_u^u)$	Unsteady pressure loading (amplitude normalised).
c	Chord of aerofoil (17.5").
cg	Centre of gravity.
d	Internal diameter of pressure tube element.
f	Frequency (Hz).
H	Height of wind tunnel working section.
H	Amplitude of unsteady hinge moment integrated over entire surface of flap.
h	Amplitude of unsteady sectional hinge moment.
h_s	Amplitude of steady section hinge moment.
$i = \sqrt{-1}$	Complex operator.
J_0, J_2	Bessel functions of the first kind of zero'th and second order.

SYMBOL	DESCRIPTION
j	Subscript defining the tube element counted from pressure tapping end.
k	Factor of the polytropic expansion of volume.
l	Length of pressure tube element.
M	Mach number.
N	Number of tube elements in a network.
np	Neutral point.
p_1	Oscillatory pressure amplitude at orifice of pressure tapping.
p_2	Oscillatory pressure amplitude measured by pressure transducer.
p_{at}	Atmospheric pressure.
p	Mean static pressure measured on surface of model.
p_∞	Freestream static pressure.
Δp	Amplitude of unsteady pressure.
p_s, p_0, p_j	Pressures used for calibration of frequency response of pressure tubing network.
Pr	Prandtl number.

SYMBOL	DESCRIPTION
$Re = \frac{Vc}{\nu}$	Reynolds number based on chord.
r	Radius of pressure tube element.
S	Planform area of fin.
S_{qa}	Charge per unit acceleration of accelerometer output.
S_{va}	Voltage per unit of acceleration of accelerometer output.
s	Semi-span of model fin (13.125").
T	Absolute temperature.
t	time.
t^{n}	Local thickness of aerofoil section.
u	Axial flow velocity of air inside pressure tube.
V_t	Internal volume of pressure transducer.
ΔV_t	Change in pressure transducer volume due to diaphragm deflection.
V	Freestream velocity in wind tunnel.
V^c	Cross-flow velocity of flow over pressure tapping.
v	Radial velocity of air inside pressure tube.

SYMBOL	DESCRIPTION
$X = x/c$	Non-dimensional chordwise distance measured from leading edge.
x	Chordwise distance measured from leading edge of aerofoil.
$Y = t/c$	Non-dimensional thickness of aerofoil.
y	Spanwise distance along fin measured from fin root.
α	Incidence of fin.
γ	Ratio of specific heats (= 1.4 for air).
δ	Steady control surface deflection.
δ_a	Amplitude of oscillatory control surface deflections ($\frac{1}{2}$ peak to peak value).
δ_m	Mean control surface deflection about which oscillation occurs.
$\eta = \frac{y}{c}$	Local co-ordinate (spanwise) used in theoretical modelling of fin.
μ	Absolute viscosity of air.
$\nu = \frac{\mu}{\rho}$	Kinematic viscosity of air.
$\xi = \frac{x}{c}$	Local co-ordinate (chordwise) used in theoretical modelling of fin.

SYMBOL	DESCRIPTION
ρ	Density of air.
ρ_s	Static density of air.
$\sigma = \frac{\Delta V_t}{V_t}$	Non-dimensional increase in volume of pressure transducer due to diaphragm deflection.
$\omega = 2\pi f$	Circular frequency.
$\omega^* = \frac{\omega c}{2V}$	Reduced frequency.

C O N T E N T S

C O N T E N T S

C O N T E N T S

1. INTRODUCTION

1.1 Background

The research described in this thesis initiated from discussions with the Admiralty Research Establishment (A.R.E.), Dorset.

Recent requirements for improving the performance of underwater vehicles have demanded the application of state-of-the-art technologies. One particular example is the torpedo (Fig. 1.1) where the need to increase its operating speed has resulted in the requirement for more powerful and therefore heavier propulsion systems. Fundamental design constraints dictate that the motors have to be located at the rear of the vehicle. This moves the centre of gravity (cg) of the torpedo to well behind its neutral point (np). In order that the instability caused by the relative position of the cg and np can be overcome it has been proposed that 'active controls' be fitted. With such a system the hydrodynamic control surfaces are deflected by commands from an onboard computer to correct for divergences from the demanded course. Onboard sensors in the form of accelerometers and gyroscopes provide the information from which the computer evaluates the required correction. With an unstable vehicle the corrections are required to be made at frequencies of up to 20 Hz in order that uncontrollable divergences do not occur. This results in continuous, small but rapid movements of the control surfaces.

In order that the control system has a stable frequency response it is necessary to know the characteristics of the load being

driven by the control surface actuators. This load comprises two components:

a). The inertia of the control surface itself.

b). The unsteady hydrodynamic pressure loads acting on the control surface.

These loads manifest themselves in the form of control surface hinge moments.

The hydrodynamic loads caused by either a rapidly deflected or oscillating control surface are generally much larger in amplitude than those generated by a steady state deflection. They also exhibit a phase lag relative to the displacement of the control surface. The relatively high density of the operating medium (sea water) means that the unsteady hydrodynamic loads on the control surface equal or exceed those due to the inertia of the control surface itself. The unsteady hydrodynamic forces are therefore significant in the analysis of the overall response of the active control system.

Fundamental hydrodynamic theory[1] reveals that the unsteady forces acting on an accelerating, lifting body are the result of two effects:-

1). The change in circulation around the body.

2). The acceleration of the entire flow field around the body (known as the 'added' or 'virtual' inertia).

These effects have been investigated both theoretically and experimentally by many researchers as a result of the increased importance of aeroelastic and active control technology in the design of modern aircraft (see Chapter 2). Theoretical models are now available for predicting with reasonable accuracy the unsteady forces acting on entire wings oscillating in pitch or heave for a wide range of flow cases (subsonic, transonic and supersonic). However, the modelling of wings and fins having an oscillating trailing edge control surface is not so advanced. This is due to the complexity of the geometry and to the flow interactions that occur with such configurations (Chapter 2).

For this reason the A.R.E. suggested that research should be undertaken to investigate the nature of flows acting on configurations with oscillating control surfaces. Of particular interest were the effects of very low aspect ratio (typically found on underwater vehicles) and the determination of unsteady control surface hinge moments. The latter being of importance in the problem of analysing the response of active control systems discussed earlier.

1.2 The Proposed Study

a). To review past and current developments (theoretical and experimental) in the field of unsteady aero/hydrodynamics to provide background on which to base further investigations (see Chapter 2).

b). To conduct an investigation (based on the findings of a. above) to determine the nature of the unsteady forces acting on a low aspect ratio fin with oscillating trailing edge control surface. The investigation was to be both theoretical and experimental with the main aim of examining the effects of the following parameters:-

1). Sealed and unsealed gap between fin and control surface.

2). Fin incidence.

3). Non-zero mean control surface deflection.

4). Vortex formations.

For simplicity, a configuration of fin and control surface typical of that found on many torpedoes was chosen for investigation.

ie.

Rectangular fin of aspect ratio	= 1.5
Thickness/chord ratio	= 12%
Control surface chord/fin chord ratio	= 25%
Typical operating speed in sea water	= 10 - 30 m/s
Small amplitude control surface oscillations	= 1° - 2°
Maximum frequency of control surface oscillation	= 20 Hz
Maximum fin incidence	= 6°

Sufficient depth of water to avoid cavitation was assumed.

The investigation was further simplified by assuming that the unsteady motion of the control surface was sinusoidal and of fixed amplitude. In reality, the motion of an actively controlled control surface would be irregular. Fortunately the use of Fourier analysis enables a random function to be constructed from a summation of sinusoids of varying frequency and amplitude.

1.3 Outline Of Thesis

Chapter 2

A review of past developments in the field of unsteady aero/hydrodynamics is presented. Areas where current knowledge is limited are highlighted with particular reference to the special features of low aspect ratio and oscillating control surfaces. The chapter concludes with a detailed definition of the research programme described in the following chapters.

Chapters 3 and 4

Description of experimental facilities and techniques established to examine the unsteady forces (by measurement of pressure distributions) acting on a low aspect ratio fin with oscillating control surface.

Chapter 5

Description of theoretical model based on a lifting surface technique which was used to produce results for comparison with experimental data.

Chapter 6

Presentation and discussion of experimental and theoretical results.

Chapter 7

Conclusions.

Chapter 8

Recomendations for future work.

2. REVIEW OF CURRENT DEVELOPMENTS IN UNSTEADY AERO/HYDRODYNAMICS AND OUTLINE OF PRESENT INVESTIGATION

2.1 Introduction

This chapter summarizes current techniques for predicting unsteady aero/hydrodynamic forces acting on oscillating lifting surfaces and bodies. Areas where further investigation is required are highlighted, especially those particular to the case of a very low aspect ratio fin with an oscillating control surface. The chapter concludes with an outline of the reasons for the approach taken in the present investigation.

In general, when an aerofoil or control surface describes an oscillatory motion, the acceleration of the fluid accompanied by the continuously changing bound vortex strength gives rise to oscillatory forces. The nature of these forces is in general terms dependent on the geometry of the configuration, the frequency of oscillation and the freestream velocity of the fluid. It is usual in unsteady aerodynamics to define the non-dimensional quantity known as the reduced frequency, where:-

$$\text{reduced frequency} \qquad \omega^{*} = \frac{\omega c}{2V}$$

(omega) ω = circular frequency of oscillation

c = chord length of aerofoil

V = freestream velocity

This enables non-dimensional comparisons to be undertaken.

2.2 Theoretical Methods

The development of theoretical techniques for predicting the behaviour of fluid flows over oscillating configurations has been rapid during the past fifteen years. Powerful methods have been developed on the basis of the 'potential theory' for attached steady and unsteady flows. For certain cases these methods yield reasonable results for both incompressible and compressible flows. These methods can be divided into two main classes:-

1). Conformal mapping methods

2). Singularity methods

The conformal mapping technique was worked out by Theodorsen[2] in 1935 to give a comprehensive theory for both steady and unsteady two-dimensional flows. However, singularity methods have become much more important since they can be readily adapted to the three-dimensional case. Due to the linearity of the subsonic potential equation the principle of superposition of solutions can be applied so that basic solutions of the equations using sources, vortices and doublets may be combined in an arbitrary way to find the required flow field. There are three main classes into which the singularity methods can be divided:-

1). Loading function methods[3,4,5]

2). Doublet/vortex lattice methods[6,7]

3). Velocity or acceleration potential panel methods[8,9,10,11]

2.2.1 Loading function methods

The loading function method, also known as the lifting surface or kernel function method, is a thin wing theory. The problem to be solved is formulated as an integral equation for the downwash of the wing. This equation is solved by introducing loading functions of unknown scale factors in both chordwise and spanwise directions to approximate the loading of the wing (Fig. 2.1). The choice of loading functions must be consistent with the singular behaviour of the wing at leading and trailing edges, the wing tip and at unsealed gaps around control surfaces[12]. After introduction of these loading functions the integral equation is reduced to a system of linear equations where the scale factors of the loading functions have to be evaluated. This is performed after introducing a number of control points on the wing where flow tangency has to be satisfied.

2.2.2 Vortex/doublet lattice method

The basis of this method is again the downwash equation of lifting surface theory and the idea of the method is to discretise the load of the wing into small elements. The wing has to be subdivided into a large number of small trapezoidal panels arranged in strips

parallel to the freestream and with aerofoil leading edge, trailing edge and hinge line coinciding with edges of the panels (Fig. 2.2). The lift of each panel is then assumed to be concentrated on the quarter chord line of each panel with trailing vortices at the tips. This horseshoe vortex whose strength has to be determined represents the steady effect on the panel. By placing a line of doublets on the quarter chord line of each panel the oscillatory effect can be accounted for. The downwash boundary condition is then satisfied at a pivot point located at the three quarter chord point along the centreline of each panel. The basic integral equation is thus reduced to a set of linear equations, which has to be solved for an unknown load.

The validity of this technique is questionable since the selection of the $\frac{1}{4}$ and $\frac{3}{4}$ chord positions on each panel, chosen for locating the singularities and satisfying the downwash boundary condition, are almost arbitrary. Justification for the method is based purely on the fact that in certain instances it gives the right answers. The use of the doublet lattice method for configurations with control surfaces where gaps are present is highly questionable[5] since it appears unable to impose the correct pressure singularities along the many boundaries of the wing.

2.2.3 Panel methods

The most recent and comprehensive approach to subsonic lifting bodies is the panel method. The basic idea of this technique is

similar to the vortex-lattice method. The surface of the body is subdivided into a large number of trapezoidal panels. Solution of the governing equation is conducted by arranging a distribution of basic singularities on body and wake surface (Fig 2.3). The effect of the discrete singularity distributions on each panel produces disturbance velocities at other points on the surface. At these 'pivot' points (each panel has one at its centre) the velocities are evaluated as an integral employing Greens theorem[11]. This integral expresses the induced velocity at a body pivot point in terms of the unknown body geometry and the unknown perturbation singularity strengths. The version most widely used in practice for steady flows has source and vortex singularities on the surface to represent the effects of thickness and circulation respectively. Unsteady effects are treated by placing doublets on the mean surface or on the body surface itself.

2.2.4 Comparison of existing theoretical methods

The loading function method has the disadvantage when compared with either the doublet-lattice or panel method in that it is necessary to know the exact form of the pressure singularities before computation can commence. This can lead to difficulties where complex geometries are involved, but once these are overcome, convergence of the solution is rapid. Lottati and Nissim[12] have developed a technique for employing the loading function method on complex geometries which include cranked leading edges and oscillating control surfaces on both leading and trailing edges. However, no comparisons with experimental data are presented.

The inability of the doublet-lattice method to apply the correct singularities on complex geometries has been mentioned in Chapter 2.2.3 . The method is therefore not considered suitable for examining forces acting on oscillating control surfaces.

The panel method has the advantage over the loading function method in that prior knowledge of the singularities is not required (they are obtained as a result of the computation). Also, the panel method can be used to simulate the effects of wing thickness. However, convergence of the solution with respect to the number of panels used must be considered if reliable answers are to be obtained. Work by Rowe and Cunningham[13] suggests a method whereby computing resources are minimised by extrapolating between the force results of two slightly different, not-so-fine panellings rather than using a single model with a fine mesh of panels.

2.3 Past Experimental Work And Comparison With Theory

2.3.1 General

The role of experiments in the field of unsteady aerodynamics is very important for:-

a). Providing data to be used directly in design.

b). Providing data for comparison with theoretical calculations for validation purposes.

c). Exploring unsteady flow phenomena.

Techniques have been developed to measure unsteady quantities such as force and pressure[14,15] and to investigate the unsteadiness within boundary layers[16]. More recently the advent of the laser-doppler anemometer has made it possible to conduct non-intrusive investigations of flow phenomena in wakes and vortices[17].

A large quantity of experimental data exists for oscillating two-dimensional aerofoils and three-dimensional wings without control surfaces. Much less data is available for wings with oscillating control surfaces, especially for configurations of very low aspect ratio. Areas of current experimental interest include transonic and separated flows, and configurations with control surfaces acting as part of active control systems[18,19].

The potential flow models (see Chapter 2.2) can be used to predict the unsteady airloads on wings (where the entire surface is oscillating) to a reasonable degree of accuracy. However, it has long been recognised that these methods are inadequate when predicting the loads on an oscillating trailing edge control surface[20,21,22,23]. One response to this has been the suggestion of introducing into the theory such effects as boundary layers and local variations of flow properties due to aerofoil thickness and control surface geometry. From the limited experimental studies already conducted it is known that these effects, which are neglected within the framework of linearised potential theory, are highly influential in the development of

unsteady airloads on oscillating controls.

2.3.2 Effect of finite thickness and incidence

It is known from theoretical investigations that the development of unsteady flow on oscillating aerofoils may be changed remarkably by thickness effects[24]. Geissler[22] also shows that the fixed incidence of the aerofoil and the steady mean deflection about which the control surface oscillates are also of importance. However, these effects are strongly coupled to the geometry of the control surface gap. The most important practical consequences of the incidence and geometry effects with regard to trailing edge controls are manifested in the control surface hinge moments. Linearised 'flat plate' theory has been found to yield rather unrealistic results for configurations with oscillating control surfaces and attention has turned to the development of panel methods in order that thickness and control surface geometry may be modelled[25]. Developments in these areas are in their early stages and much more investigation is required.

2.3.3 Effect of flow viscosity

It has often been argued that thickness effects are roughly compensated for by boundary layer effects[20]. This explains the good agreement frequently found when comparing experimental aerodynamic results with theoretical ones which neglect wing thickness and fluid viscosity. To what extent this argument is true is not clear since no results are available from wind tunnel

measurements over a wide range of Reynolds number. Förching[20] indicates that there is some evidence that the boundary layer or Reynolds number effects are of minor importance in treating unsteady aerodynamic problems of oscillating wings without controls, at least in subsonic flow at low incidence. However, from the few test results obtained for oscillating trailing edge control surfaces at various Reynolds numbers[26] it is known that hinge moments are decisively dependent upon Reynolds number. Test results show deviations from potential theory of up to 100%, even for the case of zero mean angle of attack. It is difficult to say to what extent these discrepancies may be attributed to flow viscosity effects since it must be kept in mind that the effects of gap geometry and incidence are at least of the same order of magnitude (see Chapter 2.3.2). However, it must be assumed that an interaction takes place between the boundary layer and the very complicated flow processes at the flap leading edge for open gap geometries especially when the wing-flap system is operating at non zero incidence.

2.3.3.1 methods for including the effects of thickness and viscosity in theoretical models

If linearised potential flow methods are to be used to calculate the unsteady airloads on oscillating wing and control systems the effects of thickness, and to some extent, gap geometry can be accounted for by using a panel method. The effects of viscosity can be represented by the displacement thickness of the boundary

layer. The following iterative method for calculating pressure distributions is possible in principle:-

1). Calculate pressure distributions over the original or thickened profile.

2). Calculate the boundary layer displacement thickness produced by the previously calculated pressure distribution.

3). Add the boundary layer displacement thickness to the profile and return to stage one.

For the two-dimensional case, approaches on this basis have been used[25,27]. The three-dimensional application of this approach is still in the development stage since general three-dimensional boundary layer methods with accurate prediction of transition and separation are not yet available. Attempts at the three-dimensional cases using two-dimensional boundary layer codes have been used with some degree of success for oscillating wings[10]. It appears that even the inclusion of two-dimensional boundary layer theories is in its infancy with very few practical attempts being made to include them in prediction procedures. Geissler[22] and Houwink[21] present results where a steady boundary layer thickness has been calculated from the real part of the pressure distribution, which combined with a potential flow method resulted in good agreement between theory and experiment for an oscillating wing. Only small influences of boundary layer displacement were found in the imaginary parts of the pressure distribution.

According to Telionis[16] unsteady laminar flows are well understood and experiment and theory show good agreement. However, oscillating turbulent flows are more common in engineering applications and at present the understanding of such flows is limited[16,27,28,29].

2.3.4 Modelling of the Kutta-Joukowski condition for unsteady flow calculations

One of the basic assumptions of aerofoil theory deals with the presence of the Kutta-Joukowski condition at the trailing edge. While the existence of this condition is well established for steady, non-separated flow situations, its validity for time-dependent cases is controversial especially for values of reduced frequency above 0.5. The Kutta condition is applied automatically in most numerical studies of unsteady wing theory but the conclusions of experimentalists seem to differ[30,31,32,33,34]. These evaluations have been based mainly on examinations of pressure distributions, a method which offers minimal insight into the actual behaviour of the flow in the region of the trailing edge. The conclusions of these researchers should therefore be treated with caution.

The classical Kutta condition for sharp-edged aerofoils requires that the stagnation streamline at the aft end of the aerofoil is attached to the trailing edge. This condition is sufficient to render the solution unique and it can be proved that, for steady flow at least, a number of other conditions are met at the trailing

edge:-

1). The pressure is continuous ie. the loading tends to zero.

2). The velocity is finite or zero.

3). The shedding of vorticity vanishes.

4). The stagnation streamline bisects the wedge angle of the aerofoil trailing edge.

In unsteady flow the situation changes markedly. If there is no separation upstream of the trailing edge, then the rear stagnation point again coincides with the trailing edge. However, any changes in bound vorticity require shedding of equal and opposite vorticity. Condition 3 above is therefore violated. In this case an extension to the Kutta condition for unsteady flow has been suggested by Giesing[35] and Maskell[36]. Essentially they proposed that for a changing bound circulation the stagnation streamline is an extension of the aerofoil at the sharp trailing edge. The arguments for this hypothesis are a natural extension of the steady flow theory and are mathematically consistent. However, there is a flaw in the argument because the unsteady solution does not tend asymptotically to the steady solution. For any time rate of change in the bound circulation, no matter how small, the trailing edge streamline oscillates to remain tangential to the upper and lower trailing edge surface. Nevertheless, recent experimental evidence by Poling and Telionis[37] using laser-doppler anemometry techniques supports the Giesing-Maskell model.

2.4 Conclusions

From the survey of current developments in unsteady aerodynamics the following conclusions were drawn:-

1). It is difficult to accurately predict the unsteady hinge moments acting on oscillating control surfaces, especially where unsealed gaps exist between the wing and the control surface. The discrepancies between experiment and theory can be as much as 100% for both two and three-dimensional cases. The main reasons for the bad correlation between theory and experiment are given as being the neglect of thickness, gap geometry and the effects of viscosity in the theoretical models. In some cases it has been found that the theoretical models fail to impose the correct pressure singularities at important boundaries of complex geometries.

2). Early theoretical models were based on thin-wing approximations but recent developments have seen the introduction of panel methods which allow the effects of thickness and control surface gap geometry to be modelled.

3). Little previous experimental or theoretical work has been conducted to examine the unsteady flows around very low aspect ratio, untapered wings with oscillating control surfaces. Aspect ratios of previous experiments range from about 4.0 upwards and those at the lower end of the range are usually highly tapered with rounded wing tips.

4). In the limited number of experimental cases where hinge moments have been measured on three-dimensional configurations it has been achieved by direct measurement. No work has been found which attempts to measure comprehensively the unsteady pressure distributions over an entire oscillating control surface. Usual practice has been to measure pressure data at two or three spanwise stations to obtain a general idea of the nature of the unsteady flow field.

5). Although some investigations have been conducted to examine the effects of wing-tip vortices on the unsteady flow near the tip of an oscillating wing[22], the influence of vortices on flows over oscillating control surfaces remains unexamined. These vortex flows become increasingly important as aspect ratio is reduced since a greater extent of the flow becomes affected.

2.5 Outline Of Proposed Study

2.5.1 General

An experimental programme of research was planned as a result of discussions with the A.R.E. and following the evaluation of the current state of the art in unsteady aero/hydrodynamics. This would provide design information for A.R.E. while also allowing an opportunity for the investigation of the unsteady flow phenomena peculiar to the low aspect ratio configuration. The main aim was to measure the unsteady control surface hinge moments acting over a wide range of reduced frequency ($\omega^* = 0 \rightarrow 2.0$) by integration of

unsteady pressure distributions. It was also proposed that the effects of incidence and mean control surface deflection should be examined since initial investigations indicated that, as well as gap geometry, the influence of the fin tip vortices could considerably influence the flow field over the control surface. Theoretical predictions for comparison with experimental data were to be obtained from a lifting surface model provided by the Royal Aircraft Establishment. It was hoped that the investigations would enable suggestions to be formulated for the improvement of theoretical models.

2.5.2 Selection of test facilities

A governing factor behind the selection of the form in which the research was undertaken was that of cost. The small budget available for expenditure on capital equipment (less than £1000) dictated that maximum use had to be made of the facilities and equipment owned by the University of Bath.

Initially, the possibility of using one of the following test facilities was considered:-

1). The University 7 ft x 5 ft wind tunnel.

2). The University towing tank (water).

3). Construction of a water tunnel.

Water was considered as a test medium since the magnitude of the

fluid forces in comparison to the structural inertia forces would be far greater. This would allow direct measurement of the control surface hinge moments without requiring large corrections to be made. Tests in water would also allow full scale Reynolds numbers and reduced frequencies to be obtained at small scale with moderate flow velocities and excitation frequencies. However, the use of water test facilities was ruled out due to the unsuitability of the towing tank and the absence of funds for the construction of a water tunnel. The towing tank was considered unsuitable because of its low maximum speed (< 6 kt) and the complexity of the instrumentation required. Furthermore, it was felt desirable to be able to measure pressure distributions on the model (see Chapter 2.5.4), which introduced further difficulties if this was to be achieved at small scale in water.

As the University had good aerodynamic testing facilities in the form of the 7ft x 5ft wind tunnel, investigations were conducted to assess the feasibility of its use in this study. The advantages of testing in air as opposed to water were fourfold:-

1). The facilities were readily available and their moderate utilisation offered flexibility in the planning of time tables and developing techniques during the test programme.

2). The use of air as the working fluid provided a better environment for both the model and the instrumentation.

3). A large model was possible enabling a higher resolution of the flow to be achieved together with a lower sensitivity to manufacturing tolerances.

4). Although the use of air resulted in the magnitude of the unsteady aerodynamic forces being very small, it appeared that it was possible to measure both unsteady pressures and direct forces to a high degree of accuracy[14,15].

For the reasons above it was concluded that the 7ft x 5ft wind tunnel would be suitable for use in this investigation. The next task was to determine the overall configuration of the model and decide on what flow parameters to measure.

2.5.3 Model configuration

In reality the flow over the fin of the torpedo is complicated by the propulsor (typically a contrarotating propeller) and the shape of the torpedo afterbody. In order that these effects should not mask the analysis of the unsteady forces on the control surfaces it was decided that initial tests would be conducted on a 'fin only' configuration. The effects of the rest of the torpedo geometry could be investigated later, once the basic unsteady flow field around the low aspect ratio fin had been determined.

It became clear during initial investigations that a half-model mounted on a reflection plate would be more appropriate than a full span model. The two main advantages of a half-model are the

higher Reynolds number obtainable (due to the larger model size possible) and the ability to have direct access to the root of the model. This latter was the most important since a means whereby the control surface could be oscillated was required. An actuating device small enough to fit inside the model and provide sufficient power could not be found so it was necessary to mount the actuator outside the model. The location of the actuating system had to be such that minimal aerodynamic interference was caused while still maintainting the mass and stiffness of the linkage to within reasonable limits.

A major disadvantage of the half-model was the presence of the boundary layer on the reflection plane. For tests on high aspect ratio wings (and some of low aspect ratio[14,26]) many researchers have mounted the model using the tunnel wall as the reflection plane. This method is acceptable where the regions of interest are well away from the root of the model but for the case of low aspect ratio the tunnel wall boundary layer can extend over a substantial portion of the span. In order to minimise the effects of the reflection plane boundary layer it was chosen to mount the model well away from the tunnel wall and provide a separate reflection plate (Fig. 2.4). This reflection plate extended only a short distance ahead of the model leading edge and hence minimised the boundary layer thickness in the region of the model. The amount by which the reflection plate projected forward of the fin leading edge was sufficient to ensure that flow ahead of the fin was not distorted by spillage under the plate.

The results of the feasibility study indicated that it would be possible to test a 1.25:1 scale model of the torpedo fin in the 7ft x 5ft wind tunnel and achieve Reynolds numbers of the same order of magnitude as those at full scale in water ($1x10^6$). On this scale of model, control surface oscillation frequencies of up to 60 Hz were needed to obtain reduced frequencies of up to 2.0 at the maximum tunnel speed of 40 m/s.

2.5.4 The choice between measuring forces and pressures

Of the various forces acting during an oscillation, the aerodynamic force will only be a small proportion of the inertia force due to model mass. Since it was necessary to be able to measure the unsteady aerodynamic hinge moments acting on the control surface, a method of accomplishing this accurately was required. Basically, there were two methods open to investigation; the first was to measure the hinge moments directly using strain gauge balances, and the second was to measure the pressure distributions on the control surface and by integration, obtain the overall forces.

2.5.4.1 measurement of forces

An unsteady aerodynamic force measurement is usually obtained as the difference between two measurements, one wind-on and the other wind-off. For the difference to accurately represent the aerodynamic force it is necessary for the motion of the model, including any elastic distortion,to be the same for the two

measurements; if not, any additional inertia term will appear as a spurious aerodynamic force. It is therefore evident that while measurement of unsteady aerodynamic forces may not be too difficult at low frequencies, the extraction of aerodynamic force from inertia contributions becomes more difficult with increasing frequency. It is possible to balance out the inertia terms either mechanically or electrically using signals from accelerometers, but such methods become less reliable as the working frequency increases[14]. Another disadvantage of measuring forces directly is that no information on the nature of the flow is obtained. The knowledge of the actual pressure distribution can provide a much better insight into the rather complex behaviour of unsteady flow phenomena, in particular when viscous flow effects, or vortex shedding, have pronounced influence on the flow field. Furthermore, the majority of theoretical prediction methods operate on the basis of pressure distributions and are better validated by experimentally determined pressure information than with overall force data.

2.5.4.2 measurement of unsteady pressures

Because of the problems involved in measuring unsteady aerodynamic forces it has now become more usual to measure unsteady pressures[14,15,19]. An unsteady pressure consists of a steady level and a fluctuating component. In aerodynamic experiments the steady pressure may be as high as 1 bar while the amplitude of the fluctuating component can be as little as 10^{-3} bar. Obtaining adequate percentage accuracy in the measurement of the fluctuations often requires the steady and unsteady components to

be measured separately, although not necessarily with two completely different systems. Techniques have now been developed for measuring unsteady pressures on wind tunnel models to a high degree of accuracy[38,39,40]. There are basically two different techniques:-

1). In-situ transducers

In this method, miniature pressure transducers are installed so that their pressure sensitive areas form part of the aerodynamic surface. The great advantage of this arrangement is that, in principle at least, the pressure being measured is that which would be acting on the surface of the model. Usually however, this advantage is outweighed by the difficulty of achieving a flush and correctly contoured surface in areas of high curvature. Also, the sensitive areas of the transducers,being exposed, are susceptible to damage. The cost of each transducer is approximately £400 - £500 which makes the measurement of pressure over the entire surface of a model extremely expensive. Many researchers[14] have also found that due to the mounting requirements, it is not possible to move the transducers from one position to another since they are too fragile. Although the miniature pressure transducers are very small they are usually too large to mount in thin aerofoil sections especially near trailing edges and in these cases it is usual to recess them into the model. With the latter system, transducers are connected to the surface orifices by the shortest possible passage. Compared with the tube and pressure switch system (see next paragraph) , this method largely avoids

problems of transmission, allows the pressures to be measured simultaneously and is better able to deal with non-sinusoidal variations of pressure with time. Once again the disadvantages are in the high cost of providing enough transducers to obtain an adequate resolution of pressure distributions and in the high complexity of the model required for their installation. One early problem with these miniature pressure transducers was their poor thermal stability, making them unacceptable for accurate measurement of the mean pressure component of the unsteady pressure. However, recently developed electrical compensation techniques have now eliminated this problem[41].

2). tubing and pressure switch system

The technique of measuring steady pressures using pressure tubes connected to a pressure switch (Scanivalve) containing a single pressure transducer has been in common use for a long time. This method may be extended to the measurement of unsteady pressures provided that account is taken of the dynamic response of the tube and transducer system. The transfer function, which alters the pressure along the tube both in phase and amplitude depends greatly on the geometry of the tube and the prevailing ambient conditions (see Chapter 4). It can be shown that the response of the tubing system can be calculated theoretically and that agreement with experiment is very good[38,39,40]. This method is economical since only one transducer is required to measure many pressures. It also allows for a stiff and relatively simple construction of the model.

After considering the advantages and disadvantages of the two techniques for measuring unsteady pressures it appeared that the tubing system offered greater scope for incorporating a sufficient number of tappings into the model at minimal cost (Scanivalves and compatible transducers were available within the University). The use of the tubing system also allowed for greater flexibility in locating pressure tappings where required.

In order that this system could be used, a study was conducted to develop a method whereby a tubing system could be calibrated (see Chapter 4). This was based on work by Gumley[40] which indicated that calibration to a high degree of accuracy was possible.

3. DESCRIPTION OF EXPERIMENTAL FACILITY

3.1 Wind Tunnel

The model was tested in the 7ft x 5ft low speed wind tunnel at Bath University (Fig. 3.1). The closed circuit wind tunnel had a rectangular working section with corner fillets to minimise disturbances associated with boundary layer interactions. Provision existed for either the return or working sections to be vented to atmosphere as required. All tests in this study were conducted with the working section vented. The maximum speed obtainable in the working section was just over 40 m/s. Details of the calibration of the working section and flow surveys are given in Chapter 6.

3.2 Model Fin And Control Surface

3.2.1 Geometry

The model fin (Figs. 3.2 to 3.27) had a rectangular planform of aspect ratio 1.5 and a constant NACA 0012 symmetric section with a slightly modified trailing edge. The aspect ratio, section shape and thickness to chord ratio were all typical of underwater vehicles. Modifications to the trailing edge section were made solely for the purpose of simplifying the manufacture of the control surface. The section maintained the NACA 0012 profile from the leading edge to 55% chord; a cubic curve then blended into the straight trailing edge profile which started at

68.75% chord and continued to the trailing edge. The trailing edge thickness of the NACA 0012 section was maintained (0.00252c). Differences between the true and modified NACA section were slight (Fig. 3.4).

The control surface extended from 32.4% semi-span to 97.2% semi-span and had a chord equal to 25% of the overall fin chord. The geometry of the control surface was simple, comprising a circular arc leading edge tangentially blended to a wedge section trailing edge. The geometry of the gap between the fin and the control surface was again typical of the simple construction encountered on underwater vehicles and maintained a constant gap width of 0.39% chord (Fig. 3.3). Small, unsealed gaps also existed at the inboard and outboard edges of the control surface. A part-span control surface was chosen to enable a body to be added to the configuration at a later date, thereby requiring the inboard edge of the control to be some distance away from the fin centreline. It was also necessary to provide a location for a bearing to support the outboard end of the control surface. This meant that the control could not extend to the tip of the fin.

3.2.2 Construction

FIN

The fin was constructed entirely of metal with all components forming the aerodynamic surface being machined from solid billets of aluminium alloy. The use of aluminium alloy enabled the model to be made very rigid, and unlike wood was not subject

to distortion under changing environmental conditions (temperature and humidity). Aluminiun alloy was also chosen for its ability to be easily machined and for the high quality of surface finish that could be achieved. To avoid problems of corrosion all other components were constructed of either stainless steel or brass. Brass inserts were provided for all threaded holes in aluminium components to reduce the likelihooh of stripped threads, caused by repeated dismantling.

The main portion of the fin comprised four components, an upper and lower half, a fin tip and a part forming the geometry of the control surface gap (Figs. 3.5, 3.6, 3.7). Stainless steel dowels were used to locate the components which were fixed by means of recessed machine screws. The inside of the upper half of the model was extensively machined to allow pressure tappings to be installed over most of the surface (Fig. 3.8). Provision for fewer pressure tappings was also made in the lower half of the fin (Fig. 3.8). The detachable fin tip was required to facilitate manufacture and assembly of the model. Its other function was to provide the necessary housing for the small, high precision bearing supporting the outboard end of the control surface. A separate component forming the geometry of the gap between the fin and control surface simplified manufacture and allowed for the possibility of investigating the effect of various gap geometries by having interchangeable components.

To ensure that no discontinuities in the aerofoil surface occurred

at the joints of the components, the external profile was machined after all parts had been dowelled and bolted together. As a further precaution, the leading edge joint between the two halves of the model was finished by bevelling the mating edges and filling the resulting groove with epoxy filler (Fig. 3.9). The joint was then smoothed to blend in with the rest of the aerofoil, thereby leaving no steps or roughness to interfere with the boundary layer in this critical region. This treatment of the leading edge was performed during final assembly of the model after polishing and installation of the pressure tappings and tubes. Counterbored recesses for bolt heads were filled with plasticene which was smoothed to blend with the surrounding aerofoil surface.

The aerofoil profile was achieved by the traditional method of step-milling followed by hand finishing. Accuracy of the finished profile was to within a tolerance of $\pm$ 0.002".

CONTROL SURFACE

Like the main part of the fin the control surface was machined from a solid billet of aluminium alloy (Figs. 3.10 to 3.15). The inside of the component was extensively machined to reduce its inertia and to allow pressure tappings to be installed. A cover plate forming one of the flat surfaces of the control allowed access to the inside of the model. The plate was secured by 30 8BA. countersunk screws, ensuring rigidity under dynamic conditions. Chordwise strips of sellotape covered the heads of the screws to give a smooth aerodynamic surface. The complex internal geometry

of the control surface was derived after consideration of the pressure tapping requirements; constraints were imposed by manufacturing methods and the structural stiffness of the control to avoid distortion while undergoing high frequency oscillations.

The control surface was supported by a pre-loaded, high precision ball bearing at its outboard end and by the actuating shaft at the inboard end (Figs. 3.17, 3.18). The actuating shaft was made of stainless steel and passed through the root of the fin to the underside of the reflection plate. The actuating shaft was required to be hollow in order to allow pressure tubes to pass through it into the control surface. Two pre-loaded, high precision ball bearings housed below the reflection plate provided the main support for the actuator shaft. Secondary support was provided by a phosphor bronze bush located inside the fin near the spigot joint between shaft and control surface. The purpose of this bearing was to increase the transverse (bending) stiffness of the control surface actuator shaft. It was lubricated by means of a small oil hole in the surface of the fin. One of the main considerations in the design of the actuator shaft was to achieve a flat dynamic response over the range of frequencies to be tested (0 - 60 Hz). The lowest calculated natural frequency in the torsional mode was 530 Hz, a value considered to be sufficiently high to pose no problem in the 0 - 60 Hz frequency range. Although relatively expensive, the use of high precision grade ball bearings (ABEC 7) was justified because it minimised the effects of bearing induced vibrations distorting the fundamental motion of the control surface.

The gap between the fin and control surface leading edge was sealed for some of the tests using flexible, adhesive p.v.c. tape on both upper and lower surfaces. Care had to be taken when applying the tape to ensure that it would not ripple when the control was being oscillated.

3.2.3 Control surface actuation system

The control surface was oscillated via the actuating shaft by a Ling Dynamics V404 electromagnetic vibrator mounted below the reflection plate (Fig. 3.16). Linear motion of the vibrator armature was converted to rotary motion of the actuating shaft by means of a hinged linkage and crank arm (Figs. 3.19, 3.20). Manual adjustment of the control surface mean deflection angle over a range of $\pm$ 20° was possible by slackening three screws clamping the actuator arm to the actuator shaft quadrant plate (Fig. 3.19). The mean control deflection angle was set to an accuracy of $\pm$ 0.05° using a vernier protractor against the flat portions of the flap and fin surface (Fig. 3.21). The linkage between the crank arm and the vibrator (Fig. 3.20) contained four pre-loaded, high precision ball bearings, its purpose being to eliminate bending loads being transmitted to the armature of the vibrator. The overall power requirements of the vibrator were determined from a knowledge of the desired range of frequencies and amplitudes together with calculated estimates of the moment of inertia of the control surface and actuating linkage. Over the frequency range 0 - 60 Hz it was possible to oscillate the control surface at amplitudes of up to 2° , however, most tests were conducted with amplitudes of 1°.

3.2.4 Mounting of model in wind tunnel

The fin was mounted vertically in the wind tunnel supported on a rigid stand comprising two 'A' frames and a solid steel base plate (Figs. 3.22 to 3.25). The plane of the reflection plate was 12" above the wind tunnel floor, well outside the boundary layer. In order to isolate the model from vibrations transmitted through the wind tunnel structure a framework, attached to the concrete floor of the building, was built below the wind tunnel (Figs. 3.24, 3.25). Mounted on top of this framework was a false wind tunnel floor to which the model stand was bolted. The false floor was constructed from 1" thick plywood stiffened both longitudinally and laterally with square section steel tube. A $\frac{1}{2}$" wide gap between the false floor and the surrounding wind tunnel floor ensured isolation. This gap was sealed using strips of low density foam rubber. A central pivot enabled the model fin on its stand to be set at incidence between $\pm 10^{\circ}$.

The dimensions of the reflection plate were determined from the recommendations of Förching[15] and from practical considerations. It extends a distance of 0.3c forward of the leading edge of the fin to ensure negligible flow distortion while maintaining a minimum boundary layer thickness in the region of the fin. The width and extent of the reflection plate behind the trailing edge of the fin was limited by the constraints of the wind tunnel walls when the model was at maximum incidence. Flow surveys were conducted to examine the quality of the flow over the reflection

plate (see Chapter 6). To eliminate vibration of the relatively thin reflection plate, restraining wires were provided at each of its corners and at the centre of each side. These wires were tensioned by means of small turnbuckles.

3.3 Pressure Tapping Installations

3.3.1 Distribution of pressure tappings

CONTROL SURFACE

A large number of pressure tappings was located on the control surface (Fig. 3.26) in order to obtain sufficient coverage for accurate determination of the overall control surface hinge moments by integration of the pressure distributions. Normal practice is to place pressure tappings on both surfaces of the model at the same chord and spanwise locations. This enables the loading at each point to be evaluated from the difference between the pressure readings on each surface. However, the limited space inside the control surface only made it possible to have a comprehensive distribution of pressure tappings on one surface. This meant, therefore, that for the case of zero incidence and zero mean flap deflection it had to be assumed that the flow, like the model, was symmetrical.

i.e.

a). The mean steady pressures on each surface of the flap

at a given chord and spanwise location were equal.

and b). The amplitude of the unsteady pressures on each surface at a given chord and spanwise location were equal but out of phase with each other by exactly 180°.

Experimental verification of these assumptions was obtained from the fewer pressure tappings placed on the mainly untapped surface (see Chapter 6). For the case of non-zero incidence or mean flap deflection it was possible (because of model symmetry) to treat the pressure tapped surface as the upper surface and then the lower surface by conducting tests with both positive and negative incidence and flap deflection angles.

A total of 14 chordwise rows of pressure tappings were located across the span of the control surface. Each row contained 11 pressure tappings spaced fairly evenly along the chord of the flap. A greater density of tappings was provided at the inboard and outboard ends of the control surface where three-dimensional effects would be greatest. As one of the main objectives of the investigation was to determine the hinge moments acting on the control surface, great importance was given to placing pressure tappings as near as possible to the trailing edge, The pressure loadings in this region although low in comparison to those nearer the leading edge of the flap can contribute significantly to the hinge moment as a consequence of the increased moment arm. Although it would have been desirable, it was not possible to

have pressure tappings distributed around the leading edge of the control surface due to the limited space available inside the model. However, this did not affect the evaluation of the control surface hinge moments because the leading edge of the flap was a circular arc centred about the hinge axis. This meant that the line of action of all pressures acting around the curved leading edge passed directly through the hinge axis, thereby contributing nothing to the hinge moment.

P.v.c. tubing connecting the pressure tappings to the Scanivalve had to be routed through the hollow actuating shaft of the control surface. The diameter of the shaft was limited by the thickness of the aerofoil section of the model and it was only possible to have a maximum of 13 pressure tubes plus the accelerometer cable passing into the control surface. To overcome this limitation the following procedure was adopted:-

1). Connect one chordwise row of pressure tappings to the Scanivalve with the thirteen p.v.c. tubes.

2). Conduct full series of steady and unsteady tests measuring pressure data at the connected pressure tappings only.

3). Reconnect p.v.c. tubes to pressure tappings in the next chordwise row of tappings.

4). Repeat series of steady and unsteady tests.

5). Continue the above process until data had been acquired at all the pressure tappings in the flap.

With the p.v.c. tubes being moved from one tapping to another it was important to ensure continuity of the calibrated frequency response of the tubing system. This meant that care had to be taken not to stretch or damage the tubes. It was also necessary for the overlap of the p.v.c. tube over the steel pressure tapping (5mm) to be the same in all cases. This was achieved by placing a small mark on the pressure tapping at the point to which the p.v.c. tube should overlap. The junction between the pressure tapping and flexible tubing was sealed using a coating of silicone sealant around the outside of the joint. Although a period of approximately 12 hours was required for the sealant to cure, it could be removed easily when the time came for the p.v.c. tubing to be transferred to another tapping.

FIN

Although provision had been made (by extensive internal machining) for the main surface of the fin to be comprehensively pressure tapped, only three chordwise rows of pressure tappings were used during this investigation (Fig. 3.27). The reason for this was that only two Scanivalves were available, giving a total of 96 measuring ports. As thirteen of these ports were required for pressure tappings in the control surface and eight more were needed for reference purposes, only 75 ports were available for

measuring pressures on the fin itself. The lack of full pressure measuring coverage on the fin was considered inconvenient but acceptable because the main objective of the investigation was to measure the control surface hinge moments. The spanwise locations of the pressure tappings (y/s = 0.181, 0.6213 and 0.9452) were chosen to give general information about the nature of the flow and as an aid to interpreting the pressure measurements on the control surface.

3.3.2 Construction and installation of pressure tappings

Careful construction and installation of the pressure tappings was required because of the importance of their calibrated frequency response to the success of the investigation (see Chapter 4). In order to simplify their calibration, all pressure tappings except those in areas near the trailing edge of the model were made of 20mm lengths of stainless steel tube (0.685mm bore).

Before installation, the pressure tappings were ground to a length of 20.2mm on a surface grinder (Fig. 3.28a). They were then bent as required using a small, purpose made jig (Fig. 3.28b). The jig formed a bend radius equal to four times the tubing external diameter without appreciably distorting the circular cross section of the tube. Holes were drilled in the fin and control surface to accept the pressure tappings after the profile had been formed but before it was finally polished. Great care was taken to ensure that the pressure tappings were drilled normal to

the aerofoil surface and that their chord and spanwise location was to within 0.005" of specification. After deburring and degreasing, the stainless steel pressure tappings were inserted into the holes in the surface of the model. The fit of the tappings was such that light pressure was required. A simple gauge enabled the pressure tappings to be set proud of the outside of the model by exactly 0.2mm (Fig. 3.29). Fixture of the tubes into the model was achieved using cyanoacrylate adhesive, capilliary action being relied on to draw the liquid adhesive into the joint. To make the fixture more rigid, a fillet of epoxy resin was placed around the base of the pressure tappings inside the model (Fig. 3.29). Once all the pressure tappings had been installed the protruding ends were honed flush to the aerofoil surface before final polishing of the model. After polishing, some of the tappings were blocked with the residue from the polishing process. This was removed using a trichloroethylene solvent and a high pressure airline. Each tapping was then inspected to ensure the absence of burrs before connection of the flexible p.v.c. tubing. After sealing the joint between the tapping and the flexible tube the small, oscillatory pressure generator described in Chapter 4 was used to check the calibration of the frequency response of each tapping in turn.

The technique adopted for installing pressure tappings in the trailing edge of the flap was slightly different to that described above. The thickness of the model in this region precluded the use of a bent tapping. It was therefore necessary to place a length of stainless steel tubing just below the surface of the model

into which the pressure tapping could be drilled at right angles (Fig. 3.30).

3.4 Instrumentation

3.4.1 General description

The primary role of the instrumentation system (Fig. 3.31) was to ensure the accurate measurement of mean and unsteady pressures on the surface of the model fin. To achieve this it was also necessary to measure the displacement - time history of the oscillating control surface to provide a reference for the unsteady pressure measurements. Details of the pressure tapping installations are given in Chapter 3.3 and their dynamic calibration in Chapter 4. The following sections describe the various items of instrumentation and signal conditioning used in order to obtain their optimum performance under the particular conditions prevailing during this investigation.

At the heart of the instrumentation system was the Solatron 1172 frequency response analyser (f.r.a.). This piece of equipment performed a near-real-time Fourier analysis at a selectable frequency on any two input signals. The output was displayed digitally in the form of components of the input voltages in-phase and in-quadrature with the internally generated reference signal of the f.r.a. The frequency of analysis was selectable to four digit accuracy and the number of cycles over which the

Fourier analysis was averaged could be selected from a range of 1 to 10,000 cycles. An autoranging facility enabled a wide range of input signal amplitudes (1mV to 100V) to be analysed and the results displayed to four digit accuracy (1.000mV to 100.0V) without loss of resolution.

The technique of Fourier analysis rejects components of a signal not equal to the frequency being considered, it is therefore not necessary to use filtration to remove noise from a signal. However, for the same reason it was necessary to have the flap oscillation frequency equal to the frequency being analysed by the f.r.a. This was achieved by using the internally generated signal from the f.r.a. to drive (via the power amplifier) the vibrator operating the model control surface.

3.4.2 Measurement of model motion

The displacement - time history of the control surface was measured using a small accelerometer of the delta-shear type (Bruel and Kjaer model 4375) mounted inside the control surface (Fig 3.32). The signal from the accelerometer was passed through a charge preamplifier (Bruel and Kjaer model 2651) before being measured on the frequency response analyser. The coaxial cable connecting the accelerometer to the preamplifier was routed through the control surface actuating shaft together with the pressure tubes (see Chapter 3.2). Output from the f.r.a. was in the form of in-phase and in-quadrature components of the preamplifier voltage output

with respect to the internal reference signal of the f.r.a. The motion of the flap, being sinusoidal, enabled the displacement to be derived by dividing the acceleration amplitude by ω^2 and correcting the phase angle by 180° (see Chapter 3.5).

MOUNTING OF ACCELEROMETER

The accelerometer was mounted on a specially machined pad inside the flap using a steel stud and a thin film of grease between the pad and the base of the transducer. This method was recommended by the manufacturer to maximise the rigidity of the mounting, thereby ensuring that the natural frequency of the accelerometer was as high as possible (approx. 60 kHz). When the flap was oscillating about its hinge axis, the seismic mass of the accelerometer was subject to both tangential and radial accelerations (Fig. 3.32), the former being much larger than the latter for small amplitude oscillations (tangential acceleration = 198 m/s^2, radial acceleration = 7 m/s^2 at 60 Hz for 2° amplitude). The accelerometer was therefore mounted so that its main sensitivity axis was perpendicular to a line drawn from the flap hinge axis to the centre of gravity of the seismic mass (Fig. 3.32). The low transverse sensitivity of the accelerometer (less than 1.7% of maximum sensitivity) combined with the much lower radial accelerations, resulted in the output of the transducer being only negligibly affected by the radial acceleration component (less than 0.1%).

In order to maximise the output from the accelerometer for a given

amplitude and frequency of oscillation, it was necessary to place the transducer as far away from the flap hinge axis as possible. The distance that could be achieved (40mm) was limited by the space available inside the control surface but the resulting signal to noise ratio for the worst case (1° amplitude at 5 Hz) still enabled the accelerometer output to be measured to a resolution of better than 0.5%.

Simplified theoretical analysis of the control surface indicated that distortion of the structure when undergoing forced oscillation at the maximum frequency and amplitude would be insignificant. To confirm these findings, provision was made for the accelerometer to be mounted at three spanwise stations (y/s = 0.376, 0.652 and 0.929)(Fig. 3.10). With the transducer mounted at each of these positions, the flap was oscillated at various frequencies and amplitudes and the accelerometer output recorded. The results showed that within the operating range of amplitudes and frequencies the distortion of the flap structure was undetectable. All subsequent tests were conducted with the accelerometer mounted centrally in the control surface (y/s = 0.652).

ENVIRONMENTAL SENSITIVITY

A delta-shear type accelerometer was chosen for its small size, and its insensitivity to base strain (the strains introduced into the accelerometer from distortion of the structure being measured) and variations in temperature. The effects of fluctuations in

temperature become important at low frequency where acceleration levels are low. For the Bruel and Kjaer model 4375 the charge sensitivity changes by less than 1% over the temperature range $0^{\circ}C$ to $30^{\circ}C$ and could therefore be ignored during this investigation.

FREQUENCY RESPONSE

The frequency response of an accelerometer is affected at high frequency by its own natural frequency (60 kHz). Phase and amplitude distortions of the accelerometer only become significant (greater than 5%) for frequencies greater than 1/5 of its natural frequency. Therefore, since the highest frequency for tests on the oscillating flap was only 60 Hz (1/1000th of the accelerometers mounted natural frequency) the effects of transducer response were negligible (less than 0.5% according to manufacturers specifications).

The response of an accelerometer at low frequency depends primarily on the type of preamplifier used. With voltage types, the preamplifier input resistance effectively decreases the electrical time constant of the accelerometer. Consequently, voltage preamplifiers having an exceedingly high input resistance have to be used to permit measurements at very low frequencies (0.01 Hz to 10 Hz). With charge preamplifiers there is no such problem,as capacitative feedback on the preamplifier input effectively increases the accelerometer time constant, enabling a very low frequency limit to be achieved. This was one of the

main reasons for using a charge preamplifier for these tests. The acceleration levels measured for flap oscillations between 5 Hz and 60 Hz at amplitudes from 0.5° to 2.0° were well within the linear range of the accelerometer and preamplifier combination (Fig. 3.33).

CHARGE PREAMPLIFIER

A piezoelectric accelerometer can be treated as either a charge or voltage source. Its sensitivity may therefore be expressed in terms of charge per unit acceleration:-

$$S_{qa} = pC/ms^{-2}$$

or in terms of voltage per unit acceleration:-

$$S_{va} = mV/ms^{-2}$$

In both cases, the output levels are very low, which combined with the very high impedance of the accelerometer itself ($20 \times 10^{9} \Omega$) means that a high quality preamplifier is required to condition the signal before passing it to any measuring device (a frequency response analyser in this case).

A charge preamplifier was selected for the following reasons:-

1). As discussed earlier, the charge preamplifier enables more accurate measurement of low frequency accelerations than does a voltage preamplifier.

2). The voltage sensitivity of the accelerometer depends on the capacitance of the accelerometer and connecting cable. This means that recalibration of the accelerometer is required when non-standard lengths or types of cable are used. The charge sensitivity however, is independent of cable type or length and recalibration of the accelerometer is not required for different cable arrangements.

3). The charge sensitivity of the accelerometer is less affected by thermal transients than is the voltage sensitivity.

The linear operating frequency range of the Bruel and Kjaer model 2651 charge preamplifier was from 0.3 Hz to 100 kHz and the output gain set to 10 mV/pC. The internally generated noise level of the preamplifier of 5×10^{-3} pC meant that, even at the lowest acceleration levels occurring during the tests, it was possible to measure the output to a resolution of better than 0.5%.

CALIBRATION

The calibration of an accelerometer requires the use of either sensitive laser interferometry equipment or a reference standard accelerometer. Therefore, all B. and K. accelerometers are individually calibrated by the manufacturer to an accuracy of better than 1%. An artificial ageing process carried out during

manufacture ensures a stable and predictable performance throughout their life. The charge sensitivity of the accelerometer used in these tests was 0.365 pC/ms^{-2}. This output when converted to a voltage by the charge preamplifier with a gain of 10 mV/pC resulted in an overall calibration factor of 3.65 mV/ms^{-2}.

3.4.3 Pressure measuring system

The pressure measuring system comprised the pressure tappings connected to pressure transducers via lengths of flexible p.v.c. tubing and Scanivalves. Details of the pressure tubes and the calibration of their frequency response is given in Chapter 4. The following section describes the pressure transducers, their installation and calibration, and details of the signal conditioning used to enable the system to measure both mean and unsteady pressures.

PRESSURE TRANSDUCERS

The differential, capacitative type pressure transducers (Setra model 237 and Druck P.D.C.R. 22) used in the tests were chosen for their high performance qualities, combining good linear dynamic response with very low levels of noise, hysteresis and sensitivity to thermal transients. These qualities were necessary because the transducers were used to measure both mean and unsteady pressure components simultaneously. The main difficulty was that the mean pressures were several orders of magnitude

larger than the oscillatory pressure amplitudes. Before use, the transducers were statically calibrated over their operating range using a high quality inclined manometer as a reference (Fig. 3.34). This enabled the effects of thermal transients to be determined accurately. It was found that over the range 5 C to 35 C the zero pressure output could vary significantly, whereas the overall sensitivity of the transducers changed by less than 0.3%. Furthermore, it was also discovered that the stresses induced into the diaphragm of the transducers by the mechanism used to lock them into the Scanivalves could also affect both their sensitivity and zero pressure output. In the light of these findings a procedure was developed whereby the pressure transducers were calibrated while mounted inside the Scanivalves at the beginning and end of each days testing. The transducers were also left active for a period of at least five hours before conducting any tests. This ensured that their outputs could stabilize fully after the initial thermo-electrical transients had subsided.

LOCATION OF SCANIVALVES

The two Scanivalves holding the pressure transducers were mounted on the rear 'A' frame support of the model fin, just below the reflection plate (Fig. 3.16). This ensured that the length of flexible p.v.c. tubing connecting the pressure tappings to the Scanivalve could be kept to a minimum, thereby ensuring an acceptable frequency response for the tubing network. Strips of $\frac{1}{4}$"

thick rubber were placed between the Scanivalve mounting plate and the model support frame in order to isolate the pressure transducers from excessive vibration. Tests later showed that even when the flap was being oscillated at its maximum frequency (60Hz) the vibration induced output of the pressure transducers was negligible.

SIGNAL CONDITIONING

The full range output levels of the pressure transducers were of the order 20 to 30 mV. High quality instrumentation amplifiers were therefore used to amplify the signals so that the much lower oscillatory pressure components could be measured accurately using the f.r.a. The gain of these amplifiers was set so that the highest measured pressure levels did not exceed the saturation limit of the amplifiers (approx. 10V). A facility was also included in the amplifiers for the zero pressure output to be adjusted to 0V without affecting the gain. This allowed the influence of changes in ambient temperature on the pressure transducer zero pressure output to be eliminated at the beginning of each test run. After amplification, the signal from the pressure transducer was divided so that measurements of both the mean and unsteady components could be made. To measure the mean component of the pressure signal, the fluctuating component was removed using a low pass, fourth order active filter having a 1.0 Hz cutoff. The filtered signal was then measured using a digital voltmeter.

In order that the unsteady component of the pressure transducer

output could be measured on the frequency response analyser with maximum resolution, it was first necessary to remove the very high mean D.C. component. This was because the autoranging facility of the f.r.a. did not discriminate between A.C. and D.C. inputs and would therefore autorange on the highest input voltage. As the mean component of the transducer output signal was so much higher than the magnitude of the unsteady component this would result in a great loss of accuracy when trying to measure the unsteady component. The simple, high pass, capacitative filter used to remove the D.C. component of the pressure signal was designed so that the cutoff frequency was so low that even at 5 Hz, the attenuation was less than 0.001% and the phase distortion less than 0.1°. At higher frequencies these effects were considerably reduced.

3.5 Data Acquisition And Reduction

3.5.1 Acquisition of data

It was not possible, for financial reasons, to have an automated data acquisition system, so all data had to be recorded manually. An automated system would have removed a great deal of the tedium from the testing as vast quantities of data were involved. However, the use of such a system would probably not have reduced the overall testing time by any significant degree. This is because, with any system of measuring unsteady pressures and accelerations it would be necessary to take an average over a number of cycles.

At lower frequencies, it therefore becomes almost as quick to record data manually as it would by automatic means.

For each test case (see Chapter 3.6) the components of acceleration, unsteady pressure and mean pressure were recorded on pre-prepared charts. This data, in the form of transducer output voltages was then transferred to a mainframe computer where it was manipulated using a suite of purpose written Fortran programs (Appendix 1). In all tests, the unsteady pressure and acceleration components were measured by the f.r.a. over a period of 100 cycles. This value was chosen since it was established that no improvement in repeatability of the results could be achieved by extending the sampling period.

A typical test run would proceed as follows:-

1). Set wind tunnel speed using Betz manometer and record temperature of air inside the tunnel using a thermocouple.

2). Set both Scanivalves to the 'home' position (reference port to allow zero pressure output voltage to be measured).

3). Set flap oscillating at desired frequency. The amplitude of oscillation was controlled by using the f.r.a. in 'continuous' mode to measure the

magnitude of the accelerometer output. The gain sensitivity of the power amplifier allowed the amplitude of flap oscillation to be set to within 2% of the desired value. The actual amplitude could be measured to better than 1.0%.

4). Zero the pressure transducer output voltages using the offset facilities on the amplifiers.

5). Step Scanivalve to port to be measured and sample pressures and accelerations with the f.r.a.

6). Record unsteady pressure and acceleration components and mean pressure signal.

7). Step to next port on Scanivalve.

8). Repeat steps 6 and 7 until data at all ports had been recorded.

9). Check zero pressure output using reference port on Scanivalve and record any drift (reference check occurred after approximately every 15 data points).

10). Set new test conditions and repeat tests.

The average time taken to scan 15 ports was approximately 2 minutes.

3.5.2 Data reduction

Raw data in the form of output voltages from the pressure transducers and accelerometer together with the details of each test case were loaded into the mainframe computer. A Fortran computer program (Appendix 1) was used to apply calibration factors and correct for the harmonic response of the pressure measuring system (see Chapter 4) to produce the following:-

1). Amplitude of the control surface displacement.

2). Mean pressure coefficients.

3). Values of the unsteady pressure coefficients phase referenced to the displacement of the control surface.

4). Where applicable, the steady and unsteady section hinge moment coefficients generated by the pressure distribution by numerical integration (see Chapter 6).

Input to the program was performed interactively and the raw and corrected data were stored on magnetic tape for future use. The corrections applied to the unsteady pressure data were calculated within the program taking into account the ambient conditions (wind speed, temperature and static pressure) prevailing in each test run. Account was also taken of the particular characteristics

of the pressure transducers and of the individual length of each Scanivalve inlet port (there are three different lengths; see Chapter 4).

3.6 Model Configurations And Flow Parameters Tested

The complete set of test cases for which data was recorded are given in Tables 1 and 2. The majority of tests were conducted with the model at zero incidence and with the control surface oscillating with an amplitude of 1° about a mean deflection of zero degrees. The test cases enabled the effects of reduced frequency to be examined in detail. The effects of Reynolds number were examined to some extent by testing at three wind tunnel speeds. All tests at zero incidence were carried out with the control surface gap both open and sealed.

Due to the vast quantities of data involved and the limited time available, the unsteady pressure distributions were only measured at selected spanwise stations for cases with the fin at non-zero incidence or the flap at non-zero mean deflection (Table 2). These stations were selected to obtain information where the effects of incidence and control surface deflection would be greatest.

As well as the test cases documented in Tables 1 and 2, additional tests were conducted to examine the effects of control surface oscillation amplitude and to investigate the flow using flow visualisation techniques (see Chapter 6.2.5).

4 CALIBRATION OF PRESSURE MEASURING SYSTEM

4.1 Introduction

The tubing method of pressure measurement was selected for measuring unsteady pressure as it allowed greater flexibility at much lower cost than methods employing in-situ microminiature pressure transducers (see Chapter 2.5). However, lengths of pneumatic tubing, connecting pressure tappings to pressure transducers, introduce amplitude and phase distortions in the fluctuating pressure signals. It was therefore necessary to develop a procedure to enable a tubing system, suitable for use with the model fin and control surface, to be designed and calibrated.

Work by Bergh and Tijdeman[38,39] and Gumley[40] has shown that it is possible to calibrate these pressure measuring systems, both experimentally and theoretically, and that the correlation between the two methods is excellent.

This chapter describes a theoretical and experimental study that was conducted to design and calibrate the pressure tubing system used on the wind tunnel model. A description of the fundamental design considerations is given, followed by details of the calibration procedures. The effects of changes in ambient conditions (temperature and mean static pressure) are examined together with the effects of flow across the orifice of the

pressure tapping, and of bends in the tubing.

4.2 Procedure For The Design And Calibration Of Pressure Tubing System

Once the configuration, size, and pressure tapping arrangement of the wind tunnel model had been decided, the length of tubing required to connect each pressure tapping to the pressure transducer was determined. All tubes were then standardised on the maximum length. This resulted in pressure tubes comprising two elements; a short stainless steel pressure tapping 20mm long connected by a 750mm length of flexible p.v.c. tubing to the Scanivalve and pressure transducer. This standard tube size was satisfactory for all pressure tappings except those in the region of the thin trailing edge of the model. In this area, slightly longer lengths of stainless steel pressure tappings were required (30 and 40mm). These longer lengths could not be used as the standard due to the limitation on space inside other areas of the model.

The diameter of the stainless steel pressure tappings was selected after consideration of the effect of this parameter on the distortion of the pressure reading, and with regard to the installation of the tappings in the model. A static pressure hole produces curvature in the boundary streamlines due to the removal of the constraining surface[42] ; the magnitude of this error depends on hole size and it is recommended that tappings

have internal diameters of less than 1mm to keep errors in the measurement of mean pressure coefficients below 0.005. On the other hand, a tapping of small diameter acts like an additional restrictor placed at the front of the tubing system and it is difficult to obtain a satisfactory transfer function for the network. A pressure tapping diameter of 0.685mm (standard manufactured diameter) was finally selected as it fulfilled the previously described requirements.

A final consideration in the design and construction of the pressure tappings was the quality of surface finish given to the orifice of the tapping. Burrs and specks of dust on the orifice can result in large errors in the measured pressure. All pressure tappings were therefore carefully examined using a low powered microscope and all burrs were removed.

To assist in the design and calibration of the pressure measuring system, a theoretical model was established and verified by experiment. Both are described in the following sections.

4.3 Description Of Experimental Apparatus

4.3.1 Oscillatory pressure generator for calibration of tubing systems having zero cross-flow over orifice

A device for generating a sinusoidally fluctuating pressure for determining the frequency response of a pneumatic tube system, for

the case of zero flow across the tapping orifice, was constructed based on the principle of a piston oscillating inside a cylinder (Figs. 4.1, 4.2, 4.3). The cylinder was made from steel hydraulic tube having an internal surface with a ground finish. This enabled a good fit with the piston to be achieved. The piston was oscillated inside the cylinder by a Ling Dynamics V404 electromagnetic vibrator via a hinged coupling. This latter ensured that no bending moments were applied to the armature of the vibrator. The bearings used in the coupling were of high precision grade to minimise bearing induced distortion to the fundamental motion of the piston. Provision was made in the cylinder for mounting a reference pressure transducer to monitor the pressure inside the chamber; and for an outlet to allow the oscillatory pressure to be applied to the orifice of the tubing system undergoing calibration. This outlet was terminated with a short length of soft rubber tubing to provide a seal against the pressure tapping mounting plate. The vibrator and piston-cylinder arrangement were mounted on a rigid base which in turn was fixed to the test bench using rubber vibration isolators.

The vibrator was capable of driving the piston at amplitudes from 0mm to 8mm at frequencies up to 100 Hz giving oscillatory pressure amplitudes of up to 0.1 bar. During the tests the fluctuating pressure amplitudes were kept at approximately 0.01 bar as this was the order of magnitude of the pressures expected to be measured in the wind tunnel on the model fin. Adequate sealing of the piston in the cylinder was achieved by using a thin film of lubricating oil. To check the quality of the

oscillating pressure the signal from the reference pressure transducer was compared with a pure sinusoid on an oscillascope. No difference between the two signals could be detected visually and the signal to noise ratio of the fluctuating pressure was estimated to be in excess of 400:1 for frequencies up to 60 Hz and gradually falling to about 100:1 at 100 Hz.

4.3.2 Instrumentation

The voltage outputs from the two pressure transducers were passed through high quality instrumentation amplifiers before being compared using a frequency response analyser (Fig. 4.3). The gain of each amplifier was adjusted so that the static sensitivities of both transducers were identical. This was achieved by applying a known steady pressure to both transducers simultaneously and monitoring the output on a digital voltmeter, adjusting the gain of each amplifier until equality was reached. A further range of steady pressures was then applied to check for errors in the linearity of the responses . It was found possible to set the sensitivity of both transducers to within 0.1% of each other.

Filtration of the signals was not necessary for two reasons; firstly, the signal to noise ratio was excellent; and secondly, the frequency response analyser performs a Fourier analysis of the signals and therefore rejects all components at frequencies other than that at which the harmonic content is being determined. To ensure that the frequency of the oscillating pressure was identical

to that at which the f.r.a. was operating, the built-in signal generator of the f.r.a. was used to provide the signal to drive the vibrator.

In all cases the harmonic analysis was conducted over a period of 100 cycles, since no improvement in accuracy was obtained by increasing the sampling period beyond this value. Output from the f.r.a. was in the form of either real and imaginary components or amplitude and phase, which was displayed to four digit accuracy at the end of each analysis.

The reference pressure transducer (Kulite xcs-093) was selected because it had a flat frequency response at the frequencies under investigation (0 to 100 Hz), its natural frequency being in excess of 100 kHz. The pressure transducer, which formed part of the pneumatic tubing system being calibrated, was chosen for its suitability for use in tests on the model fin in the wind tunnel (sensitivity, linearity, thermal compensation and frequency response). Two different transducers were chosen for this purpose (Druck P.D.C.R. 22 $\pm$0.5 p.s.i and Setra 237 $\pm$0.1 p.s.i), and since, according to specifications they had diaphragms with natural frequencies between 1 kHz and 5 kHz, it was necessary to calibrate the frequency response of each transducer (Chapter 4.5.1). Corrections could then be applied to the results for a complete tubing system to eliminate the effects of diaphragm response.

4.3.3 Measurement of tube components and ambient conditions

The internal diameter of tube elements was measured to an accuracy of 0.005mm using a travelling microscope. For elements made from stainless steel hypodermic tube the measured values were found to correspond exactly with the manufacturers specification but, as could be expected, the bore of the flexible p.v.c. tubing was found to vary slightly along its length ($\pm$ 0.01mm). Tests showed that accurate measurement of the tube bore was necessary to achieve satisfactory calibration of frequency response (see Chapter 4.5.5) so an average value was calculated from a series of measurements along a length of tube.

The length of pressure tubes was measured either with vernier calipers for lengths up to 150mm or with a ruler for longer lengths. The accuracy obtained was found to be sufficient to give no significant errors when comparing experimental and theoretical frequency responses.

The internal volumes of the pressure transducers were obtained from manufacturers specifications and by direct measurement of the volume enclosed within the Scanivalve adaptor cap. For the particular pressure transducers used in the tests the change in volume due to diaphragm deflection was negligible.

The ambient temperature and pressure (atmospheric) were measured at the start of each test run. A thermometer gave sufficient accuracy for temperature measurements (resolution to 0.5°C) and

an instrument standard barometer (accurate to ± 0.001" Hg.) was used to obtain the atmospheric pressure. The mean steady pressure inside the oscillatory pressure generator was held at atmospheric for all tests.

4.3.4 Aerofoil model for calibrating pneumatic tubing systems having flow across the pressure tapping orifice

In order to check the calibration of the pneumatic tubing system in conditions with a flow across the orifice of the pressure tapping, a series of tests was conducted using an oscillating aerofoil mounted in the 30" diameter open-jet wind tunnel (Figs. 4.4 to 4.8). The model had two pressure tappings situated very close to each other, one being connected to a reference pressure transducer mounted just below the surface of the aerofoil and the second, forming part of the tube and transducer system being calibrated.

The aerofoil (Figs. 4.5, 4.6) had a NACA 0012 aerofoil section, an aspect ratio of 2.0 and was mounted between endplates to improve the two-dimensionality of the flow. The model was constructed of aluminium, the whole being machined from one solid block. In order to reduce mass and inertia, a series of holes was drilled to remove the majority of the core of the aerofoil. A small, removable plug located at mid-span was used to house the two pressure tappings. One of these tappings was connected via narrow bore p.v.c. tubing to an external Scanivalve

and pressure transducer. The other led directly to a microminiature pressure transducer (Kulite xcs-093), which was itself housed in the removable plug. The position of the two pressure tappings was such that they were both at a chordwise distance $x/c = 0.15$ from the leading edge of the aerofoil. In order to obtain the largest possible magnitude for the oscillatory pressure amplitude, it was necessary to locate the pressure tappings near to the leading edge. The ability to do so was limited by the requirement of a minimum aerofoil thickness in which to house the in-situ pressure transducer. Ideally, the miniature pressure transducer should have been mounted with its diaphragm flush with the surface of the model in order to register the true surface pressure. However, since the surface of the aerofoil was curved and the transducer diaphragm was flat, and also because the protective screen over the diaphragm was fairly rough, it was necessary to recess the transducer slightly. This avoided disruption to the flow field caused by roughness and discontinuities in the aerofoil surface. In fact, the transducer diaphragm was located approximately 0.3mm below the surface of the model and connected to the surface by a hole of equal diameter to the bore of the pressure tapping of the network being calibrated. It has been shown[14] that such a mounting arrangement does not give rise to significant transmission errors due mainly to the very short length of the passage connecting the model surface to the diaphragm of the pressure transducer, even in cases where the velocity of flow across the orifice is very high.

The model was mounted in high precision bearings between the stiffened support arms of the 30" diameter open-jet wind tunnel (Fig. 4.8). A simple lever system connected the model to an electromagnetic vibrator bolted to the floor below the wind tunnel. The power of the vibrator was sufficient to oscillate the aerofoil in pitch about its quarter chord with amplitudes of up to 1.5°, and at frequencies of up to 60 Hz. Initial test results indicated that a slight transverse vibration of the model occurred above 40 Hz but this was eliminated by using bracing wires attached to the support arms of the model.

The instrumentation used for the tests was identical to that used with the zero cross-flow rig (Fig. 4.3). The acceleration sensitivity of the Kulite pressure transducer, along its longitudinal axis, was sufficiently high (approx. 0.0001 p.s.i./g) for only a small correction to be required at frequencies above 30 Hz. This correction was evaluated as follows:-

1). Cover the pressure tapping orifice of the Kulite transducer with p.v.c. tape so that when the model was oscillated, the transducer output was entirely due to acceleration of the transducer diaphragm.

2). Oscillate the model at the same frequencies and amplitudes as it would be during later tests for measuring unsteady pressures. The output from the 'sealed' transducer was measured on the f.r.a.

and a correction evaluated for the effects of transducer acceleration response.

For the worst case (highest frequency and lowest cross-flow velocity) the correction to the Kulite pressure transducer output amounted to less than 4% of the measured unsteady pressures.

4.4 Theory

The problem of determining the response to a sinusoidal input pressure (p_i) of a narrow bore tube connected at one end to the internal volume (V_T) of a pressure transducer (Fig. 4.9) can be solved analytically by applying the Navier-Stokes equations, the equation of continuity, the equation of state and the energy equation[38]. Since the behaviour of sinusoidal oscillations in a fluid without steady velocity is considered it may be assumed that:-

$$p = p_s + \bar{p}e^{i\omega t} \qquad \rho = \rho_s + \bar{\rho}e^{i\omega t} \qquad T = T_s + \bar{T}e^{i\omega t}$$

$$u = \bar{u}e^{i\omega t} \qquad v = \bar{v}e^{i\omega t}$$

Where suffix s denotes the corresponding static quantities. With the further assumptions that the sinusoidal disturbances are very small, the internal radius of the tube is small in comparison to its length and the flow is laminar throughout the tube system, the aforementioned equations can be considerably simplified.

To solve the equations for the five unknown quantities p,ρ,T,u and v the relevant boundary conditions must be introduced. Thus at the rigid wall of the tube the velocity components u and v must be zero, and due to the axial symmetry of the problem the radial velocity component must also be zero at the centreline of the tube. Furthermore, at the wall of the tube, T has to be taken as zero, assuming that heat conduction at the wall is so large that no variation in temperature occurs. The two remaining boundary conditions must be specified at both ends of the tube. At the closed end of the tube where the volume V_t of the pressure transducer is connected, the increase in mass must be equal to the mass leaving the tube. The final boundary condition at the open entrance of the tube is of substantial importance as it is necessary to distinguish whether there is an external flow velocity V^cacross the orifice (as in wind tunnel measurements) or not (as in still air). In the latter case ($V^c=0$) the pressure variation must be equal to the input pressure disturbance $p_i e^{i\omega t}$ which leads to a non-zero velocity of the air at the tube entrance. This means that the air moves periodically in and out of the tube orifice (Fig. 4.9a). However, when an airstream flows across the tube entrance, the air leaving the tube interacts with the external cross-flow. This leads locally to additional oscillatory pressures at the tube entrance, as schematically illustrated in Fig. 4.9b. Thus, the boundary condition at the tube entrance has to be modified to :-

$$p = p_i + \Delta p \quad \text{at } x = 0$$

Δp can generally be expressed in terms of the freestream velocity V^c, the tube entrance velocity u_0, the local mean density ρ_s and an unknown coefficient C as follows[39].

$$\Delta p = C.\rho_s.u_0.V^c$$

The coefficient C is a function of Mach number and must be derived from experiments. Previous researchers[39,40] have determined that a value of C = 0.9 gives satisfactory agreement between theory and experiment for Mach numbers up to 0.9.

Actual tube pressure measuring systems usually consist of a series connection of N tubes and N volumes (Fig. 4.9c), for such a system the complex transfer function for each tube segment is given by (see Appendix 2 for derivation):-

$$\left(\frac{p_{j-1}}{p_j}\right) = \cosh(\phi_j L_j) + \frac{V_j}{\pi R_j^2}\left(\phi_j + \frac{1}{k_j}\right) n_j \phi_j \sinh(\phi_j L_j)$$

$$+\left\{\left(\frac{R_{j+1}}{R_j}\right)^2 \cdot \left(\frac{\phi_{j+1}}{\phi_j}\right) \cdot \left(\frac{J_0(\alpha_j)}{J_0(\alpha_{j+1})}\right)\left(\frac{J_2(\alpha_{j+1})}{J_2(\alpha_j)}\right) \cdot \right.$$

$$\left. \frac{\sinh(\phi_j L_j)}{\sinh(\phi_{j+1} L_{j+1})} \cdot \left\{ \cosh(\phi_{j+1} L_{j+1}) - \frac{P_{j+1}}{p_j} \right\} \right\}$$

where:-

$$\phi_j = \frac{\omega}{a_0}\sqrt{\frac{J_0(\alpha_j)}{J_2(\alpha_j)}}\qquad\sqrt{\frac{\gamma}{n_j}}$$

$$n_j = \left[1 + \left(\frac{\gamma - 1}{\gamma}\right) \cdot \frac{J_2(\alpha\sqrt{Pr})}{J_0(\alpha\sqrt{Pr})}\right]^{-1}$$

$$\alpha_j = i^{3/2}\, R_j \sqrt{\frac{\omega\rho_s}{\mu}}$$

$$Pr = \text{Prandtl number} = \frac{\mu C_p}{k}$$

k = factor of the polytropic expansion of the volume (experimentally it can be shown that a value of $k=1.4$ is suitable for air in practical networks[38]).

σ = dimensionless increase of the volume due to deflection under full range pressure ($\sigma = 0$ for tube elements but may be non-zero for transducer volume).

a_0 = local mean speed of sound.

R_j and L_j = radius and length of tube element j.

j = subscript denoting tube element counted from tapping end.

γ = ratio of specific heats of air.

α = non-dimensional shear number (ratio of inertial to viscous damping) relating mean density ρ_s, molecular viscosity μ, frequency $\omega = 2\pi f$ and tube radius.

J_0 and J_2 are Bessel functions of the first kind and zeroth and second order, best computed by evaluating the Kelvin functions BER(J = 1) and BEI(J = 2) of the complex Bessel function BE(J ,I,Y) for orders I = 0 and I = 2 and argument Y. The Kelvin functions take the form $J_I(x \exp(3\ i/4)) = J_I(i^{1.5}x)$.

The correction term for the first tube element when there are substantial entrance crossflows is:-

$$\left(\frac{p_0}{p_1}\right)_{V_{fs}^c \neq 0} = \left(\frac{p_0}{p_1}\right)_{V_{fs}^c = 0} - \frac{C.V_{fs}^c.\phi_1}{i\omega}.\frac{J_2(\alpha_1)}{J_0(\alpha_1)} \left\{ \sinh(\phi_1 L_1) - \right.$$

$$\frac{n_1 \phi_1 V_1}{\pi R_1^2} \left(\sigma_1 + \frac{1}{k_1}\right) \cosh(\phi_1 L_1) +$$

$$\left. \frac{R_2^2}{R_1^2} \cdot \frac{\phi_2}{\phi_1} \cdot \frac{J_0(\alpha_1)}{J_0(\alpha_2)} \cdot \frac{J_2(\alpha_2)}{J_2(\alpha_1)} \cdot \frac{\cosh(\phi_1 L_1)}{\sinh(\phi_1 L_1)} \left\{ \cosh(\phi_2 L_2) - \left(\frac{p_2}{p_1}\right)_{V_{fs=0}^c} \right\} \right\}$$

Once the transfer function for each element has been evaluated the overall network transfer function can be calculated using

the recursion formula:-

$$\left(\frac{p_n}{p_0}\right) = \left(\frac{p_N}{p_{N-1}}\right)\left(\frac{p_{N-1}}{p_{N-2}}\right) \cdots\cdots\cdots \left(\frac{p_2}{p_1}\right)\left(\frac{p_1}{p_0}\right)$$

From these equations it can be seen that the pressure transfer function depends basically on the following parameters:-

1). The radius R and length L of the tubes.

2). The volume V_T of the pressure transducer and the dimensionless increase of the transducer volume due to deflection of the diaphragm at peak pressure amplitudes (σ).

3). The factor k of the polytropic expansion of the volume.

4). The frequency ω of the oscillating pressure.

5). The mean static pressure p_s and mean density ρ_s.

6). The mean temperature T_s.

7). The kinematic viscosity $\nu = \mu/\rho$ and the specific heat ratio γ of the air within the tube system.

COMPUTER PROGRAM

Since the equations governing the frequency response of pressure tubing systems are complex, a Fortran computer program was written based on the work presented in reference 40 (Appendix 2). This program allowed many tubing configurations to be analysed rapidly during initial design stages and proved useful in investigating the sensitivity to changes in ambient conditions, and to the accuracy of measurement of individual tube elements. The program was later incorporated as a subroutine into the suite of programs used to process wind tunnel data on the fin with oscillating flap (Chapter 3.5), enabling changes in ambient conditions to be accounted for. A listing of the relevant subroutines can be found in Appendix 2.

The program is capable of calculating the transfer function in terms of amplitude ratio and phase angle (or in complex form) of tubing systems having up to six tube elements of varying length and internal diameter connected to a pressure transducer.

4.5 Discussion Of Results

4.5.1 Comparison of frequency response of Druck and Setra pressure transducers with Kulite reference transducer

The natural frequencies of the Druck and Setra pressure transducers (5 kHz and 1 kHz respectively) were low enough for it

to be thought that significant attenuation and phase distortions could exist in the frequency range 0 to 100 Hz. Each pressure transducer was therefore calibrated against the Kulite reference pressure transducer whose frequency response was known to be flat (manufacturers specifications showed no attenuation and less than 0.1° phase lag at 100 Hz). The reference transducer and the transducer being calibrated were clamped in a holder such that an oscillating pressure (supplied from the sinusoidal pressure generator) could be applied to both their diaphragms simultaneously (Fig. 4.10). The outputs of both transducers were then compared over a frequency range of 0 to 100 Hz in steps of 5 Hz.

The results of the calibration (Fig. 4.10) show that the two transducers tested had markedly different frequency responses. The Druck P.D.C.R 22 transducer had a better response with no attenuation of amplitude and only a small phase lag (0.8°) at the maximum frequency (100 Hz). However the Setra 237 transducer, while only having a slight degree of attenuation (0.3%) at the higher frequencies, did show a significant phase lag with increasing frequency (11° at 100 Hz). Repeatability of the tests was to within the resolution of the f.r.a. (0.001 on amplitude ratio and 0.1° on phase angle).

Correction factors were evaluated for each transducer to apply to the experimental results obtained for complete tubing systems in order to remove the effects of transducer diaphragm response.

This enabled comparisons to be made with theoretical predictions where only the effects of tubing dimensions and transducer volume were accounted for. Corrections to phase lag varying linearly with frequency were calculated from a linear regression fit to the experimentally determined data points, whereas the effects of attenuation were evaluated individually according to frequency.

4.5.2 Frequency response of tubing systems without scanivalves

Initial tests were conducted using tubing systems constructed from single lengths of stainless steel hypodermic tubing, connected via a zero-volume adaptor, directly to the pressure transducer. The bore diameter of this tubing was very accurate in comparison to that of the p.v.c. tubing used later and more confidence could be held in initial comparisons with theoretical predictions. The effects of both tube length and tube diameter were examined and are presented in Figs. 4.11 and 4.12. Agreement between theory and experiment is excellent with maximum differences of approximately 2% occurring in the region of the resonance peak. These results imply that most of the assumptions made in the theoretical analysis are true in practice and that measurement of the tube dimensions and internal transducer volume is sufficiently accurate. Figs. 4.11 and 4.12 show how the fundamental natural frequency and damping of a pneumatic tube system depend on the length and internal diameter of the tube elements. Lengthening a tube of a given diameter results in lower resonance peaks at smaller values of the frequency whereas for a

tube of given length, a wider tube produces higher resonance peaks at roughly the same frequency.

The accuracy of the theoretical predictions is consistent with work presented by Bergh and Tijdeman[38].

Once the ability of the theoretical model to predict the frequency response of single element tubing systems had been verified, further tests were conducted with systems comprising several tubes of varying dimensions. The results for a pneumatic system having three tube elements, one of which was made of flexible p.v.c., show good agreement between theory and experiment (Fig. 4.13). This implies that the internal diameter of the p.v.c. tube, obtained by averaging several measurements taken along its length, is sufficiently accurate. Later investigations (see Chapter 4.5.5), however, highlighted the need for careful quality control when using this type of tubing.

4.5.3 Tubing systems incorporating a Scanivalve

4.5.3.1 Theoretical modelling of the Scanivalve

Due to the complex internal geometry of the internal passageways inside the Scanivalve (Fig. 4.14) and the need to simplify input to the theoretical model, it was found necessary to calculate the length and bore of a single tube having an equivalent frequency response. Practical considerations ruled out experimental

determination of the frequency response of the Scanivalve in isolation so a theoretical technique was used. This was later verified by comparison of theoretical and experimental results for a complete tubing network incorporating a Scanivalve.

The theoretical model was used firstly to evaluate the frequency response of the actual Scanivalve tubing, assuming straight tubes without kinks, over a wide frequency range (0 to 180 Hz). Determination of the length and diameter of a single tube having the same response was then conducted by trial and error. As the internal diameter of a large proportion of the Scanivalve tubing was approximately 1.0mm, this value was chosen for the equivalent tube. It was necessary to calculate the length of three equivalent single tubes because of the different lengths of the input ports to the Scanivalve.

Equivalent single tube lengths of 80mm, 87mm and 95mm were found to give the best results with errors of less than 0.05% in both amplitude and phase lag up to frequencies of 80 Hz (Fig. 4.15).

4.5.3.2 frequency response of tubing systems incorporating a Scanivalve

The results for a complete tubing system incorporating a Scanivalve show good agreement between theory and experiment (Figs. 4.16, 4.17). Differences are between 1 and 2 per cent and the good correlation verifies the theoretical modelling of the Scanivalve

with an equivalent single tube. Figs. 4.16 and 4.17 also show the effect of having different lengths of Scanivalve tube and of having long (40mm) and short (20mm) pressure tappings. For wind tunnel tests on the fin, a standard tapping length of 20mm was chosen as optimum for ease of installation. However, in regions near the trailing edge of the flap it was necessary to use pressure tappings 40mm in length.

4.5.4 Effect of bends in tubes

Due to restrictions on space within the wind tunnel model it was necessary to bend some of the pressure tappings to facilitate installation. In areas near the thin trailing edge of the model, pressure tappings had to be drilled at right angles into hypodermic tubing located just below the aerofoil surface (Fig. 3.30). Tests were conducted to evaluate the effects of these features on the overall transmission characteristics of the tubing system.

Results for a tubing system having a single, severe bend (centreline bend radius equal to 3 x tube O.D.) in the pressure tapping (Fig. 4.18) show little difference in the frequency response from systems with a straight tapping. Further tests with the bend placed in the centre of the tube and near the pressure transducer yielded similar results, showing that the position of the bend was not important. Large radius bends (centreline bend radius = 10 x tube O.D.) which would be

expected as a result of routing the tube inside the wind tunnel model had no detectable effect on frequency response.

The measured frequency response of a tubing network having a pressure tapping drilled at right angles into hypodermic tubing was similar to that of tubing systems having a severe bend (Fig. 4.19).

These results show that although right angle and small radius bends do act as a restriction in the line, their effects are very small and for practical pressure measuring networks can be ignored. It should be noted that these results are for the case of a single bend in the pressure tubing and that increasing the number of small radius bends will have an increasing effect on the frequency response.

4.5.5 Sensitivity of frequency response to accuracy of measurement of internal diameter of pressure tubing

A sensitivity study was conducted to evaluate the effects of errors in measuring the dimensions of tube system components. It was found that the measurement of tube lengths and transducer volumes could be performed with sufficient accuracy to result in errors of less than 0.1% when matching theory with experiment. However, it became evident that accuracy in measuring the internal diameter of tube elements was of the utmost importance if reliable theoretical predictions were to be obtained. The bores of the tube elements were measured using a travelling microscope to an

accuracy of ± 0.005mm. The bore of the stainless steel hypodermic tubing was found to be very consistent with manufacturers specifications with deviations of less than 0.5%. A ± 2% fluctuation was found in the bore of the p.v.c. tubing, meaning that an average value had to be taken when determining a suitable input to the theoretical model.

By running theoretical simulations of tubing systems with tubes of maximum and minimum diameter it was found that the frequency response could be altered considerably. The magnitude of these effects for a given error in tube diameter depend very much on the length of the tube, the longer the tube the greater the effect. For a tube system representative of that to be used in the model fin the effects of errors in tube bore were most evident in the attenuation of the system (Fig. 4.20). Differences in amplitude ratio of up to 5% were obtained for a 2% variation in tube diameter. The changes in phase angle for the same variations in tube diameter were less than 0.25%.

These results show that care had to be exercised when selecting p.v.c. tubing to ensure that all pressure tubes of identical length had the same effective mean bore diameter. This was confirmed by measuring the frequency response of each tube once it had been installed in the model (see Chapter 3.3).

4.5.6 Effects of ambient temperature and mean static pressure on frequency response

Theoretical investigations revealed a significant change in the frequency response of pressure tubing systems to changes in ambient temperature. In order to check these predictions, a tubing system was calibrated over the range of temperatures which could be expected to occur in the 7ft x 5ft wind tunnel (8 °C to 35 °C). The results (Fig. 4.21) show good agreement with theory, an increase in temperature giving rise to a reduction in damping while leaving the resonant frequency unchanged.

4.5.7 Effects of unsteady pressure amplitude on measured frequency response

Tests conducted to measure the effect of the amplitude of the oscillatory pressure on the frequency response of a pressure tubing system show that in the range considered, non-linear effects are negligible (Fig. 4.22). The range of oscillatory pressure amplitudes was chosen to occur within the range of those expected in later tests on the model fin (50 N/m^2 to 150 N/m^2).

4.5.8 The influence of non-zero cross-flow velocities over the pressure tapping orifice on the frequency response of the tubing system

Once again, the agreement between theory and experiment for

tubing systems having cross-flow over the orifice of the pressure tapping is very good (Fig. 4.23). Over the range of frequencies and cross-flow velocities examined, the theoretical model is able to predict the frequency response of the tubing system to within approximately 2%. A greater amount of scatter can be detected in the experimental data when compared with the data for cases of zero cross-flow. This is due to turbulence in the wind tunnel flow and slight vibration of the aerofoil model in modes other than pitch about the quarter-chord. The results show that the value of the chosen empirical cross-flow correction factor ($C = 0.9$) is satisfactory.

4.5.9 Repeatability of results

Repeatability tests were conducted on both sets of calibration apparatus (zero and non-zero cross-flow). These tests took two forms; the first involved successive testing of one particular tubing network and the second required the testing of three separate, but dimensionally identical (within the limits of constructional accuracy) tube systems.

Results for the zero cross-flow rig showed that the repeatability was within 0.5% (for both amplitude ratio and phase angle) for both types of repeatability test. The non-zero cross-flow rig showed a slightly poorer performance with repeatability of 1.5% to 2.0%. This latter is mainly due to the poorer signal to noise ratio of the pressure signals caused by wind tunnel turbulence and unwanted model vibration (see Chapter 4.5.8).

4.6 Conclusions

From the investigation into calibration of pressure tubing systems for measuring sinusoidally oscillating pressures, the following conclusions were drawn:-

1). Simple calibration rigs have been constructed and comissioned to enable the measurement of the frequency response of various pressure tubing systems for cases of both zero and non-zero cross-flow over the pressure tapping orifice. Repeatability of tests using both sets of apparatus is very good.

2). The theoretical model is capable of predicting the frequency response of the pressure measuring networks considered to a high degree of accuracy. The effects of changes in ambient conditions (temperature and mean static pressure) and of flow across the pressure tapping orifice are correctly modelled.

3). The accurate determination of tube dimensions is important. In particular, it is necessary to measure the internal diameter of tubes to an accuracy of better than 0.5% in order to keep errors in predicting frequency response below 1%.

4). Successful theoretical modelling of a 'J' type Scanivalve has been achieved by evaluating the length and diameter of

an equivalent single tube having an identical frequency response.

5). A single, small radius bend (bend radius = 3 x tube O.D.) in the tube does not affect the frequency response by more than 1% when compared with a straight tube of equal overall dimensions. Bends of much larger radius (bend radius > 10 x tube O.D.), such as would be expected when routing tubes inside wind tunnel models, had no influence on the frequency response. Pressure tubing systems having the pressure tapping drilled at right angles into stainless steel hypodermic tubing also showed differences of no more than 1% in frequency response when compared with a straight tube.

6). In the range of applied sinusoidal pressures, the non-linearities associated with pressure amplitude are negligible.

7). A pressure tubing system with frequency response characteristics suitable for measurement of unsteady pressures on the model fin has been designed. This 'standard' tube system comprised a stainless steel pressure tapping (20mm long, 0.685mm bore) connected to a Scanivalve via a length of p.v.c. tubing (750mm long, 1.065mm bore). The theoretically predicted frequency response for this system is to within 2% of that measured experimentally for the

tested range of ambient conditions and orifice cross-flow velocities.

5 DESCRIPTION OF THEORETICAL MODEL USED TO PREDICT UNSTEADY PRESSURE LOADINGS ON FIN AND CONTROL SURFACE

5.1 Introduction

As discussed in Chapter 2, several theoretical techniques have been, and are being developed to enable the prediction of unsteady airloads on oscillating configurations. The mathematics involved in these models is highly complex and its further development into a suitable computer program is a lengthy process. Time was a limiting factor in this investigation and a major experimental programme had been undertaken. It was therefore decided that any attempt to produce theoretical data for comparison with the experimental results would have to be performed using an existing model. The Royal Aircraft Establishment (R.A.E. Farnborough) kindly offered the use of their theoretical model which is based on a lifting surface technique[43,44]. This model, written as a suite of four Fortran programs was loaded onto the South West Universities Computer Centre (SWURCC) 2980 computer at Bath. The limitations of this model were fully realised especially with regard to the prediction of unsteady airloads on configurations with oscillating control surfaces (see Chapter 2).

5.2 Brief Description Of Theory

The full theoretical derivation of the model can be found in reference 43 and instructions for the use of the computer

programs in reference 44. The following paragraphs attempt to summarise the fundamental mathematical concepts.

The lifting surface theory of Multhopp[45] was for steady flow and required the loading to be approximated by a polynomial in the wing co-ordinates ξ and η multiplied by a function of ξ and η which took into account the known singular behaviour of the loading at the edges of the wing. This approximation to the loading was substituted into the integral equation to get an approximation to the upwash, which was equated to the known upwash at a set of points on the wing equal in number to the number of unknown coefficients in the expression for the approximation to the loading. A set of linear equations was thus obtained which could be solved for the unknown coefficients. The approximation to the loading was then known and an approximation to any required airforce coefficients could be obtained from it.

Multhopp's method was extended to low-frequency harmonic oscillations[46] and to general frequency harmonic oscillations by, among others Davies[4]. It was found however, that in all these methods, in which the chordwise integration was carried out first, the spanwise integral was evaluated numerically by too coarse a method, resulting in inaccurate estimation of the approximation to the upwash at points near to the leading and trailing edges of the wing. Consequently, this led to a loss of accuracy in the results for the generalised airforce coefficients. Garner and Fox[47] refined the method of

numerical integration of the spanwise integral which, after further development, was incorporated by Davies[43] into the current R.A.E. model.

In this method the coefficients are determined by equating integrals involving the approximation to the upwash to corresponding integrals involving the known upwash. This process, theoretically, leads to the generalised airforce coefficients being obtained with the highest possible precision for a loading approximation of a particular form. The integrals are evaluated numerically in the current method, and the number of integration points may exceed the number of unknown coefficients in the expression for the loading.

The current theoretical model is able to predict the unsteady airloads caused by the harmonic oscillation of wings having an arbitrary planform with or without control surfaces. Input to the computer program is in the form of geometry and flow conditions together with details of the mode of oscillation (pitch, heave, control surface oscillation or arbitrary structural distortion) and the location of the points at which the upwash boundary condition is evaluated. Output is in the form of pressure loadings at any requested point on the wing surface together with integrated force and moment coefficients.

5.3 Limitations Of The Model

Despite its mathematical complexity, the R.A.E. lifting surface model is only a relatively simple theory and has several limitations:-

The model is only a thin-wing theory, ignoring the effects of aerofoil thickness and the complex geometry that can occur where a trailing edge control surface is present.

The effects of viscosity with respect to the formation of boundary layers and vortices is completely ignored. It has already been stated (Chapter 2) that boundary layer effects have been shown to have a great influence on the nature of the flow where trailing edge control surfaces are concerned. This is especially so where complex interactions exist between the boundary layer and flow through an unsealed gap. Due to the low aspect ratio of the configuration being tested experimentally, the influence of vortices generated at the tip of the fin and at the ends of the control surface were also expected to be significant.

The theoretical model assumes that there is no gap between the fin and the control surface leading edge (unsealed gaps are assumed at the ends of the control surface), i.e. a logarithmic singularity at the control surface hinge line is applied. To enable comparisons to be made with theoretical predictions, some of the experimental tests were conducted with the control

surface gap sealed with p.v.c. tape.

A significant limitation of the theoretical model concerns the predicted chordwise pressure loadings where a control surface is included. The actual theoretical part of the loading becomes infinite like $\log(\xi - \xi_h(\eta))$ at the hinge line. However, the predicted loadings have a number of undulations along them (see Chapter 6.4). This is caused by the truncation of an infinite series implied in equation 22 of reference 43, for a function which has a logarithmic singularity at the hinge line. Viz:-

$$\hat{l}_k(x_0, y_0) = \frac{1}{c(y_0)} \cdot \exp\left(\frac{-ivx_0}{l}\right) \cdot \sum_{i=1}^{n} \sum_{p=1}^{m} A_{k:i.p} \cdot \xi_0^{i-1} \cdot \eta_0^{p-1} \cdot \sqrt{\frac{1-\xi_0}{\xi}} \cdot \sqrt{1-\eta_0^2}$$

Therefore, before making comparisons with experimental data, the theoretical loadings were smoothed manually to remove the undulations.

5.4 Geometry And Arrangement Of Upwash Collocation Points

The geometry of the theoretical model (Fig. 5.1) was defined to be as close as possible to that of the model being tested in the wind tunnel. The theoretical model differs in respect of the gaps at the ends of the control surface and the neglect of control surface leading edge geometry.

i.e.

a). Theory assumes unsealed but zero width gaps at each end of the control surface.

b). The theoretical control surface oscillates about its leading edge as a hinge line (located at $x/c = 0.75$) and has no leading edge gap.

PANELLING ARRANGEMENT

The theoretical model requires the user to define the number of spanwise and chordwise points on the wing surface where the upwash boundary condition is to be satisfied. Generally speaking, greater accuracy is achieved by increasing the number of these collocation points at the expense of increasing computing time. Davies[43] shows that approximately 24 spanwise and 10 chordwise collocation points are required for accurate convergence of the results to occur for a wing with trailing edge control surfaces. However, it was found that increasing the number of chordwise points on the collocation grid reduced the magnitude of the undulations in the pressure loading on chordwise sections containing the control surface (see Chapter 5.3). A grid having 24 spanwise and 20 chordwise points was therefore chosen for this investigation (Fig. 5.1). Increasing the number of grid points further was impractical due to the large increase in computing time associated with small increments in the number of collocation points. The typical computing time (c.p.u.) taken to

calculate the loadings on the fin at one set of flow conditions was approximately two hours for the 24x20 grid using the SURCC 2980 computer. Computation was performed with double-precision variables.

Once the number of chord and spanwise upwash collocation points had been input, the location of each point was calculated within the computer code according to the following relationships:-

$$\text{chordwise distribution } x = \cos\left(\frac{\pi p}{m+1}\right) \qquad \begin{matrix} p = 1.....m \\ m = 20 \end{matrix}$$

$$\text{spanwise distribution } y = \frac{1}{2}\left[1 - \cos\pi\left(\frac{2r-1}{2n+1}\right)\right] \qquad \begin{matrix} r = 1.....n \\ n = 24 \end{matrix}$$

This distribution of grid points ensured a greater density of collocation points near the leading edge and near the tip of the fin. It also allows for simple expressions concerning integration at a later stage of the calculation. Other choices of points may be just as good as far as numerical accuracy of the final results is concerned, but it is also possible to have an unfortunate choice of points resulting in poor conditioning of the sets of simultaneous equations.

6 RESULTS OF TESTS ON FIN WITH OSCILLATING CONTROL SURFACE

6.1 Calibration Of Wind Tunnel And Discussion Of Interference Effects

All measurements obtained from the wind tunnel tests are liable to suffer from the effects of tunnel interference. That is, the data obtained may differ from those which would be measured on the same model in a free and uniform flow. The sources of interference of importance during the present investigation were:-

1). Constraint of wind tunnel walls on the flow, including blockage caused by the model and support stand.

2). Interference of the boundary layer on the reflection plate with flow over the half-model.

3). Interference of the model stand and vibrator on the flow over the reflection plate.

4). Turbulent flow fluctuations inherent in the flow.

5). Tunnel resonance.

6). Curtailment of the wake vorticity by the wind tunnel fan.

While items 1 to 3 affect both steady and unsteady measurements, items 4 to 6 are peculiar to unsteady testing. Because of its more complicated nature, interference on unsteady measurements is poorly understood in comparison with interference on steady measurements. Since some part of the total effect on an unsteady measurement can be attributed to steady interference, it is important that as much as possible is done to account for, or minimise, the effect of this interference component. The following sections describe the effects of the interference sources tabulated above and explains what attempts have been made to account for them in the analysis discussed later in the chapter.

6.1.1 Wall constraint effects

Wall constraint interference in subsonic flow manifests itself in the following ways:-

a). Changes in stream velocity due to blockage (solid and wake).

b). Changes in model incidence due to induced upwash.

c). Changes in lift and pitching moment due to streamline curvature.

Although corrections for interference effects on steady and

oscillatory measurements can be obtained from theory for some situations[48], it is often better to choose a model size for which the effects are small enough to be neglected. For subsonic tests the choice of model size is a matter of judgement based on experience of unsteady testing. Current practice for three-dimensional tests with oscillating wings tends to choose model spans and planform areas within the following limitations:-

$$s/b < 0.4 \quad , \quad S/C < 0.15$$

where: s = span, b = tunnel width, S = planform area

C = cross-sectional area of tunnel

The effectiveness of these criteria have been largely confirmed by recent tests comparing results for one particular model tested in various wind tunnels[49]. Other results[50] suggest that a larger model ($s/b = 0.5$, $S/C = 0.25$) is acceptable when only a control surface is moving and when the main surface is near its zero steady lift condition.

For this particular investigation the model fin to tunnel size ratios were:-

$s/b = 0.27$, $S/C = 0.057$

chord to tunnel height ratio = 0.21

blockage for zero incidence (calculated from ref. 51) = 0.3%

These values fell well within the recommendations discussed previously. It was therefore argued that the tunnel wall interference effects caused by the size of the fin itself were negligibly small.

On the other hand, it was initially thought that significant flow interference could be caused by the model support stand and the vibrator mounted in the wind tunnel flow, below the reflection plate. The main effects were expected to be changes in the tunnel freestream velocity due to blockage, and distortion of the flow streamlines over the reflection plate in the vicinity of the model fin. This latter effect is discussed in a following section (6.1.3). The blockage effects of the support stand and vibrator were evaluated experimentally in the following manner. Firstly, the model support stand and vibrator together with the reflection plate were mounted in the wind tunnel. An N.P.L. standard elliptic nosed pitot-static tube was placed so that it measured the total and static pressure above the reflection plate at a position where the model fin would be at a later date (Fig. 6.1). An inclined manometer was used to measure the pressures. The wind tunnel Betz manometer was then calibrated against the readings from the pitot-static tube over the operating speed range of the tunnel (Figs. 6.1,6.2). The amount of blockage caused by the stand and vibrator was measured to be 1.6%.

6.1.2 The interference of the reflection plate boundary layer

One of the main interference problems associated with half-model testing concerns the boundary layer that forms on the reflection plate. The effects can be further increased by the adverse influence of the sharp corner that exists between model and reflection plate. In this study, attempts were made to minimise these effects by ensuring that the reflection plate boundary layer was kept as thin as possible. This was achieved by only allowing the reflection plate to project far enough ahead of the fin leading edge to avoid flow distortion (a value of 0.3c suggested by reference 15). A small fillet of silicone sealant (approx. 4mm radius) was applied at the intersection of the plate and the model to reduce interference associated with the sharp corner.

Tests were conducted to measure the approximate thickness of the reflection plate boundary layer at various stations along the reflection plate using a rake of flattened pitot tubes (Fig. 6.3). The maximum thickness of the boundary layer (near the fin trailing edge) was measured and found to be approximately 8mm. Although the adverse interference associated with the effects of pressure gradients on the fin would increase this value somewhat, it was felt that the pressure measuring stations on the fin were all far enough away from the root of the model to be negligibly affected.

6.1.3 Flow surveys above reflection plate in region of model fin

Flow surveys were conducted to measure local flow directions and the total and static pressure distributions over the reflection plate in the vicinity of the model fin. These tests were made to ascertain whether the disturbances caused by the stand and vibrator would be of significance. Tests were carried out at tunnel speeds of 20,30 and 40 m/s without the model fin in position. The surveys were made using a rake of yawmeters, pitot tubes and static tubes. The rake was calibrated in the empty working section of the wind tunnel against an N.P.L. standard pitot-static tube. The yawmeters were calibrated using the angular measuring facility on the wind tunnel telescope to an accuracy of 0.2°. The yawmeters could be used as pitchmeters by rotation of their plane of sensitivity by 90°. The flow surveys are summarised in Figs. 6.4 and 6.5. It was found that there was no significant distortion of the flow over the reflection plate, despite the large size of the vibrator. It is thought that this is due, in part, to the large size of the reflection plate (width and length) helping to restrict the transmission of flow disturbances.

6.1.4 The interference caused by wind tunnel turbulence

Turbulence in the wind tunnel is undesirable when undertaking both steady and unsteady measurements. Its presence necessitates a larger sampling time in making measurements and in some cases can

subject the model to undesirable vibratory conditions, resulting in resonance and fatigue failure.

Although no direct measurements of turbulence intensities were made within the tunnel, investigations were conducted to evaluate whether turbulence existed within the range of control surface oscillation frequencies being examined (0 to 60 Hz). The model fin was used for this purpose, with the control surface static. Signals from the pressure transducers measuring pressures at various places on the fin, were examined firstly on an oscillascope to detect the presence of turbulence in the frequency band of interest. Tests at the three wind tunnel speeds (20,30 and 40 m/s) indicated that the lowest turbulence frequencies were occurring at approximately 90 Hz. As a further check, the pressure transducer signals were examined on the frequency response analyser at discrete frequencies in the 0 to 60 Hz range at intervals of 5 Hz. The results obtained showed that turbulence levels in the frequency range of interest were unmeasurable below 30 Hz and of negligible proportions between 30 and 60 Hz. For the worst case (60 Hz, V = 20 m/s) turbulent pressure fluctuations would result in errors in measuring amplitude normalised unsteady pressure coefficients (Cp^u) of less than 0.01.

An advantage of the tubing system of pressure measurement is that it forms a natural low pass filter for the pressure signal, thereby eliminating the frequencies above 200 Hz. The f.r.a. also

helps to eliminate the effect of turbulence, as the process of Fourier analysis rejects frequencies other than that at which the analysis is being conducted.

6.1.5 Interference associated with tunnel resonance

In theory, tunnel resonance can occur when a train of reflected disturbances from an oscillating model returns with a phase delay that tends either to cancel or to reinforce the pressure changes occurring at the model. For a tunnel with solid walls the lowest frequency which corresponds to cancellation is:-

$$f_r = a_0(1-M^2)^{\frac{1}{2}} \Big/ 2H$$

a_0 = speed of sound, M = tunnel Mach no.
H = tunnel height or width (according to model orientation)

This yields a value of approximately 80 Hz for the conditions prevailing during this investigation.

Resonance has been shown to occur under two-dimensional conditions[52], however, it is doubtful whether the phenomenon occurs at all with three-dimensional models[14].

No evidence of tunnel resonance was detected during the current investigation.

6.1.6 Effect of wake curtailment

In a free atmosphere, an oscillating model leaves behind a periodic wake. In theory, the flow at the model must be consistent with the distribution of wake vorticity. If as in a wind tunnel, the natural wake is destroyed by a corner of the tunnel or by the driving fan as was the case in this investigation, it can be reasoned that the unsteady condition at the model will be affected. Although theoretical calculations have shown this to be important in certain special cases, the phenomenon is not generally regarded as important[14]. In the present study the wind tunnel fan was positioned approximately 12 chord lengths downstream of the model trailing edge. This was felt to be sufficient for the effects of wake curtailment to be negligible.

6.1.7 Transition fixing

Where tests are conducted at Reynolds numbers below those occurring at full scale it is sometimes necessary to fix the point of transition of the boundary layer using strips of roughness placed near the leading edge of the model. The desirability of fixing transition and the best position on the chord for attaching trips are debatable matters. If transition remains free, a laminar boundary layer may lead to types of flow separation that are unrepresentative of full scale. It is also possible that when natural transition is delayed to a rearward position on the chord, the cyclic movement of the transition point due to model oscillation may create spurious

oscillatory pressures. On the other hand, when transition strips are used, the turbulent boundary layer so produced is usually too thick over the rear section of the chord, thus overemphasizing viscous effects which can be especially serious if the investigations are centred on a trailing edge control surface.

Following the recommendations of reference 53, transition was allowed to remain free during the current study. However, tests were conducted at three wind tunnel speeds to obtain information regarding the effects of Reynolds number between 0.58×10^6 and 1.15×10^6.

6.1.8 Accuracy of experimental results

GENERAL

The accuracy with which the relevant quantities are measured is clearly an important matter. It may be assumed that the wind tunnel velocity, incidence, steady control deflection, oscillation frequency and steady pressures are measured with adequate accuracy. It is the accuracies of the unsteady pressures which give cause for concern since these quantities are derived from separate measurements of small changes in pressure and displacement of the model. The measurements are made with the instrumentation operating under dynamic conditions and their accuracy depends crucially on the calibration procedure.

Although the resolution of the instrumentation or the day to day repeatability, both of which set limits to the accuracy, are fairly easy to determine, the overall accuracy of a measurement is extremely difficult to quantify. A thorough analysis of the possible errors could easily entail as much work as the pressure measurements themselves. The following estimates concerning the accuracy of the pressure measurements are assessments based on knowledge and experience gained during the test programme.

PRESSURES

The accuracy of the calibration of the systems used to measure the pressures and displacement - time history of the control surface are discussed in Chapters 4.5 and 3.4 respectively. Efforts were made to ensure that errors were minimised during all stages of the testing but some factors depend very much on the exact conditions prevailing during particular tests. For example, the repeatability of the unsteady pressure measurements depended to a large extent on the tunnel speed and the frequency of control surface oscillation. Higher tunnel speeds yielded better results as the increased dynamic pressure resulted in larger absolute amplitudes for the oscillatory pressures. The pressure amplitudes were also increased by increasing the frequency of the control surface oscillation. Both these effects outweighed the effects of increased turbulence and extraneous vibration of the model associated with higher speeds and frequencies.

As the output from the accelerometer varied according to the square of the frequency, its output at very low frequencies (5 to 10 Hz) was quite low and could not be measured as accurately as it could at higher frequencies. This problem was mainly associated with the resolving power of the f.r.a. Errors in the amplitude normalised pressures were therefore slightly larger at the lower frequencies. This effect was to some extent counteracted by the fact that the accuracy of the calibration of the pressure tubing frequency response was best at low frequency. As frequency increased the accuracy diminished.

Bearing in mind all the factors involved the following estimates can only be regarded as approximate:

a). Error in unsteady pressure coefficient (amplitude normalised components in-phase and in-quadrature with displacement):- less than 3% at high frequency (60 Hz) rapidly improving at lower frequencies.

b). Error in unsteady hinge moment coefficients (in-phase and in-quadrature with displacement):- less than 6% - this is mainly a function of the integration method used on the pressure loadings (see Chapter 6.3.3).

These errors will mainly exhibit themselves systematically, as is portrayed in the measured pressure distributions where little scatter is evident (see following sections). The day to day

repeatability of the pressure measurements was very good and varied between 1 and 3% depending on the particular flow conditions.

6.2 Results For Steady Flow Over Fin (Control Surface Static)

6.2.1 Use of steady pressure distribution to set model at zero incidence

Before conducting any unsteady tests on the model it was necessary to align the model at zero incidence with respect to the tunnel freestream flow direction. As the model was symmetrical, this was achieved by using the model itself as a pitch-meter. Adjustments were made to the model incidence until the pressure distributions on both upper and lower surface at mid semi-span ($y/s = 0.6213$) were identical (to within experimental accuracy Fig. 6.6). It was found that this method enabled the model to be set to within 0.02° of zero. Non-zero incidences were set using a protractor scale on the wind tunnel floor to an accuracy of approximately 0.05°.

The measured steady pressure distribution at $y/s = 0.6213$ at zero incidence agrees very well with theoretical data for the NACA 0012 section obtained from ref. 54 for the effects of thickness alone. The measured pressure distributions on upper and lower surface correspond very well and indicate the good symmetric construction of the model and of the location of pressure

tappings. Differences exist very close to the leading edge of the model (up to $x/c = 0.025$) because of the extreme sensitivity of the pressures in this region to small differences in geometry and pressure tapping location.

6.2.2 Pressure distributions on fin and control surface at zero incidence

The effects of Reynolds number on the steady pressure distributions on the fin at three spanwise stations are shown in Fig. 6.7. Comparisons with two-dimensional theory also highlight the effects of low aspect ratio, the best agreement between experiment and theory occurring at the most inboard measuring station ($y/s = 0.181$) at the highest Reynolds number. The agreement is very good from the leading edge to approximately mid-chord, thereafter the effects of boundary layer displacement thickness (not accounted for in the theory) cause the experimentally measured pressures to differ from the theoretical ones.

6.2.3 Steady pressure distributions at non-zero incidence

Steady pressure data obtained for non-zero incidences ($\alpha = 5^\circ$, 10°) show the strong influence of three-dimensional effects on the loading over the fin and control surface (Figs. 6.8, 6.9). A reduction in the pressure peak at the fin leading edge toward the tip is noticeable. The presence of a vortex on the

upper surface near the fin tip is indicated by the pressure distribution at y/s = 0.9452. This results in a large suction over the rear portion of the upper surface of the fin and control surface, leading locally to areas of high loading and hinge moment. Flow visualisation studies (see Chapter 6.2.5) enabled the structure of the tip vortex to be more clearly defined.

6.2.4 Steady pressure distributions at non-zero control surface deflections ($\alpha = 0^\circ$)

Steady pressure distributions were measured for the case of non-zero control surface deflections of $5^\circ, 10^\circ, 15^\circ$, and 20° with the fin at zero incidence (Figs. 6.10 to 6.13). The influence of the fin tip vortex is noticeable even at $\delta = 5^\circ$ (Fig. 6.10). Compared to loadings at mid semi-span (y/s = 0.6213) the tip has a large suction on the upper surface, resulting in far greater section hinge moments. Carryover of the loading on the control surface can be seen on the main part of the fin inboard of the control surface. The presence of the unsealed gap at the leading edge of the control surface results in the sudden drop in loading on the fin just forward of the control surface leading edge.

Although flow visualisation (Chapter 6.2.5) showed that flow over the control surface at mid semi-span was separated for $\delta = 15^\circ$ and $\delta = 20^\circ$, little evidence of this can be detected in

the steady pressures. At $\delta = 20^{\circ}$, a second peak in the upper surface pressure distribution can be seen midway along the control surface chord near the tip of the fin. This is caused by interference of the fin tip vortex with flow through the gap at the end of the control surface. This interference was present for all non-zero control deflection angles but since at deflections less than 20° the tip vortex is dominant, the effect of interference is not evident in the pressure distributions. The gap which forms at the outboard end of the flap increases with increasing deflection. Flow from the lower surface is therefore more able to pass around the tip of the control surface to form a vortex on the upper surface, as flap deflection is increased. Flow visualisation studies confirmed this effect.

6.2.5 Flow visualisation studies

Flow visualisation studies (flow-vis) were conducted to examine the flow structure on the fin and control surface in order to assist in the interpretation of pressure measurements. Two techniques were used:-

1). Wool tufts.

2). Liquid film - mixture of titanium dioxide powder, oleic acid and paraffin. The proportions were obtained by experiment to achieve the best combination of density and viscosity.

In order to protect the pressure tappings in the model from contamination by the flow-vis liquid, the entire surface of the model was covered with matt-black, self-adhesive p.v.c. film. The result was a smooth aerodynamic surface against which the white flow-vis fluid contrasted well for photographic purposes.

One of the main problems encountered in the tests was that the model surfaces were vertical. This resulted in the undesirable influence of gravity on the flow-vis fluid.

ZERO INCIDENCE AND CONTROL SURFACE DEFLECTION

One of the major, and unexpected features of the flow patterns obtained using liquid film was the presence of what appeared to be a massive inflow over the main part of the fin towards the root (Figs 6.14 to 6.20). This occurred to some extent for all values of α and δ. However, tests conducted using wool tufts indicated that there was no flow towards the fin root whatsoever at zero incidence. At non-zero incidence the wool tufts only indicated a small inflow on the upper surface at mid semi-span due to the displacement caused by the tip vortex. The two types of flow-vis results are mainly due to the influence of gravity acting on the flow-vis fluid. Also, with the strong three-dimensionality of the flow over the fin, suctions present on the model would be larger at the root than at the tip. The resulting spanwise pressure gradient would tend to induce the flow within the boundary layer to travel inboard. These effects would be

expected to be shown by the liquid film flow-vis technique as the thin film of liquid was mainly in the low energy flow of the boundary layer. On the other hand, the wool tufts were big enough to be largely outside the boundary layer. They would therefore indicate the direction of the flow outside the boundary layer and would not be affected greatly by gravity.

The inflow indicated by the liquid film flow-vis method appears to have two contrasting regions; a small inflow occurring along the entire chord with a region of stronger inflow between approximately 20 and 30% chord. The region of strong inflow is thought to be caused by the increased effect of gravity on the liquid film in the region of a very low energy, almost separated, laminar boundary layer. Once transition occurs, the now turbulent boundary layer gains energy which results in the reduced effect of gravity on the flow-vis fluid aft of the mid-chord region. The change in inflow at the tip of the fin starts at a position nearer the leading edge of the fin than it does further inboard. It is thought that this is due to the effects of a vortex generated on the end of the fin tip (even at zero incidence - see next paragraph). This vortex moves onto the aerofoil surface and triggers transition of the boundary layer at a more forward point than natural transition occurs further inboard.

The flow-vis patterns on the end of the fin tip indicate the presence of a vortex formation, even at zero incidence (Figs. 6.14,

6.15, 6.16). The main cause of the vortex is the sharp corner on the fin tip near the leading edge. A separation occurs on the end of the fin close to the leading edge. This is followed by the formation of a vortex which attaches itself to the end of the fin (Fig. 6.16). The vortex forms into a horseshoe pattern as it proceeds rearwards. The arms of the horseshoe vortex are drawn towards the sharp edges of the fin end by the local pressure gradients (the pressures on the main fin surfaces are lower than those on the end of the fin). At approximately 20% chord the vortices separate at the sharp corner on each side of the fin. There is no evidence in the flow-vis patterns that these vortices reattach themselves to the aerofoil surface. However, as discussed previously, the separated vortices do appear to have the effect of tripping the laminar boundary layer on the fin surfaces near the tip.

NON-ZERO INCIDENCE (CONTROL SURFACE UNDEFLECTED)

Flow visualisation patterns on the fin at non-zero incidence (Fig. 6.15) show similar features to those at $\alpha = 0^{\circ}$. Of particular note is the fact that on the upper surface at $\alpha = 5^{\circ}$, the region of rapid inflow (as depicted by the liquid film) occurs nearer the leading edge than it does at zero incidence. This is thought to be due to the much higher velocity peak triggering boundary layer transition at an earlier point. The formation of the classical tip vortex can be seen on the upper surface of the fin (Fig. 6.15). This vortex causes displacement of the flow on inboard sections of the model resulting in a

small amount of genuine inflow (indicated by the wool tufts - Fig. 6.16).

The horseshoe vortex seen on the end of the fin tip at zero incidence also exists but its behaviour is modified by the flow around the fin tip from lower to upper surface. At $\alpha = 5^{\circ}$, the pressure gradient is sufficient to force both arms of the horseshoe vortex to separate at the sharp edge on the upper surface. However, the vortex arm which is nearer the lower surface does not achieve this until it is near the trailing edge. Careful examination of the flow patterns reveals that the direction of rotation of the fin end horseshoe vortex and the vortex on the upper surface of the fin (caused by flow around the tip of the fin due to pressure gradients) are opposite. There is obviously a complex interaction between the two vortices but it appears that the classically formed tip vortex is the most dominant.

NON-ZERO CONTROL SURFACE DEFLECTION (ZERO INCIDENCE)

$\delta = 5^{\circ}, 10^{\circ}$

The flow features of particular interest for the case of a deflected control are the fin tip vortex and the influence of unsealed gaps at the leading edge and at the ends of the control surface (Figs. 6.17,6.18). At the outboard end of the control surface the fin tip vortex appears to be dominant and affects approximately 15% of the control surface span for deflections

of 5° and 10°. Leakage through the gap at the outboard end of the control surface from lower to upper surface is detectable but it is dominated by the main fin tip vortex. Gap flow effects can also be seen to be occurring at the inboard end of the flap where wool tufts indicated the presence of a weak vortex at small control deflections. As the control surface was deflected further, the end gap increased in size, thereby enabling greater flow leakage to give a stronger vortex.

Flow visualisation patterns on the lower surface of the flap (Figs. 6.17, 6.18) show strong effects of spanwise flow towards each end of the control surface where leakage through the gaps is occurring. With the control surface deflected at 10°, a short separation bubble occurs on the upper surface of the flap near the point where the rounded nose blends into the straight profile of the trailing edge. This separation is probably caused by the rapid change of curvature at this point which results in a steep pressure gradient.

$\underline{\delta = 15^{\circ}}$

With the control deflected to 15° (Fig. 6.19) the influence of the fin tip vortex over the outboard end of the control is very strong. The short separation bubble near the leading edge of the control still exists but after reattachment, the flow on the upper surface over the mid semi-span portion of the flap separates again at approximately $\frac{3}{4}$ flap chord. At the outboard end, the fin tip vortex allows the flow to remain attached to the

control surface right to the trailing edge. Flow through the inboard edge gap is also sufficient to form another vortex over the inboard edge of the control, thereby maintaining attachment of the flow in this region.

$\delta = 20^{\circ}$

For a deflection of 20° the flow over the middle portion of the control surface separates almost immediately after reattachment of the first separation bubble (Fig. 6.20). Vortex effects at each end of the flap are very strong and maintain attachment of the flow over approximately 25% of the span, measured from each end (i.e. total of 50% of the control surface span affected by vortex flow). Strong spanwise flows towards each end of the control surface occur on the lower surface of the flap. Fig. 6.21 shows the interpretation of the flow-vis patterns for a deflected control.

The flow-vis studies show that the influence of vortex flows over the control surface are significant, even for small values of incidence and control deflection. These effects, especially those near the tip of the fin will have important consequences for both the steady and unsteady hinge moments.

6.2.6 Conversion of steady pressure measurements on control surface to hinge moments for comparison with unsteady data

Figs. 6.22 and 6.23 show how the steady pressure data at two spanwise stations was manipulated to obtain quasi-steady information for comparison with unsteady data. The procedure was as follows:-

1). Measure steady pressure distributions on upper and lower surface of model at several values of control surface deflection (Fig2. 6.22a, 6.23a).

2). Obtain the pressure difference between upper and lower surface (Figs. 6.22b,6.23b) and non-dimensionalise with respect to control surface deflection angle. For small deflection angles (up to $\delta = 6°$) these pressure loadings at each spanwise station collapse onto a single curve (Figs. 6.22c, 6.23c).

3). The control surface hinge moment coefficient was obtained by integration of the pressure loadings (see Chapter 6.3.3). The amplitude normalised quasi-steady hinge moment for small amplitude oscillations was then obtained from the slope of the $C_{h_s} - \delta$ curve at the particular value of δ

about which the oscillation occurred (Figs. 6.22d, 6.23d).

At mid semi-span (y/s = 0.6213) the $C_{h_s} - \delta$ curve is linear for control deflections of up to approximately 10°. The variation of section hinge moment with deflection at a station near the tip of the fin does not show the same degree of linearity due to the complex interaction of vortices in this area. The large suctions produced by the tip vortex on the upper surface of the control also lead to a much greater slope of the $C_{h_s} - \delta$ curve at y/s = 0.9452 when compared with that near the centre of the control. The value of the quasi-steady hinge moment for the case of zero mean control surface deflection and incidence was obtained by calculating the slope of the $C_{h_s} - \delta$ curve from the steady data measured at $\delta = 2°, 4°$ and 6° (Figs. 6.22d, 6.23d).

6.3 Unsteady Pressure Measurements On Fin And Control Surface For The Case Of Zero Incidence And Mean Control Deflection

The mean steady pressure distributions were recorded for the cases of both a stationary and for an oscillating control surface. It was found that in all of the oscillatory cases (all values of ω^*, α and δ_m) the mean pressures were the same as those measured when the control was static (to within experimental accuracy). The steady flow characteristics discussed in the previous paragraphs are therefore of relevance to the analysis of the unsteady data.

6.3.1 Unsealed gap between fin and control surface leading edge - pressure loadings

Typical unsteady pressure distributions measured at values of reduced frequency between 0.0 and 2.0 are shown in Figs. 6.24 to 6.27. The effects of the unsealed gap at the control surface leading edge can be seen in the real part of the unsteady pressure loadings where a drop in loading occurs on the fin just forward of the control surface leading edge. Comparison of the loadings at mid semi-span and at a point near the outboard end of the fin show the strong influence of three-dimensional effects. The influence of the vortex formation at the fin tip is present even for the small amplitude control deflections prevailing in the tests ($\delta_a = 1°$). For the case of symmetric mean flow conditions over the fin ($\alpha = 0°$, $\delta_m = 0°$) the tip vortex is generated cyclically on both upper and lower surface by the oscillation of the control. The main effect of the tip vortex is to increase the real part of the loading on the rear of the control surface. This will obviously increase the magnitude of the section hinge moment. The amplitude of the imaginary part of the pressure loading on the control near the tip of the fin is less than that at mid semi-span for a given frequency of oscillation. The dip in the imaginary part of the chordwise loading near the fin tip, just aft of the hinge line, is thought to be due to the complex interactions between the tip vortex and flow through the gaps at the control surface tip and leading edge. The development of the unsteady pressures on the

control surface at mid semi-span, during a cycle of oscillation is shown in Fig. 6.28. For clarity, only the upper surface pressures are shown (those on the lower surface being equal but 180° out of phase) starting at the downstroke of the control as it passes through its mean position (maximum velocity). The pressure distributions at equal time intervals during the next half cycle show how the reduced frequency parameter affects mainly the in-quadrature component of unsteady pressure at the frequencies considered.

More detailed unsteady pressure loadings on the control surface over a range of reduced frequencies are presented in Figs, 6.29 to 6.34. Three-dimensional effects are limited to areas very close to the ends of the control surface, especially at low values of reduced frequency. As frequency increases, the loadings (both real and imaginary components) become more three-dimensional. This is due to the flow structures at the middle and ends of the flap being affected to different degrees by the reduced frequency parameter.

As discussed in Chapter 3.3.1, due to the lack of space for installing pressure tappings, the pressure loadings on the control surface at zero incidence were obtained by measuring pressures on one surface only. Pressures on the other surface were obtained by assuming that unsteady loadings on each side of the control, at the same chord and spanwise location, were of equal amplitude but out of phase by 180°. This assumption was confirmed

by measurement of pressures at the few tappings provided on the sparsely tapped surface (Fig. 3.26). The real and imaginary components of unsteady pressure occurring at points on the model on opposite surfaces were found to be within 1.5% of each other This excellent degree of symmetry was found at all the span and chordwise positions on the control where comparison was possible. This problem did not arise for non-zero values of incidence or mean control deflection since the pressure tapped surface could be tested as both upper and lower surface.

6.3.2 Effect of control surface oscillation amplitude on unsteady pressure loadings.

Unsteady pressure measurements made for various amplitudes of control surface oscillation show little effect of amplitude on the results (Figs. 6.35, 6.36). This was to be expected since the measurements of steady pressures at control deflections between $\pm 6^{\circ}$ showed a high degree of linearity (see Chapter 6.2.6). These results cannot be extrapolated to cases of oscillation about extreme values of mean control deflection where even the steady pressures become non-linear ($\delta_m >$ approx. $8^{\circ} - 10^{\circ}$).

The negligible effect of amplitude on the unsteady pressures at zero incidence and control deflection indicate that comparison of amplitude normalised data for $\delta_a = 1^{\circ}$ with theoretically predicted data can be made.

6.3.3 Unsteady hinge moments

METHOD OF CALCULATION

Steady and unsteady hinge moments were obtained by integration of pressure loadings on the control surface in two stages. Firstly, the chordwise pressures were integrated to obtain the section hinge moment coefficients. The overall control surface hinge moment was then obtained by spanwise integration of the section coefficients.

Initial chordwise integrations were obtained using Simpsons rule. However, although the experimental data was fairly smooth with little scatter, an improvement in the accuracy of the integration was obtained by fitting a least squares polynomial through the pressure data. This technique was particularly useful for the in-phase pressure loadings at high frequency, due to the fact that the loadings crossed the zero pressure line. The hinge moments were therefore obtained by subtraction of two components which could be of similar magnitude. This could, therefore , give rise to the possibility for large errors to occur if consideration was not given to the accuracy of the computation.

It was found that a 5th order, unweighted, least squares curve fit produced good results (the smoothness of the fit being assessed graphically - Fig 6.37). The curve fitting routine was built into the data reduction program. Once the coefficients of

the polynomial were known, integration to obtain the hinge moment was an analytical formality. Due to the irregular spanwise distribution of section hinge moment at the ends of the flap (see following paragraph) the polynomial curve fitting method was not appropriate for performing spanwise integration of the hinge moments. A simple trapezium rule was used in this case.

VARIATION OF SECTION HINGE MOMENT WITH REDUCED FREQUENCY

The variation of section hinge moment coefficient with reduced frequency at various spanwise locations on the control surface are shown in real and imaginary form in Fig. 6.38 and in amplitude and phase representation in Fig. 6.39. There is little scatter in the experimental data. The real part of the hinge moment varies non-linearly with reduced frequency, mainly as a result of the virtual inertia term which varies as a function of $(\omega^*)^2$. Variation of the imaginary parts of the hinge moment with frequency is very linear at all spanwise stations. No unsteady data was measured below $\omega^* = 0.175$ so the dotted extrapolation of the imaginary components to zero has been performed intuitively. The in-phase components of hinge moment at $\omega^* = 0$ are the quasi-steady values.

The strong influence of end effects can be seen in the spanwise distributions of section hinge moment (Fig. 6.40). These effects are most prevalent in the real part of the section hinge moment near the outboard edge of the control surface. The main effect of the fin tip vortex is noticeable in the quasi-steady

component. As reduced frequency increases, unsteady effects are superimposed on the quasi-steady values. Three-dimensional effects over the entire span on the section hinge moment are more evident in the imaginary components than they are in the real parts, except right at the ends of the control surface.

VARIATION OF OVERALL CONTROL SURFACE HINGE MOMENT WITH REDUCED FREQUENCY

Due to the limited extent of the end effects on the control surface, the overall control surface hinge moment variation with frequency is dominated by the flow over the mid semi-span sections of the control (Figs. 6.41, 6.42). The in-phase hinge moment varies with ω^* according approximately to a square power law (the virtual inertia effect), while the in-quadrature component varies linearly. Fig. 6.42 shows that amplitude of the unsteady hinge moment at $\omega^* = 2.0$ is approximately four times the quasi-steady value and that it lags the control surface displacement by approximately 90°. The main effects of Reynolds number are that increasing Re from 0.58×10^6 to 1.15×10^6 leads to a reduction of the quasi-steady component by approximatel 15% (Figs. 6.41, 6.42). The effect of Re on the unsteady loadings as ω^* increases from zero is very small for both real and imaginary components (see next paragraph).

6.3.4 Effect of Reynolds number

Unsteady pressure loadings at mid semi-span for two values of reduced frequency show that the effects of Reynolds number on both real and imaginary components is very small (Figs. 6.43 to 6.46).The pressure loadings are most affected by Reynolds number in the region of the control surface hinge line. This is to be expected since complex interactions take place in this region between the boundary layer flow over the fin with the flow passing through the gap at the leading edge of the control surface. The interactions will be oscillatory in nature and could include areas of locally separated flow. To explain the effects of Reynolds number more fully it would be necessary to examine the boundary layer flow around the model. Although a knowledge of the steady boundary layer is of some importance, the unsteady influences of the oscillating control on the boundary layer may be more significant. The experimental determination of these latter effects would be an extremely difficult undertaking.

The effect of Reynolds number on the unsteady hinge moments is fairly constant across the span of the control surface and appears to be independent of the reduced frequency parameter (Fig. 6.47). The effect of increasing Reynolds number is to reduce the magnitude of the in-phase component and decrease that of the in-quadrature component by approximately equal amounts. This results in the amplitude of the hinge moment being reasonably

unaffected but the phase lag being increased at the higher values of Re. Increasing Re from 0.58×10^6 to 1.15×10^6 results in an increase in phase lag of approximately 6° to 8° (Fig. 6.42).

The fact that Reynolds number mainly affects the quasi-steady component of the in-phase loadings is to be expected for the following reasons: It is well known that boundary layers can have a significant effect on the steady (and therefore quasi-steady) loadings on wings, especially where control surfaces having gaps at their leading edges are concerned. However, the unsteady component of the loading in-phase with the motion of the control surface arises mainly from the virtual inertia forces associated with the acceleration of the entire flow field around the fin (especially as reduced frequency increases). Since the momentum in the boundary layer constitutes a very small part of that in the total flow field, the virtual inertia forces could be expected to be relatively independent of Reynolds number.

6.3.5 Effect of sealing the gap at the leading edge of the control surface

Theoretically, a sealed gap at the control surface leading edge results in a singularity of the type $\log (1/(x-x_{hinge}))$ in the real part of the pressure loading at the hinge line. For an open gap this singularity rapidly changes from being logarithmic to being a square root function as gap width is increased. This difference can be seen in the experimental data for unsteady

pressure loadings at mid semi-span (Figs. 6.48 to 6.51). The in-phase component of the pressure loadings towards the leading edge of the control are significantly larger for the case of an unsealed gap. However, this only results in slightly larger hinge moments due to the short length of the moment arm of the pressures in this region. Little influence of sealing the control surface gap can be found in the in-quadrature components of the unsteady loadings.

Another result of sealing the gap can be seen in the in-phase component of the unsteady loading on the fin, just forward of the control surface leading edge. For the case of an open gap, the chordwise loading in this region starts to rise due to the singularity at the hinge line but suddenly drops just in front of the control surface (theoretically it would drop to zero). When the gap is sealed, the loading on the fin increases consistently with the hinge line singularity.

The effects of sealing the control surface leading edge gap on the unsteady section hinge moment coefficients are of similar magnitude for both in-phase and in-quadrature components, and are not affected significantly by changes in Reynolds number or reduced frequency (Figs. 6.52, 6.53). The overall effects of gap sealing on the total control surface hinge moment are presented in Figs. 6.54 and 6.55.

6.4 Comparison Of Experimental Data With Theoretical Predictions

Theoretical predictions for the unsteady pressure loadings on the fin were produced using the lifting surface model described in Chapter 5. These predictions are compared with experimentally determined data obtained with the fin at zero incidence and with the control surface oscillating about a mean deflection of 0°. The following comparisons are for the case of a sealed gap between the fin and the leading edge of the control.

Before comparisons between experiment and theory could be made it was necessary to modify the theoretical predictions due to a limitation of the numerical procedures involved (see Chapter 5.3). This defect caused a spurious undulation in the chordwise pressure loadings where a control surface was included. The pressure loadings produced by the model were smoothed before comparison with experimental data by averaging the peak to peak amplitudes of the undulations (Fig. 6.56). For the chordwise section at $y/s = 0.181$, no modifications to the theoretical predictions were required since the section did not include the control surface. Comparisons of theoretical and experimental unsteady pressure loadings on the fin are presented in Figs. 6.57 to 6.63 for quasi-steady conditions and for four values of reduced frequency.

IN-PHASE COMPONENTS OF PRESSURE LOADINGS

Agreement between theory and experiment is very good for the in-phase components of unsteady pressure at a station inboard of the control surface ($y/s = 0.181$). Agreement is also reasonable for stations on the inboard edge of the control and at mid semi-span ($y/s = 0.3596, 0.6213$). At mid semi-span, theory and experiment agree very well on the fin up to about 50% chord. The rise of the loading on the fin towards the hinge line pressure singularity is overpredicted by theory, probably due to boundary layer displacement effects. For the quasi-steady case (Fig. 6.57), the difference between experiment and theory at $y/s = 0.6213$ for loadings on the control surface can be attributed to the effects of the boundary layer and aerofoil thickness. Although agreement is relatively good on the control at this spanwise position, especially near the hinge line, large differences in hinge moment can occur since the largest pressure differences exist towards the trailing edge. As reduced frequency is increased from zero (quasi-steady) the unsteady effects are well predicted by theory at the three inboard stations.

At low frequency the theoretical model severely underestimates the loading on the control surface near the tip of the fin ($y/s = 0.9452$) due to its inability to simulate the oscillating fin tip vortex. It should be regarded as fortuitous that agreement between theory and experiment at this station improves for values of reduced frequency above 1.0.

IN-QUADRATURE COMPONENTS OF PRESSURE LOADING

Agreement between experiment and theory for the in-quadrature component of the unsteady pressure loading is much better than for the in-phase components at all spanwise stations, and over the entire range of reduced frequencies. The only place where differences are marked is at the leading edge of the control surface, close to the tip of the fin, where a discontinuity in the experimental data occurs. This is undoubtedly due to the influence of the fin tip vortex and the chordwise gap at the end of the control surface.

HINGE MOMENTS

Overall control surface hinge moments were evaluated from the theoretically predicted pressure loadings for comparison with experimental data. For interest, comparisons were also made with predictions obtained from a two-dimensional flat-plate theory (Theodorsen[2]), assuming two dimensional flow over the entire control. The comparisons are presented in Figs. 6.64 and 6.65.

The two-dimensional theory fails to predict either the in-phase or in-quadrature components of hinge moment to any satisfactory degree, with errors of approximately 100% at all frequencies. The predictions obtained from the three-dimensional lifting surface theory do, however, agree fairly closely with experiment. The

quasi-steady hinge moment is overpredicted by approximately 20% but the effects of increasing ω^* on the in-phase components are accurately modelled. Differences between experiment and theory for the in-quadrature components are of the order of 10%, with the theoretical value being too large.

If the comparisons between experiment and theory are made with regard to the amplitude and phase of the overall control surface hinge moment (Fig. 6.65) the lifting surface model appears even better. Phase angle is predicted to within approximately 6% and amplitude to within about 15% at the worst case ($\omega^* = 0$). As reduced frequency increases from zero the error in the predicted hinge moment amplitude is gradually reduced until at $\omega^* = 2.0$ the difference is approximately 10% (theory overpredicting).

The inability of the theoretical model to accurately predict the unsteady airloads at very low values of ω^* is due to the strong influence of viscosity and aerofoil thickness on the loadings under almost quasi-steady conditions.However, as the frequency parameter increases, the unsteady force components relating to virtual inertia and damping become increasingly important. Since these factors are strong functions of the potential flow outside the boundary layer it would be expected that the lifting surface model would predict these fairly accurately, as confirmed by Figs. 6.64 an 6.55 . For the case of the fin at zero incidence, with the control surface oscillating about a mean undeflected condition, the influence of the tip vortex is limited to a small region at the outboard end of the

control surface. Therefore, its omission in the theoretical model is of little importance to the overall control surface hinge moment. If the fin were at non-zero incidence or the flap were oscillating about a deflected condition, the vortex would affect a larger area of the control surface. The theoretical model therefore becomes increasingly inaccurate as incidence or control deflection are increased. For the case of the control oscillating about a mean deflection, the influence of the vortex generated at the inboard end of the control further invalidates the theoretical model.

6.5 Effect Of Mean Control Deflection And Fin Incidence On Unsteady Loadings

Compared with the symmetric, non-lifting flow case, the characteristics of the steady flow around the fin were significantly affected by the model being set at incidence or the control surface being deflected (see Chapter 6.2). As the unsteady loadings are closely related to the steady flow condition,tests were conducted to evaluate the effects of both incidence and mean control surface deflection on the unsteady loadings. The study was limited to measuring the unsteady pressure distributions at spanwise positions near the centre and at each end of the control surface at a limited number of frequencies. A summary of the results is presented in Figs. 6.66 to 6.79.

6.5.1 Control oscillating about a mean deflection angle ($\alpha = 0$)

The unsteady pressures on both fin and control surface show a strong dependence on the mean control deflection angle, especially on the upper surface where the effects of gap flow and vortex formations occur (Figs. 6.66 to 6.69). At a mid semi-span position ($y/s = 0.6213$) where the influence of the tip vortex is minimal, the unsteady pressures remain only slightly affected by the mean control deflection angle until a deflection of approximately 15° is reached. At this point separation of the flow on the upper surface begins to occur, starting from the trailing edge and progressing towards the leading edge as control deflection increases further (see Chapter 6.2). The effect of this separation is shown in both the real and imaginary components of the unsteady pressure distributions. The unsteady pressures on the lower surface show only slight changes with increasing mean control deflection since the flow remains attached along the entire chord of the control. The in-phase component of unsteady pressure recorded on the lower surface, near the hinge line shows a large drop with increasing control deflection. This is thought to be mainly due to the gradual movement of the pressure tapping into the shadow of the gap between the fin and leading edge of the control. There are also complicated flow interactions occurring in this region caused by the geometry of the model and by boundary layer effects. A detailed investigation would be required to determine the exact nature of these flow phenomena.

Fortunately, the reduction in the lower surface pressure peak with increasing control deflection only happens in the region of the hinge line and does not significantly affect the hinge moment. On the other hand, the influence of gap flow interactions on the upper surface can be of critical importance as they could strongly affect the development of flow separation. The flow visualisation tests for static model conditions showed that no separation of the flow from the trailing edge occurred on the control surface at mid semi-span at $\delta_m = 10^\circ$. However, under dynamic conditions it is quite possible that unsteadiness in the flow triggers separation at much lower values of δ_m and this could be a function of ω^*. Such a phenomenon may be indicated by comparing the pressures on the upper surface for a mean control deflection of 10° at two reduced frequencies (Figs. 6.66, 6.67). At the lower reduced frequency ($\omega^* = 0.698$) the pressure loading is similar to that at $\delta_m = 0^\circ$. At $\omega^* = 1.396$, the pressure loadings at $\delta_m = 10^\circ$ look more like that at $\delta_m = 15^\circ$.

Small changes in the unsteady pressures on the main part of the fin, forward of the control surface, occur as mean control deflection is increased. This is caused mainly by non-linear effects caused by the boundary layer and profile thickness.

Compared with the unsteady pressure loadings at mid semi-span those near the tip of the fin ($y/s = 0.9452$) show a completely different variation with increasing control mean deflection (Figs. 6.68, 6.69). This is mainly due to the dominance of

vortex structures which occur near the tip of the fin. For control surface oscillation about a zero mean deflection angle, a tip vortex is produced cyclically on each surface at the same frequency as the control surface oscillation. However, if the control surface is oscillated about a non-zero mean deflection then, provided the amplitude of oscillation is less than the mean deflection angle, a tip vortex will only exist on one surface of the model (the suction side). The oscillation of the control will cause this vortex to cyclically vary in strength, resulting in an oscillatory pressure loading. The measured unsteady pressure distributions on the control (Figs. 6.68, 6.69) confirm this explanation. The in-phase components of the pressures on the control are symmetric on both surfaces for $\delta_m = 0^\circ$ with a large suction over the rear part of the control associated with the oscillating vortices. When the mean control deflection angle is non-zero, the rear suction peak on the lower surface, near the trailing edge, ceases to exist. This is due to the elimination of the vortex on this surface. Conversely, the loading on the upper surface still shows the influence of a vortex structure which grows in strength as mean control deflection increases. The chordwise gap between the outboard end of the control and the fin tip increases as control surface deflection increases, allowing flow from the lower surface to leak around the end of the control. As mean flap deflection increases, the effect of interference between the upper surface vortex and flow around the end of the control is increased. The results of this interference can be seen in the real parts of the unsteady

pressures on the upper surface especially at $\delta_m = 15^\circ$ and $\delta_m = 20^\circ$. The tip vortex associated with control deflection has very little influence on the unsteady pressure components in-quadrature with the control surface motion. It is only at very high deflection angles ($\delta_m = 20^\circ$) that the effects of interference between the tip vortex and flow around the end of the control have any effect on the imaginary pressure components. The small influence of the tip vortex on the imaginary parts of the upper surface pressures is probably due to the fact that the oscillation of the control surface causes the vortex to move in a plane normal to the fin surface. This leads to negligible phase shifts at points on the surface.

The development of the unsteady pressures on the surface of the flap during a cycle of oscillation for the case of a non-zero mean deflection is shown in Figs. 6.70 and 6.71 at spanwise stations $y/s = 0.6213$ and $y/s = 0.9452$. The asymmetry of the in-phase components of the pressures on upper and lower surface near the tip of the fin is particularly noticeable. An important point to remember is that only the first harmonic of the unsteady pressures was measured. With the equipment used it was not possible to measure higher harmonic components but a visual assessment of the pressure signals was made using an oscillascope. The ability to detect second and third harmonics was somewhat limited at higher fundamental frequencies due to the attenuation of the pressure tubing system. However, it did appear that for pressures on the control near the tip of the fin where vortex

interactions were dominant there were additional unsteady pressure harmonics present. Further investigations using a spectrum analyser would be required to confirm these observations. These harmonics, which would be associated with non-linearities in the flow, would be expected near the tip of the fin where flow interactions are complex.

For control oscillations about a non-zero mean deflection the unsteady pressures at mid semi-span were only slightly affected by sealing the gap until a mean deflection of 15° (Figs. 6.72, 6.73). With the gap open under steady conditions at this value of control deflection, the flow separated on the upper surface at approximately the $\frac{3}{4}$ flap chord position. With the gap sealed, this separation did not occur. The absence of flow separation for the case of a sealed gap is strongly evident in the in-quadrature component of unsteady pressure (Fig. 6.73). It is therefore clear that for this particular configuration of gap geometry, the influence of flow through the gap on the unsteady hinge moments is small until it becomes responsible for the formation of separations. With other gap geometries such as the more streamlined ones found on aircraft configurations, the effect of gap flow may be more significant even at very low values of incidence or control deflection.

At mid semi-span, the unsteady section hinge moments , for cases of various mean control deflection, show a strong dependence on deflection angle (Fig. 6.74). Increasing deflection results in

an increase in the real components of hinge moment with a smaller decrease in the imaginary component. The section hinge moments near the tip of the fin (Fig. 6.75) show that the tip vortex on the upper surface causes the in-phase components of hinge moment to be increased considerably as control deflection increases. The in-quadrature components remain unaffected by the tip vortex, even at large control surface deflections.

6.5.2 Unsteady loadings with fin set at incidence ($\delta_m = 0°$)

As for the case of a mean control deflection, placing the fin at incidence results in asymmetric flow conditions over the upper and lower surfaces. The resulting pressure difference causes flow through the gap at the control surface leading edge together with the formation of a tip vortex on the upper surface. Unsteady pressures measured at two spanwise stations (at mid semi-span and near the tip) show the effects of these flow conditions at incidences of $5°$ and $10°$ (Figs. 6.76, 6.77).

At mid semi-span the unsteady pressures on both upper and lower surfaces of the control are strongly affected by incidence, especially the components in-phase with the control surface motion. Undoubtedly, interaction of the gap flow and the boundary layer over the fin is the main cause for the effects of incidence shown in Fig. 6.76. Due to its complexity, the nature of the gap flow is difficult to identify. There may be areas of local flow separation and reattachment which in

turn may be significantly affected by the oscillation frequency of the control. Further studies would be required to provide adequate explanations for the pressure distributions of Fig. 6.76.

The tip vortex structure generated by placing the fin at incidence clearly explains the unsteady pressure distributions at y/s = 0.9452 (Fig. 6.77). The in-quadrature components are relatively unaffected by incidence for the reasons discussed previously in Chapter 6.5.1 for the case of non-zero mean control deflection. The in-phase components of the pressures on the upper surface show the influence of the tip vortex which increases with increasing incidence. This results in very large oscillatory pressure amplitudes near the trailing edge. However, the in-phase pressures on the lower surface show a different form than for the case of zero incidence and a deflected control. The reason for this is that although both configurations (incidence and mean control deflection) generate vortices on the tip, the exact nature of the flows in each case is different. For the case of incidence alone, the chordwise gap at the end of the control surface remains very small and does not allow significant interference from leakage; therefore the oscillation of the control about zero mean deflection will cause different vortex formations and interactions from those caused by the same oscillation about a mean deflected state at zero incidence.

The overall effect of incidence on the unsteady hinge moments is slightly less than the effects of oscillation about a mean deflected state at zero incidence (Figs. 6.78, 6.79). The main

effect of increasing incidence alone occurs near the tip of the fin where the in-phase components are significantly reduced as incidence increases. As for the case of a mean control deflection, increasing incidence does not affect the basic way in which the hinge moment varies with reduced frequency: the real part comprising a quasi-steady component which is modified by virtual inertia effects as the imaginary part increases linearly with frequency.

7 CONCLUSIONS

7.1 Survey

A study has been conducted to determine the unsteady pressure loadings acting on a rectangular fin of aspect ratio 1.5. Unsteady hinge moments have been measured on a 25% chord, part span, trailing edge control surface which was oscillating harmonically at values of reduced frequency up to 2.0. The study included an investigation of three-dimensional effects on the unsteady flow since little previous work on such a configuration had been conducted.

A wind tunnel model was designed, constructed and tested. Unsteady loadings on the model were obtained by integration of pressure measurements which were made using the tubing and Scanivalve method. To ensure maximum accuracy of the results, a detailed study was conducted in order to calibrate the transmission characteristics of the pressure measuring system.

Some comparisons of the experimental results were made with predictions obtained from a lifting surface model supplied by the R.A.E. at Farnborough.

The conclusions of these investigations can be divided into four parts:-

7.2 Pressure Loadings And Control Surface Hinge Moments

7.2.1 Variation of hinge moment with ω^*

For all values of steady incidence and mean control surface deflection the magnitude and phase of the unsteady control surface hinge moment is significantly dependent on the reduced frequency ω^*. As ω^* increases so does the magnitude of the hinge moment and its phase lag with respect to the displacement of the control. For a reduced frequency of 2.0 the amplitude of the unsteady hinge moment is approximately four times the value for a steady state deflection and it lags the displacement by approximately 90°.

The component of the unsteady hinge moment in-quadrature with the displacement of the control varies linearly with ω^*. The in-phase component comprises a quasi-steady value at $\omega^* = 0$ which varies approximately as a function of $(\omega^*)^2$:- the virtual inertia effect.

In underwater applications, the high density of the working medium results in large hydrodynamic forces compared to the inertia loads of the control itself. The significant effect of the unsteady hydrodynamic loads cannot, therefore, be neglected when analysing the response of an active control system, especially when the actuator system is reaching the limits of its capabilities.

7.2.2 Effects of Reynolds number

Within the range tested, Reynolds number did not affect the unsteady pressure loadings on the fin and control by any significant amount. Compared to results at Re = 0.58×10^6 the unsteady control surface hinge moments at Re = 1.15×10^6 were increased in amplitude by less than 5% (at zero incidence and mean control deflection). This was accompanied by an increase in phase lag of approximately 10% at low values of reduced frequency ($\omega^* < 1$). As ω^* increased to 2.0 the effect of Reynolds number on the phase lag was reduced to less than 4%.

Besides the effect on the quasi-steady component, no significant variation of Reynolds number effects with reduced frequency were noticeable on the in-phase components of the unsteady hinge moments. This was expected since the unsteady components of the in-phase hinge moment is associated with virtual inertia. The virtual inertia term arises from the acceleration of the entire flow field around the fin. As the boundary layer is only a small proportion of this flow field, the effects of Reynolds number on the virtual inertia would be expected to be small, unless changes in Reynolds number were to result in large flow separations.

7.2.3 Effects of sealing control surface gap

Sealing the gap at the leading edge of the control surface did not result in significant changes in the unsteady hinge moments for

the case of zero incidence and mean control surface deflection. The main effect of sealing the gap was to alter the shape of the in-phase pressure peak near the leading edge of the control surface. Since this effect only occurred locally in the region of the hinge line, its effect on the overall hinge moment was very small.

When the fin was at incidence or the control was oscillating about a non-zero mean deflection, the influence of sealing the gap was much larger than for the non-lifting configuration. This is due to the greater influence of flow through the control surface gap on the upper surface boundary layer. With the gap open it was found that flow separation on the upper surface of the control occurred at lower values of α and δ_m than it did for a sealed gap.

7.2.4 Effect of amplitude of control surface oscillations

For the case of low incidence and mean control surface deflection ($\alpha < 5^\circ$, $\delta_m < \pm 8^\circ$) the amplitude normalised unsteady pressures were the same for control surface oscillation amplitudes between $\pm 0.5^\circ$ and $\pm 2.0^\circ$. However, for cases of high mean incidence or control deflection, the non-linearity of the steady pressures with deflection meant that the unsteady pressures also become dependent on the control surface oscillation amplitude.

7.3 Three-Dimensional Effects

It has been found that vortex formations on the fin significantly affect both the mean and unsteady pressure loadings on the fin and control surface. These effects increase with increases in incidence and mean control deflection. The large suctions associated with these vortices result primarily in large increases in the hinge moments.

7.3.1 Zero mean lifting conditions ($\alpha = 0^\circ$, $\delta_m = 0^\circ$)

For the case of the fin at zero incidence and the control surface oscillating about a non-deflected position, unsteady pressure loadings indicate the presence of small tip vortices on both surfaces of the model. These vortices are shed alternately on each surface as the control moves from a positive to a negative deflection during a cycle of oscillation. These intermittent vortices result in large oscillatory suctions on the outboard end of the control surface and significantly increase the local section hinge moments. There is also evidence that trailing vortices are also shed at the inboard edge of the control surface but that they are much weaker than those at the tip of the fin.

In the steady state, zero lifting configuration, a horshoe vortex is formed on the end of the fin tip (the aerofoil shaped surface formed by the cutoff tip). This vortex causes transition of the boundary layer on the main surfaces at the point where the vortex

separates at the sharp corner on the end of the fin. Transition of the boundary layer near the tip of the fin therefore occurs much nearer the leading edge than it does further inboard.

7.3.2 Three-dimensional flow for the case of non-zero incidence and mean control surface deflection

As incidence or mean control surface deflection is increased, the influence of vortex formations on the tip of the fin and at the ends of the control surface become increasingly important. These vortices, which occur on the low pressure side of the fin, result in large suctions over approximately 25% to 50% (depending on exact values of α and δ_m) of the control surface span and greatly increase the magnitude of the local section hinge moments (up to 100% increase for control deflection of 15°).

Although the vortex formations associated with incidence and control deflection result in higher values of sectional hinge moment at the ends of the control, their presence helps to maintain attachment of the flow on the upper surface of the control, thereby ensuring effectiveness at high values of α and δ_m. In fact, the onset of flow separation over the mid 50% of the control surface span for mean deflections of 15° or more means that the overall unsteady control surface hinge moments do not increase by more than approximately 60% compared to the case of $\delta_m = 0°$.

As incidence or mean control surface deflection is increased, the flow over the control surface becomes strongly dependent on the interaction of the flow through the gap at the leading edge of the control with the boundary layer on the upper surface of the fin. The interference of the tip vortex with flow through the gap at the outboard edge of the control is also important and further investigations are required to examine these effects in more detail.

7.4 Theoretical Modelling

The R.A.E. lifting surface model was able to predict the unsteady control surface hinge moments to a reasonable degree of accuracy for the case of zero incidence and mean control deflection. The quasi-steady hinge moments were overpredicted by approximately 20% but the unsteady effects were predicted to a much better accuracy. At reduced frequencies above 1.0 the amplitude of the theoretically calculated hinge moment was 15% greater than that determined experimentally, and the predicted phase lag was to within 6% of the measured value.

The reasons for the poor prediction of the quasi-steady loadings are the neglect of the theoretical model to account for the effects of viscosity and aerofoil geometry (thickness). As the unsteady effects due to virtual inertia and damping are largely a function of the flow field outside the boundary layer, agreement between experiment and theory is much better for these components of the loading.

It was found that the theoretical model had several limitations which restricts its usefulness for predicting unsteady loadings on low aspect ratio fins with oscillating control surfaces.

Firstly, the theoretical model was not capable of simulating the effect of vortex formations, so the pressure loadings near the tip of the fin were not predicted accurately. Since the extent of these vortices is limited for the case of zero incidence and mean control deflection, the predictions for the overall control surface hinge moment were in reasonable agreement with the experimental values. However, when the fin was at incidence or the control oscillated about a deflected state, experimental evidence has shown that the vortices affect significant areas of the control surface (up to 50%). Therefore, in these cases the theoretical model is incapable of accurate prediction.

The second limitation of the theoretical model concerns deficiencies in the numerical procedures it incorporates. This makes it unable to deal satisfactorily with the pressure singularity which occurs at the control surface hinge line. This results in the theoretically predicted chordwise loadings having undulations along their length. These undulations were smoothed out in the current investigation by averaging of the undulations so it is felt that it was somewhat fortuitous that such good agreement between experiment and theory was achieved.

As a result of the current investigation it is suggested that any

future theoretical models for predicting the unsteady airloads on very low aspect ratio wings with oscillating control surfaces should include provision for the modelling of vortex structures. It is felt that for the case of low aspect ratio a panel method would be more appropriate than a thin wing theory as it allows the effects of thickness and control surface geometry to be included. However, it should be borne in mind that the effects of viscosity are as important as thickness and would thus require inclusion in the model.

7.5 Experimental Technique

This study has shown that small amplitude pressure fluctuations can be measured to a high degree of accuracy at minimal cost using the tubing and Scanivalve system. The method allows a large number of pressures to be measured using the minimum of equipment and enables pressure tappings to be placed in areas of a model where miniature pressure transducers are too large to be installed (e.g. thin trailing edges of wings).

The tubing/transducer system has to be carefully constructed and calibrated to determine its transmission characteristics (attenuation and phase lag). It has been shown that calibration can be achieved to within an accuracy of $\pm 2\%$ for the system used in this study (frequency range = 0 to 80Hz, temperature range = 8 °C to 35 °C, mean static pressure = atmospheric). Calibration was achieved using a computer program based on the theoretical model of Bergh and Tijdeman[38,39]. Results were

compared with experimental calibrations conducted in the laboratory for cases of zero and non-zero (V^c_{max} = 40m/s) flow across the orifice of the pressure tapping.

8 RECOMMENDATIONS FOR FUTURE WORK

The case of zero incidence and control deflection has been dealt with fairly comprehensively in this study. Less work has been conducted with the model at incidence or with the control oscillating about a mean deflection and possibilities for further work using the current experimental facility still exist. Areas for further investigation include:-

1). A more detailed experimental investigation of the nature of the vortex formations associated with incidence and control deflection. This is required for the case of a static and an oscillating control. The investigation could be achieved by using hot wire anemometry or by testing a model in a water tunnel using flow visualisation to depict the vortices using coloured dyes.

2). An investigation of the boundary layer over the fin to determine the exact position of transition and the growth of the boundary layer thickness, especially in the region of the control surface leading edge. This could be combined with a study to look at details of the flow in the vicinity of the gap at the leading edge of the control surface. In order to investigate the flow interactions in the gap region it may be necessary to use a large two-dimensional model to enhance resolution and to allow the necessary instrumentation to be installed. Information obtained from

such studies would provide useful data for assessing and improving existing theoretical models.

3). Comparison of the current experimental results with theoretical predictions obtained using a panel method to allow the effects of geometry to be modelled. This would have to be combined with a boundary layer model (perhaps only quasi-steady) for a fair comparison to be achieved. The representation of vortex formations would also have to be included as the present study has shown that they are extremely important for the case when the control is oscillating about a mean deflection or the fin is at incidence.

REFERENCES

1. Lamb, H. — Hydrodynamics. Dover Publications, 1945.

2. Theodorsen, T. — General Theory Of Aerodynamic Instability And The Mechanism Of flutter. NACA Report No. 496, 1935.

3. Laschka, B. — Interfering Lifting Surfaces In Subsonic Flow. Z. Flugwiss 18, pp 359-368 1970.

4. Davies, D.E. — Calculation Of Unsteady Generalised Airforces On A Wing Oscillating Harmonically In Subsonic Flow. A.R.C. R&M 3409, 1965.

5. Lottati, I. Nissim, E. — Three-Dimensional Oscillatory Piecewise Continuous-Kernel Function Method. Journal of Aircraft Vol. 18, No. 5 pp 346-363, 1981.

6. Hedman, S.G. — Vortex-Lattice method For Calculation Of Quasi-Steady State Loadings On Elastic Wings. F.F.A. Report No. 105, 1965.

7. Abano, E.
Rodden, W.P.
A Doublet Lattice Method For Calculating Lift Distribution On Oscillating Surfaces In Subsonic Flow.
A.I.A.A. Journal Vol. 7
pp 279-285, 1969.

8. Geising, J.P.
Nonlinear Two Dimensional Unsteady Potential Flow With Lift.
Journal of Aircraft Vol. 5
pp 135-143, 1968.

9. Hess, J.L.
The Problem Of Three Dimensional Lifting Surface Potential Flow And Its Solution By Means Of Surface Singularity Distribution.
Computer methods in applied mechanics and engineering Vol. 4
pp 283-319, 1974.

10. Geissler, W.
Nonlinear Unsteady Potential Flow Calculations For Three Dimensional Oscillating Wings.
A.I.A.A. Journal Vol 16
pp 1168-1174, 1978.

11. Morino, L.
Tseng, K.
Steady,Oscillatory And Unsteady Subsonic And Supersonic Aerodynamics (SOUSSA) For Complex Aircraft Configurations.
AGARD-CP-227, pp 3.1-3.14, 1977.

12. Ashley, H.
Some Considerations Relative To The Prediction Of Unsteady Airloads On Lifting Configurations.
Journal of Aircraft Vol. 8, No. 10,
1971.

13. Rowe, W.S.
Cunningham, H.J.
On The Convergence Of Unsteady Generalised Aerodynamic Forces. Journal of Aircraft Vol. 21, No. 6, 1984.

14. Lambourne, N.C.
Experimental Techniques In Unsteady Aerodynamics. AGARD-R-679, 1980.

15. Förching, H.
Wind Tunnel Test Techniques For The Measurement Of Unsteady Airloads On Oscillating Lifting Systems And Full Span Models. AGARD-R-679, 1980.

16. Telionis, D.P.
Unsteady Boundary Layers, Separated And Attached. AGARD-CP-227, 1978.

17. Koromilas, C.A.
Telionis, D.P.
Unsteady Laminar Separation: An Experimental Study. Journal of Fluid Mechanics Vol. 97 pp 347-384, 1980.

18. Mabey, D.G.
A Review Of Some Recent Research On Time-Dependent Aerodynamics. Aeronautical Journal, Feb. 1984.

19. Lambourne, N.C.
Et al.
Compendium Of Unsteady Aerodynamic Measurements. AGARD-R-702, 1982.

20. Försching, H.
Some Remarks On The Unsteady Airloads On Oscillating Control Surfaces In Subsonic Flow. AGARD-CP-227, 1981.

21. Houwink, R.
Some Remarks On Boundary Layer Effects On Unsteady Airloads.
AGARD-CP-296, 1981.

22. Geissler, W.
Viscous Effects On Unsteady Airloads Of Oscillating Configurations.
AGARD-CP-296, 1981.

23. Zimmermann, H.
Introductory Remarks On Boundary Layer Effects On Unsteady Airloads.
AGARD-CP-296, 1981.

24. Küssner, H.G.
Non-Stationary Theory Of Airfoils On Finite Thickness In Incompressible Flow.
AGARD manual on aeroelasticity part 11, Chapter 8.

25. Geissler, W.
Investigation Of Unsteady Airloads On Wings With Oscillating Controls For Active Control Purposes.
AGARD-R-699, 1981.

26. Lashka, B.
Unsteady Aerodynamic Prediction Methods Applied To Aeroelasticity In "Unsteady Aerodynamics".
AGARD-R-645, pp 1.1-1.31, 1975.

27. Crimi, P.
Reeves, B.L.
A Method For Analysing Dynamic Stall Of Helicopter Rotor Blades.
NASA-CR-2009, 1972.

28. Telionis, D.P.
Analytical Methods For Predicting Unsteady Laminar Boundary Layers.
AGARD-R-679, 1980.

29. Telionis, D.P.
Analytical Methods For Predicting Unsteady Turbulent Boundary Layers.
AGARD-R-679, 1980.

30. Commerford, G.L.
Carta, F.O.
Unsteady Aerodynamic Response Of A Two Dimensional Airfoil At High Reduced Frequency.
A.I.A.A. Journal Vol. 4.12
pp 43-48, 1974.

31. Archibald, F.S.
Unsteady Kutta Condition At High Values Of Reduced Frequency Parameter.
Journal of Aircraft Vol. 12
pp 542-550, 1965.

32. Satyanarayana, B.
Davis, S.
Experimental Studies Of Unsteady Trailing Edge Conditions.
A.I.A.A. Journal vol. 16
pp 125-129, 1978.

33. Kadlec, R.A.
Davis, S.
Visualisation Of Quasiperiodic Flows.
A.I.A.A. Journal Vol. 17
pp 1164-1169, 1979.

34. Fleeter, S.
Trailing Edge Condition For Unsteady Flows At High Reduced Frequency.
A.I.A.A. Paper No. 79-0152, 1979.

35. Giesing, J.P.
Vorticity And Kutta Condition For Unsteady Multi-Energy Flows. Trans. ASME. J. App.Mech.

36. Maskell, E.C.
On The Kutta-Joukowski Condition In Two-Dimensional Unsteady flow. Unpublished note, R.A.E. Farnborough.

37. Poling, D.R.
Telionis, D.P.
The Response Of Aerofoils To Periodic Disturbances - The Unsteady Kutta Condition. A.I.A.A. Report No. 84-0050 1984.

38. Bergh, H.
Tijdeman, H.
Theoretical And Experimental Results For The Dynamic Response Of Pressure Measuring Systems. N.L.R. Report No. F238, 1965.

39. Bergh, H.
Tijdeman, H.
The Influence Of Main Flow On The Transfer Function Of Tube-Transducer Systems Used For Unsteady Pressure Measurements. N.L.R. Report No. mp 72023u, 1972.

40. Gumley, S.J.
A detailed Design Method For Pneumatic Tubing Systems. Univ. of Oxford Q.U.E.L. Report No. 1407/82, 1982.

41. Welsh, B.L.
Pyne, C.R.
A Method To Improve The Temperature Stability Of Semi-Conductor Strain Gauge Pressure Transducers. R.A.E. Tech. Report No. 77155, 1977.

42. Rayle, R.E.
Influence Of Orifice Geometry On Static Pressure Measurements. A.S.M.E. Paper No. 59-A-234, 1959.

43. Davies, D.E.
Theoretical Determination Of Subsonic Oscillatory Airforce Coefficients. R.A.E. Report R&M 3804, 1976.

44. Davies, D.E.
On The Use Of Fortran Programs For Evaluating The Generalised Airforces And Aerodynamic Loading On A Flat Plate Wing Oscillating Harmonically In Subsonic Flow. R.A.E. Tech.Mem.Struc. 881

45. Multhopp, H.
Methods For Calculating The Lift Distribution Of Wings (Subsonic Lifting-Surface Theory). A.R.C. R&M No. 2884, 1950.

46. Garner, H.C.
Multhopps Subsonic Lifting-Surface Theory Of Wings In Slow Pitching Oscillations. A.R.C. R&M No. 2885, 1952.

47. Garner, H.C.
Fox, D.A.
Algol 60 Programme For Multhopps Low Frequency Subsonic Lifting Surface Theory. A.R.C. R&M No. 3517, 1966.

48. Acum, W.E.A.
Interference Effects In Unsteady Experiments. Chapter in AGARDograph 109, Subsonic Wind Tunnel Wall Corrections, 1966.

49. Lambourne, N.C.
Kienappel, K.
Destuynder, R.
Roos, R.
Comparative Measurements In Four European Wind Tunnels Of The Unsteady Pressures On An Oscillating Model. (The NORA Experiments).
AGARD-R-673, 1979.

50. Lambourne, N.C.
Wight, K.C.
Welsh, B.L.
Measurements Of Control Surface Oscillatory Derivatives On A Sweptback, Tapered Model Wing In Two Transonic Tunnels.
A.R.C. R&M No. 3806, 1977.

51. Pankhurst,
Holder,
Wind Tunnel Technique.
Pitman,1952.

52. Runyan, H.L.
Woolston, D.S.
Rainey, A.G.
Theoretical And Experimental Investigation Of The Effect Of Tunnel Walls On The Forces Acting On An Oscillating Airfoil In Two-Dimensional Flow.
NACA Report No. 1262, 1956.

53. Moore, A.W.
Scale Effects On Oscillatory Control-Surface Derivatives.
A.R.C. CP 1151, 1965.

54. Abbot, I.H.
Von Doenhoff, A.E.
Theory Of Wing Sections.
Dover Press , 1959.

APPENDIX 1

Fortran listings of programs used to process steady and unsteady wind tunnel data measured on fin with oscillating control surface.

```
00100 *
00110 *     this is the driver for the data reduction of wind tunnel test data
00120 *     for a low aspect ratio fin with oscillating flap.
00130 *
00140 *     note — a positive phase angle is a phase lag
00150 *            a negative phase angle is a phase lead
00160 *
00170 *     subroutines called:
00180 *
00190 *     1 input  - allows data input via terminal
00200 *     2 calc1  - calculates basic flow parameters
00210 *     3 calc2  - calculates steady and unsteady pressure coefficients
00220 *     4 pcalc  - calculates transfer function of pressure tubing
00230 *     5 output - outputs data to file in formatted form for printing
00240 *     6 outpu2 - outputs data to file in unformatted form for storage on t\
                                                                          ape
00250 *     7 forces - calculates lift and hinge moments on flap
00260 *     8 integ1 - performs simpsons rule for integrating forces on flap
00270 *
00280 *
00290 *     variable descriptions (common variables)
00300 *
00310 *     irun       = wind tunnel run number (integer,irun=1 to 9999)
00320 *     id1        = day part of date (integer,id1=1 to 31)
00330 *     id2        = month part of date (integer,id2=1 to 12)
00340 *     id3        = year part of of date (integer,id3=85 to 88)
00350 *     fn         = spare variable - unused
00360 *     tap1       = alpha characters to define pressure tapping row (charac\
                                                                        ter *2)
00370 *                  tap1='fu' for flap upper surface
00380 *                  tap1='fl' for flap lower surface
00390 *                  tap1='au' for fin upper surface
00400 *                  tap1='al' for fin lower surface
00410 *     itap       = numerical character to define pressure tapping row (int\
                                                                          eger)
00420 *                  itap=1,2 or 3 for inboard,middle or outboard row on fin
00430 *                  itap=1 to 13 for inboard to outboard row on flap
00440 *     ai         = incidence of fin (degrees) - uncorrected for tunnel con\
                                                                      straints
00450 *     aic        = incidence of finc (degrees) - corrected for tunnel cons\
                                                                      traints
00460 *     fi         = flap deflection angle about which oscillations occur (d\
                                                                      egrees)
00470 *     fqcy       = frequency of flap oscillations (Hz)
00480 *     vinf       = freestream wind velocity (m/s)
00490 *     ar(19)     = array of pressure tube amplitude ratio corrections
00500 *     phase(19)  = array of pressure tube phase lag correction angles
00510 *     tvol       = pressure transducer internal volume (mm3)
00520 *     vss        = pressure transducer internal volume (mm3) = tvol
00530 *
00540 *     vent       = spare variable originally intended for corrected freest\
                                                             ream velocity
00550 *     pdsy(19)   = array of steady pressures (n/m2)
00560 *     cpdsy(19)  = array of steady pressure coefficients
00570 *     op1(19)    = array of real parts of oscillatory pressure (n/m2)
00580 *     op2(19)    = array of imaginary parts of oscillatory pressure (n/m2)
00590 *     op3(19)    = array of amplitudes of oscillatory pressures (n/m2)
00600 *     op4(19)    = array of phase lags of oscillatory pressures (deg.)
00610 *     op5(19)    = array of real parts of oscillatory pressures (cp not am\
                                                                   p. norm.)
```

```
00620 *     op6(19)    = array of imaginary parts of oscillatory pressures (cp n\
                                                                  ot amp. norm.)
00630 *     op7(19)    = array of real parts of oscillatory pressures (cp amp. n\
                                                                       orm.)
00640 *     op8(19)    = array of imaginary parts of oscillatory pressures (cp a\
                                                                    mp. norm.)
00650 *     op9(19)    = array of amplitudes of oscillatory pressures (cp amp. n\
                                                                       orm.)
00660 *     op10(19)   = array of phase lags of oscillatory pressures (deg.)
00670 *
00680 *     nt         = number of data points (pressure tappings) in row of tap\
                                                                       pings
00690 *                  nt=13 for every row on flap
00700 *                  nt=19 for inboard row on fin
00710 *                  nt=15 fo middle or outboard row on fin
00720 *
00730 *     filenm     = name of output file for formatted data (character*8)
00740 *     file       = name of output file for unformatted data (character*8)
00750 *
00760 *     itype      = integer corresponding to pressure transducer type (ityp\
                                                          e = 1,2,3 or 4)
00770 *     omega      = angular frequency of flap oscillations (rad/s2)
00780 *     deltp      = difference between working section static pressure and \
                                                        atmospheric (n/m2)
00790 *     pinf       = absolute working section static pressure (n/m2)
00800 *     cls        = integrated steady lift coefficient on flap
00810 *     chs        = integrated steady hinge moment coefficient on flap
00820 *     clr        = real part of integrated unsteady lift coefficient on fl\
                                                                       ap
00830 *     cli        = imaginary part of integrated unsteady lift coefficient \
                                                                  on flap
00840 *     cla        = amplitude of integrated unsteady lift coefficient on fl\
                                                                       ap
00850 *     clt        = phase lag of integrated unsteady lift coefficient on fl\
                                                                       ap
00860 *     chr        = real part of integrated unsteady hinge moment coefficie\
                                                                 nt on flap
00870 *     chi        = imaginary part of integrated unsteady hinge moment on f\
                                                                       lap
00880 *     cha        = amplitude of integrated unsteady hinge moment on flap
00890 *     cht        = phase lag of integrated unsteady hinge moment on flap
00900 *
00910 *
00920 *     variable descriptions (non common variables)
00930 *
00940 *     ans        = holds answer from user to computer enquiry (character*1\
                                                                       )
00950 *                  ans = 'y' means yes
00960 *                  ans = 'n' means no
00970 *     i          = do loop counter
00980 *
00990 *     common blocks
01000 *
01010       common/bl1/irun,id1,id2,id3,fn,tap1,itap,ai,aic,fi,fqcy,vinf
01020       common/bl2/ar(19),phase(19),tvol,vent,temp,patmos,pcal,accal
01030       common/bl3/pstdy(19),prein(19),pimin(19),acrein(19),acimin(19)
01040       common/bl4/pzeri,pzerf,re,refqcy,rho,amu,q
01050       common/bl5/accn(19),disp(19),pdsy(19),cpsdy(19),op1(19),op2(19)
01060       common/bl6/op3(19),op4(19),op5(19),op6(19),op7(19),op8(19)
01070       common/bl7/op9(19),op10(19)
```

```
01080       common/bl8/nt
01090       common/bl9/filenm,file,itype,omega
01100       common/bl10/deltp,pinf
01110       common/bl11/cls,chs,clr,cli,chr,chi,cla,cha,clt,cht
01120 *
01130       character*8 filenm,file
01140       character*2 tap1
01150       character*1 ans
01160   200 call input
01170 *     check input data is ok
01180       print *,'IS THE INPUT DATA CORRECT'
01190       read(5,*)ans
01200       if(ans.eq.'y') goto300
01210       goto400
01220   300 do 100 i=1,24,1
01230       print *
01240   100 continue
01250       print *,'                PROCESSING DATA - PLEASE WAIT'
01260       do 110 i=1,10,1
01270       print *
01280   110 continue
01290       call calc1
01300       call calc2
01310       call output
01320       call outpu2
01330 *
01340 *
01350 *     confirm processing complete and name the data sets
01360 *
01370       do 120 i=1,15,1
01380       print *
01390   120 continue
01400       print *,'PROCESSING COMPLETE DATA STORED IN FILES'
01410       print *,filenm,file
01420       print *
01430   400 print *,'DO YOU WANT TO ENTER MORE DATA - Y OR N'
01440       read(5,*)ans
01450       if(ans.ne.'y') goto 500
01460 *
01470 *     zero arrays for calculated values
01480 *
01490       do 450 i=1,19,1
01500       ar(i)=1.
01510       phase(i)=0.0
01520       prein(i)=0.0
01530       pimin(i)=0.0
01540       acrein(i)=0.0
01550       acimin(i)=0.0
01560       accn(i)=0.0
01570       disp(i)=0.0
01580       pdsy(i)=0.0
01590       cpsdy(i)=0.0
01600   450 continue
01610       goto 200
01620   500 stop
01630       end
```

```
00100       subroutine input
00110 *
00120 *       this subroutine enables data to be entered for processing
00130 *
00140 *
00150 *
00160 *
00170 *       common blocks
00180 *
00190       common/bl1/irun,id1,id2,id3,fn,tap1,itap,ai,aic,fi,fqcy,vinf
00200       common/bl2/ar(19),phase(19),tvol,vent,temp,patmos,pcal,accal
00210       common/bl3/pstdy(19),prein(19),pimin(19),acrein(19),acimin(19)
00220       common/bl4/pzeri,pzerf,re,refqcy,rho,amu,q
00230       common/bl5/accn(19),disp(19),pdsy(19),cpsdy(19),op1(19),op2(19)
00240       common/bl6/op3(19),op4(19),op5(19),op6(19),op7(19),op8(19)
00250       common/bl7/op9(19),op10(19)
00260       common/bl8/nt
00270       common/bl9/filenm,file,itype,omega
00280 *
00290       character*2 tap1
00300       character*1ans
00310       character*8 filenm,file
00320 *
00330 *     data input routine
00340 *
00350       do 20 i=1,24,1
00360       print *
00370    20 continue
00380       print *,'DATA REDUCTION ROUTINE FOR UNSTEADY PRESSURE MEASUREMENTS
00390      & ON OSCILLATING FLAP'
00400       print *,'------------------------------------------------------------
00410      &--------------------'
00420       print *
00430       print *,'INPUT DATA AS REQUESTED'
00440       print *,'-----------------------'
00450       print *
00460       print *
00470       print *,'ENTER RUN NUMBER'
00480       read(5,*)irun
00490       print *,'ENTER DATE OF RUN IN FORM 21 10 85'
00500       read(5,*)id1,id2,id3
00510       print *,'ENTER NAME OF FILE TO WHICH FORMATTED DATA IS TO BE WRITTEN\

00520       read(5,*)filenm
00530       print *,'ENTER NAME OF FILE TO WHICH UNFORMATTED DATA IS TO BE WRITT\
                                                                          EN'
00540       read(5,*)file
00550       print *,'ENTER INCIDENCE OF FIN IN DEGREES'
00560       read(5,*)ai
00570       print *,'ENTER FLAP MEAN DEFLECTION ANGLE IN DEGREES'
00580       read(5,*)fi
00590       print *,'ENTER PRESSURE TAPPING ROW DEFINITION CODE IN FORM FL 13'
00600   105 read(5,*)tap1,itap
00610 *
00620 *     check input of tap1 and itap
00630 *
00640       if(tap1.eq.'fu'.or.tap1.eq.'fl') goto 120
00650       if(tap1.eq.'au'.or.tap1.eq.'al') goto 130
00660   110 print *,'INVALID TAPPING DEFINITION CODE - PLEASE REENTER'
00670       goto 105
```

```
00680 *
00690 *     determine number of pressure data points to be entered
00700 *
00710   120 if(itap.gt.13.or.itap.lt.1) goto 110
00720       nt=13
00730       goto 140
00740   130 if(itap.gt.3.or.itap.lt.1) goto 110
00750       if(itap.eq.1) nt=19
00760       if(itap.ne.1) nt=15
00770 *
00780 *
00790 *     enter flow parameters
00800 *
00810   140 print *,'ENTER WIND TUNNEL SPEED (m/s)'
00820       read(5,*)vinf
00830       print *,'ENTER WIND TUNNEL TEMPERATURE (deg C)'
00840       read(5,*)temp
00850       print *,'ENTER BAROMETRIC PRESSURE (mBars)'
00860       read(5,*)patmos
00870       print *,'ENTER FREQUENCY OF FLAP OSCILLATION (Hz)'
00880       read(5,*)fqcy
00890 *
00900 *     read pressure and acceleration data
00910 *
00920       print *,'ENTER INITIAL PRESSURE TRANSDUCER ZERO VOLTAGE'
00930       read(5,*)pzeri
00940       do 10 i=1,24,1
00950       print *
00960    10 continue
00970       write(6,500) nt
00980   500 format(1h ,'ENTER PRESSURE AND ACCELERATION DATA FOR ',i2,' DATA POI\
                                                                        NTS')
00990       if(fqcy.lt.1.) goto 300
01000       print *,'IN FORM - PREAL  PIMAGINARY  PSTEADY  AREAL  AIMAGINARY'
01010       print *
01011       i=1
01012       write(6,510)i
01013       read(5,*)prein(1),pimin(1),pstdy(1),acrein(1),acimin(1)
01014       print *
01020       do 200 i=2,nt,1
01030       write(6,510) i
01040   510 format(1h ,'POINT NUMBER ',i2)
01050       read(5,*)prein(i),pimin(i),pstdy(i)
01051       acrein(i)=acrein(1)
01052       acimin(i)=acimin(1)
01060       print *
01070   200 continue
01080       print *
01090       goto 410
01100 *
01110 *
01120 *     steady pressures only
01130 *
01140   300 print *,'IN FORM - PSTEADY'
01150       do 400 i=1,nt,1
01160       write(6,520) i
01170   520 format(1h ,'POINT NUMBER ',i2)
01180       read(5,*)pstdy(i)
01190       print *
01200   400 continue
```

```
01210       print *
01220   410 print *,'ENTER FINAL PRESSURE TRANSDUCER ZERO VOLTAGE'
01230       read(5,*)pzerf
01240       print *,'DO YOU WANT TO CHANGE TRANSDUCER CALIBRATION FACTORS ?'
01250       read(5,*)ans
01260       if(ans.ne.'y') goto800
01270       print *,  'ENTER PRESSURE TRANSDUCER CALIBRATION CONSTANT (V/N/M2)'
01280       read(5,*)pcal
01290       print *, 'ENTER ACCELEROMETER CALIBRATION CONSTANT (V/M/S2)'
01300       read(5,*)accal
01310 *     enter transducer type -
01320 *     1=setra +- 0.1 psi
01330 *     2=druck +- 0.5 psi
01340 *     3=druck +- 1.0 psi
01350 *     4=druck +- 2.5 psi
01360       print *,'ENTER TRANSDUCER TYPE 1,2,3,OR4'
01370       read(5,*)itype
01380   800 continue
01390       return
01400       end
```

```
00100       subroutine calc1
00110 *
00120 *     this subroutine calculates the basic flow parameters for use in data
00130 *     reduction in subroutine calc2
00140 *
00150 *
00160 *     variable descriptions (not common)
00170 *
00180 *     pi          = pi=3.1415927
00190 *     tinf        = temperature in degrees kelvin
00200 *     s     *
00210 *     a0    *
00220 *     a1    *     = constants used to calculate viscosity of air
00230 *     a2    *
00240 *     a3    *
00250 *     a4    *
00260 *     anu          = kinematic viscosity of air in tunnel (m2/s)
00270 *
00280 *
00290 *     common blocks
00300 *
00310       common/bl1/irun,id1,id2,id3,fn,tap1,itap,ai,aic,fi,fqcy,vinf
00320       common/bl2/ar(19),phase(19),tvol,vent,temp,patmos,pcal,accal
00330       common/bl4/pzeri,pzerf,re,refqcy,rho,amu,q
00340       common/bl9/filenm,file,itype,omega
00350       common/bl10/deltp,pinf
00360       character*2 tap1
00370       character*8 filenm,file
00380       pi=3.1415927
00390 *
00400 * calculate angular frequency - omega
00410       omega=2*pi*fqcy
00420 * calculate reduced frequency
00430       if(vinf.le.0.1) goto 100
00440       refqcy=(omega*0.4445)/(2*vinf)
00450 * calculate air density
00460   100 rho=1.225*patmos*288.15/((temp+273.15)*1013.25)
00470 * calculate air viscosity
00480       tinf=temp+273.15
00490       s=100/tinf
00500       a0=0.552795
00510       a1=2.81089
00520       a2=-13.5083
00530       a3=39.3531
00540       a4=-41.4194
00550       amu=(sqrt(tinf)*1.e-6)/(a0+a1*s+a2*s**2+a3*s**3+a4*s**4)
00560       anu=amu/rho
00570 * calculate reynolds number
00580       if(vinf.le.0.1) goto 200
00590       re=vinf*0.4445/anu
00600 * calculate dynamic pressure
00610       q=0.5*rho*vinf**2
00620 * calculate working section freestream static pressure (n/m2)
00630   200 deltp=(-4.209*q/9.81)+0.213
00640       pinf=(patmos*100)+deltp
00650 * return to main program
00660       return
00670       end
```

```
00100       subroutine calc2
00110 *
00120 *     this subroutine processes the pressure and acceleration data
00130 *
00140 *     variable descriptions (not common)
00150 *
00160 *     pi          = pi=3.1415927
00170 *     rad         = distance between flap pivot axis and center of accelero\
                                                                          meter
00180 *     sddotr      = real part of tangential acceleration (m/s2)
00190 *     sddoti      = imaginary part of tangential acceleration (m/s2)
00200 *     ttddr       = real part of angular acceleration (rad/s2)
00210 *     ttddi       = imaginary part of angular acceleration (rad/s2)
00220 *     thetre(19)  = array of real parts of angular flap displacement
00230 *     thetim(19)  = array of imaginary parts of angular flap displacement
00240 *     cosa        = cosine of phase angle
00250 *     sina        = sine of phase angle
00260 *     hyp         = amplitude of acceleration
00270 *
00280 *
00290 *     common blocks
00300 *
00310       common/bl1/irun,id1,id2,id3,fn,tap1,itap,ai,aic,fi,fqcy,vinf
00320       common/bl2/ar(19),phase(19),tvol,vent,temp,patmos,pcal,accal
00330       common/bl3/pstdy(19),prein(19),pimin(19),acrein(19),acimin(19)
00340       common/bl4/pzeri,pzerf,re,refqcy,rho,amu,q
00350       common/bl5/accn(19),disp(19),pdsy(19),cpsdy(19),op1(19),op2(19)
00360       common/bl6/op3(19),op4(19),op5(19),op6(19),op7(19),op8(19)
00370       common/bl7/op9(19),op10(19)
00380       common/bl8/nt
00390       common/bl9/filenm,file,itype,omega
00400       common/bl10/deltp,pinf
00410       common/bl11/cls,chs,clr,cli,chr,chi,cla,cha,clt,cht
00420 *
00430 *     declarations
00440 *
00450       dimension thetre(19),thetim(19)
00460       dimension pstdyc(19),precal(19),pimcal(19)
00470       dimension pre(19),pim(19)
00480       character*8 filenm,file
00490       character*2 tap1
00500 *
00510 *     set constants
00520 *
00530       pi=3.1415927
00540       rad=0.040
00550       *
00560 *     calculate the angular accelerations and displacements if oscillatory\
                                                          inputs are present
00570 *
00580       if(fqcy.le.0.1) goto 110
00590 * start with tangential accelerations
00600       do 100 i=1,nt,1
00610       sddotr=acrein(i)/accal
00620       sddoti=acimin(i)/accal
00630 * if tappings are on lower surface multiply accn components by -1
00640       if(tap1.eq.'fu'.or.tap1.eq.'au') goto 50
00650       sddotr=sddotr*-1
00660       sddoti=sddoti*-1
00670 * calculate components of angular acceleration
```

```
00680    50 ttddr=sddotr/rad
00690       ttddi=sddoti/rad
00700 *  calculate components of angular displacement
00710       thetre(i)=-ttddr/omega**2
00720       thetim(i)=-ttddi/omega**2
00730 *  calculate amplitude of angular displacements and accelerations
00740       disp(i)=sqrt(thetre(i)**2+thetim(i)**2)
00750       accn(i)=disp(i)*omega**2
00760 *     convert displacement to degrees
00770       disp(i)=disp(i)*180/pi
00780   100 continue
00790 *
00800 *     now do the pressures
00810 *
00820 *     first set up loop for nt data points
00830 *
00840   110 do 500 i=1,nt,1
00850 *
00860 *     now do the steady pressures if wind speed is greater than 0.1 m/s
00870 *
00880       if(vinf.le.0.1) go to 600
00890 * get rid of zero pressure reading
00900       delp=0.0
00910       if(i.eq.1) goto 200
00920       delp=(pzerf-pzeri)/(nt-1)
00930   200 pstdyc(i)=pstdy(i)-(pzeri+(i-1)*delp)
00940 * now calculate pressure in n/m2 and Cp
00950       pdsy(i)=pstdyc(i)/pcal
00960       pdsy(i)=pdsy(i)-deltp
00970       cpsdy(i)=pdsy(i)/q
00980   500 continue
00990 *
01000 *     check for steady pressure data only
01010 *
01011       print *,fqcy
01020   600 if(fqcy.le.0.1) goto 511
01030 *
01040 *     call pcalc to get transfer function of tubes
01050 *
01060       call pcalc
01070 *
01080 *
01090 *     now do the unsteady pressures
01100 *
01110       do 510 i=1,nt,1
01120 * first evaluate amplitude of unsteady pressure in n/m2
01130       precal(i)=prein(i)/pcal
01140       pimcal(i)=pimin(i)/pcal
01150 * now correct for calibration of tubing systems
01160 * evaluate transformation matrix and perform transformation
01170       cosa=cos(-phase(i)*2*pi/360)
01180       sina=sin(-phase(i)*2*pi/360)
01190       pre(i)=(precal(i)*cosa+pimcal(i)*sina)*ar(i)
01200       pim(i)=(precal(i)*(-sina)+pimcal(i)*cosa)*ar(i)
01210 * now phase reference pressures to the displacement of the flap
01220 * evaluate transformation matrix
01230       hyp=sqrt(thetre(i)**2+thetim(i)**2)
01240       cosa=thetre(i)/hyp
01250       sina=thetim(i)/hyp
01260 * perform transformation
```

```
01270       op1(i)=pre(i)*cosa+pim(i)*sina
01280       op2(i)=pre(i)*(-sina)+pim(i)*cosa
01290 * now calculate amplitude and phase in n/m2
01300       op3(i)=sqrt(op1(i)**2+op2(i)**2)
01310       if(abs(op2(i)/op1(i)).lt.1.e6) goto 250
01320       if(op2(i).gt.0.0)  op4(i)=90.0
01330       if(op2(i).lt.0.0) op4(i)=270.0
01340       goto 240
01350   250 op4(i)=atan(op2(i)/op1(i))
01360   260 op4(i)=op4(i)*360.0/(2*pi)
01370       if(op1(i).lt.0.0) op4(i)=180+op4(i)
01380       if(op2(i).lt.0.0.and.op1(i).gt.0.0) op4(i)=op4(i)+360
01384       op4(i)=360-op4(i)
01390   240 continue
01400       if(vinf.le.0.0) goto 510
01410 * now work out non amplitude normalised pressure coefficients
01420       if(vinf.le.0.1) goto 510
01430       op5(i)=op1(i)/q
01440       op6(i)=op2(i)/q
01450 * now work out amplitude normalised pressure coefficients
01460       op7(i)=op5(i)/(disp(i)*pi/180)
01470       op8(i)=op6(i)/(disp(i)*pi/180)
01480 * now work out amplitude and phase of amplitude normalised pressures
01490       op9(i)=sqrt(op7(i)**2+op8(i)**2)
01500       op10(i)=op4(i)
01510 *
01520 *
01530 *
01540 510 continue
01545 511 continue
01550 *
01560 *     if data is on flap - integrate to find lift and hinge moment
01570 *
01580       if(tap1.eq.'fu'.or.tap1.eq.'fl') call forces
01590 *
01600       return
01610       end
```

```
00100       subroutine pcalc
00110 *     ************************************************************
00120 *
00130 *     this subroutine calculates the transfer function (amplitude and phas\
                                                                        e lag)
00140 *     of the tubing system for each pressure tapping at the frequency unde\
                                                                          r
00150 *     consideration.account is taken of different scanivalve tube
00160 *     lengths and the natural response of individual pressure transducers
00170 *
00180 *     **** warning **** ensure correct connection of tubes on scanivalve
00190 *                       ports and the type of transducer being used
00200 *
00210 *
00220 *     computation of pressure ratio of transducer measurement
00230 *     to the averaged sum of the input pressures for multiple
00240 *     pneumatic systems with mp identical primary manifolds
00250 *     each with ma identical tube inputs.
00260 *     provision made for internal scanivalve tubing
00270 *     provision made for orifice crossflow effects
00280 *     for each tube the mean static pressure and air density are calculate\
                                                                          d
00290 *     from the value of the mean steady pressure and the wind tunnel tempe\
                                                                     rature
00300 *     this subroutine calls function 'bei' to calculate kelvin functions b\
                                  ei(i=1)and bei(j=2) for orders i=0 and i=2
00310 *
00320 *     ************************************************************
00330 *
00340 *     variable descriptions (not common)
00350 *
00360 *     d(6)        = array of tube diameters in each tube network
00370 *     l(19,6)     = array of tube lengths for each individual pressure tapp\
                                                                        ing
00380 *                   accounts for different lengths of scanivalve tube and p\
                                                    ressure tapping length
00390 *     mu          = viscosity of air in tube
00400 *     ma          = number of inputs to each tube system
00410 *     mp          = number of primary manifolds =1
00420 *     prav        = volume of primary manifold =0.0
00430 *     secav       = volume of secondary manifold 0.0
00440 *     dd4a        = polytropic expansion index for air = 1.4
00450 *     ss          = volume increase in transducer due to diaphragm deflecti\
                                                              on = 0.0
00460 *     slm         = local crossflow velocity over pressure tapping = vinf
00470 *     cec         = constant for calculation of effect of orifice crossflow\
                                                                      = 0.9
00480 *     prnd        = prandtl number
00490 *     pr          = square root of prandtl number
00500 *     g           = 1-(1/gamma)
00510 *     pstat       = absolute local mean static pressure at tapping orifice \
                                                                    (n/m2)
00520 *     stpr        = pstat/100
00530 *     vismol      = molecular viscosity of air in tube
00540 *     rho         = density of air in tubes
00550 *     delt        = correction term to phase lag due to transducer response
00560 *     delu        = correction term to amplitude ratio due to transducer re\
                                                                     sponse
00570 *     fact        = correction term to amplitude ratio due to transducer re\
                                                                     sponse
```

```
00580 *      w          = angular frequency = 2*pi*fqcy
00590 *
00600 *
00610 *      common blocks
00620 *
00630        common/bl1/irun,id1,id2,id3,fn,tap1,itap,ai,aic,fi,fqcy,vinf
00640        common/bl2/ar(19),phase(19),vss,vent,temp,patmos,pcal,accal
00650        common/bl4/pzeri,pzerf,re,refqcy,rho,amu,q
00660        common/bl5/accn(19),disp(19),pdsy(19),cpsdy(19),op1(19),op2(19)
00670        common/bl8/nt
00680        common/bl9/filenm,file,itype,omega
00690        common/bl10/deltp,pinf
00700 *
00710 *      declarations
00720 *
00730        character*2 tap1
00740        character*8 filenm,file
00750        real d(6),l(19,6),mu,k2
00760        complex b6,bz,u,v,n(6),bfo(6),bf2(6),phi(6),ch(6)
00770        complex a(6),z,s,t,q6,q5,q4,q3,q1,qa(19),sh(6),q2,qv
00780 *
00790 *      determine which row of tappings and assign lengths to tubes
00800 *
00810        if(tap1.eq.'fu'.or.tap1.eq.'fl') goto 100
00820        if(itap.eq.1) goto 115
00830 *
00840 *      middle or outboard row on fin
00850 *
00860        do 10 i=2,14,2
00870        l(i,1)=20.0
00880        l(i,6)=80.0
00890     10 continue
00900        do 20 i=1,13,4
00910        l(i,1)=20.0
00920        l(i,6)=87.0
00930     20 continue
00940        do 30 i=3,15,4
00950        l(i,1)=20.0
00960        l(i,6)=95.0
00970     30 continue
00980        goto 400
00990 *
01000 *      inboard on fin
01010 *
01020    115 do 130 i=2,18,2
01030        l(i,1)=20.0
01040        l(i,6)=80.0
01050    130 continue
01060        do 140 i=1,17,4
01070        l(i,1)=20.0
01080        l(i,6)=95.0
01090    140 continue
01100        do 150 i=3,19,4
01110        l(i,1)=20.0
01120        l(i,6)=87.0
01130    150 continue
01140        l(19,1)=98.0
01150        goto 400
01160 *
01170 *      flap
```

```
01180 *
01190   100 do 110 i=2,12,2
01200       l(i,1)=20.0
01210       l(i,6)=80.0
01220   110 continue
01230       do 120 i=1,13,4
01240       l(i,1)=20.0
01250       l(i,6)=87.0
01260   120 continue
01270       do 125 i=3,11,4
01280       l(i,1)=20.0
01290       l(i,6)=95.0
01300   125 continue
01310       l(10,1)=30.0
01320       l(11,1)=40.0
01330 *
01340 *
01350 *     set other geometry components
01360 *
01370 *
01380 * set tube lengths
01390   400 do 300 i=1,nt,1
01400       l(i,2)=100.0
01410       l(i,3)=100.0
01420       l(i,4)=100.0
01430       l(i,5)=450.0
01440   300 continue
01450 * shorten tube by 5mm for 4th
01460       if(tap1.eq.'fu'.or.tap1.eq.'fl') goto 380
01470       if(itap.ne.3) goto 380
01480       l(4,5)=445.0
01490 * now set tube diameters
01500   380 d(1)=0.685
01510       d(2)=1.065
01520       d(3)=1.065
01530       d(4)=1.065
01540       d(5)=1.065
01550       d(6)=1.000
01560 *     convert tube diameters to quasi areas
01570       do 4 i=1,6,1
01580       d(i)=0.25e-6*d(i)*d(i)
01590     4 continue
01600 *
01610 *
01620       ma=1
01630       mp=1
01640       prav=0.0
01650       secav=0.0
01660       dd4a=1.4
01670       ss=0.0
01680       slm=vinf
01690       cec=0.9
01700 *
01710 *      set transducer volume
01720 *
01730       if(itype.eq.1) vss=82.0
01740       if(itype.eq.2) vss=136.0
01750       if(itype.eq.3) vss=98.0
01760       if(itype.eq.4) vss=98.0
01770 *
```

```
01780 *     set fluid properties
01790 *
01800       prnd=0.72-.0002*temp
01810       pr=sqrt(prnd)
01820       g=1.0-1.0/1.4
01830       bz=cmplx((ss+1.0/dd4a)*vss*1.0e-9/(3.1415793*d(6)),0.0)
01840       w=6.2831853*fqcy
01850       do 600 k=1,nt,1
01860       pstat=pdsy(k)+pinf
01870       stpr=pstat/100
01880       rho=1.2256*stpr*288./((temp+273.)*1013.)
01890       vismol=rho*(1.326+0.009*temp)*1013./stpr
01900       p=sqrt(rho/pstat)
01910       mu=sqrt(rho/(vismol*0.000010))
01920 * convert tube lengths to meters
01930       do 5 m=1,6,1
01940       l(k,m)=0.001*l(k,m)
01950     5 continue
01960 *
01970 *     now calculate transfer function
01980 *
01990       do 2 i=1,6
02000       x=mu*sqrt(w*d(i))
02010       y=x*pr
02020       s=cmplx(bei(1,0,y),bei(2,0,y))
02030       t=cmplx(bei(1,2,y),bei(2,2,y))
02040       bfo(i)=cmplx(bei(1,0,x),bei(2,0,x))
02050       bf2(i)=cmplx(bei(1,2,x),bei(2,2,x))
02060       n(i)=(s+cmplx(g,0.0)*t)/s
02070       phi(i)=cmplx(w*p,0.0)*csqrt(n(i)*bfo(i)/bf2(i))
02080       z=cmplx(l(k,i),0.0)*phi(i)
02090       u=cexp(z)
02100       v=cexp(-z)
02110       ch(i)=cmplx(0.5,0.0)*(u+v)
02120       sh(i)=cmplx(0.5,0.0)*(u-v)
02130     2 continue
02140       do 3 i= 1,5
02150       j=i+1
02160       a(i)=cmplx(d(j)/d(i),0.0)*phi(j)*bfo(i)*bf2(j)*
02170      &sh(i)/(phi(i)*bfo(j)*bf2(i)*sh(j))
02180     3 continue
02190       b6=bz*phi(6)*sh(6)/n(6)
02200       q6=ch(6)+b6
02210       q5=ch(5)+a(5)*(ch(6)-cmplx(1.0,0.0)/q6)
02220       q4=ch(4)+a(4)*(ch(5)-cmplx(1.0,0.0)/q5)
02230       q3=ch(3)+a(3)*(ch(4)-cmplx(1.0,0.0)/q4)
02240       q2=ch(2)+a(2)*(ch(3)-cmplx(1.0,0.0)/q3)
02250       q1=ch(1)+a(1)*(ch(2)-cmplx(1.0,0.0)/q2)
02260       qv=q1-((cmplx(slm,0.0)*cmplx(cec,0.0)*phi(1)*bf2(1))/(bfo(1)*
02270      &cmplx(w,0.0)*cmplx(0.0,1.0)))*(sh(1)+a(1)*
02280      &(ch(1)/sh(1))*(ch(2)-cmplx(1.0,0.0)/q2))
02290       qa(k)=cmplx(1.0,0.0)/(qv*q2*q3*q4*q5*q6)
02300       ar(k)=cabs(qa(k))
02310       phase(k)=-57.29578*atan2(aimag(qa(k)),real(qa(k)))
02320       if(phase(k).lt.0.0) phase(k)=phase(k)+360.0
02330   600 continue
02340 *
02350 *      correct for response of transducer diaphragm
02360 *
02370       goto(410,420,440,460),itype
```

```
02380 * setra +- 0.1 psi
02390   410 delt=0.1181102
02400       delu=0.68
02410       goto 470
02420 * druck +- 0.5 psi
02430   420 delt=0.0
02440       delu=0.0
02450       goto 470
02460 * druck +- 1.0 psi
02470   440 delt=0.005
02480       delu=0.0
02490       goto 470
02500 * druck +- 2.5 psi
02510   460 delt=0.0
02520       delu=0.0
02530 * now do the corrections
02540   470 do 480 i=1,nt,1
02550       phase(i)=phase(i)+(delt*fqcy-delu)
02560   480 continue
02570       if(itype.ne.1) goto 490
02580 * correct amplitude for setra +- 0.1 psi transducer
02590       if(fqcy.le.60.0) goto 490
02600       fact=1-((fqcy-60.0)*0.0002)
02610       do 485 i=1,nt,1
02620       ar(i)=ar(i)/fact
02630   485 continue
02640   490 do 800 i=1,nt,1
02650   800 continue
02660       return
02670       end
```

```
00100 *     ****************************************************************
00110 *
00120 *
00130       function bei(j,i,y)
00140 *
00150 *     computation of kelvin functions ber(j=1) and bei(j=2)
00160 *     for orders i=0 and i=2 and argument y
00170 *
00180 *     ****************************************************************
00190 *
00200       x=0.25*y*y
00210       t=0.0
00220       go to (1,2,3,4),i+j
00230     1 s=1.0
00240       f1=0.0
00250       f2=0.0
00260       go to 5
00270     2 s=x
00280       f1=1.0
00290       f2=1.0
00300       go to 5
00310     3 s=x*x/6.0
00320       f1=1.0
00330       f2=3.0
00340       go to 5
00350     4 s=-0.5*x
00360       f1=0.0
00370       f2=2.0
00380     5 x=x*x
00390     6 bei=s+t
00400       if(abs(s).lt.0.00000001) return
00410       t=bei
00420       f1=f1+2.0
00430       f2=f2+2.0
00440       s=-s*x/(f1*f2*(f1-1.0)*(f2-1.0))
00450       go to 6
00460       end
```

```
00100       subroutine forces
00110 *
00120 *     this subroutine works out lift and hinge moments acting on the flap
00130 *     Simpsons rule is used to perform integrations using subroutine 'inte\
                                                                          g1'
00140 *
00150 *     common blocks
00160 *
00170       common/bl1/irun,id1,id2,id3,fn,tap1,itap,ai,aic,fi,fqcy,vinf
00180       common/bl2/ar(19),phase(19),tvol,vent,temp,patmos,pcal,accal
00190       common/bl3/pstdy(19),prein(19),pimin(19),acrein(19),acimin(19)
00200       common/bl4/pzeri,pzerf,re,refqcy,rho,amu,q
00210       common/bl5/accn(19),disp(19),pdsy(19),cpdsy(19),op1(19),op2(19)
00220       common/bl6/op3(19),op4(19),op5(19),op6(19),op7(19),op8(19)
00230       common/bl7/op9(19),op10(19)
00240       common/bl8/nt
00250       common/bl9/filenm,file,itype,omega
00260       common/bl10/deltp,pinf
00270       common/bl11/cls,chs,clr,cli,chr,chi,cla,cha,clt,cht
00280 *
00290 *     declarations
00300 *
00310       character*2 tap1
00320       character*8 filenm,file
00330       dimension y(11),xi(11)
00340       data xi/0.0,0.02377,0.04754,0.07131,0.09508,0.11874,0.14262,0.16639,\
                                                  0.19016,0.21371,0.24280/
00350 *
00360 *     constants
00370 *
00380       pi=3.1415927
00390 *
00400 *     start with steady lift coefficient
00410 *
00420       if(vinf.le.0.1) goto 310
00430       call integ1(cpdsy,cls)
00440 *
00450 *     now work out steady hinge moment coefficient
00460 *
00470       do 100 i=1,11,1
00480       y(i)=cpdsy(i)*xi(i)
00490   100 continue
00500       call integ1(y,chs)
00510 *
00520 *     check for case of no flap oscillations
00530 *
00540   105 if(fqcy.le.0.1) goto 310
00550 *
00560 *     now work out unsteady lift coefficient
00570 *
00580       call integ1(op7,clr)
00590       call integ1(op8,cli)
00600 *
00610 *     now work out unsteady hinge moments - real then imaginary
00620 *
00630       do 110 i=1,11,1
00640       y(i)=op7(i)*xi(i)
00650   110 continue
00660       call integ1(y,chr)
00670 *
```

```
00680       do 120 i=1,11,1
00690       y(i)=op8(i)*xi(i)
00700   120 continue
00710       call integ1(y,chi)
00720 *
00730 *
00740 *     now calculate amplitude and phase of hinge moments
00750 *
00760 *
00770       cla=sqrt(clr**2+cli**2)
00780       cha=sqrt(chr**2+chi**2)
00790 *
00800 *     check for angle of 90 deg
00810 *
00820       at=cli/clr
00830       ht=chi/chr
00840       if(abs(at).lt.1.e6) goto 200
00850       if(cli.gt.0.0)clt=90.0
00860       if(cli.lt.0.0)clt=270.0
00870       goto 210
00880   200 clt=atan(at)
00890       clt=clt*180./pi
00900       if(clr.le.0.0) clt=180.+clt
00910       if(cli.le.0.0.and.clr.gt.0.0) clt=360.+clt
00920 *
00930 *
00940 *
00950 *     now do hinge moment phase angles
00960 *
00970   210 if(abs(ht).lt.1.e6) goto 300
00980       if(chi.gt.0.0) cht=90.0
00990       if(chi.lt.0.0) cht=270.0
01000       goto 310
01010   300 cht=atan(ht)
01020       cht=cht*180./pi
01030       if(chr.le.0.0) cht=180.+cht
01040       if(chi.le.0.0.and.chr.gt.0.0) cht=360.+cht
01050 *
01060   310 return
01070       end
```

```
00100       subroutine integ1(y,result)
00110 *
00120 *     this subroutine performs an integration using simpsons rule
00130 *     to evaluate the hinge moments on the flap
00140 *
00150 *     the first ten data points are evenly spoced but give uneven number o\
                                                                              f
00160 *     panels.
00170 *
00180 *     therefore simpsons 1/3 rule is used on first 6 panels
00190 *               simpsons 3/8 rule is used on next 3 panels
00200 *               trapezium rule used on last two panels (uneven spacing)
00210 *
00220 *     note - the last panel has data point 11 as its first ordinate and
00230 *     zero at the trailing edge
00240 *
00250       dimension y(11)
00260 *
00270 *     do simpsons 1/3 rule on first 6 panels
00280 *
00290       result=0.0
00300       h=0.023746
00310 *
00320 *     do 1st and last values
00330 *
00340       result=h/3*(y(1)+4.*y(2)+y(7))
00350 *
00360 *     now add in middle terms
00370 *
00380       do 100 i=3,5,2
00390       result=result+(h/3.*(2.*y(i)+4*y(i+1)))
00400   100 continue
00410 *
00420 *     now add next three panels using simpsons 3/8 rule
00430 *
00440       result=result+(3.*h/8*(y(7)+3.*y(8)+3.*y(9)+y(10)))
00450 *
00460 *     now add final two panels using trapezium rule
00470 *
00480       result=result+(0.5*(y(10)+y(11))*0.02909)+(0.5*y(11)*0.003)
00490 *
00500 *
00510       return
00520       end
```

```
00100       subroutine output
00110 *
00120 *     this subroutine outputs processed data to a formatted file of name
00130 *     'filenm'.
00140 *
00150 *
00160 *     common blocks
00170 *
00180       common/bl1/irun,id1,id2,id3,fn,tap1,itap,ai,aic,fi,fqcy,vinf
00190       common/bl2/ar(19),phase(19),tvol,vent,temp,patmos,pcal,accal
00200       common/bl3/pstdy(19),prein(19),pimin(19),acrein(19),acimin(19)
00210       common/bl4/pzeri,pzerf,re,refqcy,rho,amu,q
00220       common/bl5/accn(19),disp(19),pdsy(19),cpsdy(19),op1(19),op2(19)
00230       common/bl6/op3(19),op4(19),op5(19),op6(19),op7(19),op8(19)
00240       common/bl7/op9(19),op10(19)
00250       common/bl8/nt
00260       common/bl9/filenm,file,itype,omega
00270       common/bl10/deltp,pinf
00280       common/bl11/cls,chs,clr,cli,chr,chi,cla,cha,clt,cht
00290 *
00300 *     declarations
00310 *
00320       character*8 filenm,file
00330       character*2 tap1
00340 *
00350 *     open file
00360 *
00370       open(7,file=filenm,carriage=.true.,form='formatted')
00380 *
00390 *     output first page - config definition and tubing calibration
00400 *
00410       write(7,100)
00420   100 format(1h1,36x,'TEST DATA FOR UNSTEADY FORCES ON FIN WITH OSCILLATIN\
                                                                              G
00430      & FLAP'/37x,58('-')////)
00440       write(7,105)irun,id1,id2,id3,filenm,file
00450   105 format(1h ,1x,'RUN No. = ',i4,15x,'RUN DATE = ',i2,':',i2,':',i2,10
00460      &x,'FORMATTED FILE NAME = ',a8,5x,'UNFORMATTED FILE NAME = ',a8)
00470       write(7,110)tap1,itap
00480   110 format(1h0,1x,'PRESSURE TAPPING ROW DEFINITION',7x,'= ',a2,i2)
00490       write(7,115)ai
00500   115 format(1h0,1x,'AIRFOIL MEAN INCIDENCE (deg)   ',7x,'= ',f6.2)
00510       write(7,120)fi
00520   120 format(1h0,1x,'FLAP MEAN DEFLECTION ANGLE (deg)',6x,'= ',f6.2)
00530       write(7,125)fqcy
00540   125 format(1h0,1x,'FLAP OSCILLATION FREQUENCY (Hz)',7x,'= ',f6.2)
00550       write(7,130)vinf
00560   130 format(1h0,1x,'WIND TUNNEL SPEED (m/s)',15x,'= ',f6.2)
00570 *
00580 *     now output the pressure tube calibrations
00590 *
00600       write(7,150)
00610   150 format(1h0,//////////35x,'PRESSURE TUBING CALIBRATION CONSTANTS')
00620       write(7,155)
00630   155 format(1h ,34x,37('-')//)
00640       write(7,160)
00650   160 format(1h ,10x,'DATA POINT NUMBER',13x,'AMPLITUDE RATIO',15x,'PHASE
00660      & LAG (deg)')
00670       write(7,165)
00680   165 format(1h ,10x,17('-'),13x,15('-'),15x,15('-'),/)
```

```
00690       do 500 i=1,nt,1
00700       write(7,170)i,ar(i),phase(i)
00710   170 format(1h ,16x,i2,26x,f7.3,23x,f7.2)
00720   500 continue
00730       write(7,175)tvol
00740   175 format(1h0,///10x,'TRANSDUCER VOLUME (mm3) = ',f10.4)
00750 *
00760 *     second page of output data - raw data values
00770 *
00780       write(7,200)
00790   200 format(1h1,//55x,'UNCORRECTED RAW DATA'/55x,20('-'))
00800       write(7,205)vinf,temp
00810   205 format(1h0,//11x ,'WIND TUNNEL SPEED (m/s)    = ',f7.3,12x,'WIND TU
00820      &NNEL TEMPERATURE (deg C)     = ',f7.3)
00830       write(7,210)patmos,fqcy
00840   210 format(1h0,10x,'BAROMETRIC PRESSURE (mBar) = ',f7.2,12x,'FREQUENCY
00850      & OF FLAP OSCILLATIONS (Hz) = ',f7.3/////)
00860       write(7,215)
00870   215 format(1h ,4x,'DATA POINT',6x,'STEADY',6x,'REAL PART',5x,'IMAG. PA
00880      &RT',4x,'REAL PART',5x,'IMAG. PART')
00890       write(7,220)
00900   220 format(1h ,6x,'NUMBER',7x,'PRESSURE',4x,'OSCILLATORY',3x,'OSCILLAT
00910      &ORY',6x,'ACC,N',9x,'ACC,N')
00920       write(7,225)
00930   225 format(1h ,20x,'VOLTS',9x,'VOLTS',9x,'VOLTS',9x,'VOLTS',9x,'VOLTS'
00940      &)
00950       write(7,230)
00960   230 format(1h ,3x,6(12('-'),2x)/)
00970       do 600 i=1,nt,1
00980       write(7,240)i,pstdy(i),prein(i),pimin(i),acrein(i),acimin(i)
00990   240 format(1h ,8x,i2,4x,5(4x,f10.6))
01000   600 continue
01010       write(7,245)pzeri,pzerf
01020   245 format(1h0,//10x,'INITIAL ZERO PRESSURE READING (Volts)       = ',f1\
                                                                        0.6//10x,
01030      &'FINAL ZERO PRESSURE READING (Volts)         = ',f10.6)
01040       write(7,250)pcal
01050   250 format(1h0,9x,'PRESSURE TRANSDUCER CALIBRATION (VOLT/N/M2) = ',f10.7\
                                                                            )
01060       write(7,255)accal
01070   255 format(1h0,9x,'ACCELEROMETER CALIBRATION (VOLT/M/S2)       = ',f10.7\
                                                                            )
01080       goto(260,265,270,275),itype
01090   260 write(7,261)
01100   261 format(1h0,9x,'PRESSURE TRANSDUCER TYPE = SETRA +- 0.1 PSI')
01110       goto 278
01120   265 write(7,266)
01130   266 format(1h0,9x,'PRESSURE TRANSDUCER TYPE = DRUCK +- 0.5 PSI')
01140       goto 278
01150   270 write(7,271)
01160   271 format(1h0,9x,'PRESSURE TRANSDUCER TYPE = DRUCK +- 1.0 PSI')
01170       goto 278
01180   275 write(7,276)
01190   276 format(1h0,9x,'PRESSURE TRANSDUCER TYPE = DRUCK +- 2.5 PSI')
01200   278 continue
01210 *
01220 *     output third page of data - corrected data
01230 *
01240       write(7,300)
01250   300 format(1h1,/58x,'CORRECTED DATA'/58x,14('-')//)
```

```
01260       write(7,305)vinf,re
01270   305 format(1h0,8x,'WIND TUNNEL VELOCITY (m/s)      = ',f8.3,10x,
01280      &'REYNOLDS NUMBER (BASED ON CHORD)       = ',e12.4)
01290       write(7,310)fqcy,refqcy
01300   310 format(1h0,8x,'FLAP OSCILLATION FREQUENCY (Hz) = ',f8.3,10x,'REDUC
01310      &ED FREQUENCY (BASED ON SEMICHORD) = ',f8.4)
01320       write(7,315)patmos,temp
01330   315 format(1h0//9x,'ATMOSPHERIC PRESSURE (mBar)     = ',f8.3,10x,'AIR T
01340      &EMPERATURE (deg C)                = ',f8.4)
01350       write(7,320)rho,amu
01360   320 format(1h0,8x,'AIR DENSITY (kg/m3)             = ',f8.5,10x,'DYNAM
01370      &IC VISCOSITY (Mu) OF AIR (Ns/m2)  = ',e12.4)
01380       write(7,325)q,pinf
01390   325 format(1h0,8x,'DYNAMIC PRESSURE (N/m2)         = ',f8.3,10x,'FREEST
01400      &REAM STAIC PRESSURE (N/m2)        = ',f9.2/)
01410       write(7,330)ai,fi
01420   330 format(1h0,8x,'FIN INCIDENCE (deg)             = ',f8.5,10x,'FLAP
01430      & DEFLECTION ANGLE (deg)            = ',f8.5////)
01440 *
01450 *
01460 *
01470       write(7,340)
01480   340 format(1h0,20x,'TAPPING    ACCELERATION    DISPLACEMENT',8x,'STEADY
01490      & PRESSURE ')
01500       write(7,345)
01510   345 format(1h ,20x,'NUMBER      AMPLITUDE       AMPLITUDE',6x,22('-'))
01520       write(7,350)
01530   350 format(1h0,33x,'(rad/s2)',9x,'(deg)',10x,'(N/m2)',7x,
01540      &'(Cp)'/21x,7('-'),2(4x,12('-')),4x,10('-'),2x,10('-')/)
01550 *
01560 *
01570 *
01580       do 650 i=1,nt,1
01590       write(7,360)i,accn(i),disp(i),pdsy(i),cpsdy(i)
01600   360 format(1h ,23x,i2,7x,f10.3,6x,f10.3,5x,f10.3,2x,f10.4)
01610   650 continue
01620 *
01630 *     output fourth page of data if oscillatory data is present
01640 *
01650       if(fqcy.le.0.1) goto 670
01660       write(7,400)
01670   400 format(1h1,//2x,'TAPPING',54x,'OSCILLATORY PRESSURE'/2x,'NUMBER',
01680      &5x,120('-')/23x,'NEWTONS/SQUARE METRE',28x,'Cp',24x,'AMPLITUDE NOR
01690      &MALISED Cp'/13x,47('-'),3x,22('-'),3x,45('-')/16x,'REAL',8x,
01700      &'IMAG',6x,'AMPLITUDE',6x,'PHASE',8x,'REAL',8x,'IMAG',9x,'REAL',8x,
01710      &'IMAG',5x,'AMPLITUDE',5x,'PHASE')
01720       write(7,410)
01730   410 format(1h ,1x,7('-'),4x,10('-'),2x,10('-'),3x,10('-'),2x,10('-')
01740      &,3x,10('-'),2x,10('-'),3x,10('-'),2x,10('-'),2x,10('-'),2x,9('-')/)
01750 *
01760 *
01770       do 670 i=1,nt,1
01780       write(7,420)i,op1(i),op2(i),op3(i),op4(i),op5(i),op6(i),op7(i),op8(i\
                                                          ),op9(i),op10(i)
01790   420 format(1h ,3x,i2,7x,f10.4,2x,f10.4,3x,f10.4,2x,f10.4,3x,f10.4,2x,
01800      &f10.4,3x,f10.4,2x,f10.4,2x,f10.4,2x,f10.4,2x,f9.4)
01810   670 continue
01820 *
01830 *     output integrated forces and moments if on flap
01840 *
```

```
01850       if(tap1.ne.'fu'.and.tap1.ne.'fl') goto 800
01860       if(fqcy.le.0.1)write(7,700)
01870   700 format(1h1,///)
01880       write(7,715)
01890   715 format(1h0)
01900       if(vinf.le.0.1) goto 850
01910       write(7,705)cls
01920   705 format(1h ,10x,'STEADY SECTION LIFT COEFFICIENT ACTING ON FLAP      \
                                                                    = ',f12.6)
01930       write(7,710)chs
01940   710 format(1h ,10x,'STEADY SECTION HINGE MOMENT COEFFICIENT ACTING ON FL\
                                          AP                        = ',f12.6/)
01950   850 if(fqcy.le.0.1) goto 800
01960       write(7,720)clr
01970   720 format(1h ,10x,'REAL PART OF UNSTEADY SECTION LIFT COEFFICIENT ACTIN\
                                          G ON FLAP                 = ',f12.6)
01980       write(7,725)cli
01990   725 format(1h ,10x,'IMAGINARY PART OF UNSTEADY SECTION LIFT COEFFICIENT \
                                          ACTING ON FLAP            = ',f12.6)
02000       write(7,730)cla
02010   730 format(1h ,10x,'AMPLITUDE OF UNSTEADY SECTION LIFT COEFFICIENT ACTIN\
                                          G ON FLAP                 = ',f12.6)
02020       write(7,735)clt
02030   735 format(1h ,10x,'PHASE LAG OF UNSTEADY SECTION LIFT COEFFICIENT ACTIN\
                                          G ON FLAP (Deg.)          = ',F8.3/)
02040       write(7,740)chr
02050   740 format(1h ,10x,'REAL PART OF UNSTEADY SECTION HINGE MOMENT COEFFICIE\
                                          NT ACTING ON FLAP         = ',f12.6)
02060       write(7,745)chi
02070   745 format(1h ,10x,'IMAGINARY PART OF UNSTEADY SECTION HINGE MOMENT COEF\
                                          FICIENT ACTIN ON FLAP     = ',f12.6)
02080       write(7,750)cha
02090   750 format(1h ,10x,'AMPLITUDE OF UNSTEADY SECTION HINGE MOMENT ACTING ON\
                                           FLAP COEFFICIENT         = ',f12.6)
02100       write(7,755)cht
02110   755 format(1h ,10x,'PHASE LAG OF UNSTEADY SECTION HINGE MOMENT COEFFICIE\
                                          NT ACTING ON FLAP (DEG.) = ',f12.6)
02120   800 close(7)
02130       return
02140       end
```

```
00100       subroutine outpu2
00110 *
00120 *     this subroutine writes data to an unformatted file of name 'file'
00130 *
00140 *     common blocks
00150 *
00160       common/bl1/irun,id1,id2,id3,fn,tap1,itap,ai,aic,fi,fqcy,vinf
00170       common/bl2/ar(19),phase(19),tvol,vent,temp,patmos,pcal,accal
00180       common/bl3/pstdy(19),prein(19),pimin(19),acrein(19),acimin(19)
00190       common/bl4/pzeri,pzerf,re,refqcy,rho,amu,q
00200       common/bl5/accn(19),disp(19),pdsy(19),cpsdy(19),op1(19),op2(19)
00210       common/bl6/op3(19),op4(19),op5(19),op6(19),op7(19),op8(19)
00220       common/bl7/op9(19),op10(19)
00230       common/bl8/nt
00240       common/bl9/filenm,file,itype,omega
00250       common/bl10/deltp,pinf
00260       common/bl11/cls,chs,clr,cli,chr,chi,clo,cho,clt,cht
00270 *
00280       character*8 filenm,file
00290       character*2 tap1
00300 *
00310 *     puts data into unformatted file for storage on tape
00320 *
00330 *     first open file
00340 *
00350       open(8,file=file,status='new')
00360 *
00370 *     write data to file - start with raw data
00380 *
00390       write(8) irun,id1,id2,id3,fn,tap1,itap
00400       write(8) ai,fi,fqcy,vent,nt
00410       write(8) (ar(i),i=1,nt),(phase(i),i=1,nt),tvol
00420       write(8) temp,patmos,fqcy
00430       write(8) (pstdy(i),i=1,nt)
00440       write(8) (prein(i),i=1,nt)
00450       write(8) (pimin(i),i=1,nt)
00460       write(8) (acrein(i),i=1,nt)
00470       write(8) (acimin(i),i=1,nt)
00480       write(8) pzeri,pzerf,pcal,accal
00490 *
00500 *     now write the corrected data
00510 *
00520       write(8) vinf,re,refqcy,rho,amu,q,aic
00530       write(8) (accn(i),i=1,nt)
00540       write(8) (disp(i),i=1,nt)
00550       write(8) (pdsy(i),i=1,nt)
00560       write(8) (cpsdy(i),i=1,nt)
00570       write(8) (op1(i),i=1,nt)
00580       write(8) (op2(i),i=1,nt)
00590       write(8) (op3(i),i=1,nt)
00600       write(8) (op4(i),i=1,nt)
00610       write(8) (op5(i),i=1,nt)
00620       write(8) (op6(i),i=1,nt)
00630       write(8) (op7(i),i=1,nt)
00640       write(8) (op8(i),i=1,nt)
00650       write(8) (op9(i),i=1,nt)
00660       write(8) (op10(i),i=1,nt)
00670       write(8) filenm,file,itype,omega
00680       write(8) deltp,pinf
00690       write(8) cls,chs,clr,cli,chr,chi,clo,cho,clt,cht
```

```
00700 *
00710 *     tidy up and return to main program
00720 *
00730       close(8)
00740       return
00750       end
```

```
00100 *     this program reads data from unformatted file into correct variables
00110 *     for use in manipulation of wind tunnel test data on oscillating flap
00120 *
00130 *     common blocks
00140 *
00150       common/bl1/irun,id1,id2,id3,fn,tap1,itap,ai,aic,fi,fqcy,vinf
00160       common/bl2/ar(19),phase(19),tvol,vent,temp,patmos,pcal,accal
00170       common/bl3/pstdy(19),prein(19),pimin(19),acrein(19),acimin(19)
00180       common/bl4/pzeri,pzerf,re,refqcy,rho,amu,q
00190       common/bl5/accn(19),disp(19),pdsy(19),cpsdy(19),op1(19),op2(19)
00200       common/bl6/op3(19),op4(19),op5(19),op6(19),op7(19),op8(19)
00210       common/bl7/op9(19),op10(19)
00220       common/bl8/nt
00230       common/bl9/filenm,file,itype,omega
00240       common/bl10/deltp,pinf
00250       common/bl11/cls,chs,clr,cli,chr,chi,clo,cho,clt,cht
00260 *
00270       character*8 filenm,file
00280       character*2 tap1
00290       character*1 ans
00300 *
00310 *     first ask operator for name of file from whick data is to be read
00320 *
00330       print *,'ENTER NAME OF FILE FROM WHICH DATA IS TO BE READ'
00340       read(5,*) file
00350 *
00360 *     reads data from unformatted file specified by operator
00370 *     first open file
00380 *
00390       open(8,file=file,status='old')
00400 *
00410 *     read data from file
00420 *
00430       read(8) irun,id1,id2,id3,fn,tap1,itap
00440       read(8) ai,fi,fqcy,vent,nt
00450       read(8) (ar(i),i=1,nt),(phase(i),i=1,nt),tvol
00460       read(8) temp,patmos,fqcy
00470       read(8) (pstdy(i),i=1,nt)
00480       read(8) (prein(i),i=1,nt)
00490       read(8) (pimin(i),i=1,nt)
00500       read(8) (acrein(i),i=1,nt)
00510       read(8) (acimin(i),i=1,nt)
00520       read(8) pzeri,pzerf,pcal,accal
00530 *
00540 *     now read the corrected data
00550 *
00560       read(8) vinf,re,refqcy,rho,amu,q,aic
00570       read(8) (accn(i),i=1,nt)
00580       read(8) (disp(i),i=1,nt)
00590       read(8) (pdsy(i),i=1,nt)
00600       read(8) (cpsdy(i),i=1,nt)
00610       read(8) (op1(i),i=1,nt)
00620       read(8) (op2(i),i=1,nt)
00630       read(8) (op3(i),i=1,nt)
00640       read(8) (op4(i),i=1,nt)
00650       read(8) (op5(i),i=1,nt)
00660       read(8) (op6(i),i=1,nt)
00670       read(8) (op7(i),i=1,nt)
00680       read(8) (op8(i),i=1,nt)
00690       read(8) (op9(i),i=1,nt)
```

```
00700       read(8) (op10(i),i=1,nt)
00710       read(8) filenm,file,itype,omega
00720       read(8) deltp,pinf
00730       read(8) cls,chs,clr,cli,chr,chi,cla,cha,clt,cht
00740       close(8)
00750 *
00760 *     ask user if a formatted output file is needed
00770 *
00780       print *,'DO YOU WANT TO HAVE THE DATA FORMATTED INTO OUTPUT FILE'
00790       read(5,*)ans
00800       if(ans.ne.'y') goto 200
00810       call output
00820 *
00831   200 call plot(cpsdy,nt)
00832       stop
00840       end
```

Example of output from data reduction program for data measured on control surface at $y/s = 0.3357$.

TEST DATA FOR UNSTEADY FORCES ON FIN WITH OSCILLATING FLAP

RUN No. = 238 RUN DATE = 17: 7:85 FORMATTED FILE NAME = f238 UNFORMATTED FILE NAME = f238o

PRESSURE TAPPING ROW DEFINITION = fu 1

AIRFOIL MEAN INCIDENCE (deg) = 0.00

FLAP MEAN DEFLECTION ANGLE (deg) = 0.00

FLAP OSCILLATION FREQUENCY (Hz) = 20.00

WIND TUNNEL SPEED (m/s) = 40.00

PRESSURE TUBING CALIBRATION CONSTANTS

DATA POINT NUMBER	AMPLITUDE RATIO	PHASE LAG (deg)
1	1.015	27.53
2	1.015	27.23
3	1.014	27.86
4	1.015	27.22
5	1.015	27.52
6	1.015	27.22
7	1.014	27.85
8	1.015	27.21
9	1.015	27.50
10	1.006	29.07
11	0.995	31.58
12	1.015	27.23
13	1.015	27.52

TRANSDUCER VOLUME (mm3) = 82.0000

UNCORRECTED RAW DATA

WIND TUNNEL SPEED (m/s) = 40.000

WIND TUNNEL TEMPERATURE (deg C) = 22.000

BAROMETRIC PRESSURE (mBar) = 1005.37

FREQUENCY OF FLAP OSCILLATIONS (Hz) = 20.000

DATA POINT NUMBER	STEADY PRESSURE VOLTS	REAL PART OSCILLATORY VOLTS	IMAG. PART OSCILLATORY VOLTS	REAL PART ACC,N VOLTS	IMAG. PART ACC,N VOLTS
1	-4.950000	-0.240000	0.286000	-0.034300	0.021900
2	-4.460000	-0.176000	0.135000	-0.034300	0.021900
3	-4.380000	-0.177000	0.120000	-0.034300	0.021900
4	-4.200000	-0.151000	0.076000	-0.034300	0.021900
5	-4.020000	-0.111000	0.027000	-0.034300	0.021900
6	-3.850000	-0.090000	0.007000	-0.034300	0.021900
7	-3.680000	-0.081000	0.000000	-0.034300	0.021900
8	-3.500000	-0.071000	-0.005000	-0.034300	0.021900
9	-3.300000	-0.056000	-0.016000	-0.034300	0.021900
10	-3.020000	-0.036000	-0.020000	-0.034300	0.021900
11	-2.560000	-0.005000	-0.019000	-0.034300	0.021900
12	-4.570000	0.192000	-0.161000	-0.034300	0.021900
13	-4.570000	0.192000	-0.161000	-0.034300	0.021900

INITIAL ZERO PRESSURE READING (Volts) = 0.532000

FINAL ZERO PRESSURE READING (Volts) = 0.535000

PRESSURE TRANSDUCER CALIBRATION (VOLT/N/M2) = 0.0108878

ACCELEROMETER CALIBRATION (VOLT/M/S2) = 0.0036500

PRESSURE TRANSDUCER TYPE = SETRA +- 0.1 PSI

CORRECTED DATA

WIND TUNNEL VELOCITY (m/s)	= 40.000	REYNOLDS NUMBER (BASED ON CHORD)	= 0.1154E+07
FLAP OSCILLATION FREQUENCY (Hz)	= 20.000	REDUCED FREQUENCY (BASED ON SEMICHORD)	= 0.6982
ATMOSPHERIC PRESSURE (mBar)	= 1005.370	AIR TEMPERATURE (deg C)	= 22.0000
AIR DENSITY (kg/m3)	= 1.18197	DYNAMIC VISCOSITY (Mu) OF AIR (Ns/m2)	= 0.1829E-04
DYNAMIC PRESSURE (N/m2)	= 949.317	FREESTREAM STAIC PRESSURE (N/m2)	= 100129.91
FIN INCIDENCE (deg)	= 0.00000	FLAP DEFLECTION ANGLE (deg)	= 0.00000

TAPPING NUMBER	ACCELERATION AMPLITUDE (rad/s2)	DISPLACEMENT AMPLITUDE (deg)	STEADY PRESSURE (N/m2)	STEADY PRESSURE (Cp)
1	278.734	1.011	-96.406	-0.1016
2	278.734	1.011	-51.424	-0.0542
3	278.734	1.011	-44.100	-0.0465
4	278.734	1.011	-27.590	-0.0291
5	278.734	1.011	-11.081	-0.0117
6	278.734	1.011	4.510	0.0048
7	278.734	1.011	20.101	0.0212
8	278.734	1.011	36.610	0.0386
9	278.734	1.011	54.956	0.0579
10	278.734	1.011	80.650	0.0850
11	278.734	1.011	122.876	0.1294
12	278.734	1.011	-61.757	-0.0651
13	278.734	1.011	-61.780	-0.0651

TAPPING NUMBER	OSCILLATORY PRESSURE									
	NEWTONS/SQUARE METRE				Cp		AMPLITUDE NORMALISED Cp			
	REAL	IMAG	AMPLITUDE	PHASE	REAL	IMAG	REAL	IMAG	AMPLITUDE	PHASE
1	-34.2573	-6.0960	34.7955	169.9099	-0.0361	-0.0064	-2.0444	-0.3638	2.0765	169.9099
2	-19.1338	-7.8451	20.6796	157.7057	-0.0202	-0.0083	-1.1419	-0.4682	1.2341	157.7057
3	-17.8629	-8.8219	19.9226	153.7167	-0.0188	-0.0093	-1.0660	-0.5265	1.1890	153.7167
4	-13.2085	-8.5985	15.7606	146.9367	-0.0139	-0.0091	-0.7883	-0.5131	0.9406	146.9367
5	-7.3423	-7.7106	10.6473	133.5984	-0.0077	-0.0081	-0.4382	-0.4602	0.6354	133.5984
6	-4.7881	-6.9218	8.4165	124.6730	-0.0050	-0.0073	-0.2857	-0.4131	0.5023	124.6730
7	-3.7268	-6.5624	7.5468	119.5923	-0.0039	-0.0069	-0.2224	-0.3916	0.4504	119.5923
8	-2.9303	-5.9543	6.6363	116.2030	-0.0031	-0.0063	-0.1749	-0.3553	0.3960	116.2030
9	-1.3127	-5.2675	5.4286	103.9934	-0.0014	-0.0055	-0.0783	-0.3144	0.3240	103.9934
10	0.0455	-3.8061	3.8063	89.3156	0.0000	-0.0040	0.0027	-0.2271	0.2272	89.3156
11	1.3633	-1.1688	1.7958	40.6058	0.0014	-0.0012	0.0814	-0.0698	0.1072	40.6058
12	21.9786	7.9148	23.3603	340.1953	0.0232	0.0083	1.3117	0.4723	1.3941	340.1953
13	21.9304	8.0257	23.3528	339.8993	0.0231	0.0085	1.3088	0.4790	1.3937	339.8993

STEADY SECTION LIFT COEFFICIENT ACTING ON FLAP = 0.002793
STEADY SECTION HINGE MOMENT COEFFICIENT ACTING ON FLAP = 0.001305

REAL PART OF UNSTEADY SECTION LIFT COEFFICIENT ACTING ON FLAP = -0.119289
IMAGINARY PART OF UNSTEADY SECTION LIFT COEFFICIENT ACTING ON FLAP = -0.093571
AMPLITUDE OF UNSTEADY SECTION LIFT COEFFICIENT ACTING ON FLAP = 0.151609
PHASE LAG OF UNSTEADY SECTION LIFT COEFFICIENT ACTING ON FLAP (Deg.) = 218.111

REAL PART OF UNSTEADY SECTION HINGE MOMENT COEFFICIENT ACTING ON FLAP = -0.006553
IMAGINARY PART OF UNSTEADY SECTION HINGE MOMENT COEFFICIENT ACTIN ON FLAP = -0.009679
AMPLITUDE OF UNSTEADY SECTION HINGE MOMENT ACTING ON FLAP COEFFICIENT = 0.011689
PHASE LAG OF UNSTEADY SECTION HINGE MOMENT COEFFICIENT ACTING ON FLAP (DEG.) = 235.898170

APPENDIX 2

Derivation of equations governing the dynamic response of pneumatic tubing systems to sinusoidal pressure fluctuations

NOTATION

SYMBOL	DESCRIPTION
$a_0 = \sqrt{\gamma p_s / \rho_s}$	Mean velocity of sound.
C_p	Specific heat at constant pressure.
C_v	Specific heat at constant volume.
g	Acceleration due to gravity.
$i = \sqrt{-1}$	Complex operator.
$J_{n'}$	Bessel function of first kind and order n'.
k	Polytropic constant for expansion in a volume.
l	Tube length.
m	Mass of fluid in motion.
n	Kind of polytropic constant given in equation 1.

SYMBOL	DESCRIPTION
N	Number of tubes and volumes.
$\bar{p} = p_s + pe^{i\omega t}$	Total pressure.
p_s	Mean pressure.
p	Amplitude of oscillatory pressure.
$Pr = \mu g C_p / \lambda$	Prandtl number.
r	co-ordinate in radial direction.
R	Radius of tube.
R_0	Universal gas constant.
t	Time
$\bar{T} = T_s + Te^{i\omega t}$	Total temperature
T_s	Mean temperature.
T	Amplitude of fluctuating temperature.
$\bar{u} = ue^{i\omega t}$	Velocity component in axial direction.
u	Amplitude of velocity disturbance in axial direction.
$\bar{v} = ve^{i\omega t}$	Velocity component in radial direction.
v	Amplitude of velocity disturbance in radial direction.
V_t	Pressure transducer volume.

SYMBOL	DESCRIPTION
$V_v = \pi R^2 l$	Volume of tube.
x	Axial co-ordinate along tube.
$z = \alpha r\sqrt{Pr} \Big/ R$	
$\alpha = i^{1.5} R \sqrt{\rho_s \omega / \mu}$	Shear wave number.
$\gamma = C_p \Big/ C_v$	Specific heat ratio
λ	Thermal conductivity.
μ	Absolute fluid viscosity.
$\omega = 2\pi / t$	Circular frequency.
$\bar{\rho} = \rho_s + \rho e^{i\omega t}$	Fluid density.
ρ_s	Mean density.
ρ	Amplitude of density disturbance.
$\sigma = \Delta V_t \Big/ V_t$	Dimensionless increase in transducer volume due to diaphragm deflection.

$$\phi = \frac{\omega}{a_0}\sqrt{\frac{J_0[\alpha]}{J_2[\alpha]}}\sqrt{\frac{\gamma}{n}}$$

SUBSCRIPTS

j	Refers to pressure transducer j or tube j.
v	Refers to pressure transducer volume.

BASIC FORMULAE AND ASSUMPTIONS

The equations governing the motion of a fluid in a tube of circular cross-section (Fig. A1a) are:-

a). The Navier-Stokes equations (for constant absolute fluid viscosity):

$$\bar{\rho}\frac{\partial \bar{u}}{\partial t}+\bar{v}\frac{\partial \bar{u}}{\partial r}+\bar{u}\frac{\partial \bar{u}}{\partial x}=-\frac{\partial \bar{p}}{\partial x}+\mu\left[\left[\frac{\partial^2 \bar{u}}{\partial x^2}+\frac{\partial^2 \bar{u}}{\partial r^2}+\frac{1}{r}\frac{\partial \bar{u}}{\partial r}\right]+\frac{1}{3}\frac{\partial}{\partial x}\left[\frac{\partial \bar{u}}{\partial x}+\frac{\partial \bar{v}}{\partial r}+\frac{\bar{v}}{r}\right]\right] \qquad \text{A2.1}$$

$$\bar{\rho}\frac{\partial \bar{v}}{\partial t}+\bar{v}\frac{\partial \bar{v}}{\partial r}+\bar{u}\frac{\partial \bar{v}}{\partial x}=-\frac{\partial \bar{p}}{\partial r}+\mu\left[\left[\frac{\partial^2 \bar{v}}{\partial r^2}+\frac{1}{r}\frac{\partial \bar{v}}{\partial r}-\frac{\bar{v}}{r^2}+\frac{\partial^2 \bar{v}}{\partial x^2}\right]+\frac{1}{3}\frac{\partial}{\partial r}\left[\frac{\partial \bar{u}}{\partial x}+\frac{\partial \bar{v}}{\partial r}+\frac{\bar{v}}{r}\right]\right] \qquad \text{A2.2}$$

b). The equation of continuity:

$$\frac{\partial \bar{\rho}}{\partial t}+u\frac{\partial \bar{\rho}}{\partial x}+v\frac{\partial \bar{\rho}}{\partial r}+\bar{\rho}\left[\frac{\partial \bar{u}}{\partial x}+\frac{\partial \bar{v}}{\partial r}+\frac{\bar{v}}{r}\right]=0 \qquad \text{A2.3}$$

c). The equation of state for an ideal gas:

$$\bar{p} = \bar{\rho} R_0 \bar{T} \qquad \text{A2.4}$$

d). The energy equation:

$$\bar{\rho} g C_p \left[\frac{\partial \bar{T}}{\partial t} + \bar{u}\frac{\partial \bar{T}}{\partial x} + \bar{v}\frac{\partial \bar{T}}{\partial r}\right] = \lambda\left[\frac{\partial^2 \bar{T}}{\partial r^2} + \frac{\partial \bar{T}}{r\partial r} + \frac{\partial^2 \bar{T}}{\partial x^2}\right] + \frac{\partial \bar{p}}{\partial t} + \bar{u}\frac{\partial \bar{p}}{\partial x} + \bar{v}\frac{\partial \bar{p}}{\partial r} + \mu\phi \qquad \text{A2.5}$$

Where ϕ is the dissipation function that represents the heat transfer due to internal friction:

$$\phi = 2\left[\left(\frac{\partial \bar{u}}{\partial x}\right)^2 + \left(\frac{\partial \bar{v}}{\partial r}\right)^2 + \left(\frac{\bar{v}}{r}\right)^2\right] + \left[\frac{\partial \bar{v}}{\partial x} + \frac{\partial \bar{u}}{\partial r}\right]^2 - \frac{2}{3}\left[\frac{\partial \bar{u}}{\partial x} + \frac{\partial \bar{v}}{\partial r} + \frac{\bar{v}}{r}\right]^2 \qquad \text{A2.5a}$$

putting:

$$\bar{p} = p_s + pe^{i\omega t}$$

$$\bar{\rho} = \rho_s + \rho e^{i\omega t}$$

$$\bar{T} = T_s + Te^{i\omega t}$$

$$\bar{u} = ue^{i\omega t}$$

$$\bar{v} = ve^{i\omega t}$$

and assuming that:-

a). The sinusoidal disturbances are small.

b). The internal radius of the tube is small in comparison with its length.

c). The flow is laminar throughout the system.

the equations A2.1 to A2.5 can be simplified to:-

$$i\omega u = -\frac{1}{\rho_s}\cdot\frac{\partial p}{\partial x} + \frac{\mu}{\rho_s}\left[\frac{\partial^2 u}{\partial r^2} + \frac{1}{r}\cdot\frac{\partial u}{\partial r}\right] \qquad \text{A2.6}$$

$$0 = -\frac{\partial p}{\partial r} \qquad \text{A2.7}$$

$$i\omega\rho = -\rho_s\left[\frac{\partial u}{\partial x} + \frac{\partial v}{\partial r} + \frac{v}{r}\right] \qquad \text{A2.8}$$

$$\rho = \frac{\gamma}{a_0^2}\left[1 + \frac{\rho_s}{T_s}\cdot\frac{T}{\rho}\right] \quad \underline{\text{or}} \quad \rho = \frac{\gamma}{a_0^2}\left[p - \rho_s R_0 T\right] \qquad \text{A2.9}$$

$$i\omega\rho_s g C_p T = \lambda\left[\frac{\partial^2 T}{\partial r^2} + \frac{1}{r}\cdot\frac{\partial T}{\partial r}\right] + i\omega p \qquad \text{A2.10}$$

The unknown quantities p, ρ, T, u, and v must satisfy the following boundary conditions:

At the wall of the tube (r = R):

1). Zero radial and axial velocity, i.e. $u = 0$, $v = 0$ A2.11

2). The conductivity of the wall is supposed to be so large that the variation in temperature at the wall will be zero: $T = 0$ A2.12

At the centre of the tube (r = 0):

1). Due to axial symmetry $v = 0$ A2.13

A further requirement is that the values of u, T, p, and remain finite.

GENERAL SOLUTION

From equation A2.7 it follows that the amplitude of the pressure disturbance p is a function of the x co-ordinate only. Equation A2.10 can be written as:-

$$T - \frac{\lambda}{i\omega\rho_s g C_p}\left[\frac{\partial^2 T}{\partial r^2} + \frac{1}{r}\frac{\partial T}{\partial r}\right] = \frac{p}{\rho_s g C_p} \qquad \text{A2.14}$$

introducing the notation $\alpha = -i^{\frac{1}{2}} R\sqrt{\frac{\rho\omega}{\mu}}$ and $Pr = \mu g C_p / \lambda$ (the so called Prandtl number) and putting $T = f\langle x\rangle \cdot h\langle z\rangle$, where $z = \frac{\alpha r}{R}\sqrt{Pr}$ equation A2.14 reads:-

$$\frac{d^2 h\langle z\rangle}{dz^2} + \frac{1}{z}\cdot\frac{dh\langle z\rangle}{dz} + h\langle z\rangle = \frac{p}{\rho_s g C_p}\cdot\frac{1}{f\langle x\rangle} \qquad \text{A2.15}$$

with the solution:-

$$h\langle x\rangle = C_1 J_0\langle z\rangle + C_2 Y_0\langle z\rangle + \frac{p}{\rho_s g C_p} \cdot \frac{1}{f\langle x\rangle} \qquad \text{A2.16}$$

From the condition that T must remain finite for r = 0, it follows that $C_2 = 0$. For r = R, T must be zero, so:-

$$f\langle x\rangle = -\frac{1}{C_1 J_0\langle \alpha\sqrt{Pr}\rangle} \cdot \frac{p}{\rho_s g C_p} \qquad \text{A2.17}$$

From A2.16 and A2.17

$$T = f\langle x\rangle . h\langle z\rangle = \left[1 - \frac{J_0\left\langle \frac{\alpha r}{R}\sqrt{Pr}\right\rangle}{J_0\langle \alpha\sqrt{Pr}\rangle}\right] \frac{p}{\rho_s g C_p} \qquad \text{A2.18}$$

and substituting this result in equation A2.9

$$\rho = \frac{\gamma}{a_0^2} p \left[1 - \left[\frac{\gamma - 1}{\gamma}\right]\left\{1 - \frac{J_0\left\langle \frac{\alpha r}{R}\sqrt{Pr}\right\rangle}{J_0\langle \alpha\sqrt{Pr}\rangle}\right\}\right] \qquad \text{A2.19}$$

Equation A2.6 can be written as:-

$$u - \frac{\mu}{i\omega\rho_s}\left[\frac{\partial^2 u}{\partial r^2} + \frac{1}{r}\frac{\partial u}{\partial r}\right] = -\frac{1}{i\omega\rho_s}\frac{dp}{dx} \qquad \text{A2.20}$$

This equation can be solved in a similar way as equation A2.14. The solution that fulfils the requirements that u remains finite for r = 0 and is zero for r = R yields:-

$$u = \left[\frac{J_0 \left\langle \frac{\alpha r}{R} \right\rangle}{J_0 \langle \alpha \rangle} - 1 \right] \cdot \frac{1}{i\omega\rho_s} \cdot \frac{dp}{dx} \qquad \text{A2.21}$$

Finally the equation of continuity, equation A2.8, has to be satisfied, thus:-

$$\frac{1}{r} \cdot \frac{\partial (vr)}{\partial r} = iv \frac{\rho}{\rho_s} - \frac{\partial u}{\partial x} \qquad \text{A2.22}$$

or with the aid of the expressions A2.19 and A2.21:-

$$\frac{1}{r}\frac{\partial(vr)}{\partial r} = \frac{1}{i\omega\rho_s} \left[\frac{\omega^2}{a_0^2} \gamma p \left\{ 1 - \left[\frac{\gamma - 1}{\gamma} \right] \left\{ 1 - \frac{J_0 \left\langle \frac{\alpha r}{R} \sqrt{Pr} \right\rangle}{J_0 \left\langle \alpha \sqrt{Pr} \right\rangle} \right\} \right\} - \frac{d^2 p}{dx^2} \left\{ \frac{J_0 \left\langle \frac{\alpha r}{R} \right\rangle}{J_0 \langle \alpha \rangle} - 1 \right\} \right] \qquad \text{A2.23}$$

After integration with respect to r:-

$$vr = \frac{1}{i\omega\rho_s}\left[\frac{\omega^2}{a_0^2}\gamma p\left\{\frac{r^2}{2}-\left(\frac{\gamma-1}{\gamma}\right)\left(\frac{r^2}{2}-\frac{rR}{\alpha\sqrt{Pr}}\,\frac{J_1\left\langle\frac{\alpha r}{R}\sqrt{Pr}\right\rangle}{J_0\left\langle\alpha\sqrt{Pr}\right\rangle}\right)\right\}\right.$$

$$\left.-\frac{d^2p}{dx^2}\left\{\frac{rR}{\alpha}\cdot\frac{J_1\left\langle\frac{\alpha r}{R}\right\rangle}{J_0\left\langle\alpha\right\rangle}-\frac{r^2}{2}\right\}+f\left\langle x\right\rangle\right] \qquad \text{A2.24}$$

From the boundary condition v = 0 at r = R it follows that:-

$$-f\left\langle x\right\rangle = \frac{\omega^2}{a_0^2}\gamma\frac{R^2}{2}\cdot p\left\{1+\left\{\frac{\gamma-1}{\gamma}\right\}\cdot\frac{J_2\left\langle\alpha\sqrt{Pr}\right\rangle}{J_0\left\langle\alpha\sqrt{Pr}\right\rangle}\right\}-\frac{R^2}{2}\cdot\frac{d^2p}{dx^2}\cdot\frac{J_2\left\langle\alpha\right\rangle}{J_0\left\langle\alpha\right\rangle} \qquad \text{A2.25}$$

Due to the axial symmetry, it must hold that $\lim_{r\to 0} v = 0$ A2.26

This requirement is fulfilled if $f\left\langle x\right\rangle = 0$, or

$$\frac{\omega^2}{a_0^2}\gamma p\left\{1+\frac{\gamma-1}{\gamma}\,\frac{J_2\left\langle\alpha\sqrt{Pr}\right\rangle}{J_0\left\langle\alpha\sqrt{Pr}\right\rangle}\right\}-\frac{J_2\left\langle\alpha\right\rangle}{J_0\left\langle\alpha\right\rangle}\cdot\frac{d^2p}{dx^2}=0 \qquad \text{A2.27}$$

From this differential equation p can be solved as:-

$$p = A\exp\left[\frac{\omega x}{a_0}\sqrt{\frac{J_0\langle\alpha\rangle}{J_2\langle\alpha\rangle}}\left\{\gamma+[\gamma-1]\cdot\frac{J_2\langle\alpha\sqrt{Pr}\rangle}{J_0\langle\alpha\sqrt{Pr}\rangle}\right\}^{\frac{1}{2}}\right]$$

$$+ B\exp\left[\frac{-\omega x}{a_0}\sqrt{\frac{J_0\langle\alpha\rangle}{J_2\langle\alpha\rangle}}\left\{\gamma+[\gamma-1]\ \frac{J_2\langle\alpha\sqrt{Pr}\rangle}{J_0\langle\alpha\sqrt{Pr}\rangle}\right\}^{\frac{1}{2}}\right] \qquad \text{A2.28}$$

introducing the notation

$$n = \frac{1}{1+\frac{\gamma-1}{\gamma}\cdot\frac{J_2\langle\alpha\sqrt{Pr}\rangle}{J_0\langle\alpha\sqrt{Pr}\rangle}} \qquad \text{A2.29}$$

the general solution for the fluid motion in a tube yields:-

$$p = A\exp\left[\frac{\omega x}{a_0}\sqrt{\frac{J_0\langle\alpha\rangle}{J_2\langle\alpha\rangle}}\sqrt{\frac{\gamma}{n}}\right] + B\exp\left[\frac{-\omega x}{a_0}\sqrt{\frac{J_0\langle\alpha\rangle}{J_2\langle\alpha\rangle}}\sqrt{\frac{\gamma}{n}}\right] \qquad \text{A2.30}$$

$$u = \frac{i}{a_0\rho_s}\sqrt{\frac{J_0\langle\alpha\rangle}{J_2\langle\alpha\rangle}}\sqrt{\frac{\gamma}{n}}\left\{\frac{J_0\langle\frac{\alpha r}{R}\rangle}{J_0\langle\alpha\rangle}-1\right\}\left\{A\exp\left[\frac{\omega x}{a_0}\sqrt{\frac{J_0\langle\alpha\rangle}{J_2\langle\alpha\rangle}}\sqrt{\frac{\gamma}{n}}\right]\right.$$

$$\left. - B\exp\left[\frac{-\omega x}{a_0}\sqrt{\frac{J_0\langle\alpha\rangle}{J_2\langle\alpha\rangle}}\sqrt{\frac{\gamma}{n}}\right]\right\} \qquad \text{A2.31}$$

$$v = \frac{i\omega}{a_0^2 \rho_s}\left[\frac{r}{2}\left\{1 + \frac{J_0\langle\alpha\rangle}{J_2\langle\alpha\rangle}\cdot\frac{\gamma}{n}\right\} + \frac{(\gamma-1)R}{\alpha\sqrt{Pr}}\cdot\frac{J_1\left\langle\frac{\alpha r}{R}\sqrt{Pr}\right\rangle}{J_2\langle\alpha\sqrt{Pr}\rangle} - \frac{R\gamma}{n\alpha}\cdot\frac{J_1\left\langle\frac{\alpha r}{R}\right\rangle}{J_2\langle\alpha\rangle}\right] p \qquad \text{A2.32}$$

$$\rho = \frac{\gamma}{a_0^2}\left[1 - \left\{\frac{\gamma-1}{\gamma}\right\}\left\{1 - \frac{J_0\left\langle\frac{\alpha r}{R}\sqrt{Pr}\right\rangle}{J_0\langle\alpha\sqrt{Pr}\rangle}\right\}\right] p \qquad \text{A2.33}$$

$$T = \frac{1}{\rho_s g\, C_p}\left[1 - \frac{J_0\left\langle\frac{\alpha r}{R}\sqrt{Pr}\right\rangle}{J_0\langle\alpha\sqrt{Pr}\rangle}\right] p \qquad \text{A2.34}$$

The constants A and B can be determined after the boundary conditions at both ends of the tube have been defined.

APPLICATION

With the aid of the solutions A2.30 to A2.34 a system consisting of a series connection of N tubes and N volumes (Fig. A1b) can be treated. To solve this problem some additional assumptions are made:-

1). The pressure and density in the instrument volumes time dependent.

2). The pressure expansion in the instrument volume is a polytropic process, described by:-

$$\left(\frac{\bar{p}_v}{\bar{\rho}_v}\right)^{k_j} = \text{constant} \qquad \text{A2.35}$$

For the flow through tube j the following expressions are valid

$$p = A_j \exp(\phi_j X_j) - B_j \exp(-\phi_j X_j) \qquad \text{A2.36}$$

and

$$u = \frac{i}{\omega \rho_{sj}} \cdot \phi_j \left\{ \frac{J_0 \left\langle \frac{\alpha_j R_j}{r} \right\rangle}{J_0 \left\langle \alpha_j \right\rangle} - 1 \right\} \left\{ A_j \exp(\phi_j X_j) - B_j \exp(-\phi_j X_j) \right\} \qquad \text{A2.37}$$

where $$\phi_j = \frac{\omega}{a_{0j}} \sqrt{\frac{J_0 \left\langle \alpha_j \right\rangle}{J_2 \left\langle \alpha_j \right\rangle}} \cdot \sqrt{\frac{\gamma}{n_j}} \quad \text{and } j = 1,2,3\ldots N \qquad \text{A2.38}$$

For tube j it holds:

At the entrance: $X_j = 0 : p_{j-1} = A_j + B_j$ A2.39

At the exit: $X_j = l_j : p_j = A_j \exp(\phi_j l_j) + B_j \exp(-\phi_j l_j)$ A2.40

$$u_{ji} = \frac{i}{\omega \rho_{sj}} \cdot \phi_j \left\{ \frac{J_0 \left\langle \frac{\alpha_j R_j}{r} \right\rangle}{J_0 \left\langle \alpha_j \right\rangle} - 1 \right\} \left\{ A_j \exp(\phi_j l_j) + B_j (-\phi_j l_j) \right\} \qquad \text{A2.41}$$

and the mass leaving tube j :-

$$m_{ji} = \int_0^{R_j} \rho_{sj} u_{ji} 2\pi r dr$$

$$m_{ji} = \frac{\pi R_j^2 \phi_j}{i\omega} \cdot \frac{J_2 \left\langle \alpha_j \right\rangle}{J_0 \left\langle \alpha_j \right\rangle} \cdot \left\{ A_j \exp(\phi_j l_j) - B_j \exp(-\phi_j l_j) \right\} \qquad \text{A2.42}$$

for the tube j+1 it holds:-

at the entrance: $X_{j+1} = 0$

$$p_j = A_{j+1} + B_{j+1} \qquad \text{A2.43}$$

$$u_{j0} = \frac{i}{\omega \rho_{sj+1}} \cdot \phi_{j+1} \left\{ \frac{J_0 \left\langle \frac{\alpha_{j+1} R_{j+1}}{r} \right\rangle}{J_0 \left\langle \alpha_{j+1} \right\rangle} - 1 \right\} + \left\{ A_{j+1} - B_{j+1} \right\} \qquad \text{A2.44}$$

the mass entering tube j+1:

$$m_{j0} = \int_0^{R_{j+1}} \rho_{sj+1} u_{j0} 2\pi r dr = \frac{\pi R_{j+1}^2 \phi_{j+1}}{i\omega} \cdot \frac{J_2 \left\langle \alpha_{j+1} \right\rangle}{J_0 \left\langle \alpha_{j+1} \right\rangle} \cdot \left\{ A_{j+1} - B_{j+1} \right\} \qquad \text{A2.45}$$

at the exit: $X_{j+1} = l_{j+1}$

$$p_{j+1} = A_{j+1} \exp(\phi_{j+1} l_{j+1}) + B_{j+1} \exp(-\phi_{j+1} l_{j+1}) \qquad \text{A2.46}$$

From equations A2.39 and A2.40 it can easily be found that:-

$$A_j = \frac{p_j - p_{j-1} \exp(-\phi_j l_j)}{\exp(\phi_j l_j) - \exp(-\phi_j l_j)} \quad \text{and} \quad B_j = \frac{p_{j-1} \exp(\phi_j l_j) - P_j}{\exp(\phi_j l_j) - \exp(-\phi_j l_j)} \qquad \text{A2.47}$$

and from equations A2.43 and A2.46 it follows:-

$$A_{j+1} = \frac{p_{j+1} - p_j \exp(-\phi_{j+1} l_{j+1})}{\exp(\phi_{j+1} l_{j+1}) - \exp(-\phi_{j+1} l_{j+1})}$$

A2.48

$$B_{j+1} = \frac{p_j \exp(\phi_{j+1} l_{j+1}) - p_{j+1}}{\exp(\phi_{j+1} l_{j+1}) - \exp(-\phi_{j+1} l_{j+1})}$$

For the instrument volume it is assumed that

$$\frac{p_v}{\rho_v} \cdot k_j = \frac{p_s + p_v e^{ivt}}{\rho_s + \rho_v e^{ivt}} \cdot k_j = \frac{p_s}{\rho_{sj}} \cdot k_j \qquad \text{A2.49}$$

Considering small values of p_v $(=p_j)$ and ρ_v equation A2.49 can be simplified to:-

$$p_j = a_{0j}^2 \; k_j \; p_v / \gamma \qquad \text{A2.50}$$

The instrument volume corrected for diaphragm deflection is defined as follows:-

$$V_{vj} = \left[1 + \frac{\sigma_j \; p_j}{p_s} \; e^{i\omega t} \right] \qquad \text{A2.51}$$

The mass of air within this volume is then:-

$$m_v = V_{vj} \left\{ 1 + \frac{\sigma_j p_j}{p_s} \; e^{i\omega t} \right\} \left\{ \rho_{sj} + \rho_v e^{i\omega t} \right\}$$

$$m_v = V_{vj} \left\{ \rho_{sj} + \frac{\sigma_j \rho_{sj}}{p_s} \; p_j e^{i\omega t} + \frac{\gamma}{a_0^2 k_j} \; p_j e^{i\omega t} \right\} \qquad \text{A2.52}$$

The variation of mass within the instrument volume is :-

$$\frac{dm_v}{dt} = \frac{i\omega\gamma}{a_{0j}^2} \cdot V_{vj} \cdot \left\{ \sigma_j + \frac{1}{k_j} \right\} p_j e^{i\omega t} \qquad \text{A2.53}$$

The mass increase of the instrument volume must be equal to the difference in mass leaving tube j and the mass entering tube j+1, thus:-

$$\frac{dm_v}{dt} = \left\{ m_{ji} - m_{j0} \right\} \; e^{i\omega t}$$

Substituting the expressions A2.42, A2.45, A2.47, A2.48 and A2.53 in equation A2.54 the following recursion formula can be derived:

$$\frac{p_j}{p_{j-1}} = \left[\cosh(\phi_j l_j) + \frac{V_{vj}}{V_{tj}} \; \phi_j + \frac{1}{k_j} \; n_j \phi_j l_j \sinh(\phi_j l_j) + \right.$$

$$\left\{ \frac{V_{tj+1}}{V_{tj}} \cdot \frac{\phi_{j+1}}{\phi_j} \cdot \frac{l_j}{l_{j+1}} \cdot \frac{J_0\langle \alpha_j \rangle}{J_0\langle \alpha_{j+1} \rangle} \cdot \frac{J_2\langle \alpha_{j+1} \rangle}{J_2\langle \alpha_j \rangle} \cdot \frac{\sinh(\phi_j l_j)}{\sinh(\phi_{j+1} l_{j+1})} \right\}$$

$$\left. \left\{ \cosh(\phi_{j+1} l_{j+1}) - \frac{p_{j+1}}{p_j} \right\} \right]^{-1} \qquad \text{A2.55}$$

with $v_{tj} = R_j^2 l_j$, the volume of tube j.

From the recursion formula A2.55 the expressions for the complex ratio of the pressure fluctuation of each transducer j to the sinusoidal input pressure p_0 can be derived by successively putting j = N,N-1,....2,1. It will be noticed that for j = N the last two terms of expression A2.55 disappear.

APPENDIX 3

Fortran listings of program used to evaluate the frequency response of a pneumatic tube system for measuring small amplitude oscillatory pressures.

Length of tube elements = l1,l2,l3,l4,l5,l6

Diameters of tube lengths = d1,d2,d3,d4,d5,d6

```
00100 *     ************************************************************
00110 *
00120 *
00130 *     computation of pressure ratio of transducer measurement
00140 *     to the averaged sum of the input pressures for multiple
00150 *     pneumatic systems with mp identical primary manifolds
00160 *     each with ma identical tube inputs.
00170 *     provision made for internal scanivalve tubing
00180 *     provision made for orifice crossflow effects
00190 *
00200 *     ************************************************************
00210 *
220 real d(6),l(6),phas(500),mu,k2
00230       complex b6,bz,u,v,n(6),bfo(6),bf2(6),phi(6),ch(6)
00240       complex a(6),z,s,t,q6,q5,q4,q3,q1,qa,sh(6),q2,qv
00250       common mes
00260       real*4 mes
00270       open(7,carriage=.true.,form='formatted')
00280    60 continue
00290       write(6,150)
00300   150 format( ' type (non zero) tube d1,d2,d3,d4,d5 in mm ')
00310       read(5,*,err=250) d(1),d(2),d(3),d(4),d(5)
00320       write(6,160)
00330   160 format( ' type tube l1,l2,l3,l4,l5 in mm ')
00340       read(5,*,err=250) l(1),l(2),l(3),l(4),l(5)
00350       write(6,166)
00360   166 format( ' type diameter and length of internal scanivalve tube')
00370       read(5,*,err=250) d(6),l(6)
00380       do 168 i=1,6
00390   168 if(d(i).eq.0.0) goto 250
00400       write(6,210)
00410   210 format( ' type air temp(deg c),type static pressure(millibar)')
00420       read(5,*,err=250) temp,stpr
00430       goto 260
00440   250 continue
00450       write(6,252)
00460   252 format( ' inputting error,repeat input of data for this run')
00470       goto60
00480   260 prnd=0.72-0.0002*temp
00490       pstat=100.*stpr
00500       rho=1.2256*stpr*288./((temp+273.)*1013.)
00510       vismol=rho*(1.326+0.009*temp)*1013./stpr
00520       write(6,270)
00530   270 format( ' type trans. int. vol. (mm3),type expansion index')
00540       read(5,*,err=250) vss,dd4a
00550       write(6,272)
00560   272 format(' dimensionless diaphragm deflection correction to vol?')
00570       read(5,*,err=250) ss
00580       write(6,275)
00590   275 format( ' type local tunnel speed (m/sec), empirical value of c ')
00600       read(5,*,err=250)slm,cec
00610       write(6,285)
00620   285 format( ' type y if parameters are correct ')
00630       read(5,290) mes
00640   290 format(a1)
00650       if(mes.ne.'y') go to 250
00660       write(7,500)
00670   500 format(1h1,'**************************************************')
00680       write(7,505)
00690   505 format(1h0,5x,'frequency response of pressure tubing system')
```

```
00700       write(7,510)
00710   510 format(1h ,5x,'frequency range = 0 - 180 hz')
00720       write(7,515)
00730   515 format(1h ,5x,' correction for crossflow over orifice')
00740       write(7,520)
00750   520 format(1h0,'**************************************************'//)
00760       write(7,300) l(1),l(2),l(3),l(4),l(5)
00770   300 format( ' l1=',f8.2,' l2=',f8.2,' l3=',f8.2,' l4=',f8.2,' l5=',
00780      &f8.2/)
00790       write(7,310) d(1),d(2),d(3),d(4),d(5)
00800   310 format( ' d1=',f8.4,' d2=',f8.4,' d3=',f8.4,' d4=',f8.4,' d5=',
00810      &f8.4/)
00820       write(7,315) d(6),l(6)
00830   315 format( ' scanivalve d6=',f8.4//' scanivalve l6=',f8.2/)
00850       write(7,350) temp,stpr
00860   350 format( ' air temp=',f7.2//' stat. press.=',f7.2,' millibar'/)
00870       write(7,355) rho
00880   355 format( ' air density =',f7.4,' kg/m3'/)
00890       write(7,360) prnd
00900   360 format( ' prandtl number=',f8.4/)
00910       write(7,370) vss
00920   370 format( ' transducer internal volume=',f9.3/)
00930       write(7,380) dd4a
00940       write(7,375) ss
00950   375 format( ' dimensionless diaphragm deflection correction=',f10.6/)
00960   380 format( ' expansion index=',f9.3/)
00970       write(7,390) vismol
00980   390 format( ' 1.0e5 times the molecular viscosity=',f7.5/)
00990       write(7,395) slm
01000   395 format( ' local tunnel speed = ',f8.3,' m/sec'/)
01010       write(7,397) cec
01020   397 format( ' empirical value of c = ',f8.3/)
01030       write(7,410)
01040   410 format(1h1,3x,'frequency',8x,'amplitude ratio',10x,'phase')
01050       write(7,415)
01060   415 format(1h ,5x,'(hz.)',35x,'(deg)')
01070       write(7,420)
01080   420 format(1h ,'---------------     ---------------     ',
01090      &'---------------')
01100       write(7,425)
01110   425 format(1h )
01120       do 400 i=1,6
01130       l(i)=0.001*l(i)
01140       d(i)=0.25e-6*d(i)*d(i)
01150   400 continue
01160       pr=sqrt(prnd)
01170       p=sqrt(rho/pstat)
01180       mu=sqrt(rho/(vismol*0.000010))
01190       g=1.0-1.0/1.4
01200       bz=cmplx((ss+1.0/dd4a)*vss*1.0e-9/(3.1415793*d(6)),0.0)
1210 do 1 m=5,500,5
01220       w=6.2831853*float(m)
01230       do 2 i=1,6
01240       x=mu*sqrt(w*d(i))
01250       y=x*pr
01260       s=cmplx(be(1,0,y),be(2,0,y))
01270       t=cmplx(be(1,2,y),be(2,2,y))
01280       bfo(i)=cmplx(be(1,0,x),be(2,0,x))
01290       bf2(i)=cmplx(be(1,2,x),be(2,2,x))
01300       n(i)=(s+cmplx(g,0.0)*t)/s
```

```
01310       phi(i)=cmplx(w*p,0.0)*csqrt(n(i)*bfo(i)/bf2(i))
01320       z=cmplx(l(i),0.0)*phi(i)
01330       u=cexp(z)
01340       v=cexp(-z)
01350       ch(i)=cmplx(0.5,0.0)*(u+v)
01360       sh(i)=cmplx(0.5,0.0)*(u-v)
01370       2 continue
01380       do 3 i= 1,5
01390       j=i+1
01400       a(i)=cmplx(d(j)/d(i),0.0)*phi(j)*bfo(i)*bf2(j)*
01410      &sh(i)/(phi(i)*bfo(j)*bf2(i)*sh(j))
01420     3 continue
01430       b6=bz*phi(6)*sh(6)/n(6)
01440       q6=ch(6)+b6
01450       q5=ch(5)+a(5)*(ch(6)-cmplx(1.0,0.0)/q6)
01460       q4=ch(4)+a(4)*(ch(5)-cmplx(1.0,0.0)/q5)
01470       q3=ch(3)+a(3)*(ch(4)-cmplx(1.0,0.0)/q4)
01480       q2=ch(2)+a(2)*(ch(3)-cmplx(1.0,0.0)/q3)
01490       q1=ch(1)+a(1)*(ch(2)-cmplx(1.0,0.0)/q2)
01500       qv=q1-((cmplx(slm,0.0)*cmplx(cec,0.0)*phi(1)*bf2(1))/(bfo(1)*
01510      &cmplx(w,0.0)*cmplx(0.0,1.0)))*(sh(1)+a(1)*
01520      &(ch(1)/sh(1))*(ch(2)-cmplx(1.0,0.0)/q2))
01530       qa=cmplx(1.0,0.0)/(qv*q2*q3*q4*q5*q6)
01540       phas(m)=-57.29578*atan2(aimag(qa),real(qa))
01550       if(phas(m).lt.0.0) phas(m)=phas(m)+360.0
01560       write(7,430) m,cabs(qa),phas(m)
01570   430 format(1h ,6x,i3,14x,f9.5,11x,f9.5)
01580     1 continue
01590       write(6,65)
01600    65 format( ' type yes or y for another run')
01610       read(5,70) mes
01620    70 format(a1)
01630       if(mes.eq.'y') go to 60
01640       close(7)
01650       stop
01660       end
```

Example of output from program showing frequency response of a tube system used on the model fin.

```
**************************************************

     frequency response of pressure tubing system
     frequency range = 0 - 180 hz
      correction for crossflow over orifice

**************************************************

l1=   20.00 l2=  100.00 l3=  100.00 l4=  100.00 l5=  450.00

d1=  0.6850 d2=  1.0650 d3=  1.0650 d4=  1.0650 d5=  1.0650

scanivalve d6=  1.0000

scanivalve l6=   80.00

air temp=   8.00

stat. press.= 998.00 millibar

air density = 1.2375 kg/m3

prandtl number=  0.7184

transducer internal volume=   98.000

expansion index=    1.400

dimensionless diaphragm deflection correction=  0.000000

1.0e5 times the molecular viscosity=1.75607

local tunnel speed =   20.000 m/sec

empirical value of c =    0.900
```

frequency (hz.)	amplitude ratio	phase (deg)
5	1.00283	5.45556
10	1.01125	10.99460
15	1.02500	16.70078
20	1.04361	22.65723
25	1.06624	28.94448
30	1.09154	35.63523
35	1.11754	42.78581
40	1.14151	50.42348
45	1.16016	58.53130
50	1.16999	67.03515
55	1.16812	75.80030
60	1.15307	84.64451
65	1.12532	93.36761
70	1.08715	101.78773
75	1.04196	109.77011
80	0.99333	117.23903
85	0.94436	124.17343
90	0.89735	130.59352
95	0.85376	136.54536
100	0.81442	142.08816
105	0.77967	147.28547
110	0.74954	152.20002
115	0.72389	156.89100
120	0.70250	161.41319
125	0.68509	165.81694
130	0.67141	170.14863
135	0.66119	174.45147
140	0.65420	178.76613
145	0.65022	183.13146
150	0.64902	187.58500
155	0.65038	192.16327
160	0.65406	196.90178
165	0.65978	201.83471
170	0.66717	206.99388
175	0.67580	212.40736
180	0.68512	218.09713
185	0.69444	224.07620
190	0.70299	230.34513

LIST OF TABLES

control surface oscillation frequency (Hz)	freestream velocity (m/s)		
	20	30	40
0	0	0	0
5	0.349	0.233	0.175
7.5	0.524	-	-
10	0.698	0.466	0.349
12.5	0.873	-	-
15	1.047	0.698	0.524
17.5	1.222	-	-
20	1.396	0.931	0.698
22.5	1.571	-	-
25	1.746	1.164	0.873
30	2.095	1.396	1.047
35	-	1.629	1.222
40	-	1.862	1.396
45	-	2.095	1.571
50	-	-	1.746
60	-	-	2.095
	reduced frequencies $\omega^* = \frac{\omega c}{2v}$		

Test cases at $\alpha = 0^\circ$, $\delta_m = 0^\circ$, gap open and gap sealed.

Mean and unsteady pressures measured at all pressure tappings on model for all above test cases.

Table 1. Reduced frequencies at which tests were conducted with model at zero incidence and control surface at zero mean deflection.

$\alpha = 0^\circ$, $\delta_m = 5^\circ, 10^\circ, 15^\circ, 20^\circ$

ω^* (gap open)	ω^* (gap sealed)
0	0
0.349	0.349
0.524	0.698
0.698	1.396
1.047	
1.396	
2.095	

$\delta_m = 0^\circ$, $\alpha = 5^\circ, 10^\circ$

ω^* (gap open)	ω^* (gap sealed)
0	0
0.349	0.349
0.524	0.698
0.698	1.396
1.047	
1.396	
2.095	

mean and unsteady pressures recorded at spanwise stations y/s = 0.181, 0.3596, 0.6213 and 0.9452 at tunnel speed of 40 m/s.

Table 2. Reduced frequencies at which tests were conducted for non-zero values of incidence and mean control deflection.

LIST OF FIGURES

Fig. No.	DESCRIPTION
3.7	Internal details of fin components.
3.8	Installation of pressure tappings and tubes in fin.
3.9	Section through fin at y/s = 0.0857.
3.10	Details of internal machining of control surface.
3.11	Cross sections through control surface.
3.12	Cross sections through control surface.
3.13	Control surface and actuating shaft - machining of control surface incomplete and pressure tappings not installed.
3.14	Installation of pressure tappings in control surface.
3.15	Outboard end of control surface - cover plate fitted - showing spigot forming outboard hinge.
3.16	View below reflection plate showing vibrator, actuating linkage, lower bearing housing and location of Scanivalves.
3.17	Scrap section through model fin showing arrangement of bearings for supporting the control surface and actuating shaft.
3.18	Details of spigot joint between control surface and actuating shaft.
3.19	Attachment of control surface operating arm to actuating shaft allowing the control surface deflection to be adjusted $\pm 20°$.
3.20	Details of linkage connecting vibrator to actuating arm of control surface.
3.21	Use of vernier protractor to set mean deflection angle of control surface.
3.22	Front view of model fin mounted in 7ft x 5ft wind tunnel.
3.23	Rear view of model fin mounted in 7ft x 5ft wind tunnel.

4. CALIBRATION OF PRESSURE MEASURING SYSTEM

Fig. No.	DESCRIPTION
4.5	General layout of aerofoil model used to calibrate the frequency response of tubing systems with cross flow over tapping orifice.
4.6	Section through instrumented section of aerofoil model used to calibrate the frequency response of pressure tubing systems with cross-flow over tapping orifice.
4.7	Detail of insert holding pressure transducer and pressure tapping for calibration of pressure tubing systems with cross-flow over tapping orifice.
4.8	Suspension of aerofoil model in 30" dia. open jet wind tunnel for calibration of pressure tubing systems with flow across tapping orifice.
4.9	Boundary conditions at both ends of pressure tubing systems when used to measure sinusoidally oscillating pressures.
4.10	Measured frequency response of two pressure transducers used in wind tunnel tests on model fin with oscillating control surface.
4.11	Effect of tube internal diameter on frequency response of single tube connected to pressure transducer (stainless steel hypodermic tube).
4.12	Effect of tube length on frequency response of single tube connected to pressure transducer (stainless steel hypodermic tubing).
4.13	Frequency response of tubing system comprising a pressure tapping connected to a pressure transducer via a length of flexible p.v.c. tube (no Scanivalve).
4.14	Internal passages of 'J' type scanivalve.
4.15	Comparison of theoretical frequency response of actual Scanivalve with equivalent single tube.
4.16	Amplitude ratio of tubing system comprising stainless steel tapping, p.v.c. tubing, Scanivalve and pressure transducer (effect of two pressure tapping lengths and two Scanivalve tubing lengths).

Fig. No.	DESCRIPTION
4.17	Phase lag of tubing system comprising stainless steel pressure tapping, p.v.c. tubing, Scanivalve and pressure transducer (effect of two pressure tapping lengths and two Scanivalve tubing lengths).
4.18	Effect of sharp bend in tube on frequency response of pressure tubing systems.
4.19	Effect of pressure tapping drilled at 90° to tube wall on frequency response of pressure tubing systems.
4.20	Effect of small errors in measurement of tube diameter on frequency response of pressure tubing system.
4.21	Effect of ambient temperature on frequency response of pressure tubing system.
4.22	Effect of variation in amplitude of applied oscillatory pressure on frequency response of pressure tubing system.
4.23	Effect of flow across orifice on frequency response of pressure tubing system with Scanivalve.

5. DESCRIPTION OF THEORETICAL MODEL USED TO PREDICT UNSTEADY PRESSURE LOADINGS ON FIN AND CONTROL SURFACE

5.1	Location of collocation points used in lifting surface model of fin to determine unsteady pressure loadings due to oscillation of control surface.

6. RESULTS OF TESTS ON FIN WITH OSCILLATING CONTROL SURFACE

6.1	Calibration of tunnel freestream velocity and blockage effects of model support stand and vibrator.
6.2	Calibration of tunnel working section static pressure and blockage effect of model support stand and vibrator.

Fig. No.	DESCRIPTION
6.3	Boundary layer thickness on reflection plate measured at three stations along centreline of model.
6.4	Flow surveys in region above reflection plate at two tunnel speeds (V = 20 m/s, V = 40 m/s).
6.5	Flow surveys in region above reflection plate along centreline of model at two tunnel speeds (V = 20 m/s, V = 40 m/s).
6.6	Comparison of steady pressure distributions on upper and lower surface at y/s = 0.6213 to confirm setting of model at zero incidence.
6.7	Steady pressure distributions on surface of fin at three Reynolds numbers ($\alpha = 0^\circ$, $\delta = 0^\circ$, gap open).
6.8	Steady pressure distributions on fin and control surface ($\alpha = 5^\circ$, $\delta = 0^\circ$).
6.9	Steady pressure distributions on fin and control surface ($\alpha = 10^\circ$, $\delta = 0^\circ$).
6.10	Steady pressure distributions on fin and control surface ($\alpha = 0^\circ$, $\delta = 5^\circ$).
6.11	Steady pressure distributions on fin and control surface ($\alpha = 0^\circ$, $\delta = 10^\circ$).
6.12	Steady pressure distributions on fin and control surface ($\alpha = 0^\circ$, $\delta = 15^\circ$).
6.13	Steady pressure distributions on fin and control surface ($\alpha = 0^\circ$, $\delta = 20^\circ$).
6.14	Flow visualisation on fin and control surface ($\alpha = 0^\circ$, $\delta = 0^\circ$).
6.15	Flow visualisation on fin and control surface ($\alpha = 5^\circ$, $\delta = 0^\circ$).
6.16	Vortex formations on tip of fin at zero and at 5° incidence.
6.17	Flow visualisation on fin and control surface ($\alpha = 0^\circ$, $\delta = 5^\circ$).
6.18	Flow visualisation on fin and control surface ($\alpha = 0^\circ$, $\delta = 10^\circ$).

Fig. No.	DESCRIPTION
6.19	Flow visualisation on fin and control surface ($\alpha = 0^\circ$, $\delta = 15^\circ$).
6.20	Flow visualisation on fin and control surface ($\alpha = 0^\circ$, $\delta = 20^\circ$).
6.21	Vortices and flow separations on upper surface of fin for the case of a deflected control (V = 40m/s, gap open).
6.22	Evaluation of control surface steady section hinge moment coefficients from pressure data ($y/s = 0.6213$, V = 40m/s, gap open, $\alpha = 0^\circ$).
6.23	Evaluation of control surface steady section hinge moment coefficients from pressure data ($y/s = 0.9452$, V = 40m/s, gap open, $\alpha = 0^\circ$).
6.24	Effect of reduced frequency on real part of unsteady pressure loading at mid semi-span ($y/s = 0.6213$, $\alpha = 0^\circ$, $\delta_m = 0^\circ$, $\delta_a = 1^\circ$).
6.25	Effect of reduced frequency on imaginary part of unsteady pressure loading at mid semi-span ($y/s = 0.6213$, $\alpha = 0^\circ$, $\delta_m = 0^\circ$, $\delta_a = 1^\circ$).
6.26	Effect of reduced frequency on real part of unsteady pressure loading near tip of fin ($y/s = 0.9452$, $\alpha = 0^\circ$, $\delta_m = 0^\circ$, $\delta_a = 1^\circ$).
6.27	Effect of reduced frequency on imaginary part of unsteady pressure loading near tip of fin ($y/s = 0.9452$, $\alpha = 0^\circ$, $\delta_m = 0^\circ$, $\delta_a = 1^\circ$).
6.28	Development of unsteady pressures on control surface during half cycle of oscillation.
6.29	Unsteady pressure loading on control surface ($\omega^* = 0.349$, V = 40m/s, gap open, $\alpha = 0^\circ$, $\delta_m = 0^\circ$, $\delta_a = 1^\circ$).
6.30	Unsteady pressure loading on control surface ($\omega^* = 0.698$, V = 40m/s, gap open, $\alpha = 0^\circ$, $\delta_m = 0^\circ$, $\delta_a = 1^\circ$).
6.31	Unsteady pressure loading on control surface ($\omega^* = 1.047$, V = 40m/s, gap open, $\alpha = 0^\circ$, $\delta_m = 0^\circ$, $\delta_a = 1^\circ$).
6.32	Unsteady pressure loading on control surface ($\omega^* = 1.396$, V = 40m/s, gap open, $\alpha = 0^\circ$, $\delta_m = 0^\circ$, $\delta_a = 1^\circ$).

Fig. No.	DESCRIPTION
6.33	Unsteady pressure loading on control surface (ω^*= 1.745, V = 40m/s, gap open, α = 0°, δ_m = 0°, δ_a = 1°).
6.34	Unsteady pressure loading on control surface (ω^*= 2.095, V = 40m/s, gap open, α = 0°, δ_m = 0°, δ_a = 1°).
6.35	Effect of control surface oscillation amplitude on real part of unsteady pressure loading (α = 0°, δ_m = 0°).
6.36	Effect of control surface oscillation amplitude on imaginary part of unsteady pressure loading (α = 0°, δ_m = 0°).
6.37	The fit of a 5th order least squares polynomial to unsteady pressure data on control surface to simplify integration into hinge moment.
6.38	Variation of unsteady section hinge moment coefficient with reduced frequency at selected spanwise locations across control surface (V = 40m/s, gap open, α = 0°, δ_m = 0°, δ_a = 1°).
6.39	Variation of amplitude and phase of unsteady section hinge moment coefficient with reduced frequency at selected spanwise stations across control surface (V = 40m/s, gap open, α = 0°, δ_m = 0°, δ_a = 1°).
6.40	Spanwise distribution of unsteady section hinge moment coefficient at various values of reduced frequency (V = 40m/s, gap open, α = 0°, δ_m = 0°, δ_a = 1°).
6.41	Variation of overall control surface hinge moment with reduced frequency (gap open, α = 0°, δ_m = 0°, δ_a = 1°).
6.42	Variation of amplitude and phase of overall control surface hinge moment with reduced frequency (gap open, α = 0°, δ_m = 0°, δ_a = 1°).
6.43	Effect of Reynolds number on real part of unsteady pressure loading at mid semi-span (y/s = 0.6213, α = 0°, δ_m = 0°, δ_a = 1°).
6.44	Effect of Reynolds number on imaginary part of unsteady pressure loading at mid semi-span (y/s = 0.6213, α = 0°, δ_m = 0°, δ_a = 1°).

Fig. No.	DESCRIPTION
6.45	Effect of Reynolds number on real part of unsteady pressure loading at mid semi span ($y/s = 0.6213$, $\alpha = 0°$, $\delta_m = 0°$, $\delta_a = 1°$).
6.46	Effect of Reynolds number on imaginary part of unsteady pressure loading at mid semi-span ($y/s = 0.6213$, $\alpha = 0°$, $\delta_m = 0°$, $\delta_a = 1°$).
6.47	Effect of Reynolds number on control surface hinge moments ($\alpha = 0°$, $\delta_m = 0°$, $\delta_a = 1°$, gap open).
6.48	Effect of sealing control surface gap on real part of unsteady pressure loading at mid semi-span ($y/s = 0.6213$, $\alpha = 0°$, $\delta_m = 0°$, $\delta_a = 1°$).
6.49	Effect of sealing control surface gap on imaginary part of unsteady pressure loading at mid semi-span ($y/s = 0.6213$, $\alpha = 0°$, $\delta_m = 0°$, $\delta_a = 1°$).
6.50	Effect of sealing control surface gap on real part of unsteady pressure loading at mid semi-span ($y/s = 0.6213$, $\alpha = 0°$, $\delta_m = 0°$, $\delta_a = 1°$).
6.51	Effect of sealing control surface gap on imaginary part of unsteady pressure loading at mid semi-span ($y/s = 0.6213$, $\alpha = 0°$, $\delta_m = 0°$, $\delta_a = 1°$).
6.52	Effect of sealing gap on control surface unsteady hinge moment coefficients ($V = 20m/s$, $\alpha = 0°$, $\delta_m = 0°$, $\delta_a = 1°$).
6.53	Effect of sealing gap on control surface unsteady hinge moment coefficients ($V = 40m/s$, $\alpha = 0°$, $\delta_m = 0°$, $\delta_a = 1°$).
6.54	Effect of sealing gap on variation of overall control surface hinge moment with reduced frequency ($Re = 0.58 \times 10^6$, $\alpha = 0°$, $\delta_m = 0°$, $\delta_a = 1°$).
6.55	Effect of sealing gap on variation of overall control surface hinge moment with reduced frequency ($Re = 1.15 \times 10^6$, $\alpha = 0°$, $\delta_m = 0°$, $\delta_a = 1°$).
6.56	Result of filtering unsteady pressure loadings predicted by theoretical model to remove distortion caused by shortfalls in the numerical procedure.
6.57	Comparison of theoretical and experimental quasi-steady pressure loadings on fin and control surface ($\omega^* = 0$, $\alpha = 0°$, $\delta_m = 0°$, $\delta_a = 1°$).

Fig. No.	DESCRIPTION
6.58	Comparison of theoretical and experimental unsteady pressure loadings on fin and control surface - real parts - ($\omega^* = 0.698$, $\alpha = 0°$, $\delta_m = 0°$, $\delta_a = 1°$).
6.59	Comparison of theoretical and experimental unsteady pressure loadings on fin and control surface - imaginary parts - ($\omega^* = 0.698$, $\alpha = 0°$, $\delta_m = 0°$, $\delta_a = 1°$).
6.60	Comparison of theoretical and experimental unsteady pressure loadings on fin and control surface - real parts - ($\omega^* = 1.396$, $\alpha = 0°$, $\delta_m = 0°$, $\delta_a = 1°$).
6.61	Comparison of theoretical and experimental unsteady pressure loadings on fin and control surface - imaginary parts - ($\omega^* = 1.396$, $\alpha = 0°$, $\delta_m = 0°$, $\delta_a = 1°$).
6.62	Comparison of theoretical and experimental unsteady pressure loadings on fin and control surface - real parts - ($\omega^* = 2.091$, $\alpha = 0°$, $\delta_m = 0°$, $\delta_a = 1°$).
6.63	Comparison of theoretical and experimental unsteady pressure loadings on fin and control surface - imaginary parts - ($\omega^* = 2.091$, $\alpha = 0°$, $\delta_m = 0°$, $\delta_a = 1°$).
6.64	Comparison of theoretically and experimentally determined overall unsteady hinge moments on oscillating control surface ($Re = 1.15 \times 10^6$, $V = 40m/s$, gap sealed, $\alpha = 0°$, $\delta_m = 0°$, $\delta_a = 1°$).
6.65	Comparison of theoretically and experimentally determined overall unsteady control surface hinge moments - amplitude and phase - ($Re = 1.15 \times 10^6$, $V = 40m/s$, gap sealed, $\alpha = 0°$, $\delta_m = 0°$, $\delta_a = 1°$).
6.66	Effect of varying mean control surface deflection angle on unsteady pressure distributions on fin and control surface at mid semi-span ($y/s = 0.6213$, $V = 40m/s$, gap open, $\alpha = 0°$, $\delta_a = 1°$).
6.67	effect of varying mean control surface deflection angle on unsteady pressure distribution on control surface at mid semi-span ($y/s = 0.6213$, $V = 40m/s$, $\alpha = 0°$, $\delta_a = 1°$).

Fig. No.	DESCRIPTION
6.68	Effect of varying mean control surface deflection angle on unsteady pressure distributions on fin and control surface near tip of fin (y/s = 0.9452, V = 40m/s, gap open, $\alpha = 0°$, $\delta_a = 1°$).
6.69	Effect of varying mean control surface deflection angle on unsteady pressure distributions on control surface near tip of fin (y/s = 0.9452, V = 40m/s, gap open, $\alpha = 0°$, $\delta_a = 1°$).
6.70	Development of unsteady pressures on control surface during half cycle of oscillation for non-zero mean control surface deflection (y/s = 0.9452).
6.71	Development of unsteady pressures on control surface during half cycle of oscillation for non-zero mean control surface deflection (y/s = 0.6213).
6.72	Unsteady pressure distributions on control surface showing effect of gap with a mean control deflection of 10°(y/s = 0.6213, $\alpha = 0°$, $\delta_m = 10°$, $\delta_a = 1°$,).
6.73	Unsteady pressure distributions on control surface showing effect of gap with a mean control deflection of 15° (y/s = 0.6213, $\alpha = 0°$, $\delta_m = 15°$, $\delta_a = 1°$).
6.74	Effect of mean control surface deflection on unsteady section hinge moment coefficients measured at mid semi-span (y/s = 0.6213, V = 40m/s, gap open, $\alpha = 0°$, $\delta_a = 1°$).
6.75	Effect of mean control surface deflection on unsteady section hinge moment coefficients measured near tip of fin (y/s = 0.9452, V = 40m/s, gap open, $\alpha = 0°$, $\delta_a = 1°$).
6.76	Effect of incidence on unsteady pressures on fin and control surface at mid semi-span (y/s = 0.6213, V = 40m/s, $\delta_m = 0°$, $\delta_a = 1°$).
6.77	Effect of incidence on unsteady pressures on fin and control surface near tip of fin (y/s = 0.9452, V = 40m/s, $\delta_m = 0°$, $\delta_a = 1°$).

Fig. No.	DESCRIPTION
6.78	Effect of incidence on unsteady section hinge moments measured at mid semi-span (y/s = 0.6213, V = 40m/s, gap open, $\delta_m = 0°$, $\delta_a = 1°$).
6.79	Effect of incidence on unsteady section hinge moments measured near tip of fin (y/s = 0.9452, V = 40m/s, gap open, $\delta_m = 0°$, $\delta_a = 1°$).

APPENDIX 1

A1	Notation used for evaluating the frequency response of pressure tubing systems.

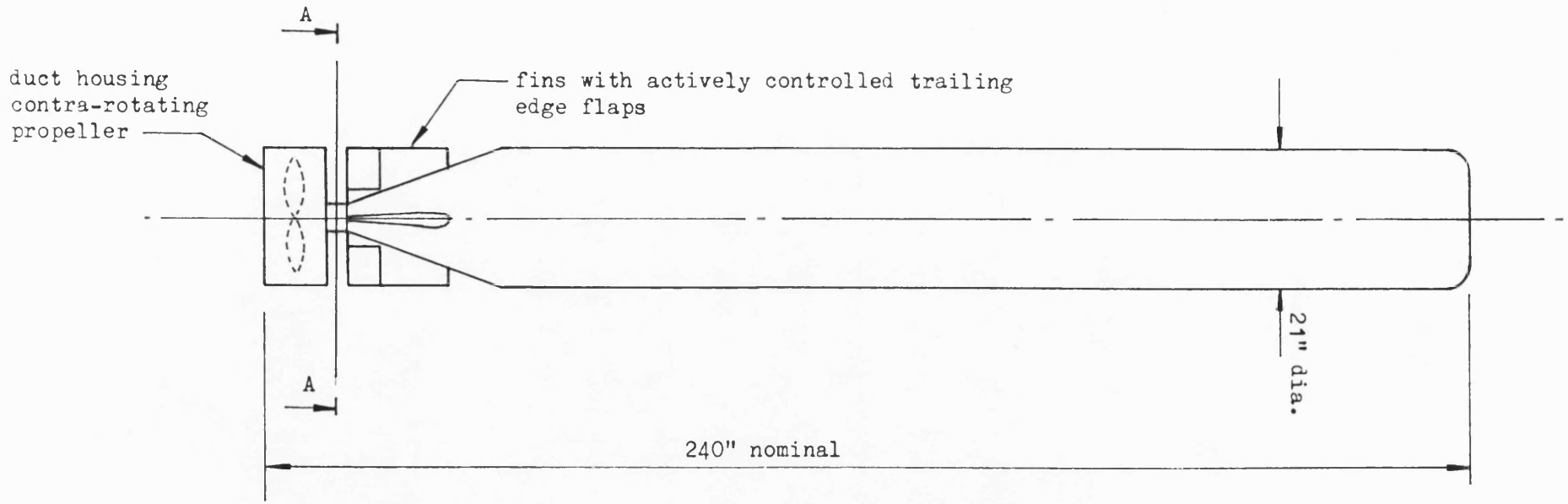

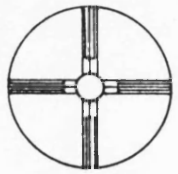

section AA - showing cruciform arrangement of fins

typical details of fins

aspect ratio	= 1.5
aerofoil thickness/chord ratio	= 12%
flap chord/fin chord ratio	= 0.25

typical performance

speed :- up to 60 kt
operating frequency of active control system :- up to 20 Hz.

Fig. 1.1

Fig. 1.1 Typical configuration of a torpedo

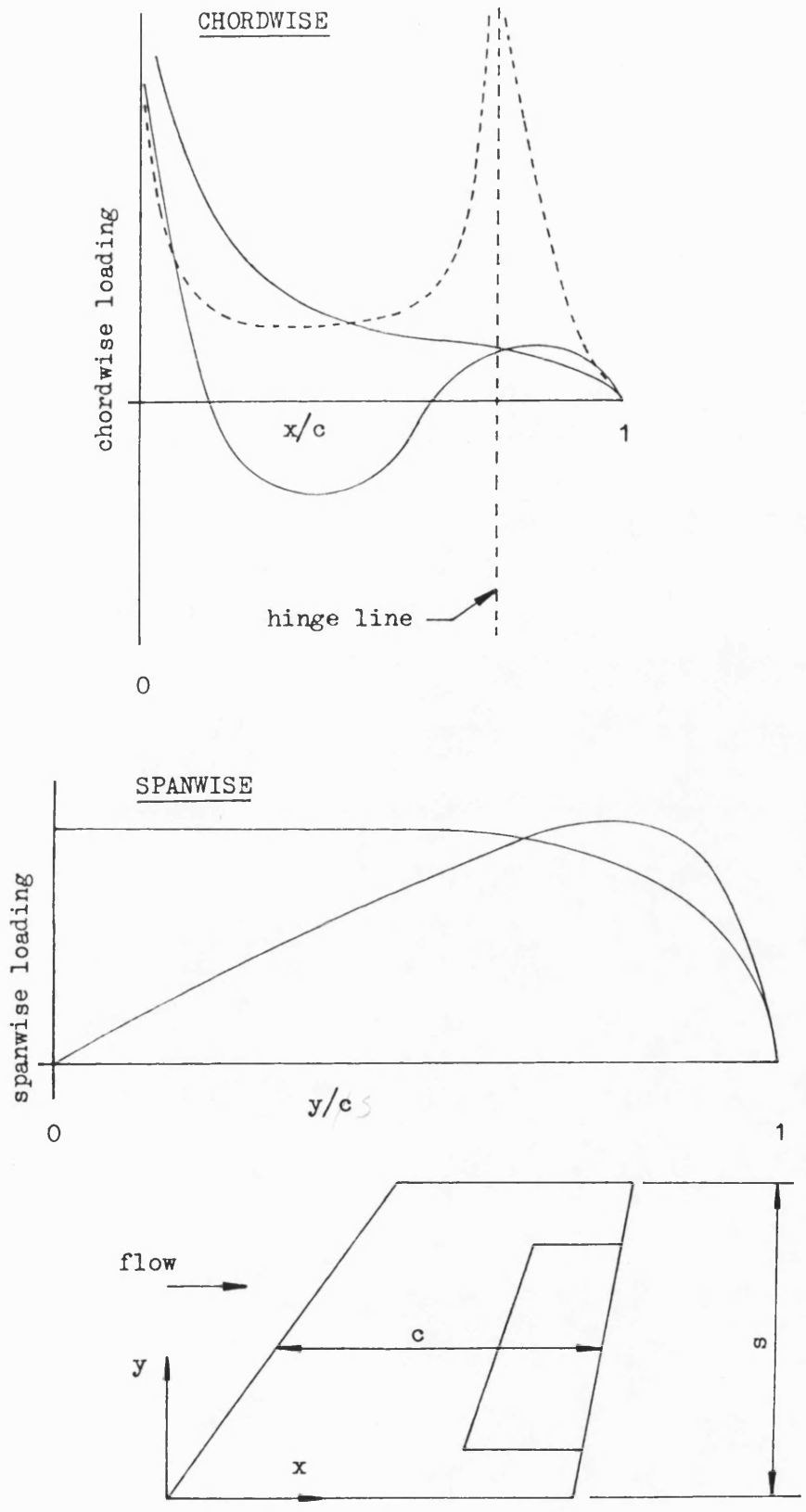

Fig. 2.1 Examples of loading functions used in lifting surface theory.

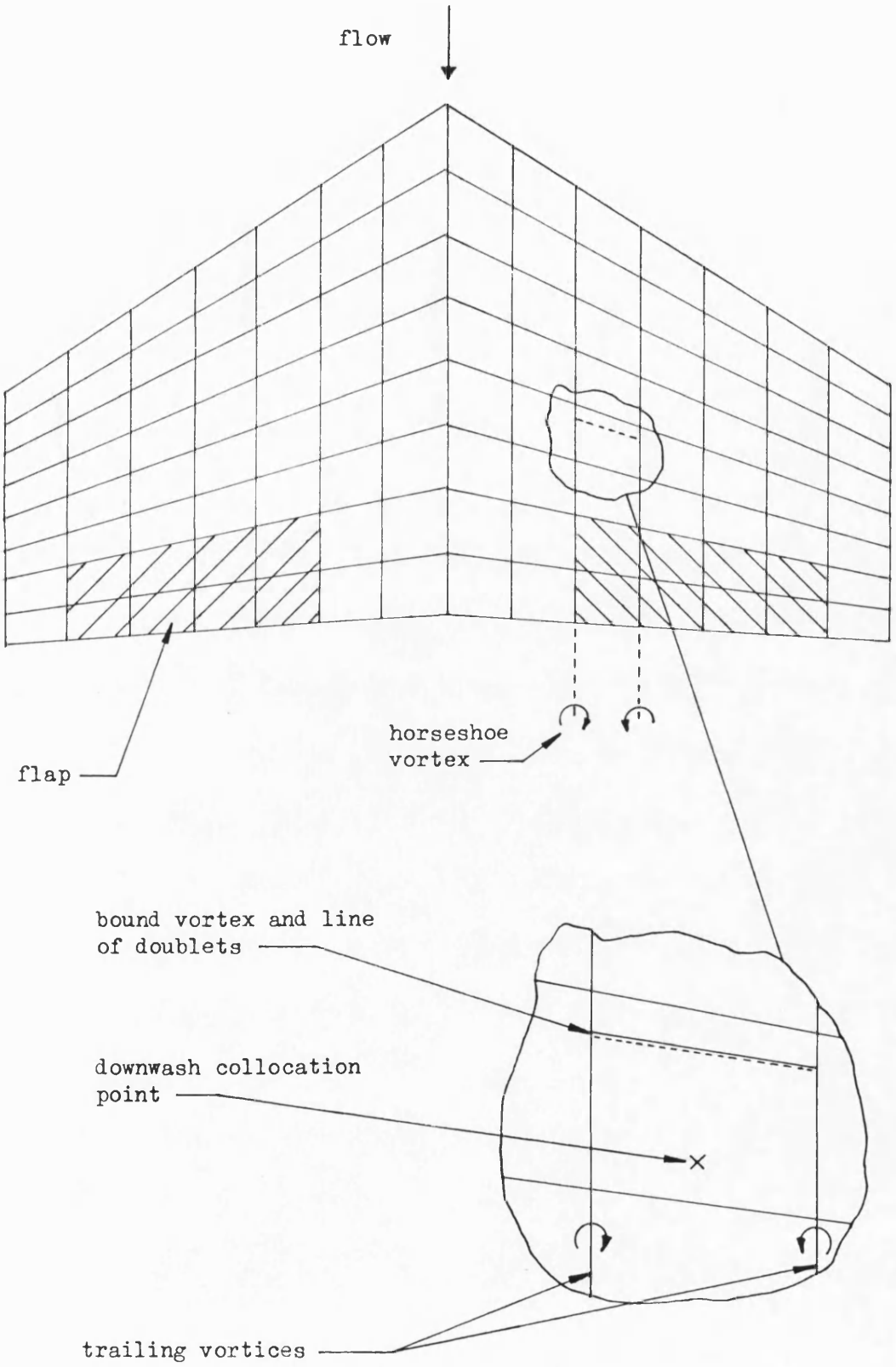

Fig. 2.2 Discretisation of a wing for the vortex/doublet lattice method.

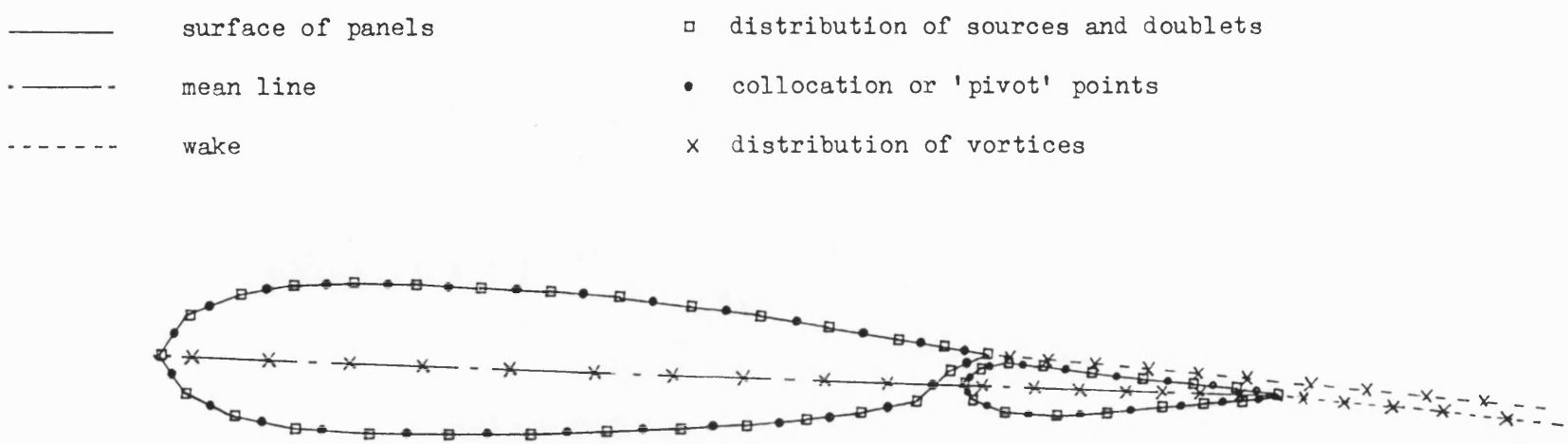

Fig. 2.3 Discretisation of a flapped aerofoil for the panel method.

Fig. 2.3

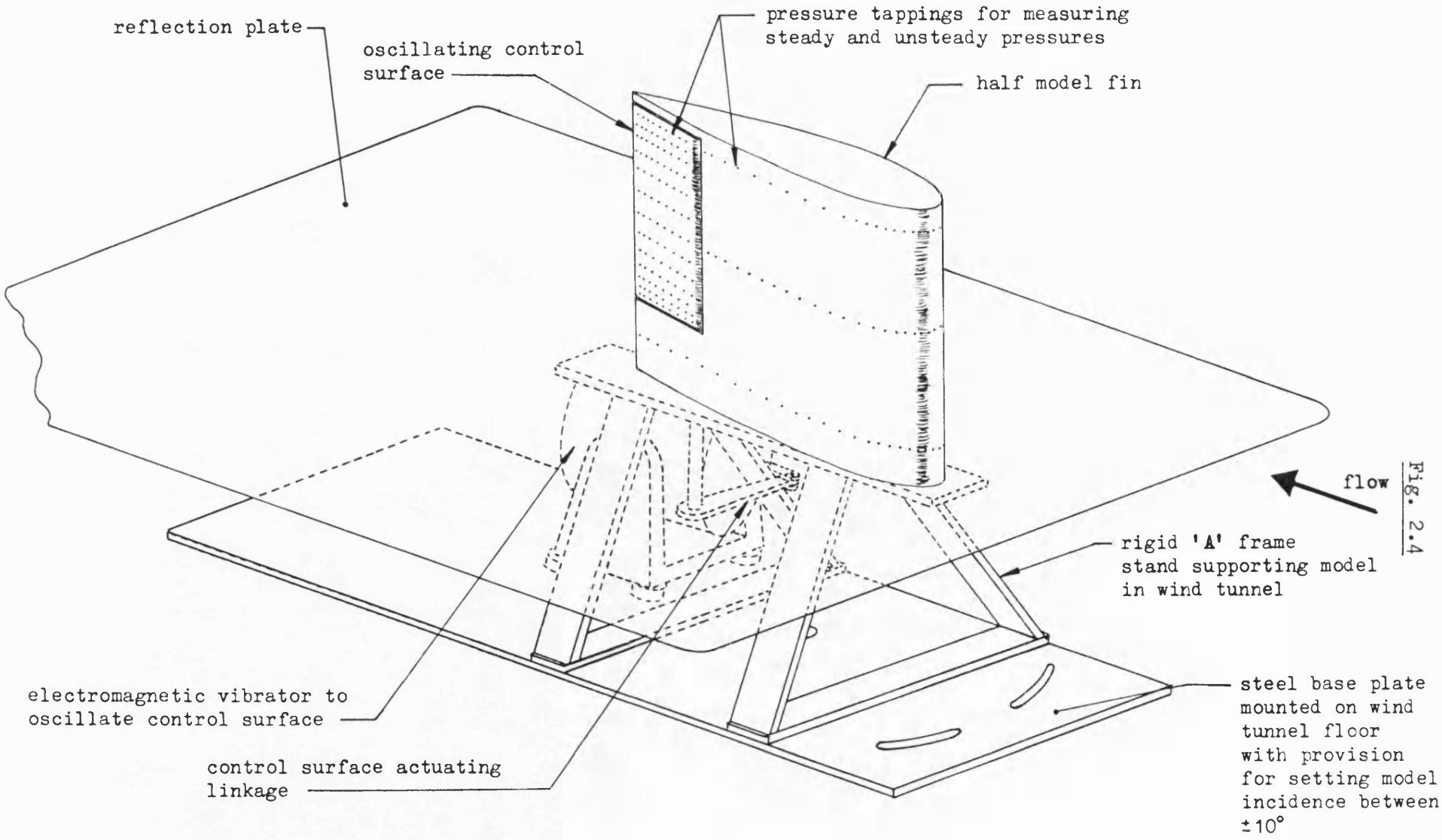

Fig. 2.4 Pictorial view of 'half' model fin with oscillating control surface

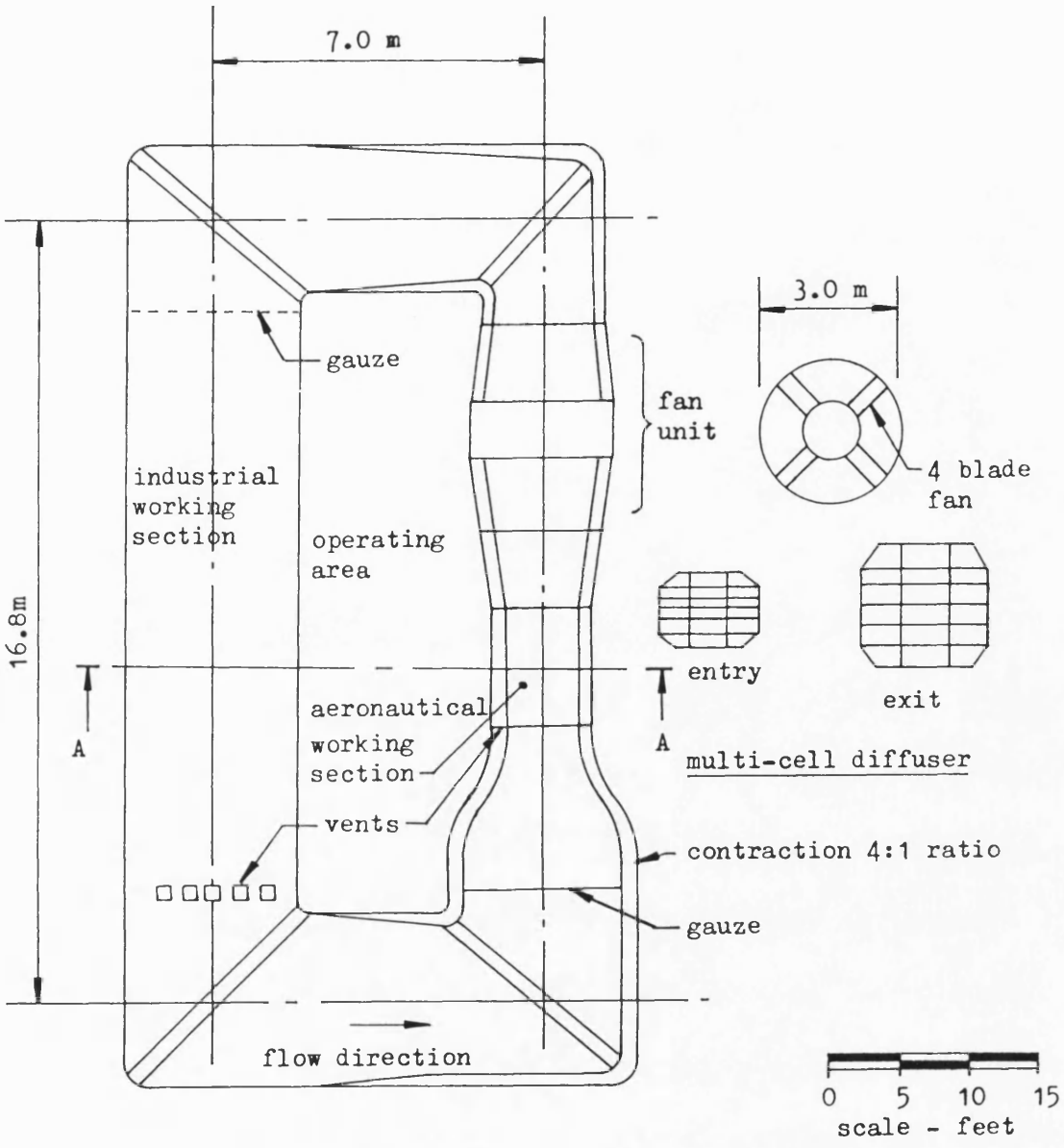

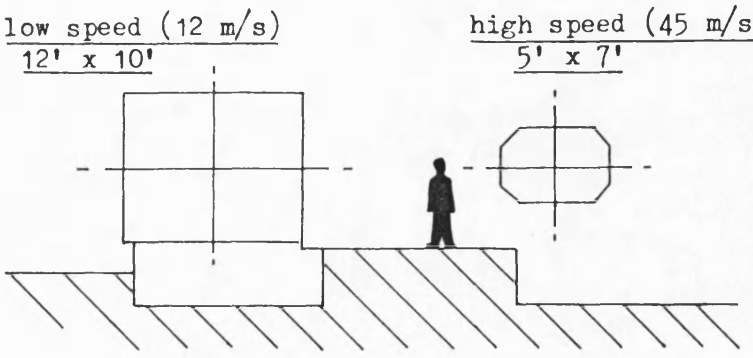

section AA showing the two working sections either of which may be operated at ambient pressure

Fig. 3.1 Layout of large dual purpose wind tunnel, University of Bath.

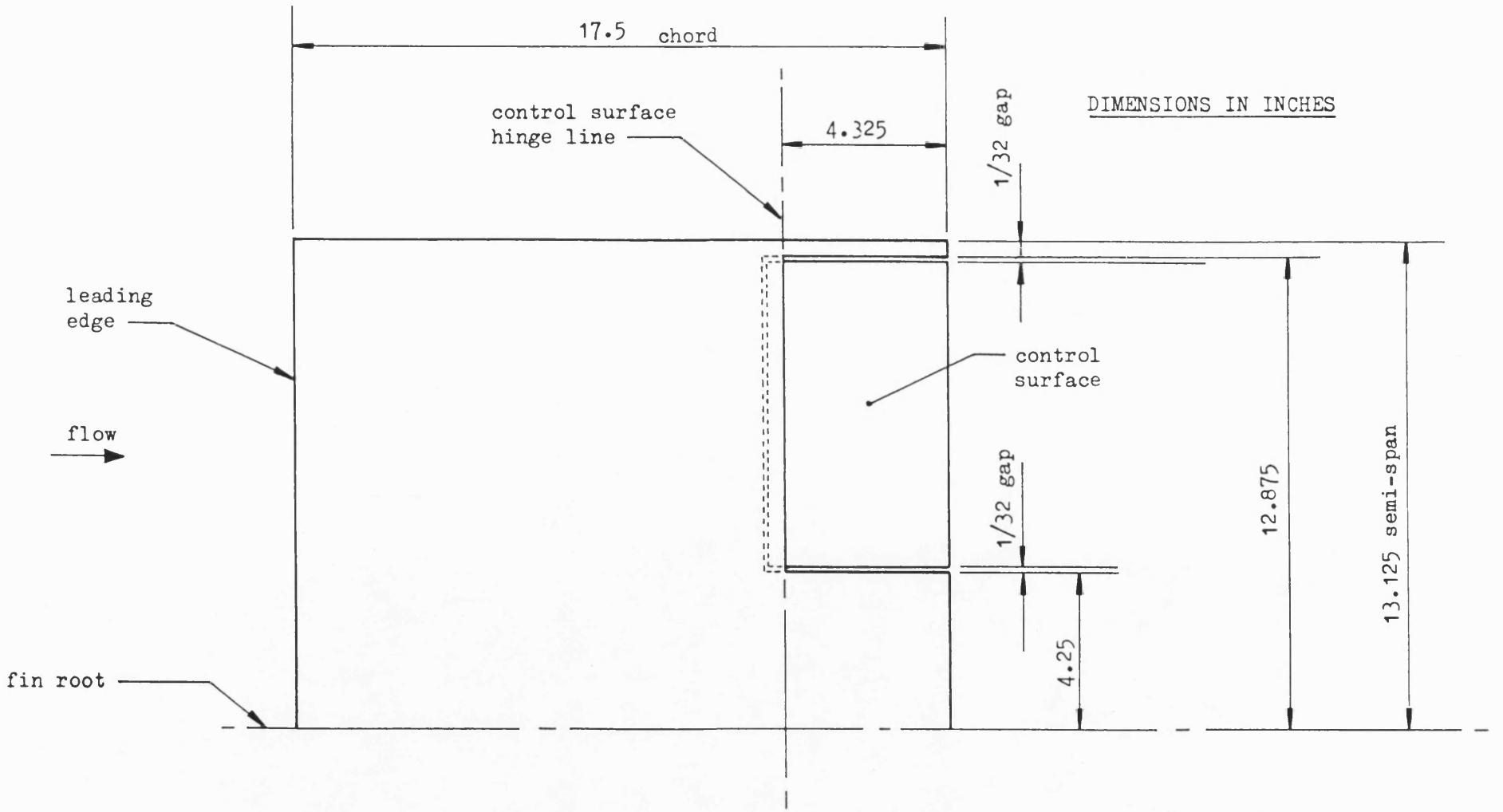

Fig. 3.2 Planform geometry of model fin and control surface

Fig. 3.2

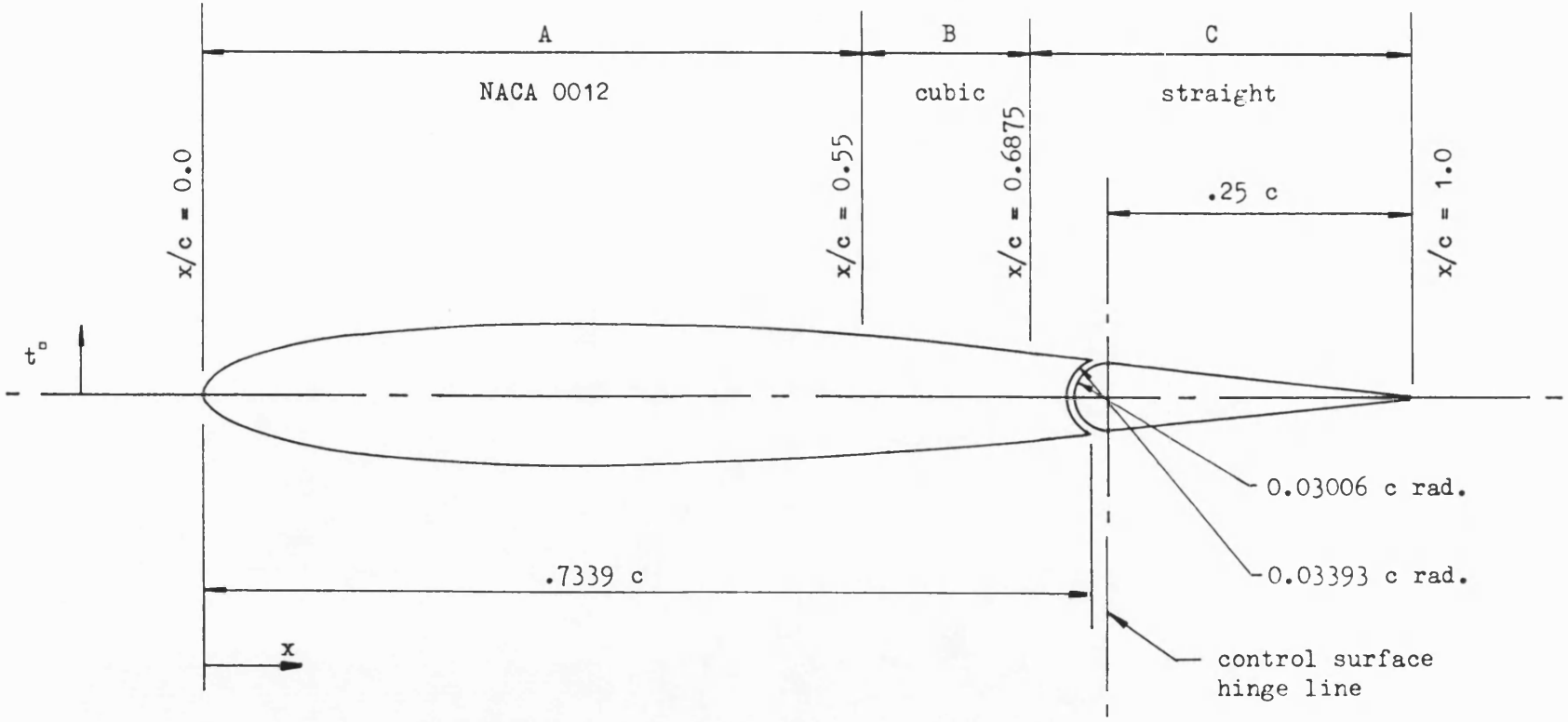

A). $Y = 0.6(0.2969X^{\frac{1}{2}}-0.126X-0.3516X^2+0.2843X^3-0.1015X^4)$

B). $Y = 0.026888X^3-0.150525X^2+0.06789X+0.053242$

C). $Y = 0.037511-((X-0.6875)0.116003)$

$X = x/c$

$Y = t°/c$

$c = 17.5"$

Fig. 3.3 Aerofoil profile of model fin and control surface.

Fig. 3.3

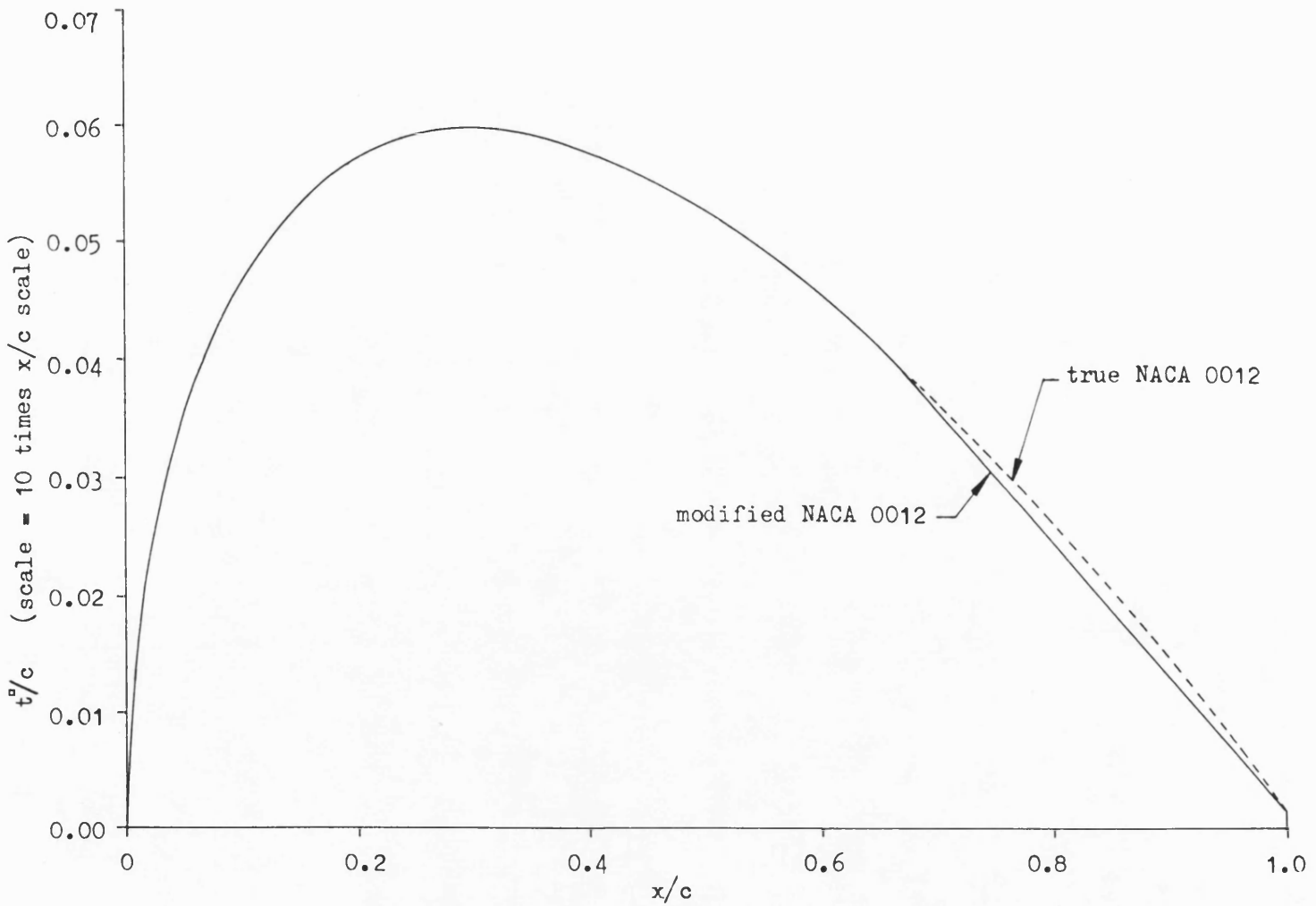

Fig. 3.4

Fig. 3.4 Comparison of modified aerofoil section with true NACA 0012 section.

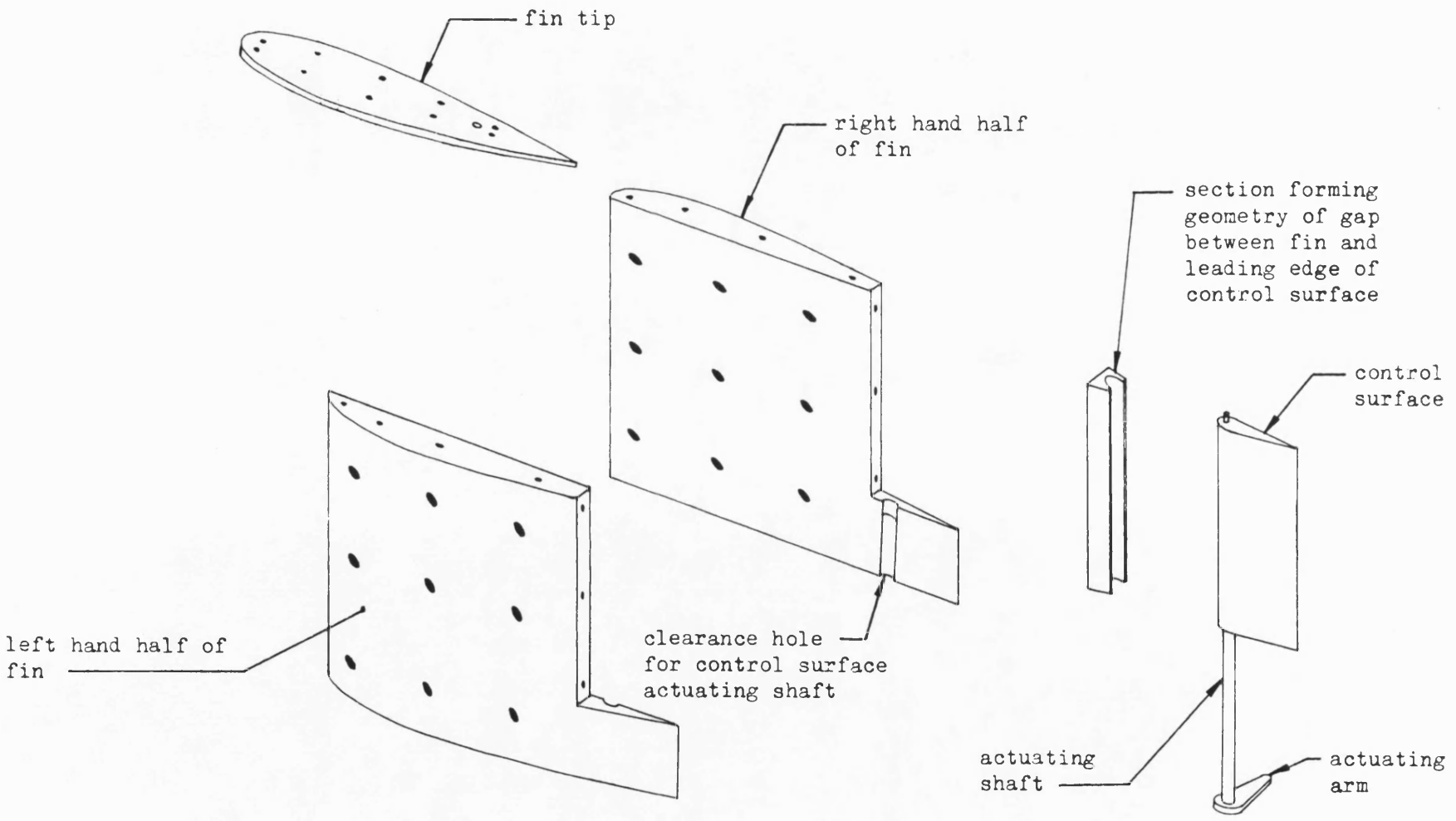

Fig. 3.5

Fig. 3.5 Exploded view of main components of model fin and control surface.

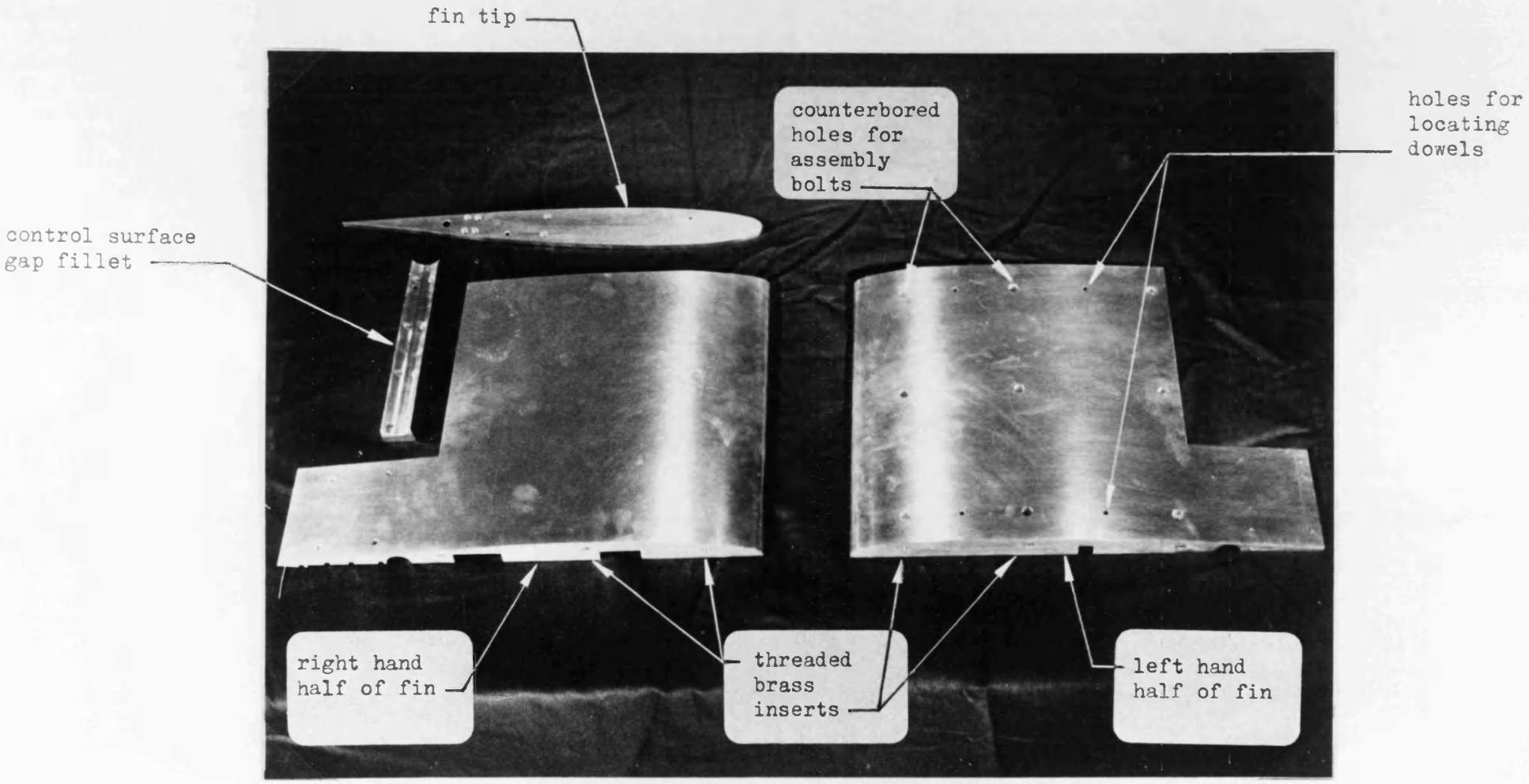

Fig. 3.6

Fig. 3.6 Components of fin machined from solid aluminium billets (holes for pressure tappings not drilled).

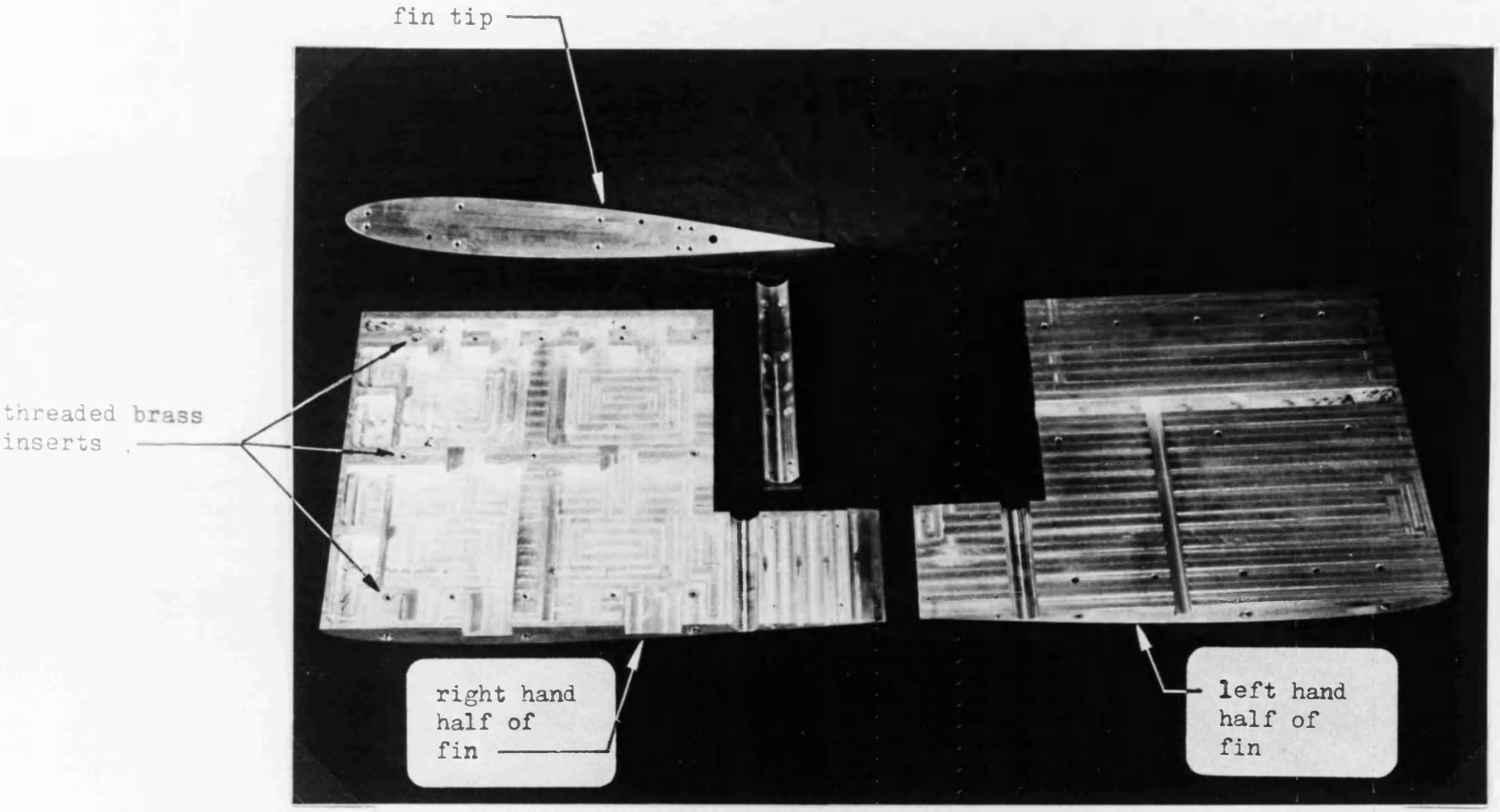

Fig. 3.7 Internal details of fin components.

Fig. 3.7

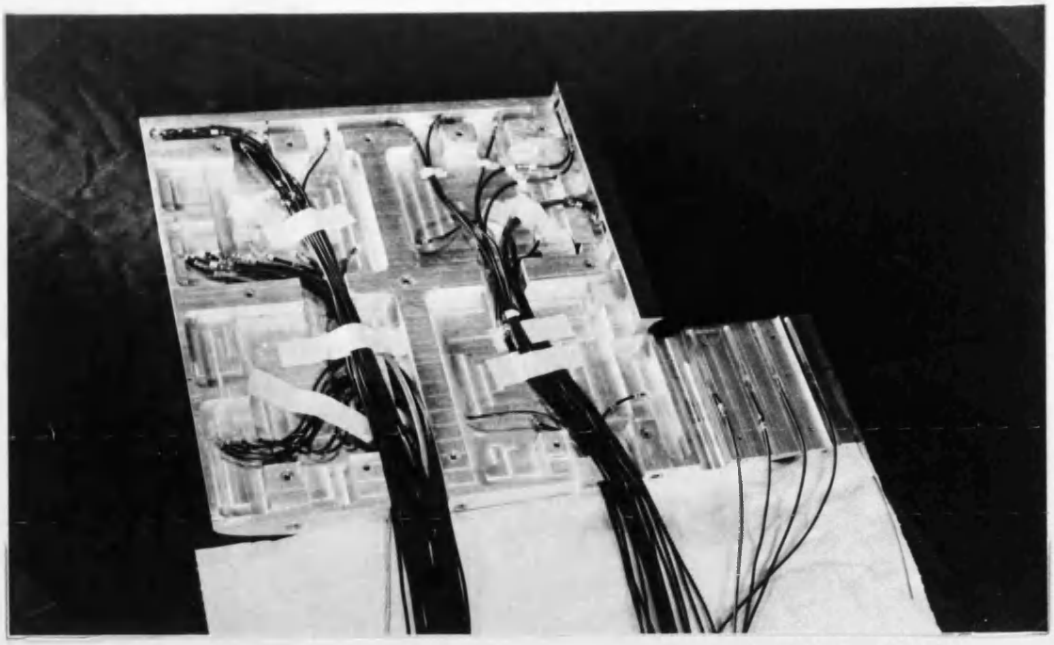

right hand half of fin

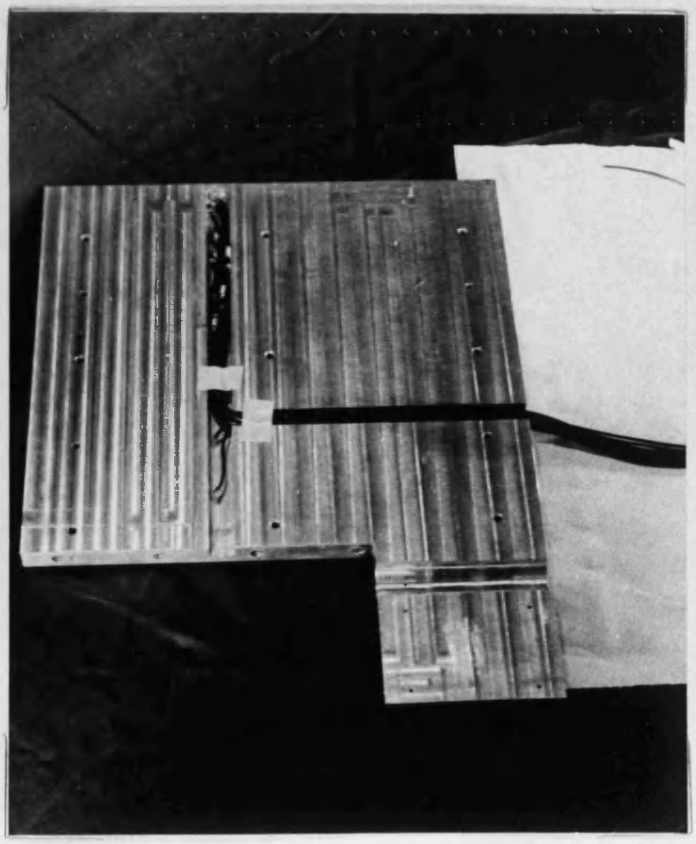

left hand half of fin

Fig. 3.8 Installation of pressure tappings and tubes in fin.

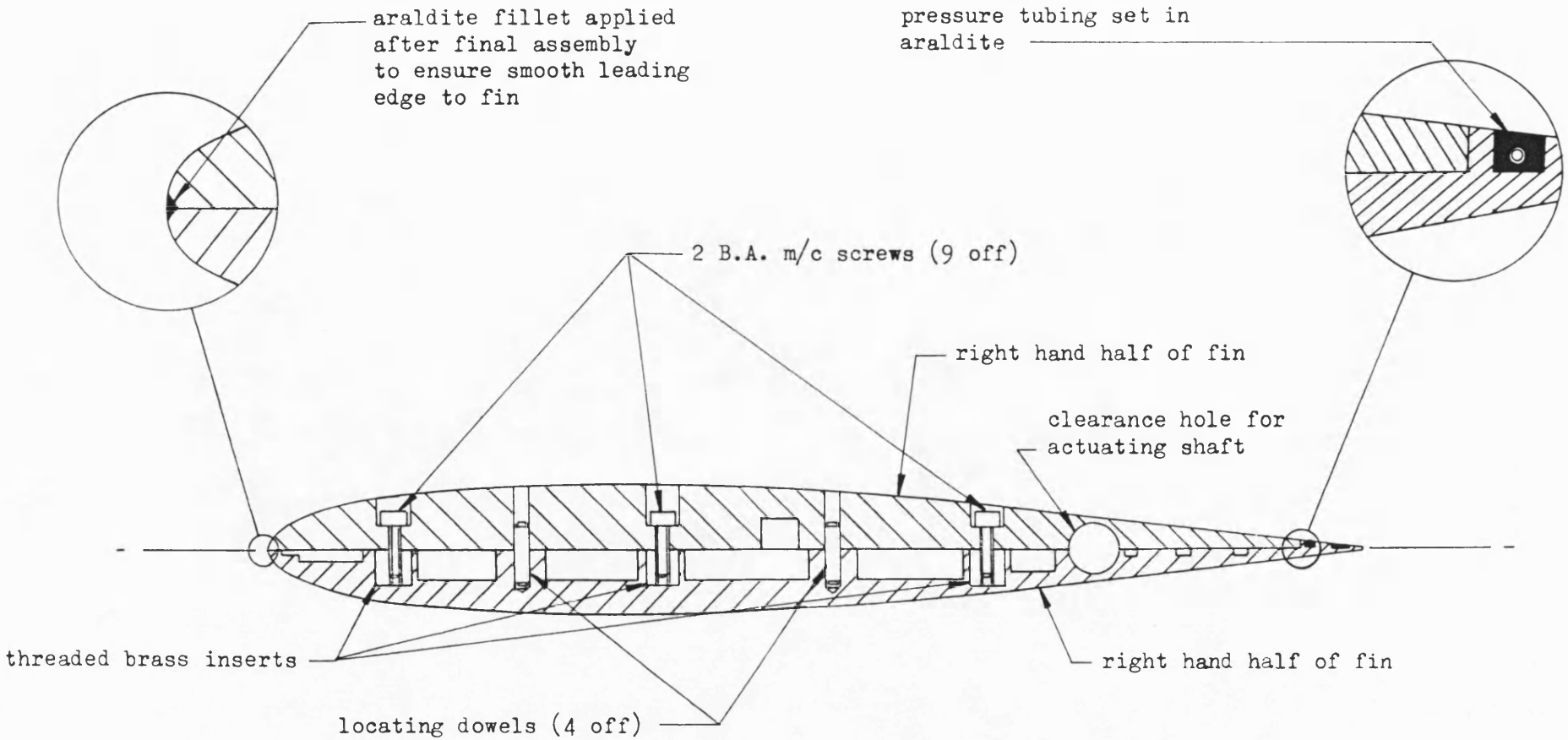

Fig. 3.9 Section through fin at y/s = 0.0857.

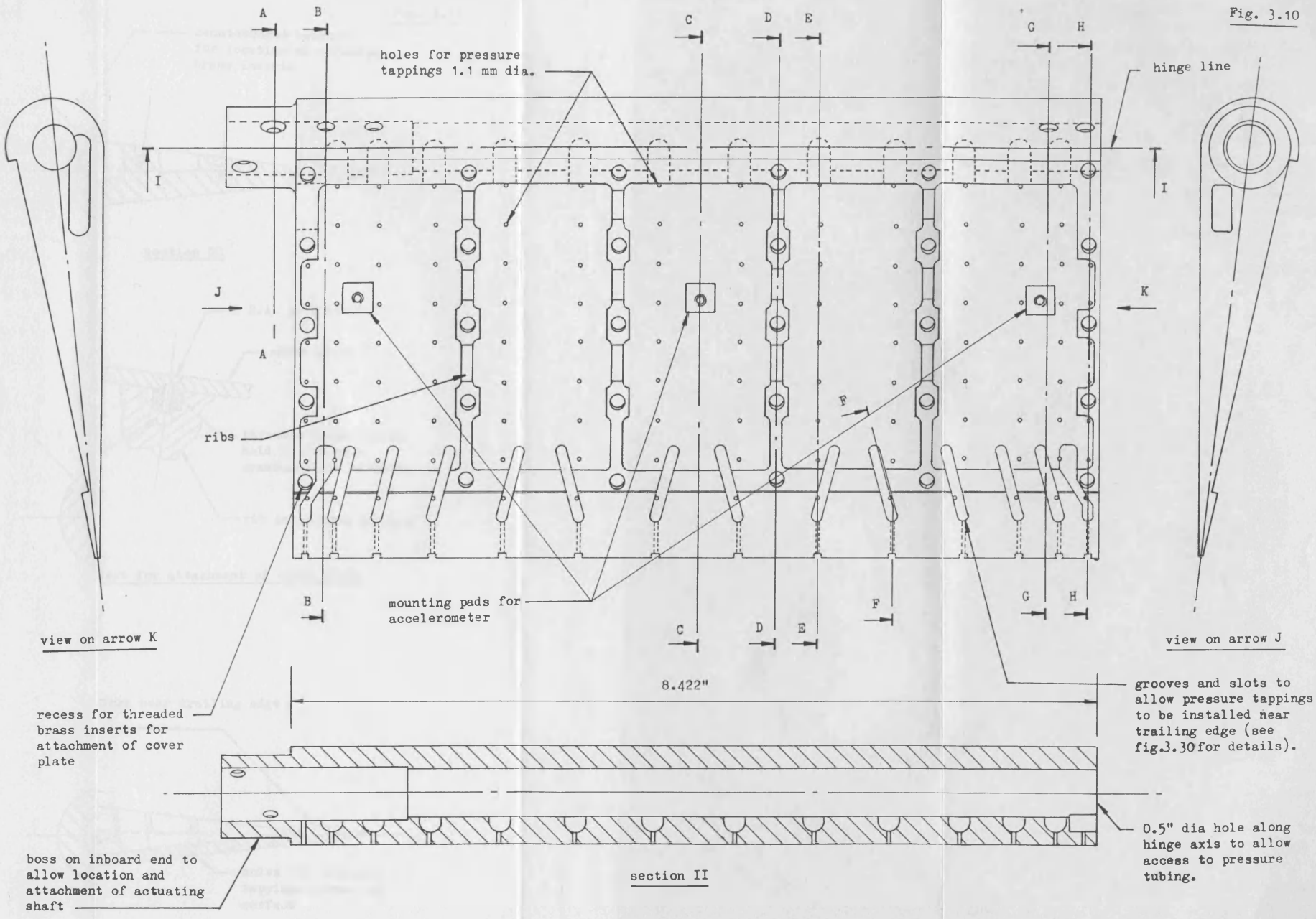

Fig. 3.10 Details of internal machining of control surface (refer to figs.3.11,3.12 for details of sections).

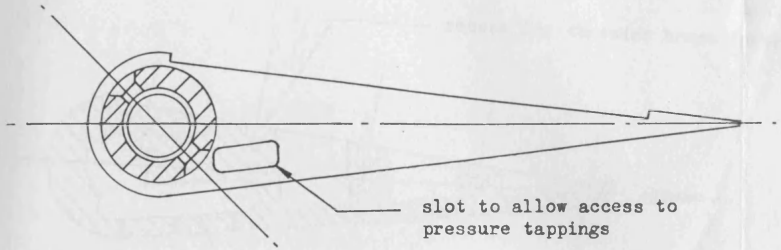

section AA

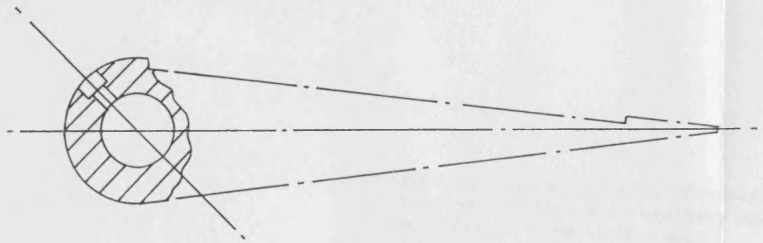

section BB,GG

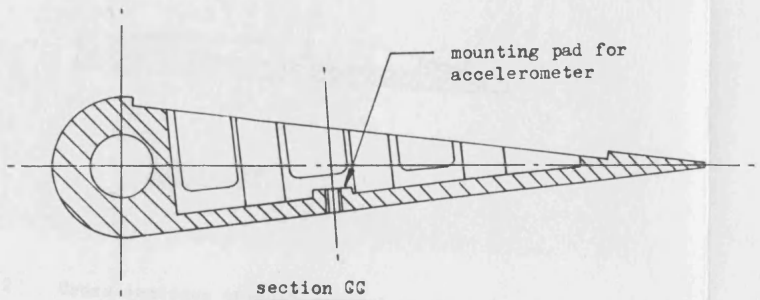

section CC

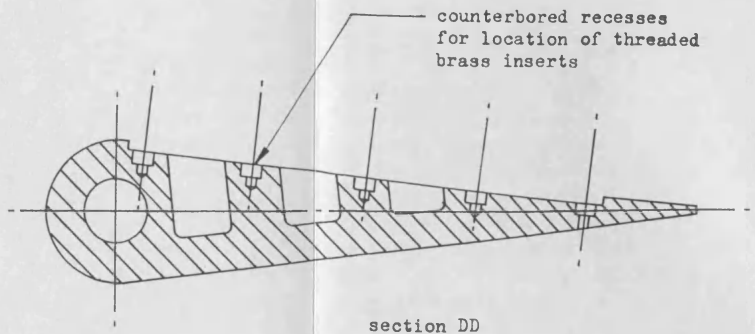

section DD

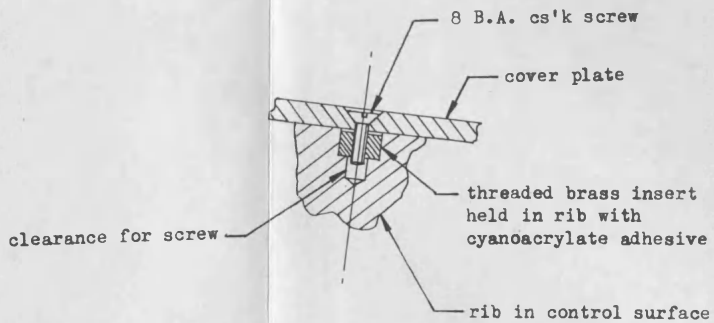

detail of brass insert for attachment of cover plate

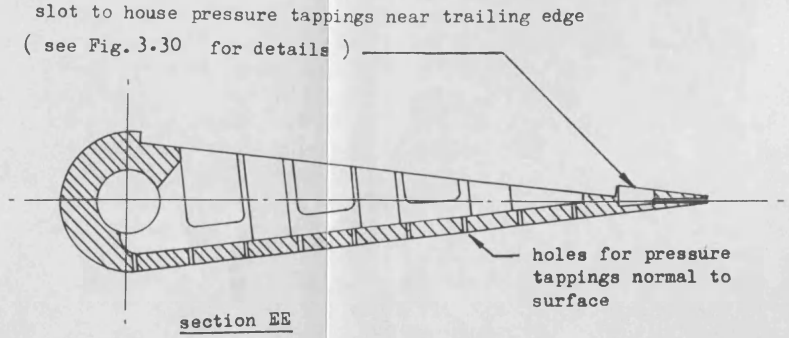

section EE

Fig. 3.11 cross sections through control surface (refer to Fig. 3.10 for location of each section.).

Fig. 3.12

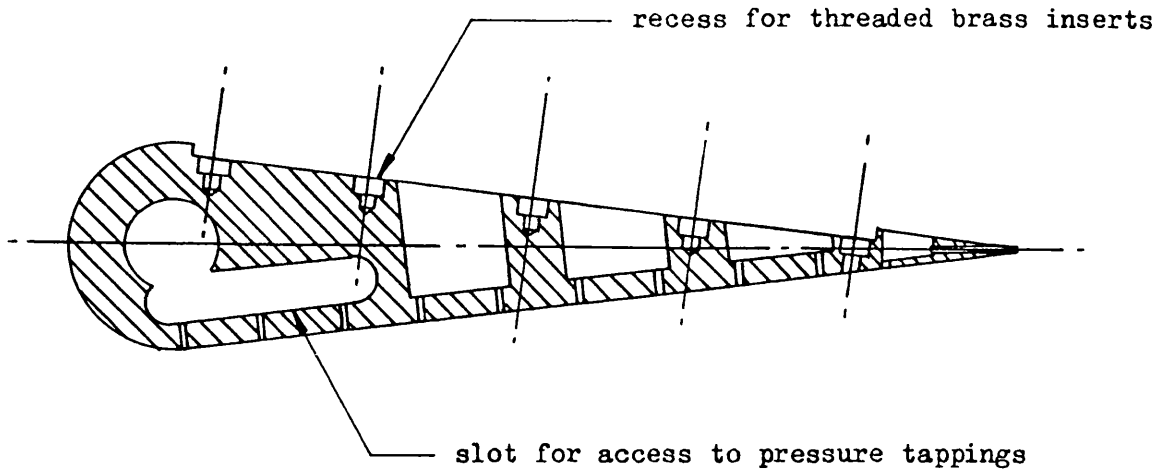

section HH

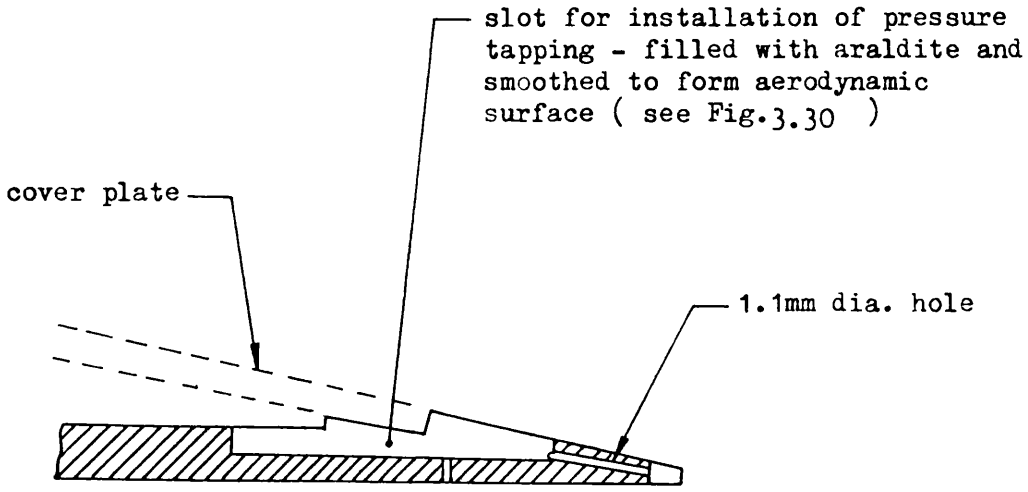

section FF

Fig. 3.12 Cross sections through control surface (see Fig. 3.10 for location of each section).

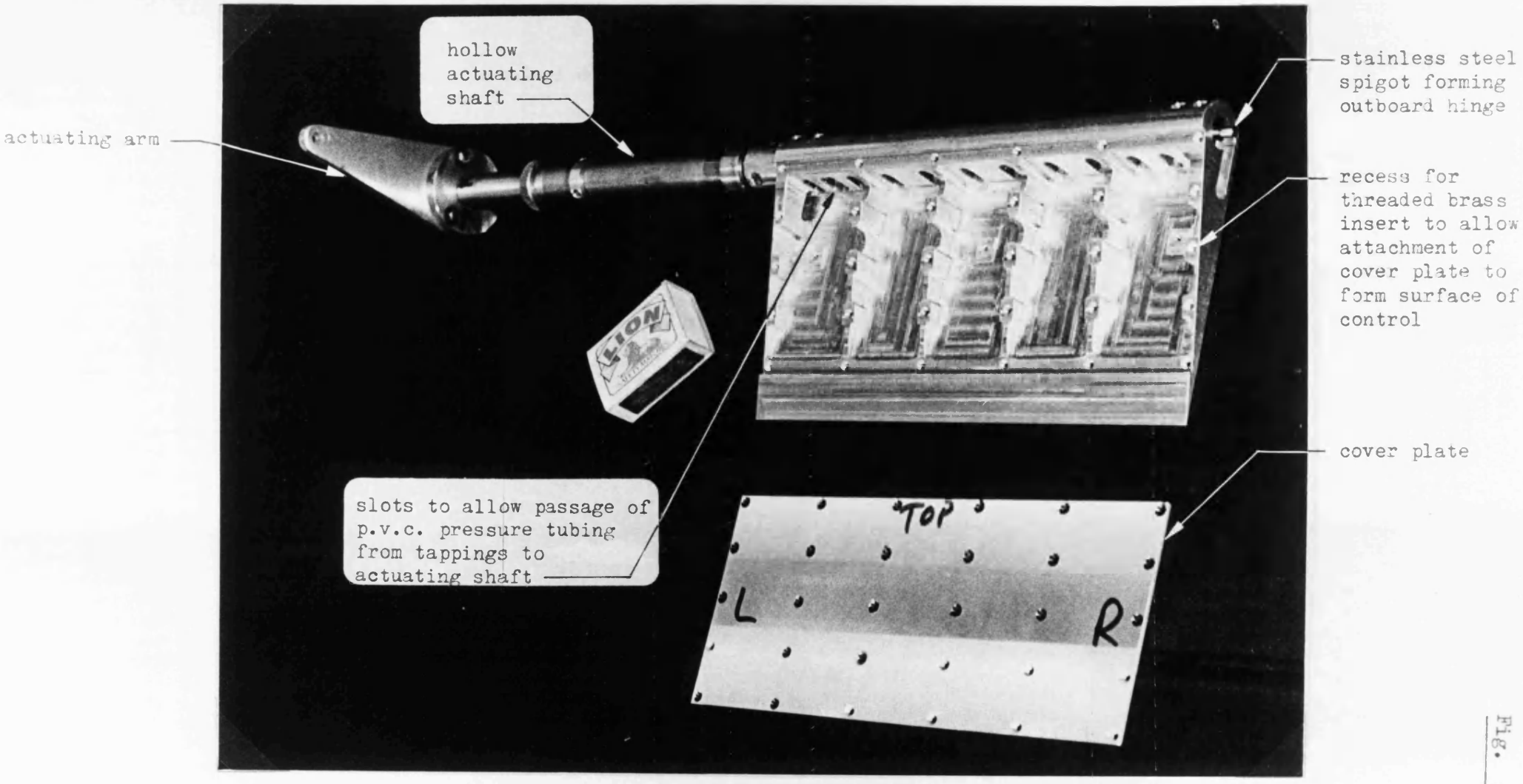

Fig. 3.13

Fig. 3.13 Control surface and actuating shaft - machining of control surface incomplete and pressure tappings not installed.

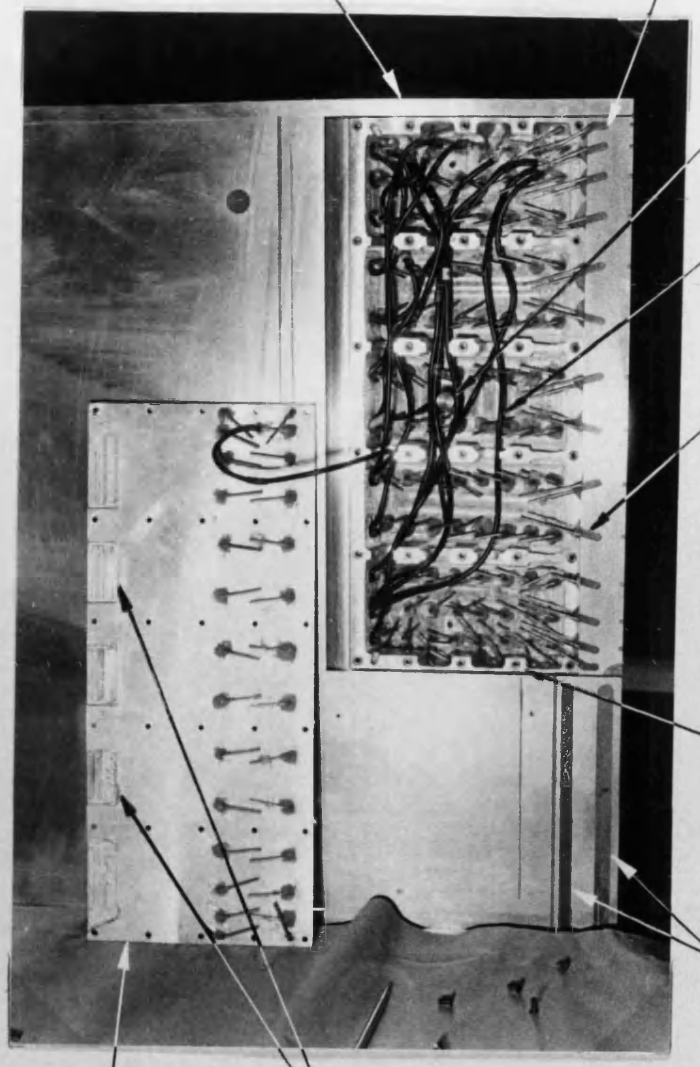

Fig. 3.14 Installation of pressure tappings in control surface.

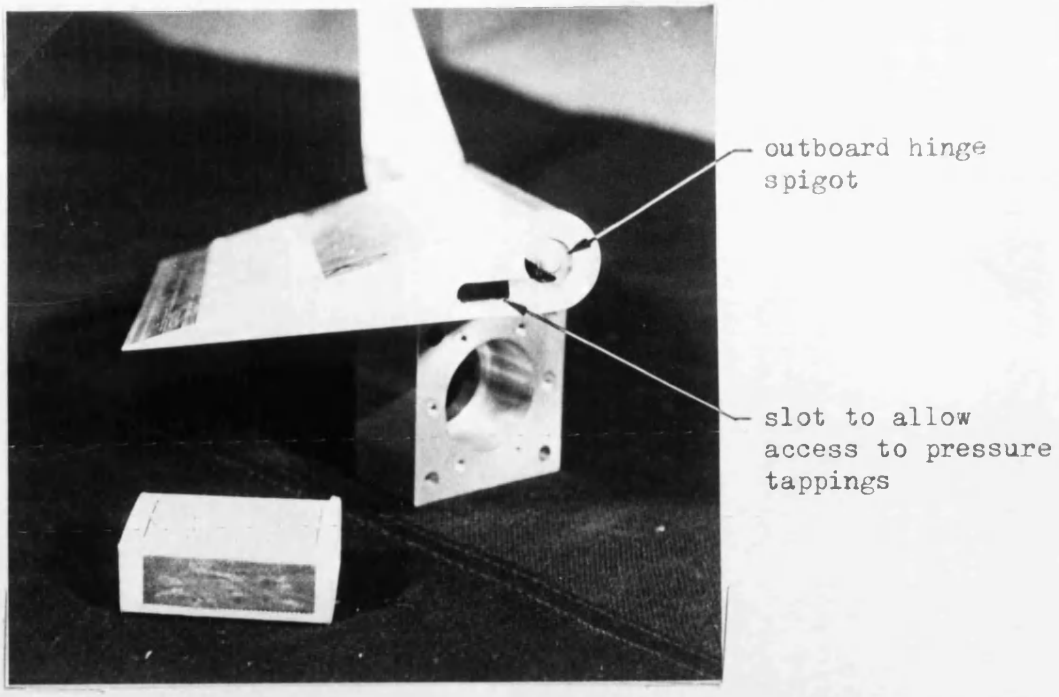

Fig. 3.15 Outboard end of control surface - cover plate fitted - showing spigot forming outboard hinge.

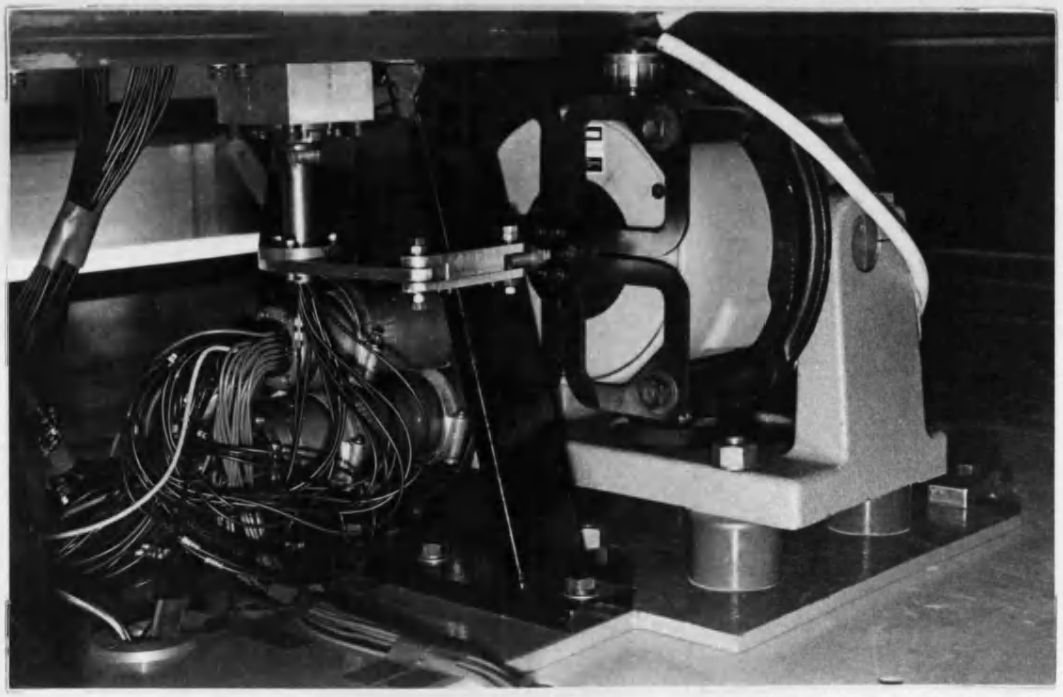

Fig. 3.16 View below reflection plate showing vibrator, actuating linkage, lower bearing housing and location of Scanivalves.

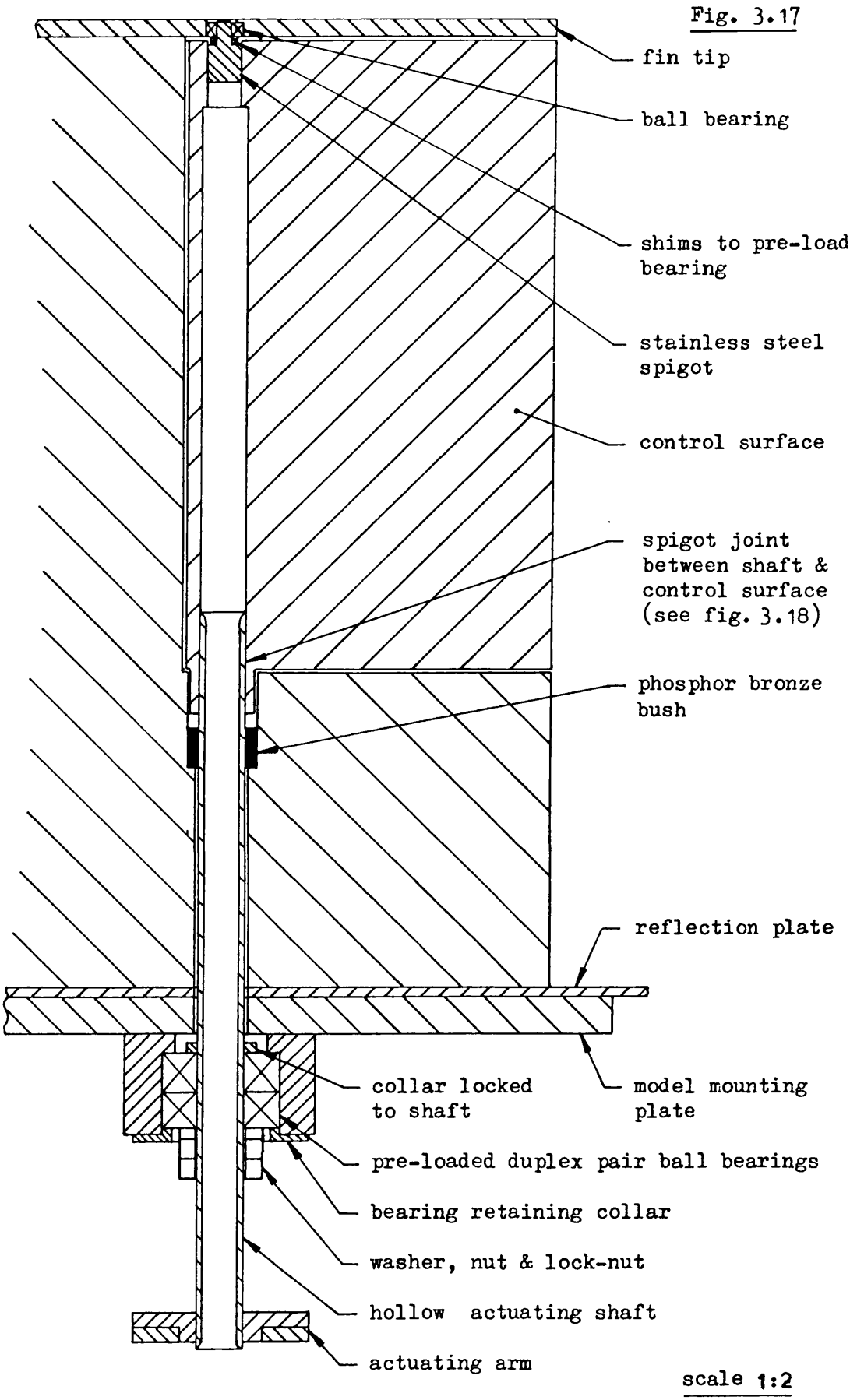

Fig. 3.17 Scrap section through model fin showing arrangement of bearings for supporting the control surface and actuating shaft.

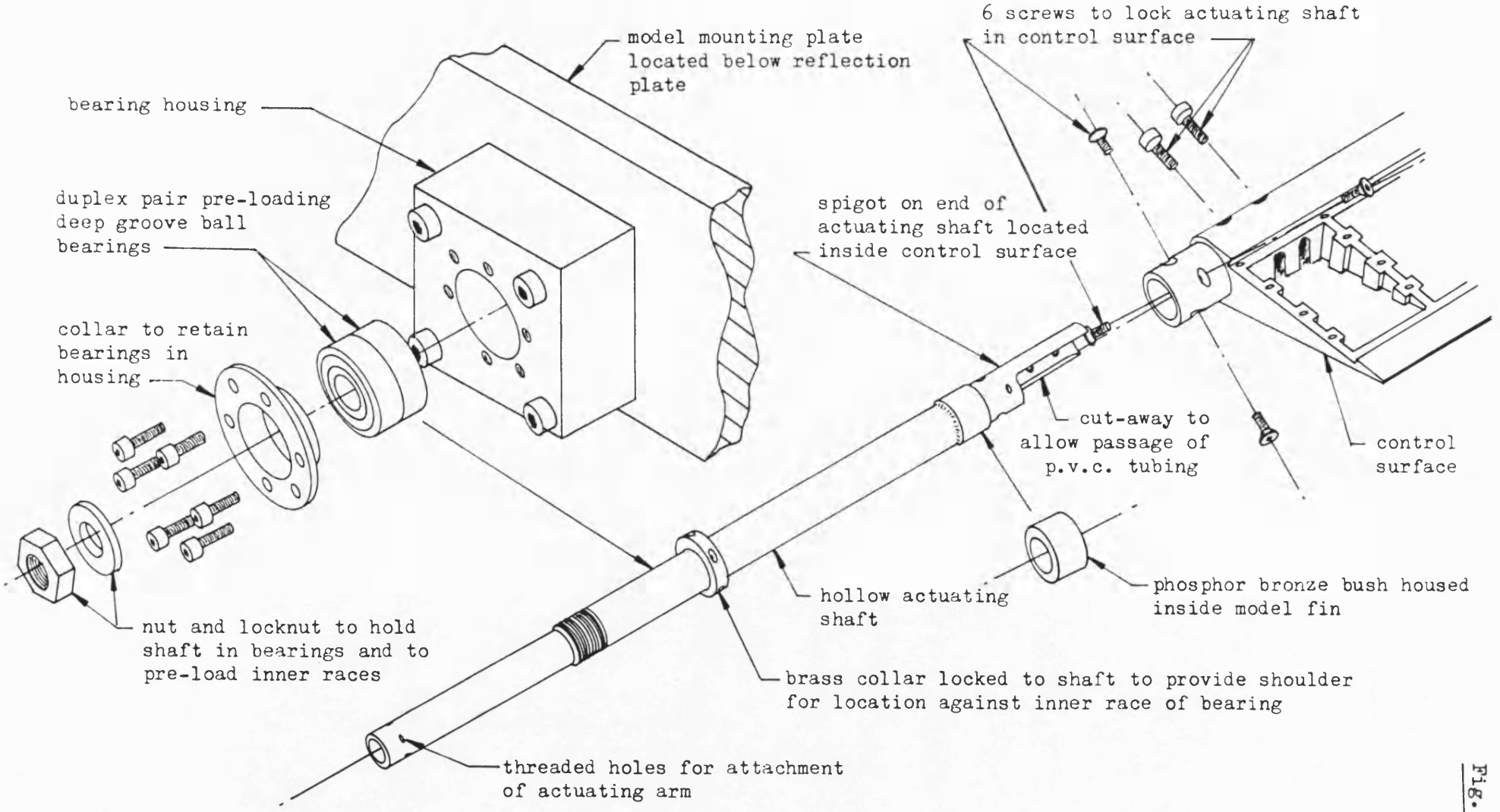

Fig. 3.18

Fig. 3.18 Details of spigot joint between control surface and actuating shaft.

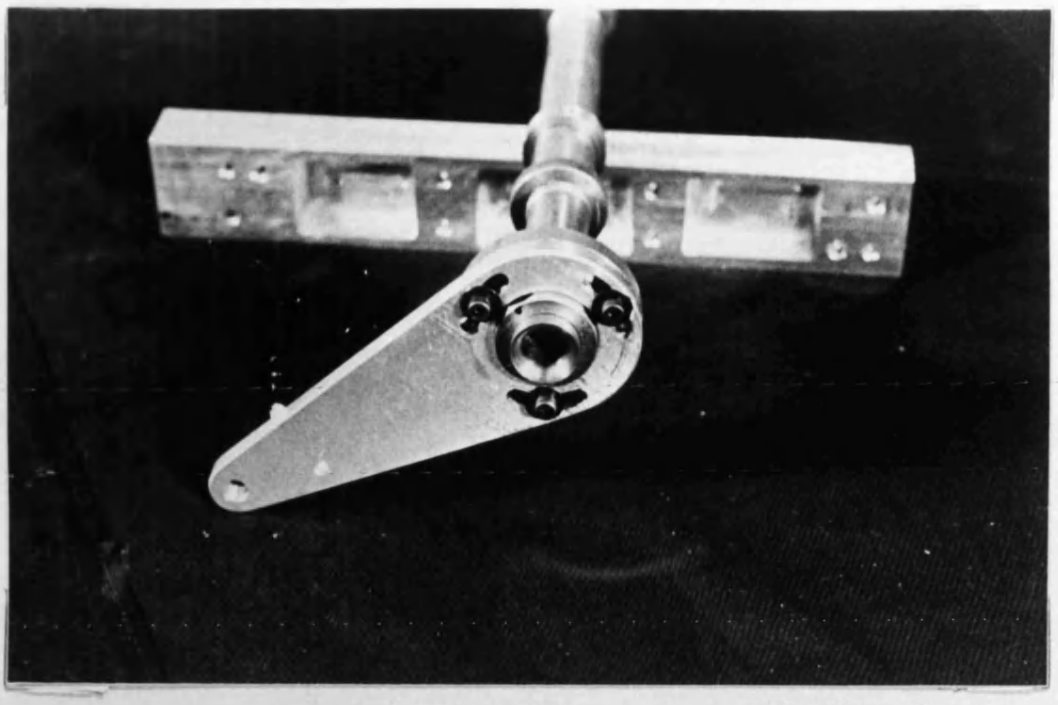

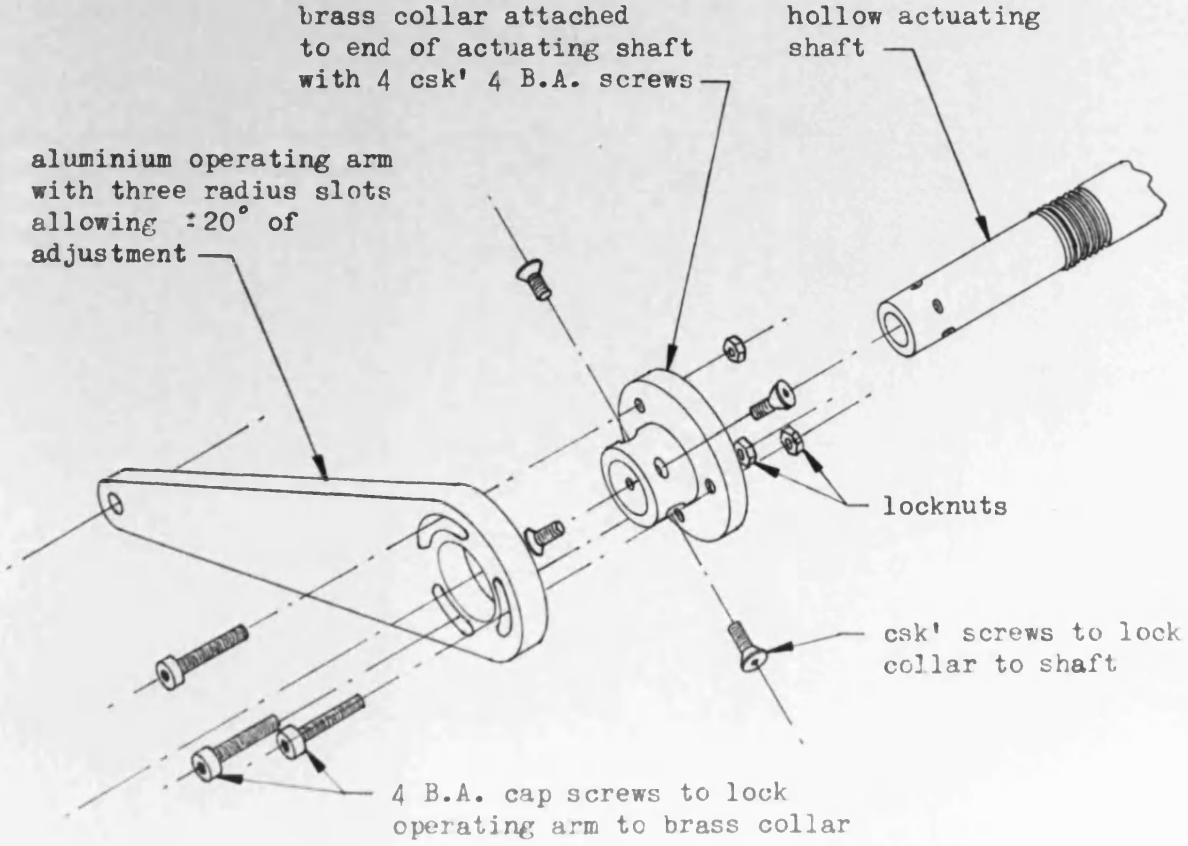

Fig. 3.19 Attachment of control surface operating arm to actuating shaft allowing the control surface deflection to be adjusted ±20°.

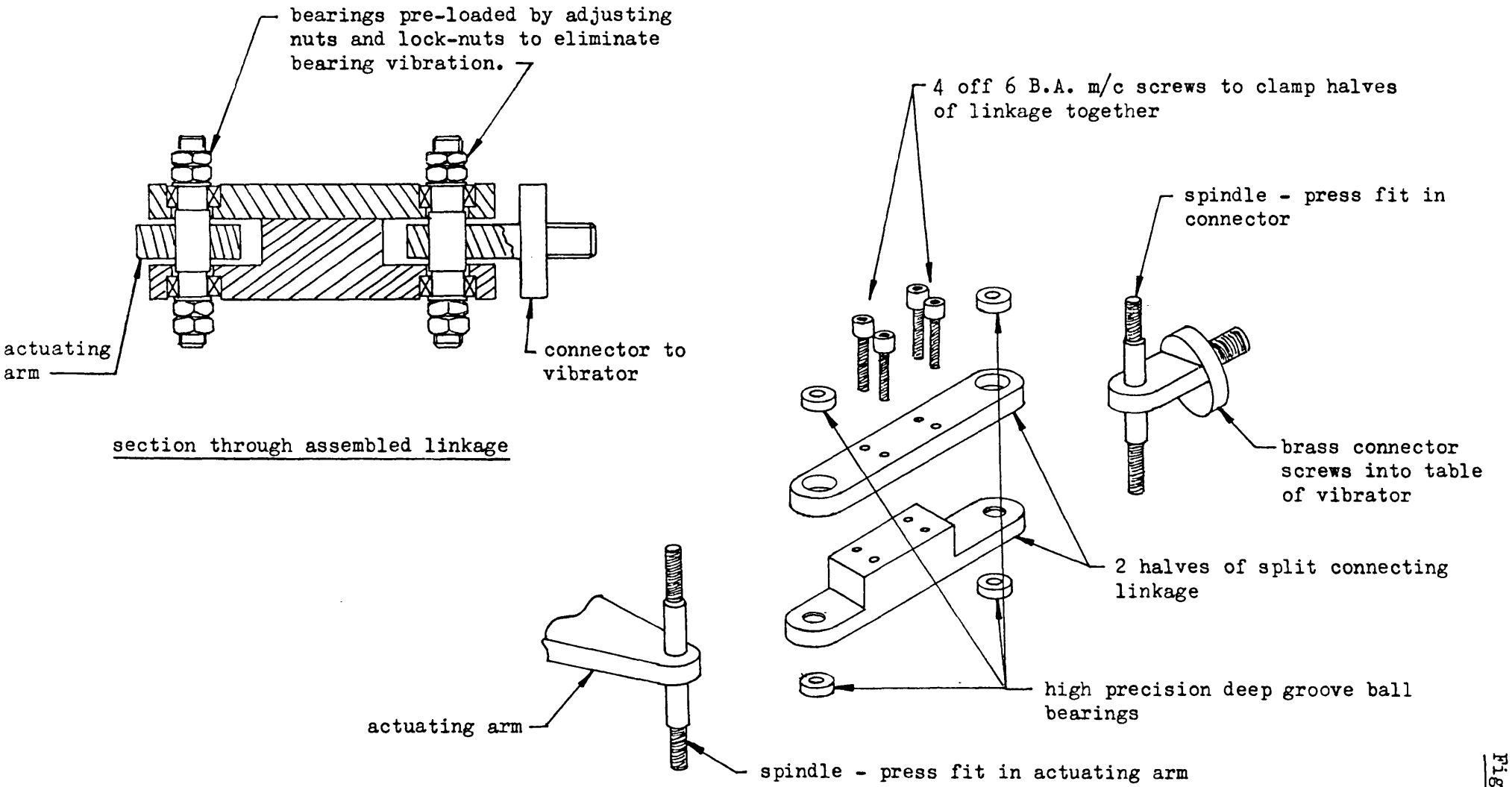

Fig. 3.20

Fig. 3.20 Details of linkage connecting vibrator to actuating arm of control surface.

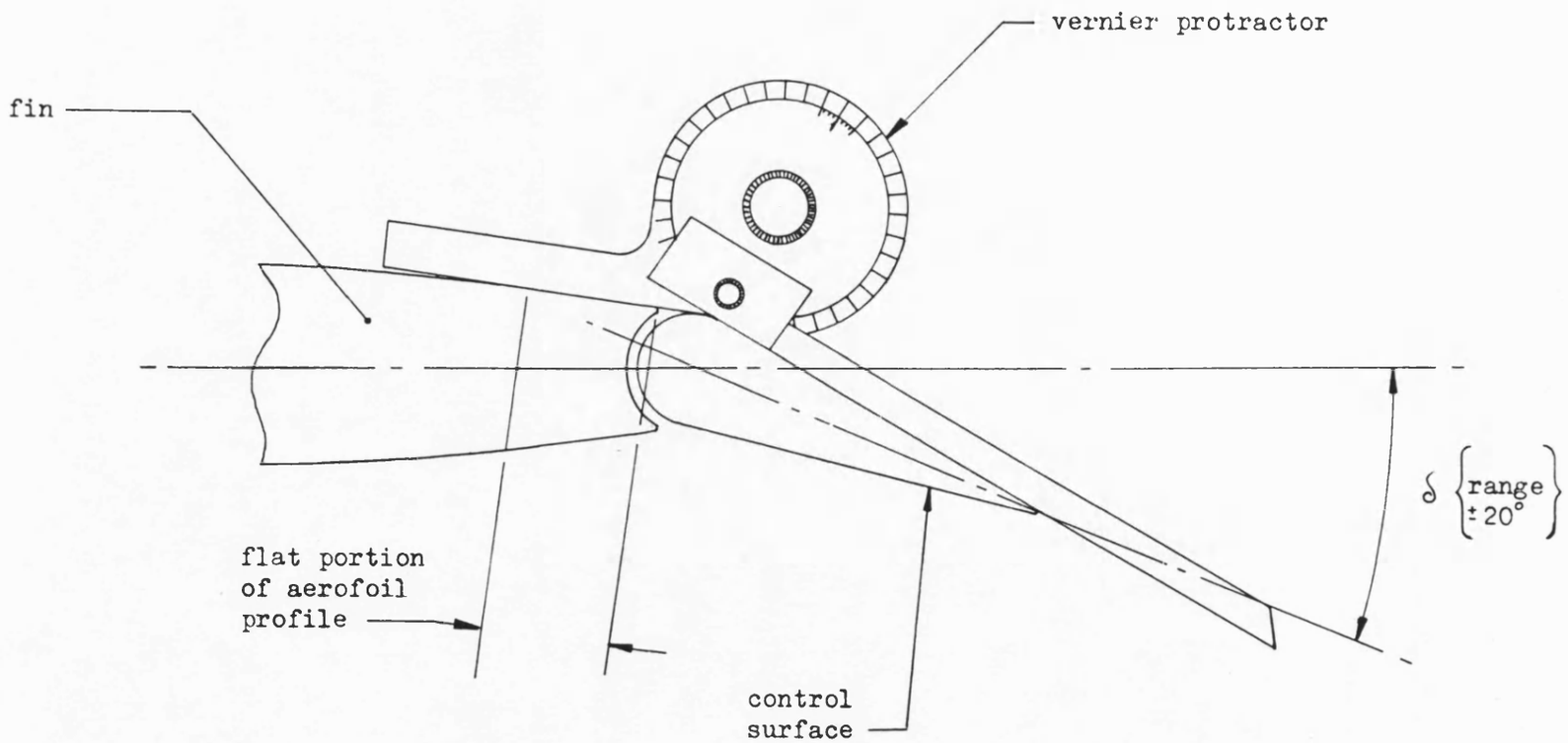

Fig. 3.21

Fig. 3.21 Use of vernier protractor to set mean deflection angle of control surface.

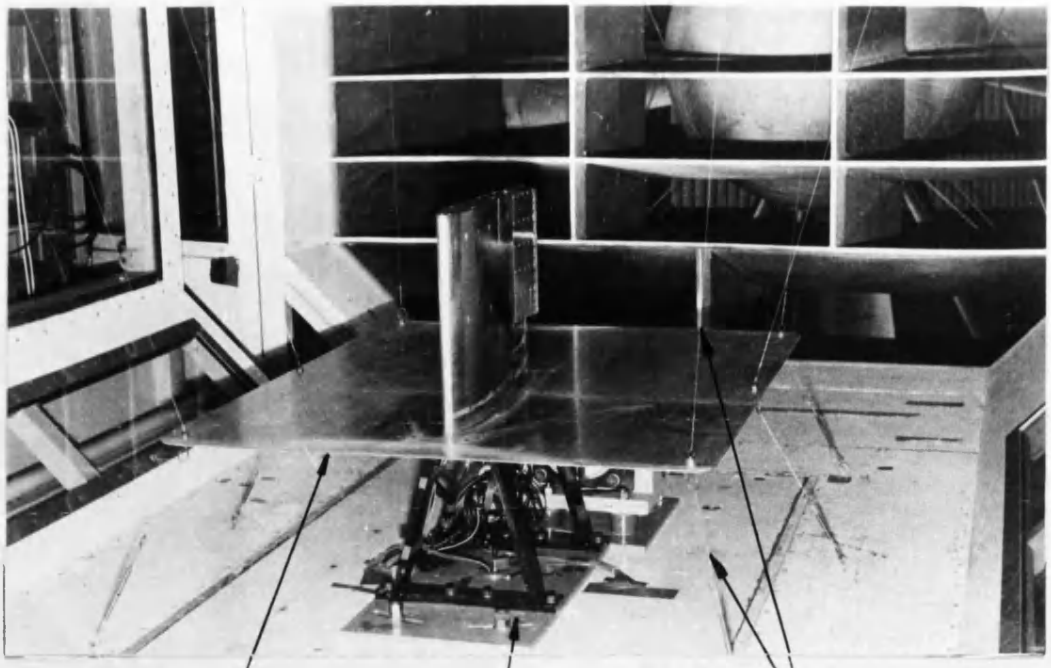

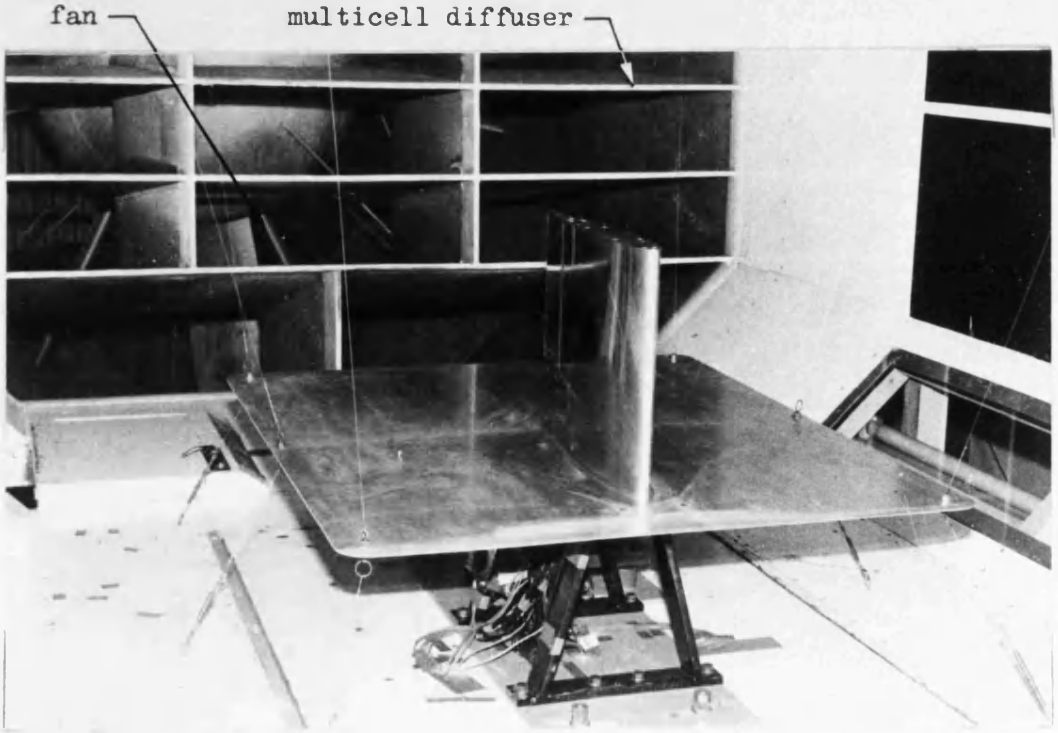

Fig. 3.22 Front view of model fin mounted in 5' x 7' wind tunnel.

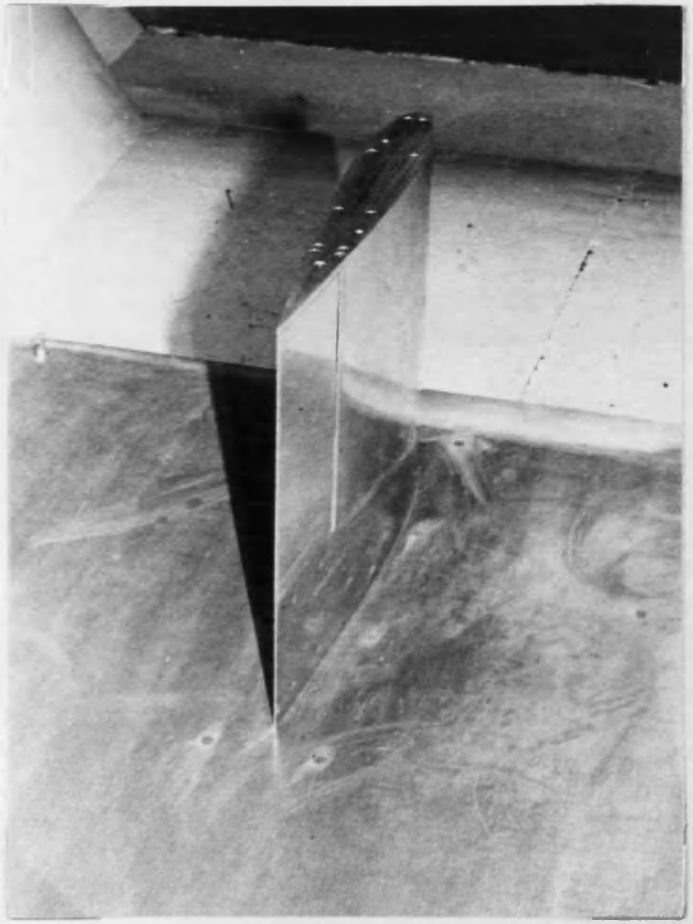

note:

all recessed screw heads were filled with plasticene and smoothed to blend into aerofoil surface

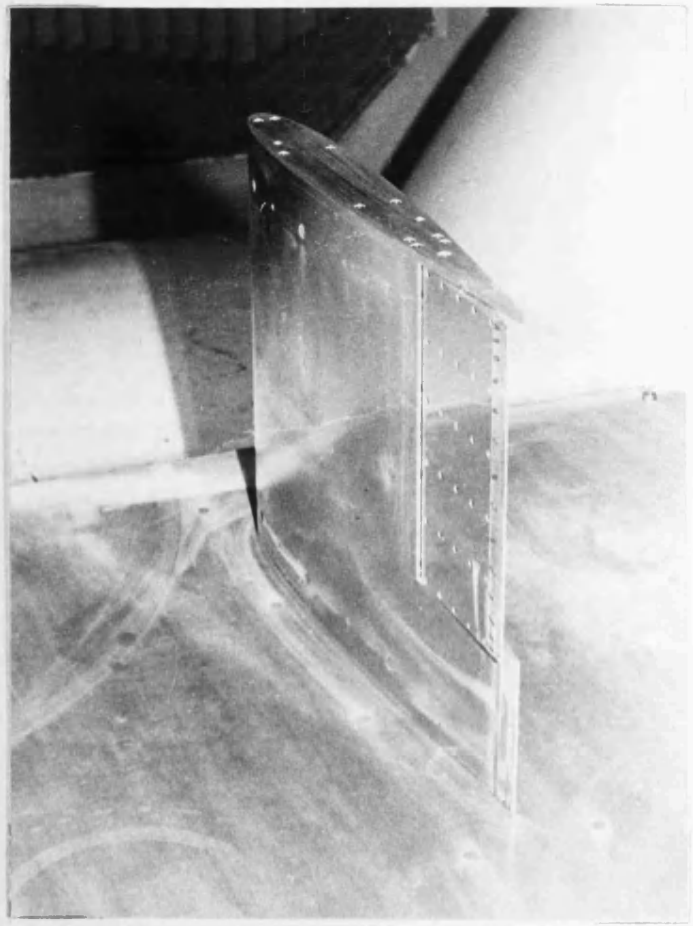

Fig. 3.23

Fig. 3.23 Rear view of model fin mounted in 5' x 7' wind tunnel.

Fig. 3.24

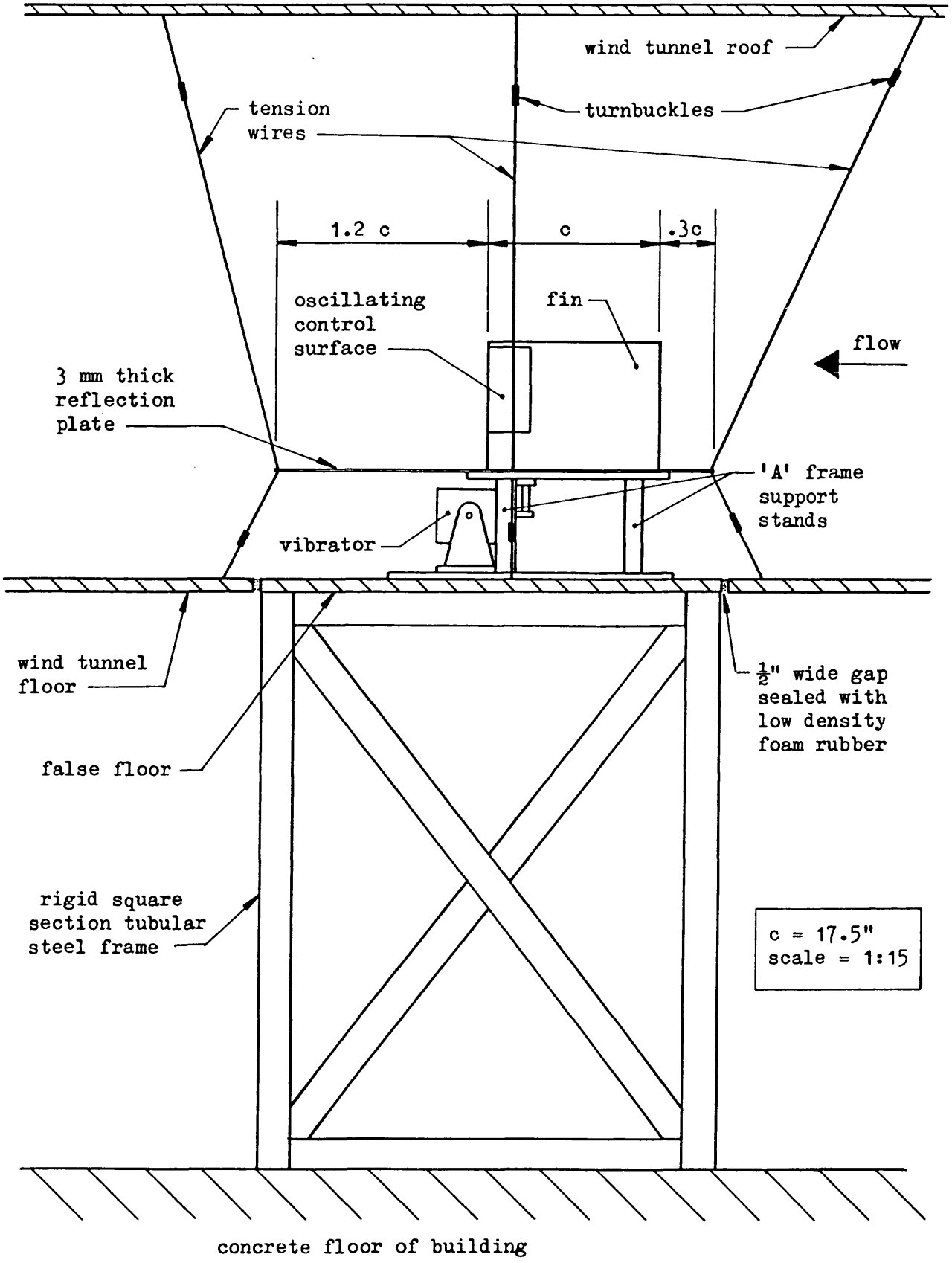

Fig. 3.24 Side elevation of model mounted in 7'x5' wind tunnel.

Fig. 3.25

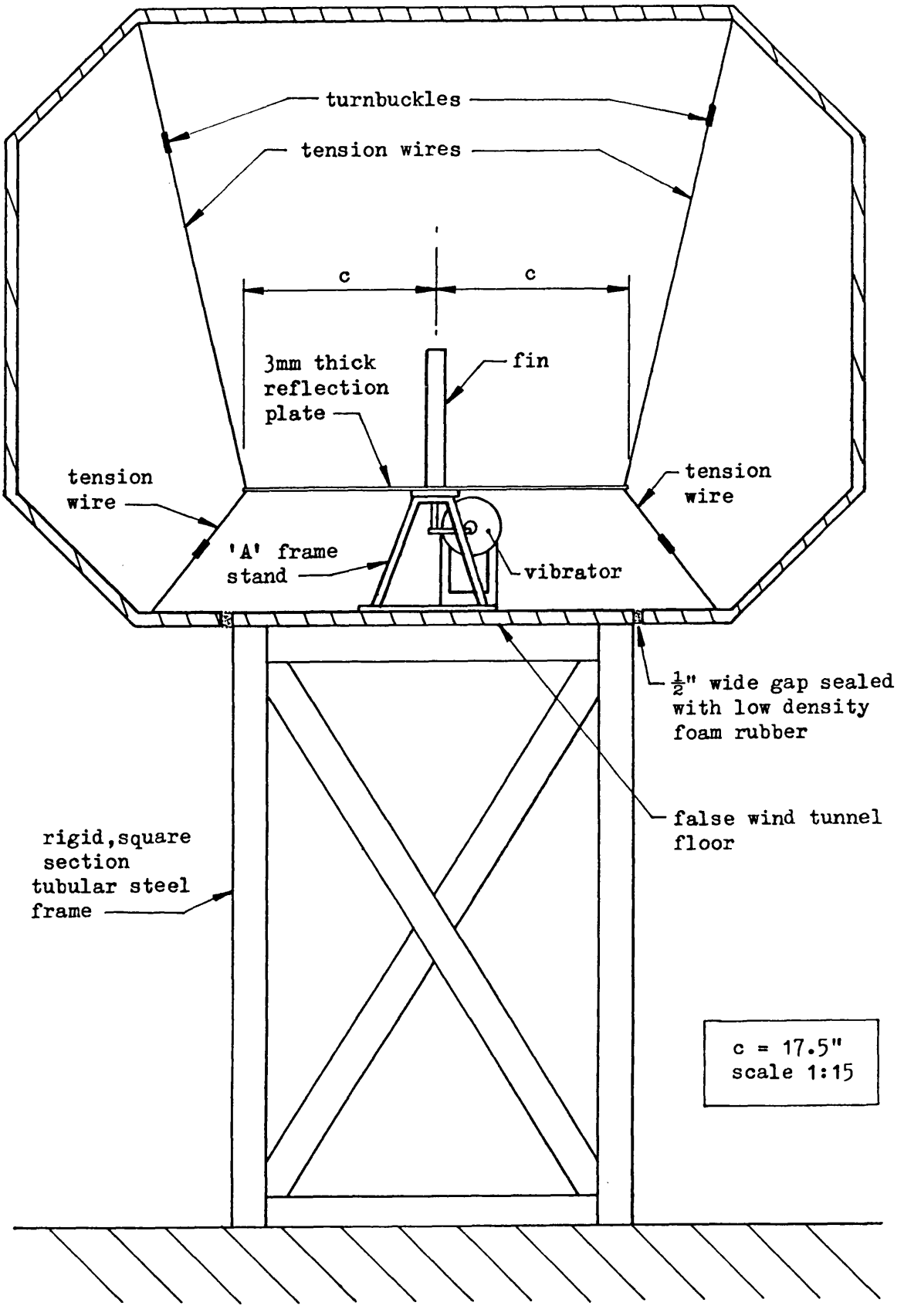

Fig. 3.25 Front elevation of model mounted in 7'x5' wind tunnel.

Fig. 3.26

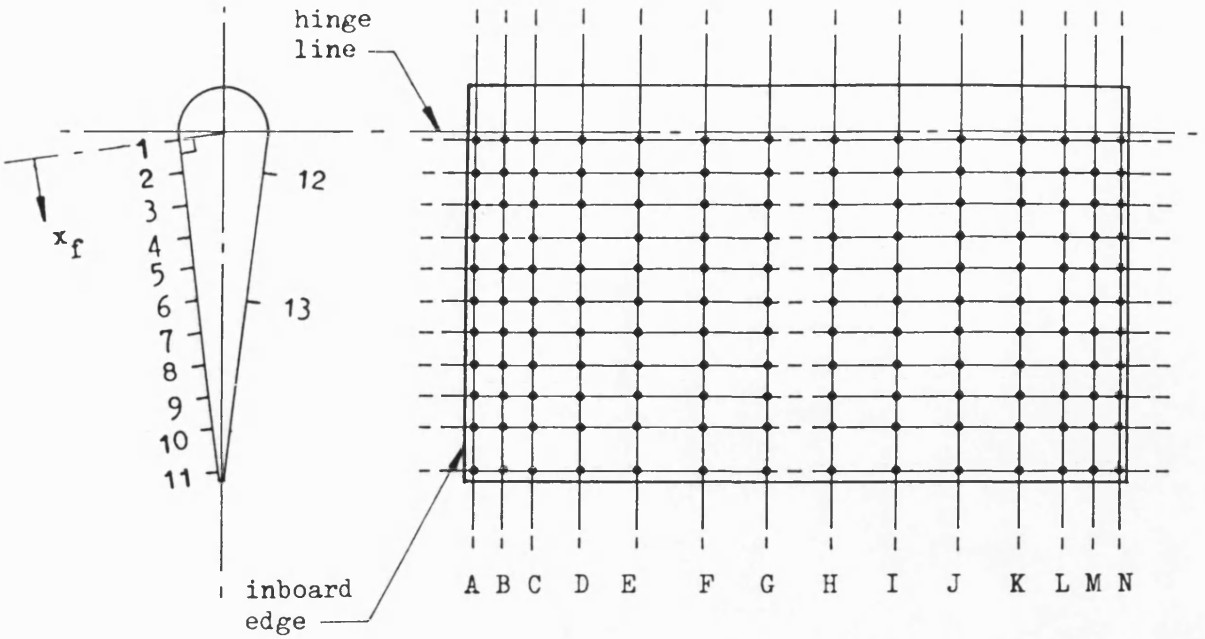

tapping row no.	x/c	x_f/c
1	.7534	.0000
2	.7770	.0238
3	.8006	.0475
4	.8242	.0713
5	.8478	.0950
6	.8714	.1187
7	.8949	.1425
8	.9185	.1662
9	.9421	.1899
10	.9658	.2137
11	.9946	.2428
12	.7770	.0238
13	.8714	.1187

chordwise distribution

tapping row no.	y/s
A	.3357
B	.3596
C	.3952
D	.4381
E	.4953
F	.5571
G	.6213
H	.6834
I	.7476
J	.8095
K	.8667
L	.9119
M	.9452
N	.9691

spanwise distribution

x = chordwise distance from L.E. of fin
y = spanwise distance from fin centreline
c = chord length of fin = 17.5"
s = semi-span of fin = 13.125"

Fig. 3.26 Distribution of pressure tappings on control surface

Fig. 3.27

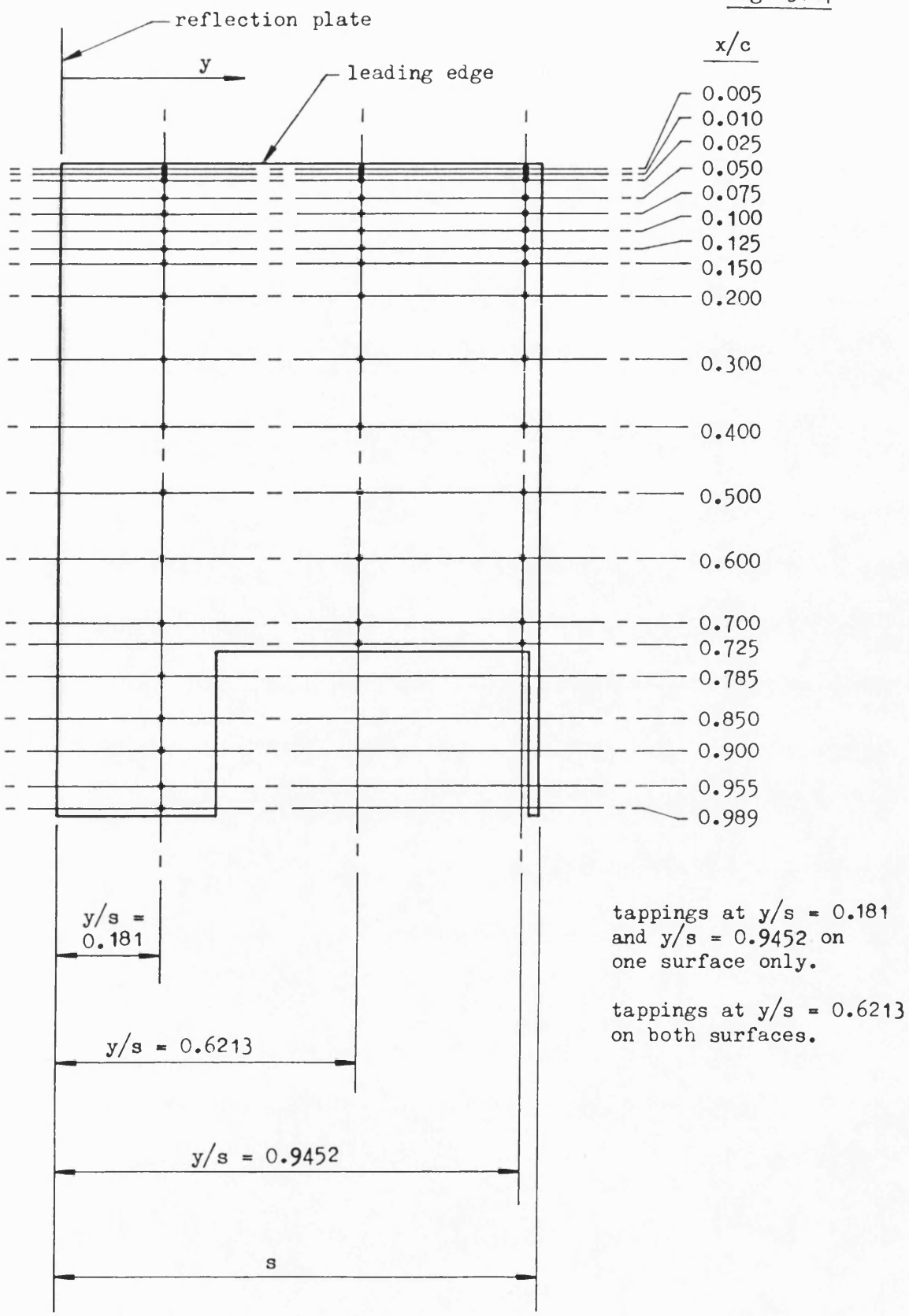

Fig. 3.27 Distribution of pressure tappings on fin.

Fig. 3.28

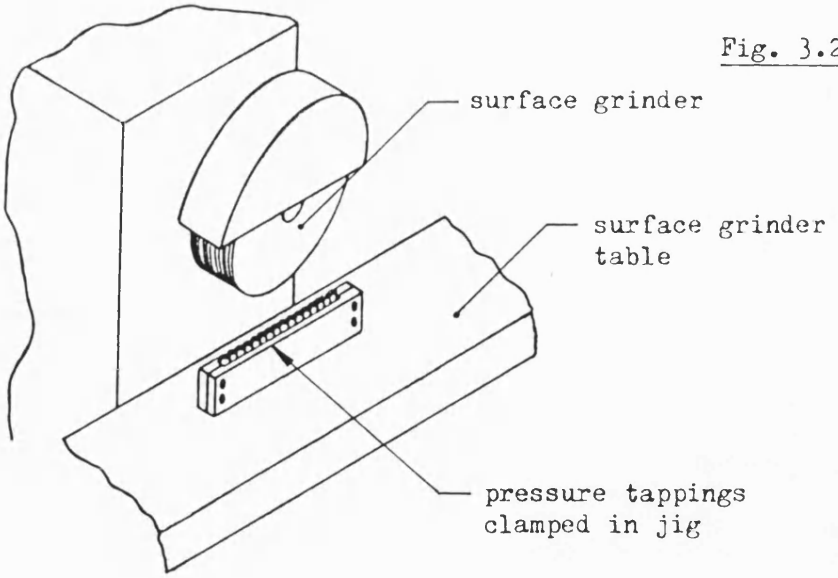

a). pressure tappings accurately ground to a length of 20.2mm

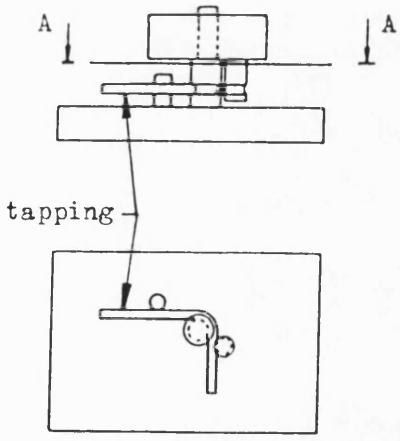

section AA

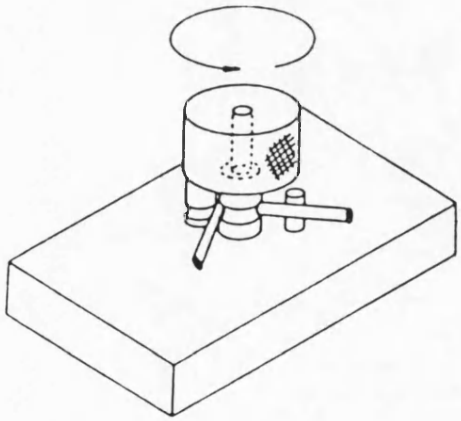

bend radius = 4 x tube O.D.

b). pressure tappings bent in special jig without deformation of tube cross-section

Fig. 3.28 Initial stages in the manufacture of pressure tappings from stainless steel hypodermic tubing.

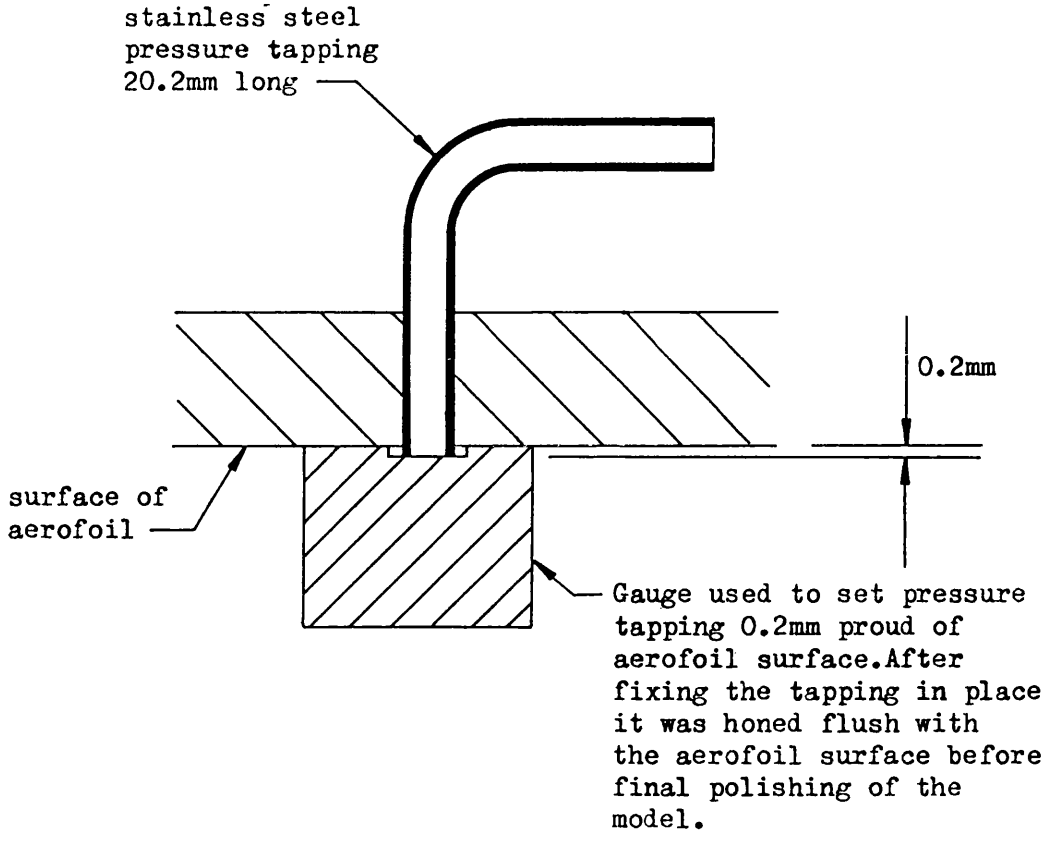

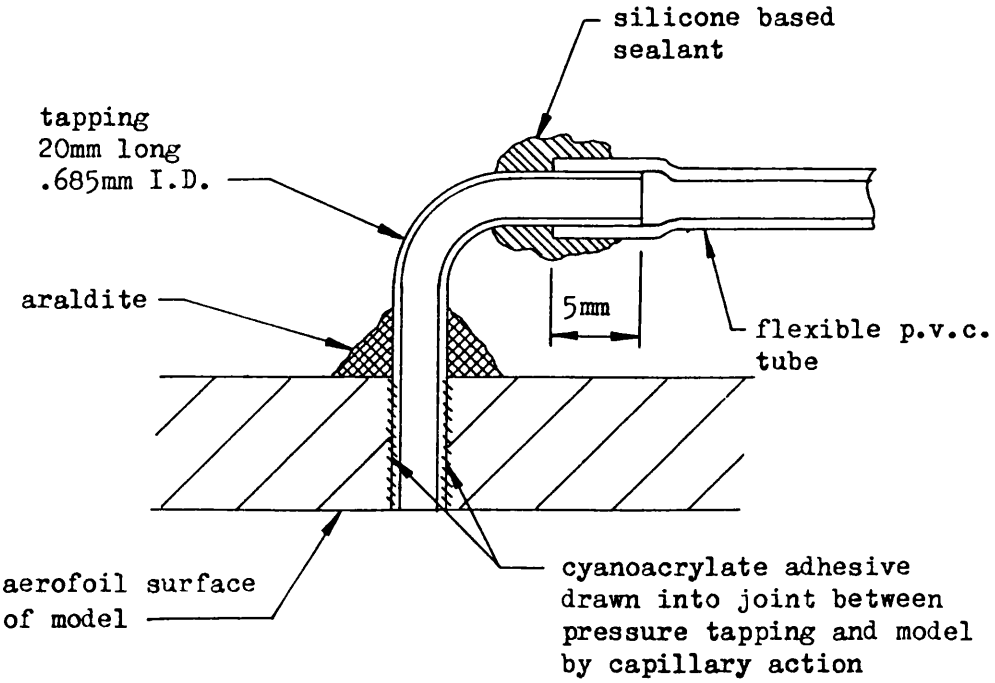

Fig. 3.29 Mounting of pressure tappings in surface of model.

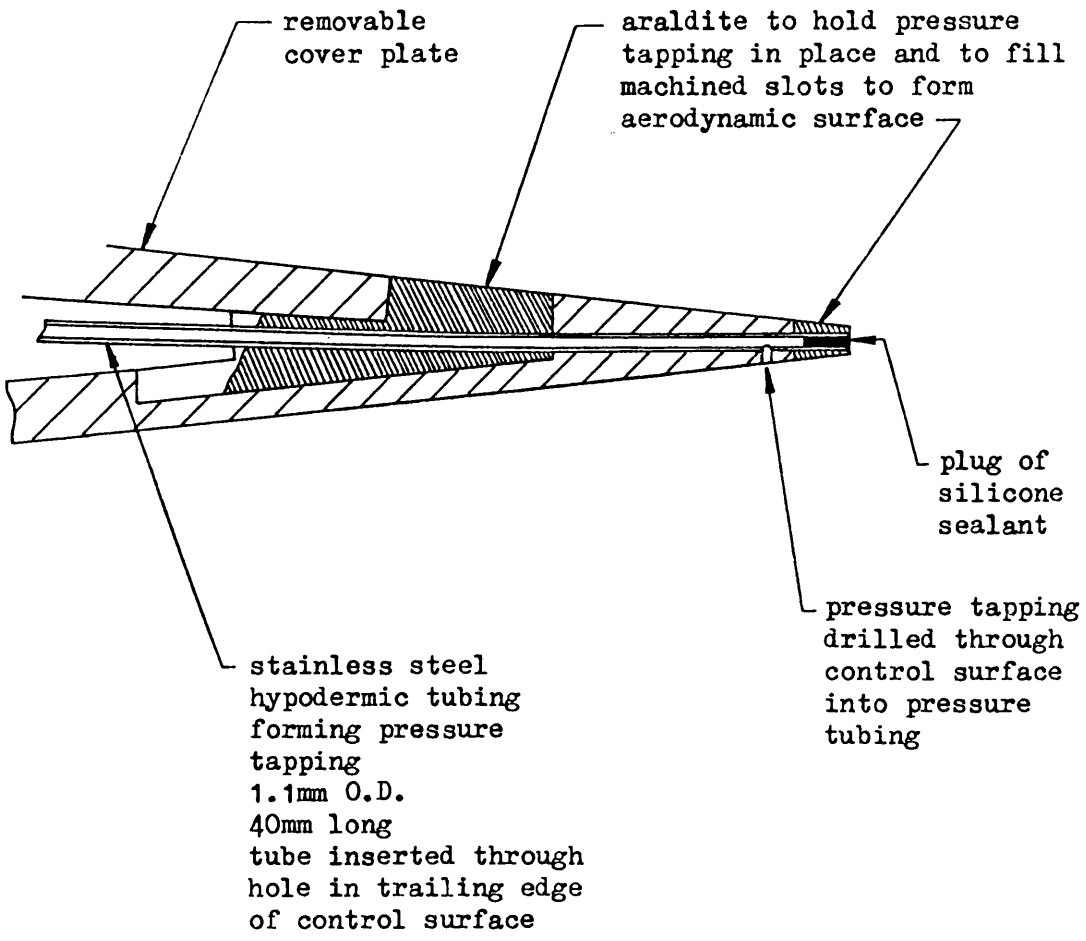

Fig. 3.30 Installation of pressure tapping near trailing edge of control surface.

Fig. 3.31

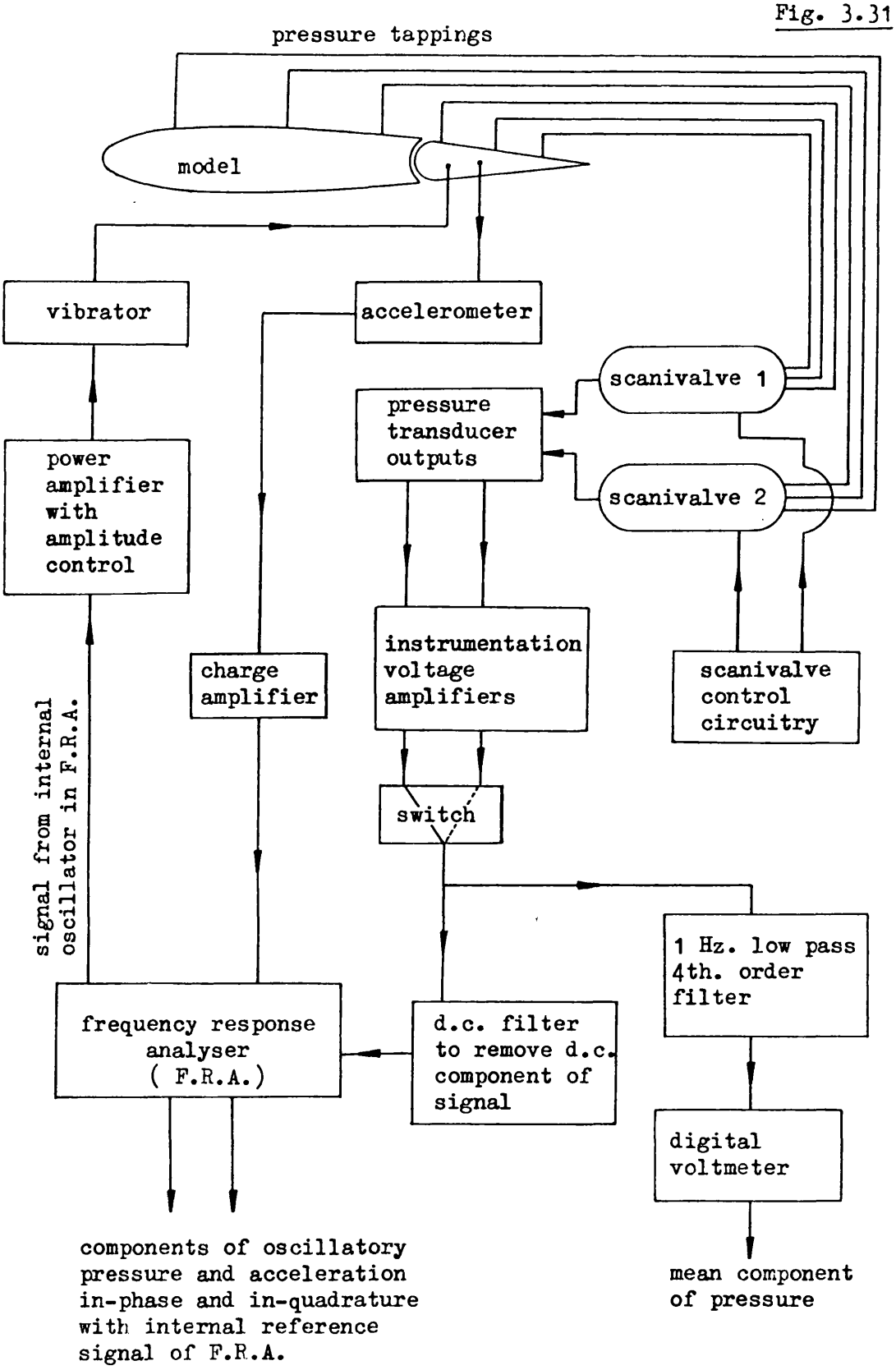

Fig. 3.31 Schematic layout of instrumentation for measuring steady and unsteady pressures on fin with oscillating control surface.

Fig. 3.32

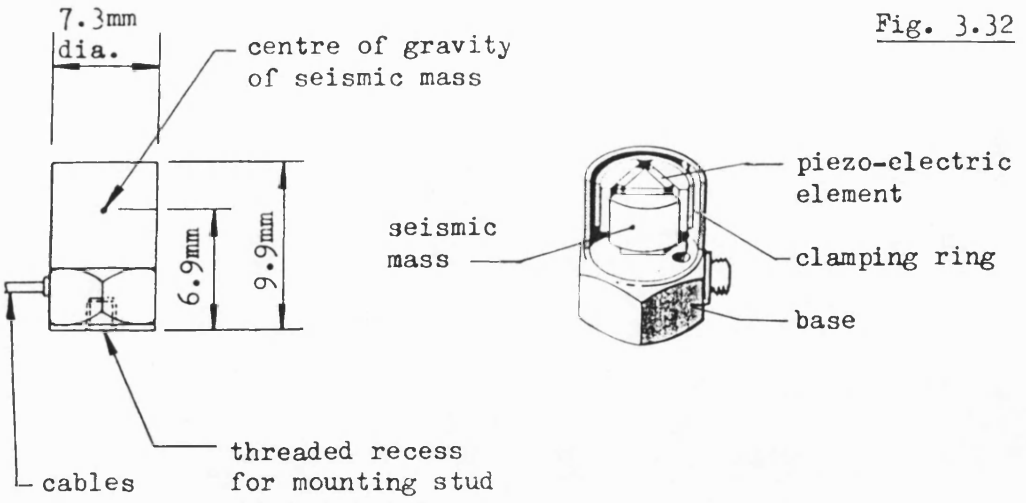

Details of B & K model 4375 delta shear type accelerometer
approx 2.5 x full size

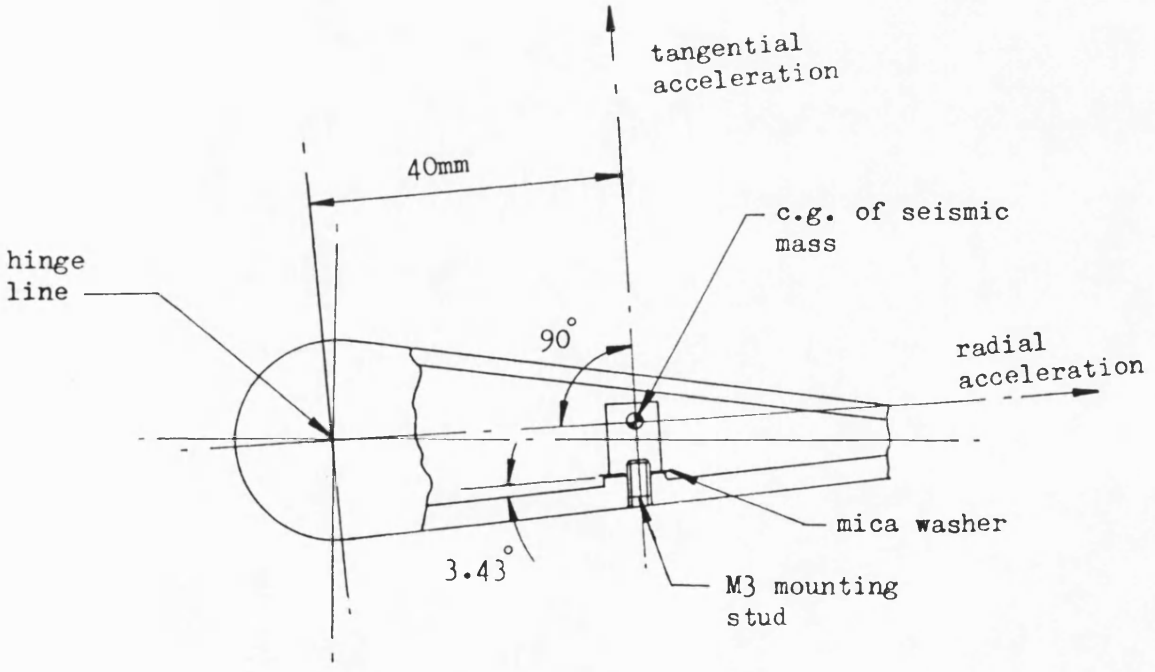

Fig. 3.32 mounting of accelerometer inside control surface.

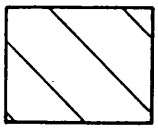

envelope of vibration levels for which the response of the Bruel and Kjaer model 4375 accelerometer is linear.

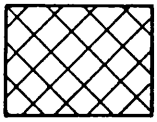

range of vibration levels measured during tests on oscillating flap by accelerometer mounted inside model.

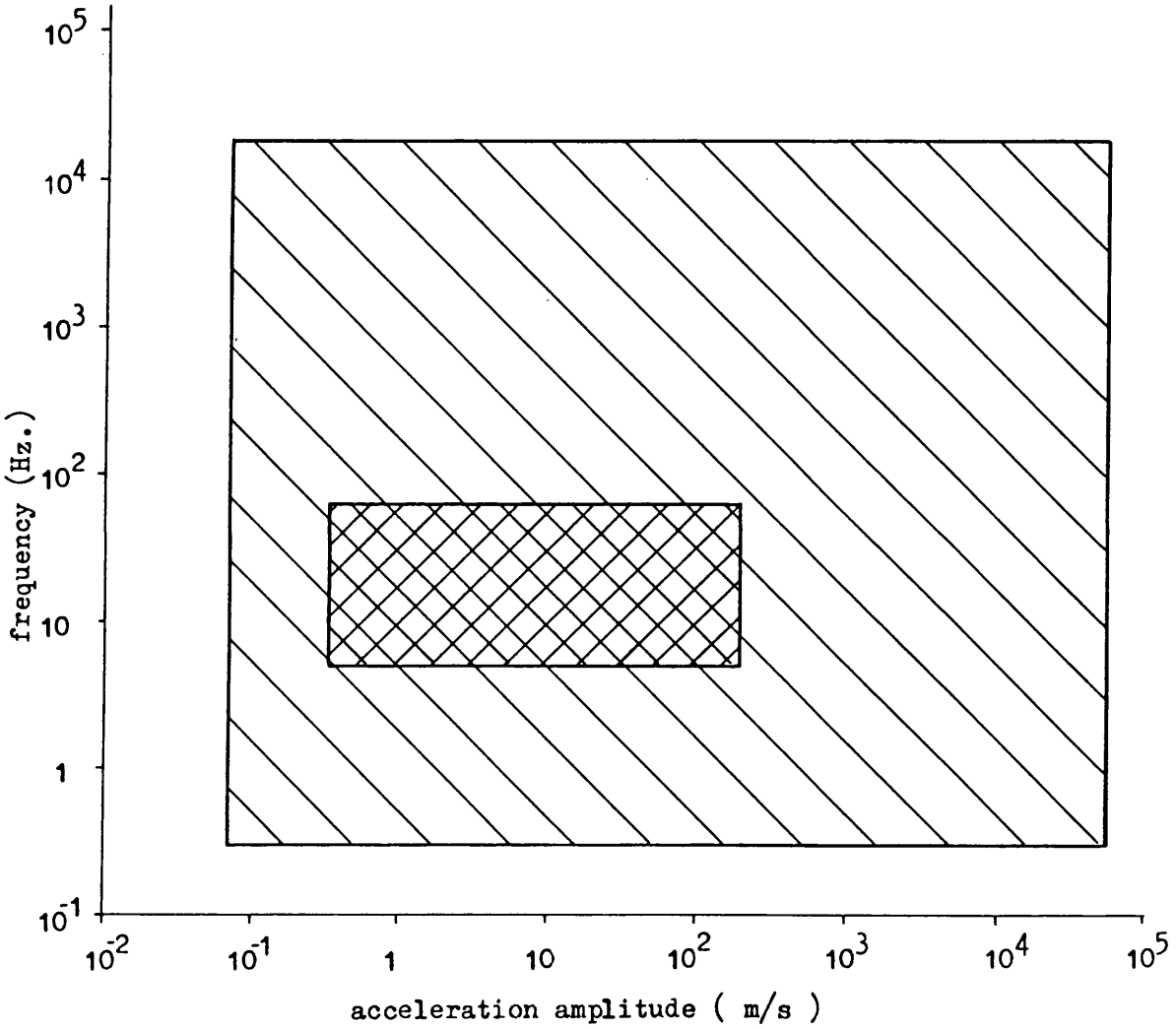

Fig. 3.33 Range of acceleration levels measured by the accelerometer mounted inside the oscillating control surface.

Fig. 3.34

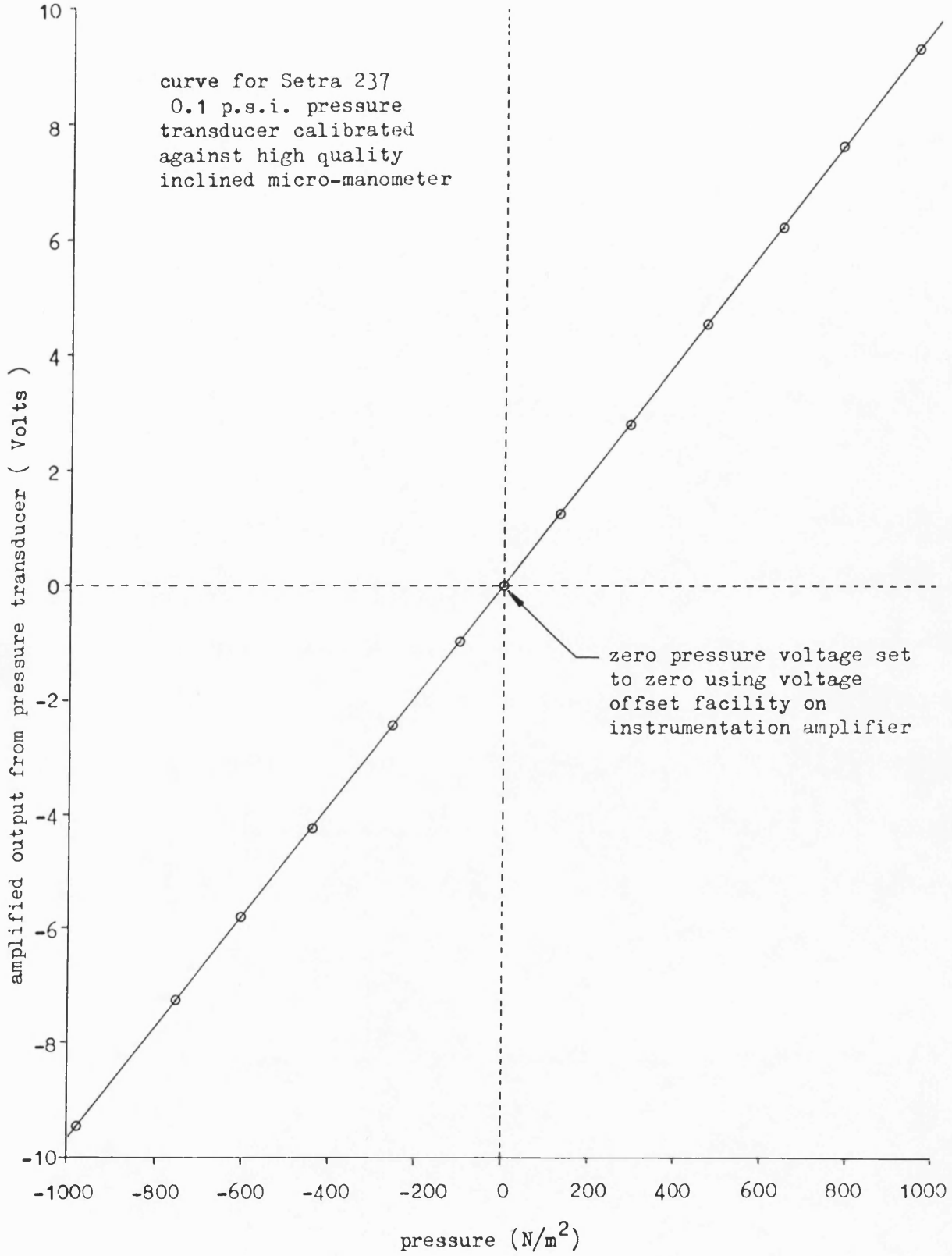

Fig. 3.34 Typical calibration curve for pressure transducer (under static conditions) used in tests on model fin.

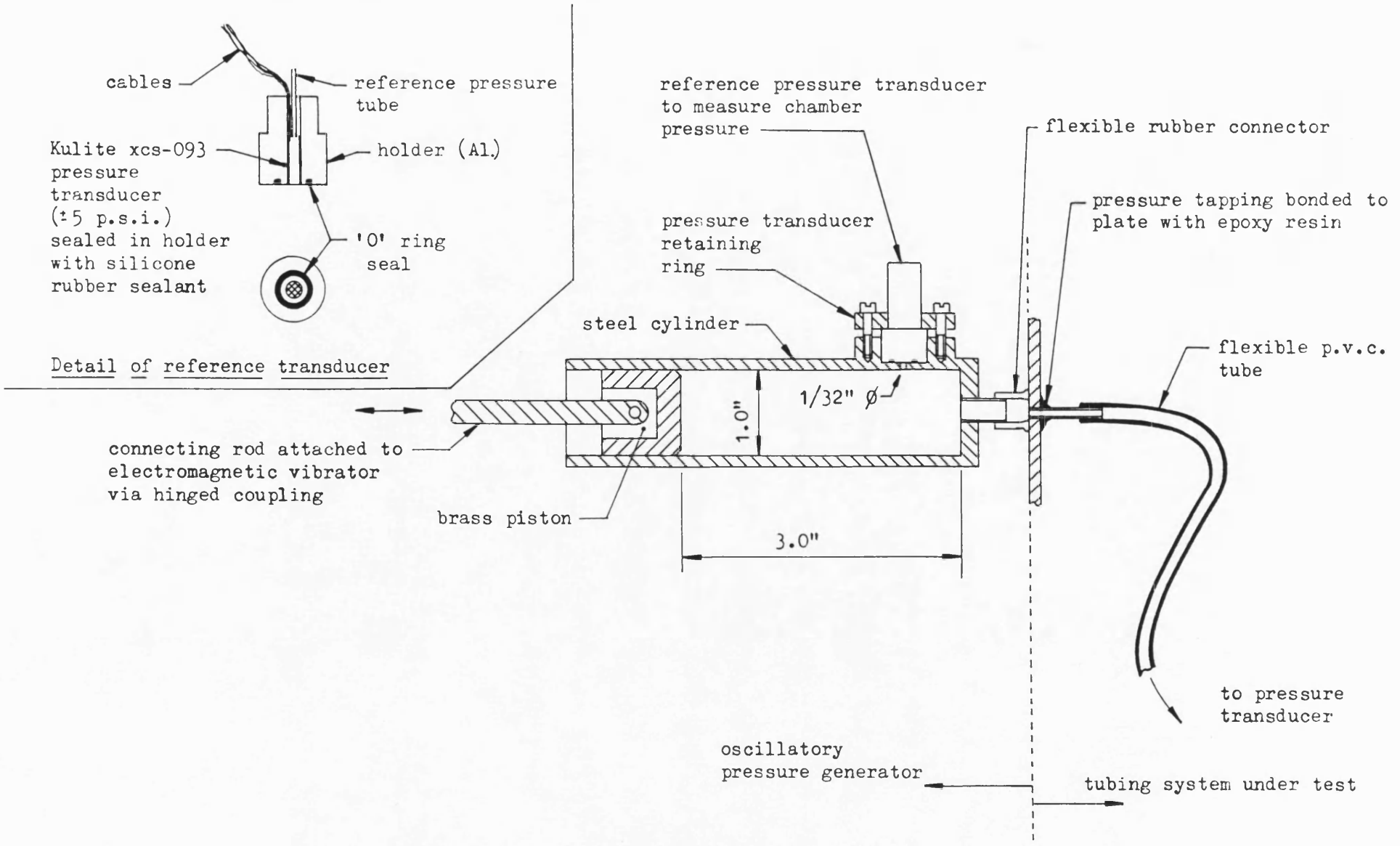

Fig. 4.1

Fig. 4.1 Details of oscillatory pressure generator for calibration of pressure tubing systems for frequency response (zero crossflow over pressure tapping orifice).

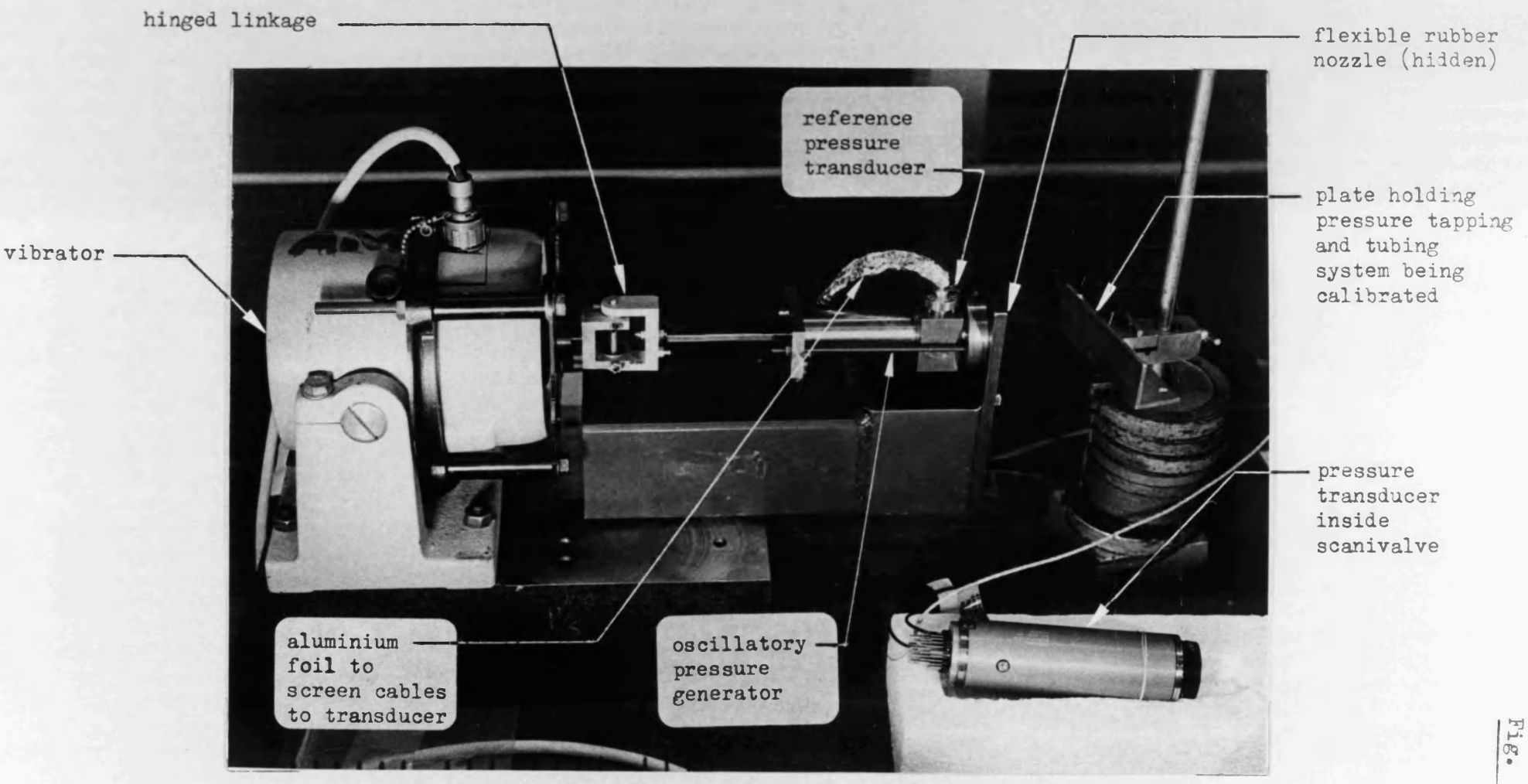

Fig. 4.2

Fig. 4.2 System for calibrating pressure tubing systems with zero crossflow over pressure tapping orifice.

Fig. 4.3

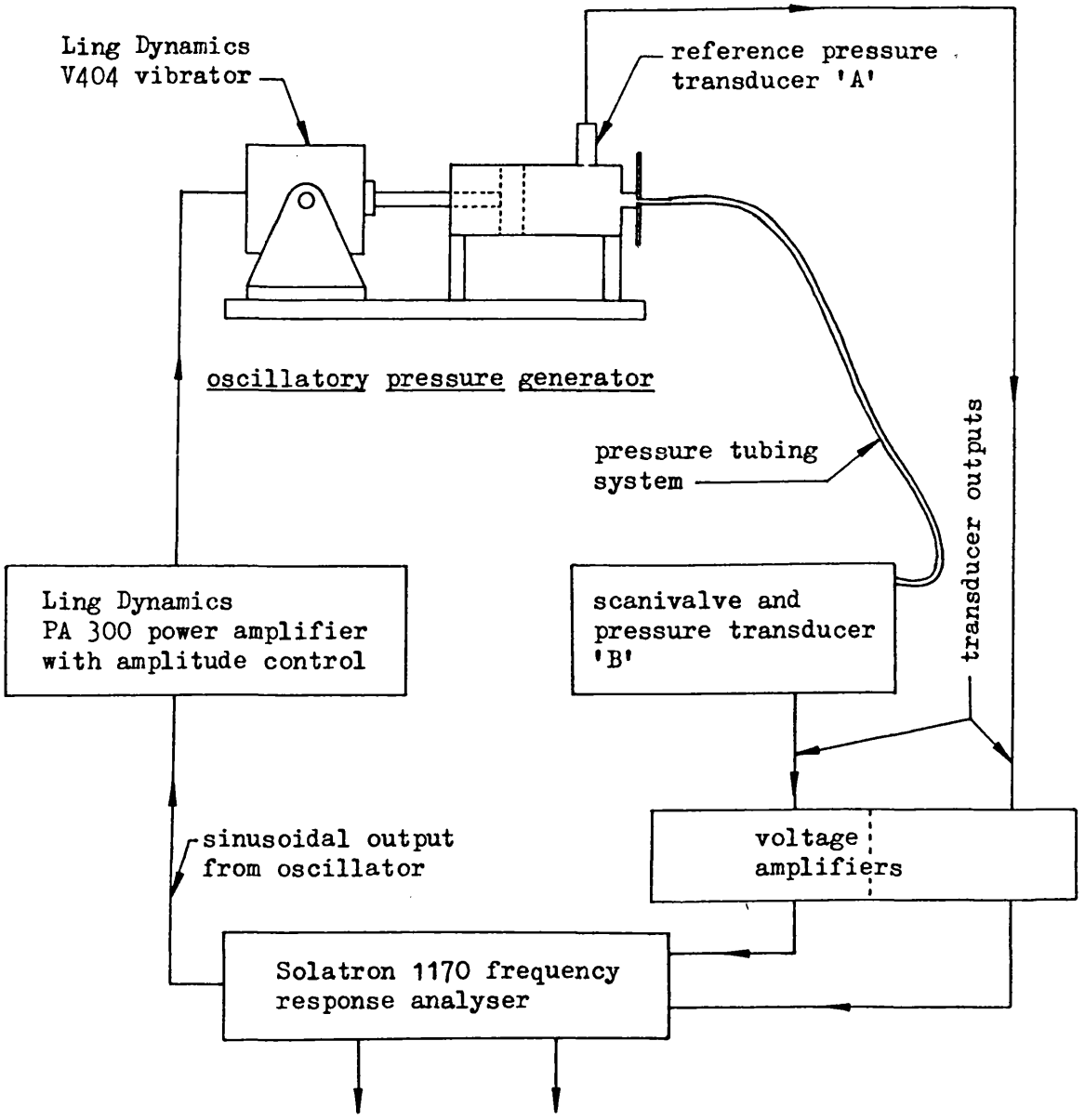

Fig. 4.3 Schematic layout of instrumentation for measurement of frequency response of pressure tubing systems.

Fig. 4.4

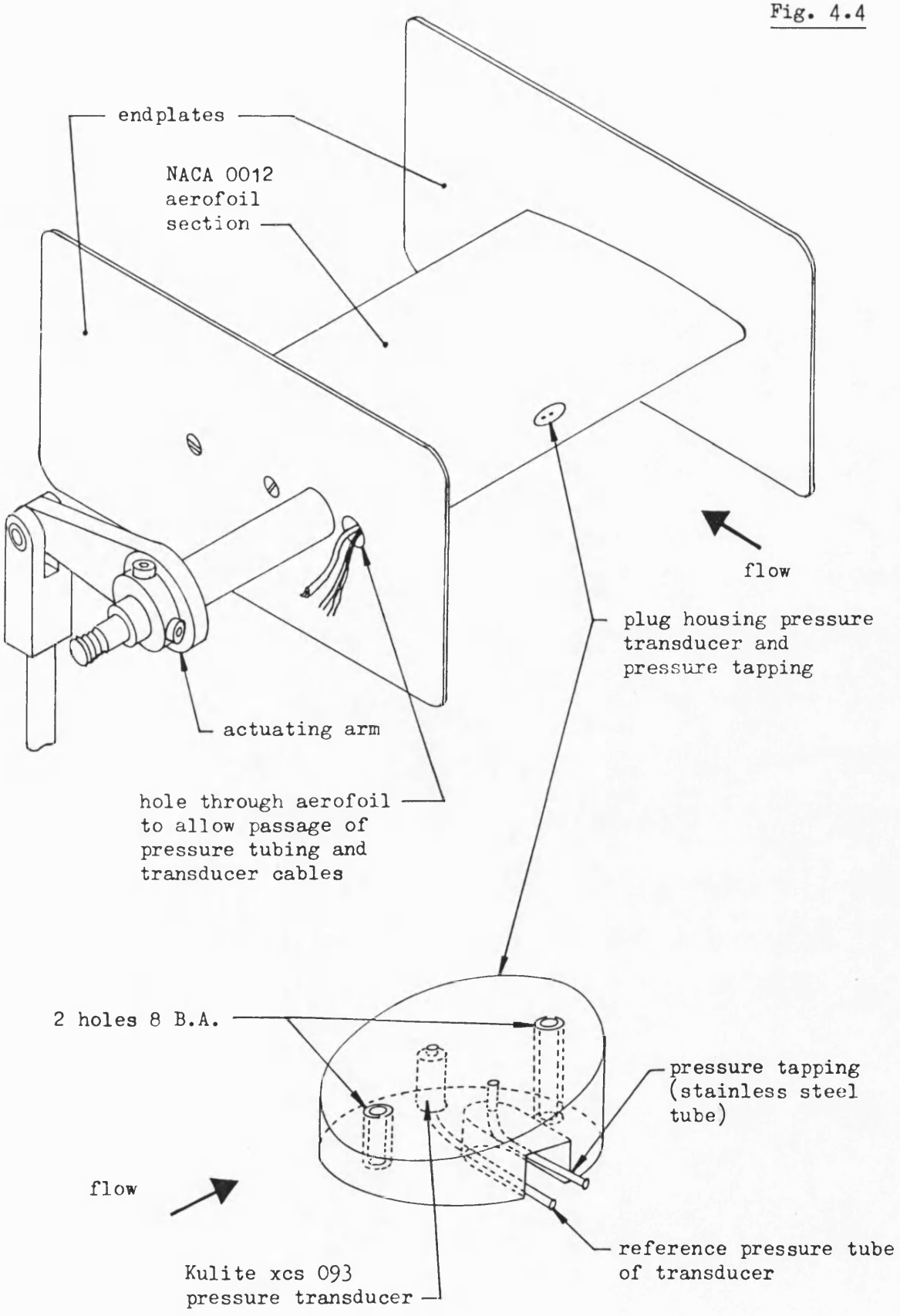

Fig. 4.4 Pictorial view of aerofoil model and instrumentation for calibration of pressure tubing systems with flow across tapping orifice.

Fig. 4.5

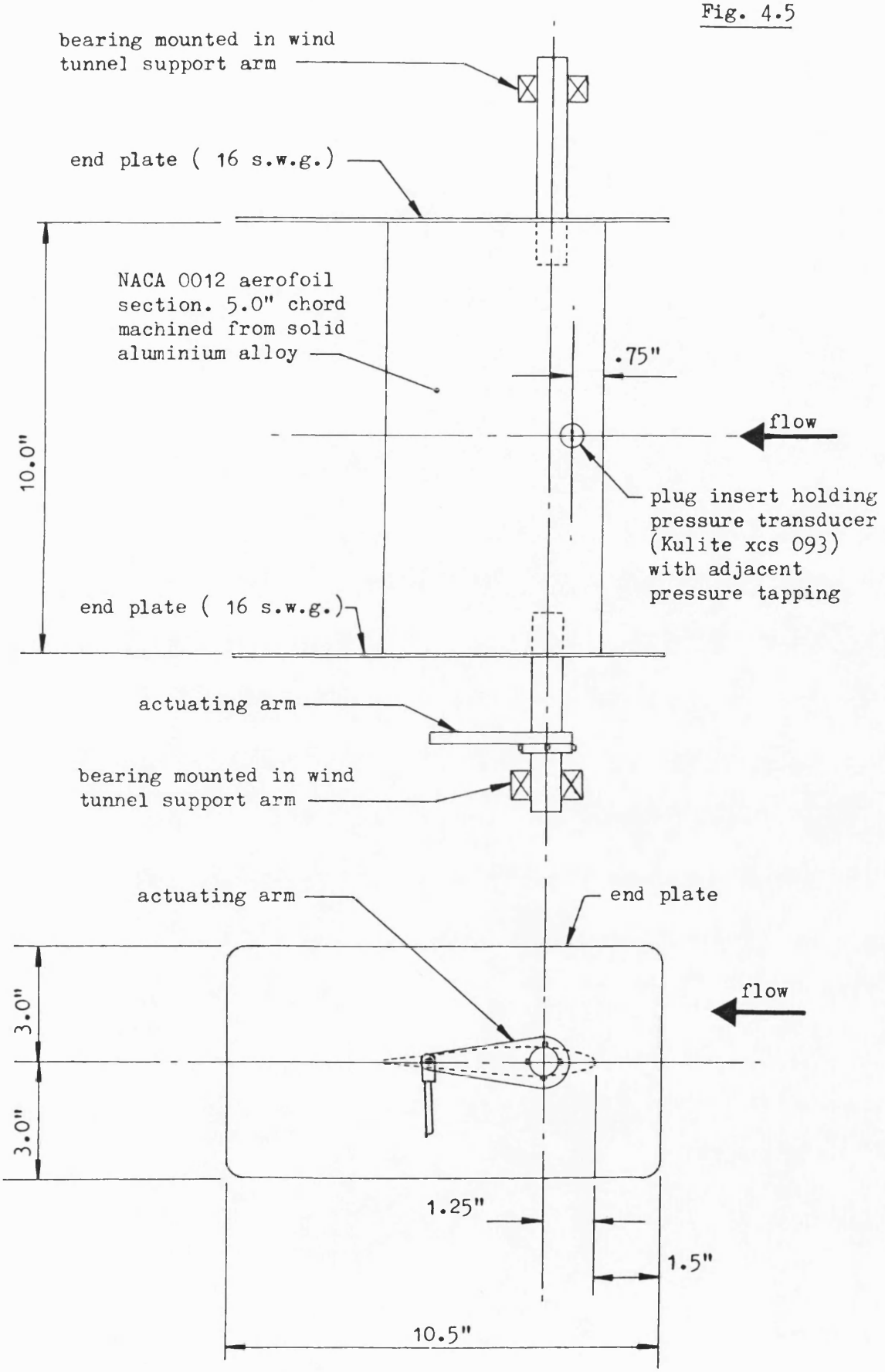

Fig. 4.5 General layout of aerofoil model used to calibrate the frequency response of pressure tubing systems with crossflow over the tapping orifice.

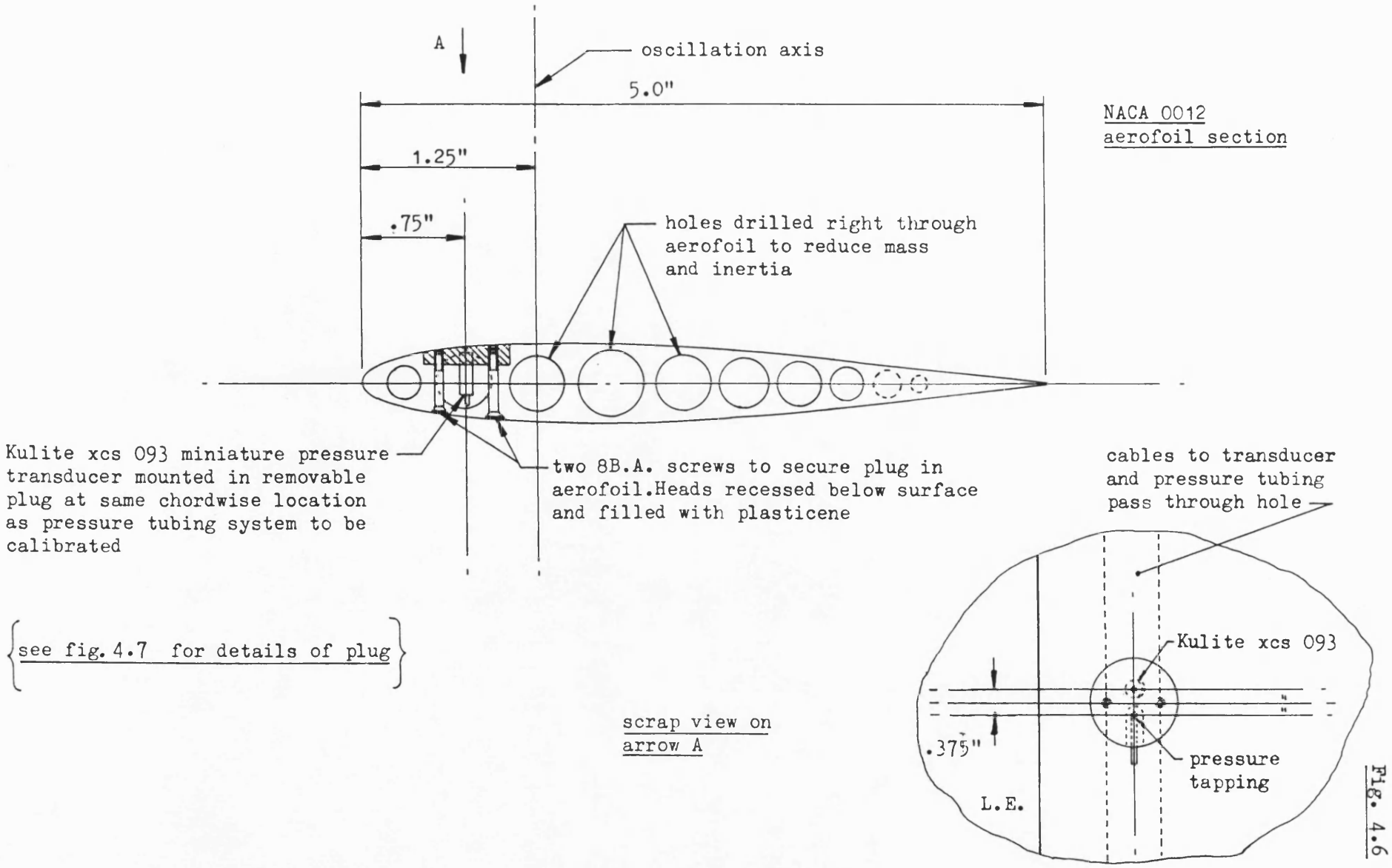

Fig. 4.6 Section through instrumented section of aerofoil model used to calibrate the frequency response of pressure tubing systems with crossflow over tapping orifice.

Fig. 4.7

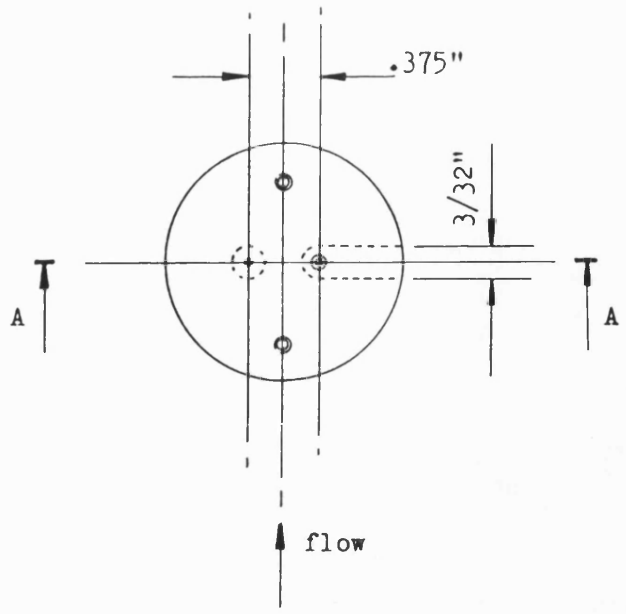

plan view

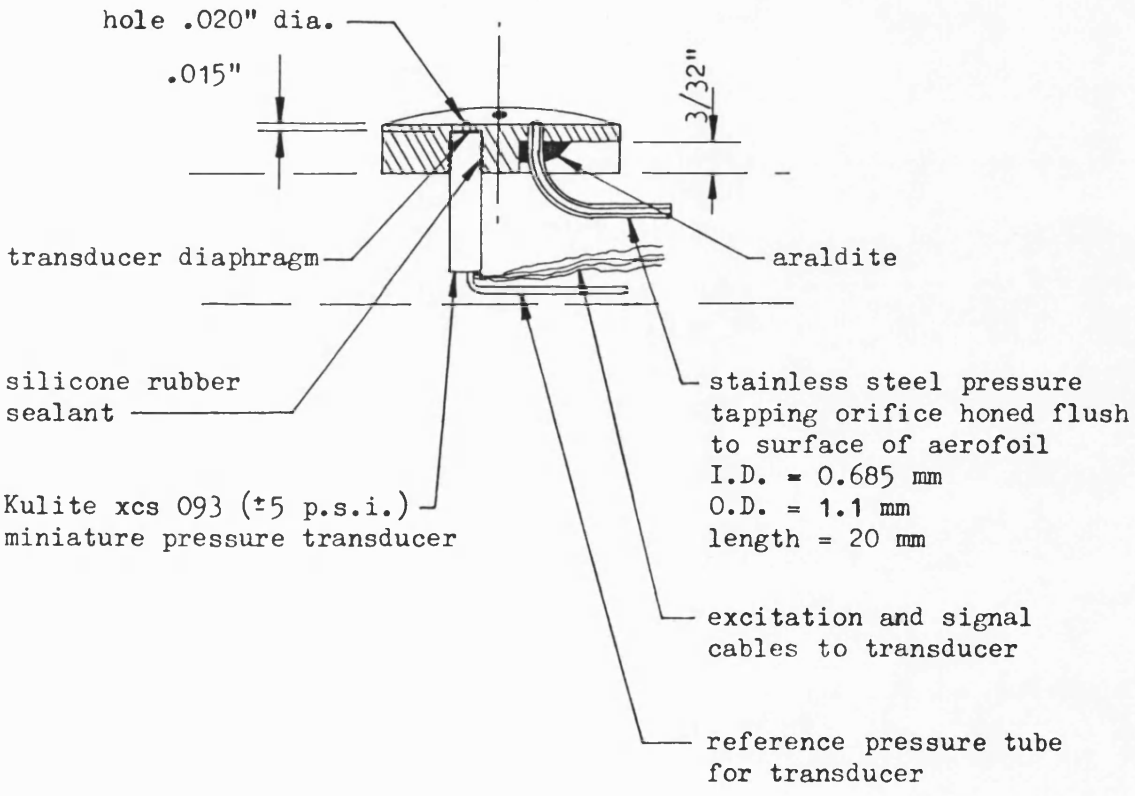

section AA

Fig. 4.7 Detail of insert holding pressure transducer and pressure tapping for calibration of pressure tubing system with crossflow over tapping orifice (scale 2:1).

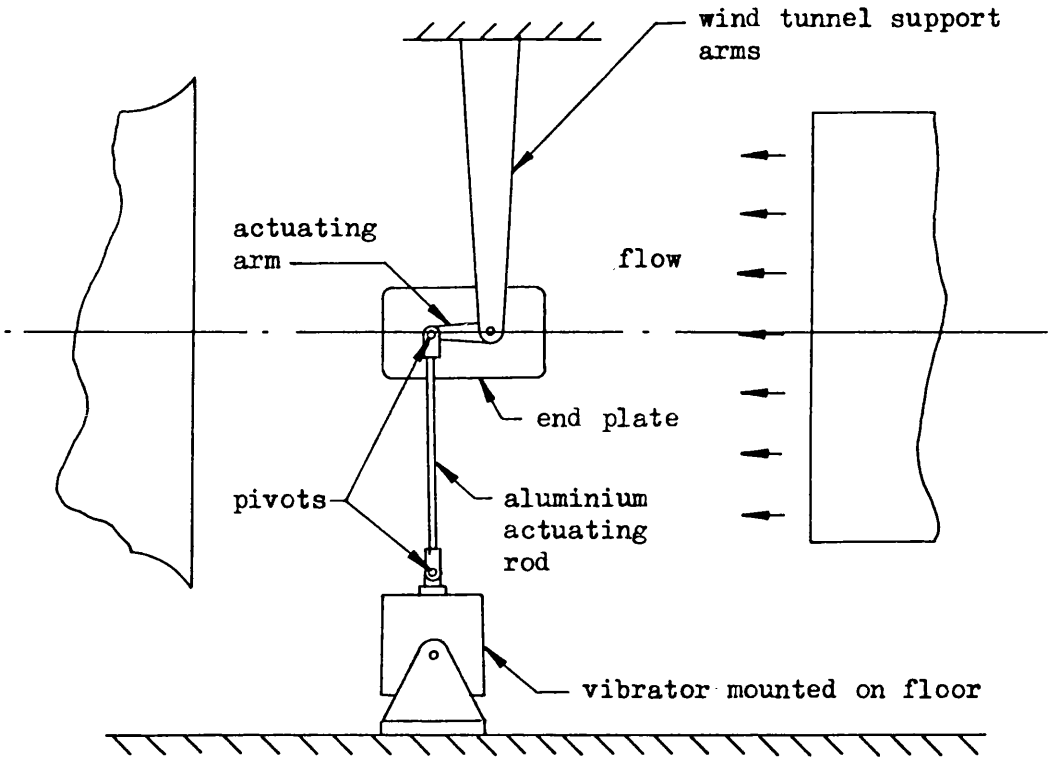

side elevation

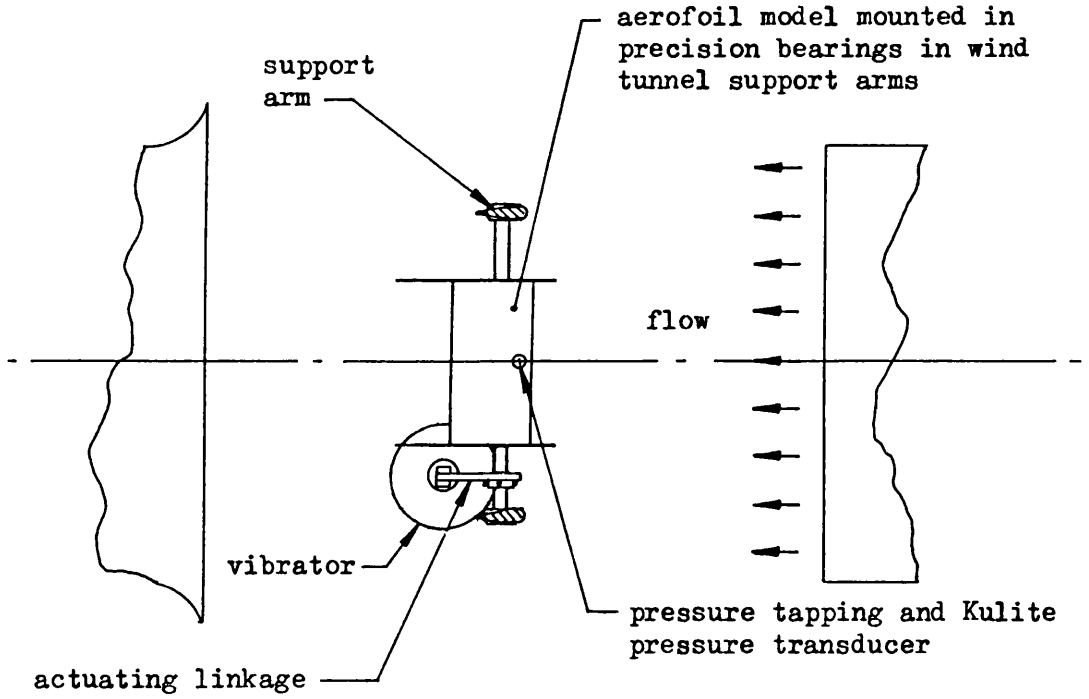

plan

Fig. 4.8 suspension of aerofoil model in 30" dia. open jet wind tunnel for calibration of pressure tubing system with flow across tapping orifice.

Fig. 4.9

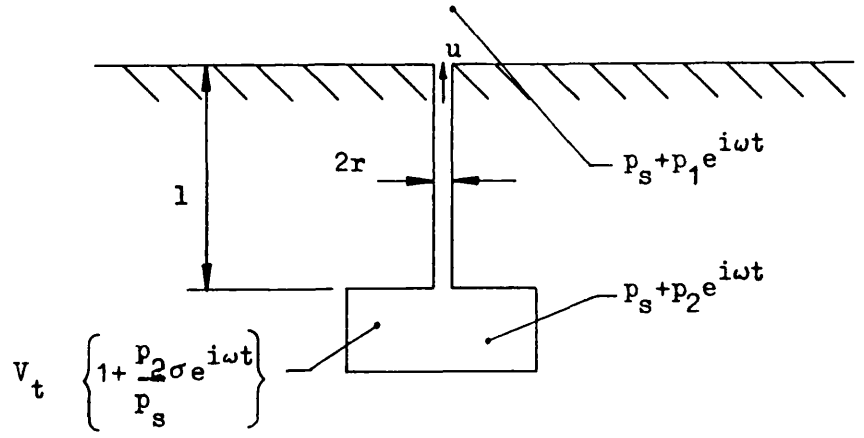

a). still air (single tube + transducer)

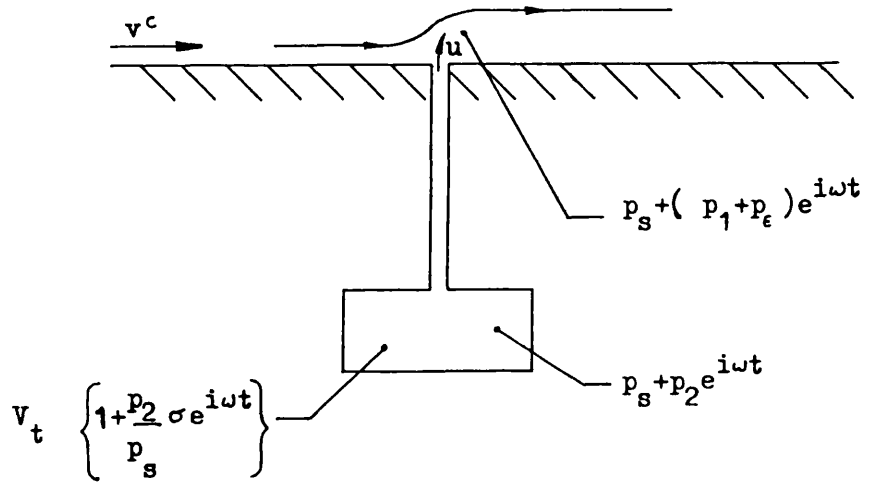

b). with crossflow (single tube + transducer)

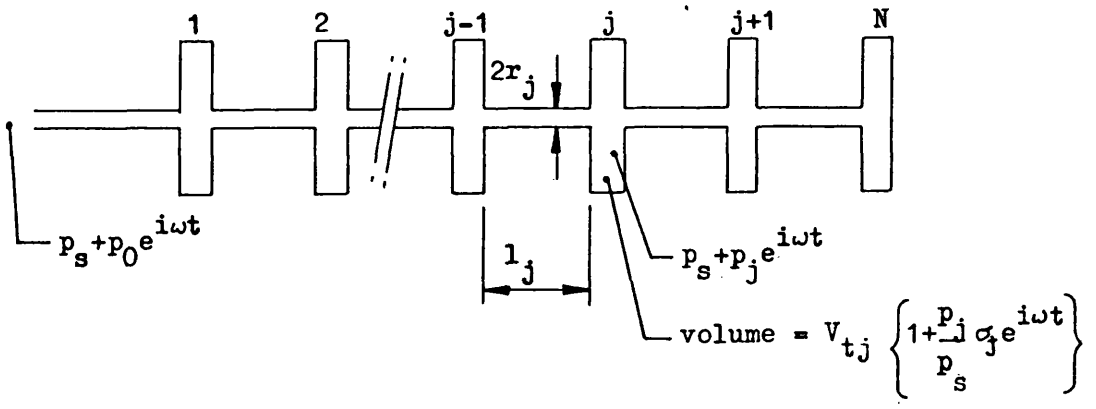

c). series connection of N tubes and N volumes

Fig. 4.9 Boundary conditions at both ends of pressure tubing systems when used to measure sinusoidally oscillating pressures.

Fig. 4.10

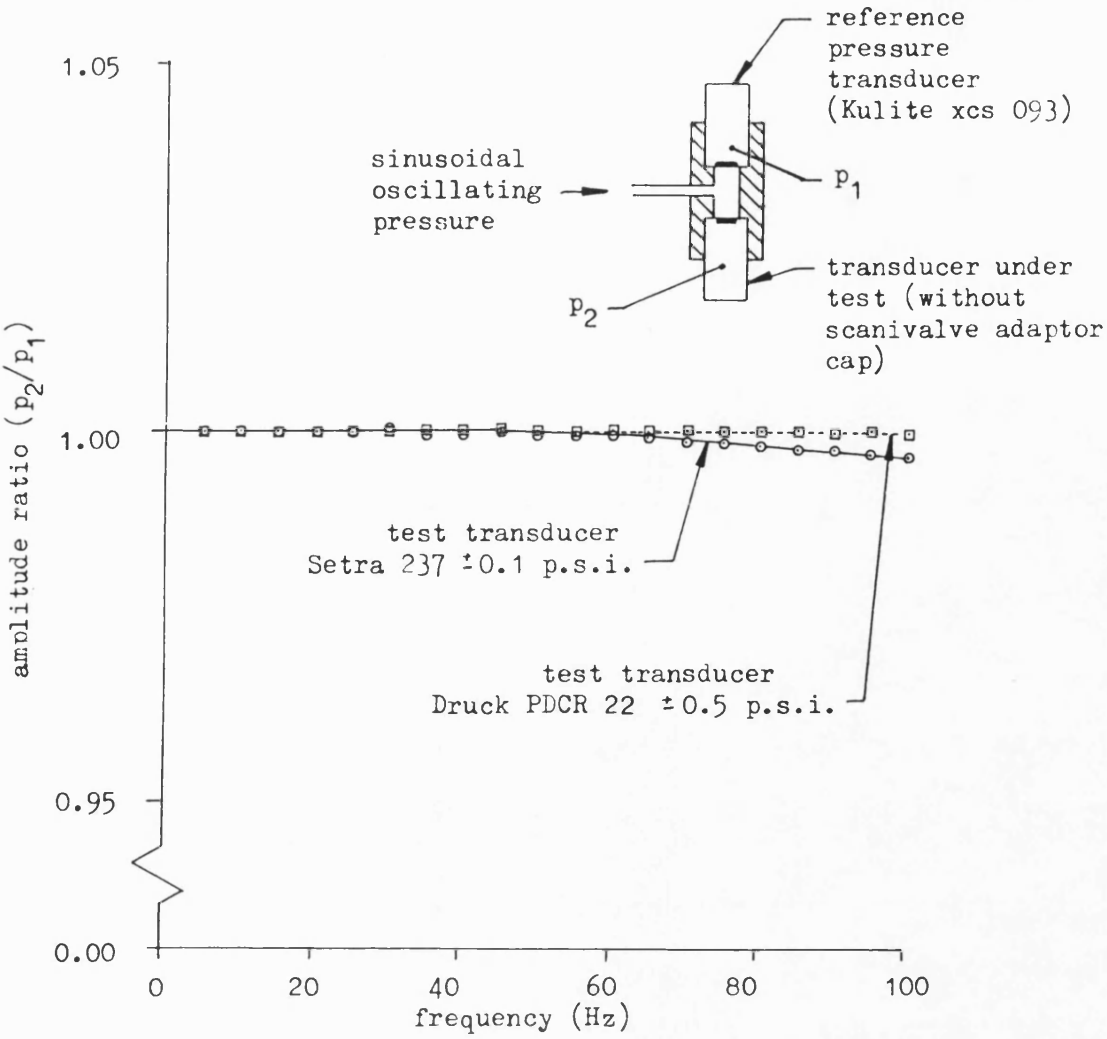

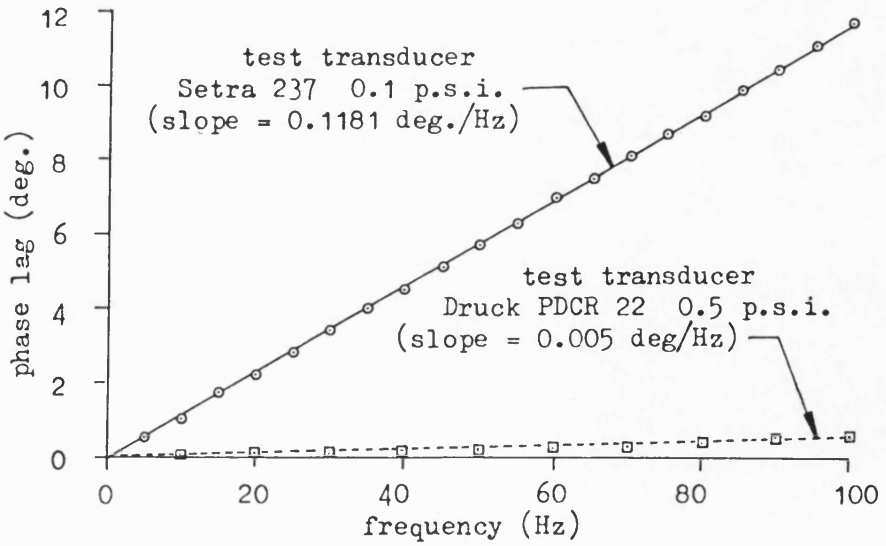

Fig. 4.10 Measured frequency response of two pressure transducers used in wind tunnel tests on model fin with oscillating control surface.

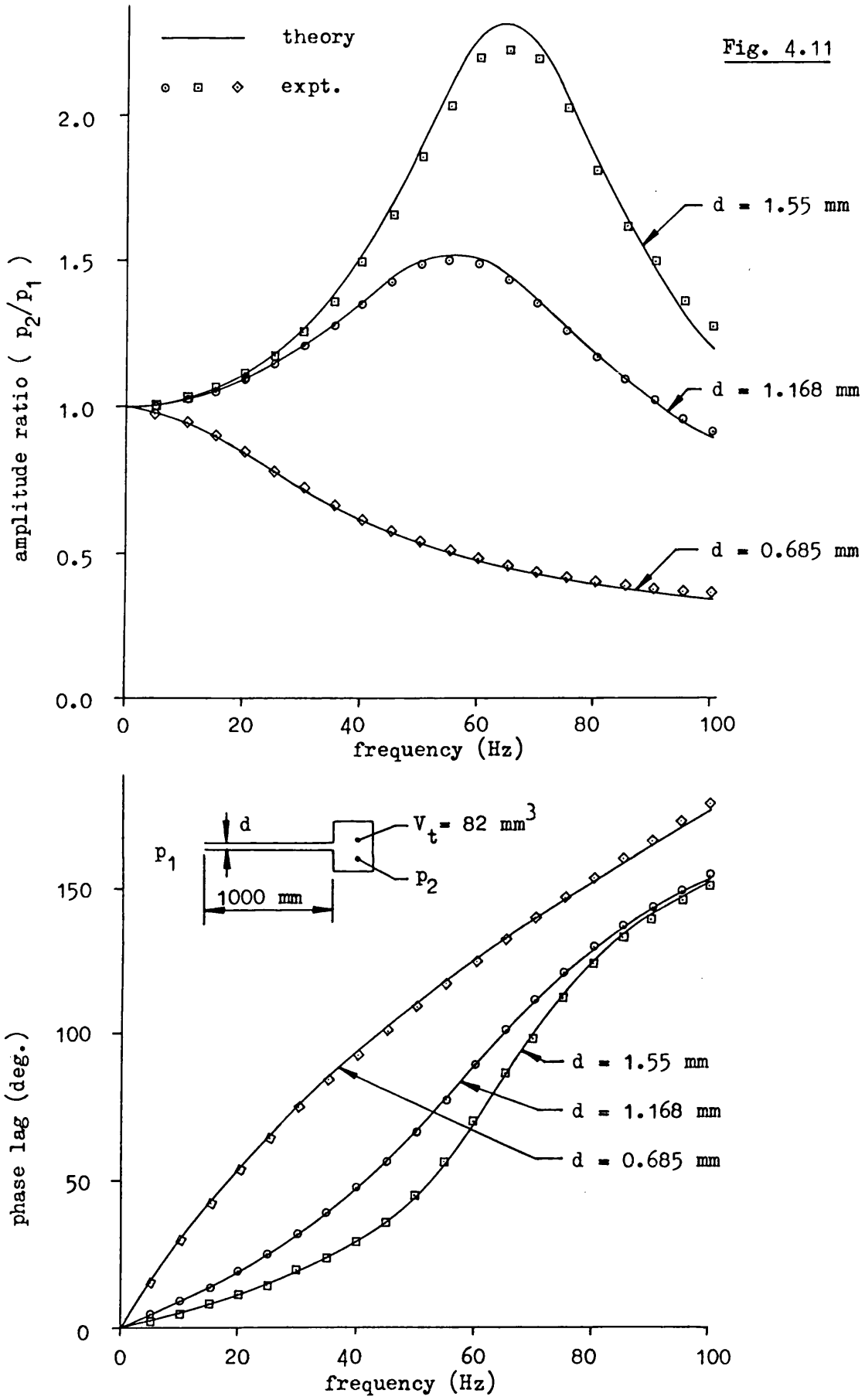

Fig. 4.11 Effect of tube internal diameter on frequency response of single tube connected to pressure transducer (stainless steel hypodermic tubing).

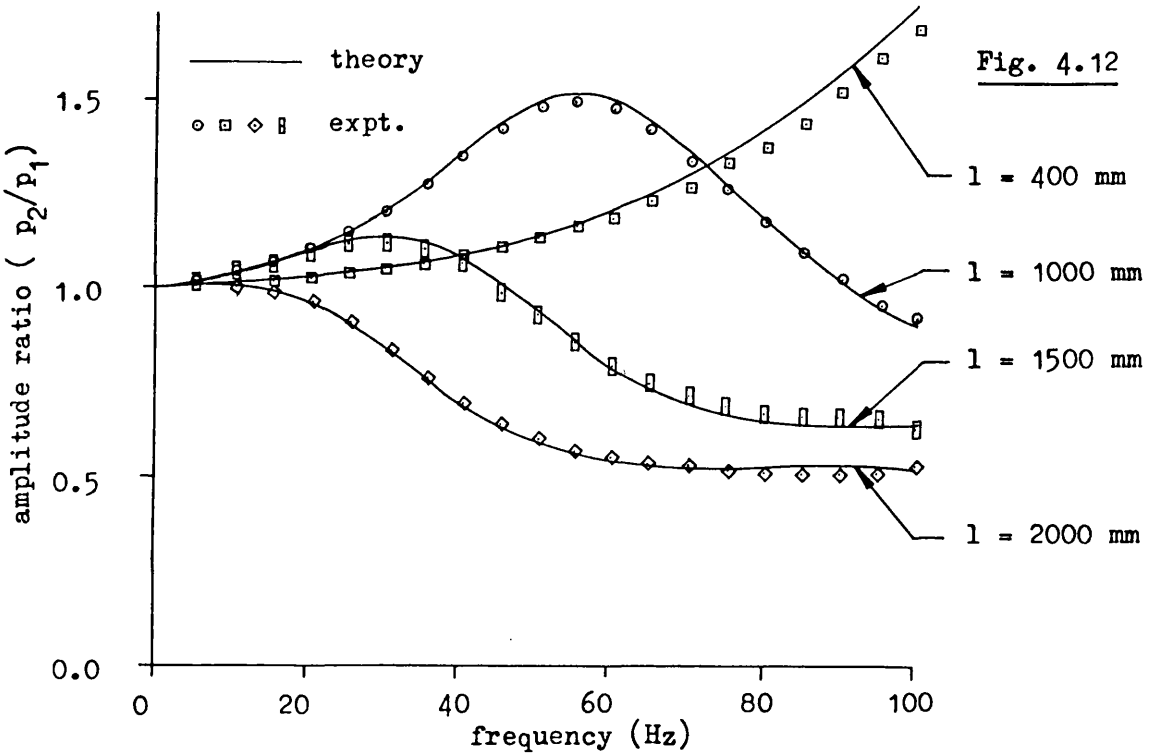

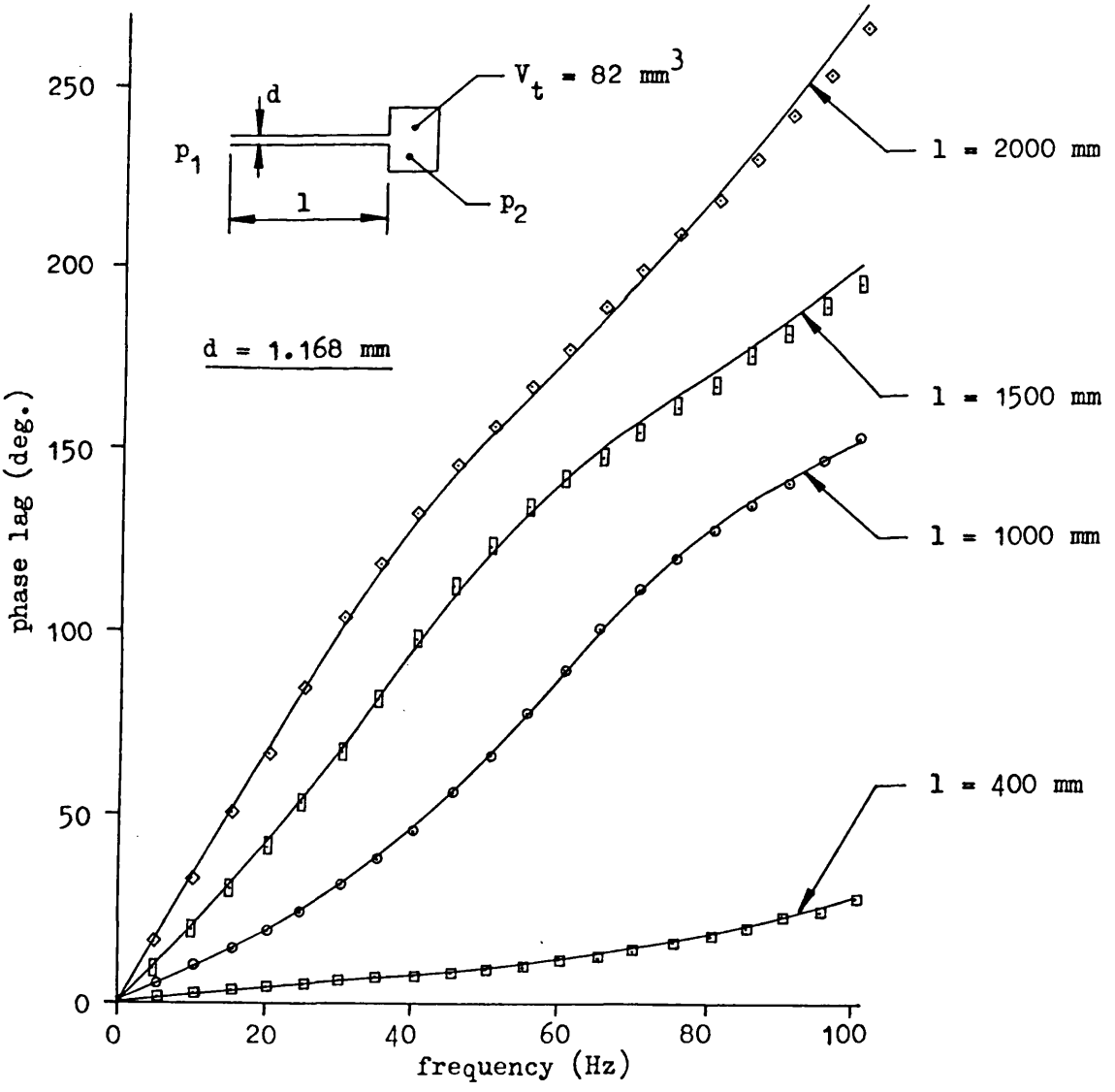

Fig. 4.12 Effect of tube length on frequency response of single tube connected to pressure transducer (stainless steel hypodermic tubing).

Fig. 4.13

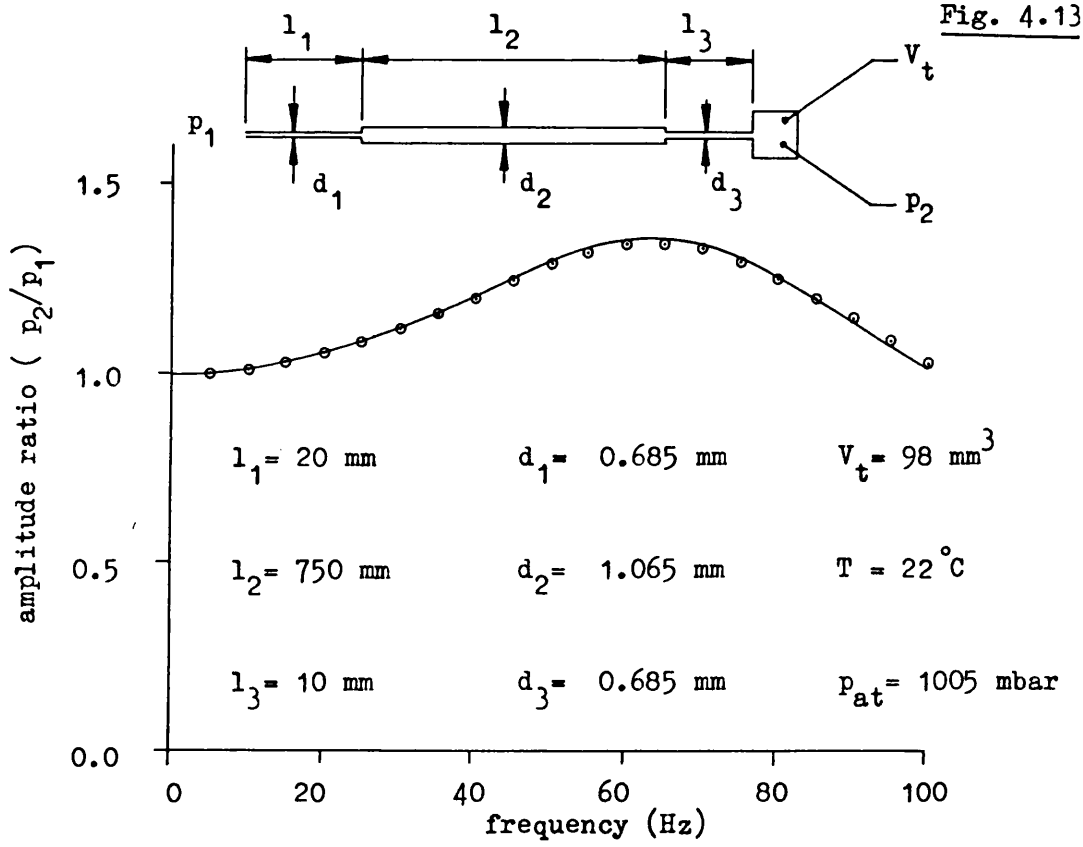

l_1 and l_3 are stainless steel tube

l_2 is flexible p.v.c. tube

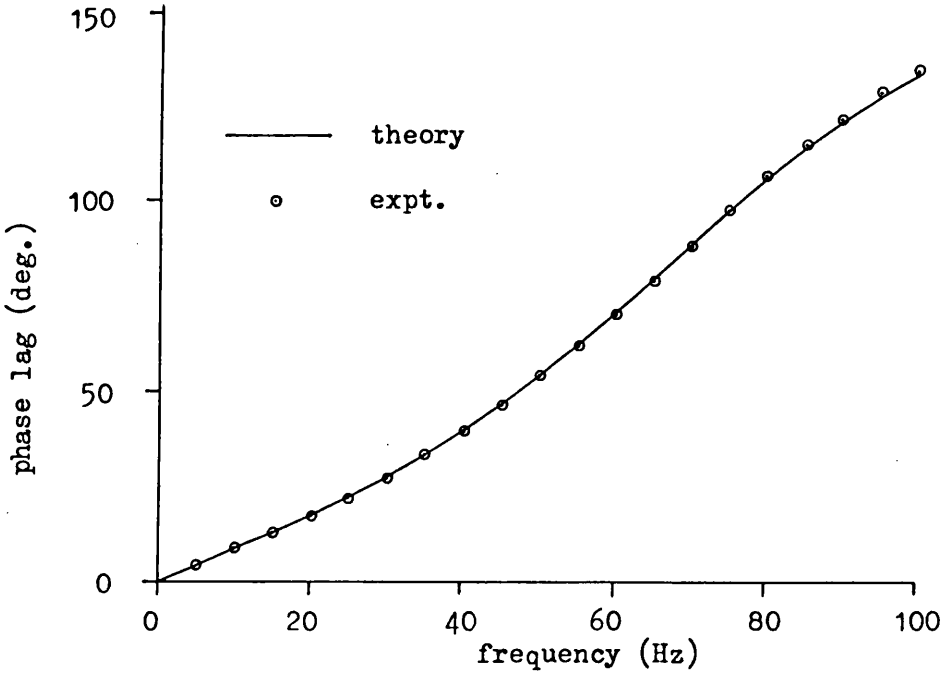

Fig. 4.13 Frequency response of tubing system comprising a pressure tapping connected to a pressure transducer via a length of flexible p.v.c. tube (no scanivalve).

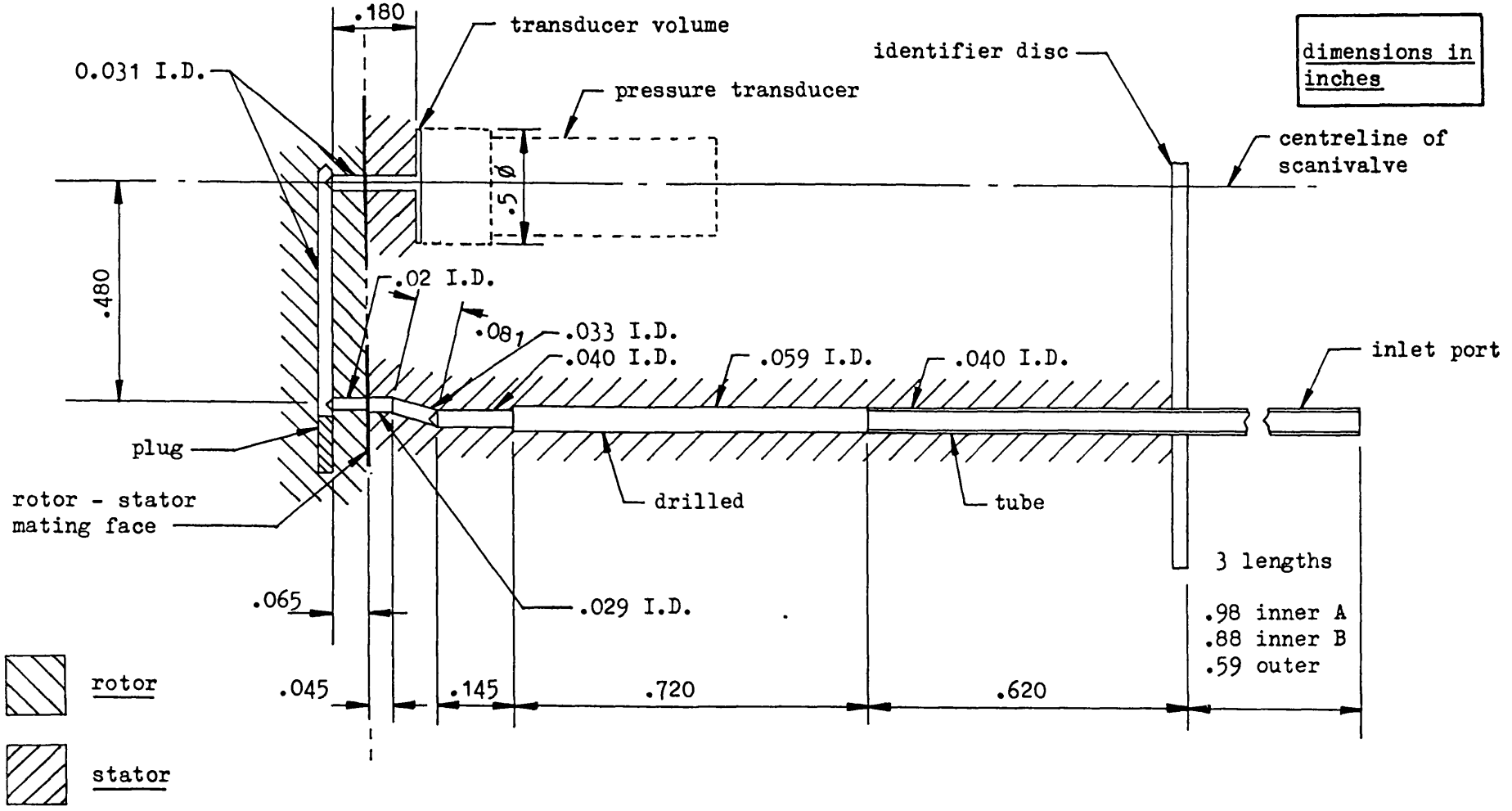

Fig. 4.14 Internal passages of 'J' type scanivalve

Fig. 4.14

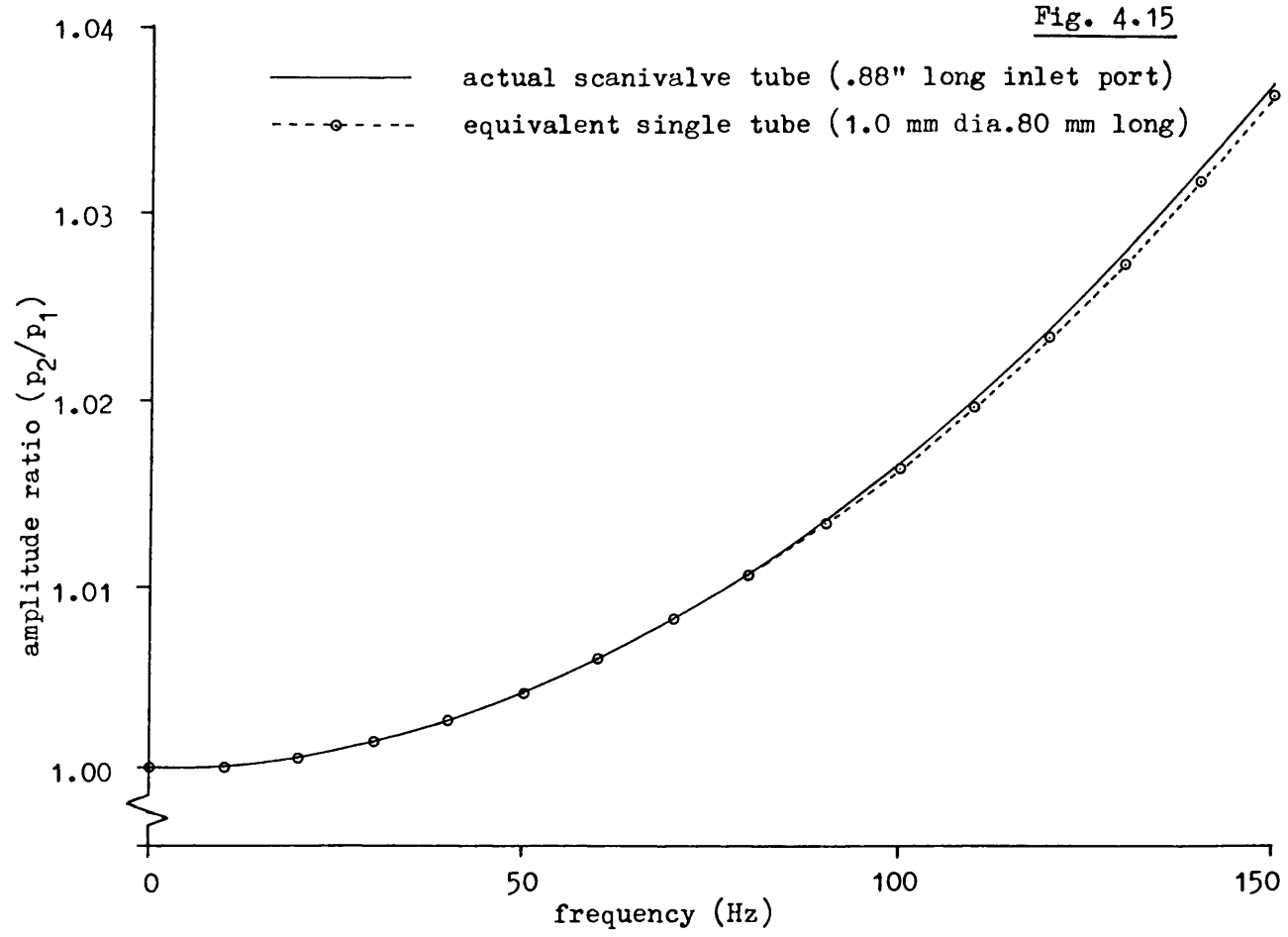

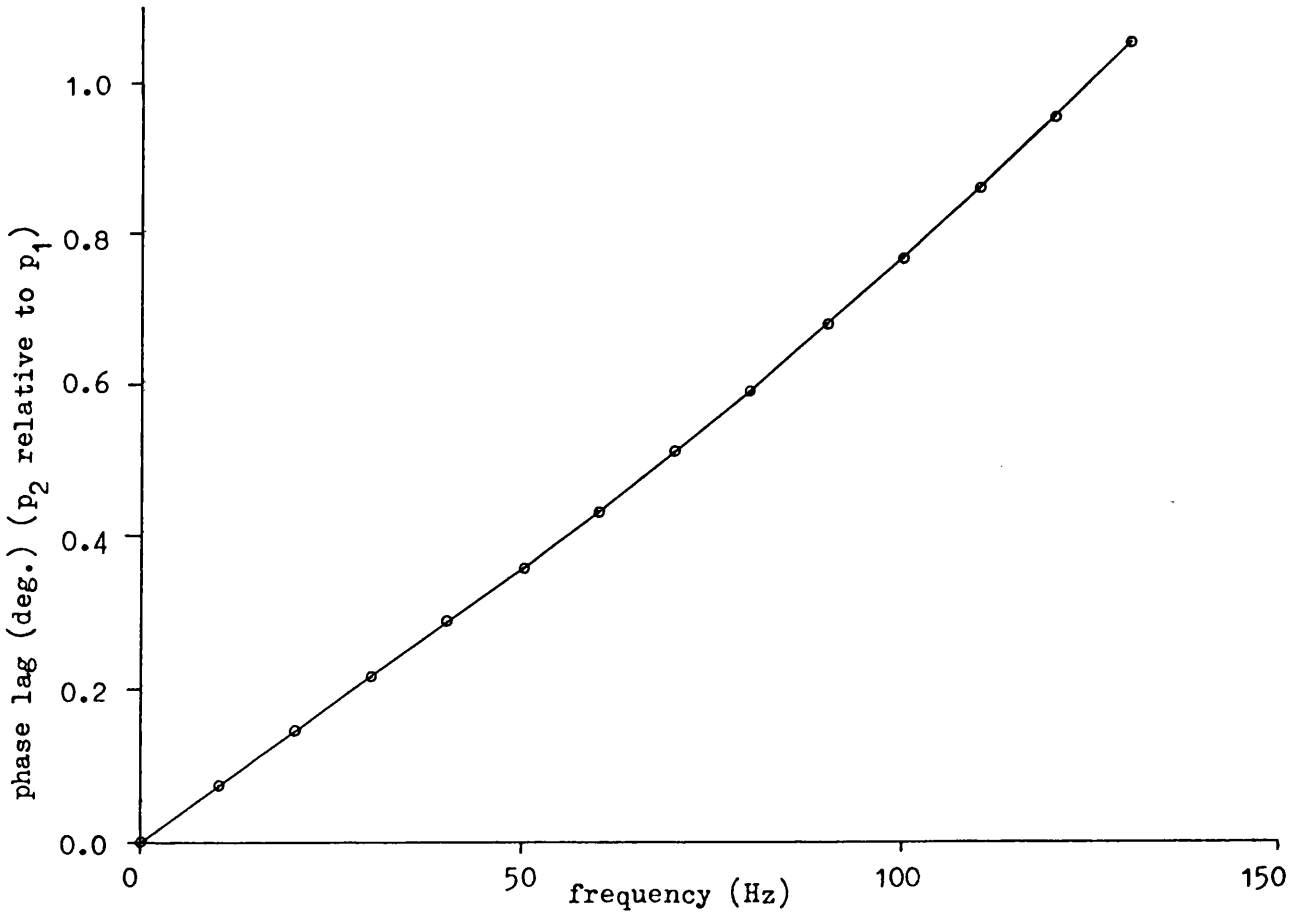

Fig. 4.15 comparison of theoretical frequency response of actual scanivalve with equivalent single tube.

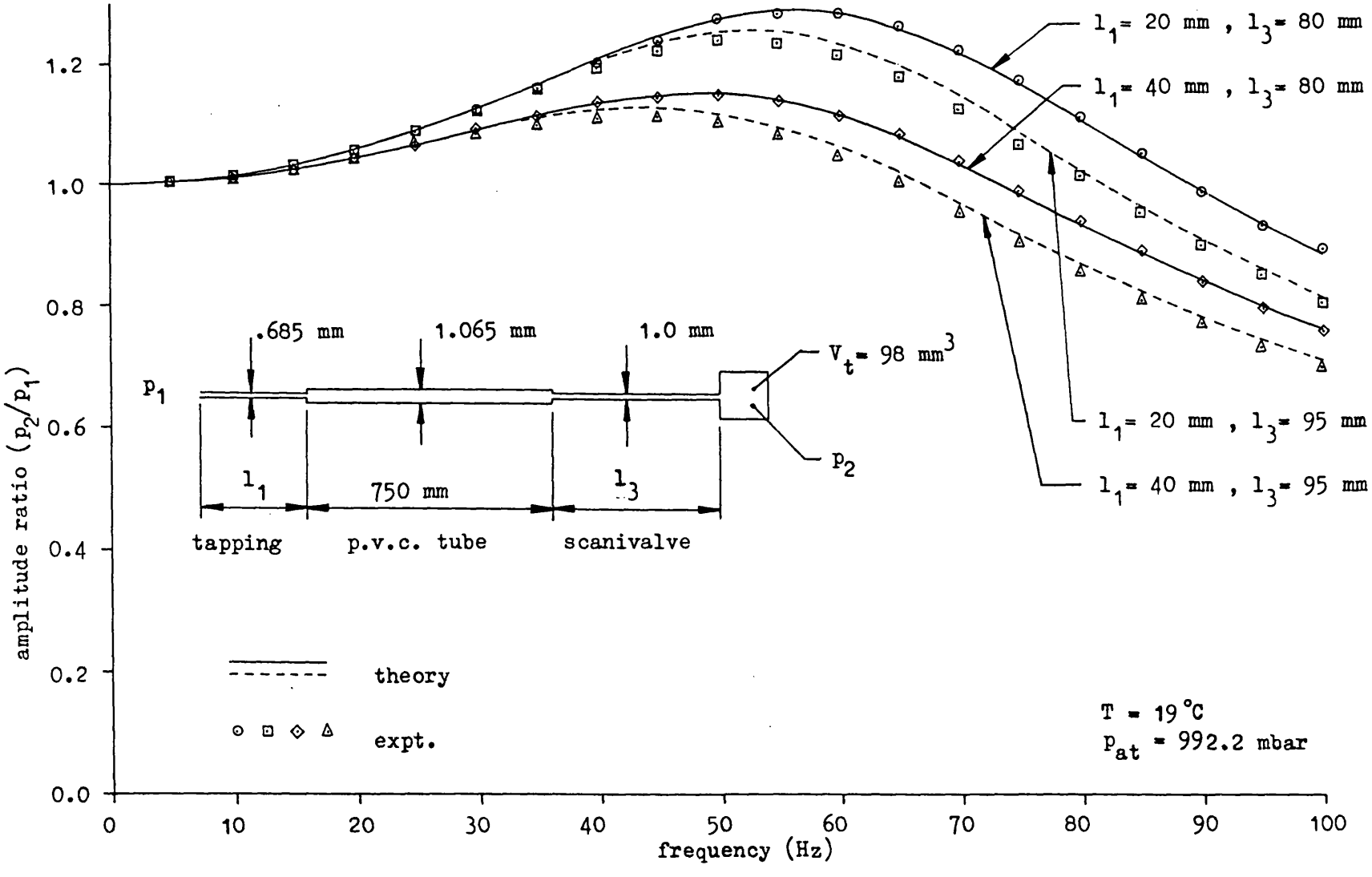

Fig. 4.16

Fig. 4.16 Amplitude ratio of tubing system comprising stainless steel pressure tapping, p.v.c. tubing, scanivalve and pressure transducer (effect of two pressure tapping lengths and two scanivalve tube lengths)+ see fig. 4.17 for phase lag.

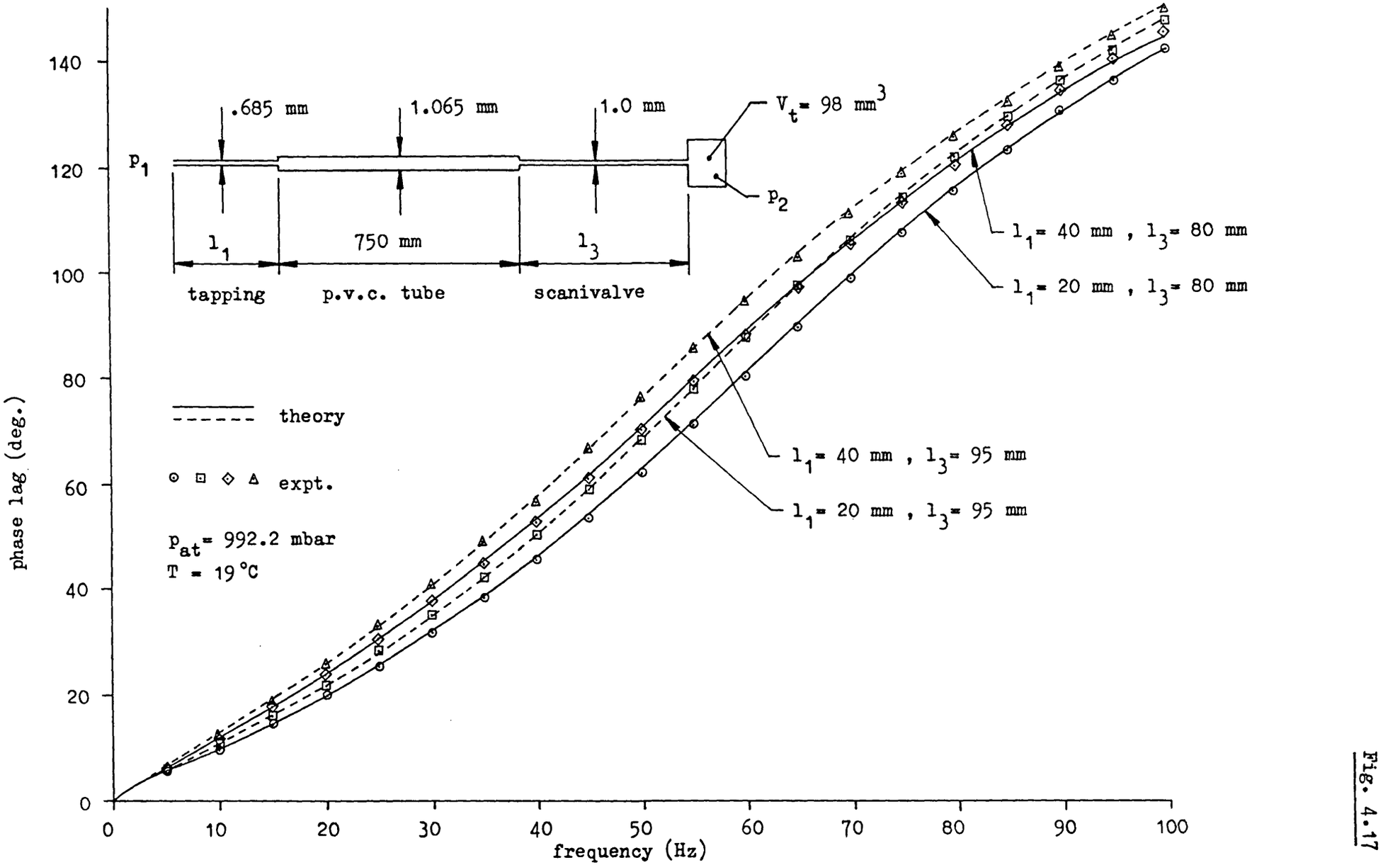

Fig. 4.17

Fig. 4.17 Phase lag of tubing system comprising stainless steel pressure tapping, p.v.c. tube, scanivalve and pressure transducer (effect of two pressure tapping lengths and two scanivalve tube lengths).

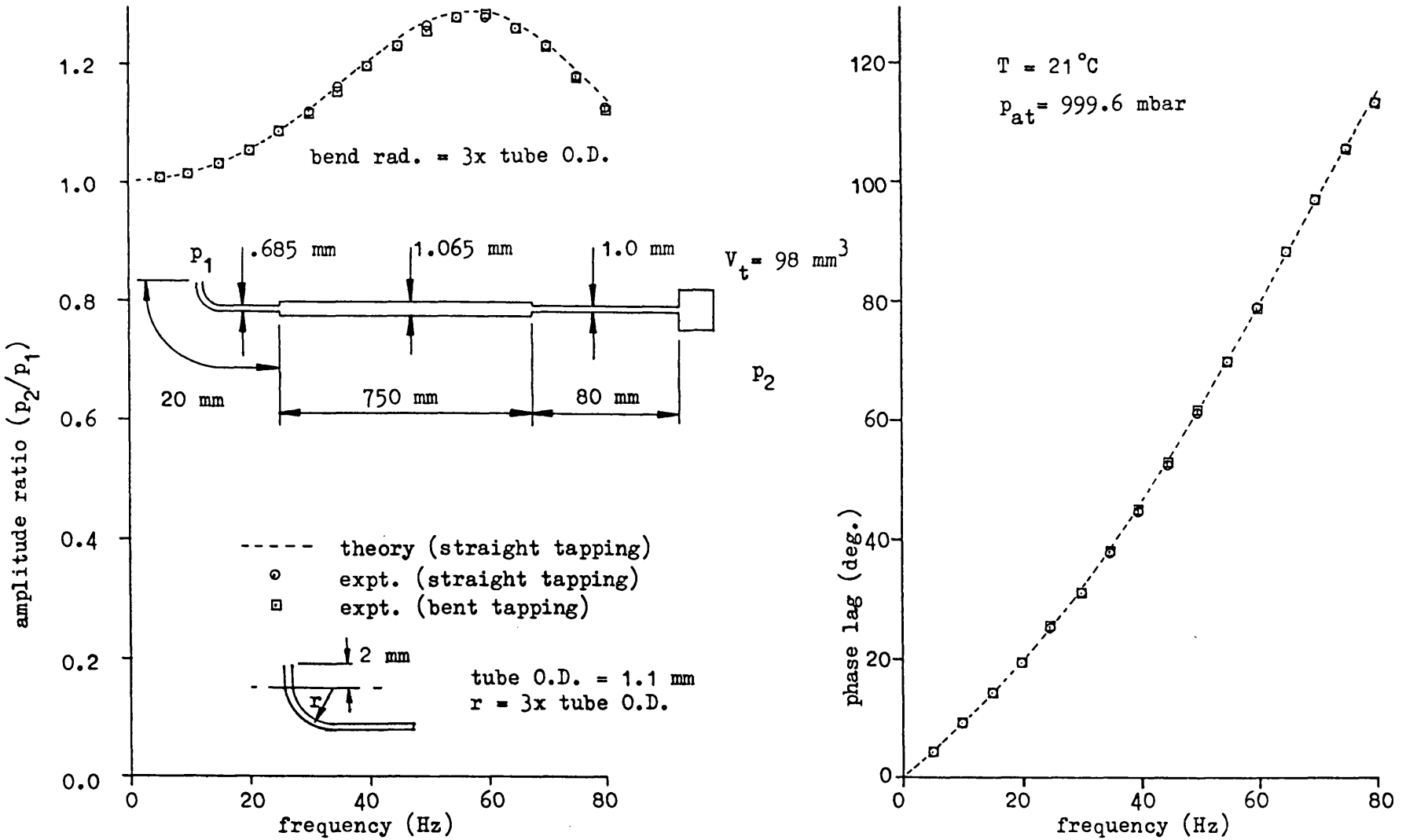

Fig. 4.18

Fig. 4.18 Effect of sharp bend in tube on frequency response of pressure tubing system.

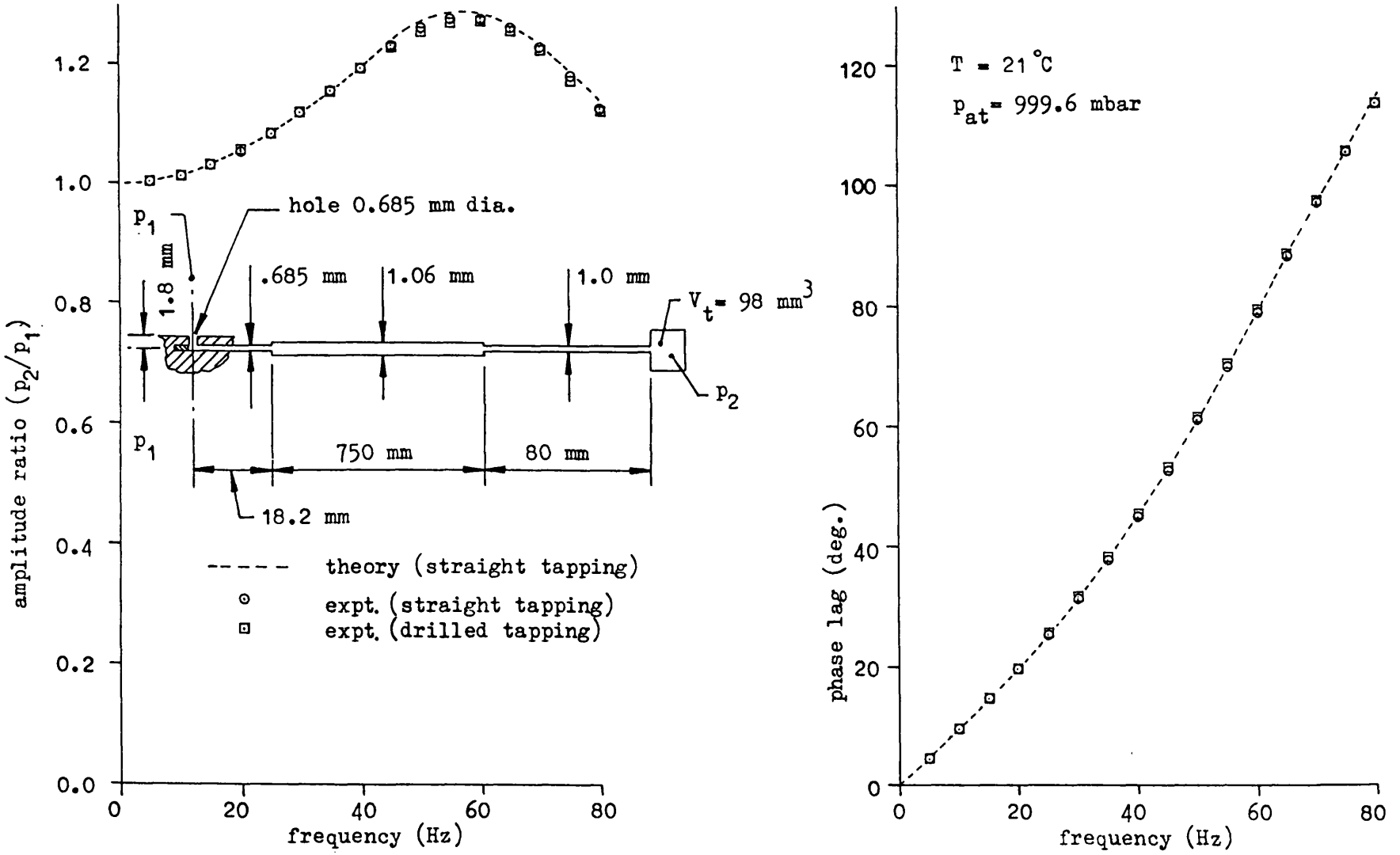

Fig. 4.19

Fig. 4.19 Effect of pressure tapping drilled at 90° to tube wall on frequency response of pressure tubing system.

Fig. 4.20

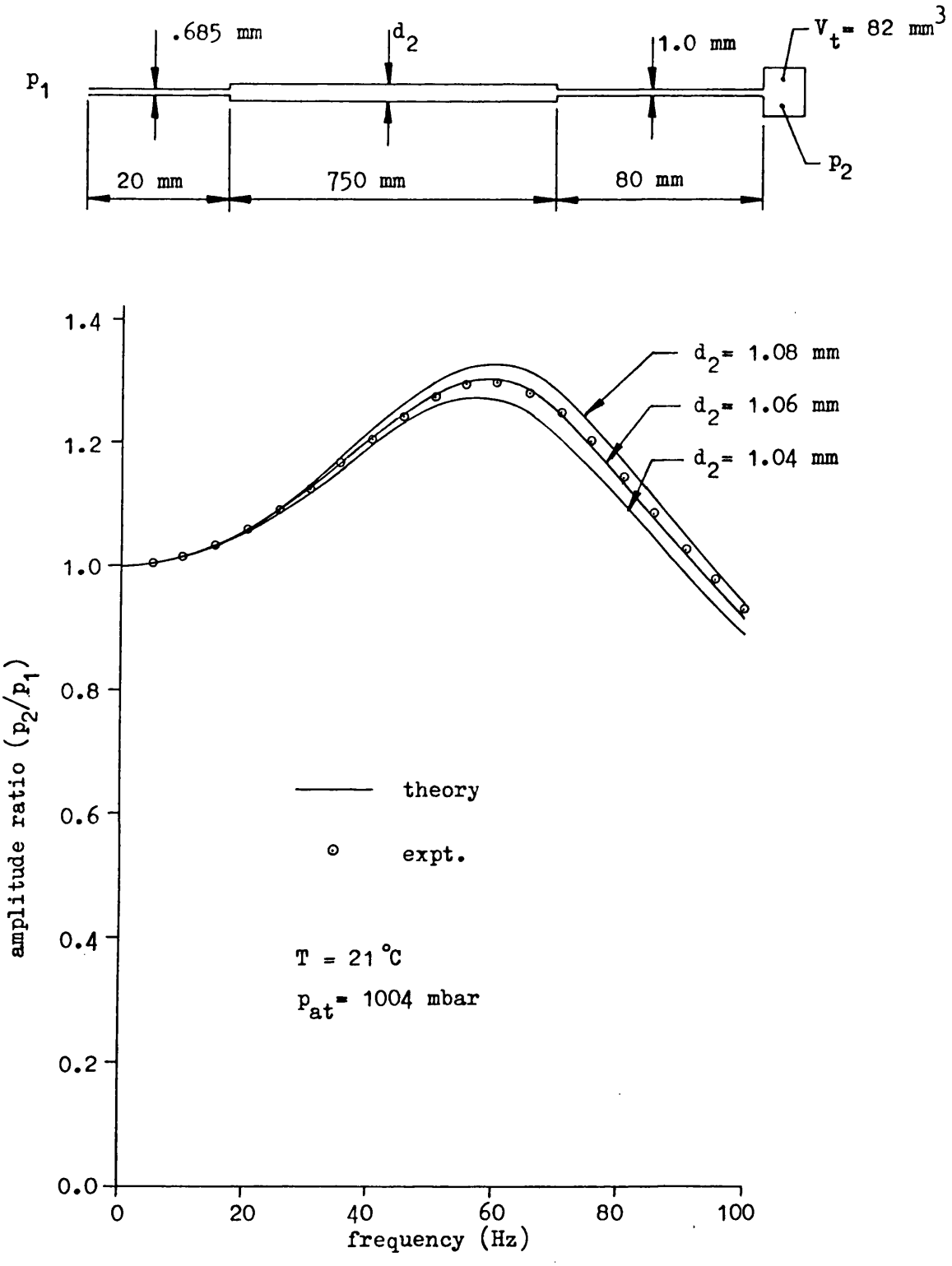

Fig. 4.20 Effect of small errors in measurement of tube diameter on frequency response of pressure tubing system.

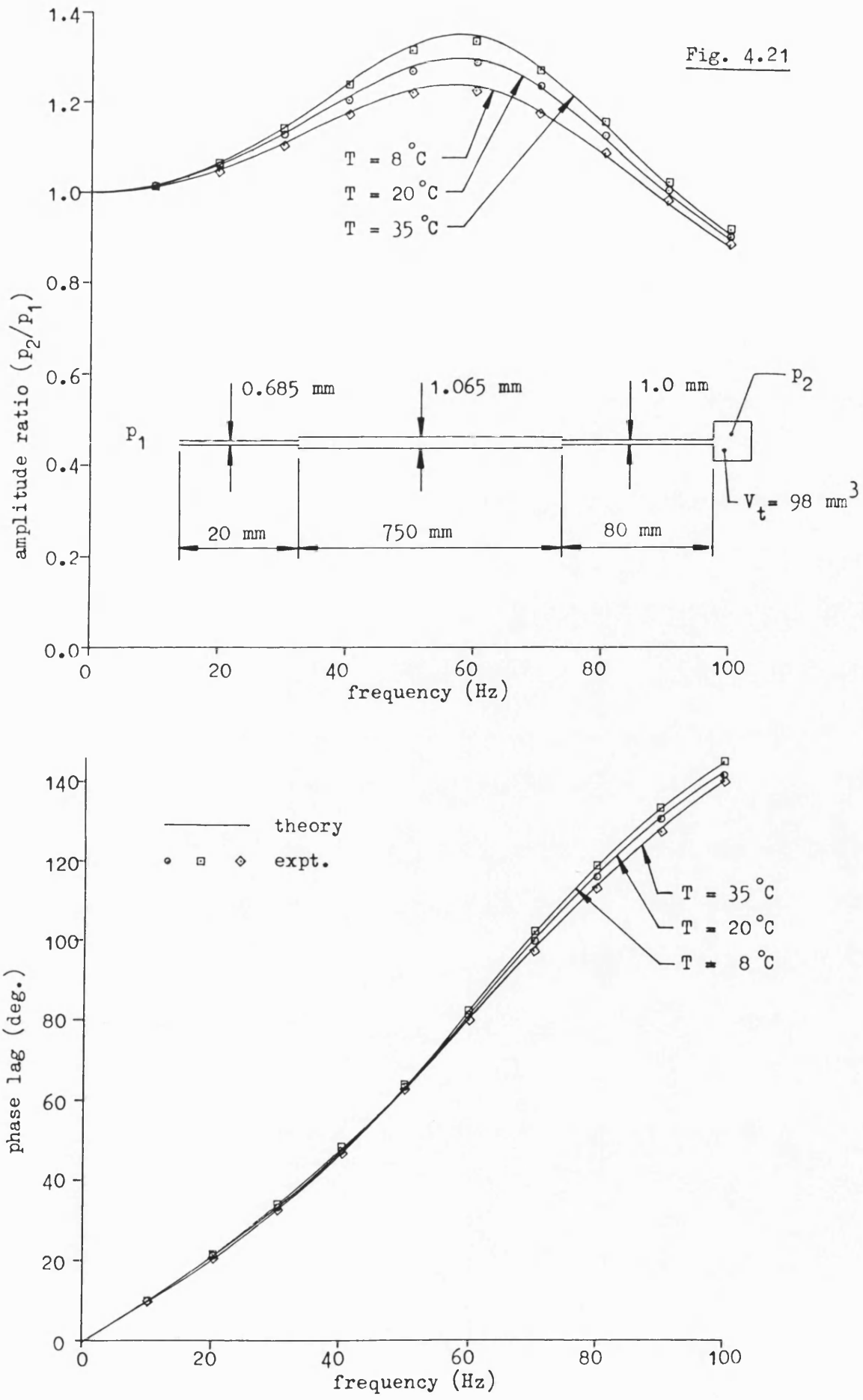

Fig. 4.21 Effect of ambient temperature on frequency response of pressure tubing system.

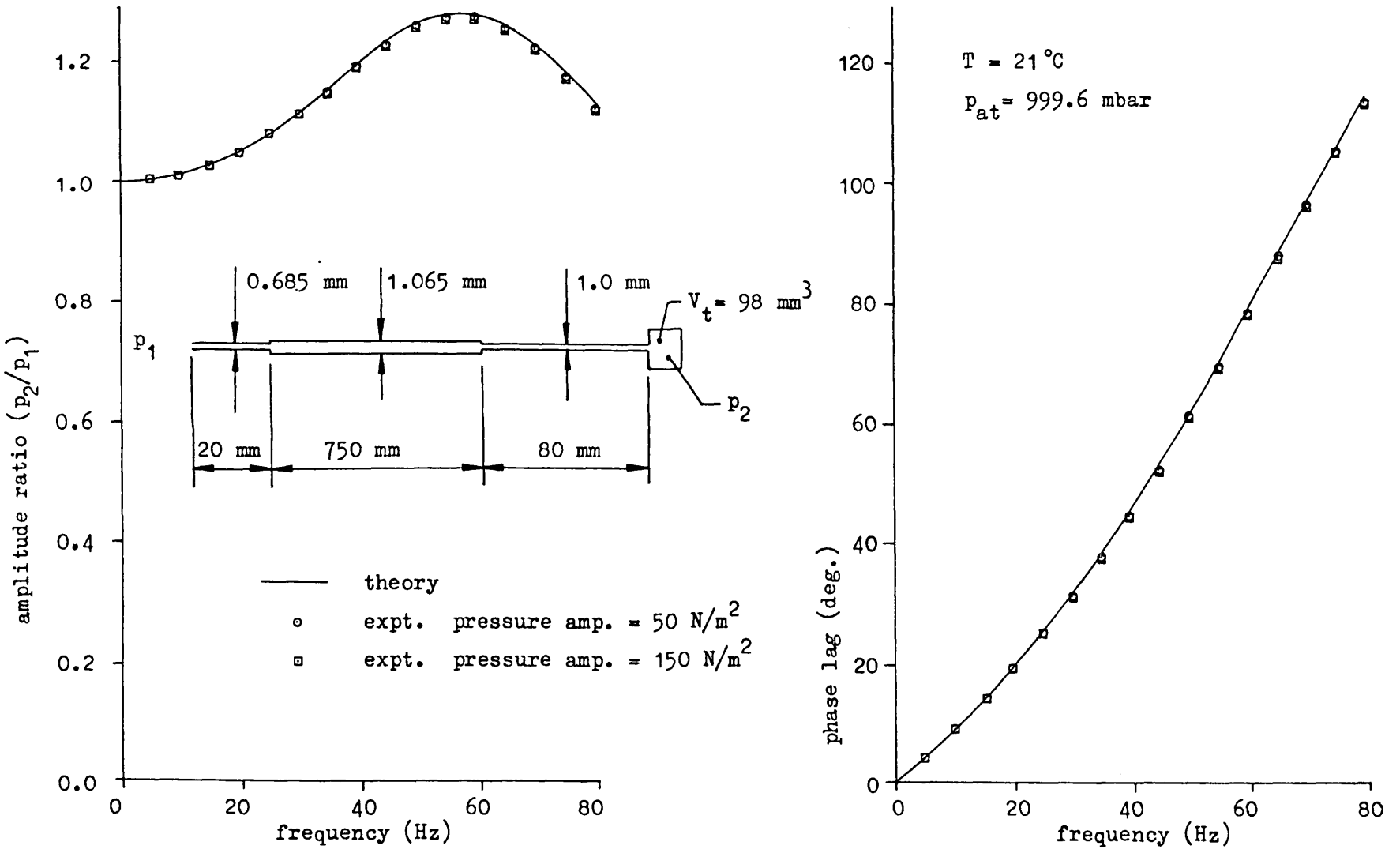

Fig. 4.22

Fig. 4.22 Effect of variation in amplitude of applied oscillatory pressure on frequency response of pressure tubing system.

Fig. 4.23

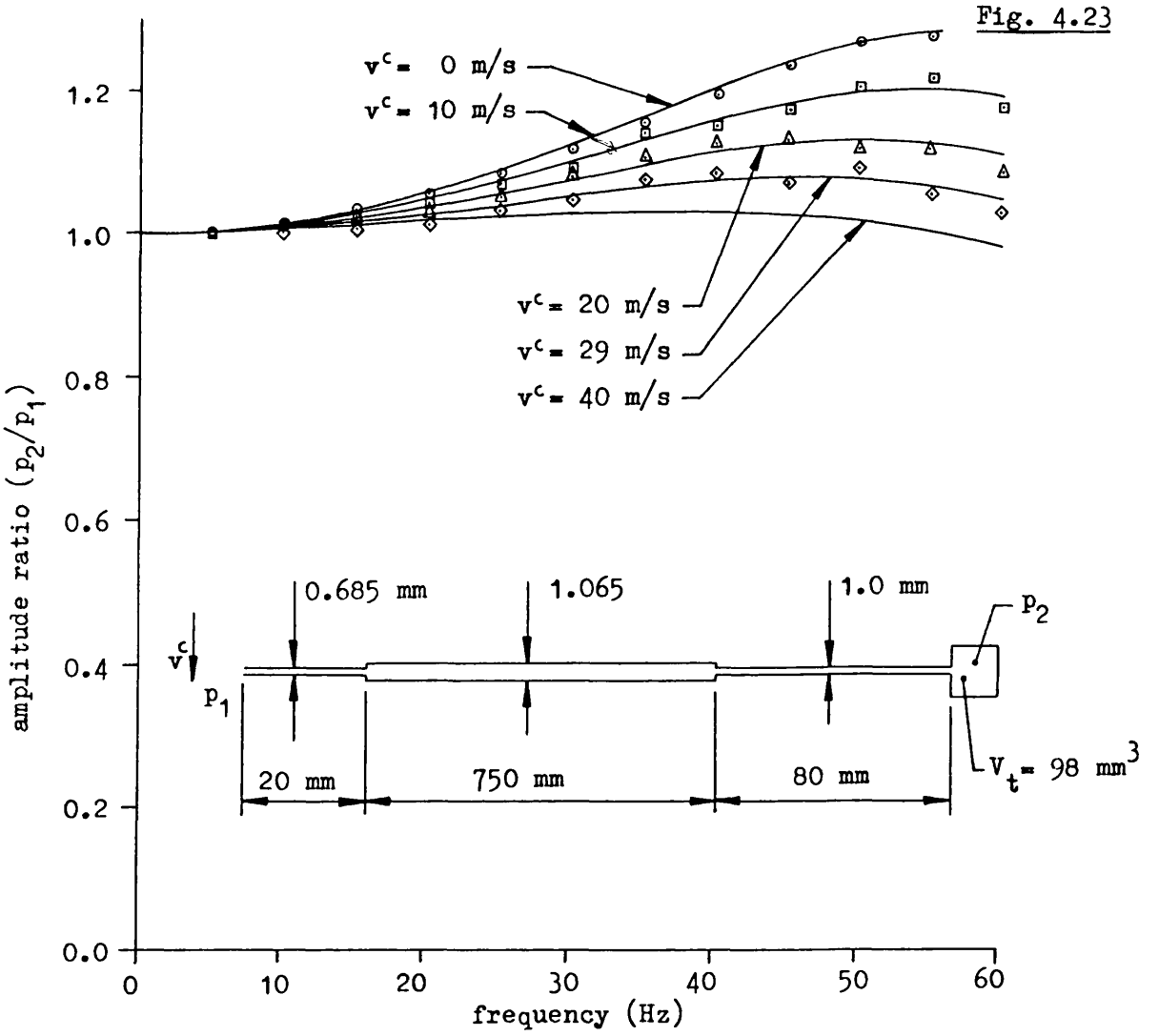

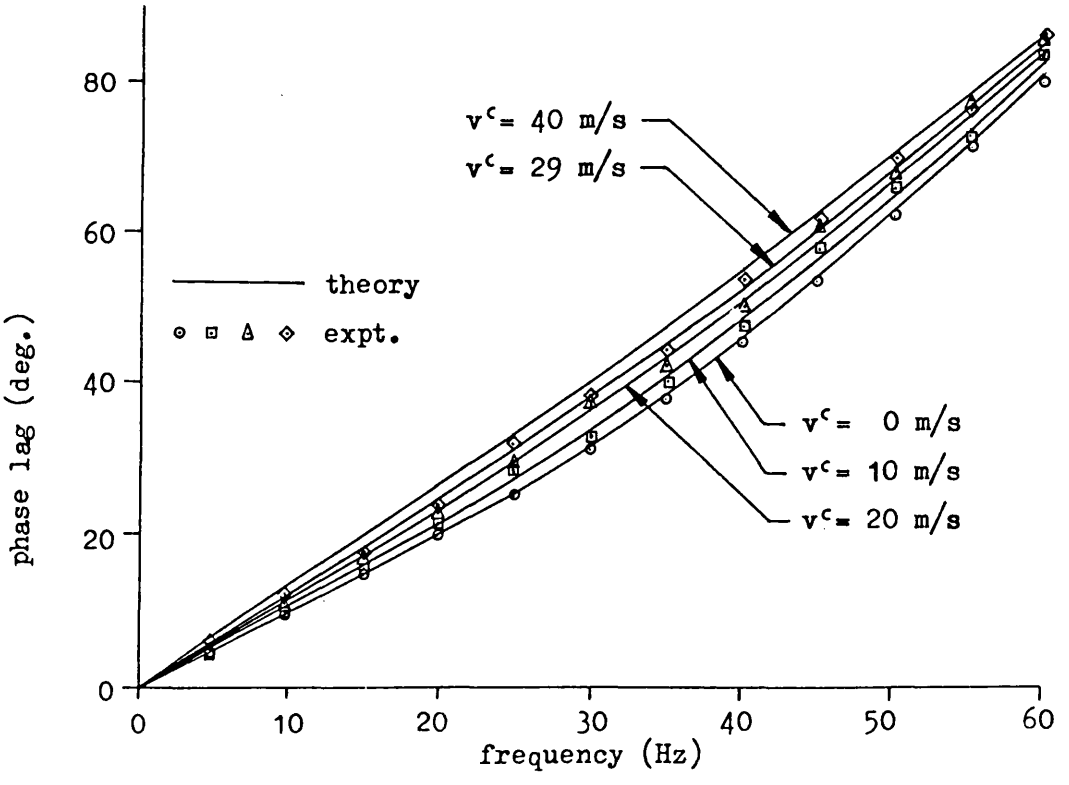

Fig. 4.23 Effect of flow across orifice on frequency response of pressure tubing system with scanivalve.

Fig. 5.1

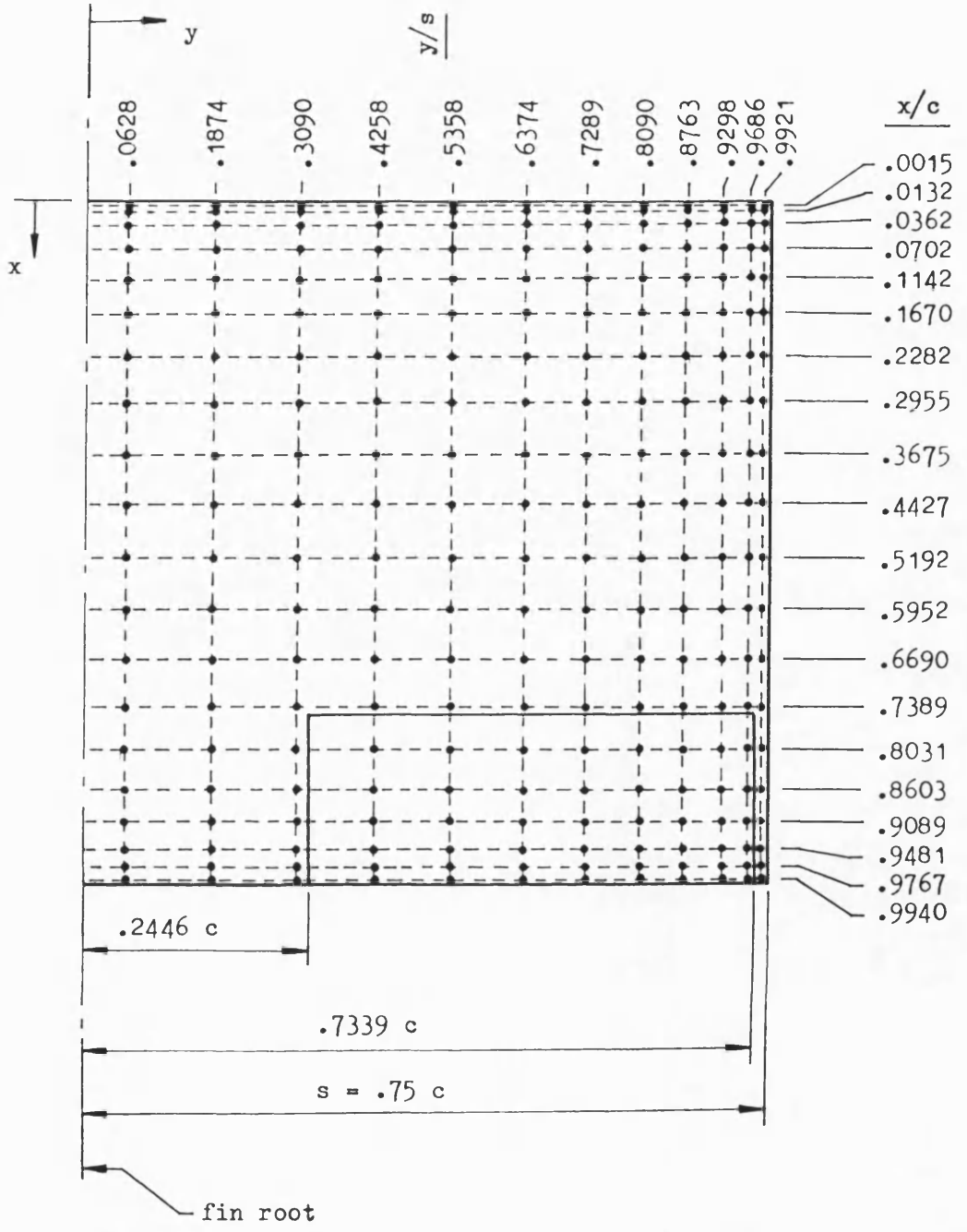

24 spanwise points defined by:- $y/s = \cos\left\{\frac{p\pi}{m+1}\right\}$ $p = 1,\ldots,m$ $m = 24$

20 chordwise points defined by:- $x/c = \frac{1}{2}\left\{1-\cos\left(\frac{2r-1}{2n+1}\pi\right)\right\}$ $r = 1,\ldots,n$ $n = 20$

Fig. 5.1 Location of collocation points used in lifting surface model of fin to determine unsteady pressure loadings due to oscillation of control surface.

Fig. 6.1

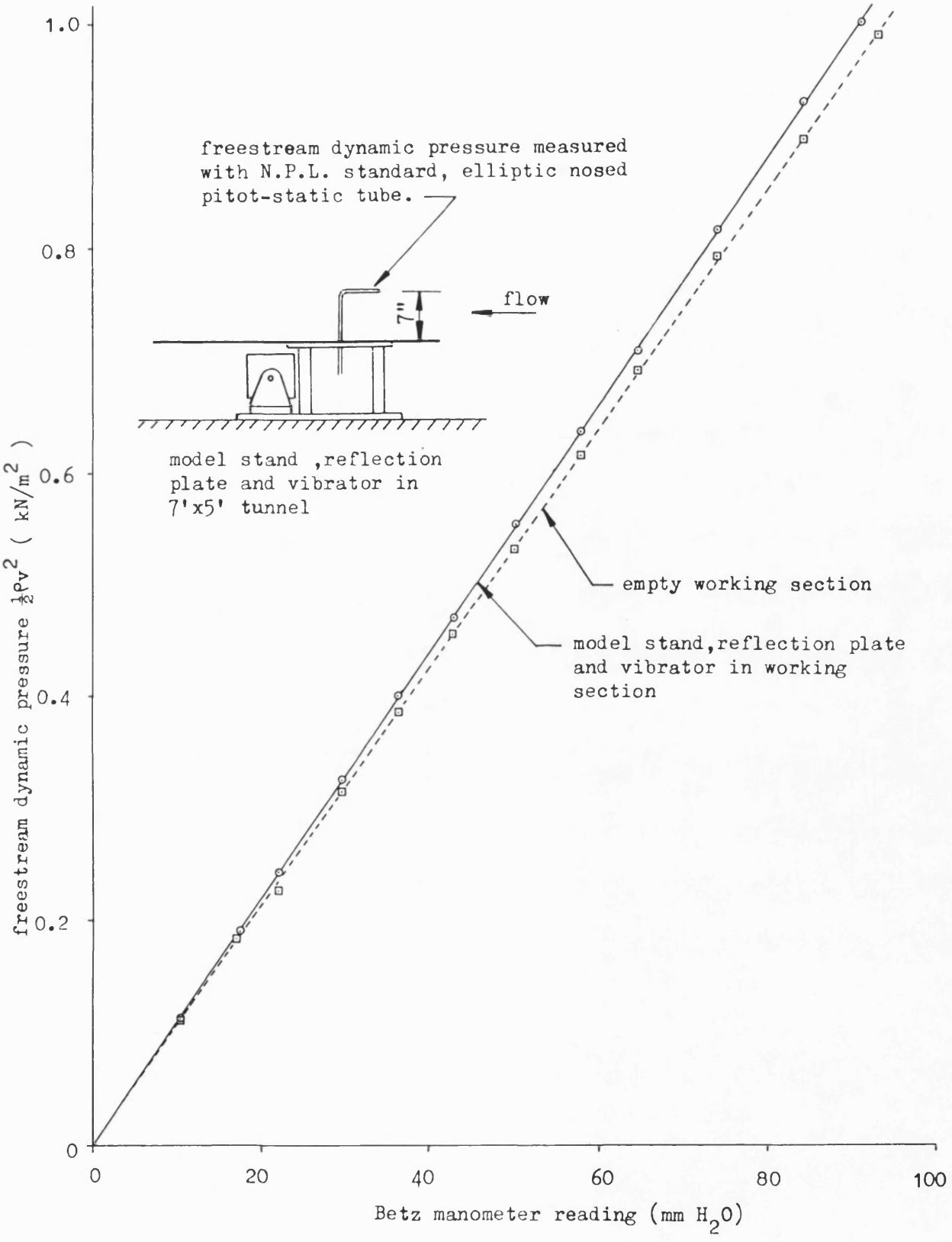

Fig. 6.1 Calibration of tunnel freestream velocity and blockage effect of model support stand and vibrator.

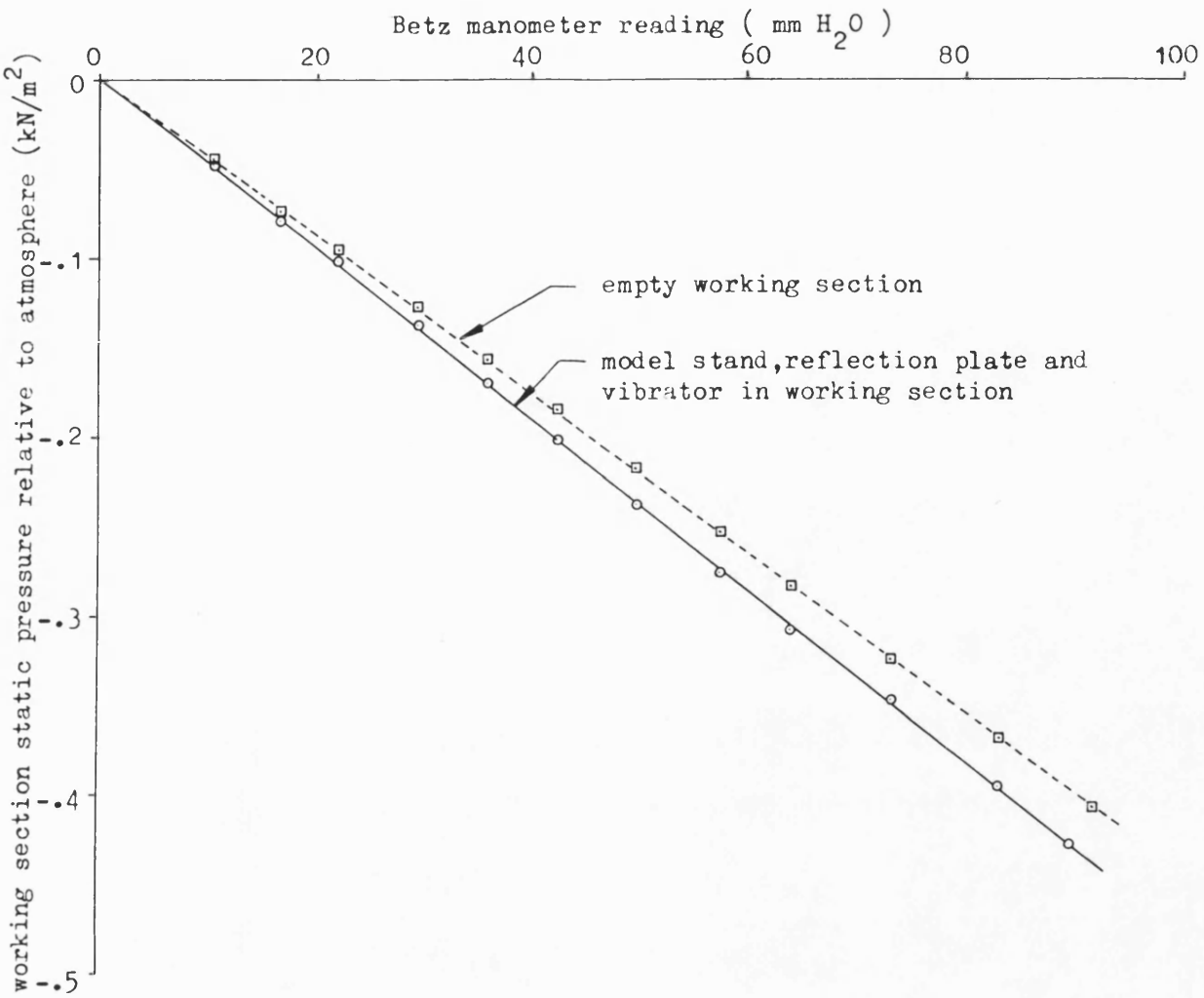

Fig. 6.2 Calibration of tunnel working section static pressure and blockage effect of model support stand and vibrator.

Fig. 6.3

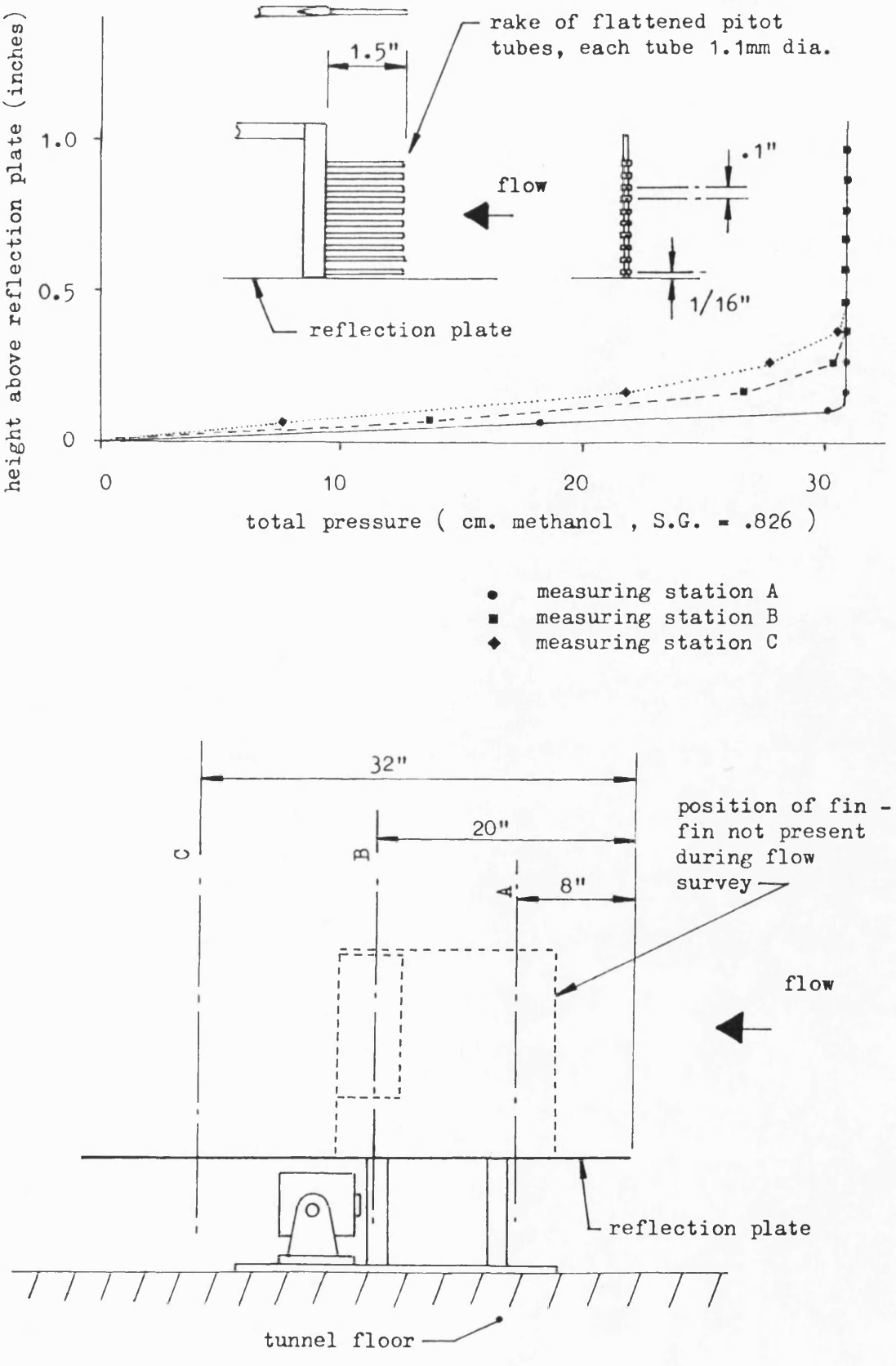

Fig. 6.3 Boundary layer thickness on reflection plate measured at three stations along centreline of model.

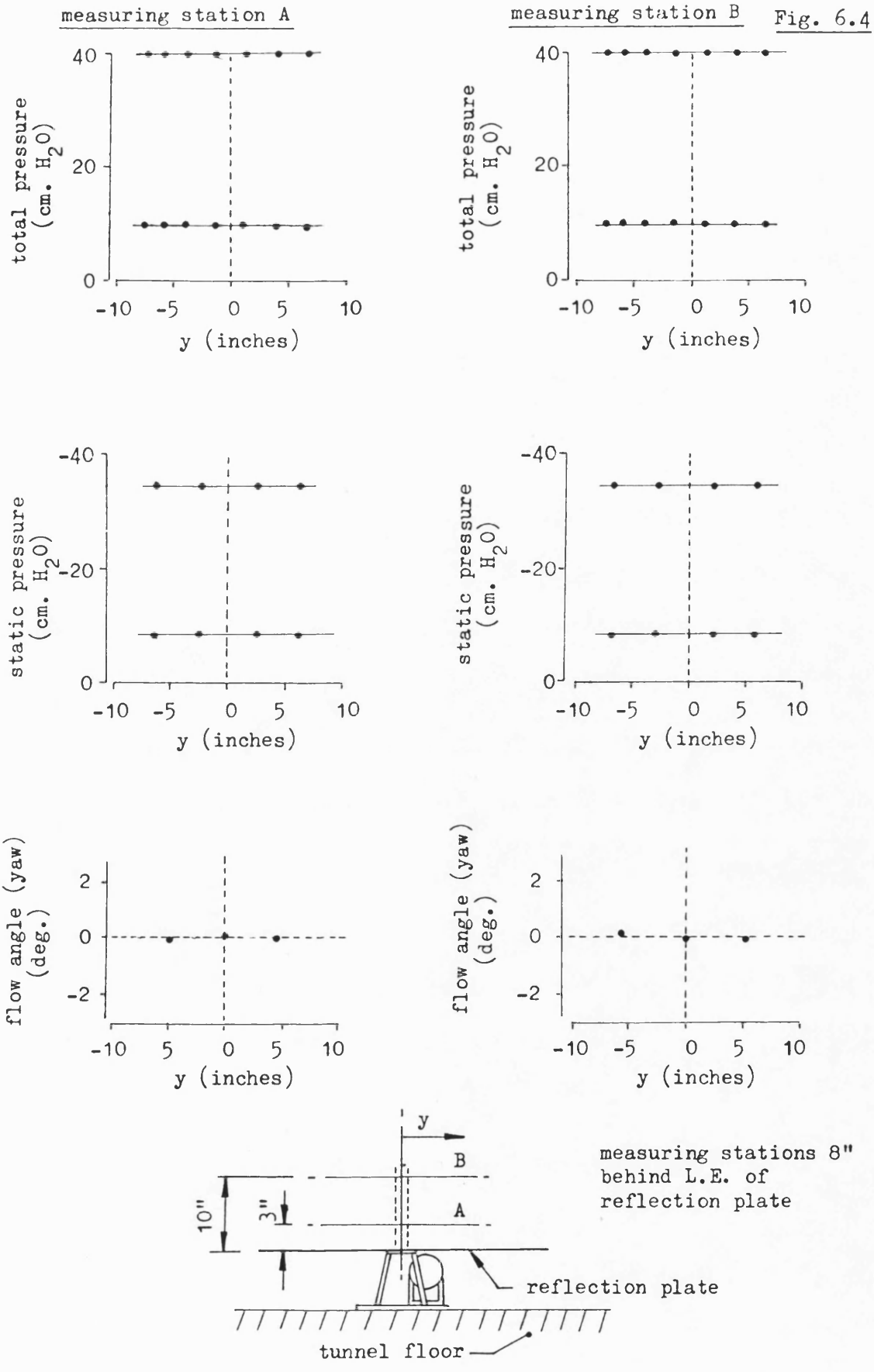

Fig. 6.4 Flow surveys in region above reflection plate at two tunnel speeds (V = 20, 40 m/s)

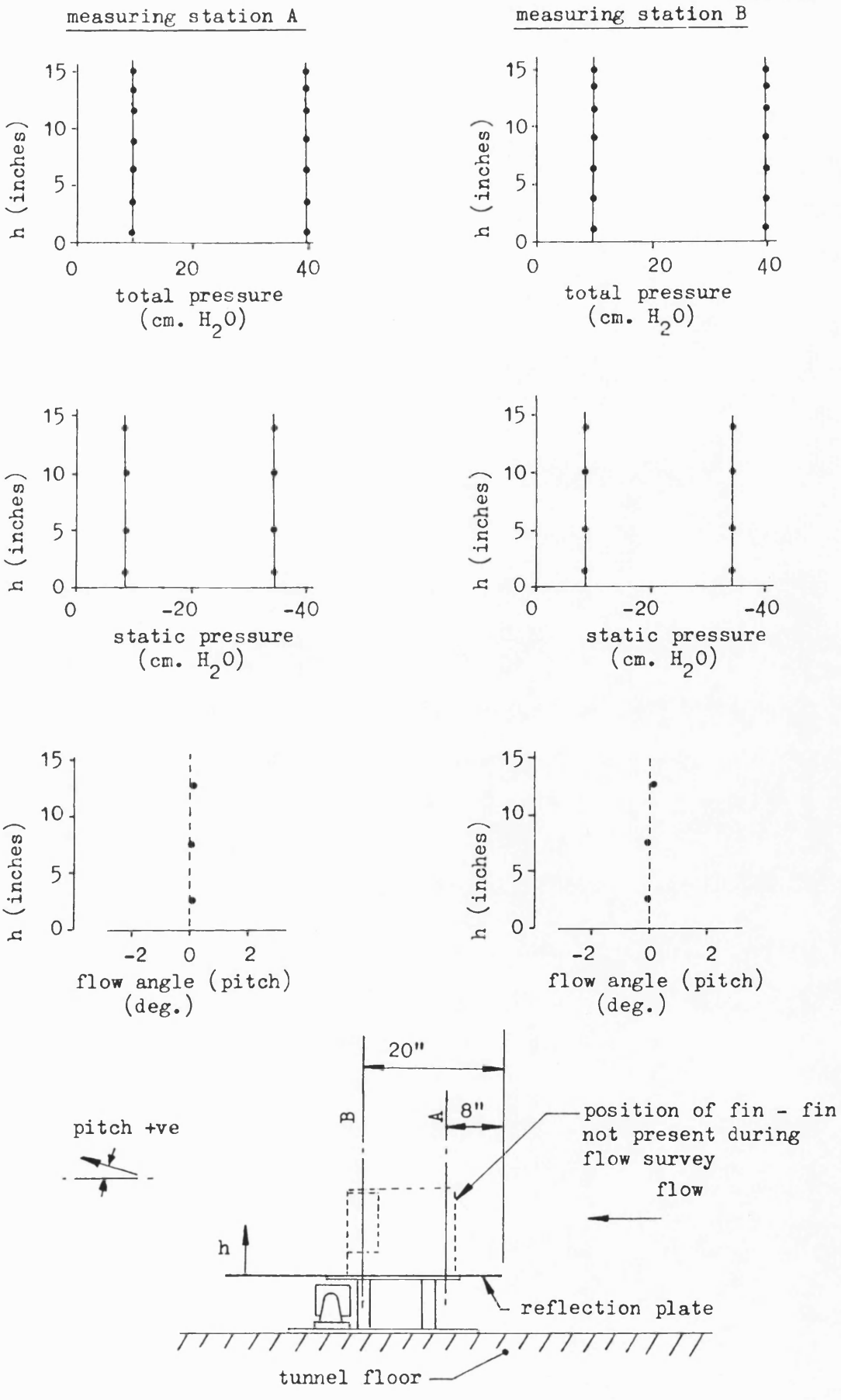

Fig. 6.5 Flow surveys in region above reflection plate along centreline of model at two speeds (V = 20, 40 m/s).

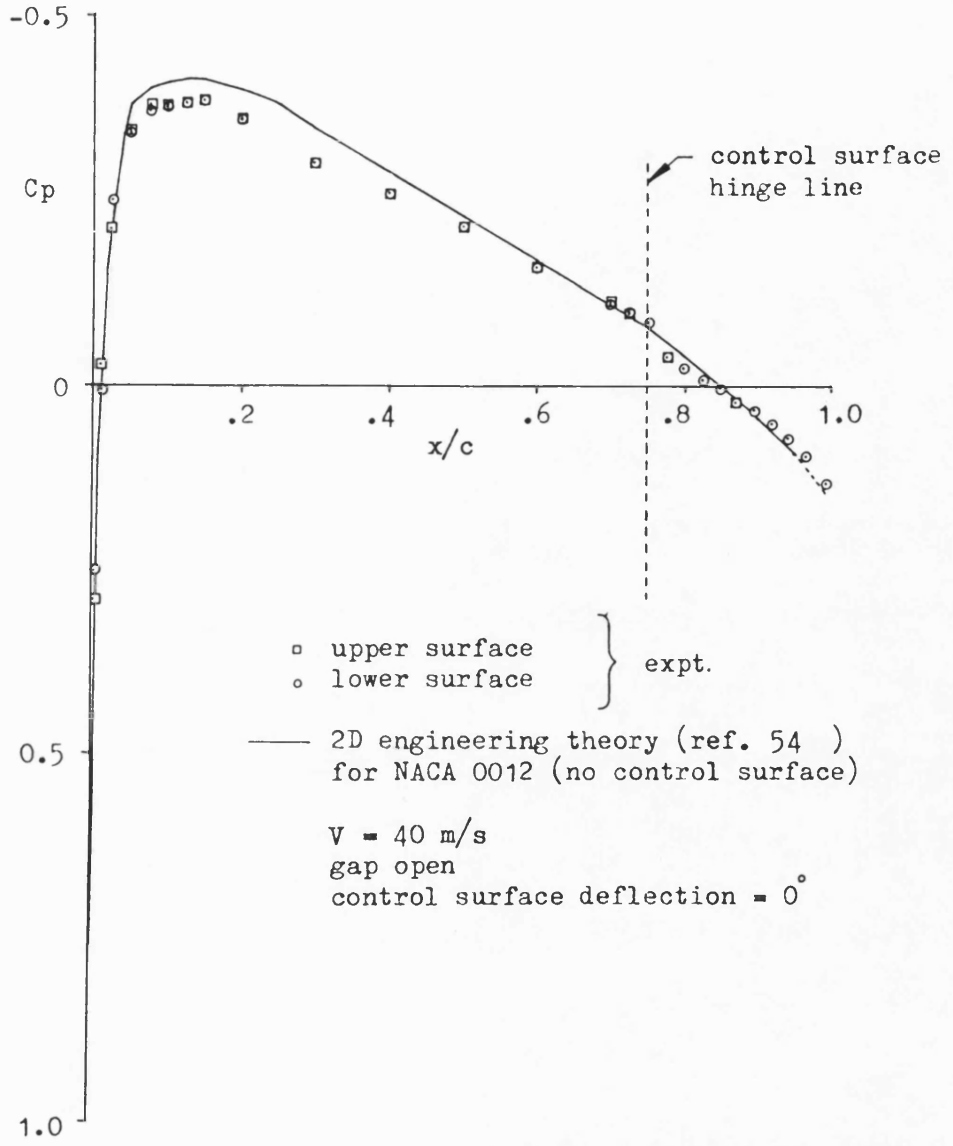

Fig. 6.6 Comparison of steady pressure distributions on upper and lower surface of fin at y/s = 0.6213 to confirm setting of model at zero incidence.

Fig. 6.7

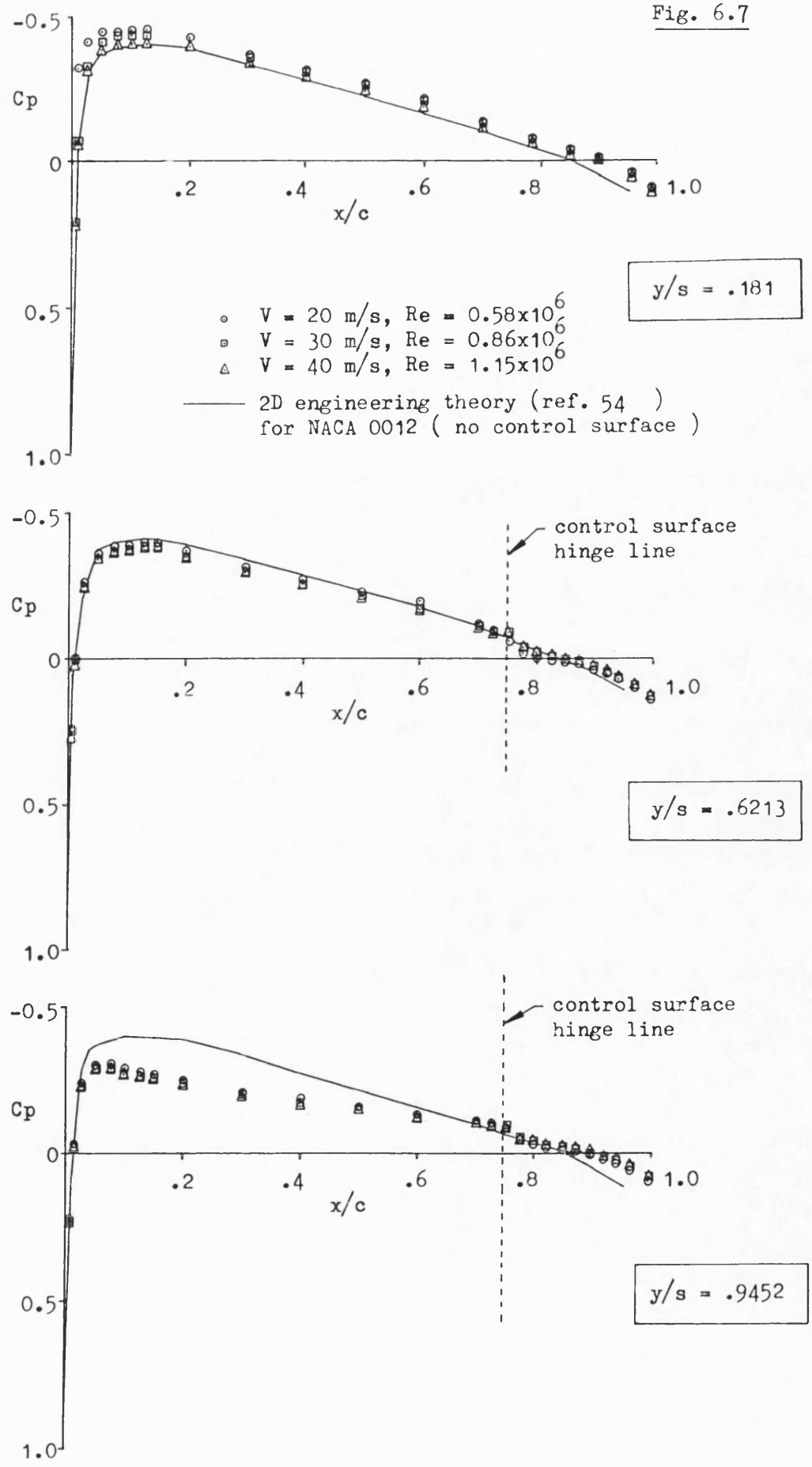

Fig. 6.7 Steady pressure distributions on surface of fin at three Reynolds numbers ($\alpha = 0^\circ$, $\delta = 0^\circ$, gap open)

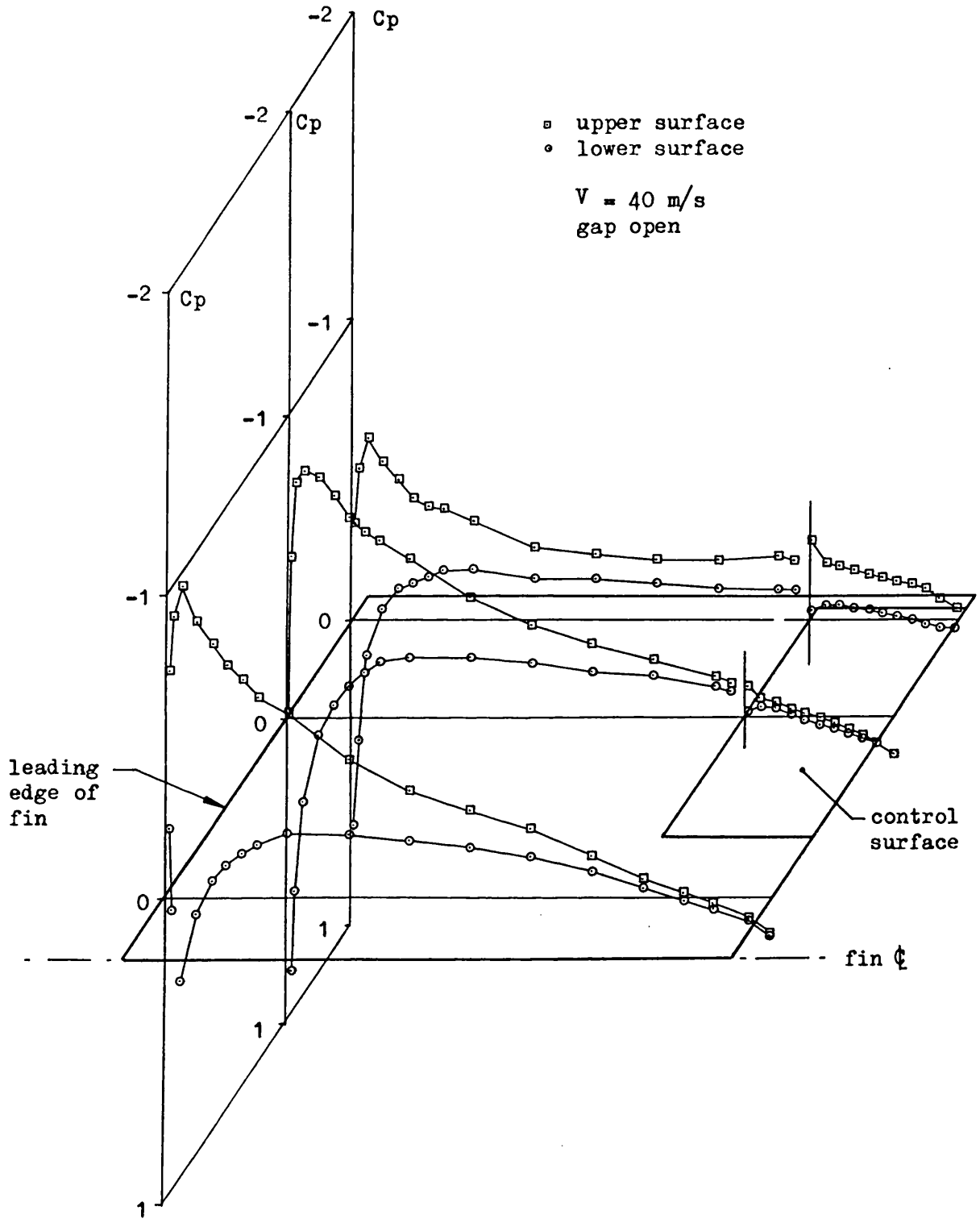

Fig. 6.8 Steady pressure distribution on fin and control surface ($\alpha = 5^{\circ}$, $\delta = 0^{\circ}$)

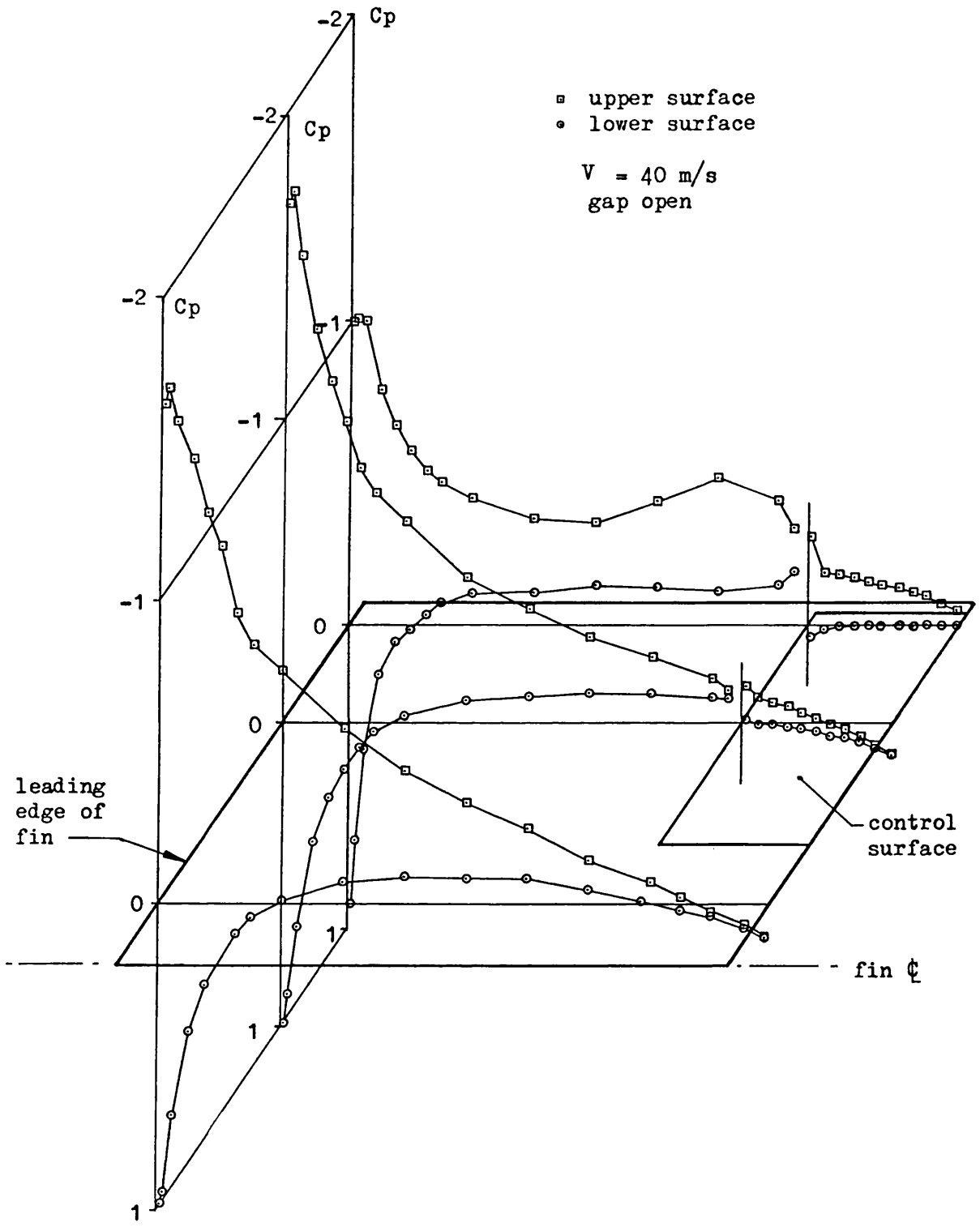

Fig. 6.9 Steady pressure distribution on fin and control surface ($\alpha = 10^{\circ}$, $\delta = 0^{\circ}$).

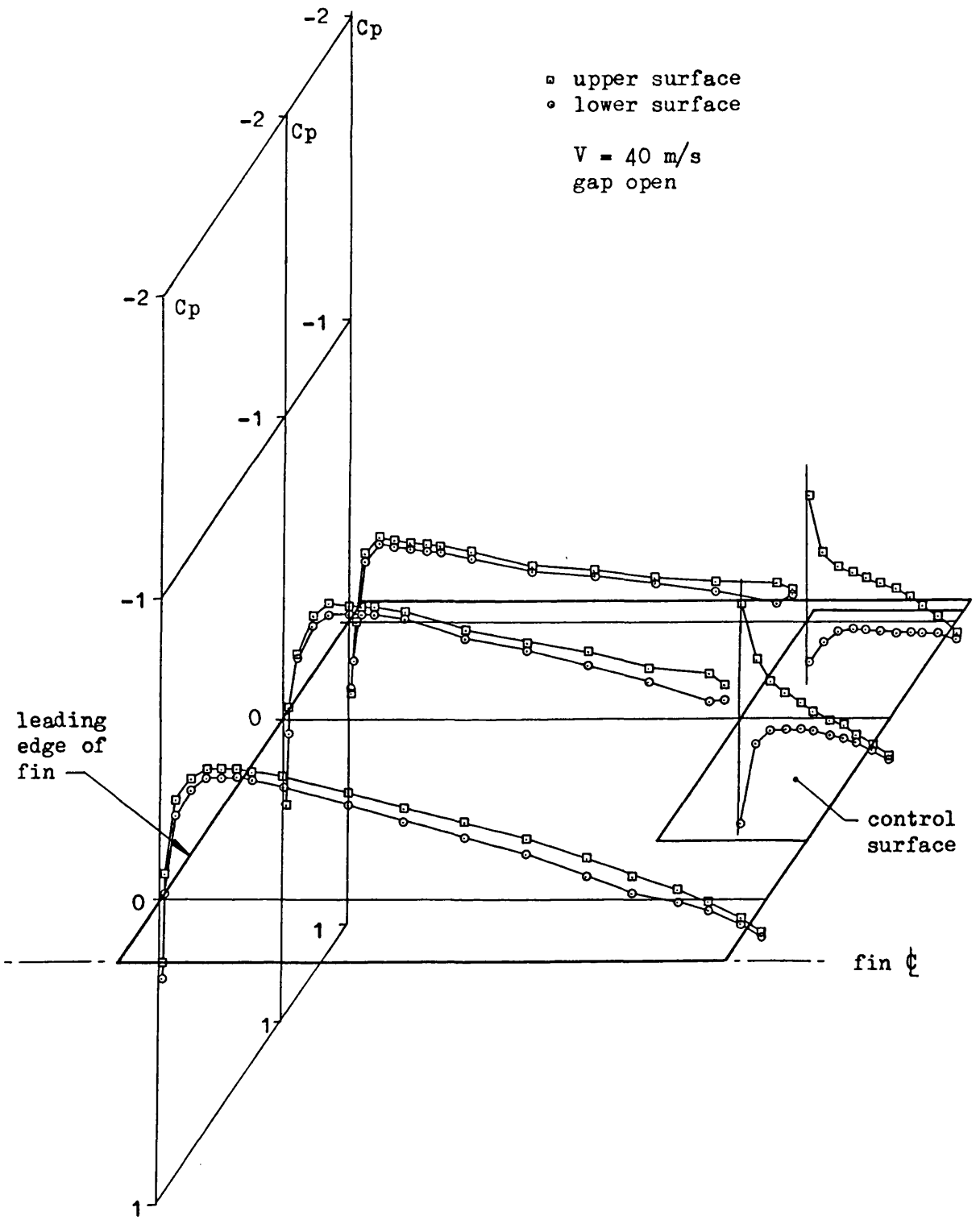

Fig. 6.10 Steady pressure distributions on fin and control surface ($\alpha = 0^\circ$, $\delta = 5^\circ$).

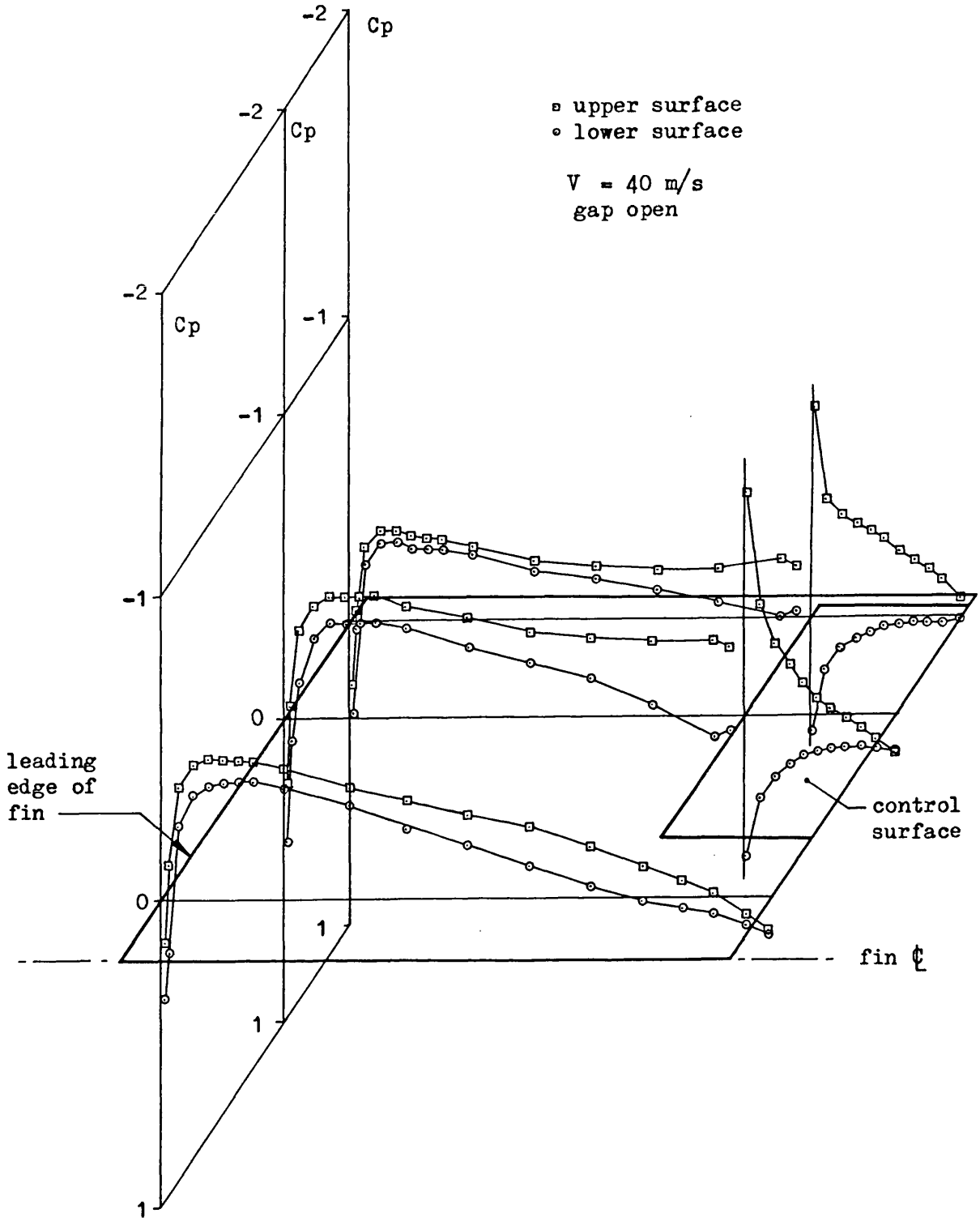

Fig. 6.11 Steady pressure distribution on fin and control surface ($\alpha = 0^{\circ}$, $\delta = 10^{\circ}$).

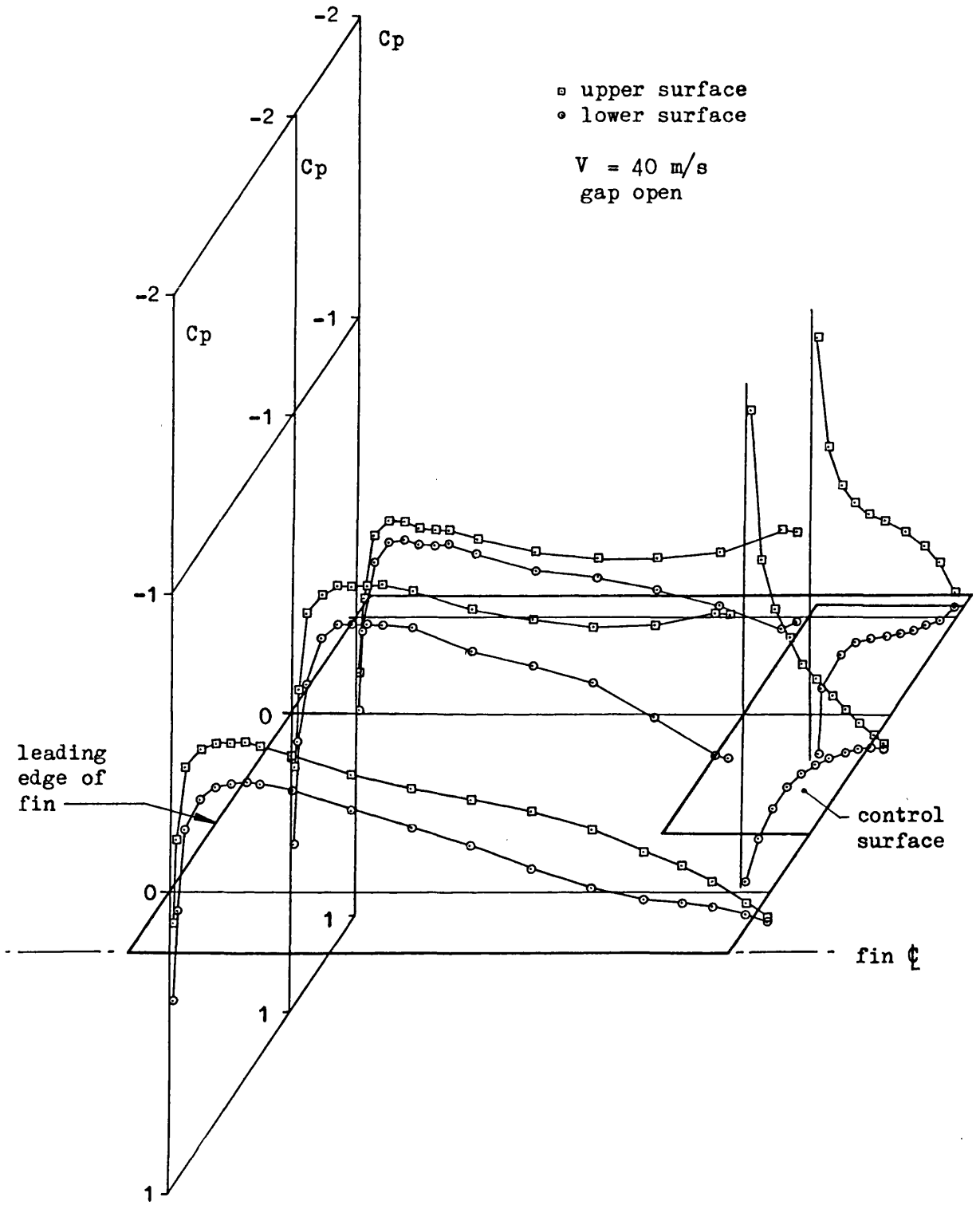

Fig. 6.12 Steady pressure distribution on fin and control surface ($\alpha = 0^{\circ}$, $\delta = 15^{\circ}$).

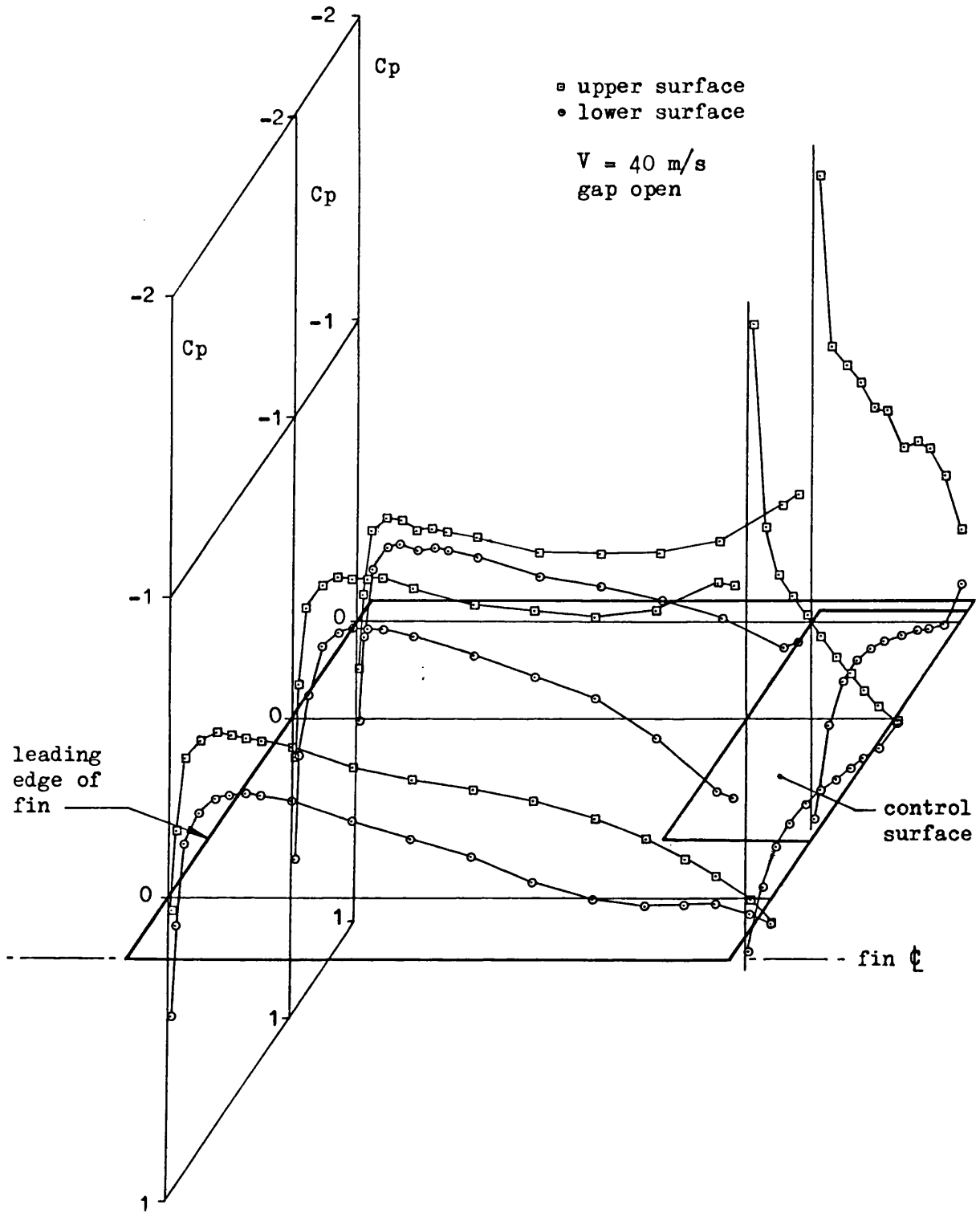

Fig. 6.13 Steady pressure distribution on fin and control surface ($\alpha = 0^{\circ}$, $\delta = 20^{\circ}$).

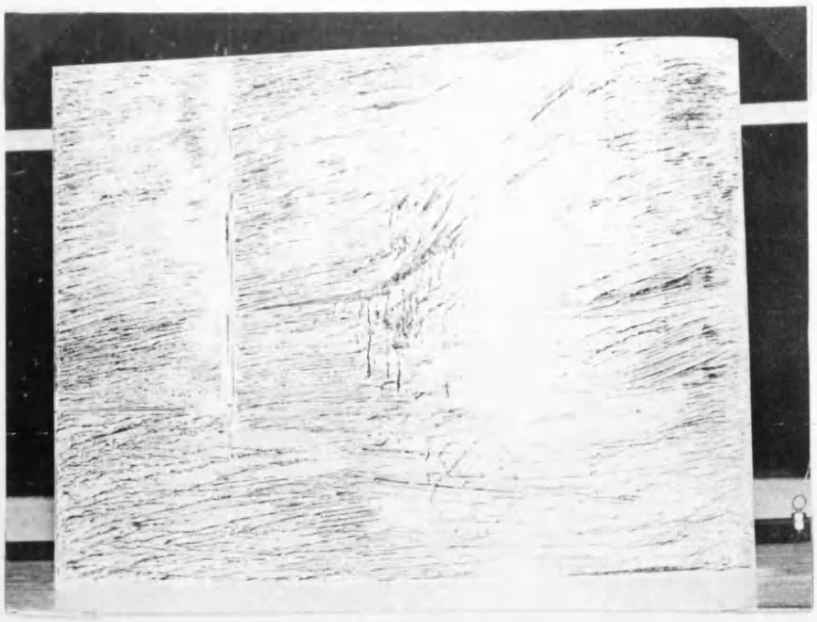

liquid film

liquid film - fin tip

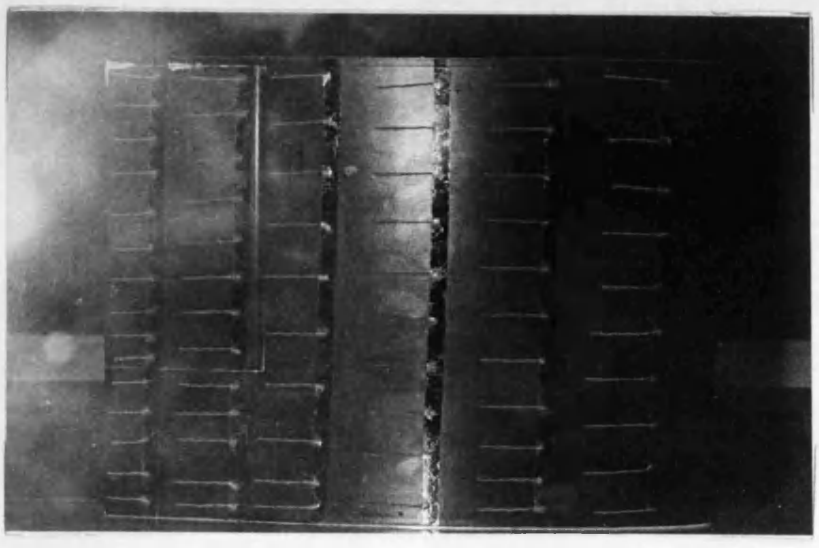

wool tufts

Fig. 6.14 Flow visualisation on fin and control surface ($\alpha = 0^\circ, \delta = 0^\circ$)

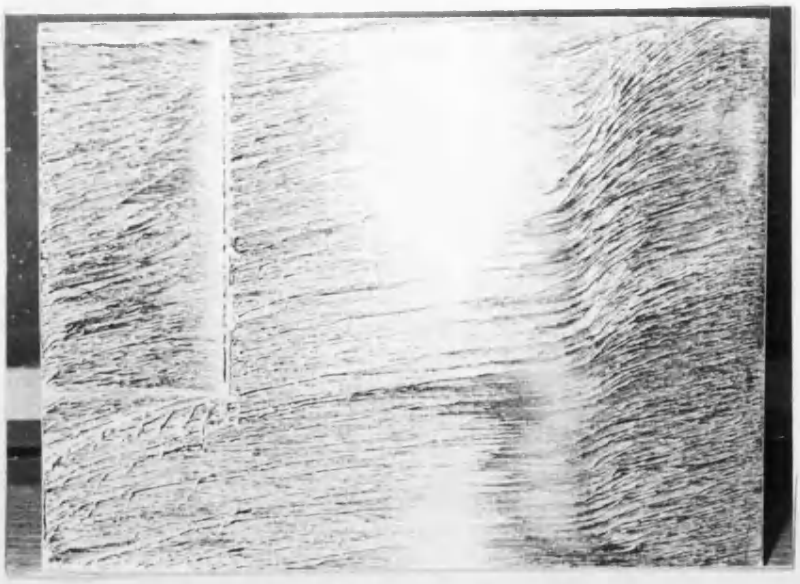

upper surface - liquid film

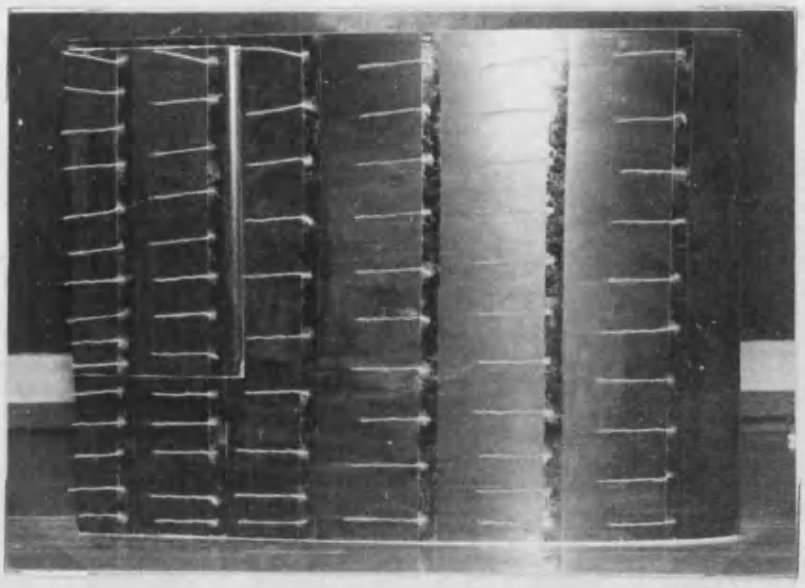

upper surface - wool tufts

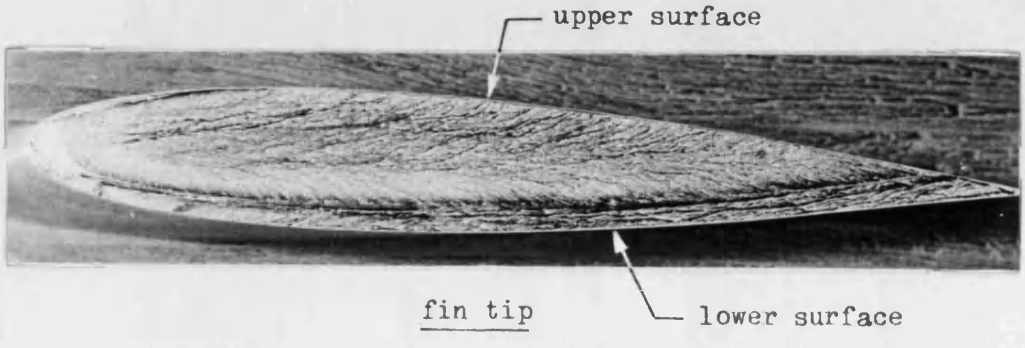

Fig. 6.15 Flow visualisation on fin and control surface ($\alpha = 5^\circ, \delta = 0^\circ$)

Fig. 6.16

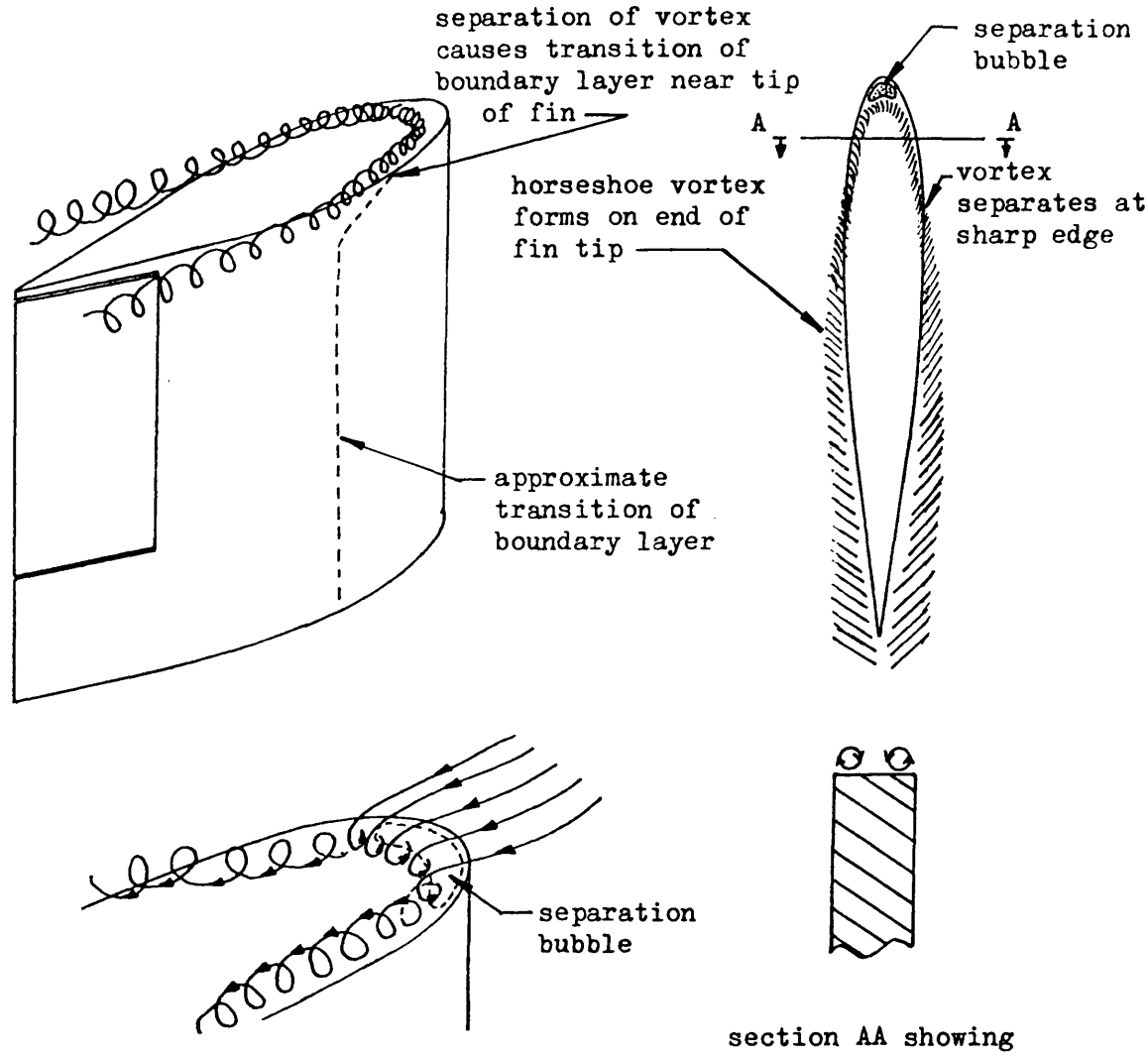

$\alpha = 0^\circ$

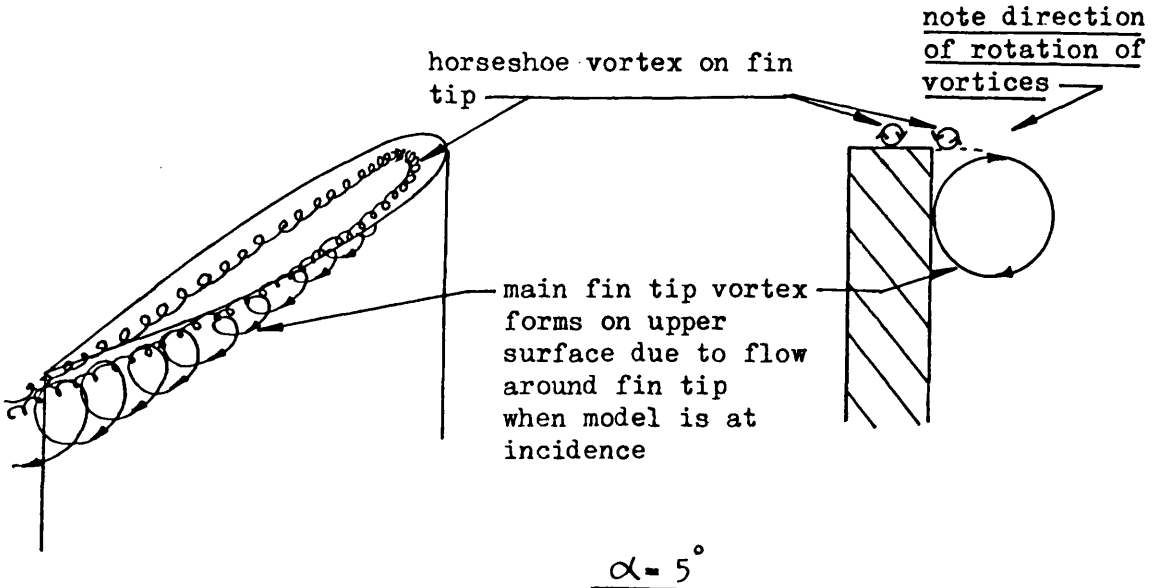

$\alpha = 5^\circ$

Fig. 6.16 vortex formations on tip of fin at zero and at 5° incidence

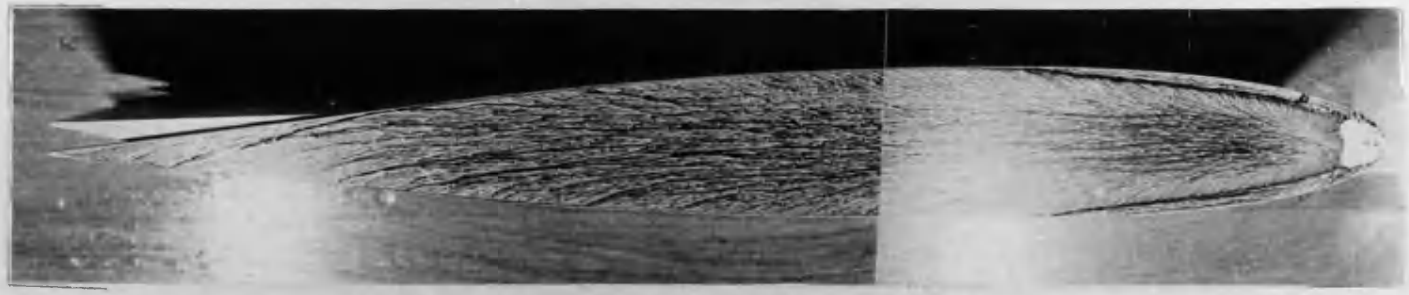

fin tip

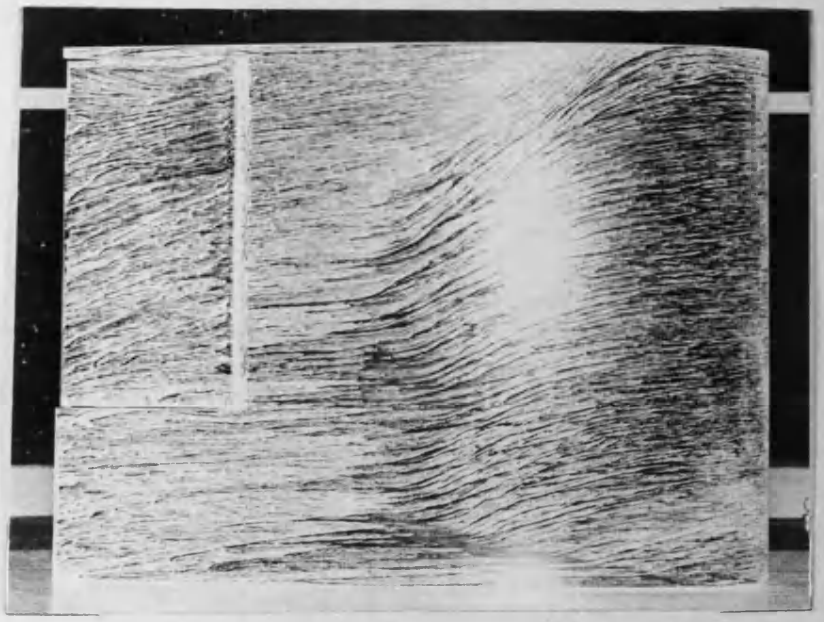

upper surface

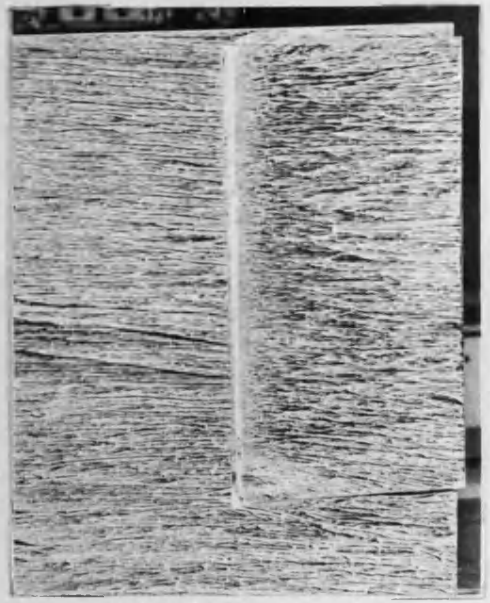

lower surface

Fig. 6.17

Fig. 6.17 Flow visualisation on fin and control surface ($\alpha = 0^\circ, \delta = 5^\circ$).

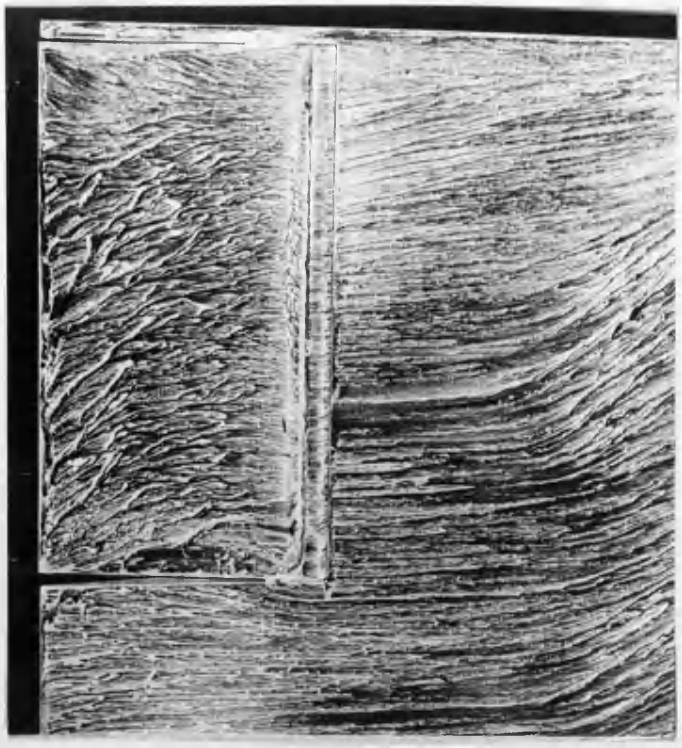

upper surface

fin tip

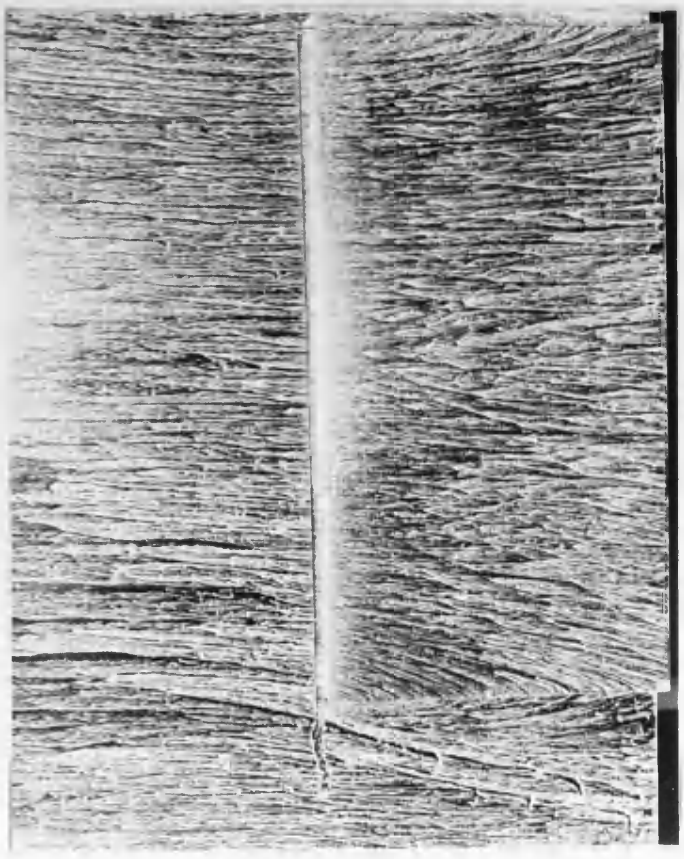

lower surface

Fig. 6.18 Flow visualisation on fin and control surface ($\alpha = 0^{\circ}$, $\delta = 10^{\circ}$).

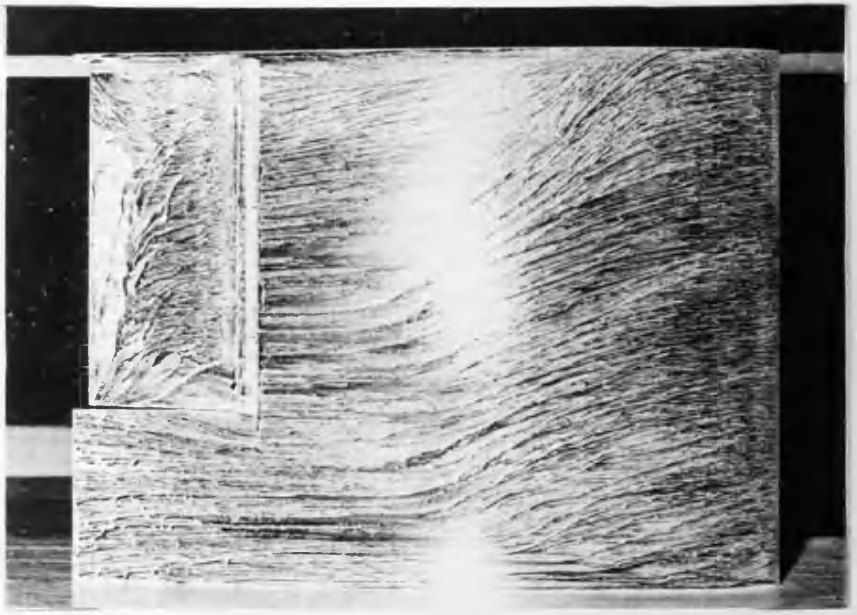

upper surface

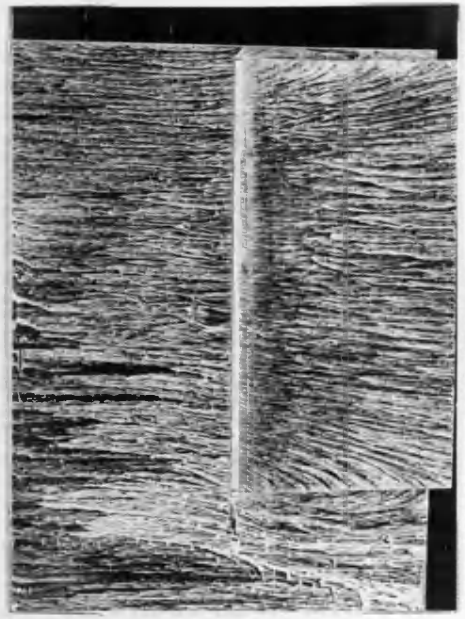

lower surface

fin tip

Fig. 6.19 Flow visualisation on fin and control surface ($\alpha = 0^\circ, \delta = 15^\circ$).

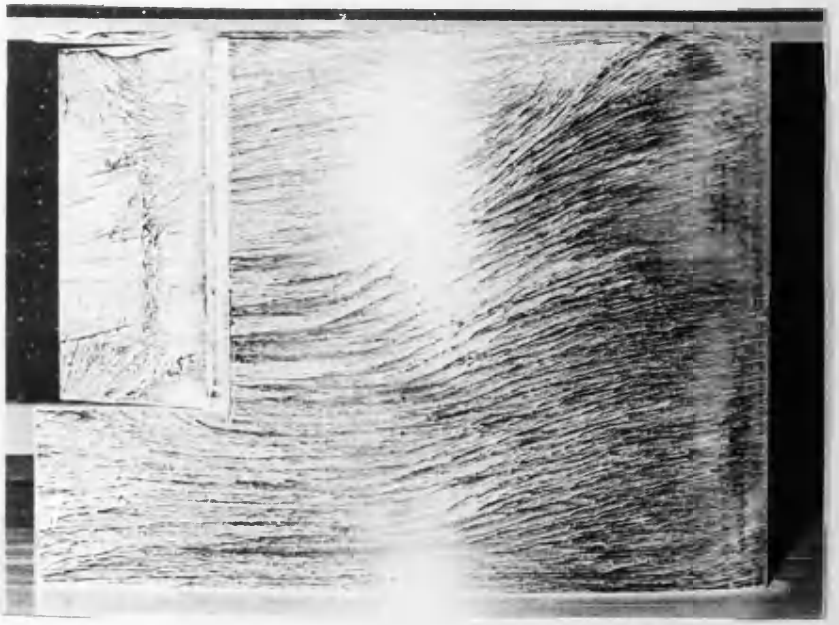

upper surface

fin tip

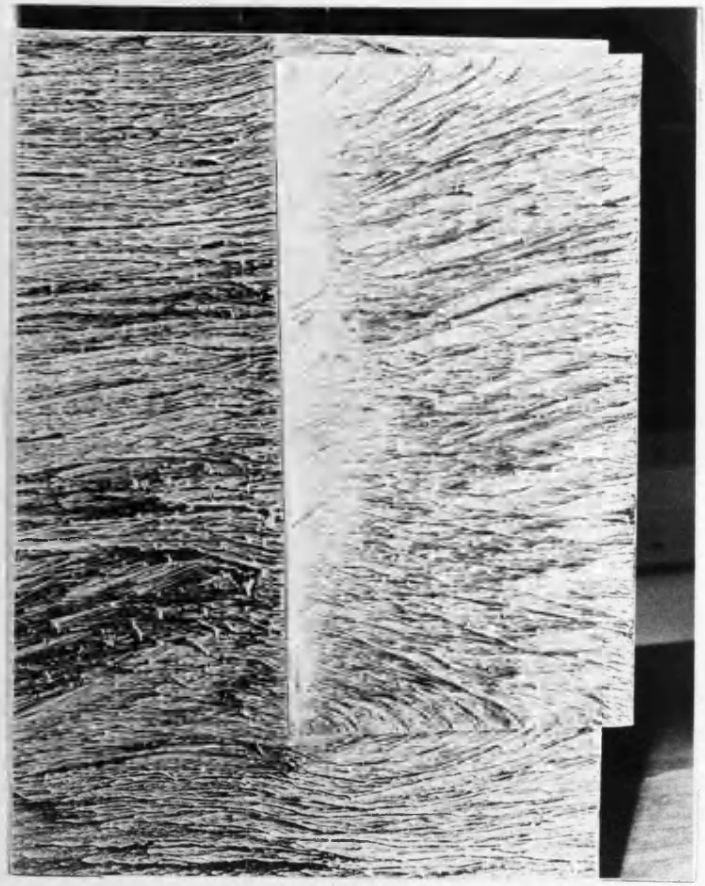

lower surface

Fig. 6.20

Fig. 6.20 Flow visualisation on fin and control surface ($\alpha = 0^\circ$, $\delta = 20^\circ$).

Fig. 6.21

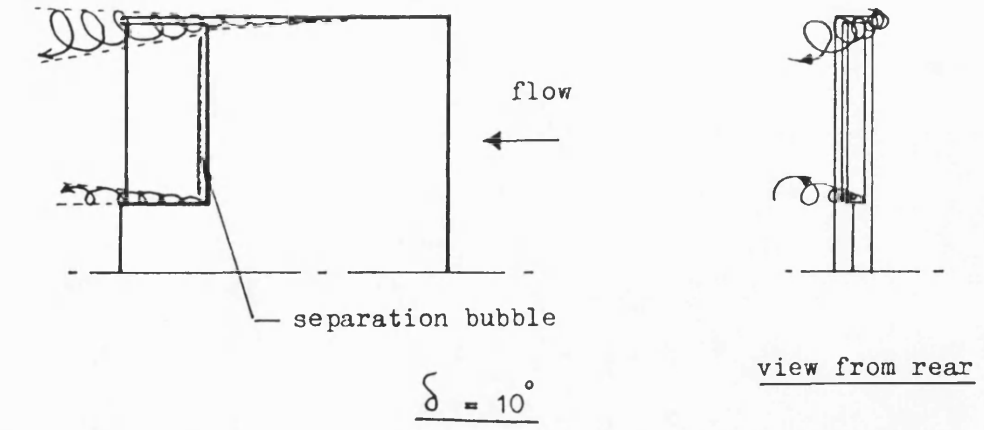

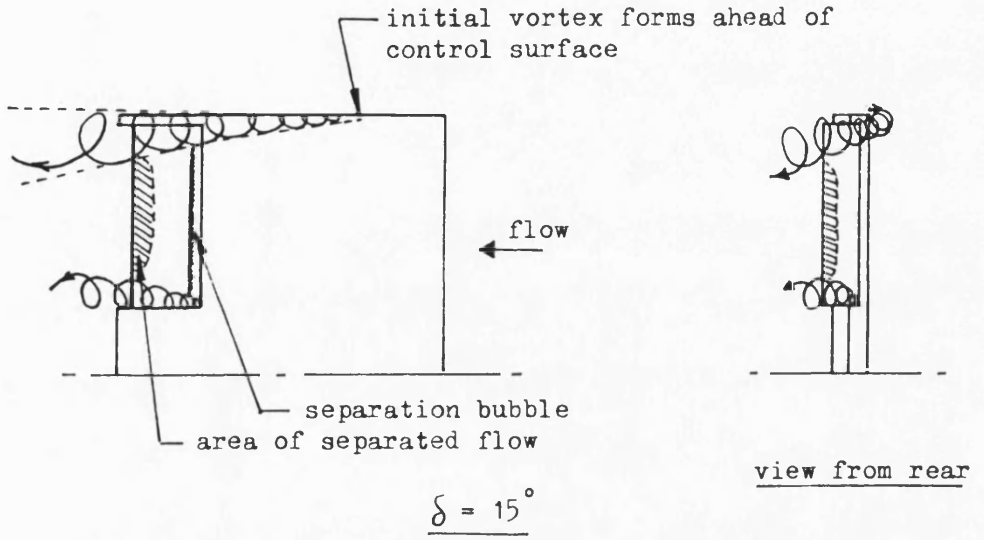

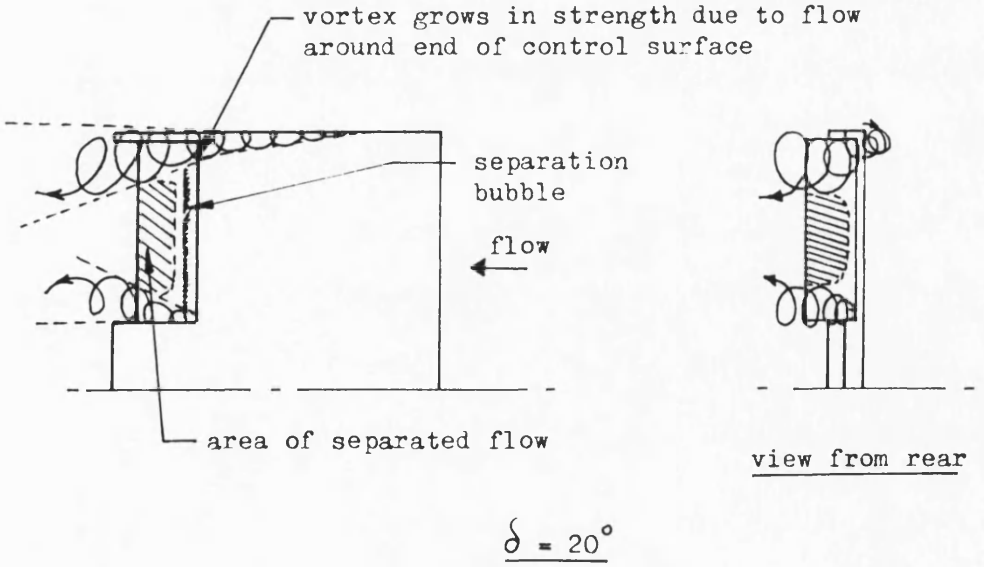

Fig. 6.21 Vortices and flow separations on upper surface of fin for the case of a deflected control (V = 40 m/s,gap open).

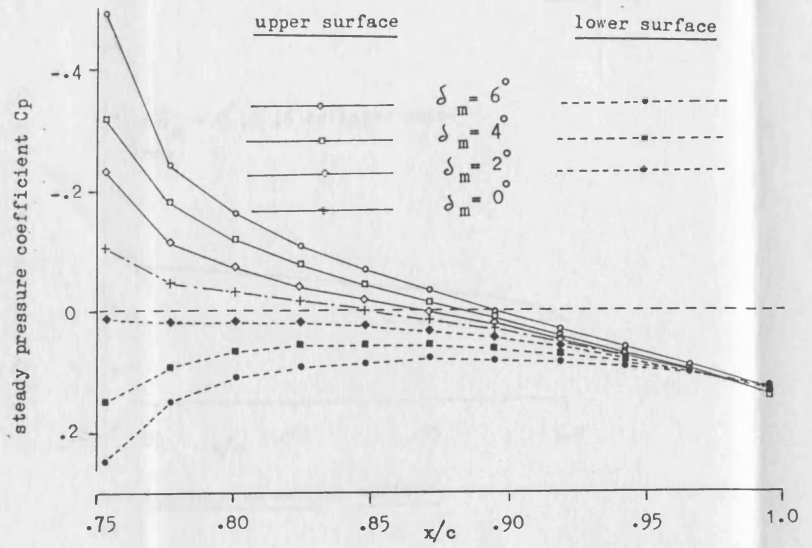

a). upper and lower surface pressure distributions on control surface

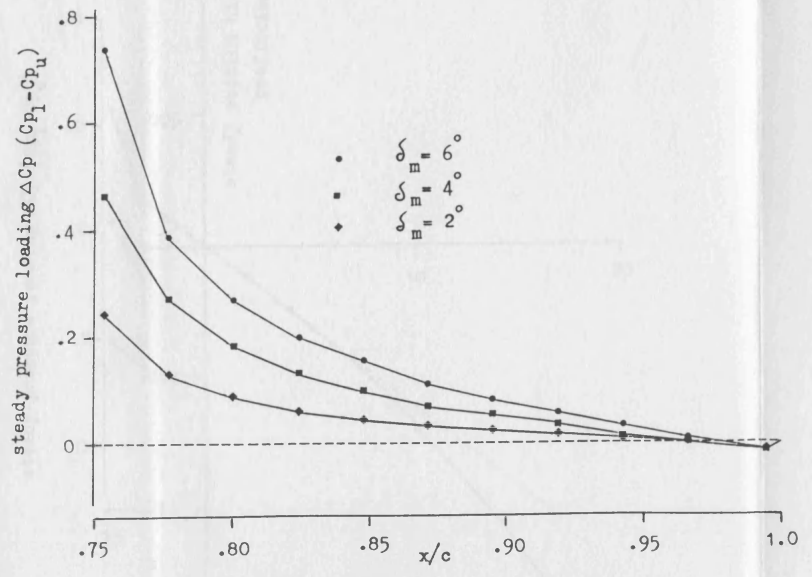

b). pressure loadings on control surface

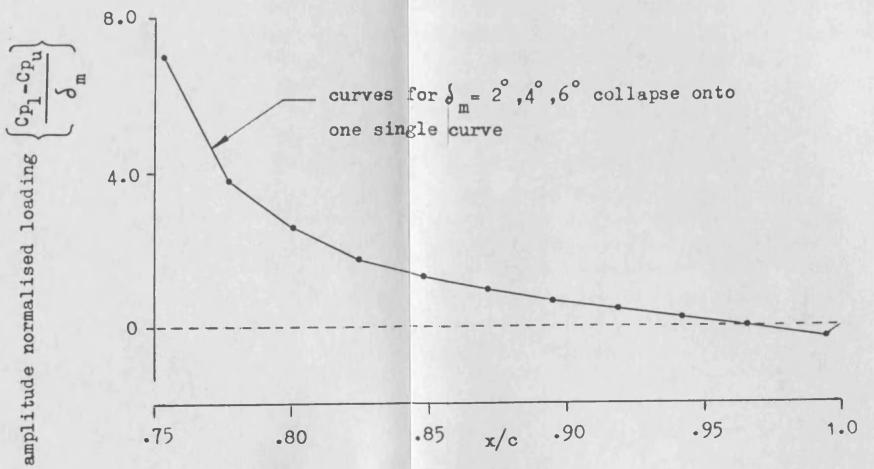

c). amplitude normalised loadings on control surface

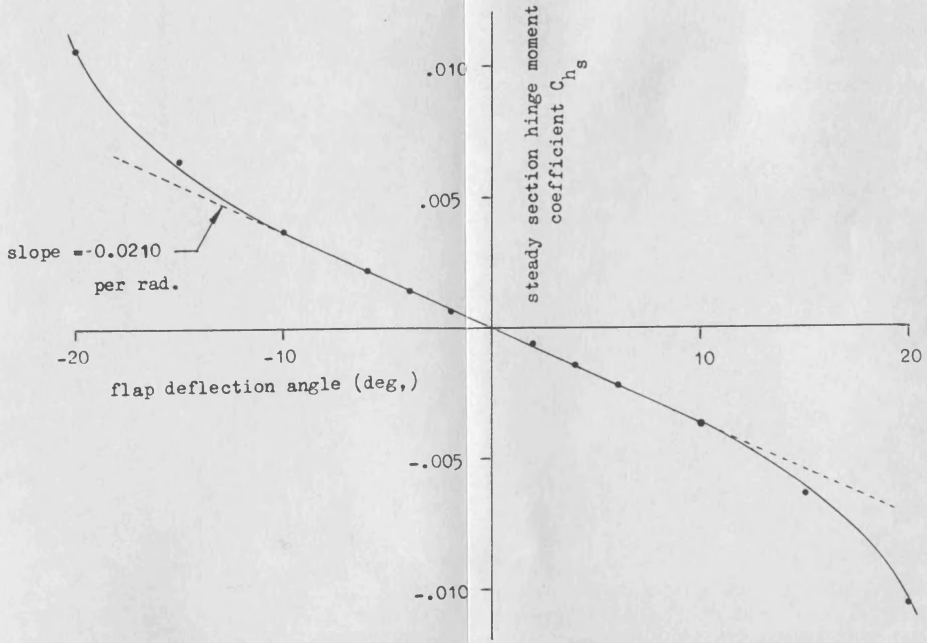

d). variation of section hinge moment coefficient with control surface deflection

Fig. 6.22 Evaluation of control surface steady section hinge moment coefficients from pressure data (y/s = .6213, v = 40 m/s, gap open, $\alpha = 0°$)

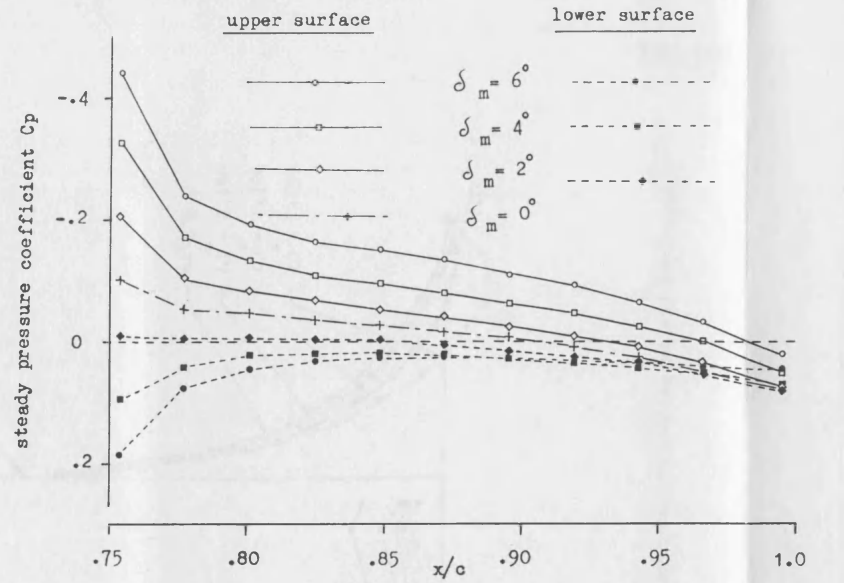

a). upper and lower surface pressure distributions on control surface

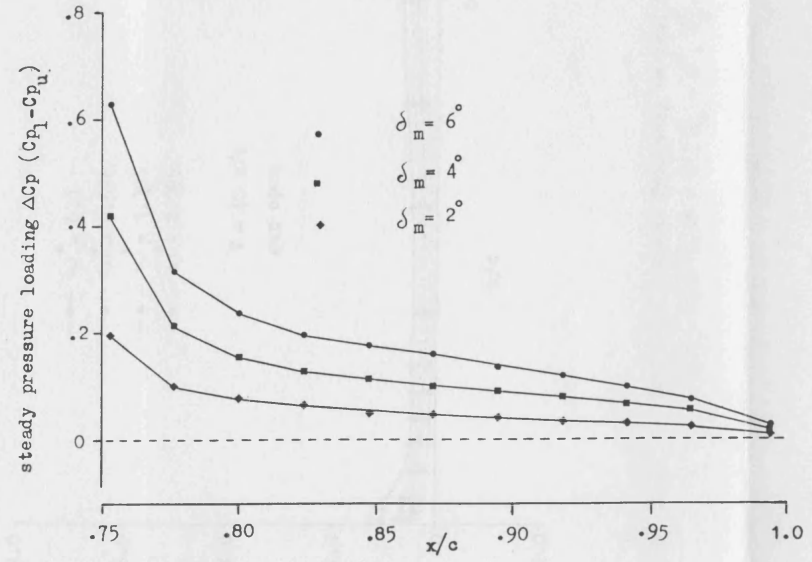

b). pressure loadings on control surface

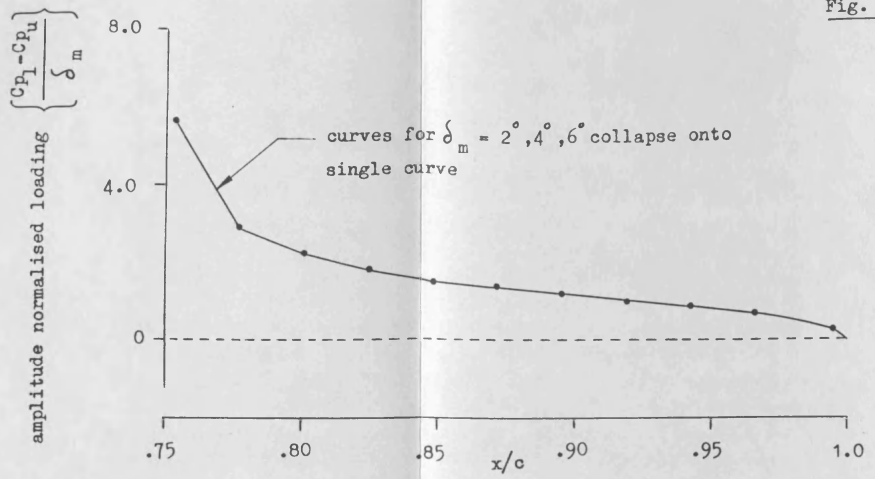

c). amplitude normalised loadings on control surface

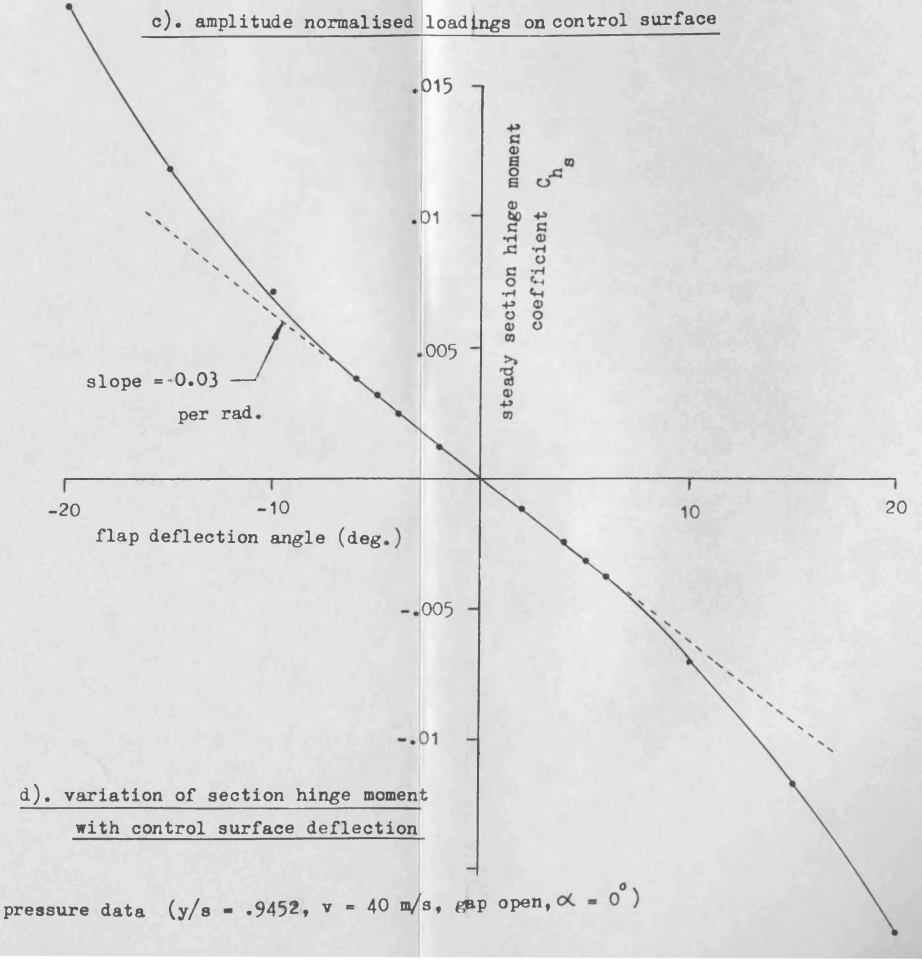

d). variation of section hinge moment with control surface deflection

Fig. 6.23 Evaluation of control surface steady section hinge moment coefficients from pressure data (y/s = .9452, v = 40 m/s, gap open, $\alpha = 0°$)

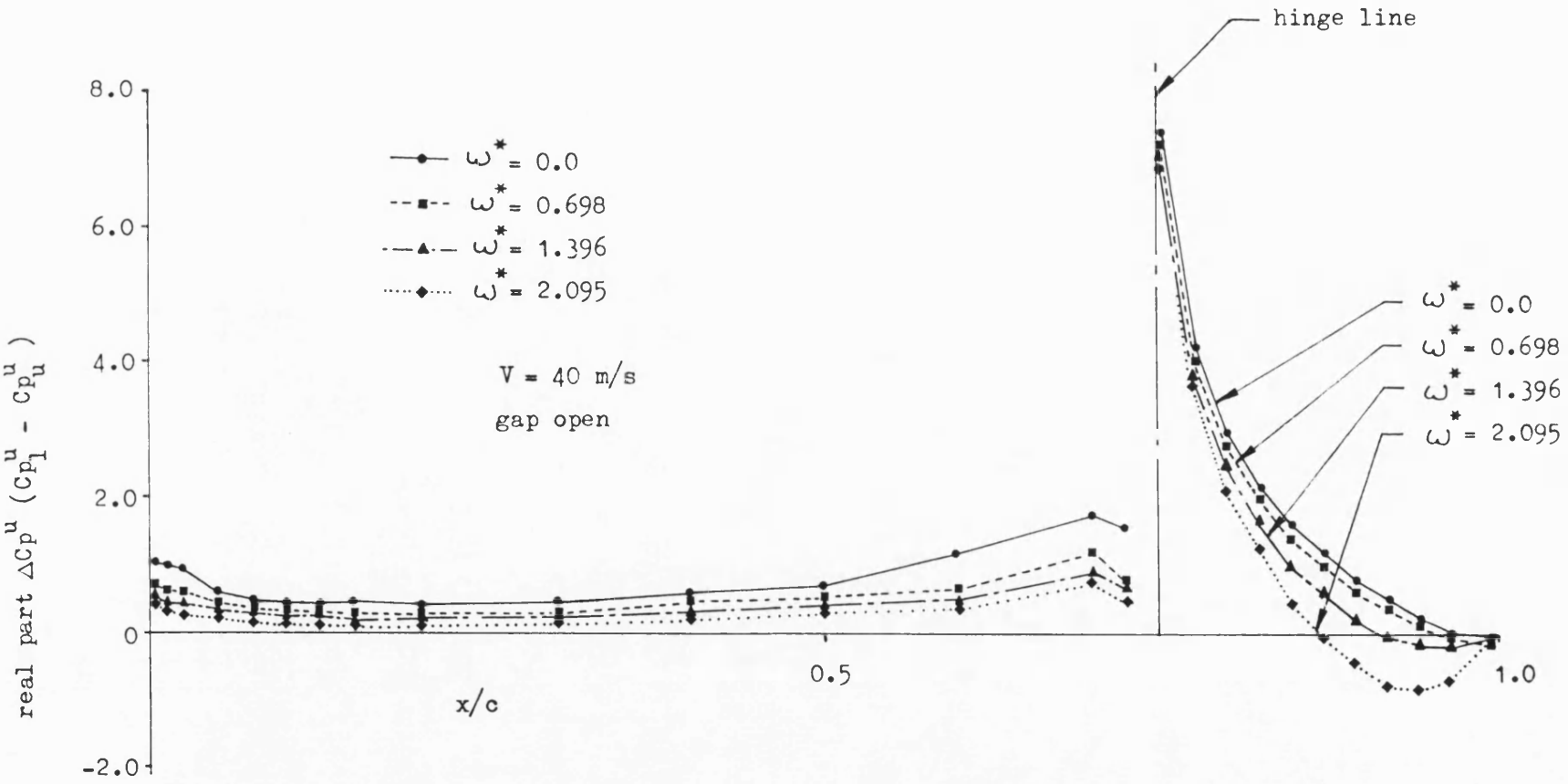

Fig. 6.24 Effect of reduced frequency on real part of unsteady pressure loading at mid semi-span ($y/s = 0.6213, \alpha = 0^\circ, \delta_m = 0^\circ, \delta_a = 1^\circ$).

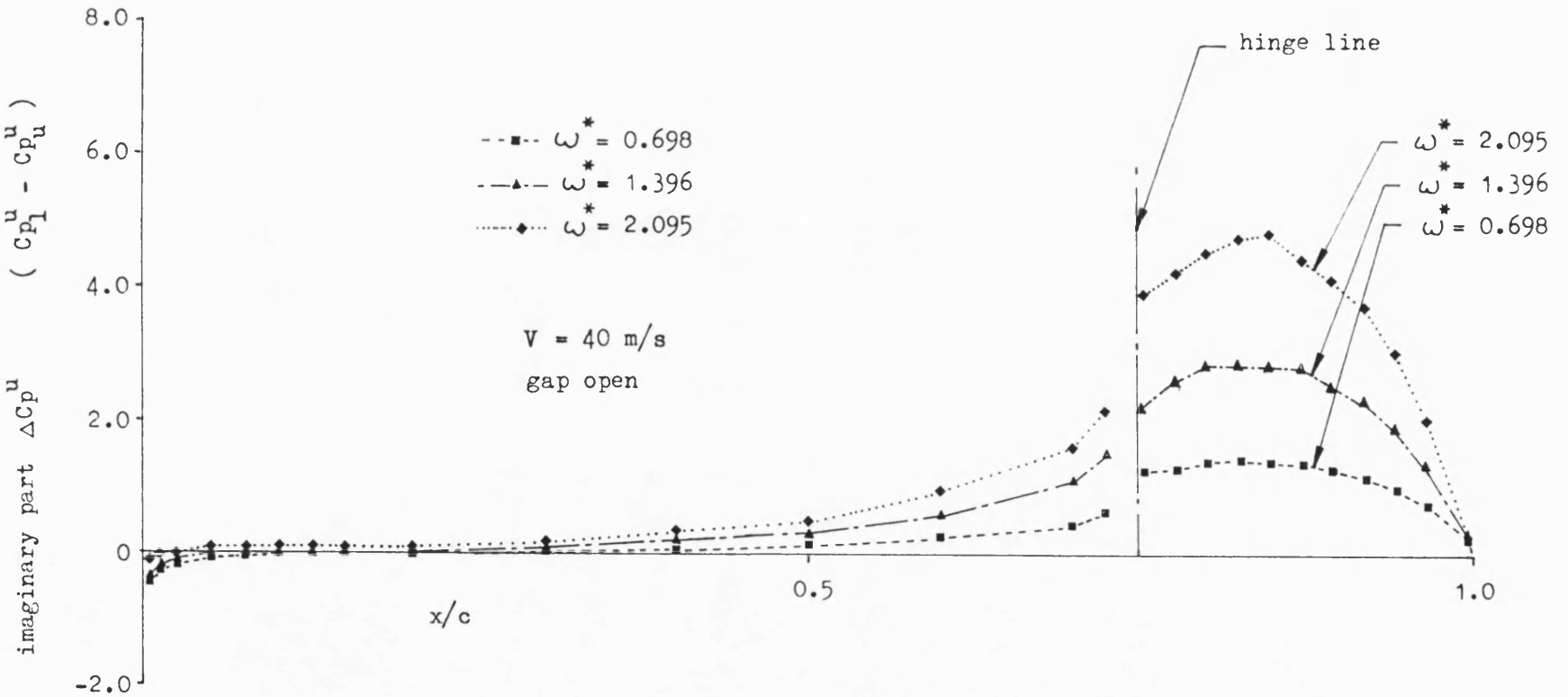

Fig. 6.25 Effect of reduced frequency on imaginary part of unsteady pressure loading at mid semi-span ($y/s = 0.6213$, $\alpha = 0^\circ$, $\delta_m = 0^\circ$, $\delta_a = 1^\circ$).

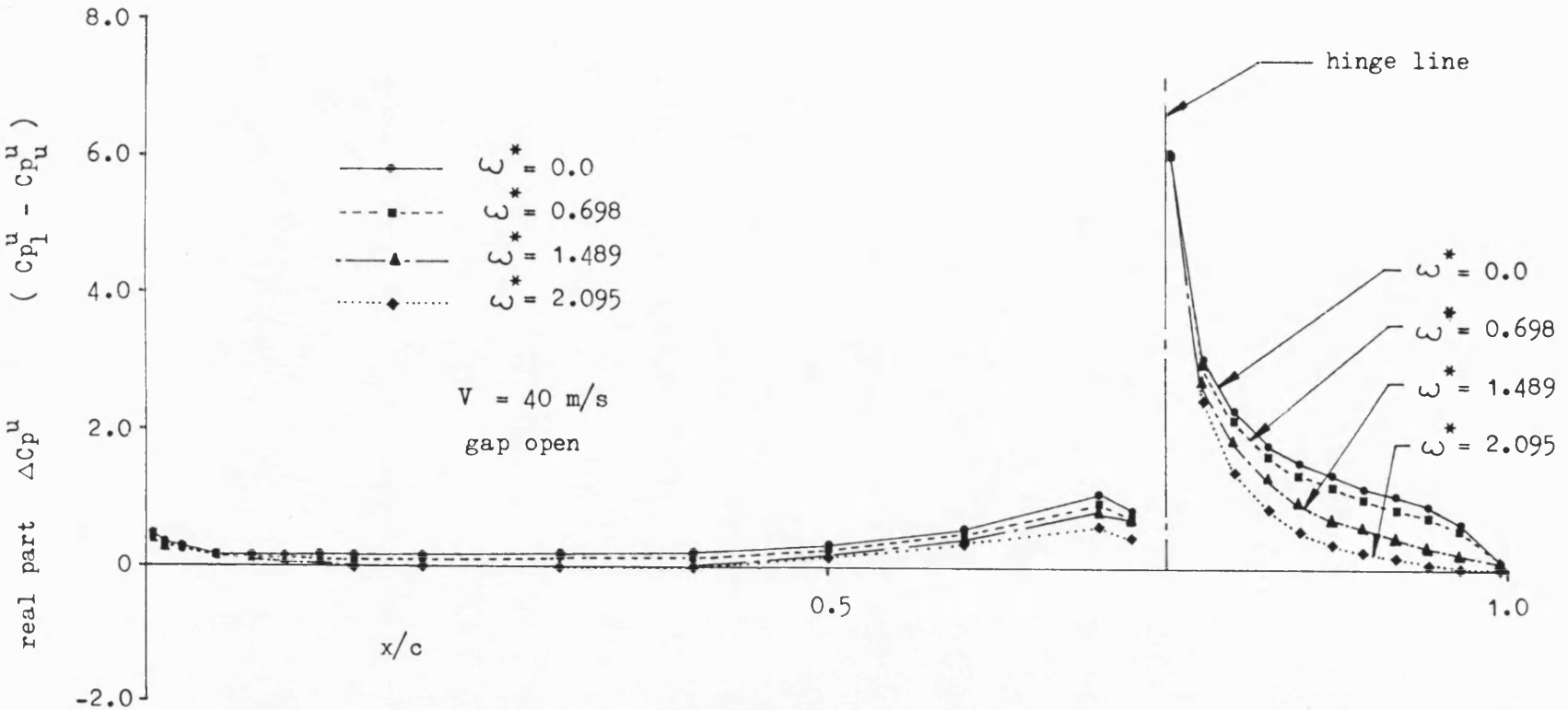

Fig. 6.26 Effect of reduced frequency on real part of unsteady pressure loading near the fin tip (y/s = 0.9452, $\alpha = 0^\circ$, $\delta_m = 0^\circ$, $\delta_a = 1^\circ$).

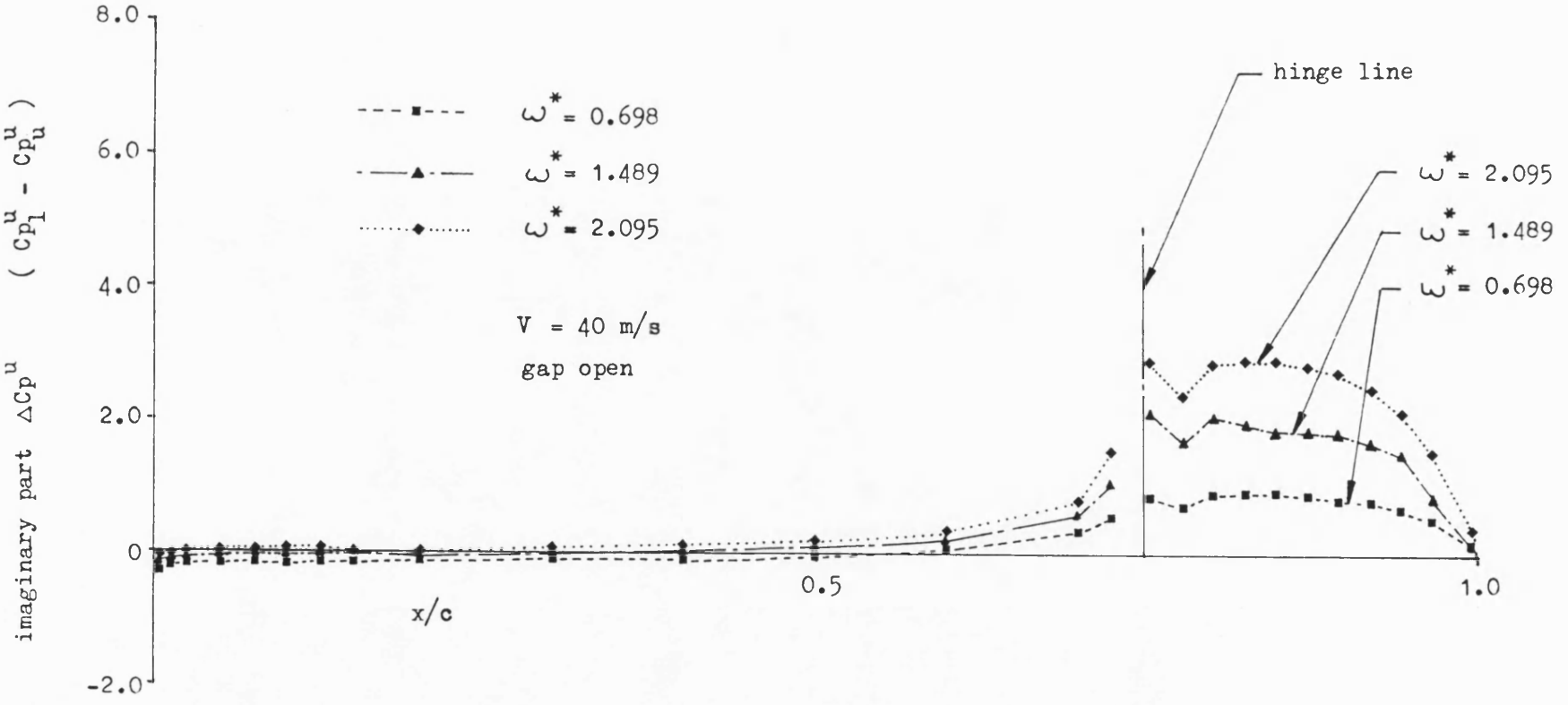

Fig. 6.27 Effect of reduced frequency on imaginary part of unsteady pressure loading near the fin tip ($y/s = 0.9452, \alpha = 0^\circ, \delta_m = 0^\circ, \delta_a = 1^\circ$).

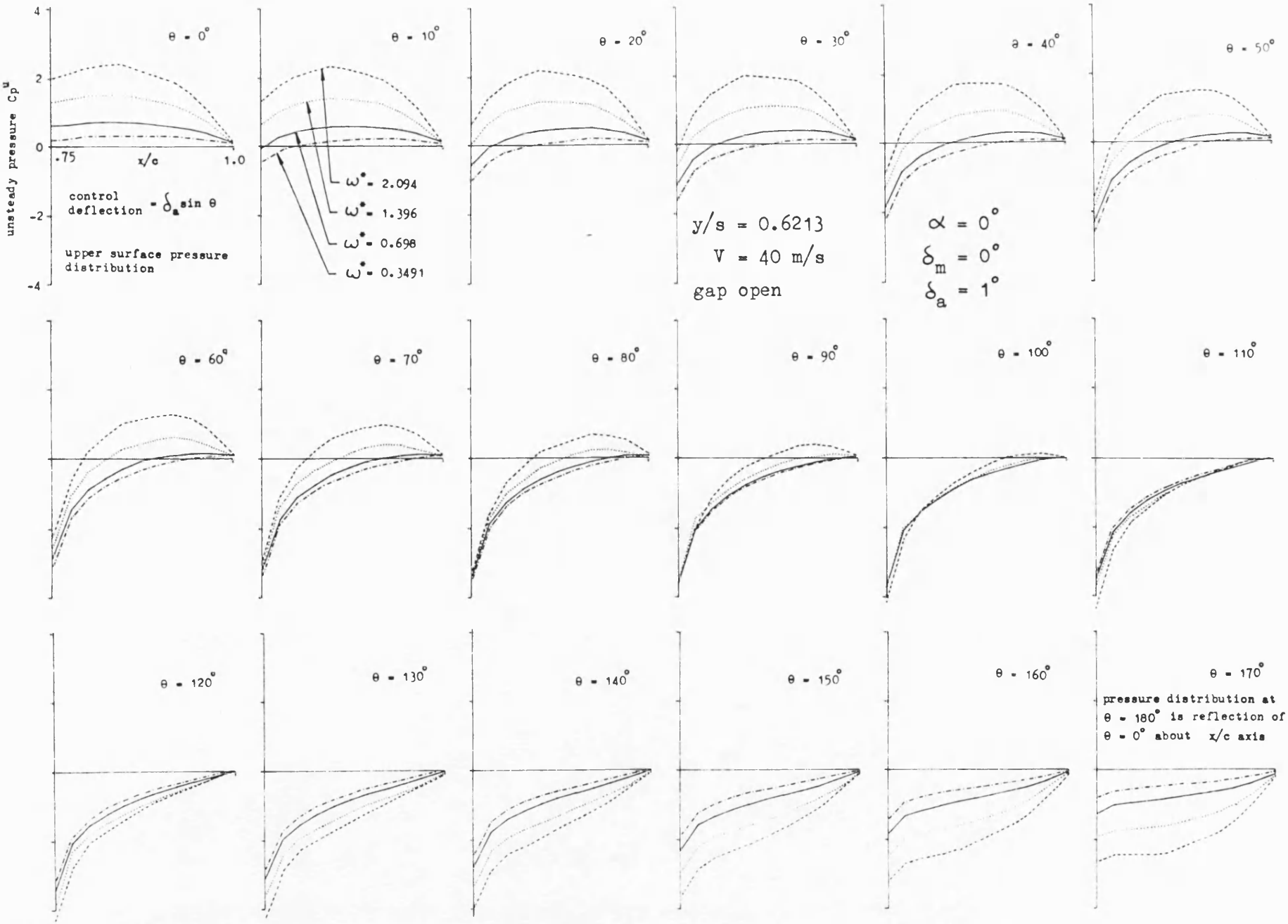

Fig. 6.28

Fig. 6.28 Development of unsteady pressures on control surface during half cycle of oscillation.

Fig. 6.29

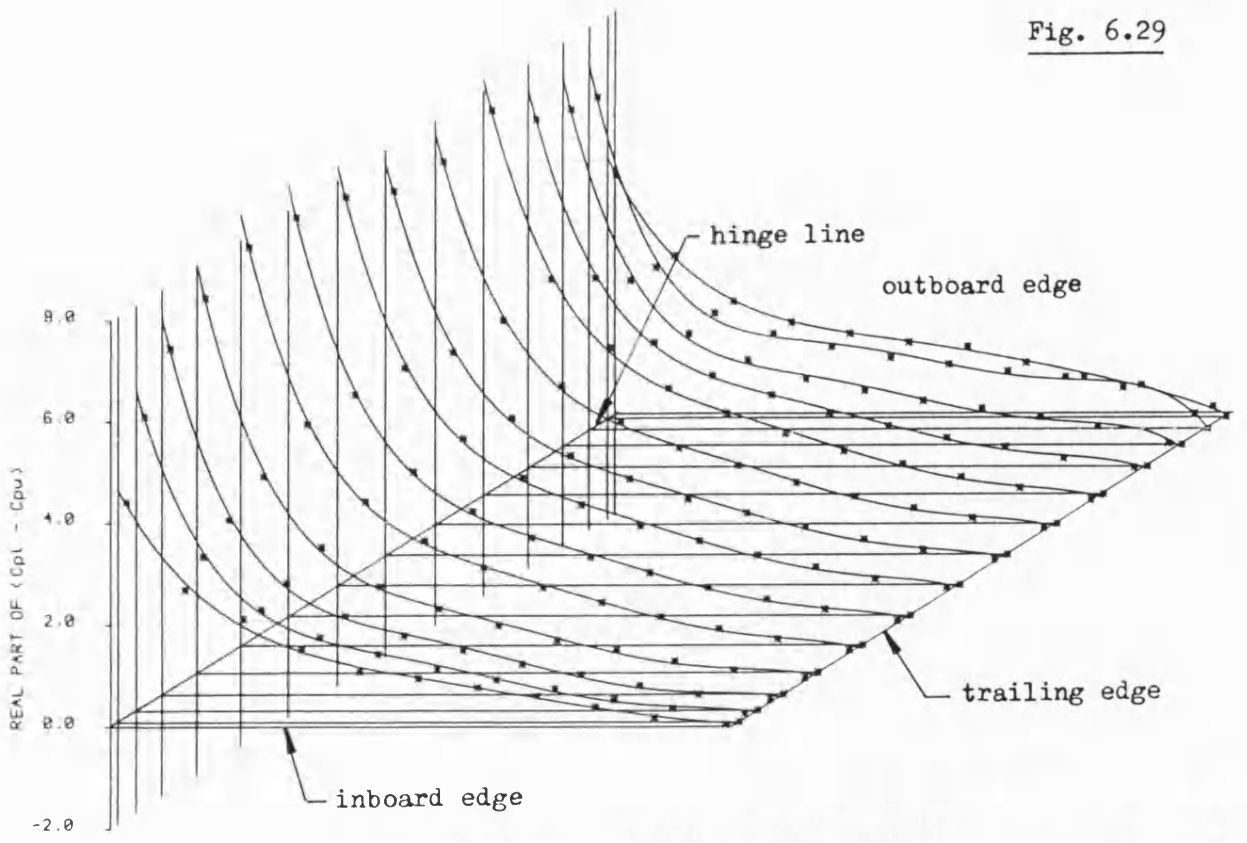

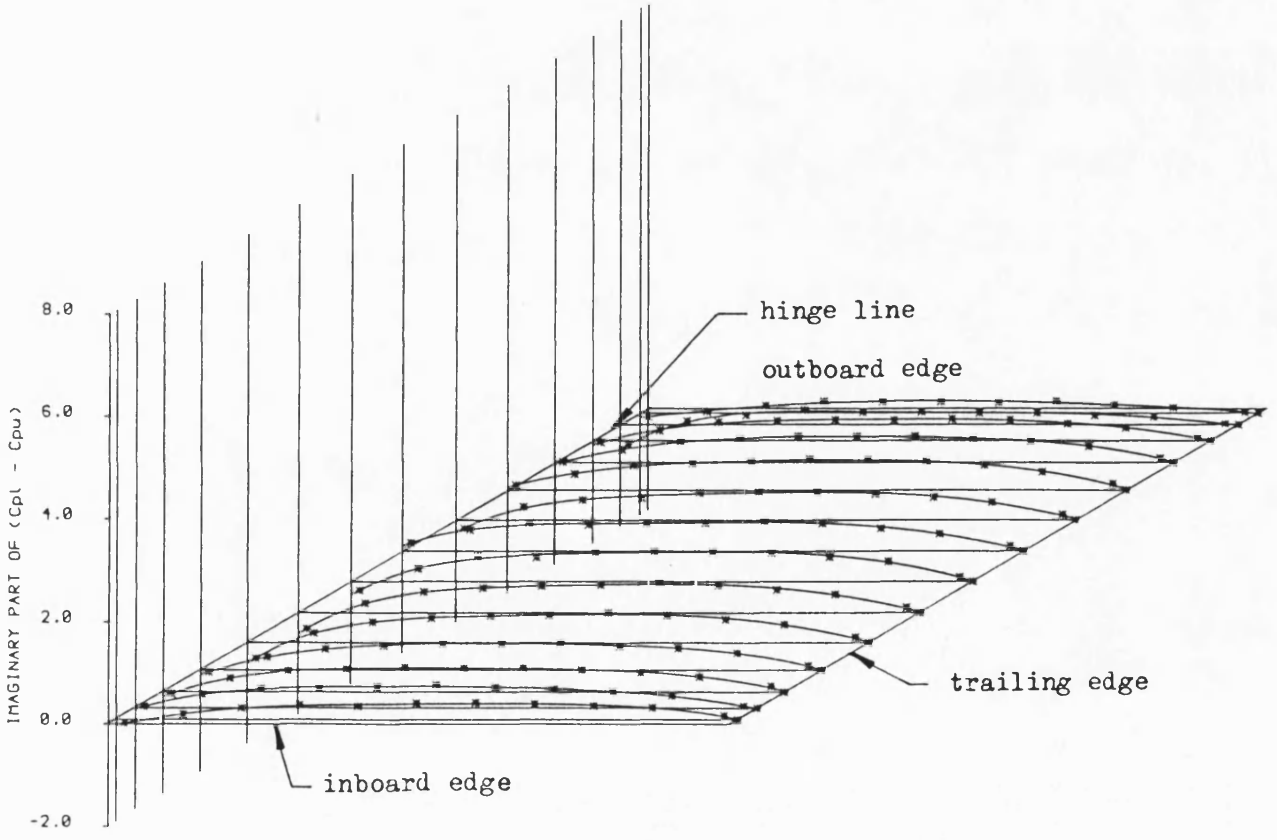

Fig. 6.29 unsteady pressure loading on control surface ($\omega^* = 0.349$)
(V = 40 m/s, gap open, $\alpha = 0^\circ$, $\delta_m = 0^\circ$, $\delta_a = 1^\circ$)

Fig. 6.30

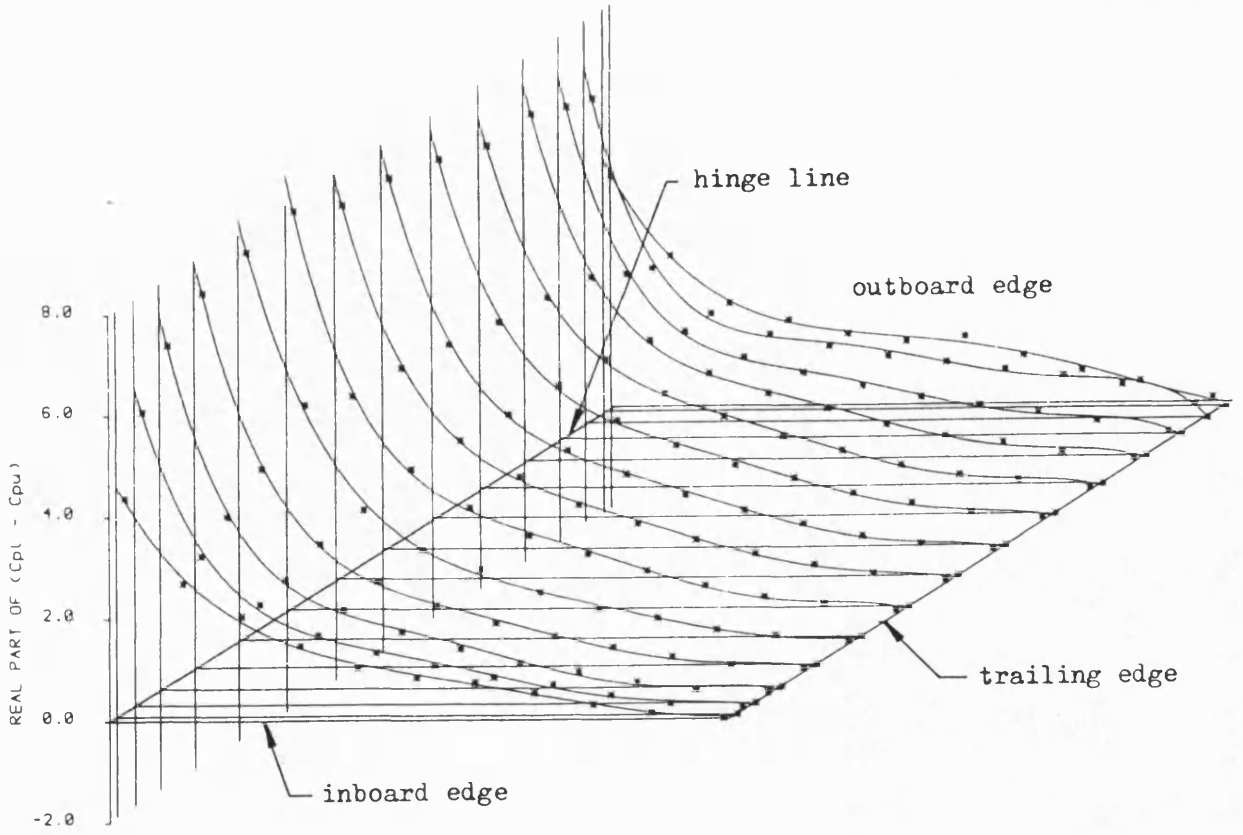

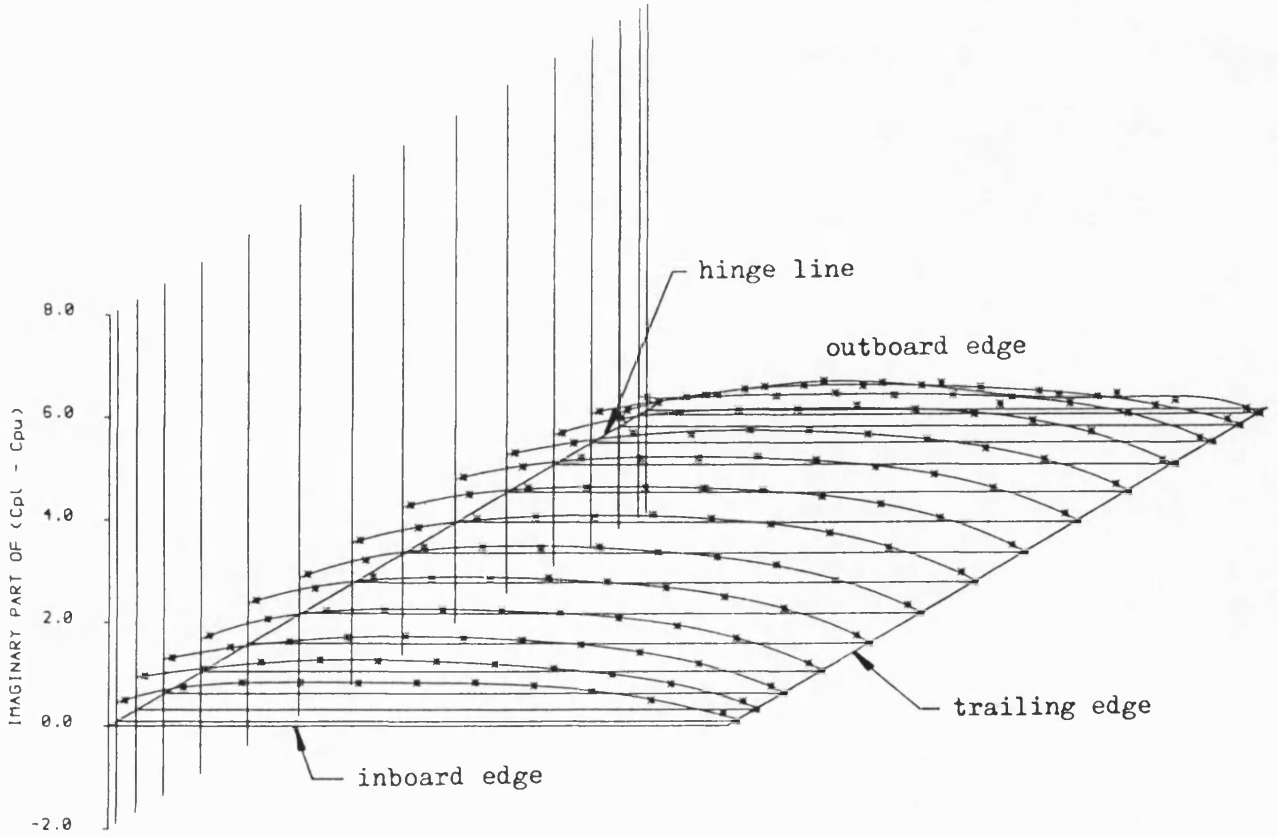

Fig. 6.30 Unsteady pressure loading on control surface ($\omega^* = 0.698$)
(V = 40 m/s, gap open, $\alpha = 0^\circ$, $\delta_m = 0^\circ$, $\delta_a = 1^\circ$)

Fig. 6.31

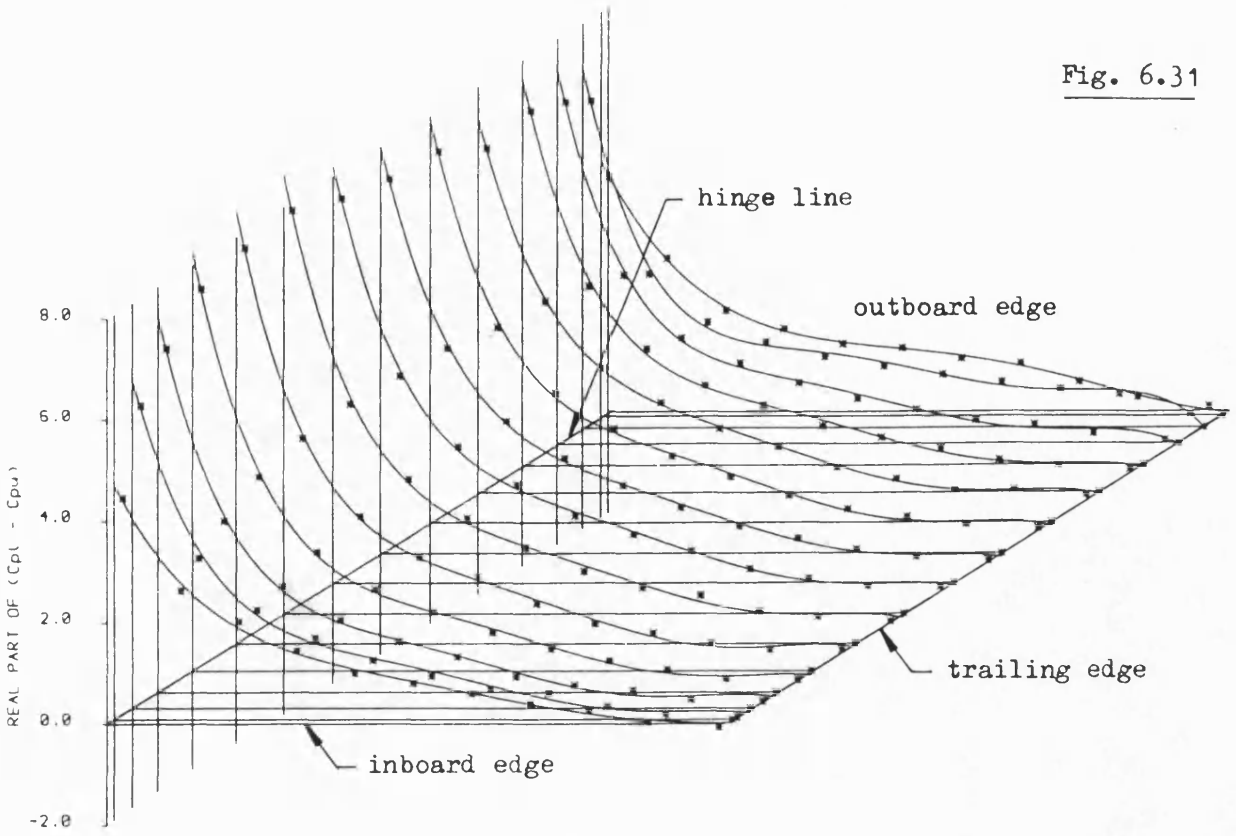

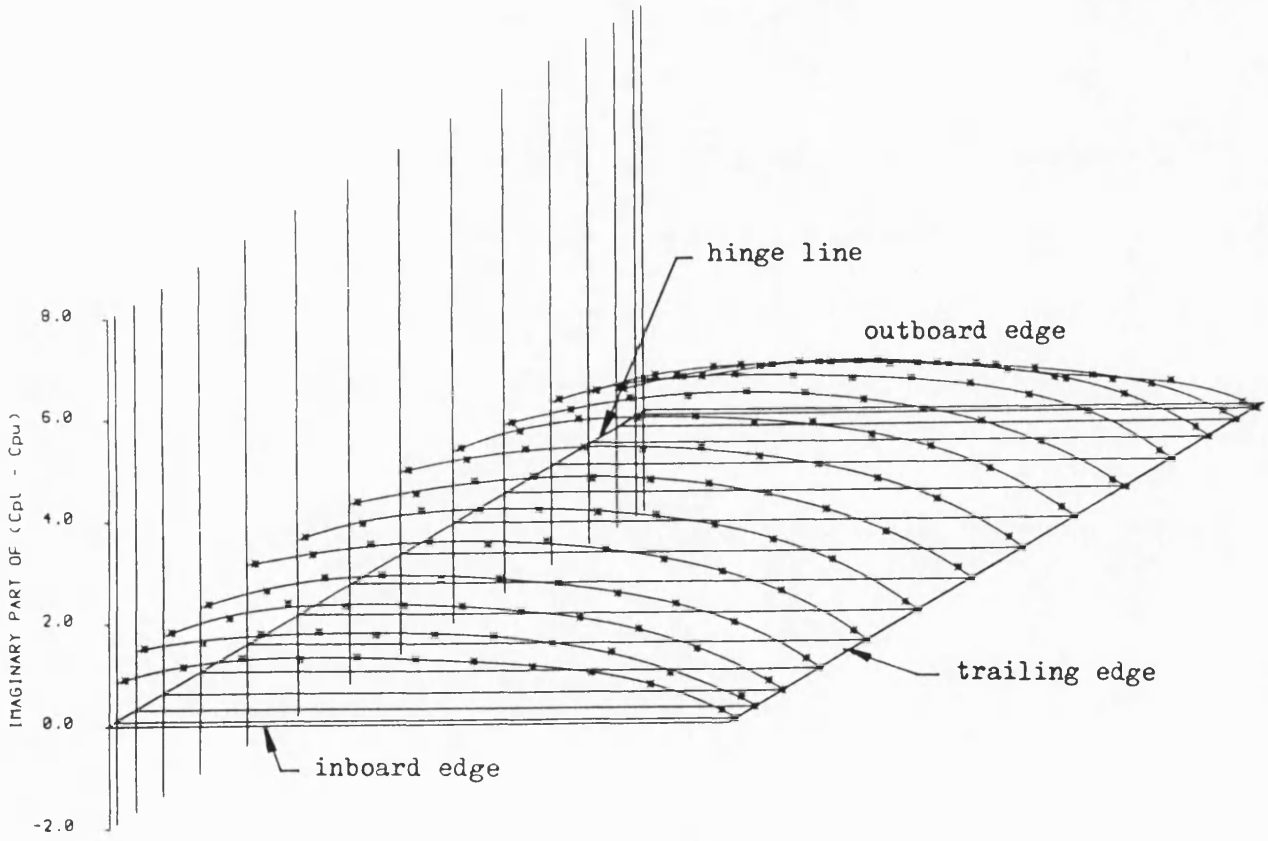

Fig. 6.31 Unsteady pressure loading on control surface ($\omega^* = 1.047$) (V = 40 m/s, gap open, $\alpha = 0^\circ$, $\delta_m = 0^\circ$, $\delta_a = 1^\circ$).

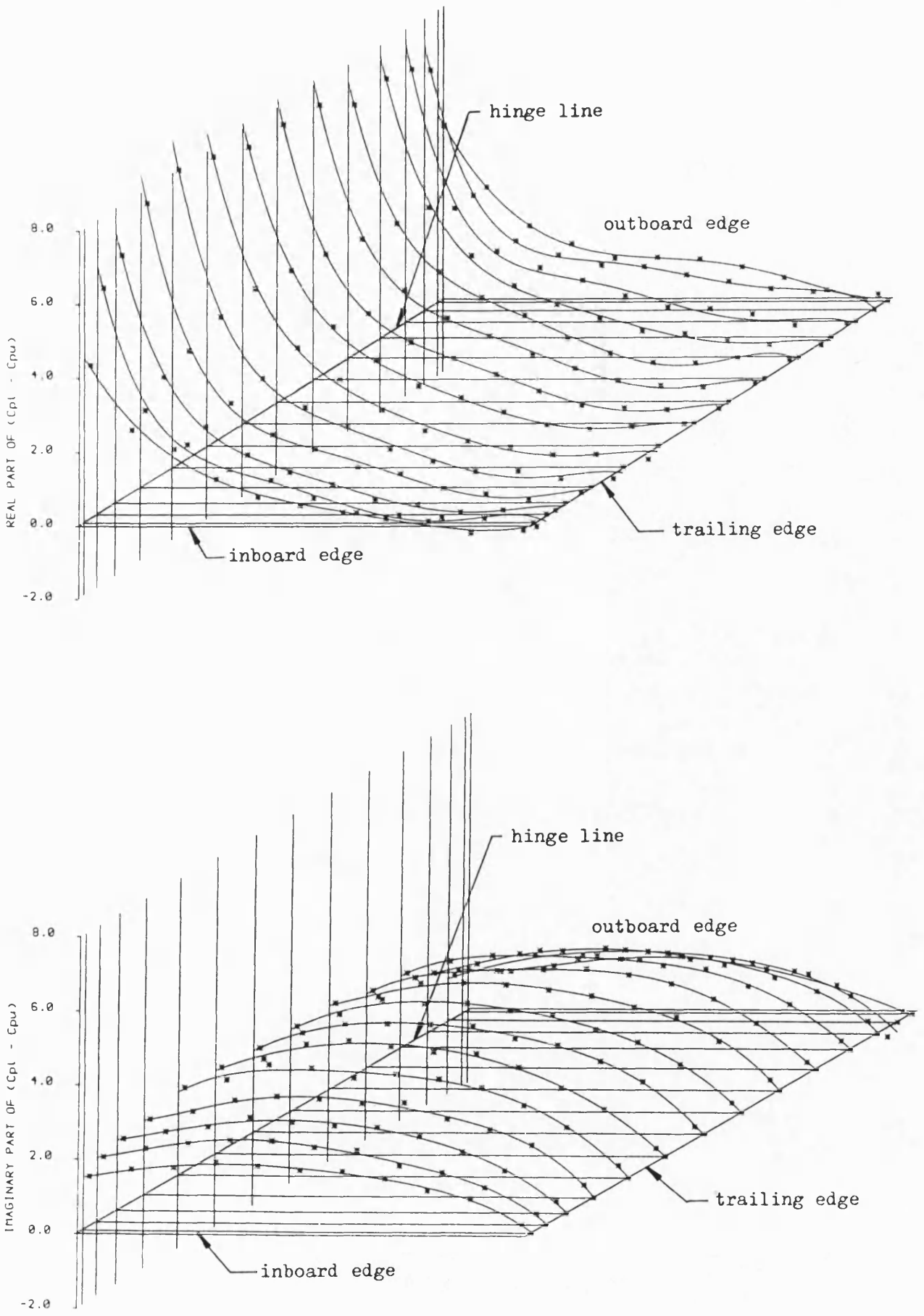

Fig. 6.32 Unsteady pressure loading on control surface ($\omega^* = 1.396$)
(V = 40 m/s, gap open, $\alpha = 0^\circ$, $\delta_m = 0^\circ$, $\delta_a = 1^\circ$)

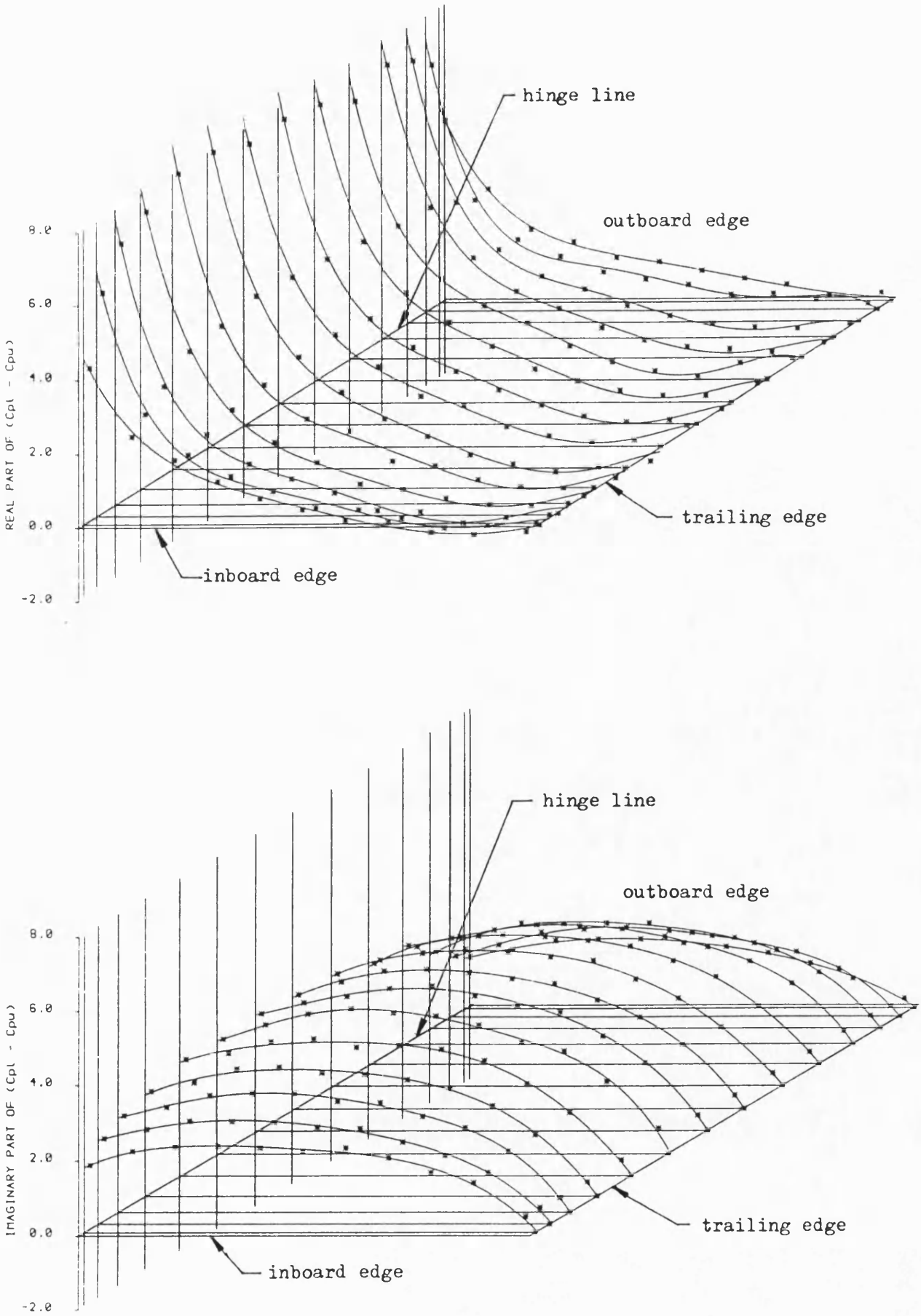

Fig. 6.33 Unsteady pressure loading on control surface ($\omega^* = 1.745$) (V = 40 m/s, gap open, $\alpha = 0^\circ$, $\delta_m = 0^\circ$, $\delta_a = 1^\circ$).

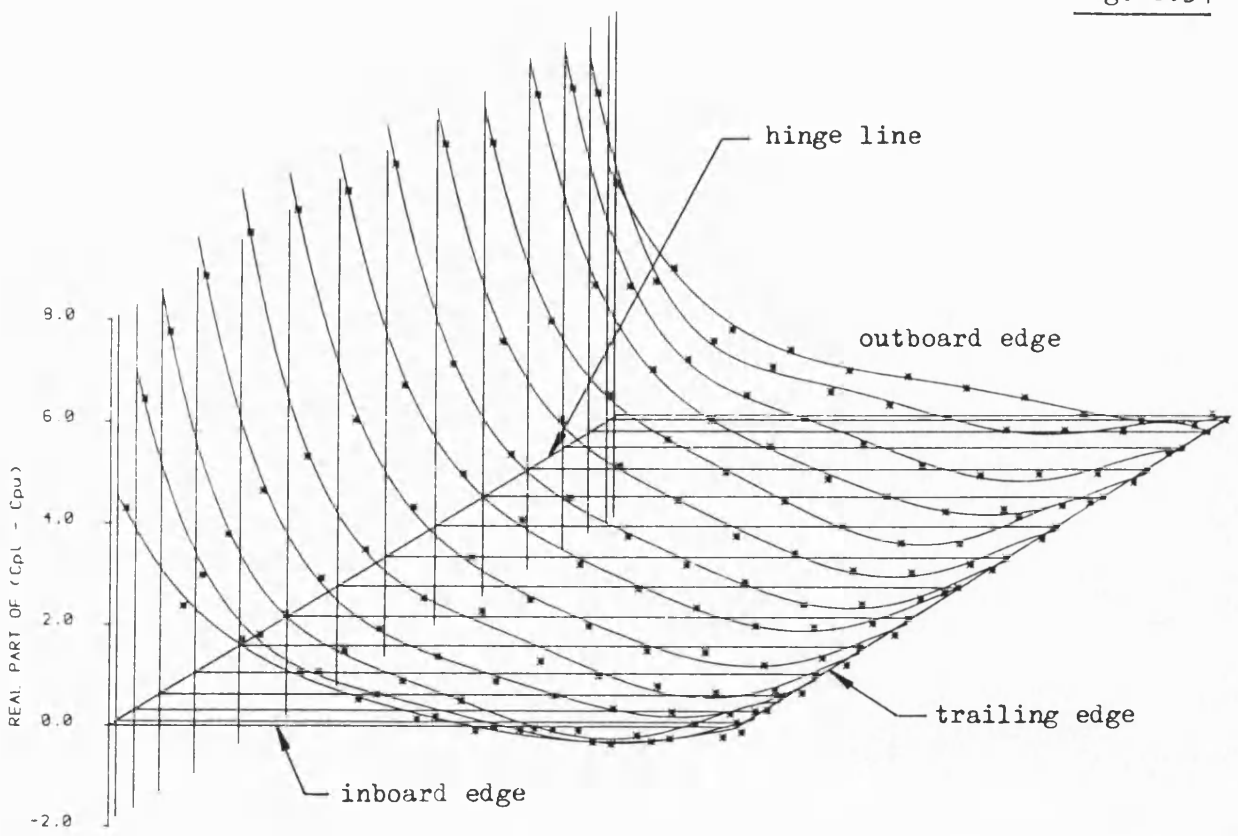

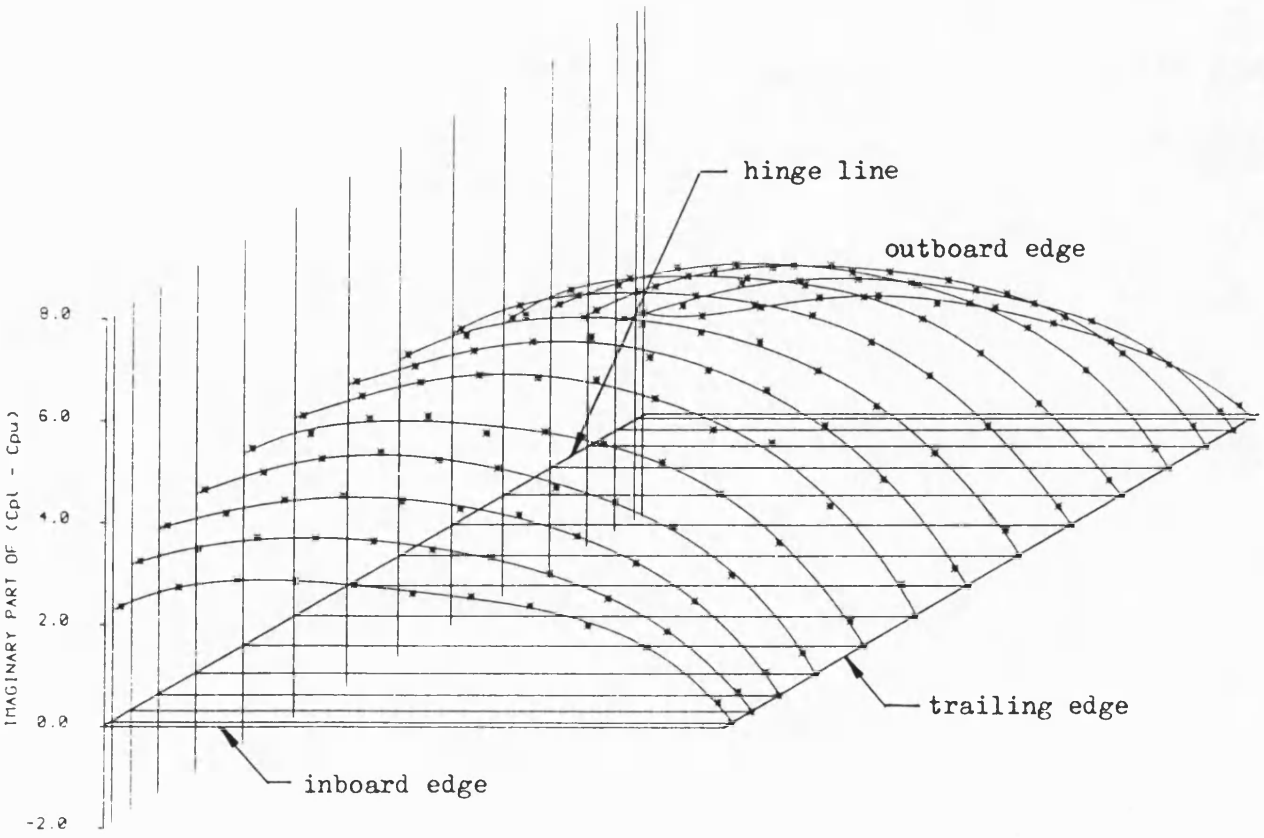

Fig. 6.34 Unsteady pressure loading on control surface ($\omega^* = 2.095$)
(V = 40 m/s, gap open, $\alpha = 0^\circ$, $\delta_m = 0^\circ$, $\delta_a = 1^\circ$)

Fig. 6.35

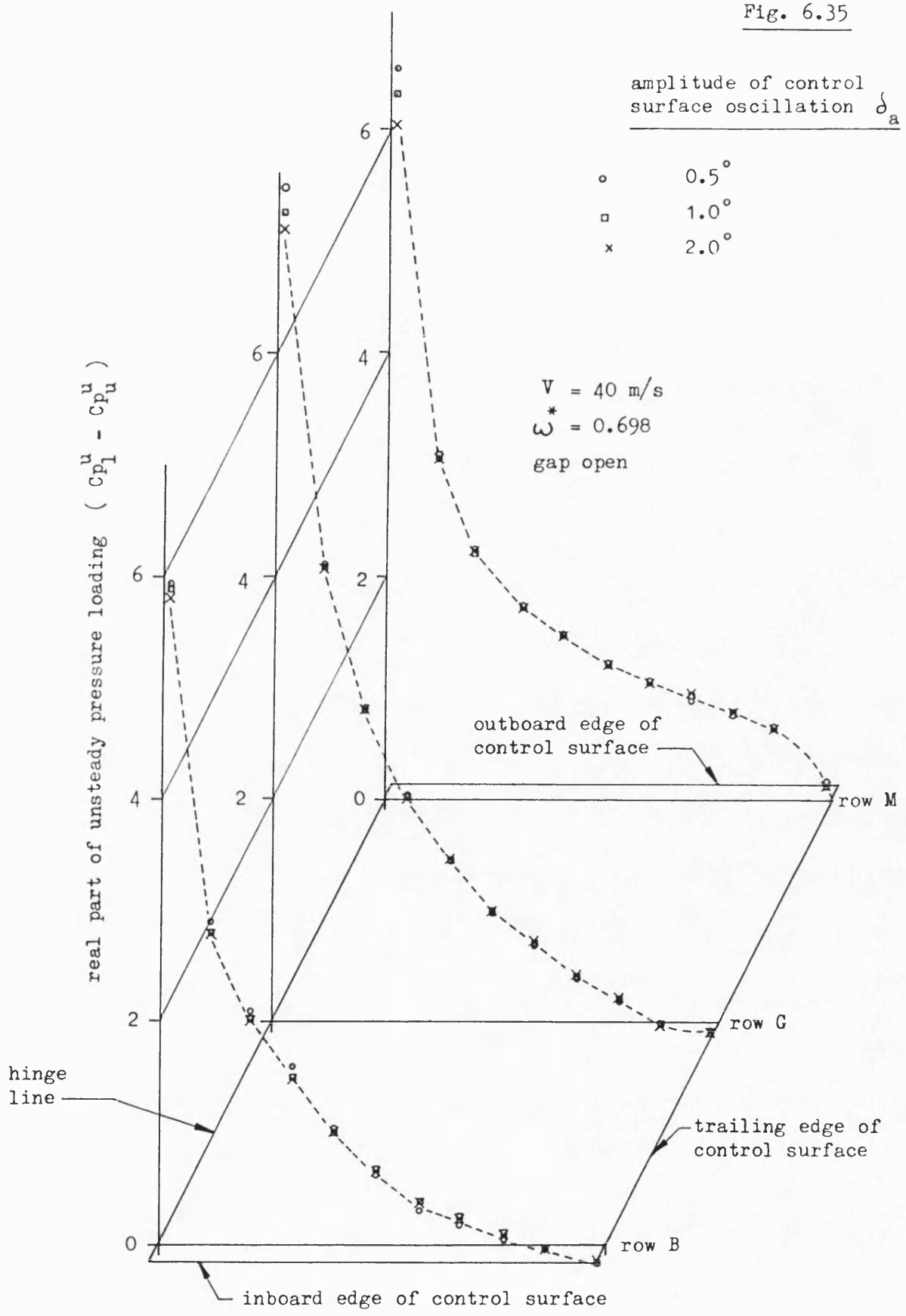

Fig. 6.35 Effect of control surface oscillation amplitude on real part of unsteady pressure loading ($\alpha = 0°, \delta_m = 0°$).

Fig. 6.36

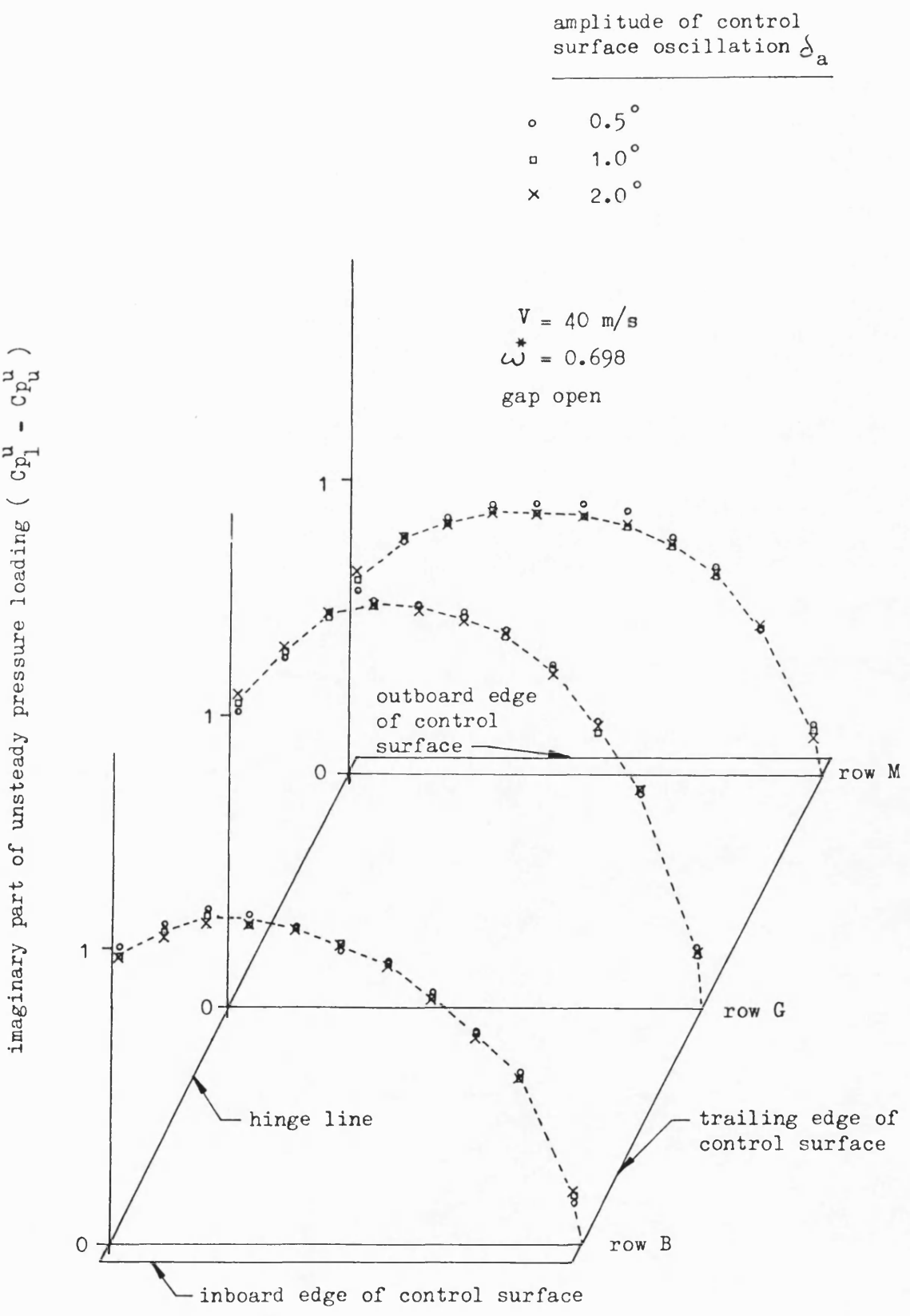

Fig. 6.36 Effect of control surface oscillation amplitude on imaginary part of unsteady pressure loading ($\alpha = 0^\circ$, $\delta_m = 0^\circ$)

Fig. 6.37

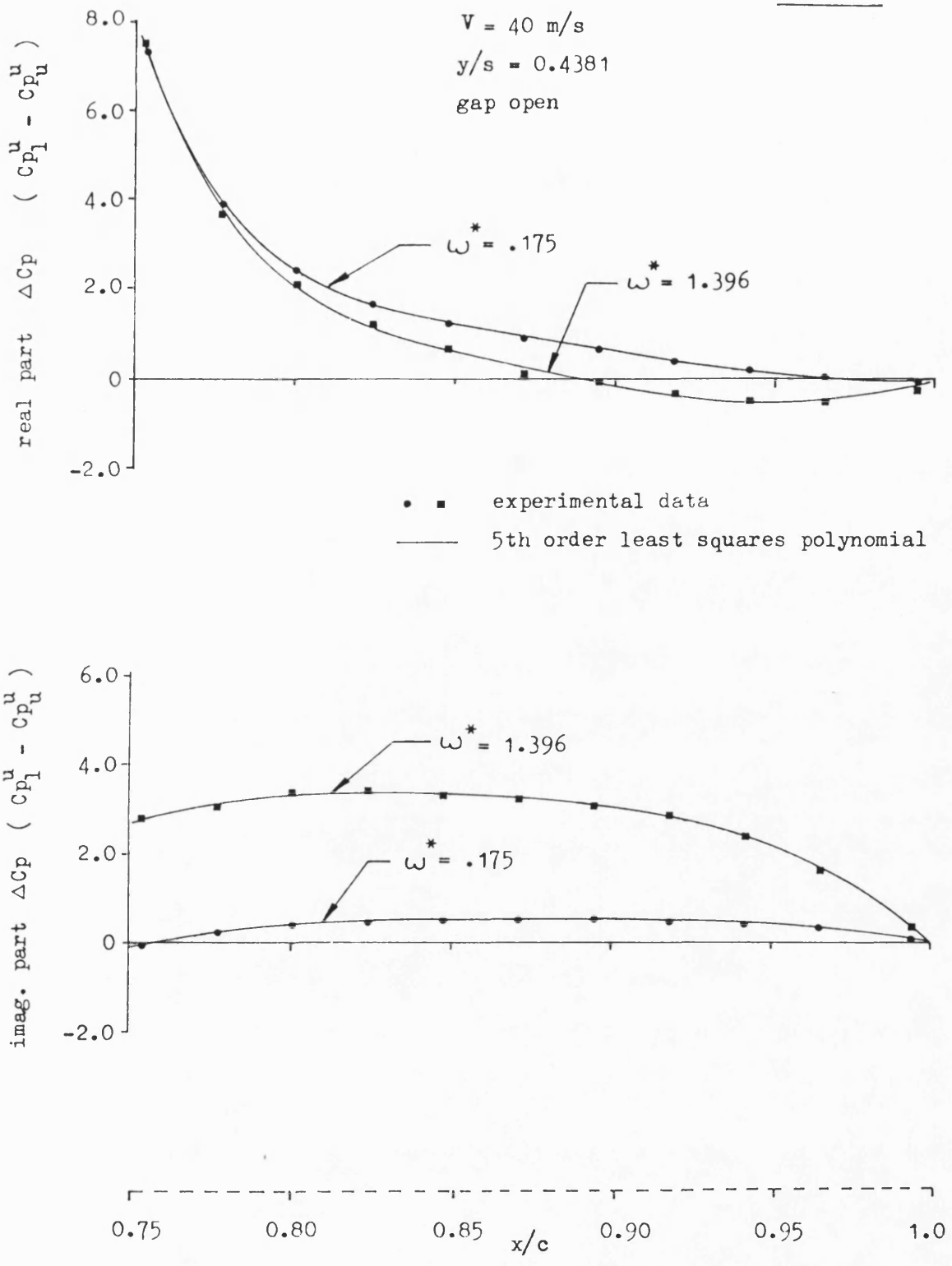

Fig. 6.37 The fit of 5th order least squares polynomials to unsteady pressure data on control surface to simplify integration into hinge moments.

Fig. 6.38

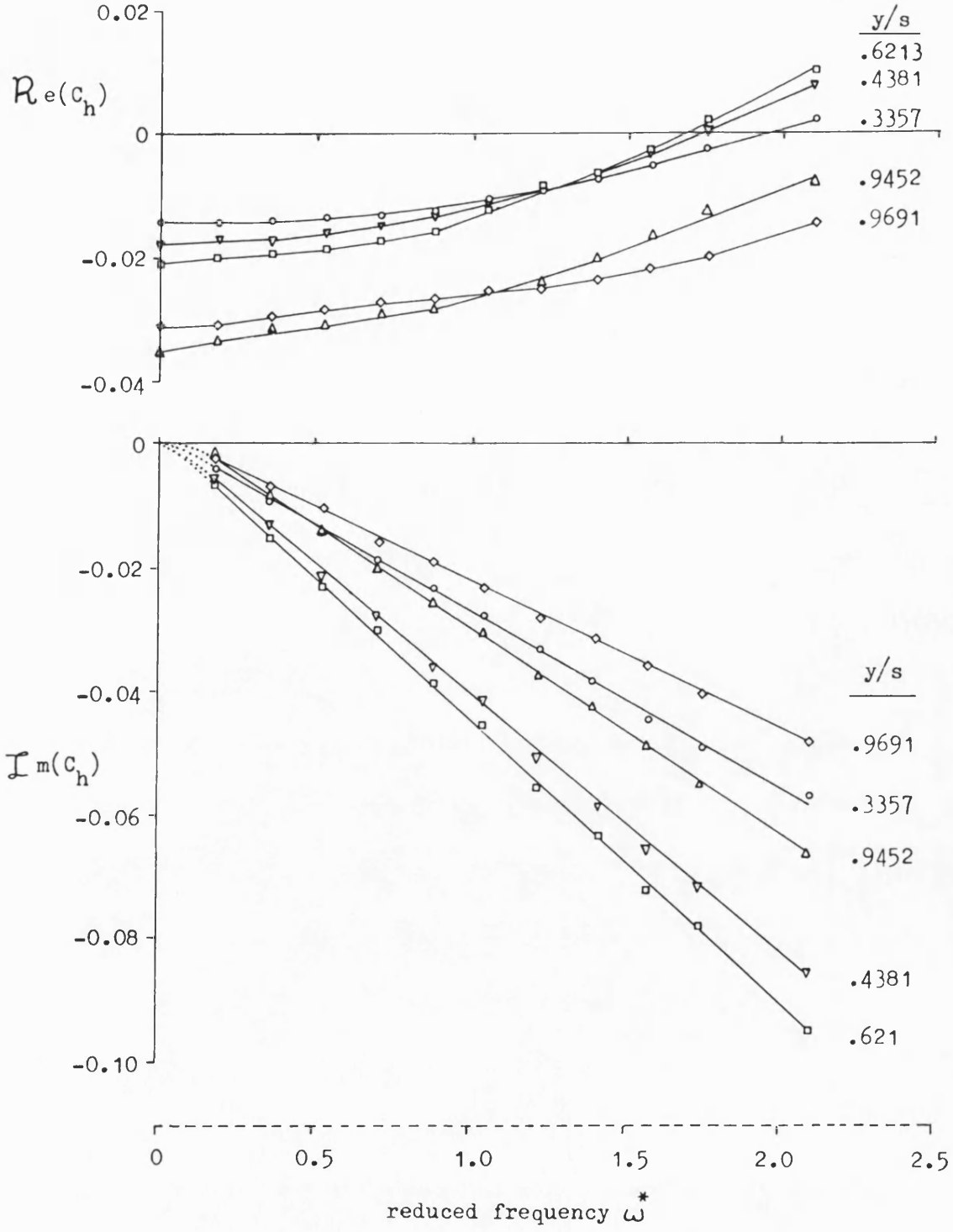

- ○ y/s = .3357, row A
- ▽ y/s = .4381, row D
- □ y/s = .6213, row G
- △ y/s = .9452, row M
- ◇ y/s = .9691, row N

Fig. 6.38 Variation of unsteady section hinge moment coefficient with reduced frequency at selected spanwise locations across control surface (V = 40 m/s, gap open, $\alpha = 0^\circ$, $\delta_m = 0^\circ$, $\delta_a = 1^\circ$).

Fig. 6.39

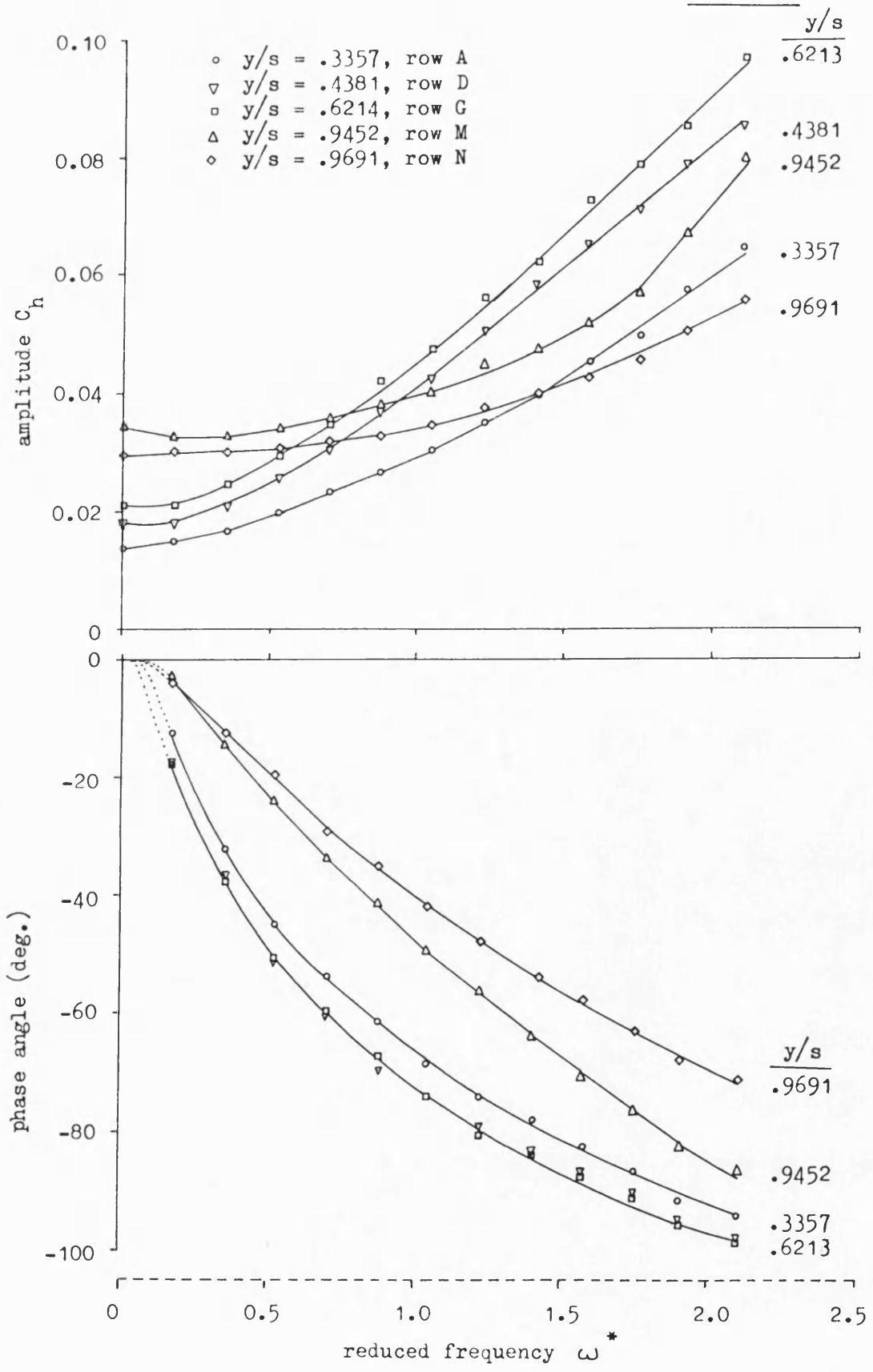

Fig. 6.39 Variation of amplitude and phase of unsteady section hinge moment coefficient with reduced frequency at selected spanwise locations across control surface (V = 40 m/s, gap open, $\alpha = 0^\circ$, $\delta_m = 0^\circ$, $\delta_a = 1^\circ$).

Fig. 6.40

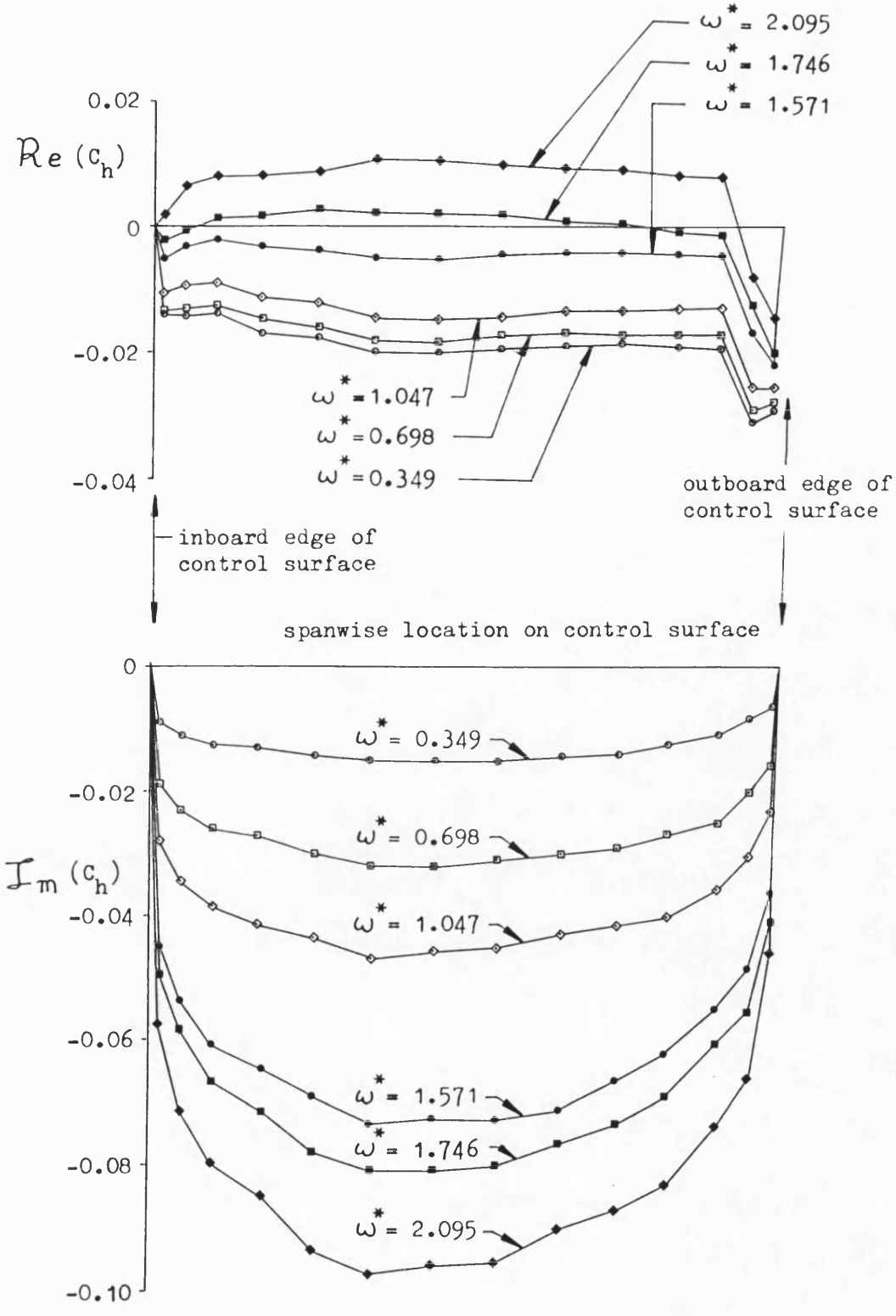

Fig. 6.40 Spanwise distribution of unsteady section hinge moment coefficient at various values of reduced frequency (V = 40 m/s, gap open, $\alpha = 0^\circ$, $\delta_m = 0^\circ$, $\delta_a = 1^\circ$).

Fig. 6.41

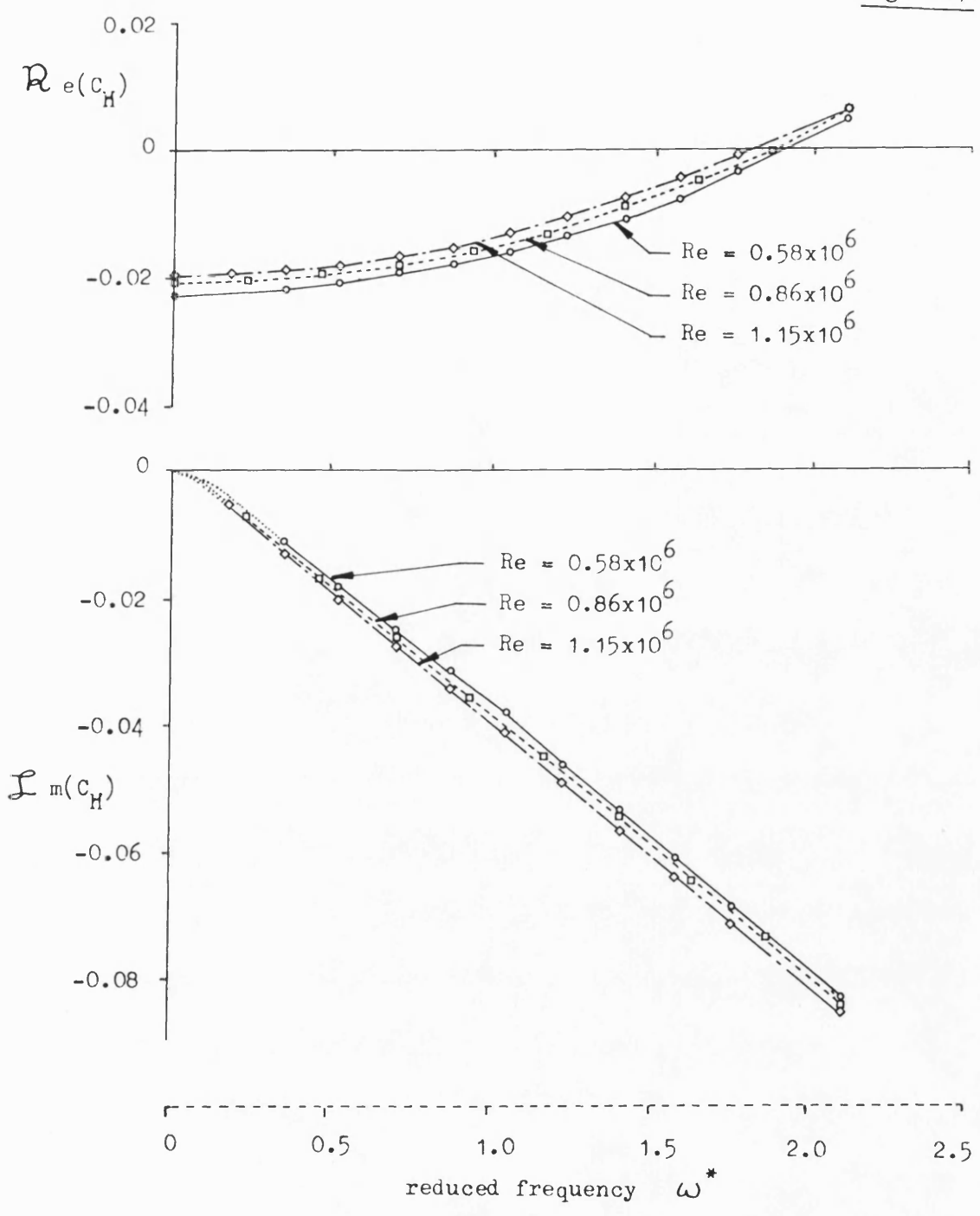

Fig. 6.41 Variation of overall control surface hinge moment with reduced frequency (gap open, $\alpha = 0°$, $\delta_m = 0°$, $\delta_a = 1°$).

Fig. 6.42

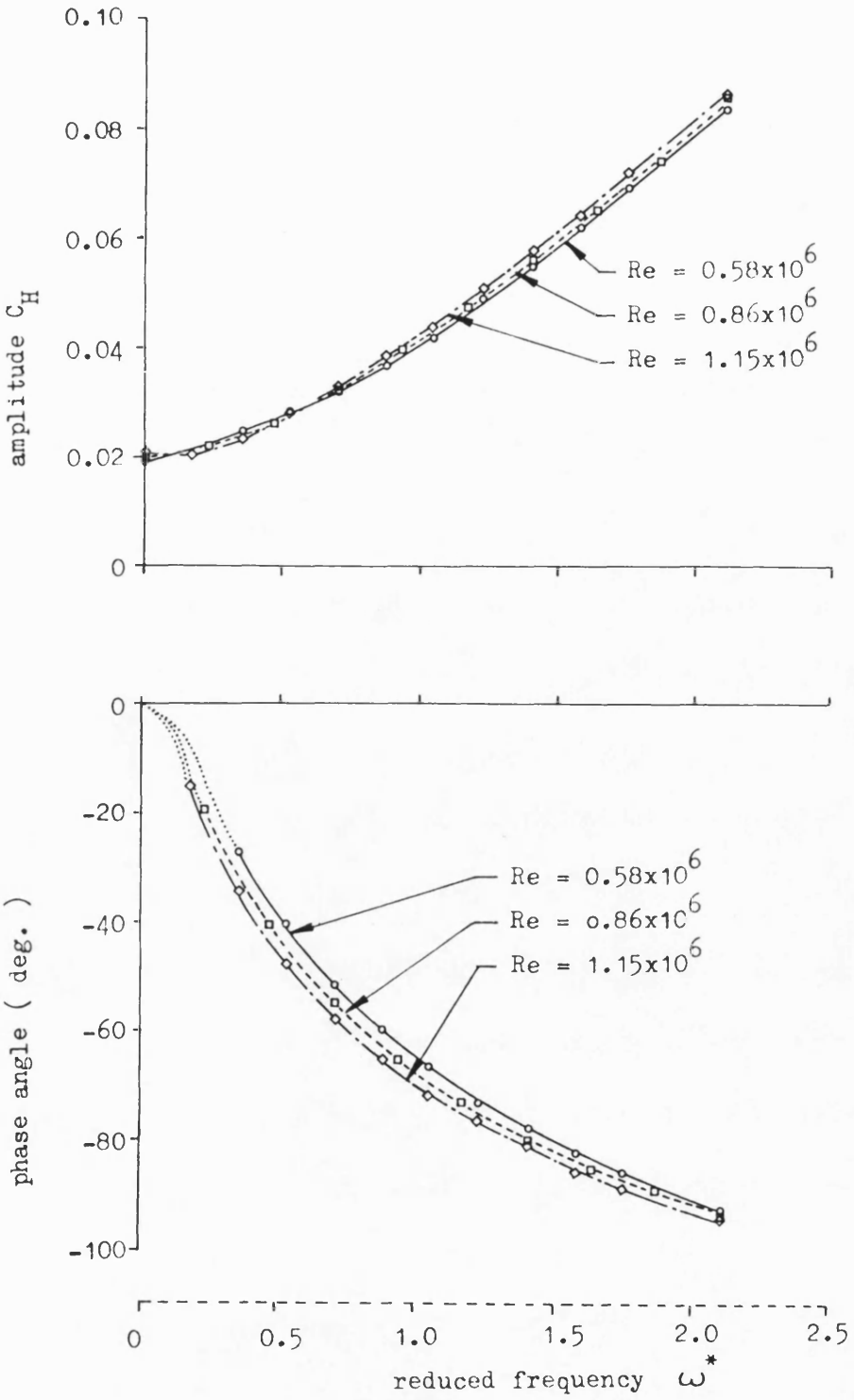

Fig. 6.42 Variation of amplitude and phase of overall control surface hinge moment with reduced frequency (gap open, $\alpha = 0^\circ$, $\delta_m = 0^\circ$, $\delta_a = 1^\circ$).

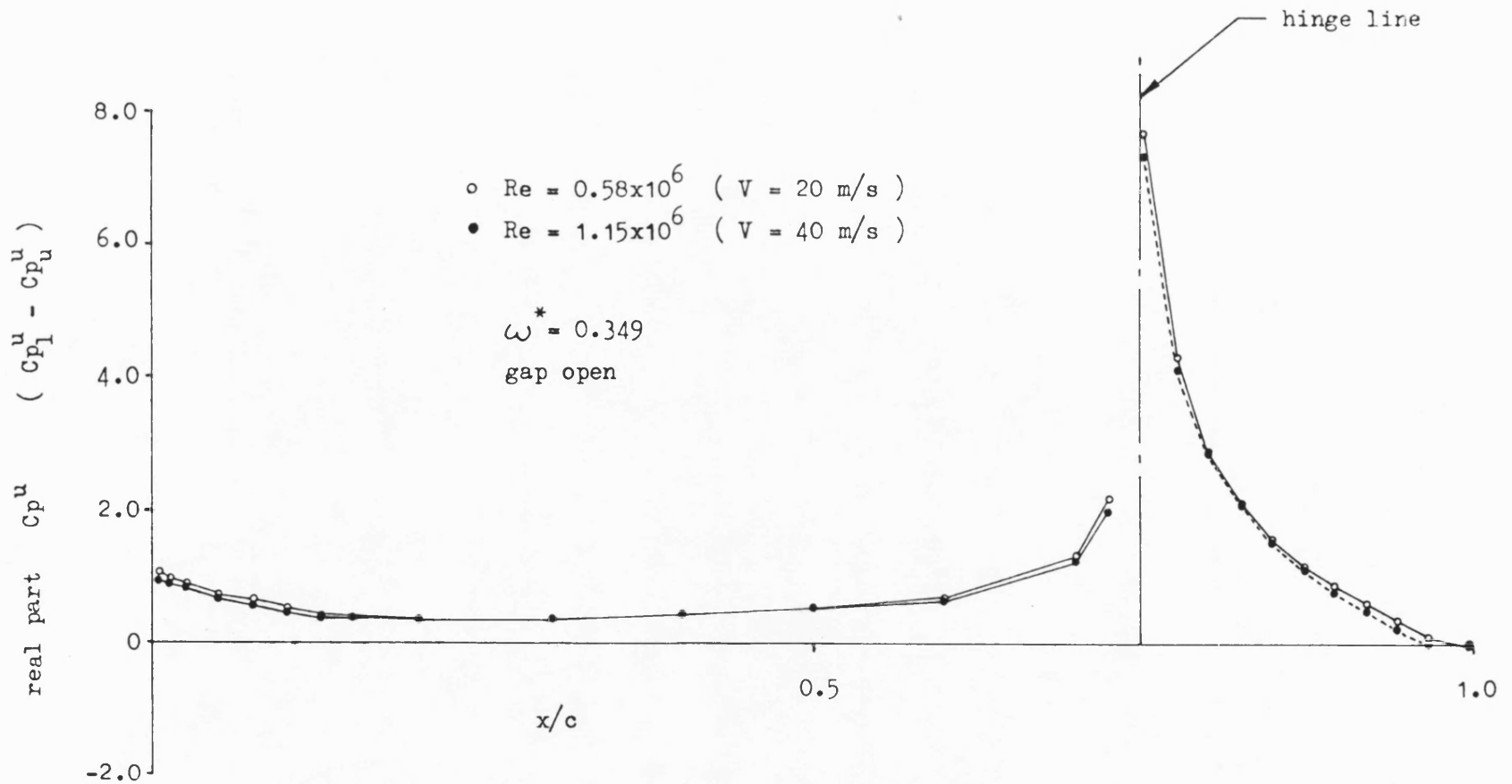

Fig. 6.43

Fig. 6.43 Effect of Reynolds number on real part of unsteady pressure loading at mid semi-span ($y/s = 0.6213, \alpha = 0^\circ, \delta_m = 0^\circ, \delta_a = 1^\circ$).

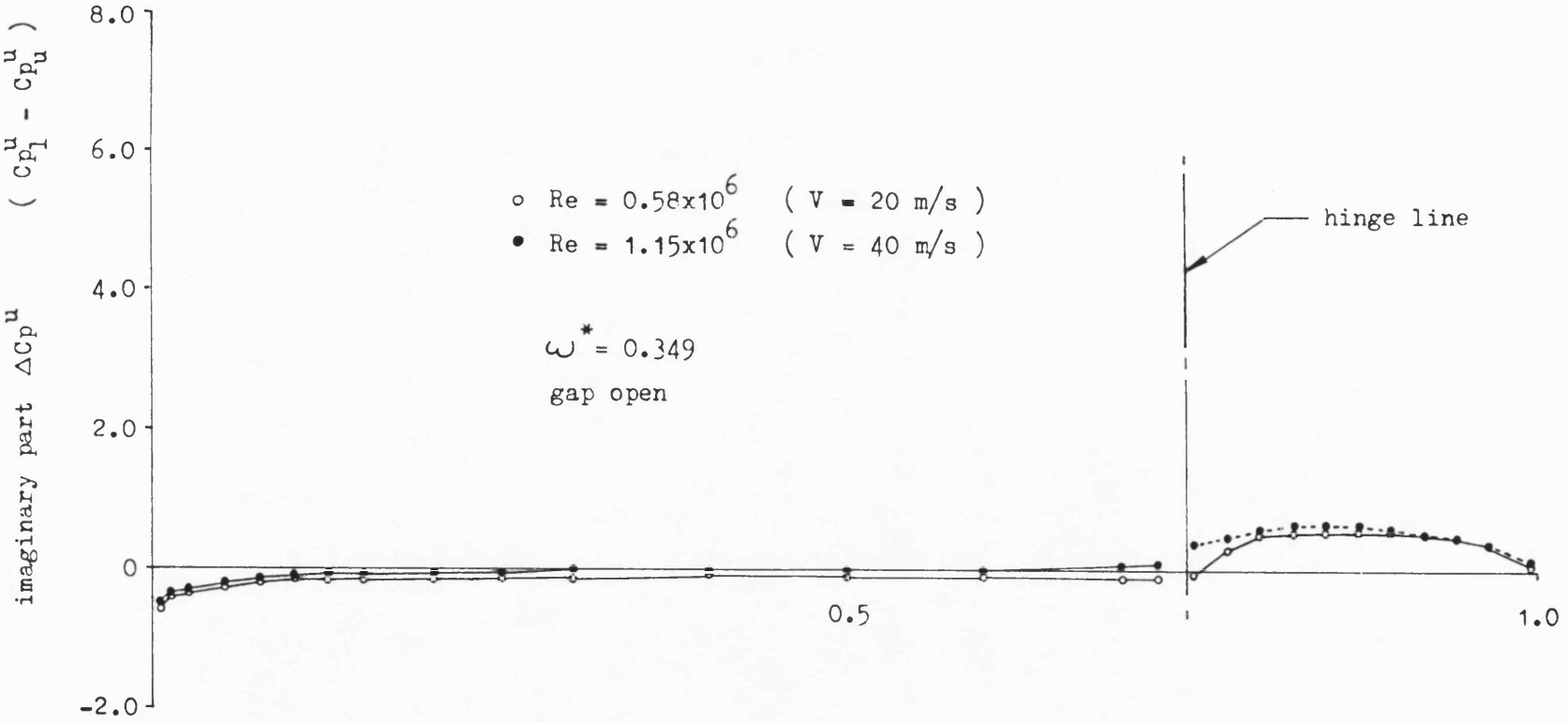

Fig. 6.44 Effect of Reynolds number on imaginary part of unsteady pressure loading at mid semi-span ($y/s = 0.6213$, $\alpha = 0^\circ$, $\delta_m = 0^\circ$, $\delta_a = 1^\circ$).

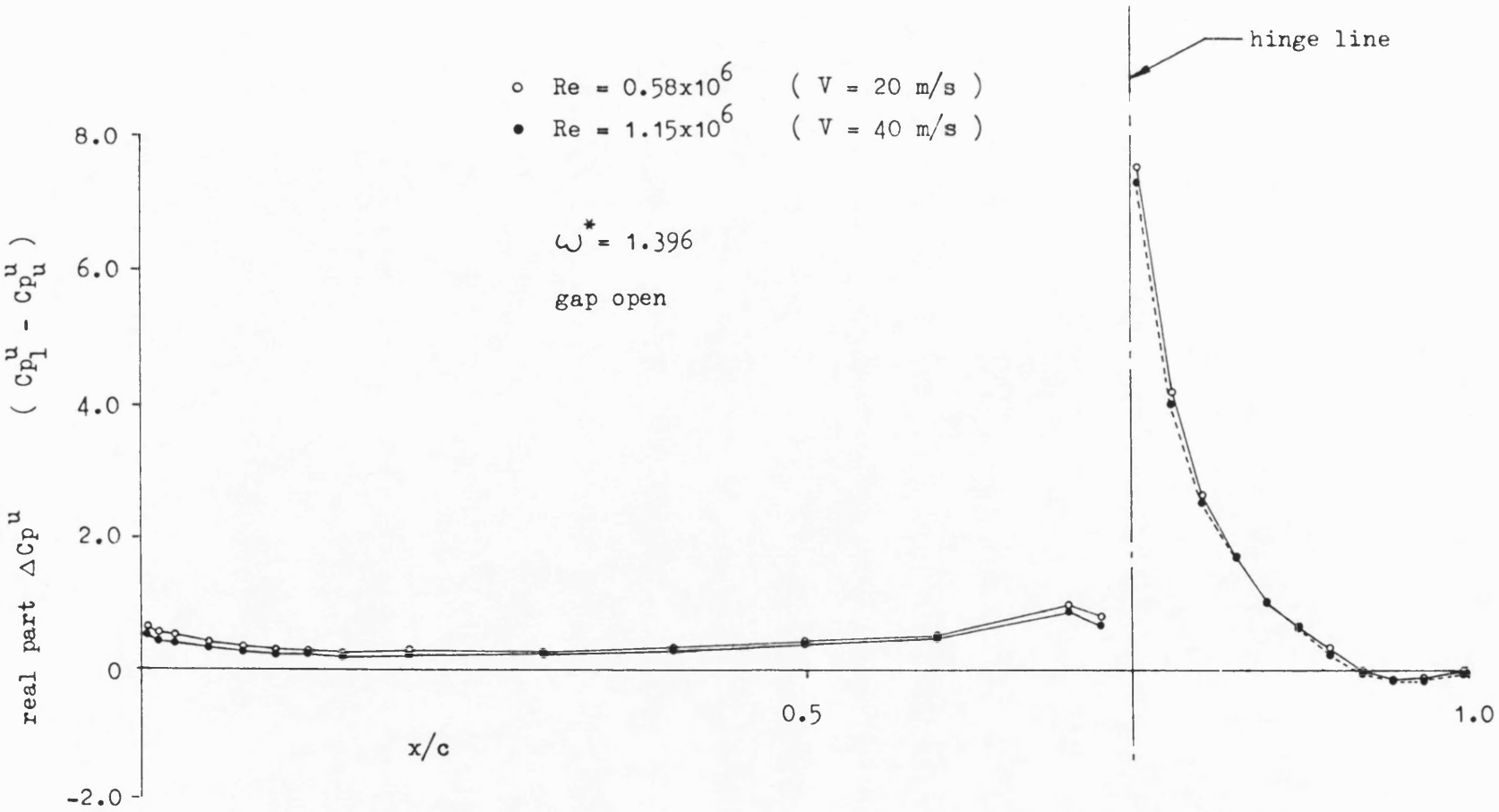

Fig. 6.45

Fig. 6.45 Effect of Reynolds number on real part of unsteady pressure loading at mid semi-span ($y/s = 0.6213$, $\alpha = 0^\circ$, $\delta_m = 0^\circ$, $\delta_a = 1^\circ$)

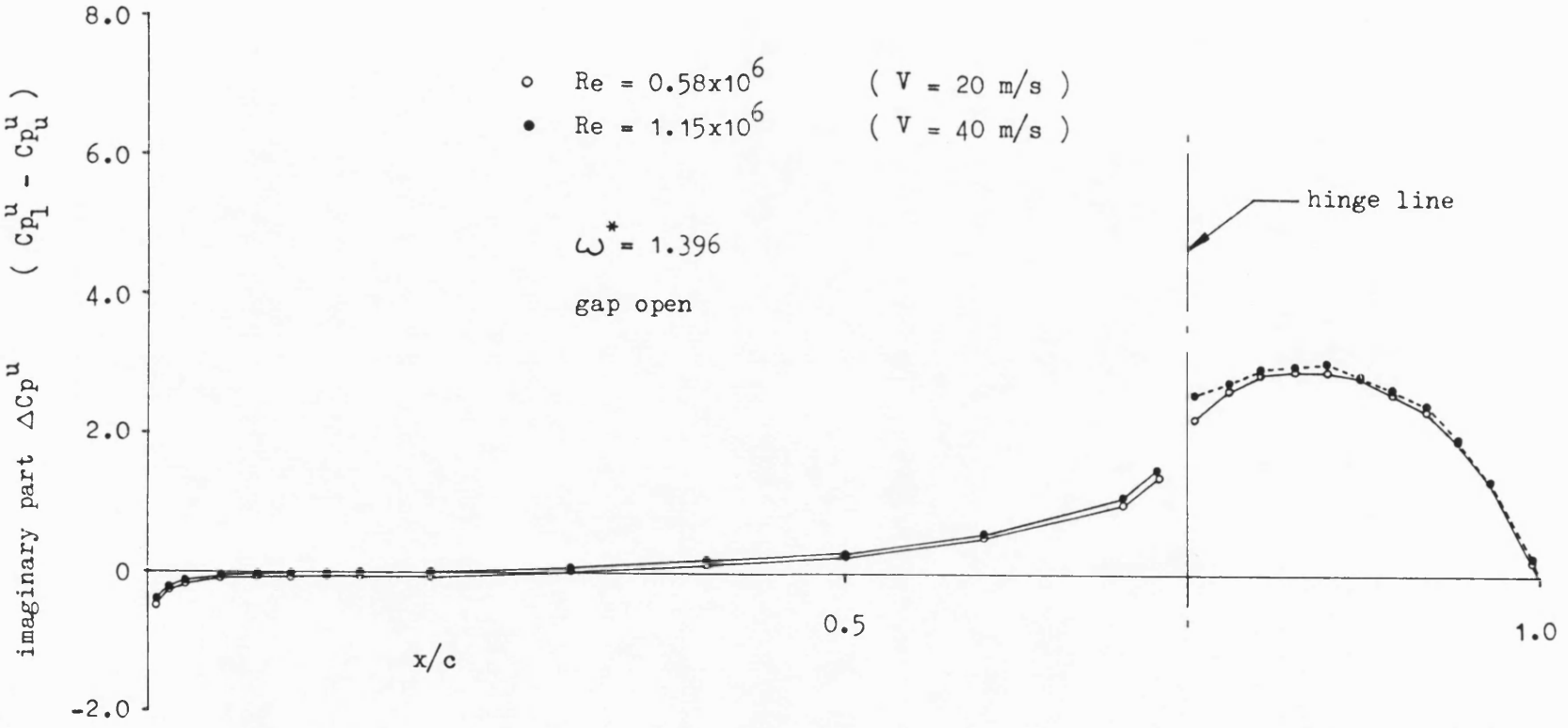

Fig. 6.46 Effect of Reynolds number on imaginary part of unsteady pressure loading at mid semi-span ($y/s = 0.6213$, $\alpha = 0^\circ$, $\delta_m = 0^\circ$, $\delta_a = 1^\circ$).

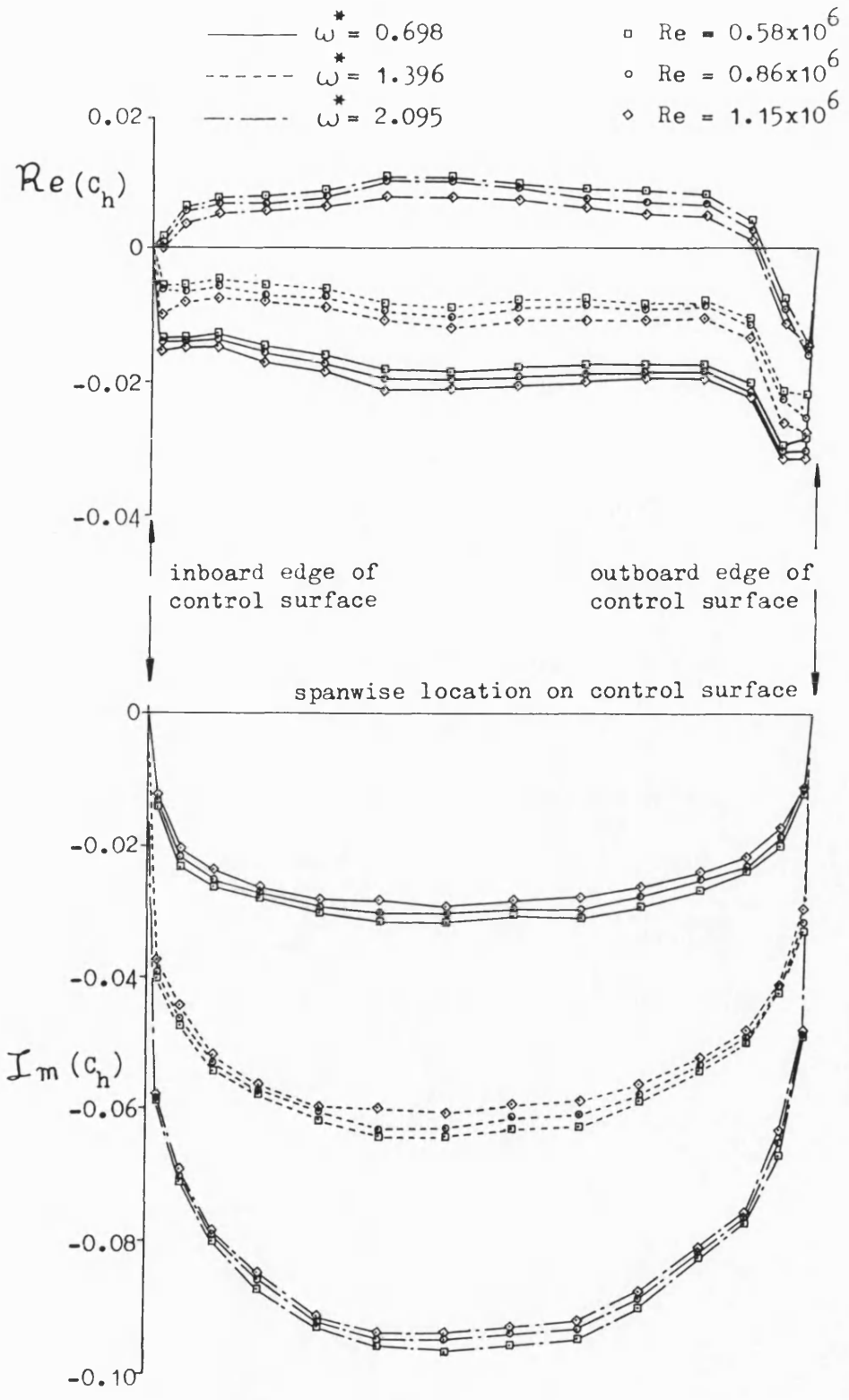

Fig. 6.47 Effect of reynolds number on control surface unsteady hinge moments ($\alpha = 0^\circ, \delta_m = 0^\circ, \delta_a = 1^\circ$; gap open).

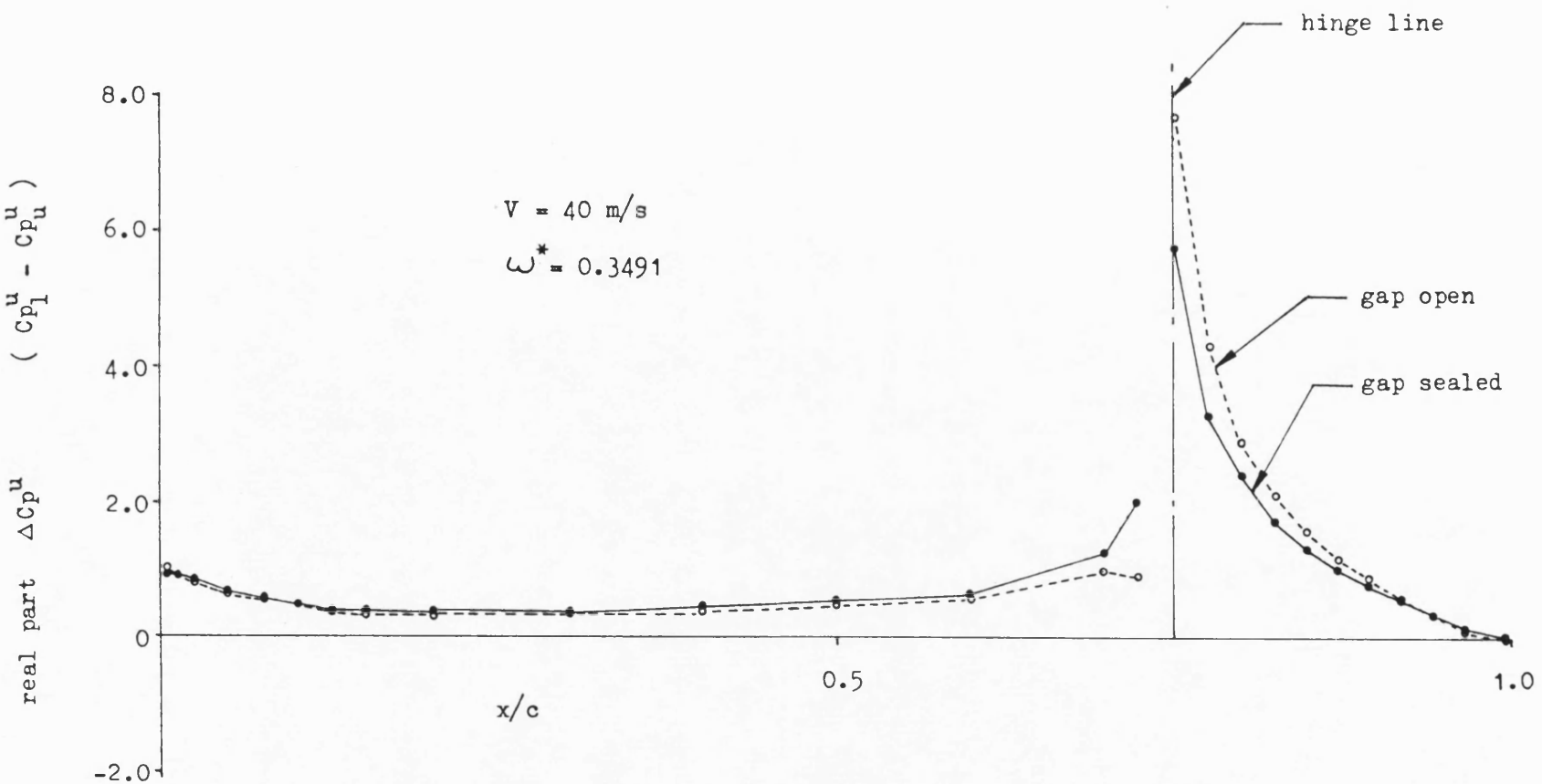

Fig. 6.48 Effect of sealing control surface gap on real part of unsteady pressure loading at mid semi-span (y/s = 0.6213, $\alpha = 0^\circ$, $\delta_m = 0^\circ$, $\delta_a = 1^\circ$)

Fig. 6.48

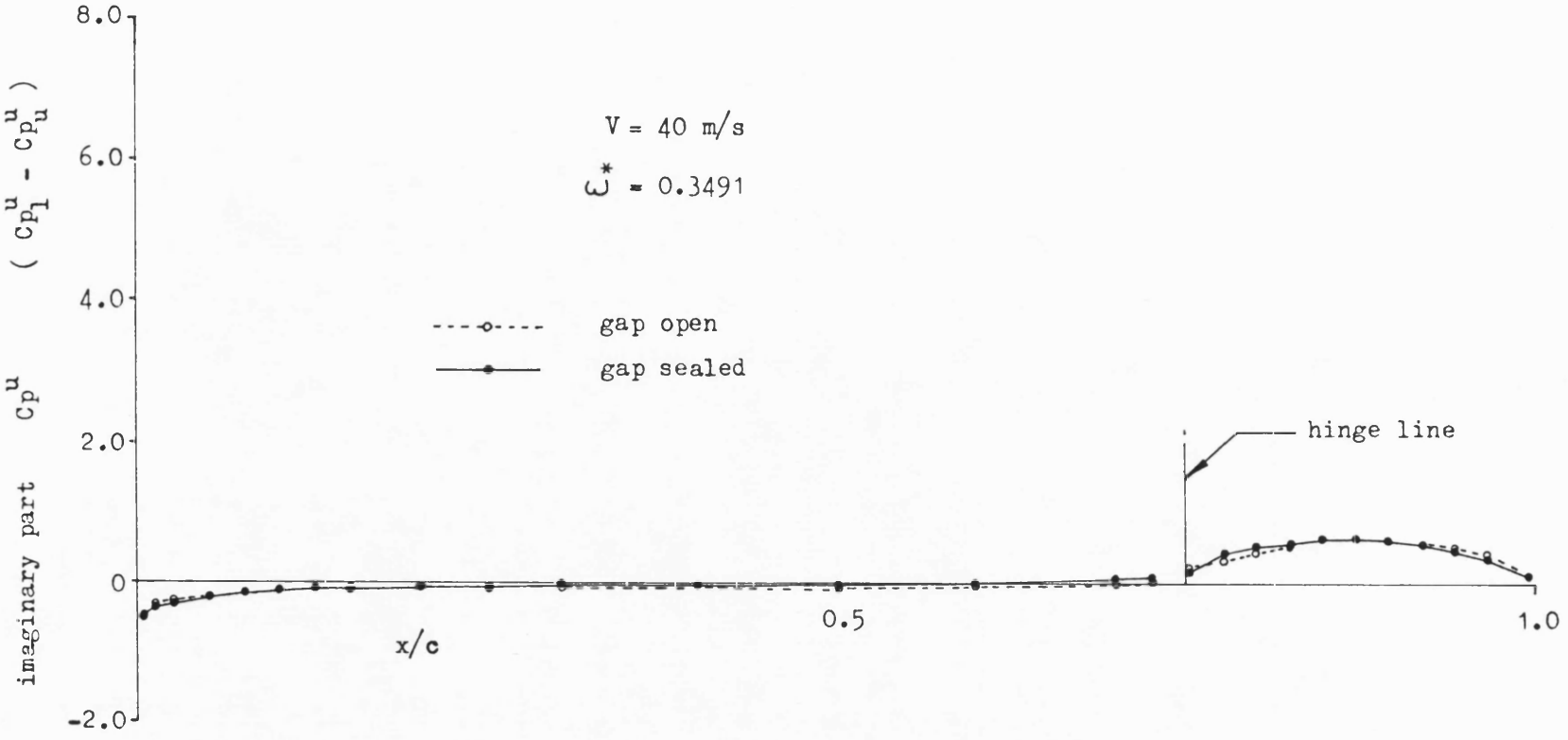

Fig. 6.49 Effect of sealing control surface gap on imaginary part of unsteady pressure loading at mid semi-span (y/s = 0.6213, α = 0°, δ_m = 0°, δ_a = 1°).

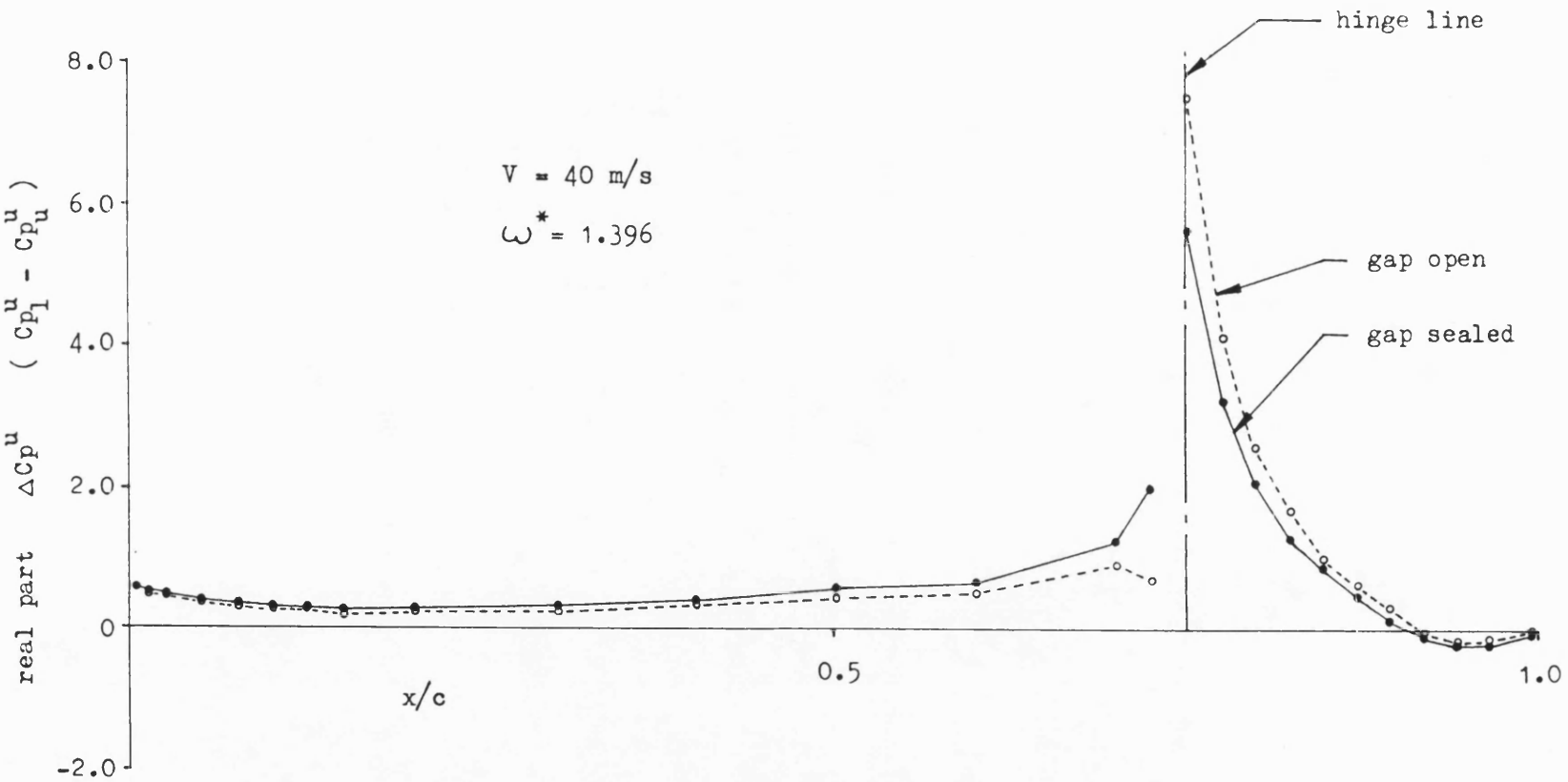

Fig. 6.50 Effect of sealing control surface gap on real part of unsteady pressure loading at mid semi-span (y/s = 0.6213, $\alpha = 0^\circ$, $\delta_m = 0^\circ$, $\delta_a = 1^\circ$).

Fig. 6.50

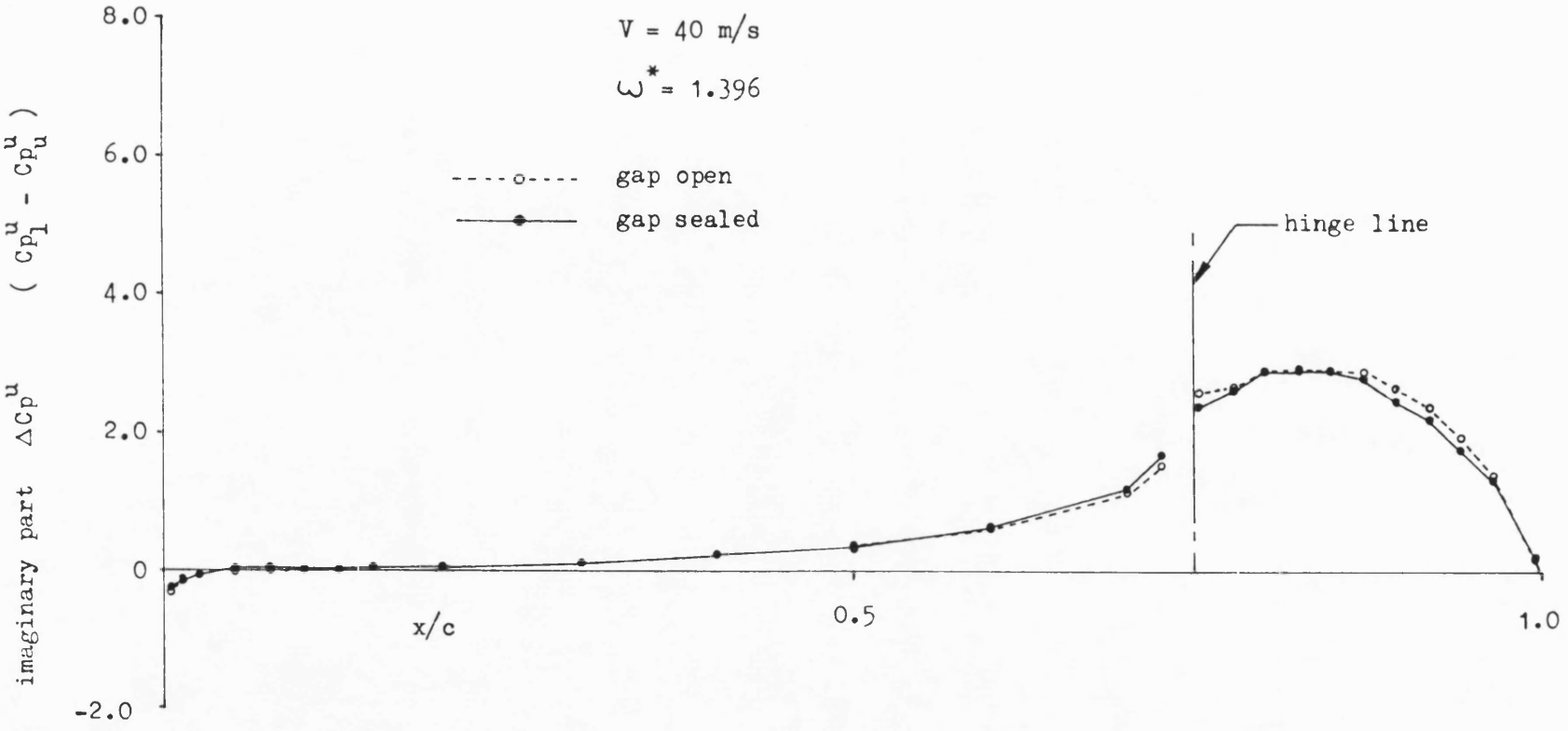

Fig. 6.51 Effect of sealing control surface gap on imaginary part of unsteady pressure loadings at mid semi-span (y/s = 0.6213, $\alpha = 0^\circ$, $\delta_m = 0^\circ$, $\delta_a = 1^\circ$).

Fig. 6.52

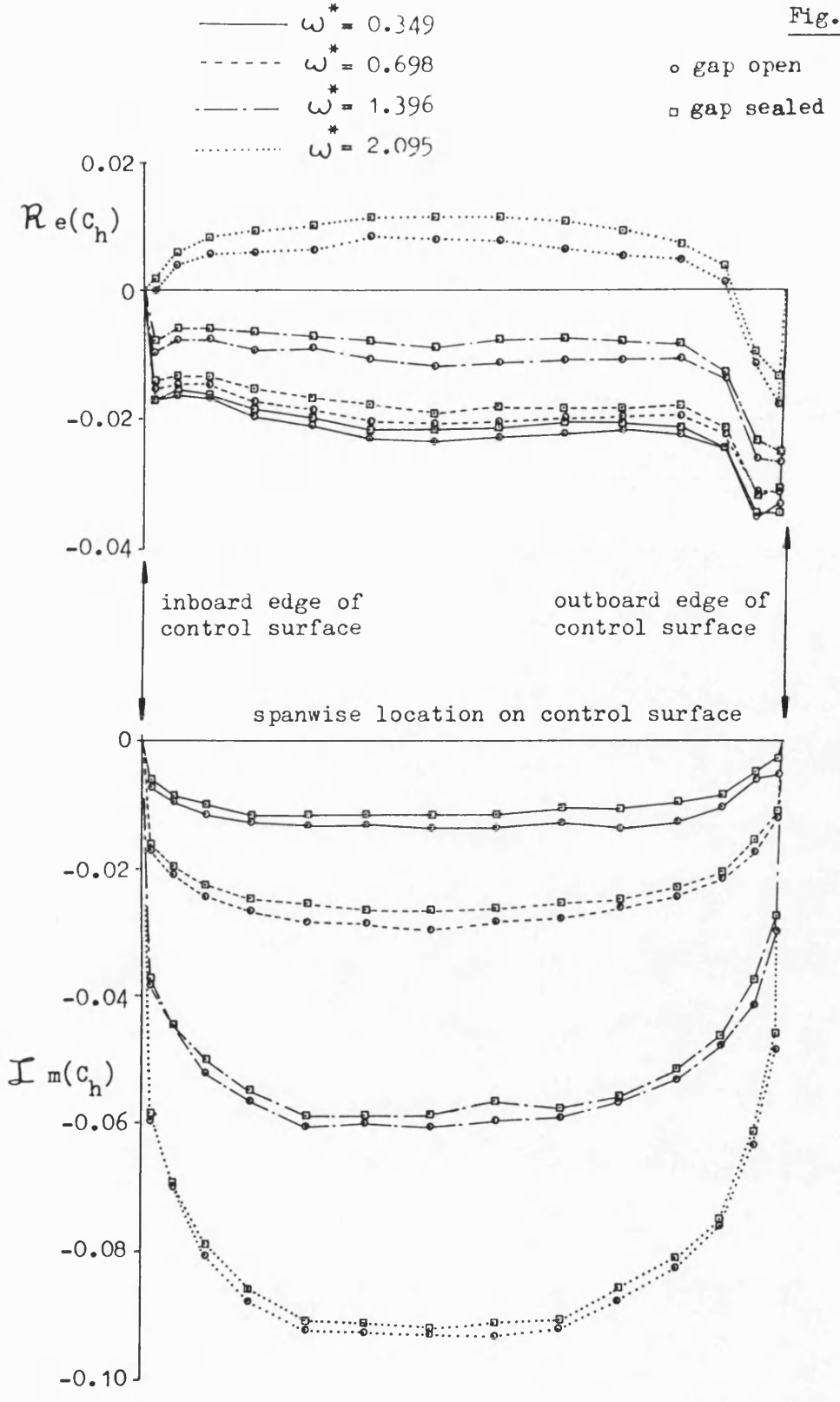

Fig. 6.52 Effect of sealing gap on control surface unsteady hinge moment coefficients (V = 40 m/s, $\alpha = 0^\circ$, $\delta_m = 0^\circ$, $\delta_a = 1^\circ$).

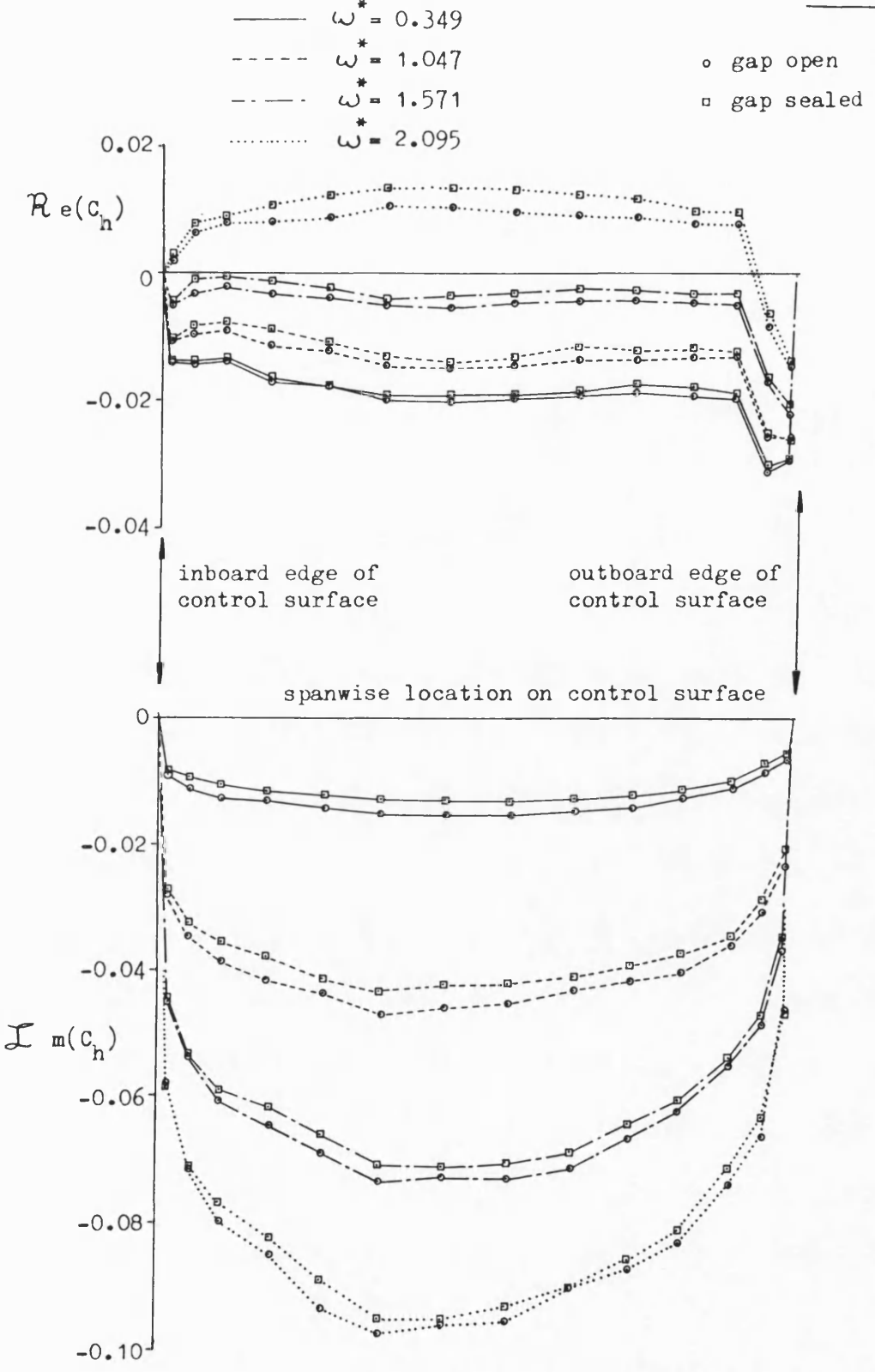

Fig. 6.53 Effect of sealing gap on control surface unsteady hinge moment coefficients (V = 40 m/s, $\alpha = 0^\circ$, $\delta_m = 0^\circ$, $\delta_a = 1^\circ$)

Fig. 6.54

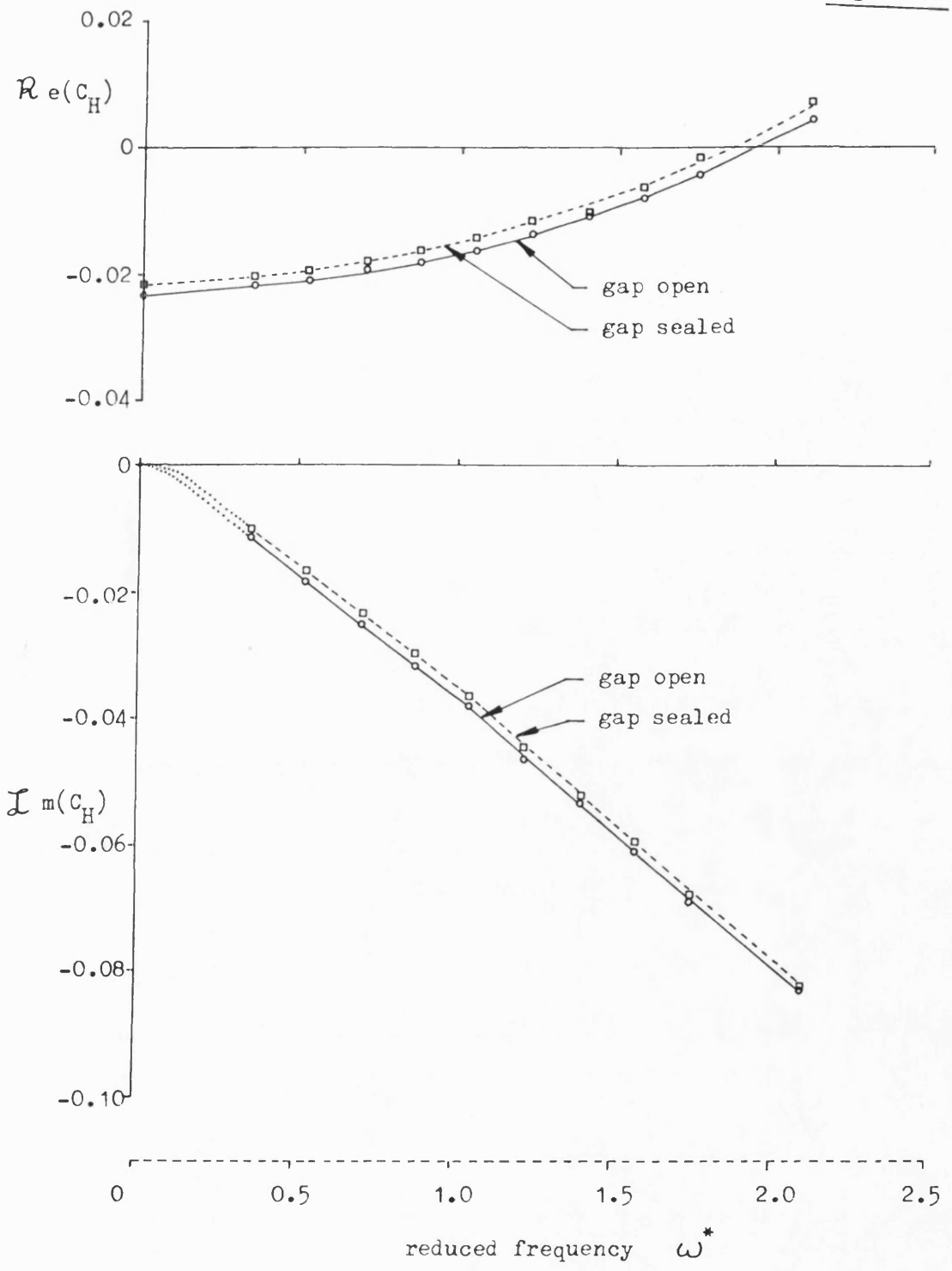

Fig. 6.54 Effect of sealing gap on variation of overall control surface hinge moment with reduced frequency (Re = 0.58×10^6, $\alpha = 0^\circ$, $\delta_m = 0^\circ$, $\delta_a = 1^\circ$).

Fig. 6.55

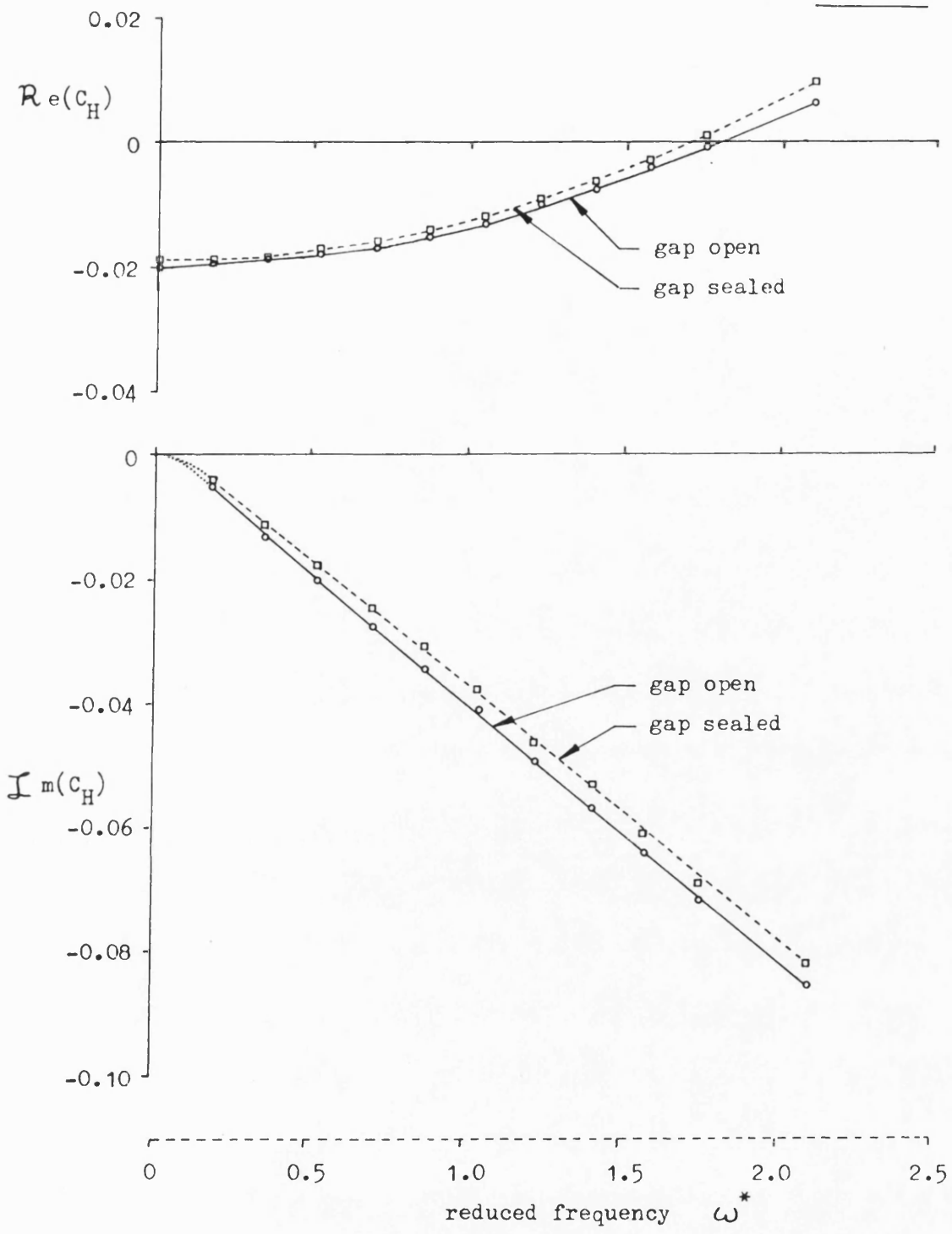

Fig. 6.55 Effect of sealing gap on variation of overall control surface hinge moment with reduced frequency (Re = 1.15×10^6, $\alpha = 0^\circ$, $\delta_m = 0^\circ$, $\delta_a = 1^\circ$).

Fig. 6.56

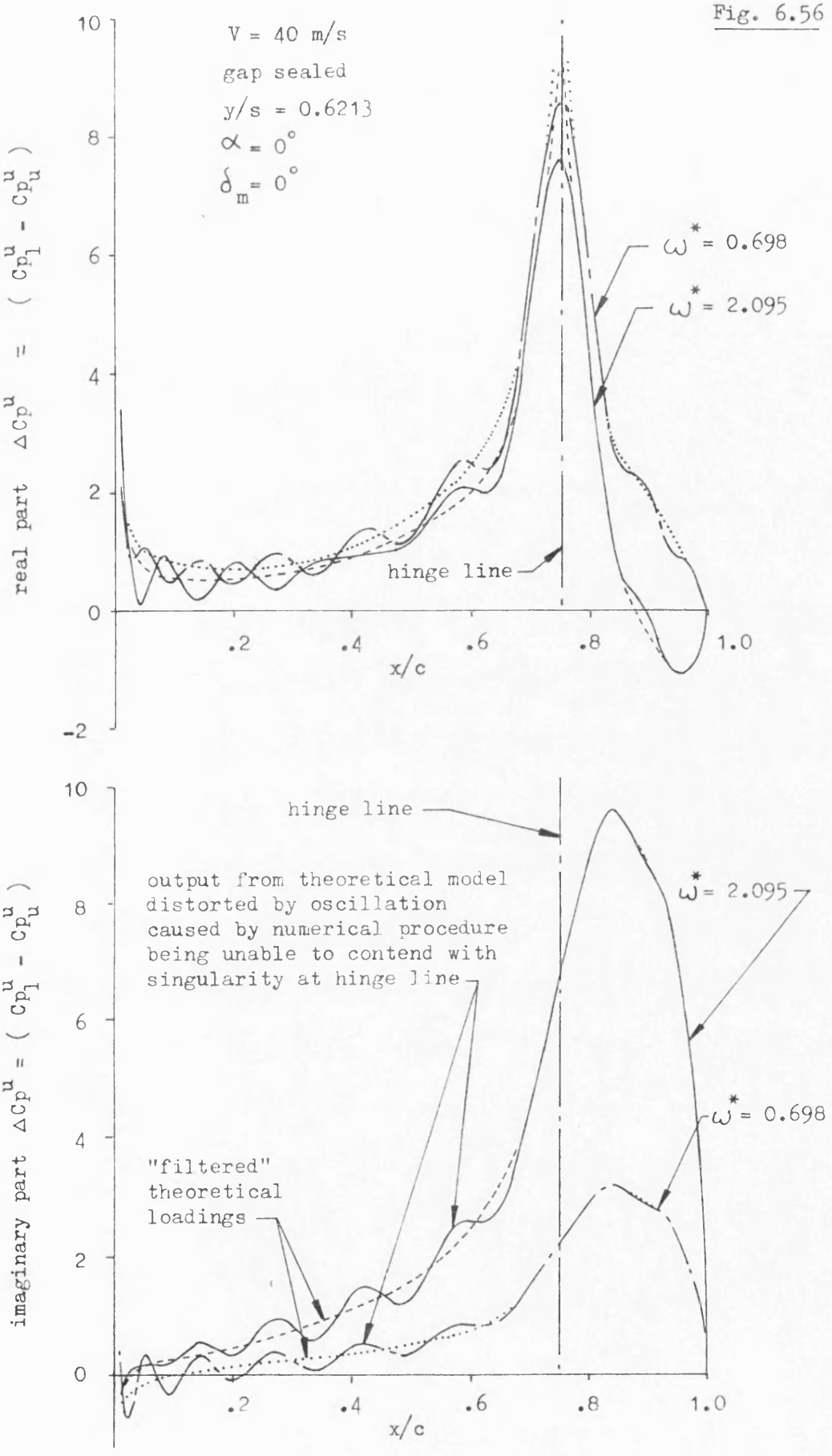

Fig. 6.56 Result of "filtering" unsteady pressue loadings predicted by theoretical model to remove distortion caused by shortfalls in the numerical procedure.

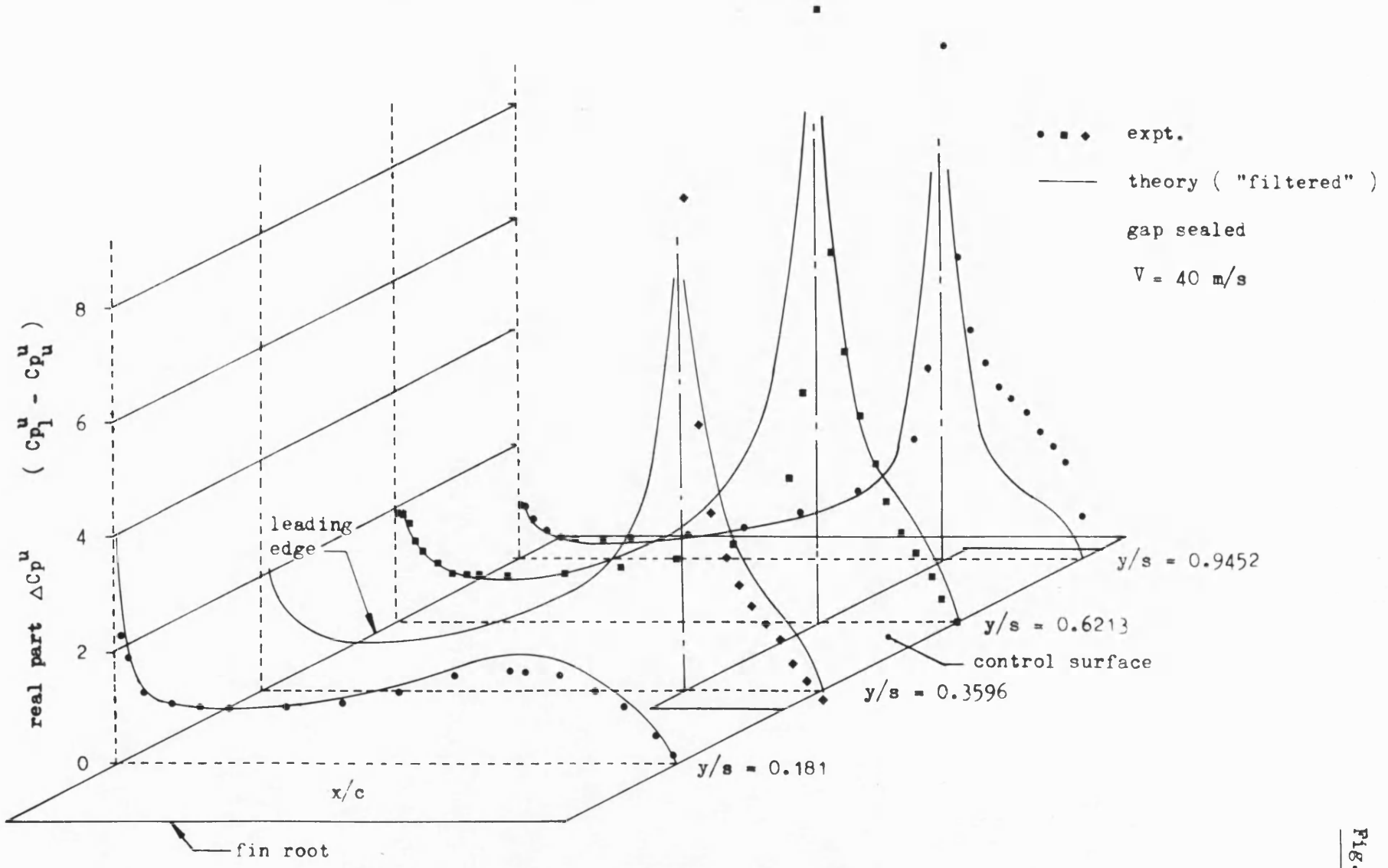

Fig. 6.57

Fig. 6.57 Comparison of theoretical and experimental quasi- steady pressure loadings on fin and control surface $\omega^* = 0$ ($\alpha = 0^\circ$, $\delta_m = 0^\circ$, $\delta_a = 1^\circ$).

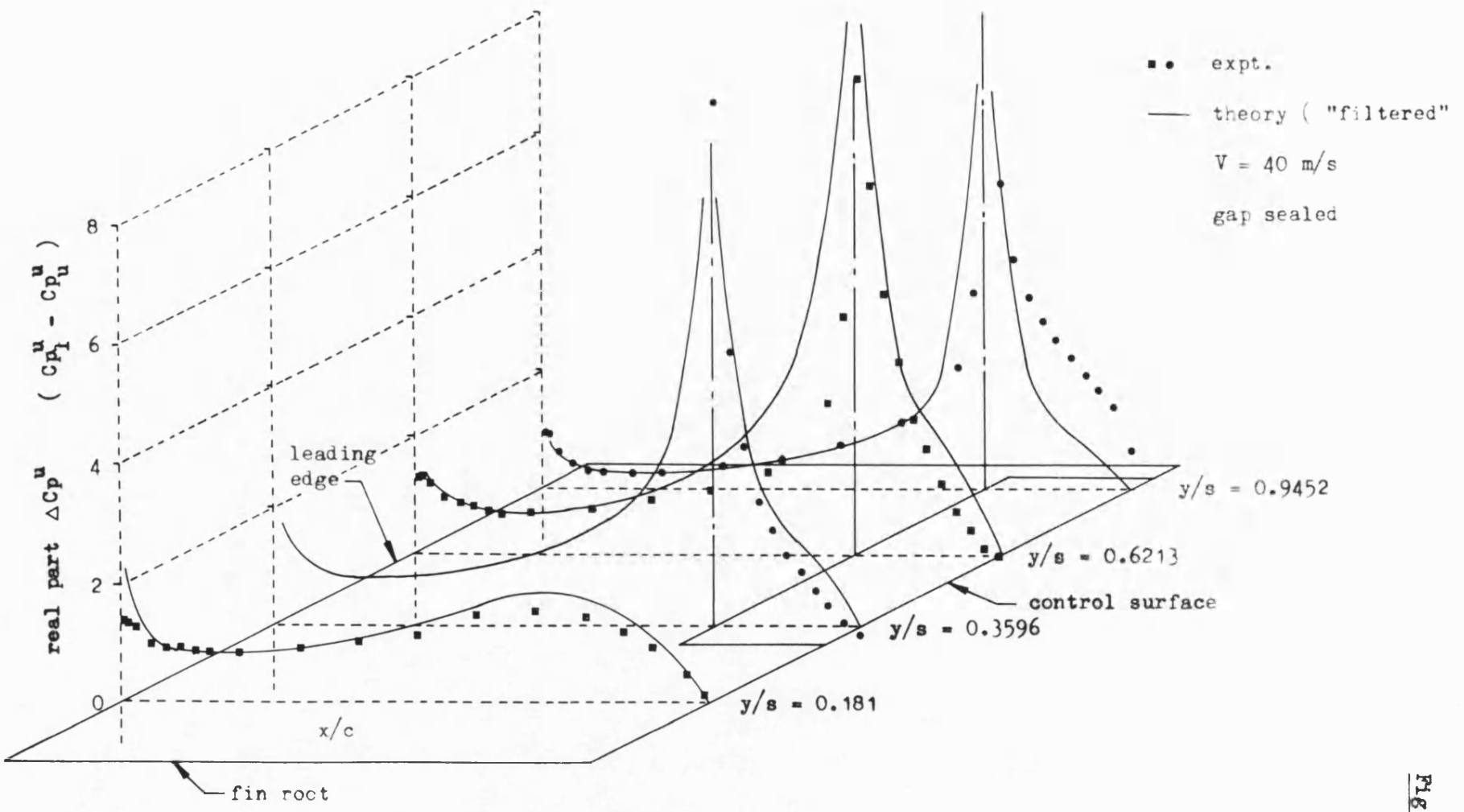

Fig. 6.58

Fig. 6.58 Comparison of theoretical and experimental unsteady pressure loadings on fin and control surface real parts - $\omega^* = 0.698$ - ($\alpha = 0^\circ$, $\delta_m = 0^\circ$, $\delta_a = 1^\circ$).

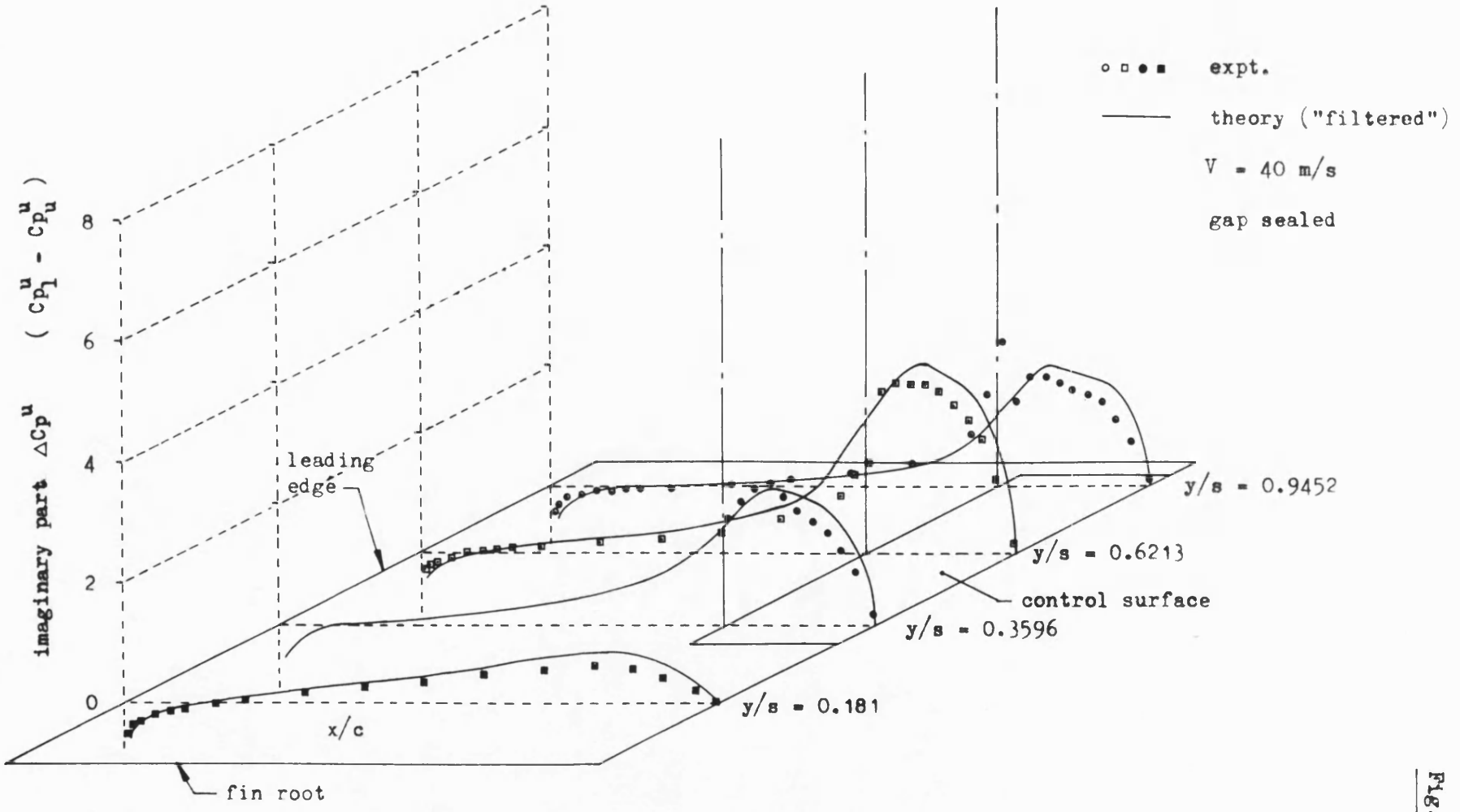

Fig. 6.59

Fig. 6.59 Comparison of theoretical and experimental unsteady pressure loadings on fin and control surface imaginary parts - $\omega^* = 0.698$ ($\alpha = 0^\circ$, $\delta_m = 0^\circ$, $\delta_a = 1^\circ$).

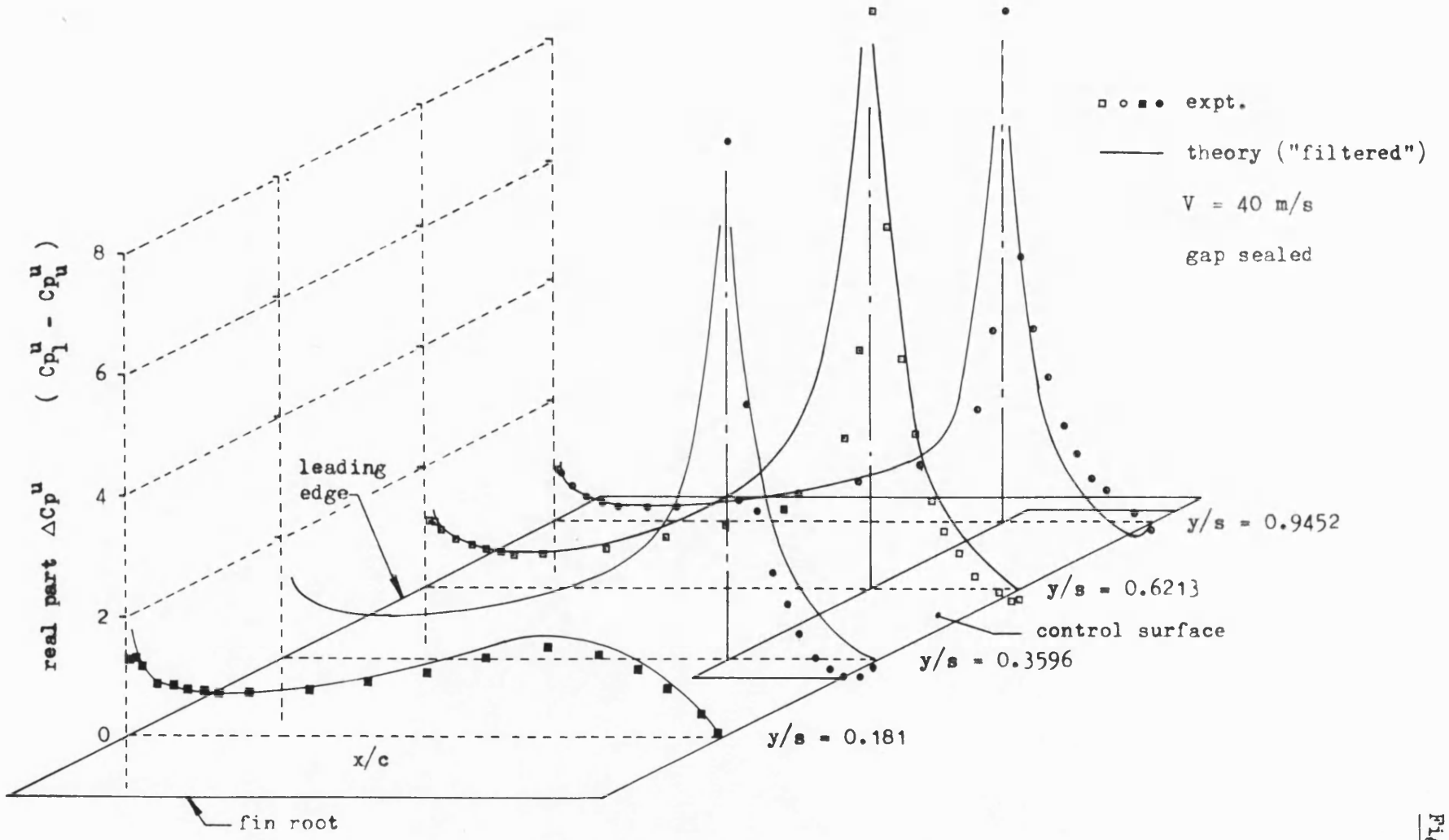

Fig. 6.60

Fig. 6.60 Comparison of theoretical and experimental unsteady pressure loadings on fin and control surface real parts - $\omega^* = 1.396$ ($\alpha = 0°$, $\delta_m = 0°$, $\delta_a = 1°$)

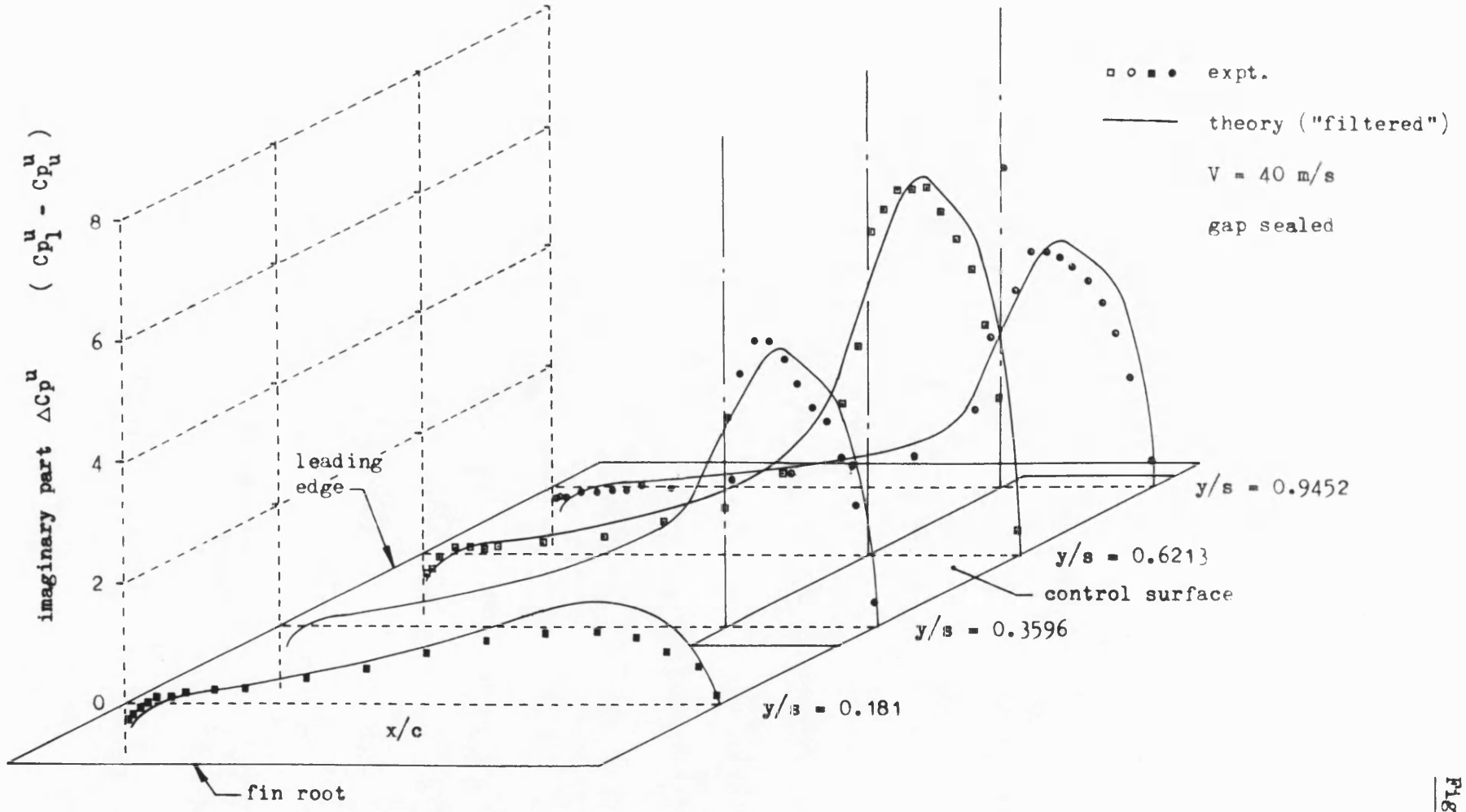

Fig. 6.61

Fig. 6.61 Comparison of theoretical and experimental unsteady pressure loadings on fin and control surface imaginary parts - $\omega^* = 1.396$ ($\alpha = 0°, \delta_m = 0°, \delta_a = 1°$).

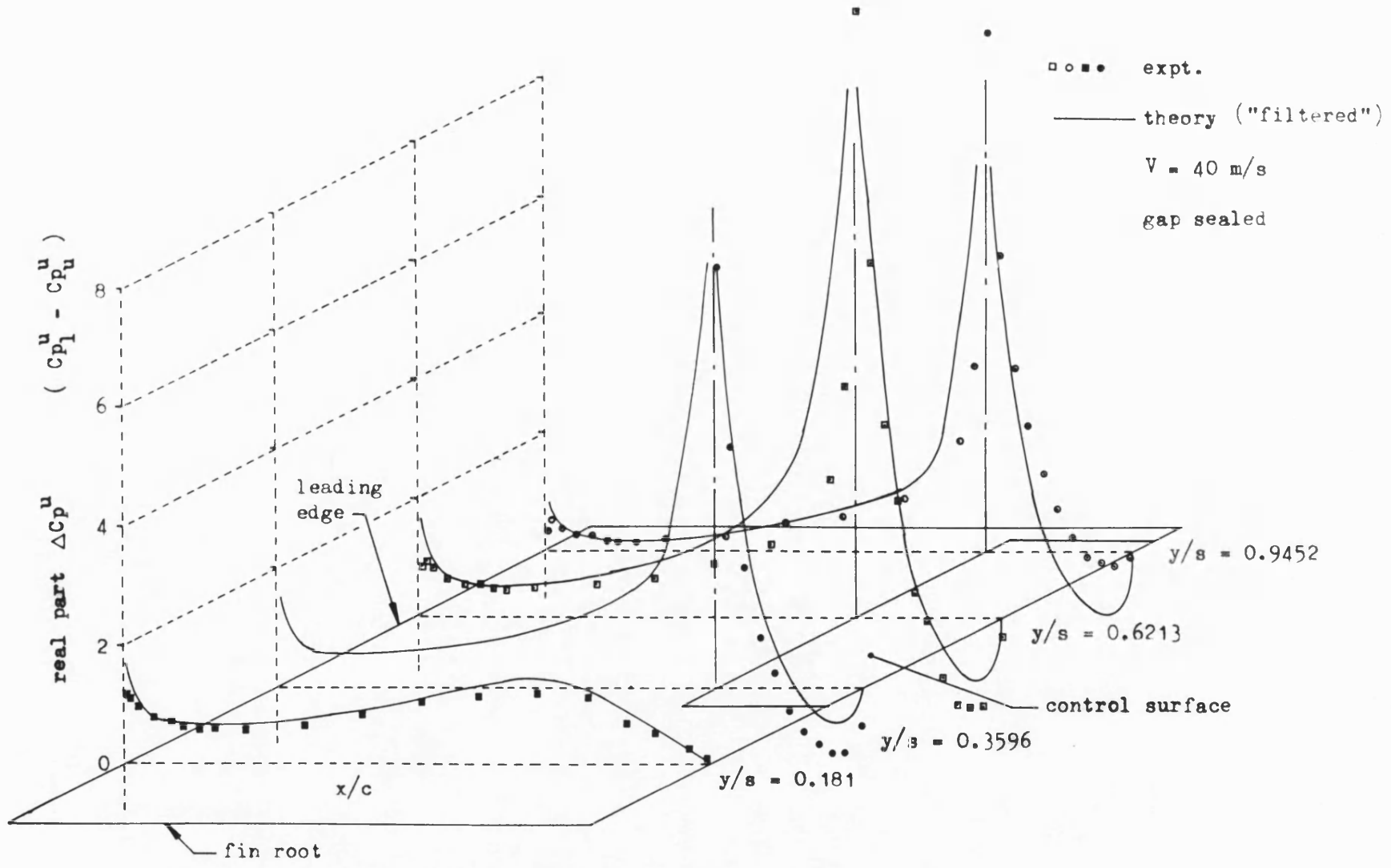

Fig. 6.62

Fig. **6.62** Comparison of theoretical and experimental unsteady pressure loadings on fin and control surface real parts - $\omega^* = 2.091$ ($\alpha = 0^\circ, \delta_m = 0^\circ, \delta_a = 1^\circ$)

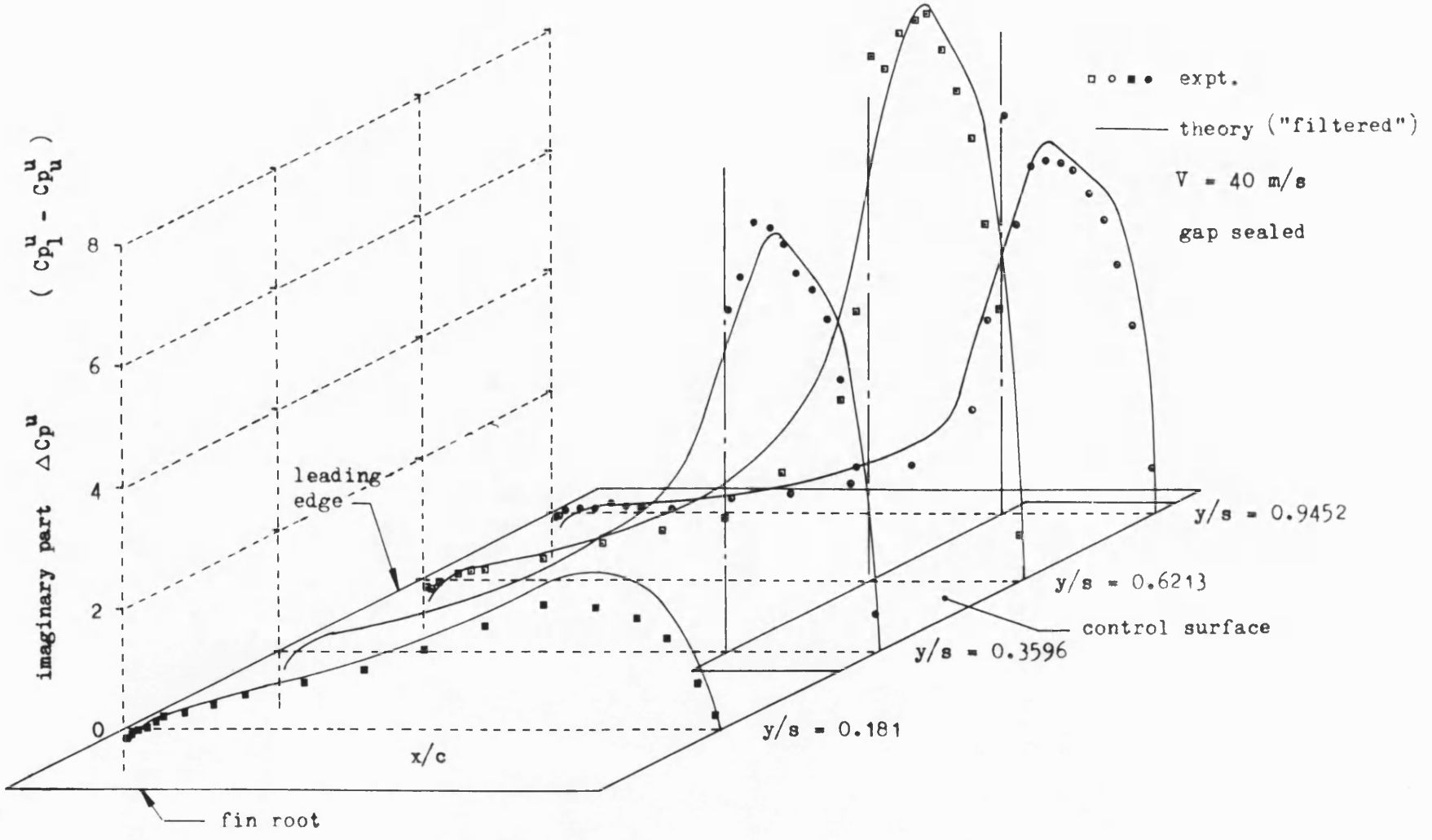

Fig. 6.63

Fig. 6.63 Comparison of theoretical and experimental unsteady pressure loadings on fin and control surface imaginary parts - $\omega^* = 2.091$ ($\alpha = 0°$, $\delta_m = 0°$, $\delta_a = 1°$)

Fig. 6.64

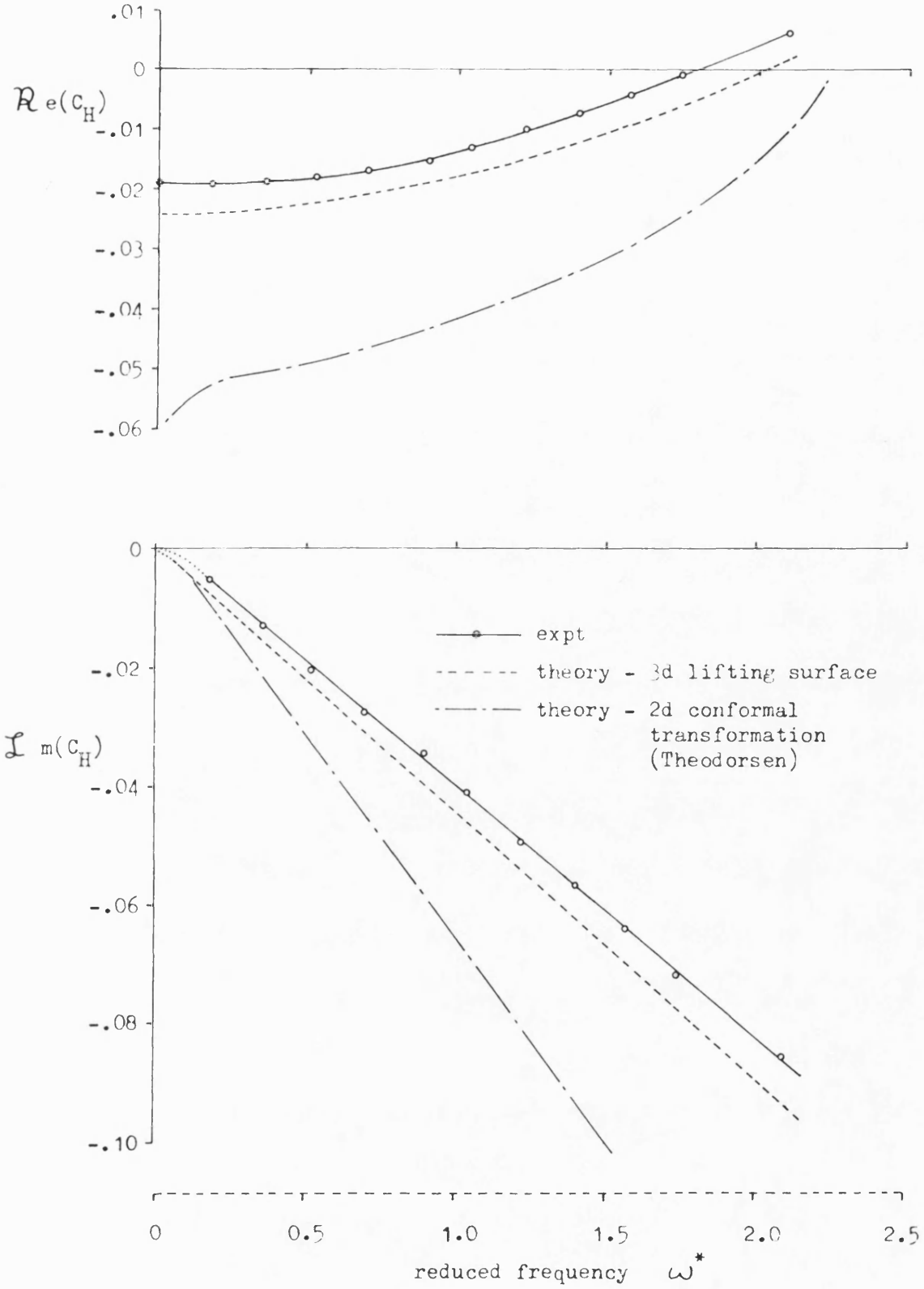

Fig. 6.64 Comparison of theoretically and experimentally determined overall unsteady hinge moments on oscillating control surface (Re = 1.15×10^6, V = 40 m/s, gap sealed, $\alpha = 0^\circ$, $\delta_m = 0^\circ$, $\delta_a = 1^\circ$).

Fig. 6.65

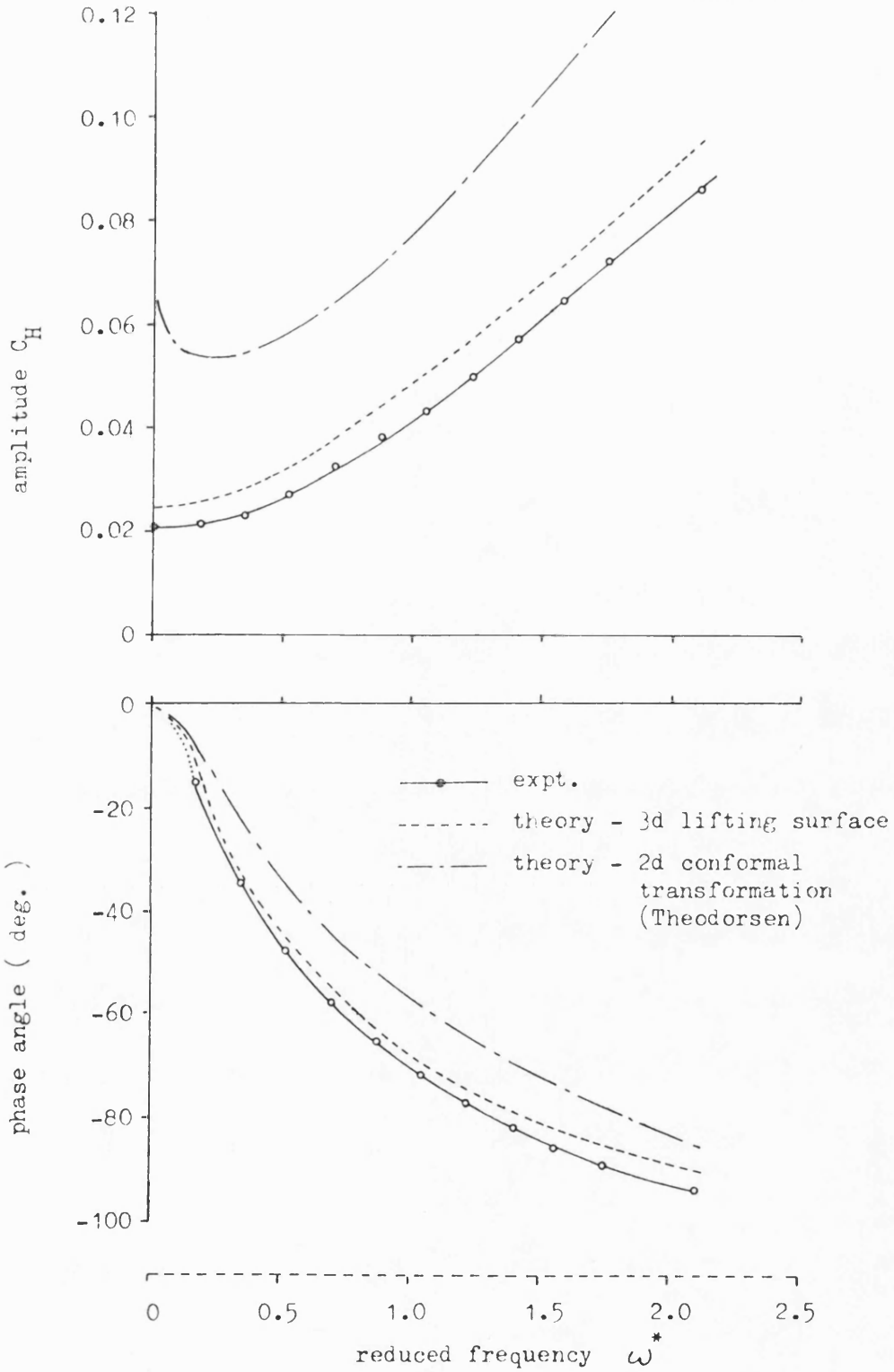

Fig. 6.65 Comparison of theoretically and experimentally determined overall unsteady hinge moments on oscillating control surface - amplitude and phase - (Re = 1.15×10^6, gap sealed, $\alpha = 0^\circ$, $\delta_m = 0^\circ$, $\delta_a = 1^\circ$).

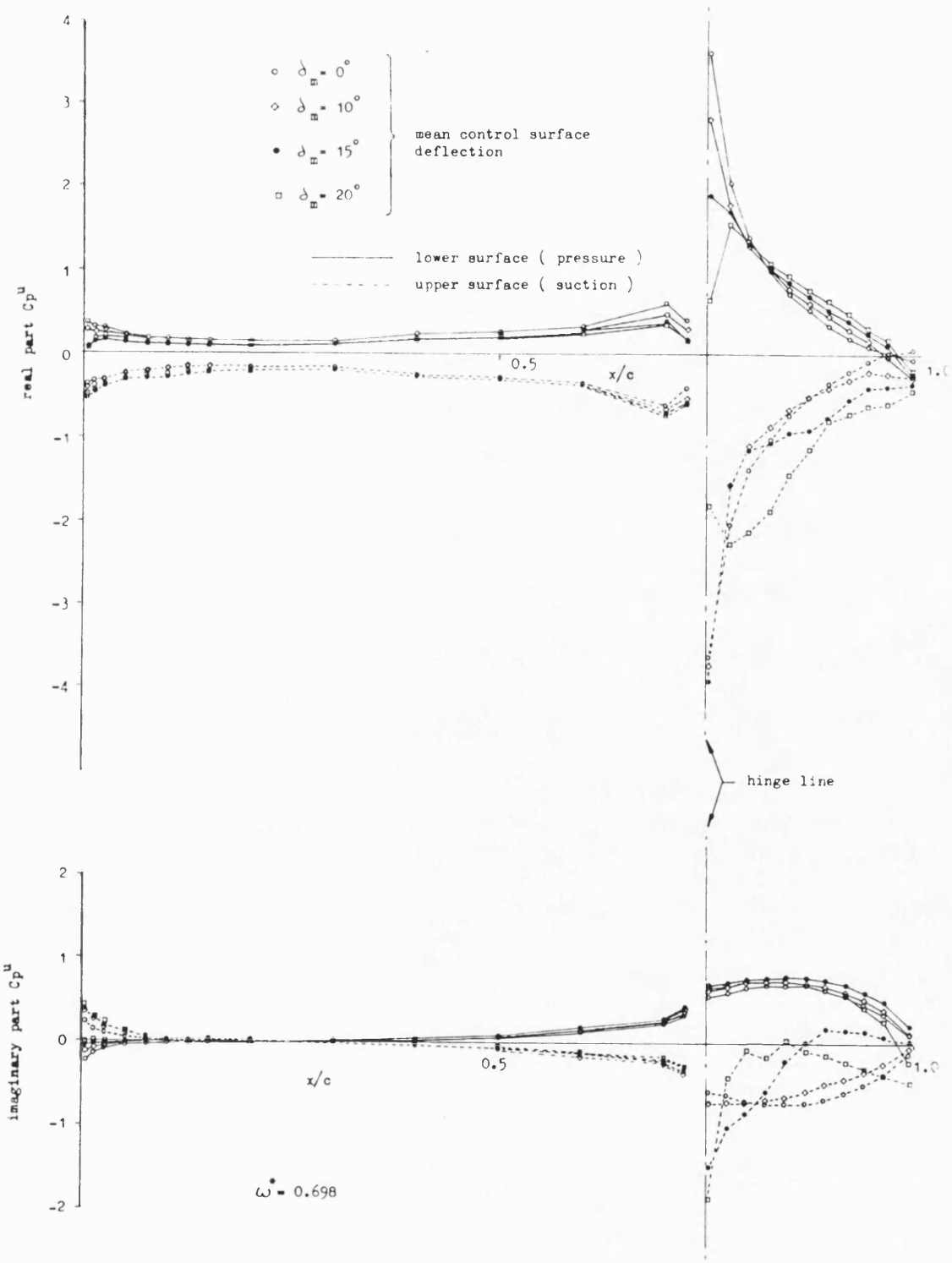

Fig. 6.66 Effect of varying mean control surface deflection angle on unsteady pressure distributions on fin and control at mid semi-span (y/s = 0.6213, V = 40m/s, gap open, α = 0°, δ_a = 1°).

Fig. 6.67

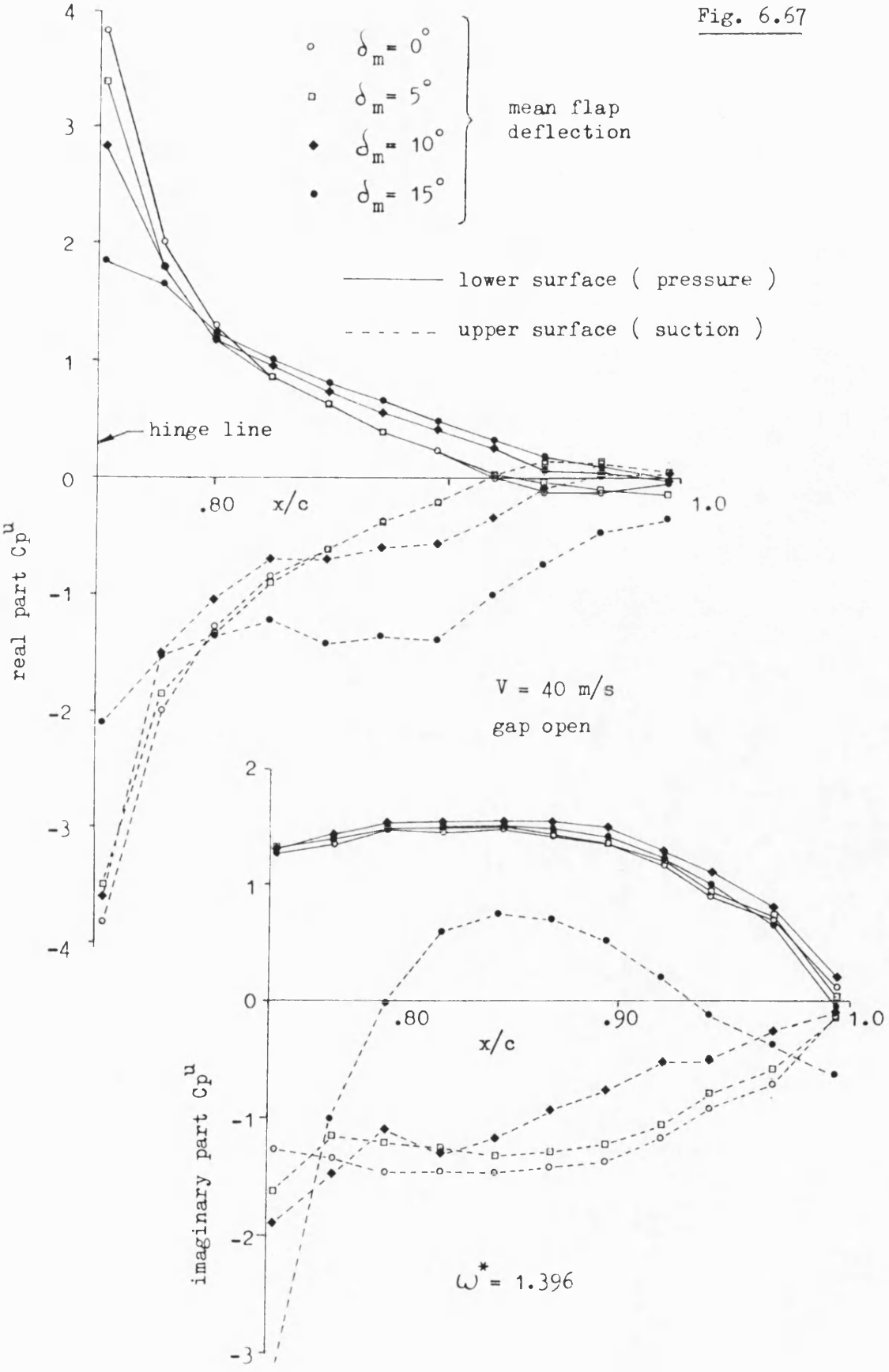

Fig. 6.67 Effect of varying mean control surface deflection angle on unsteady pressure distributions on control surface at mid semi-span ($y/s = 0.6213, \alpha = 0°, \delta_a = 1°$)

Fig. 6.68

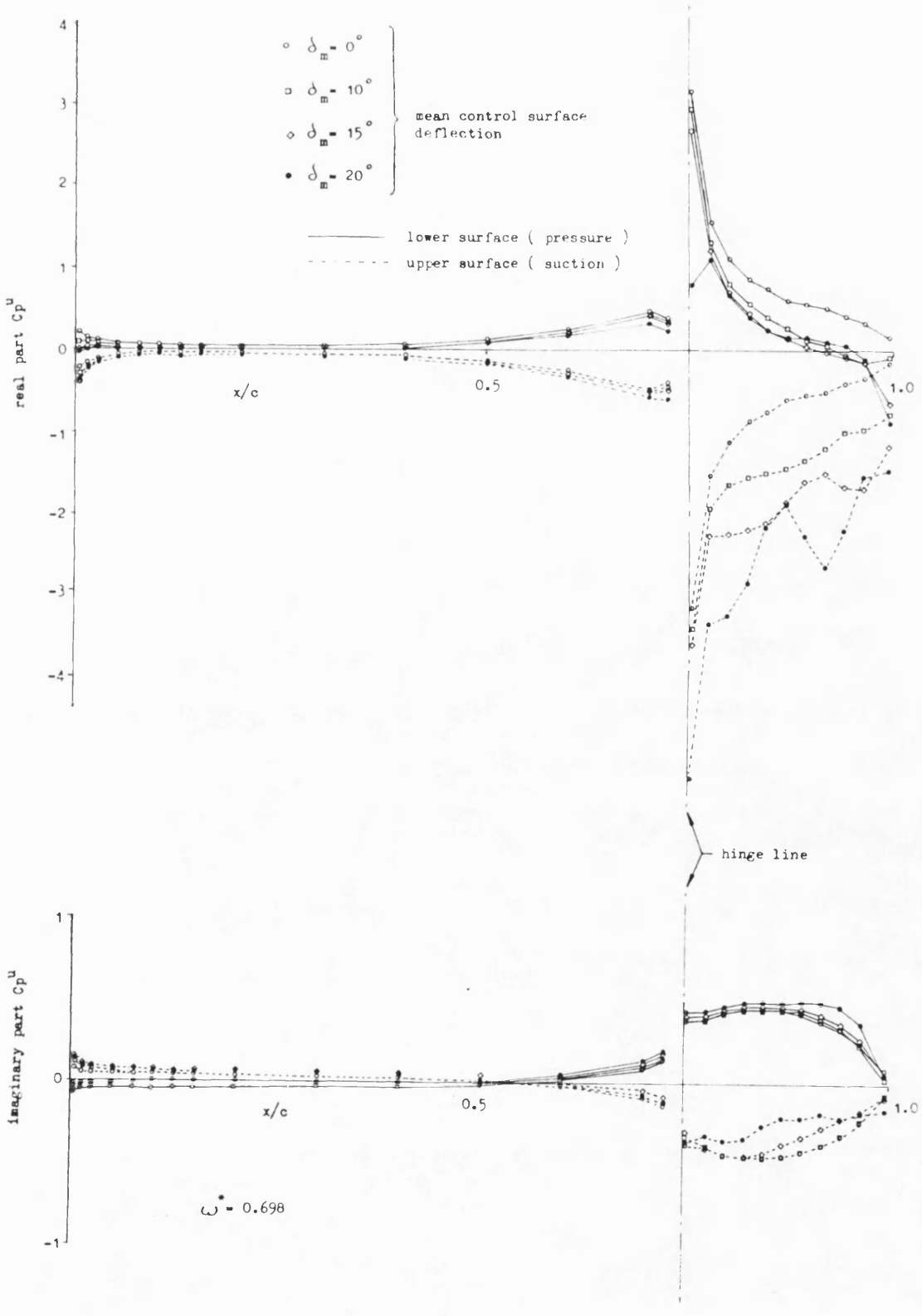

Fig. 6.68 Effect of varying mean control surface deflection angle on unsteady pressure distributions on fin and control surface near tip of fin (y/s = 0.9452, V = 40m/s, gap open, $\alpha = 0°$, $\delta_g = 1°$).

Fig. 6.69

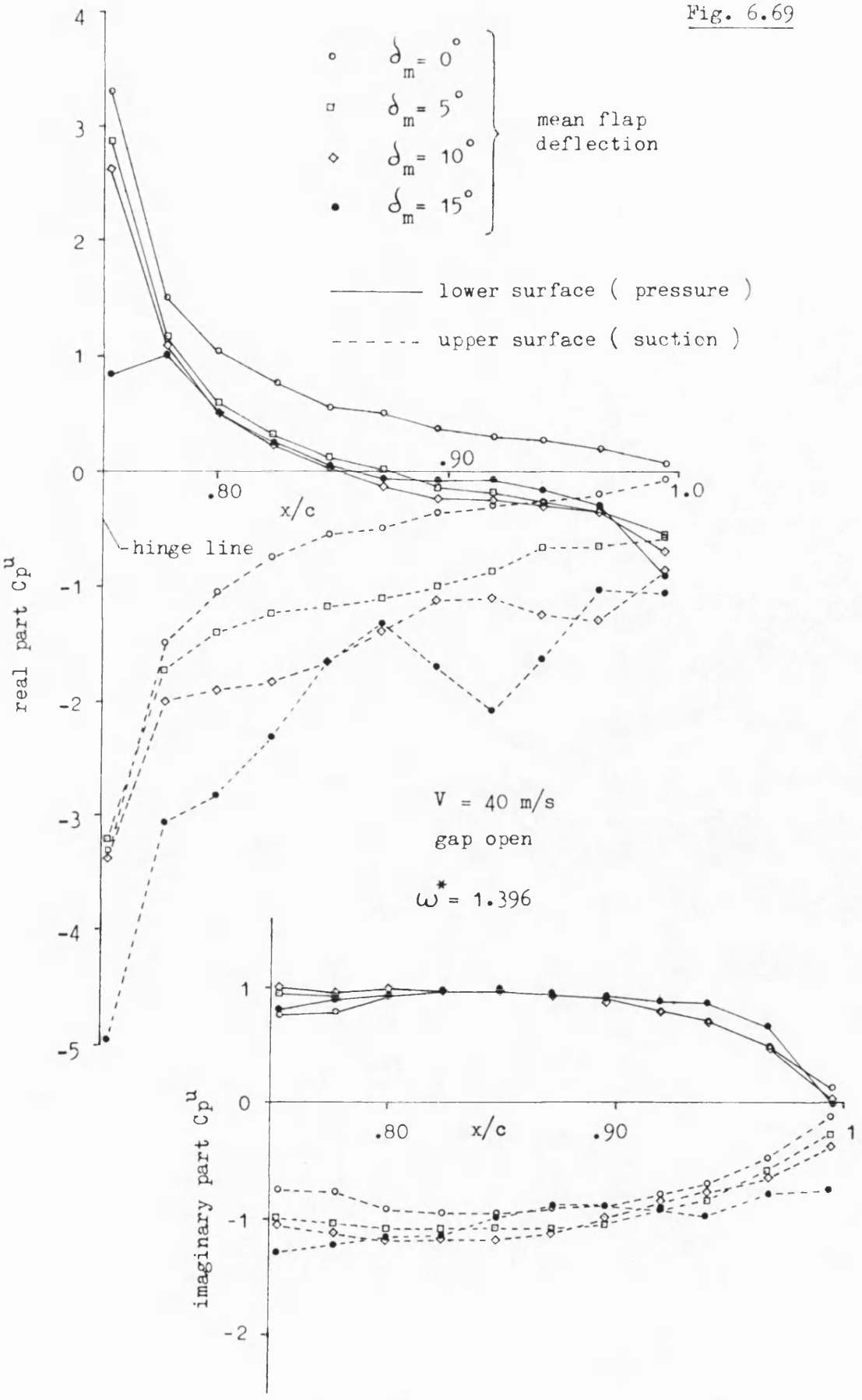

Fig. 6.69 Effect of varying mean control surface deflection angle on unsteady pressure distributions on control surface near fin tip ($y/s = 0.9452$, $\alpha = 0°$, $\delta_a = 1°$).

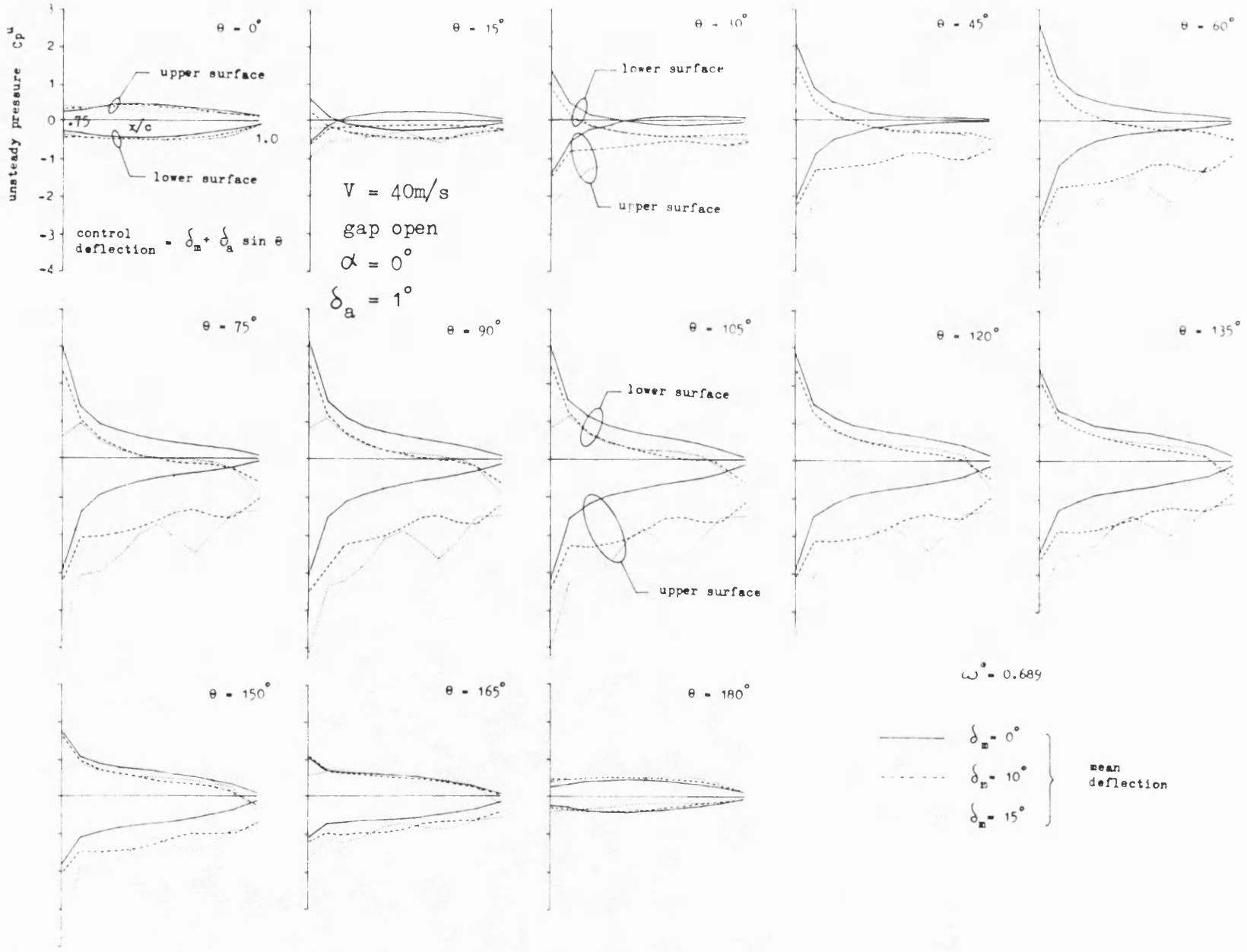

Fig. 6.70

Fig. 6.70 Development of unsteady pressures on control surface during half cycle of oscillation for non-zero mean control surface deflection (y/s = 0.9452).

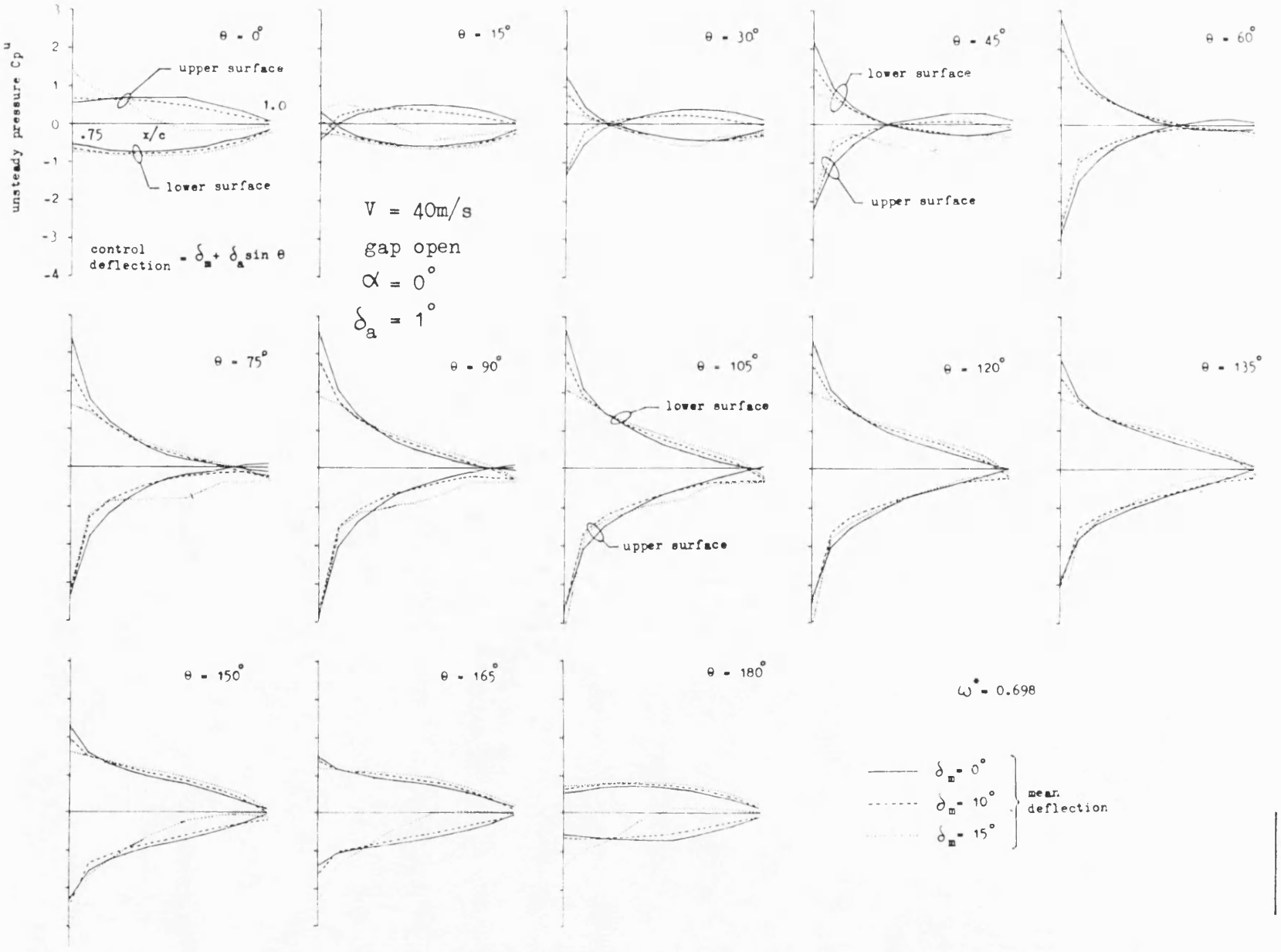

Fig. 6.71

Fig. 6.71 Development of unsteady pressures on control surface during half cycle of oscillation for non-zero mean control surface deflection (y/s = 0.6213).

Fig. 6.72

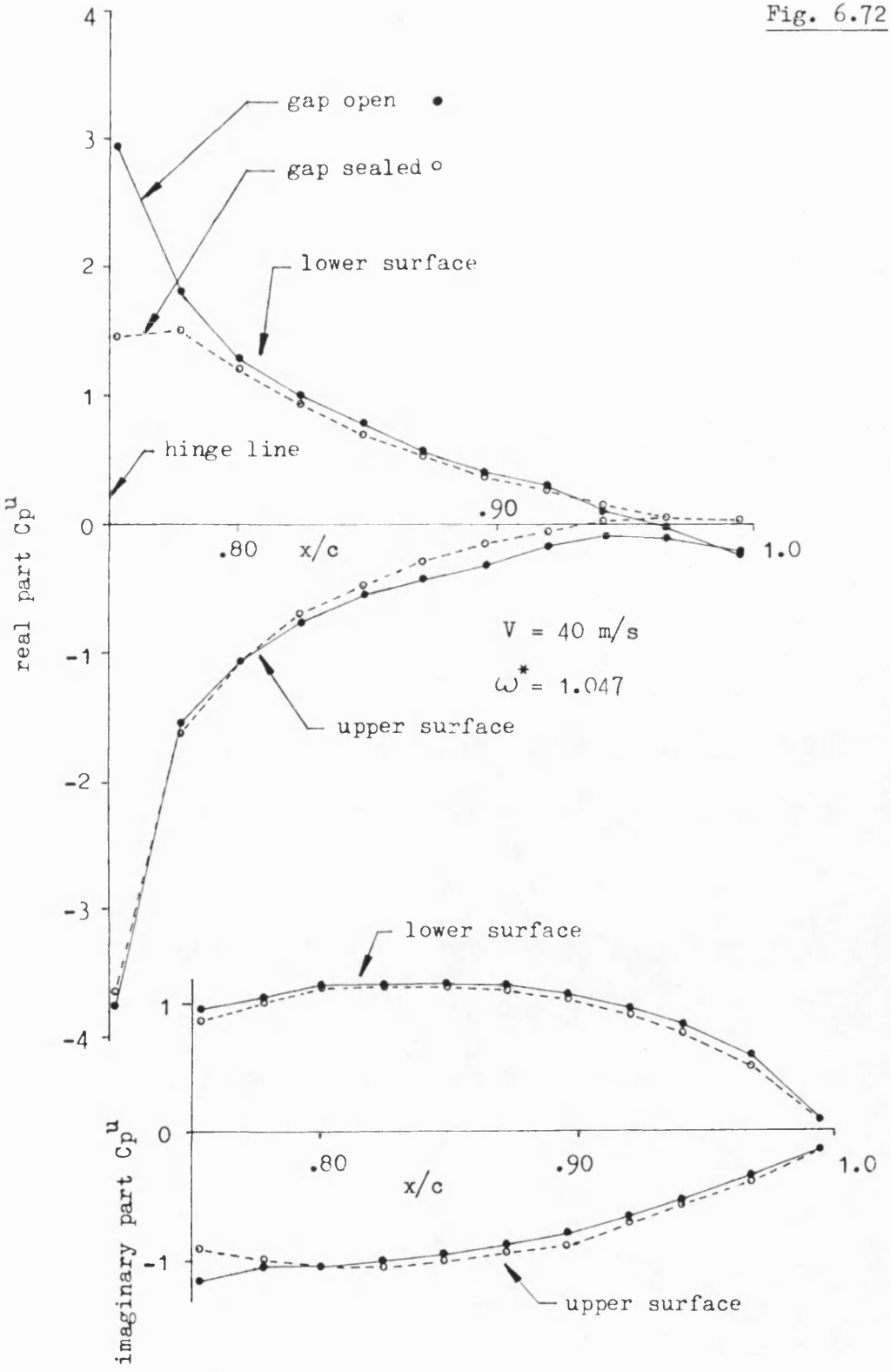

Fig. 6.72 Unsteady pressure distributions on control surface showing effect of gap with a mean control deflection of 10° ($y/s = 0.6213$, $\alpha = 0°$, $\delta_m = 10°$, $\delta_a = 1°$).

Fig. 6.73

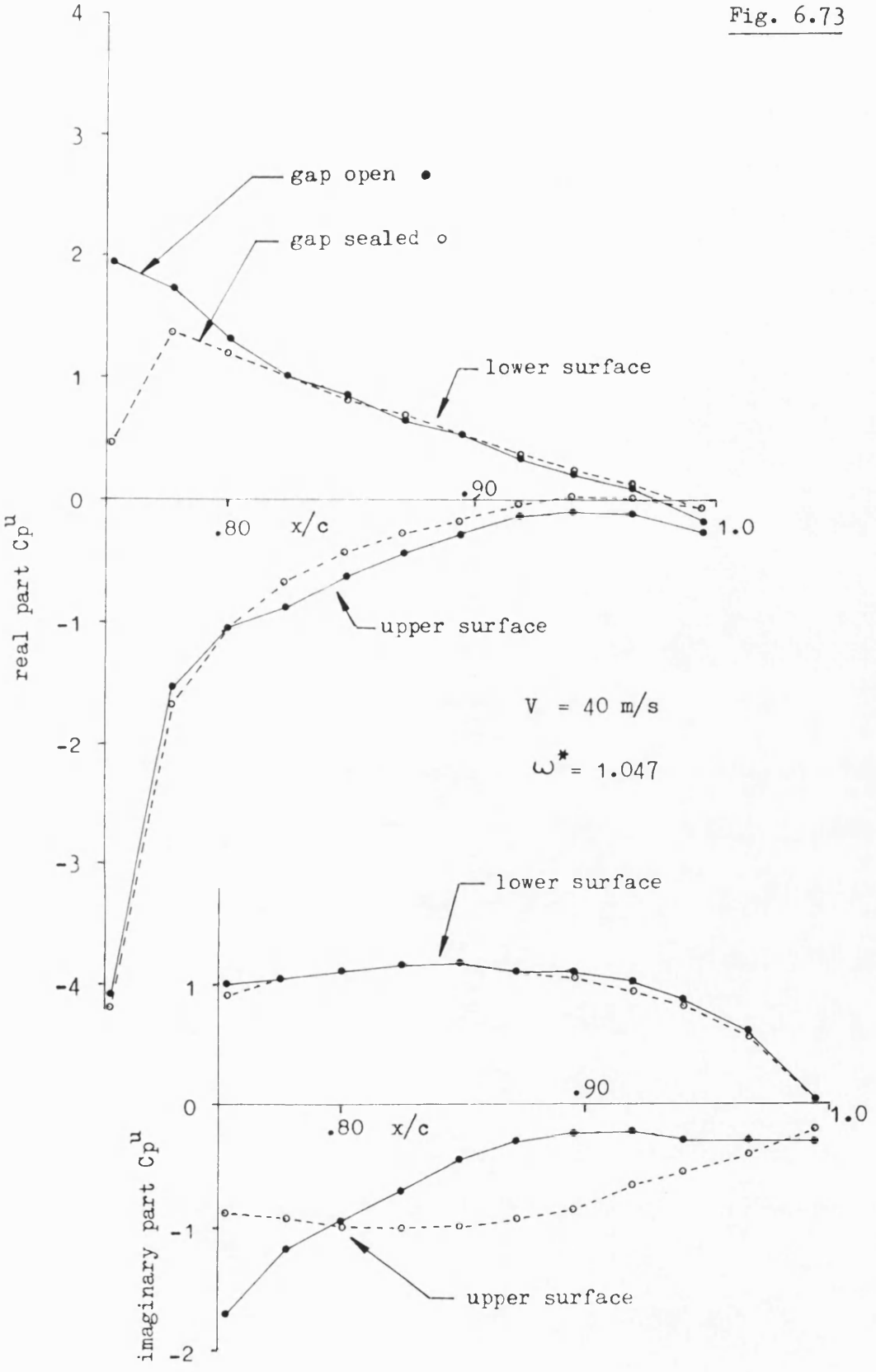

Fig. 6.73 Unsteady pressure distributions on control surface showing effect of gap with a mean control deflection of 15°
($y/s = 0.6213$, $\alpha = 0°$, $\delta_m = 15°$, $\delta_a = 1°$).

Fig. 6.74

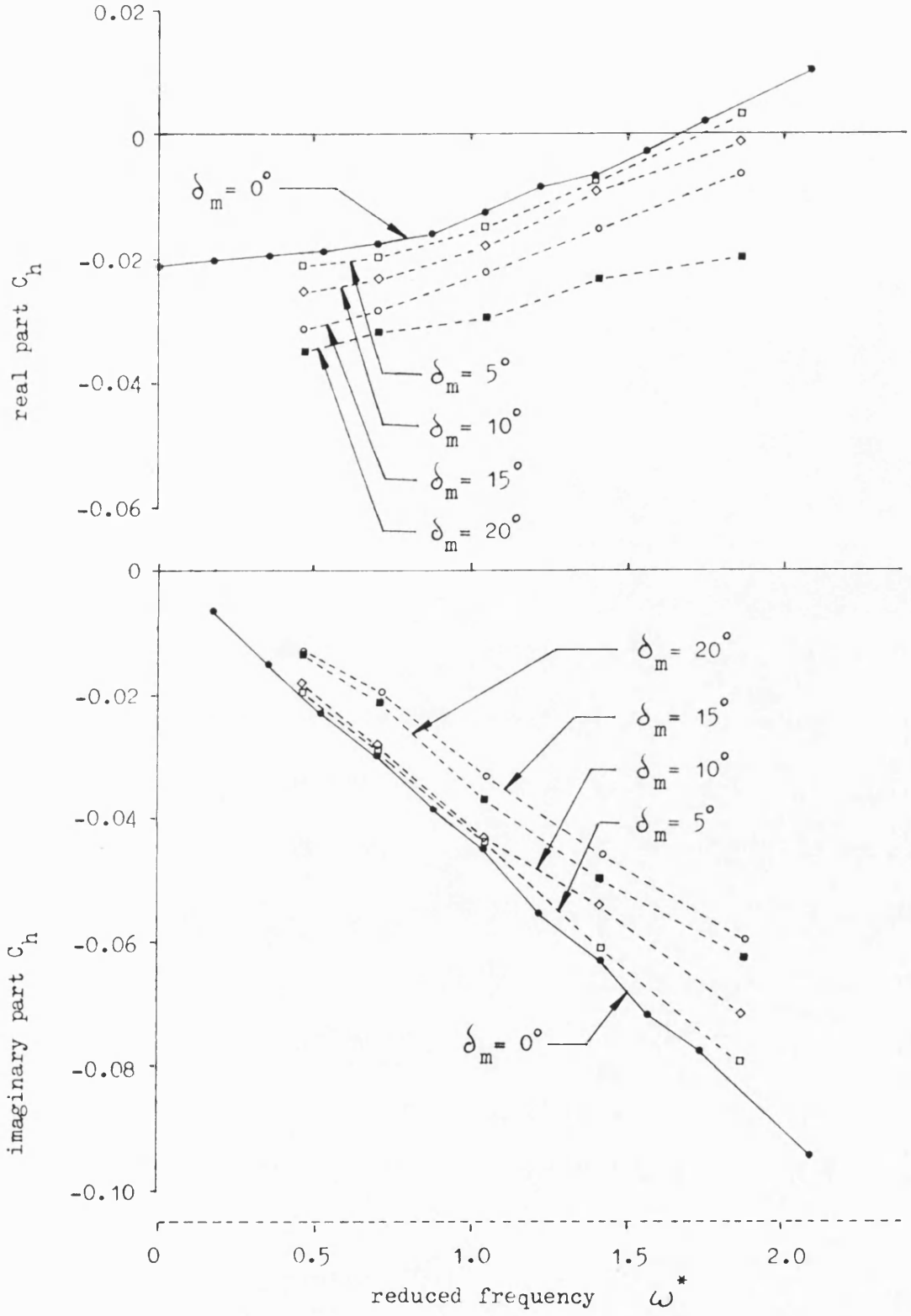

Fig. 6.74 Effect of mean control surface deflection on unsteady section hinge moment coefficients measured at mid semi-span (y/s = 0.6213, V = 40 m/s, gap open, α = 0°, δ_a = 1°).

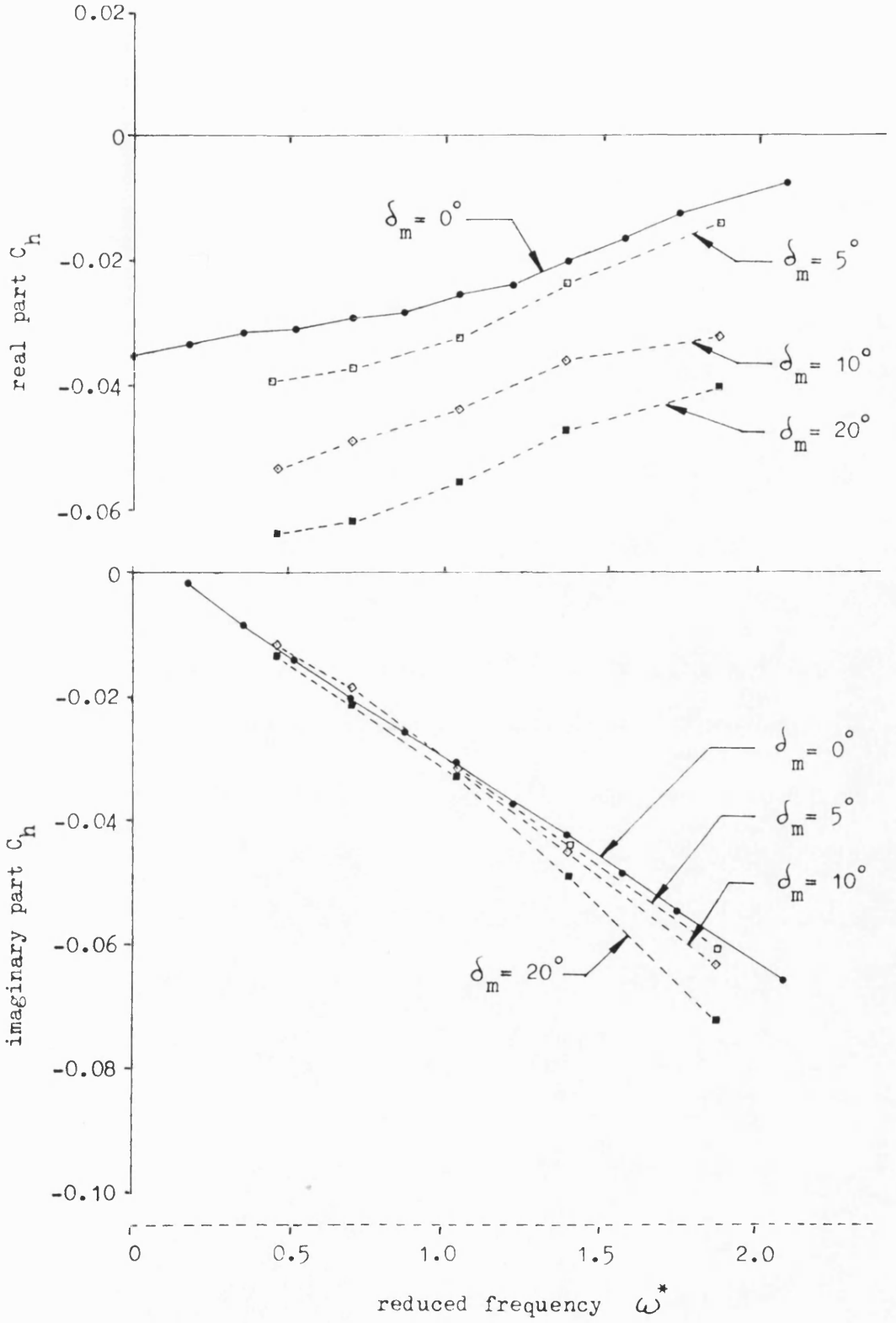

Fig. 6.75 Effect of mean control surface deflection on unsteady section hinge moments measured near fin tip (y/s = 0.9452, V = 40 m/s, gap open, $\alpha = 0°$, $\delta_a = 1°$).

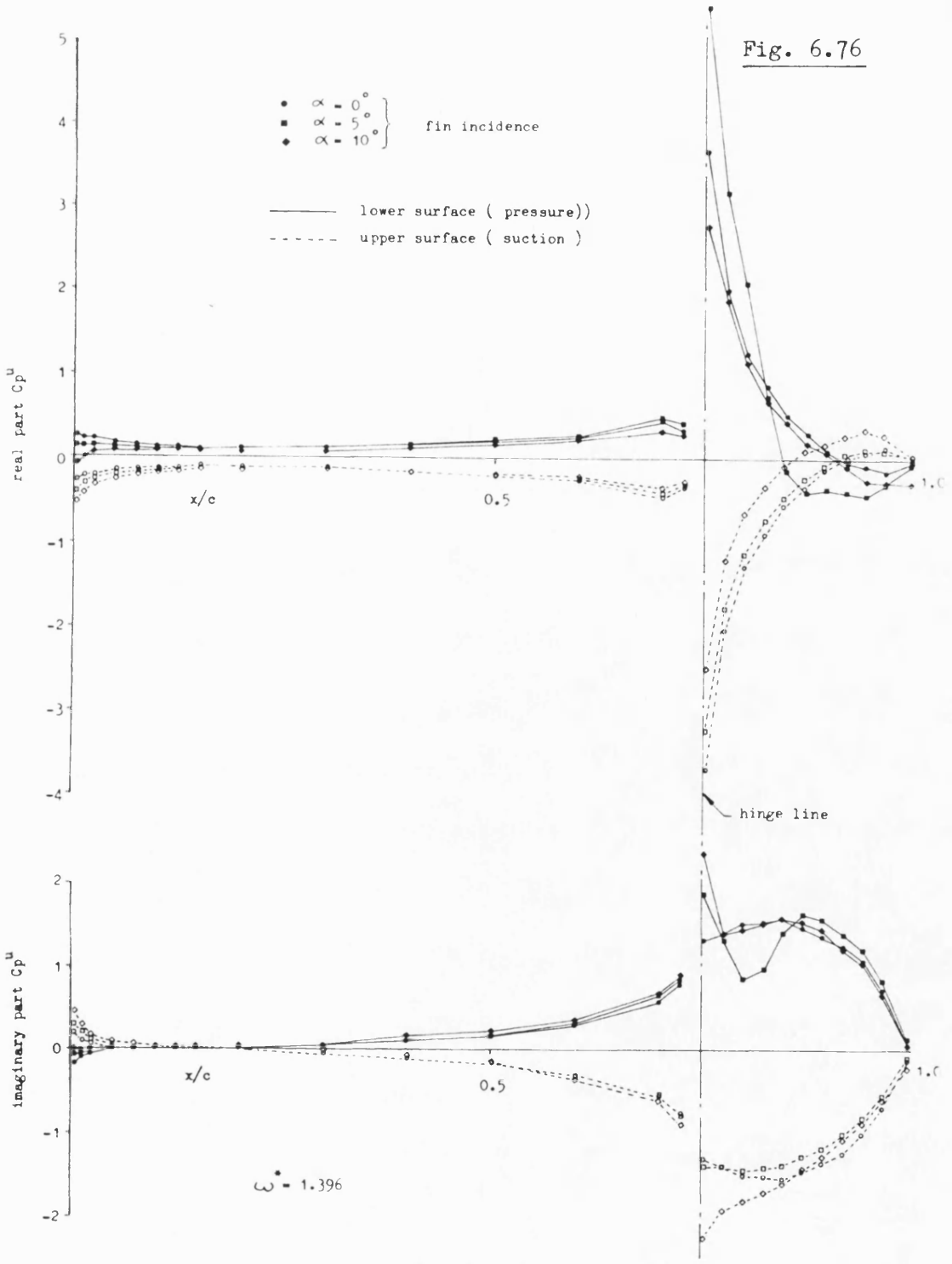

Fig. 6.76 Effect of incidence on unsteady pressures on fin and control surface at mid semi-span (y/s = 0.6213, V = 40m/s, $\delta_m = 0°$, $\delta_a = 1°$).

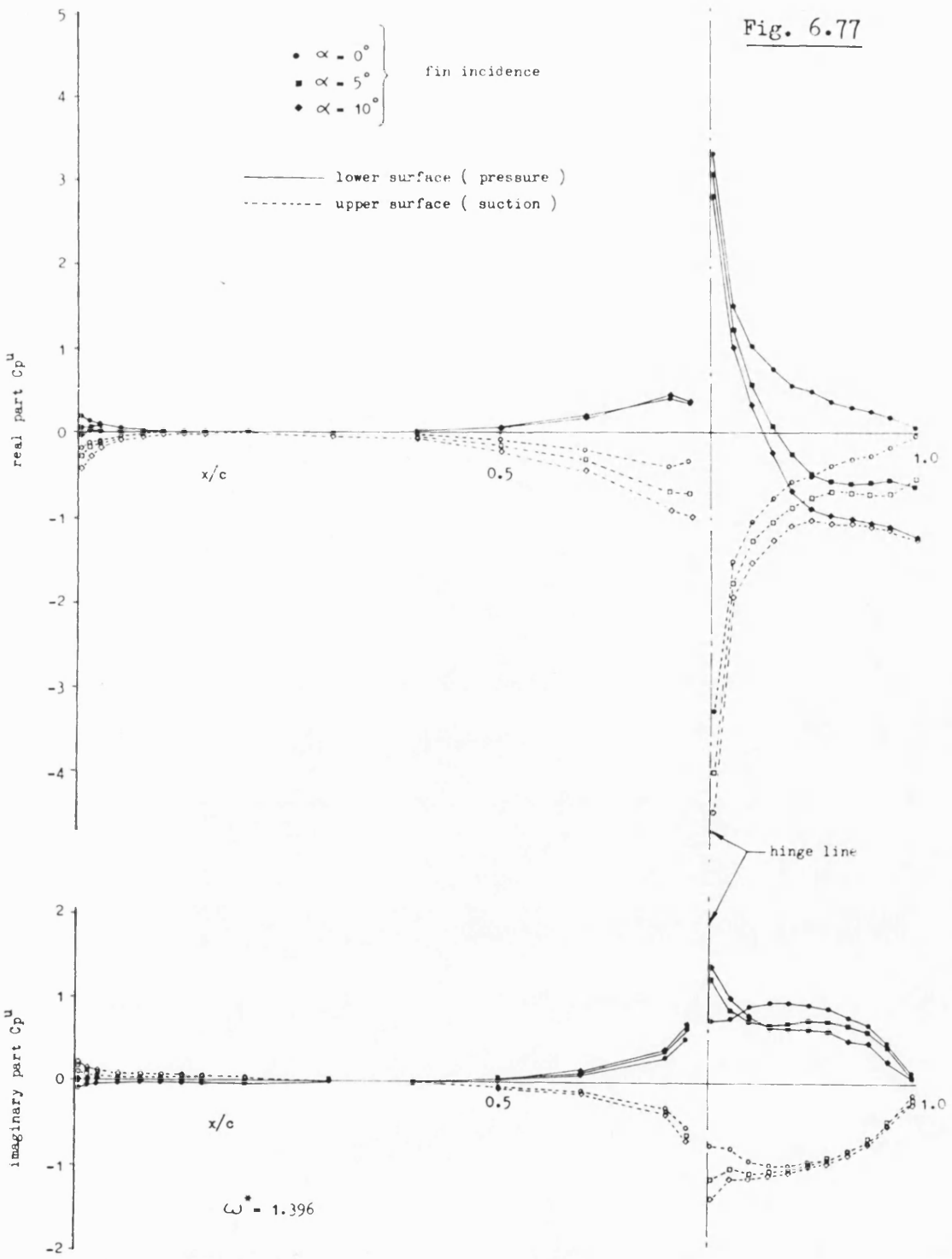

Fig. 6.77 Effect of incidence on unsteady pressures on fin and control surface near the tip of the fin (y/s = 0.9452, V = 40m/s, gap open, $\delta_m = 0°$, $\delta_a = 1°$).

Fig. 6.78

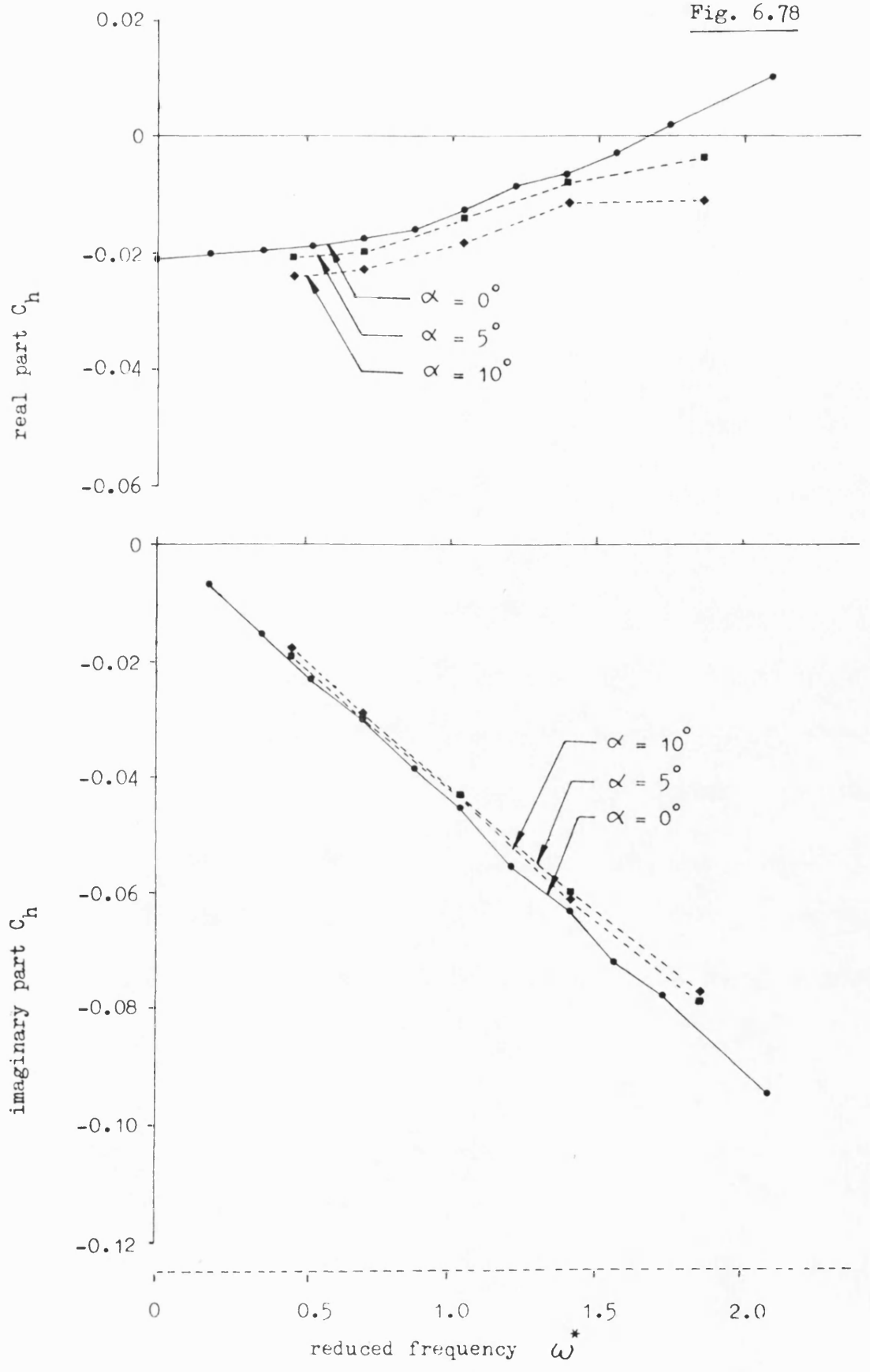

Fig. 6.78 Effect of incidence on unsteady section hinge moments measured at mid semi-span (y/s = 0.6213, V = 40 m/s, gap open, $\delta_m = 0°$, $\delta_a = 1°$).

Fig. 6.79

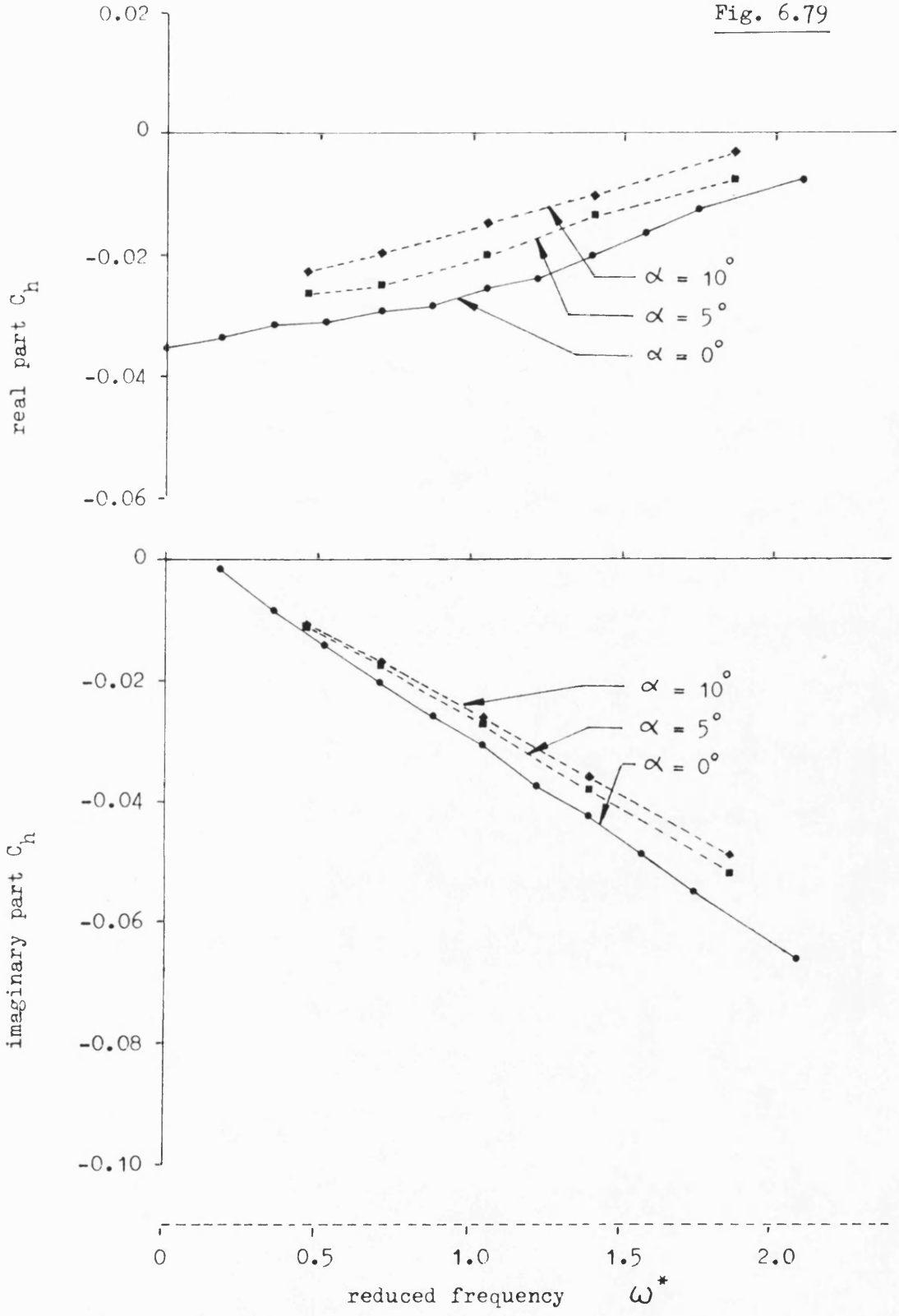

Fig. 6.79 Effect of incidence on unsteady section hinge moments measured near fin tip (y/s = 0.9452, V = 40 m/s, gap open, $\delta_m = 0°$, $\delta_a = 1°$).

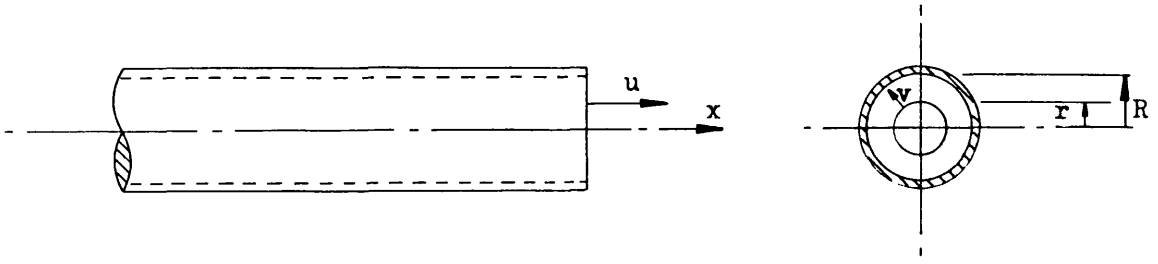

a). co-ordinate system

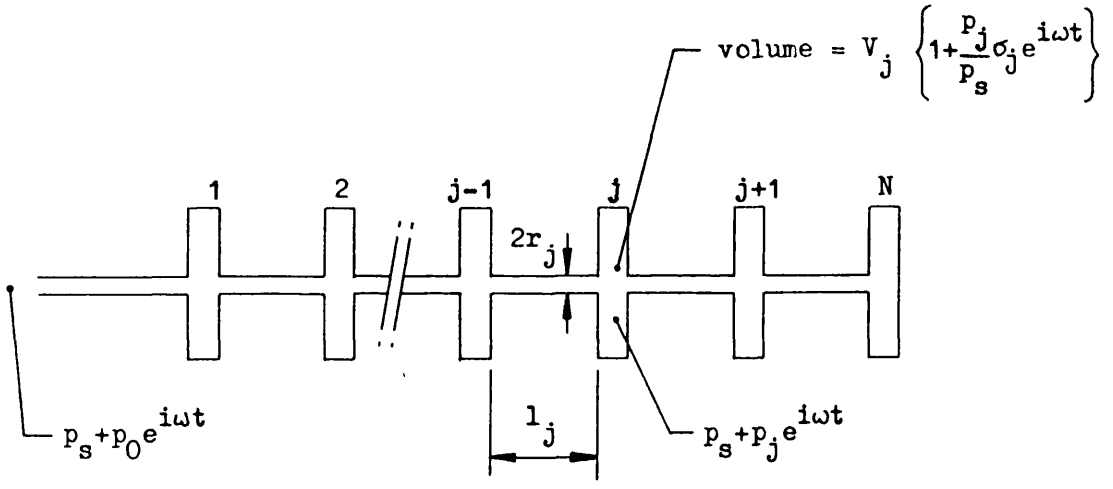

b). series connection of tubes and volumes

Fig. A1 Notation used for evaluating the frequency response of pressure tubing systems.